

ÉCOLE DOCTORALE DE SCIENCES CHIMIQUES

**Institute de Chimie pour les Procédés, l'Énergie, l'Environnement et la Santé,
UMR 7515**

THÈSE

présentée par :

Irene LARA IBEAS

soutenue le 12 décembre 2019

pour obtenir le grade de : **Docteur de l'université de Strasbourg**

Discipline / Spécialité : Chimie / Chimie Physique

**Composés Organiques Volatils dans l'air : étude
de l'adsorption et la désorption sur différents
matériaux, développement d'un préconcentrateur
microfluidique et mesures sur le terrain**

THÈSE dirigée par :

Monsieur LE CALVE Stéphane Directeur de Recherche, CNRS, Université de Strasbourg

Monsieur COLIN Stéphane Professeur des Universités, INSA Toulouse

RAPPORTEURS :

Monsieur PETITPREZ Denis Professeur des Universités, Université de Lille 1

Monsieur MORINI Gian Luca Professeur des Universités, Università di Bologna

AUTRES MEMBRES DU JURY :

Madame RIFFAULT Véronique Professeur des Universités, École nationale supérieure des Mines-
Télécom de Lille-Douai

"Live as if you were to die tomorrow. Learn as if you were to live forever"

Mahatma Gandhi

Table of contents

<i>Remerciements (en français)</i>	VII
<i>List of figures</i>	IX
<i>List of tables</i>	XIV
<i>List of abbreviations</i>	XV
<i>Symbols</i>	XVI
<i>General introduction</i>	1
Chapter 1. Introduction and literature review	5
1.1 Air quality	5
1.1.1 Ambient air.....	6
1.1.2 Indoor air	7
1.1.3 Health effects.....	9
1.1.4 Legislation	11
1.2 Methods for airborne VOC detection	12
1.2.1 Chromatographic methods (GC-TCD/PID/FID/MS).....	12
1.2.2 Non-chromatographic methods	15
1.2.3 Portable devices for air quality monitoring.....	17
1.3 Gaseous VOC Preconcentrators: state-of-the-art	19
1.3.1 Principle of thermal desorption.....	19
1.3.2 Recent developments and trends in miniaturized gas preconcentrators	22
1.3.2.1 Materials used.....	24
1.3.2.2 Microstructures designs	28
1.3.2.3 Heating system	31
1.3.2.4 Adsorbent Materials.....	33
1.3.2.5 Applications	37

1.4 Sorption/Desorption of VOCs	38
1.4.1 Theoretical background.....	38
1.4.2 VOC Adsorption on different materials.....	45
1.4.2.1 Carbon-based adsorbents.....	45
1.4.2.2 Porous polymers.....	47
1.4.2.3 Mesoporous Silica	48
1.4.2.4 Metal Organic Frameworks (MOF).....	49
1.4.2.5 Zeolites.....	51
1.4.3 General adsorption behaviour of aldehydes and aromatics compounds.....	52
1.4.3.1 BTEX adsorption behaviour.....	53
1.4.3.2 Aldehydes adsorption	55
1.4.4 VOC removal methods for air pollution control.....	58
1.5 Objectives of this work	60
Chapter 2. Materials and Methods	83
2.1 Study of VOC adsorption/desorption behaviour	83
2.1.1 Selected adsorbents	83
2.1.1.1 Carbopack™ B	84
2.1.1.2 Basolite™ C300	84
2.1.1.3 SBA-16.....	85
2.1.1.4 ZSM-5 zeolites.....	86
2.1.2 Characterization Techniques	88
2.1.2.1 Scanning Electron Microscopy (SEM)	88
2.1.2.2 N ₂ physisorption: specific surface area (BET method).....	89

2.1.2.3	Thermogravimetric Analysis – Differential Scanning Calorimetry (TGA-DSC).....	90
2.1.2.4	Temperature-Programmed Desorption (TPD).....	91
2.1.3	Dynamic VOC adsorption experiments	94
2.1.3.1	Experimental setup for dynamic adsorption experiments of aromatics compounds 96	
2.1.3.2	Experimental setup for dynamic adsorption experiments of formaldehyde.....	97
2.1.3.3	Experimental setup for dynamic adsorption experiments of hexanal.....	99
2.2	Development of microfluidic devices for BTEX preconcentration	101
2.2.1	Analyser operating principle	101
2.2.2	Development of a BTEX preconcentrator.....	102
2.2.2.1	Macro Aluminium Preconcentrator (MAP).....	102
2.2.2.2	MEMS Preconcentrator (MEMS-P)	103
2.2.2.3	Mixed Aluminium/Polymer Preconcentrator	117
2.2.2.4	Micro Aluminium Preconcentrator (μ AP1).....	118
2.2.2.5	Micro Aluminium Preconcentrator (μ AP2).....	119
2.3	Conclusions.....	121
 <i>Chapter 3. Field Measurements: BTEX near real-time monitoring in two primary schools in La Rochelle, France</i>		
3.1	Impact'Air Project.....	127
3.2	Article 1 published in Air Quality, Atmosphere & Health: "BTEX near real-time monitoring in two primary schools in La Rochelle, France.....	128
3.3	Conclusions.....	146
 <i>Chapter 4. Development of a preconcentrator for BTEX quantification.....</i>		

4.1	Macro Aluminium Preconcentrator (MAP)	149
4.1.1	Leakage test	149
4.1.2	Temperature tests	151
4.1.3	Main results obtained.....	153
4.1.4	Article 2 published in Micromachines “Sub-ppb Level Detection of BTEX Gaseous Mixtures with a Compact Prototype GC Equipped with a Preconcentration Unit “	159
4.2	MEMS Preconcentrator (MMP)	173
4.2.1	Flow Simulations	173
4.2.2	Temperature tests	176
4.2.3	Preconcentration tests	180
4.3	Mixed Aluminium/Polymer Preconcentrator (MAAP)	182
4.3.1	Temperature tests	183
4.3.2	Preconcentration tests	184
4.4	Micro Aluminium Preconcentrator (μAP1)	186
4.4.1	Temperature tests	186
4.4.2	Preconcentration tests	187
4.5	Micro Aluminium Preconcentrator (μAP2)	188
4.5.1	Temperature tests	189
4.5.2	Preconcentration tests	189
4.5.2.1	SBA-16.....	190
4.5.2.2	Carbopack® B.....	193
4.6	Comparison with existing instruments	198
4.7	Conclusions	203
Chapter 5. VOC adsorption on different materials		209

5.1	BTEX adsorption on commercial adsorbents.....	209
5.1.1	Introduction.....	209
5.1.2	Article 3 published in Journal of Environmental Chemical Engineering.....	210
5.1.3	Conclusions	226
5.2	BTEX adsorption on zeolites.....	226
5.2.1	Introduction.....	226
5.2.2	Article 4 published in Journal of Environmental Chemical Engineering.....	227
5.2.3	Conclusions	240
5.3	Aldehydes adsorption on different materials	240
5.3.1	Hexanal adsorption.....	241
5.3.1.1	Dynamic adsorption experiments.....	243
5.3.1.2	Comparison with the literature	245
5.3.1.3	Conclusions	247
5.3.2	Formaldehyde adsorption.....	247
5.3.2.1	Formaldehyde adsorption on commercial adsorbents	249
5.3.2.2	Formaldehyde adsorption on zeolites.....	252
5.3.2.3	Performance evaluation of formaldehyde removal by conventional adsorbents ...	256
5.3.2.4	Conclusions	261
	<i>General conclusions and perspectives</i>	267
	<i>Résumé (en français).....</i>	273
1.	Introduction générale.....	273
a)	La qualité de l'air intérieur.....	273
b)	Effets sur la santé et législation.....	276

c) Objectifs de ce travail	277
2. Campagne de mesure des BTEX dans deux écoles primaires à La Rochelle.....	279
3. Développement d'un préconcentrateur pour l'analyse des BTEX.....	283
4. Etude de l'adsorption des VOC sur des différents matériaux.....	292
5. Conclusions générales.....	298
6. References.....	301
<i>Communications</i>	309
<i>Appendix</i>	312

Remerciements (en français)

Ce travail de thèse en co-direction a été réalisé au sein de l'équipe de Physico Chimie de l'Atmosphère de l'Institut de la Chimie pour les Procédés, l'Energie et l'Environnement et la Santé à l'Université de Strasbourg et l'Institut Clément Ader de l'Institut National des Sciences Appliquées de Toulouse. Il est maintenant venu le moment de remercier toutes les personnes qui ont fait partie d'une manière ou d'une autre de ce travail, grâce à chacun de vous ce travail a été possible !

Tout d'abord, j'aimerais remercier aux membres du jury Madame Véronique Riffault et Messieurs Gian Luca Morini et Denis Petitprez d'avoir accepté d'évaluer ce travail de thèse.

Je souhaite exprimer ma profonde gratitude à mes directeurs de thèse Messieurs Stéphane Colin et Stéphane Le Calvé pour l'opportunité que vous m'avez donnée de réaliser ce travail de thèse. Stéphane Colin (Steph) merci de m'avoir toujours apporté ta vision « ingénieure » des choses qui m'a permis d'observer les problèmes d'un autre point de vue et d'élargir mes connaissances dans d'autres domaines un peu éloignés de la chimie mais toujours très intéressants. Merci pour l'accueil que vous m'avez réservé à Toulouse, il a été vraiment facile de travailler dans ces conditions.

Stéphane Le Calvé, je ne sais par où commencer... tu m'as déjà permis de renouer à nouveau avec ma passion, la chimie quand tu m'as accepté pour ce stage de master il a presque 4 ans ! Merci pour la confiance que tu m'as accordée dès le début, pour tes précieux conseils scientifiques ainsi que personnels qui m'ont permis de réaliser ce travail. Et surtout merci de m'avoir soutenue dans les moments les plus difficiles, de m'avoir encouragée dans les moments de doute, de ne jamais m'avoir laissée baisser les bras et de toujours avoir su trouver les bons mots pour me motiver. J'espère que ce n'était que le début des projets communs ! Je tiens à remercier tous mes collègues de Toulouse : Lucien, Marcos, Cristine, Silvio, Daniel, Dong Hai... pour m'avoir aidé en tout moment et pour cette bonne ambiance au travail. Je me sentais chez moi. Je remercie également Nicolas Laurien de m'avoir dédié beaucoup de temps et d'efforts pour que je puisse faire toutes mes expériences à Toulouse. Un grand merci aussi à Dominique et Francesco pour tous les bons moments qu'on a passés ensemble et pour m'avoir adoptée pour une petite période, vous m'avez fait me sentir vraiment à la maison !

Merci à Guillermo (el Diablo) pour tous les bons moments passés ensemble, j'espère qu'on se rencontrera dans les prochaines conférences et sinon on aura toujours l'occasion de se voir à Madrid.

J'adresse également mes remerciements à Monique Dilhan et Adrian Laborde de m'avoir apporté leurs conseils et leur expertise en micro fabrication. Vous avez pris le temps de tout m'expliquer et j'ai pu beaucoup apprendre avec vous.

Je tiens à remercier toutes les personnes de l'Université de Strasbourg qui ont rendu possible ce travail : Michel Wolf, Benoît Louis, Maurice Millet, Laura Bom, Thierry Dintzer, Christophe Sutter, Alain Rach. J'aimerais remercier également mes collègues avec qui j'ai partagé mes enseignements : Quentin, Nicole, Thomas, Gad, Alain, Aline... c'était vraiment une très belle expérience !

J'exprime aussi ma profonde gratitude à toute l'équipe de In'Air Solutions : Mathias, Rouba, Stéphanette, Thierry et Pierre pour la bonne ambiance dès le début de ce travail. Merci à Vincent de m'avoir appris à

toujours me poser « la bonne question » et de toujours m'avoir aidée dès que j'en ai eu besoin. Merci pour ces bières after work qui faisaient aussi du bien. Un remerciement spécial à Claire Trocquet d'avoir été toujours là. Je n'ai presque jamais rencontré une personne aussi professionnelle que toi. Dès le début, tu as toujours trouvé le temps de m'aider quand j'en avais besoin et de m'apprendre des choses au laboratoire mais pas seulement pratiques, tu m'as démontré les vraies significations de la rigueur et l'esprit d'équipe. Un grand merci à Christina Andrikopolou, une grande partie de ce travail est grâce à toi. Merci pour tous les bons et aussi les mauvais moments passés ensemble et pour nos fous rires au labo. Je suis vraiment contente d'avoir pu partager cette expérience avec toi !

Je remercie également Cristina Megías Sayago pour toutes les collaborations qu'on a développées ensemble, elles ont été très fructueuses ! Merci de m'avoir apporté de bons conseils scientifiques et une vision différente de mon travail, ça m'a permis d'avancer dans d'autres directions.

Un remerciement très très spécial à Alberto Rodríguez Cuevas. Merci de m'avoir accompagné une bonne partie de cette aventure et d'avoir été toujours là aussi bien comme collègue que comme ami, ce travail aurait été impossible sans toi ! Je te remercie pour tous les bons moments passés au labo et les fous rires pour des conneries. On fait une super équipe et tu vas beaucoup me manquer !

Je remercie Patricia García Muñoz pour le soutien dans les moments difficiles et aussi pour ces bières et les millions de fous rires ! Pour moi, tu es un vrai exemple personnel ainsi que professionnel. Merci à tous mes camarades et amis de l'ICPEES et de Strasbourg : Javi, Anaïs B., Paula, Kim, Thomas, Faustine pour le soutien, les cafés, les soirées et tous les bons moments passés et ceux qui restent à venir ! Un remerciement particulier à Anaïs Rodrigues pour avoir accepté de me donner un coup de main en français et surtout pour rendre beaucoup plus agréable la fin de cette thèse, on s'est rencontré tard mais ça c'est juste le début !

Un énorme merci à mes parents et à ma sœur, malgré la distance, vous avez toujours été là et vous m'avez donné la force pour continuer. Merci de m'avoir encouragé dès que j'étais petite à suivre mes rêves et de me montrer que tout est possible. C'est grâce à vous qu'aujourd'hui je suis arrivée ici !

Finalement, un remerciement très spécial pour Elena, tu m'as accompagné pendant une des étapes les plus compliquées de ma vie. Merci d'avoir été avec moi, pour me motiver tous les jours, même pendant les moments difficiles, d'avoir su me montrer que la plupart des problèmes ne sont pas aussi importants que ce que l'on croit. Je te remercie de m'avoir supporté alors que je ne parlais que de la thèse pendant des mois, tu as une sacrée patience ! Enfin, merci pour ta confiance illimitée, tu m'as fait croire que j'étais capable de faire tout ce que je voulais dans la vie.

MERCI A TOUS !

Irene

List of figures

Figure 1-1. Main emission sources of ambient air pollution [8].....	6
Figure 1-2. Structure of the molecules investigated in this work.	7
Figure 1-3. Main sources of indoor air pollution [32].....	8
Figure 1-4. Schematic diagram of a gas chromatograph [55]	13
Figure 1-5. Analyte separation in a chromatography column [56].....	13
Figure 1-6. Working principle of a μ GC [81]	20
Figure 1-7. Diagram of adsorption-desorption cycle.....	21
Figure 1-8. Sampling tubes commercialised by Sigma Aldrich [103].....	23
Figure 1-9. Schematic view of the first MEMS PC with a cavity etched by deep reactive ion etching (DRIE).....	23
Figure 1-10. Micro preconcentrators made from diverse materials: (a) silicon-glass [89], (b) cooper [123], (c) stainless steel [105], (d) ceramics [107] and (e) polyimide foil [114].....	28
Figure 1-11. Schematic representation of a planar PC. Reprinted from [125].....	29
Figure 1-12. Preconcentrators with different geometries: circular spiral (a) [112], array of parallel channels (b) [85] and U-shape channel (c) [116].	29
Figure 1-13. (a) Flow simulation in a PC with inlet/outlet angle $> 120^\circ$ [90]; (b) Preconcentrator containing micropillars and having inlet and outlet angles $> 120^\circ$ [81]; (c) Pressure (green) and flow velocity (blue) simulations in a PC with inlet/outlet manifold fluidic system [127].....	30
Figure 1-14. Preconcentrator containing crisscross shaped (a) [129] and U-shaped (b) [104] pillars ..	31
Figure 1-15. Diverse heating systems found in micropreconcentrators: (a) Ni-Cr wire [81], (b) gold layer deposited by electroless plating technology [83], (c) platinum heater [112] and (d) gold layer deposited by electron beam [115].....	32
Figure 1-16. Schematic diagram of different categories of adsorbents employed in micro preconcentrators: (a) granular, (b) thin film and (c) foam adsorbents. Reprinted from [86]	34

Figure 1-17. QxCav (a) and EtQxBox (b) cavitands employed for the selective preconcentration of aromatic compounds. Reprinted from [109].....	35
Figure 1-18. (a) Thin film layer of zeolite Day [89] and (b) CNT foam [86].....	37
Figure 1-19. Example of adsorption isotherms at different temperatures from the lowest (black line) to the highest (green line).	40
Figure 1-20. Freundlich isotherm at different n_f values [140].....	41
Figure 1-21. Example of Langmuir isotherm at different values of K [141]	42
Figure 1-22. Types of adsorption isotherms according to the IUPAC classification [143]	44
Figure 1-23. Different structures of mesoporous silica [172]. SG: Space Group	49
Figure 1-24. Structures of several MOF and their linkers. The yellow and green spheres represent the pore volume. [186].....	50
Figure 1-25. Structures of four commercial zeolites and their building units (reprinted from [193]) .	51
Figure 2-1. a) Schematic view of Basolite™ C300 three-dimensional structure. The spheres represent the pore volume. Atoms are displayed in the following colours: Carbon (grey), Hydrogen (white), Oxygen (red) and Copper (brown) and b) Representation of different cages and windows in Basolite™ C300. Atoms are displayed in the following colours: Carbon (white), Oxygen (red) and Copper (blue). For simplicity, hydrogen atoms are not displayed [8].	85
Figure 2-2. Pore structure and geometry of ZSM-5 [17].....	87
Figure 2-3. Example of breakthrough curve.	95
Figure 2-4. Schematic representation of thermal desorption tube employed in breakthrough tests...	96
Figure 2-5. Schematic drawing of experimental setup for Toluene or BTEX breakthrough experiments	97
<i>Figure 2-6. Schematic drawing of experimental setup for formaldehyde breakthrough experiments.</i>	<i>98</i>
Figure 2-7. Schematic drawing of experimental setup for hexanal breakthrough experiments	99
Figure 2-8. Schematic drawing of GC laboratory prototype	102
Figure 2-9. Macro Aluminium Preconcentrator (MAP).	103
Figure 2-10. Structure of MEMS-based Preconcentrator.....	104

Figure 2-11. Designs proposed for the microfluidic cavity: a) square shape and b) serpentine.....	105
Figure 2-12. Schematic view of mesh 1 (a) and mesh 2 (b) at the inlet of the microdevice with serpentine configuration.	107
Figure 2-13. Design of thin film masks employed for Ti deposition (heating elements in orange and temperature sensors in black) (a); Ag deposition (b) and SiO ₂ sputtering (c) for the first heating system	110
Figure 2-14. Overview of the fabrication protocol of heating systems by photolithography followed by metal deposition	111
Figure 2-15. Process flow of porous gold deposition.....	113
Figure 2-16. Patterns for the fabrication of masks for: (a) SU-8 deposition and (b) gold deposition to form the porous layer.....	114
Figure 2-17. Patterns for the fabrication of chromium masks for: (a) titanium and gold deposition, (b) gold etching and (c) SiO ₂ deposition.....	114
Figure 2-18. Process flow of the fabrication of titanium and gold resistances.....	115
Figure 2-19. Manufacturing the microfluidic cavity by SU-8 patterning.....	116
Figure 2-20. Overview of sandblasting process and SU-8 deposition.....	116
Figure 2-21. Process flow of adhesive bonding	117
Figure 2-22. 3D design of MAPP preconcentrator: (a) aluminium board with the cavity and the O-ring microfluidic cavity and (b) aluminium board with ceramic resistance; (c) fluidic connections were integrated in a PEEK block and (d) the overall structure was fixed using a housing made of two polymer pieces joined by screws.....	118
Figure 2-23. μ PA 3D design: (a) copper tube, (b) copper tube, aluminium cube and ceramic resistances and (c) whole assembly including the fluidic connections.....	119
Figure 2-24. μ AP2 3D design: (a) aluminium block; (b) aluminum block, Swagelok standard connectors and ceramic resistances; (c) first draft of the housing of μ AP2 prototype including two fans for rapid cooling.	120
Figure 5-1. Schematic diagram of the first setup employed for hexanal dynamic adsorption experiments	243

Figure 5-2. Breakthrough curves of gaseous hexanal on different materials (flow rate = 20mL/min, C_0 = 3289.3 ppm)	245
Figure 5-3. Hexanal adsorption capacity of each adsorbent (mg/g adsorbent)	245
Figure 5-4. Formaldehyde adsorption isotherms for ACF (\diamond), GAC1 (\square), and GACF (Δ) representing the adsorption capacity at different formaldehyde concentrations ($T = 299$ K) [29].	249
Figure 5-5. Formaldehyde adsorption isotherms on AC (black), SBA-15 (orange) and MIL-53 (blue) representing the adsorption capacity of these materials at different formaldehyde partial pressures ($T = 298$ K) [28].	249
Figure 5-6. (a) Breakthrough curves of gaseous formaldehyde on Carbopack® B, SBA-16 and HKUST-1 (formaldehyde concentration = 201 ppb, flow rate = 15 mL/min) and (b) enlarged view of the first 150 min of the experiment.....	251
Figure 5-7. Breakthrough curves of gaseous formaldehyde over ZSM-5 zeolites with different Si/Al ratios (formaldehyde concentration = 164 ppb, flow rate = 15 mL/min).....	254
Figure 5-8. Formaldehyde adsorption capacities of ZSM-5 with different Si/Al ratios.....	254
Figure 5-9. EDX mapping of Mg loaded CBV3020E zeolite	256
Figure 5-10. Breakthrough curves of gaseous formaldehyde over CBV3020E and CBV3020E-Mg zeolites.....	256
Figure 5-11. Formaldehyde adsorption capacities of diverse materials at different formaldehyde concentrations	257
Figure 1. Principaux causes de mortalité dans le monde enregistrées ces dernières années [6]	274
Figure 2. Schéma de fonctionnement du GC portable utilisé au cours de cette thèse (a), prototype de GC développé au laboratoire (b) et prototype de GC pré-industriel (c).....	278
Figure 3. Les trois scénarios étudiés pendant la campagne de terrain : salle de cours vide (a), salle de cours avec le mobilier (b) et salle de cours pendant l'activité courante de l'école (c). Concentrations de benzène (d) et toluène (e) et CO_2 mesurées pendant la cinquième semaine à l'école des Grandes Varennes. Comparaison des concentrations de toluène mesurées à l'école des Grandes Varennes pendant la troisième, quatrième et cinquième semaines (f).	282

- Figure 4. a) Schéma de fonctionnement de l'analyseur de BTEX avec l'étape de préconcentration et b) version commercial (μ -BTEX-1, In'Air Solutions) utilisé pour l'intégration du préconcentrateur.... 284
- Figure 5. Différentes versions du préconcentrateur de BTEX développés au cours de ce travail de thèse. Masses thermiques avec connecteurs (rouge) et sans connecteurs (bleu). 285
- Figure 6. Design 3D du préconcentrateur μ AP2 (a). Performance du système de chauffage et refroidissement (b). Exemple d'un chromatogramme d'un échantillon de BTEX obtenu avec le prototype du GC intégrant le μ AP2 (V échantillon = 50 mL, C_{BTEX} = 20 ppb, température de désorption = 330 °C, temps d'injection = 75 s) 286
- Figure 7. Résultats des tests de répétabilité obtenus pour 7 échantillons de BTEX analysés consécutivement le même jour : (a) aires de pic et (b) temps de rétention. Résultats des tests de reproductibilité obtenus pour 3 échantillons de BTEX analysés sur trois jours différents : (c) aires de pic et (d) temps de rétention. V = 20 mL, C = 20 ppb, température de désorption = 330 ° C, temps d'injection = 75 s. Les barres d'erreur verticales représentent l'écart type des triplicats. 289
- Figure 8. Dispositifs expérimentaux utilisés pour l'adsorption des BTEX (a) et du formaldéhyde (b) 293
- Figure 9. Courbes de perçage des BTEX sur Carbopack® B (a), SBA-16 (b) et HKUST-1 (c). Concentration BTEX = 10 ppm, débit = 5 mL / min. Capacités d'adsorption de BTEX des trois adsorbants étudiés (d)..... 294
- Figure 10. a) Courbe de perçage typique des BTEX sur une zéolithe ZSM-5, b) exclusion stérique des métha et ortho xylènes des pores de la zéolithe ZSM-5 et c) capacité d'adsorption des différents BTEX en fonction du rapport Si/Al. 295
- Figure 11. a) Courbes de perçage du formaldéhyde sur des adsorbants commerciaux, b) courbes de perçage du formaldéhyde sur des zéolithes ZSM-5 avec différents rapport Si/Al et c) corrélation linéaire de la capacité d'adsorption de formaldéhyde des zéolithes ZSM-5 avec le rapport Si/Al.... 296

List of tables

Table 1-1. Commercially available portable instruments for VOC detection	18
Table 1-2. Summary of micro preconcentrators developed in the last years	25
Table 1-3. General properties of the investigated VOC.....	53
Table 2-1. Main characteristics of commercially available adsorbents selected for the study.....	84
Table 2-2. Parameters employed in hexanal analysis method by ATD-GC-FID	100
Table 2-3. Parameters employed in flow simulations for both designs of MEMS Preconcentrator ..	106
Table 2-4. Summary of mesh parameters employed in flow simulations for MEMS Preconcentrator	107
Table 2-5. Features of each heating system design.	110
Table 4- 1. Calibration equations and coefficients of determination obtained from the linear fittings	154
Table 4-2. Pressure drop and maximum velocity obtained at different flow rates in absence of granular adsorbent	174
Table 4-3. Equations from the volume calibration curves	188
Table 4-4. Summary of the experimental conditions employed in a series of tests with μ AP2.	190
Table 4-5. Performances obtained for the GC prototype integrating μ AP2 filled with SBA-16.....	191
Table 4-6. Data from calibration (volume) obtained for the GC prototype integrating μ AP2 filled with SBA-16.....	192
Table 4-7. Performances obtained for the GC prototype integrating μ AP2 filled with Carboxpack® B	195
Table 4-8. Equation and determination coefficients obtained in sample volume variation tests.....	195
Table 4-9. Summary of miniaturized GC with integrated PC developed in the last years.	201
Table 5-1. Textural properties and adsorption capacities of studied materials towards gaseous hexanal	243
Table 5-2. Literature review of gaseous hexanal adsorption on various materials.....	246
Table 5-3. Textural properties and adsorption capacities of studied materials towards gaseous formaldehyde.....	250
Table 5-4. Chemical composition, acid site density, textural and adsorption properties of as-prepared H-ZSM-5 zeolites.	253
Table 5-5. Formaldehyde adsorption capacities of various zeolites obtained in previous studies classified in ascending order of the value of K_H	259
Tableau 1. Propriétés physico-chimiques des composés étudiés dans ce travail.	275
Tableau 2. Performances obtenues avec le prototype de l'analyseur de BTEX intégrant le μ AP2	287

List of abbreviations

AC	Activated Carbon
ATD	Automated Thermal Desorption
COD	Cancer Odor Database
DOAS	Differential Optical Absorption Spectroscopy
EEA	European Environment Agency
EHT	Electron High Tension
FAU	Faujasite
FT-IR	Fourier Transform Infrared Spectroscopy
GC	Gas Chromatography
ICP-RIE	Inductively Coupled Plasma-Reactive Ion Etching
IUPAC	International Union of Pure and Applied Chemistry
LOD	Limit of Detection
LOQ	Limit of Quantification
MFC	Mass Flow Controller
MOS	Metal Oxide Semiconductor
OCS	Open Coordination Sites
PC	Preconcentrator
PECVD	Plasma-Enhanced Chemical Vapor Deposition
PEEK	Polyether Ether Ketone
PID	Photoionisation Detector
PTR-MS	Proton-Transfer-Reaction Mass Spectrometry
PVD	Physical Vapor Deposition
RH	Relative Humidity
SAR	Si/Al Ratio
SSA	Specific Surface Area
S _{BET}	Surface area calculated by the Brunauer Emmett Teller method
t _b	Breakthrough time
TCD	Thermal conductivity detector
TCR	Temperature Coefficient of Resistance
TEOS	Tetraethoxysilane
TPD	Temperature Programmed Desorption
t _s	Saturation time
WHO	World Health Organization

Symbols

E_d	Activation energy of the desorption	J mol ⁻¹
XZ	Adsorbed gaseous molecule	
A_m	Area occupied by one molecule	m ² molecule ⁻¹
N_A	Avogadro's number	molecules mol ⁻¹
K_f	Constant of Freundlich isotherm	
n_f	Exponent of non-linearity in Freundlich isotherm	
c	Constant related to the energy of adsorption of the first layer	
h_c	Convective heat transfer coefficient assuming free convection	W m ⁻² K ⁻¹
S_e	Cross section of the heating element	m ²
I	Current	A
ρ	Density	kg m ⁻³
A	Desorption rate coefficient	s ⁻¹
q	Dynamic adsorption capacity	kg kg ⁻¹ of adsorbent
ρ_e	Electrical resistivity	Ω m
P_f	Formaldehyde partial pressure	Pa
X	Free gaseous molecule	
Q	Gas flow rate	m ³ min ⁻¹
Q_H	Heat	J
β	Heating rate	K min ⁻¹
h	Height	m
K_H	Henry constant	mol kg ⁻¹ Pa ⁻¹
D_h	Hydraulic diameter	m
R	Ideal gas constant	J mol ⁻¹ K ⁻¹
ρ_{e0}	Initial electrical resistivity	Ω m
T_0	Initial temperature	K
S_i	Inlet cross section area	m
v	Inlet mean velocity	m s ⁻¹
Q_i	Inlet volume flow rate	m ³ min ⁻¹
ν_{air}	Kinematic viscosity of air	m ² s ⁻¹
L	Length	m
L_e	Length of the heating element	m
Π_{lost}	Lost heat flux	W
m	Mass	kg
x	Mass of the adsorbed gas	kg
M	Molecular weight	kg mol ⁻¹
M_f	Molecular weight of formaldehyde	kg mol ⁻¹
n_m	Monolayer capacity	mol
n	Order of the reaction	
P	Partial pressure of a gas	Pa
P_B	Partial pressure of the gas B	Pa
Π	Power	W
Π_i	Power per heater	W
k_a	Rate of adsorption	

k_d	Rate of desorption	
P_{ref}	Reference pressure	Pa
R_i	Resistance per element	Ω
Re	Reynolds number	
P_0	Saturation pressure	Pa
c_{Si}	Specific heat of silicon	$\text{J kg}^{-1} \text{K}^{-1}$
θ	Surface coverage	
T	Temperature	K
T_p	Temperature at a maximum of the desorption peak	K
α_0	Temperature coefficient of resistance	K^{-1}
ΔT	Temperature difference	K
N	Total number of sites	
S_t	Total surface area	m^2
Z	Unoccupied site on the adsorbent's surface	
Π_{useful}	Useful power	W
U	Voltage supply	V
V_p	Volume of gas adsorbed at partial pressure P	m^3
V_m	Volume of gas required to form a monolayer	m^3
S_w	Wafer section area	m^2
P_w	Wetted perimeter	m
w	Width	m

General introduction

Air pollution is defined as “the contamination of the indoor or outdoor environment by any chemical, physical or biological agent that modifies the natural characteristics of the atmosphere” according to the World Health Organization (WHO). Nowadays, air pollution is one of the major environmental risk factors for the global burden of disease. Only in 2015, exposure to air pollution was estimated to cause over 7.0 million deaths which represented 7.6% of total global mortality this year [1]. The health effects of exposure to air pollution are diverse and can range from slight nose and eyes irritation to more serious pathologies such as heart disease, lung cancer, and chronic and acute respiratory diseases including allergy and asthma.

This context highlighted the need of air pollution regulations at the global level to prevent the deterioration of public health. For example, in the last decade, several laws have been entered into force to limit vehicle entry in hundreds of European cities and promote the use of public transport. In general, people appear to be more aware of outdoor air pollution since it is more “visible”. Indeed, who has never observed large columns of smoke arising from factories or enormous clouds of pollution on top of cities? According to the WHO, 4.2 million deaths every year are attributed to ambient air pollution whereas 3.8 million can be ascribed to indoor air pollution. Therefore, the difference is not as significant as we think. This high mortality is mainly due to the fact that people spend more than 80 % of time indoors [2] where the levels of some organic pollutants are usually from 2 to 10 times higher than outdoors [3], [4]. Additionally, the existence of multiple pollutant emission sources, together with the conditions to live in comfort characteristics of closed environments (temperature, humidity, ventilation), promotes chemical reactions generating by-products that can be as harmful as their precursors. The continuous exposure to this mixture of diverse pollutants can provoke serious detrimental effects on human health. Therefore, the European Union has established indoor air quality (IAQ) guidelines aiming to limit benzene and formaldehyde exposure to $5 \mu\text{g m}^{-3}$ (1-year period) and $100 \mu\text{g m}^{-3}$ (30 min), respectively. In France, IAQ legislation in public buildings has become stricter fixing a limit value of $30 \mu\text{g m}^{-3}$ for long-term exposure to formaldehyde from 1st January 2015 and decreasing the benzene threshold for long term exposure to $2 \mu\text{g m}^{-3}$ from 1st January 2016 [5].

In this context, the objective of this thesis is the development of a portable analytical instrument for BTEX monitoring in near real-time at very low concentrations. To this purpose, a micro gas preconcentrator was developed and integrated in a portable GC prototype to achieve a LOD for benzene lower than the threshold value set by the French government, i.e. $2 \mu\text{g m}^{-3}$ (0.6 ppb). In order to possibly enlarge the range of pollutants analysed by this instrument, a part of this thesis was focused on the study of different adsorbents for the capture of indoor pollutants.

In **chapter 1**, general aspects on air pollution and theoretical bases on VOC measurement and adsorption needed to understand this research work are provided. To complete the socioeconomic context of the development of this project, the health effects associated to this “silent killer” and the current European air quality regulations are described. Most common methods for VOC detection and the state of the art of preconcentration devices are presented to highlight the lack of analytical devices presenting simultaneously high sensitivity and portability. In the last section of this chapter, the main aspects on VOC adsorption are explained to give the reader a brief introduction prior to the discussion of the obtained results.

Chapter 2 is divided in two sections: VOC adsorption and preconcentrator development. In the first part, the materials employed for VOC adsorption and the techniques employed for their characterization are detailed. Afterwards, the different homemade experimental setups used for the adsorption experiments are described.

In **chapter 3**, the results obtained in field campaign of indoor air quality conducted in two French primary schools for 5 weeks are presented. This campaign was developed in the framework of the IMPACT’Air project aiming to determine BTEX concentrations in indoor air, identify their main emission sources and evaluate the efficacy of different ventilation methods.

Chapter 4 summarizes the characterization in terms of heating performance and BTEX preconcentration of the different BTEX preconcentrator prototypes developed throughout this work. The analytical performances are evaluated in terms of linearity, detection and quantification limits, overall sensitivity considering the gaseous sample volume used, repeatability and reproducibility.

In **chapter 5**, the adsorption/desorption of BTEX, formaldehyde and hexanal is investigated on different solid materials and the influence of the different textural and chemical properties affecting

adsorption is discussed. The results are discussed and compared with the literature in terms of quantity of VOC adsorbed per mass of adsorbent for a given gas concentration.

Finally, in the last section, the **general conclusions and future perspectives** of this work are provided.

References

- [1] S. S. Babatola, "Global burden of diseases attributable to air pollution," *J Public Health Afr*, vol. 9, no. 3, Dec. 2018.
- [2] M. C. McCormack et al., "Common household activities are associated with elevated particulate matter concentrations in bedrooms of inner-city Baltimore pre-school children," *Environmental Research*, vol. 106, no. 2, pp. 148–155, Feb. 2008.
- [3] J. Madureira et al., "Source apportionment of CO₂, PM₁₀ and VOCs levels and health risk assessment in naturally ventilated primary schools in Porto, Portugal," *Building and Environment*, vol. 96, pp. 198–205, Feb. 2016.
- [4] L. Zhong, F.-C. Su, and S. Batterman, "Volatile Organic Compounds (VOCs) in Conventional and High Performance School Buildings in the U.S.," *International Journal of Environmental Research and Public Health*, vol. 14, no. 1, p. 100, Jan. 2017.
- [5] Décret n° 2011-1727 du 2 décembre 2011 relatif aux valeurs-guides pour l'air intérieur pour le formaldéhyde et le benzène. 2011.

Chapter 1. Introduction and literature review

Air pollution is a current environmental and global public health issue. In this chapter, a brief introduction about airborne pollutants, their related health effects and the current legislation is given to introduce the reader to the context of this research work. Afterwards, a summary of the most common methods for volatile organic compounds (VOC) detection followed by the state of art of gaseous micro preconcentrators is provided. Then, some technical background on general adsorption and desorption processes and, more specifically, VOC adsorption/desorption is presented. Finally, the objectives of this work are listed.

1.1 Air quality

Air pollution has become a growing concern in the past few years, with an increasing number of intense air pollution events in many cities worldwide. In 2016, it was estimated that about 91 % of people live in urban areas where the levels of pollutants exceed the World Health Organisation (WHO) guideline values [1, p. 10]. This continuous exposure to high levels of pollutants causes about 7 million of premature deaths every year [2]. More of these deaths occur in low- and middle-income countries, mainly in Asia and Africa, followed by low- and middle-income countries of the Eastern Mediterranean region, Europe and the Americas. In the last years, a large amount of scientific evidence has demonstrated the link between air pollution exposure and the development of a large number of pathologies such as stroke heart disease, lung cancer, chronic obstructive pulmonary diseases and respiratory infections [3]–[6]. Additionally, air pollution has also notable economic impact due to the deterioration of public health, the decrease of the employees' productivity and the degradation of the environment. In that respect, environmental policies are being implemented to protect both human health and environment. However, to properly evaluate air quality (AQ) and thereby propose actions to improve it, more experimental AQ data are required, especially in less developed countries where the lack of these data is particularly notable. The type of pollutants found and their levels strongly depend on the investigated environment. Two main environments can be distinguished: outdoors and indoors.

1.1.1 Ambient air

Ambient outdoor air pollution differs in composition and pollutants levels from indoor air pollution. Particulate matter (PM_{2.5} and PM₁₀), ground-level ozone (O₃), nitrogen dioxide (NO₂), sulphur dioxide (SO₂) and carbon monoxide (CO) are considered the five more common pollutants of ambient air according to the WHO and the United States Environmental Protection Agency (US EPA). Other pollutants such as VOC are also encountered but to a lesser extent compared to the abovementioned. In ambient air, the type of pollutants and their concentrations are closely related to the nature of the emission sources, the atmospheric conditions and the geographic location.

The principal emission sources responsible for ambient air pollution are shown in Figure 1-1. Most pollutants are emitted by anthropogenic sources such as motor vehicles, heat and power generation plants, industrial facilities, municipal and agricultural waste treatment and cities [7]. Natural sources such as forest fires, wind erosion or volcanic eruptions also contribute to the degradation of air quality but to a much lesser extent compared to anthropogenic sources [7].

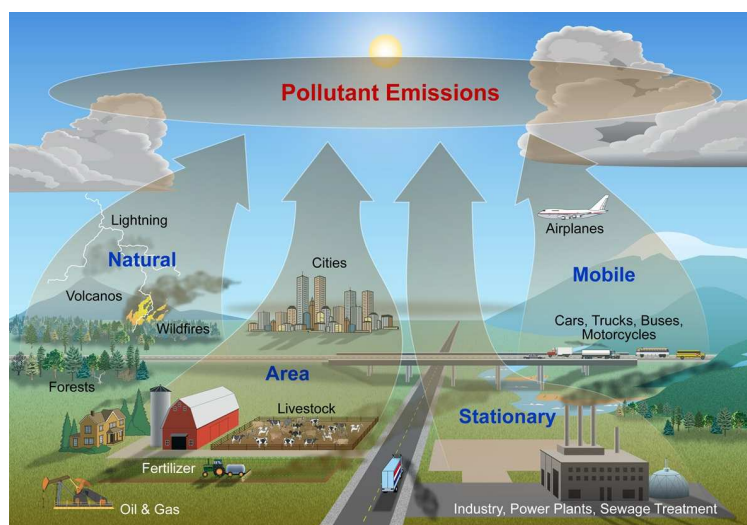


Figure 1-1. Main emission sources of ambient air pollution [8]

Although most emissions of ambient air pollution are from local or regional sources, pollutants can travel long distances under certain atmospheric conditions. Therefore, ambient air pollution can affect people far away from its original emission source. Weather conditions can also drastically influence pollution levels, leading to serious pollution events such as the great smog of London in 1952. In this incident, a combination of cold weather and windless conditions with an anticyclone over London

city resulted in the formation of a thick layer of smog that lasted for five days. Recent studies suggest that more than 12,000 deaths could be attributed to this pollution event [9], [10]. Apart from meteorology, geographic location plays a major role in ambient air pollution. Cities surrounded by mountains such as Skopje, Sarajevo or the best-known example, Mexico, suffer from extremely high levels of pollution. The mountains act indeed as a barrier for the pollution, preventing the air renewal and thus promoting the accumulation of pollutants over the city.

1.1.2 Indoor air

The WHO established that about 3.8 millions of premature deaths per year are attributed to indoor air pollution. Therefore, indoor air quality has become an issue of major importance. Some research reported that people spend more than 80 % of time indoors [11] where the pollutant levels are usually from 2 to 10 times higher than outdoors [12], [13]. These pollutants can be classified according to their nature as biological (mold, mite), physical (particulate matter, asbestos) and chemical (CO, pesticides, VOC). Among the chemical pollutants, VOC are the most abundant in indoor air [14]. This group of molecules is defined by the European council as compounds having a vapour pressure of 0.01 kPa or more at 293 K. VOC includes a broad spectrum of molecules characterized by structures formed by carbon chains and, in some cases, other atoms like oxygen, sulphur, or nitrogen. This work is focused on the study of formaldehyde, hexanal and a family of aromatic compounds called BTEX (benzene, toluene, ethylbenzene and xylene isomers), presented in Figure 1-2. These compounds have adverse effects on human health, and are frequently encountered at high levels in indoor air [15]–[17].

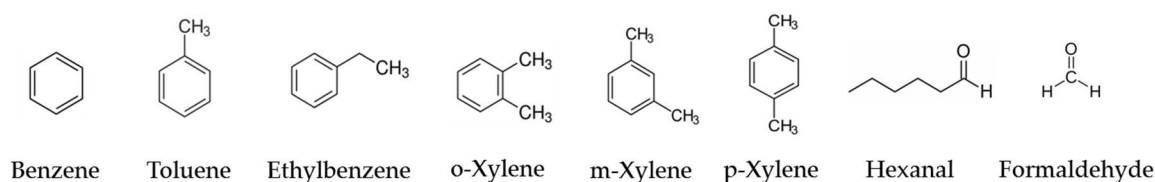


Figure 1-2. Structure of the molecules investigated in this work.

A study in 22 dwellings in Strasbourg reported maximum concentrations of formaldehyde and hexanal ranging between 13.3–123.4 $\mu\text{g m}^{-3}$ and 0–47.2 $\mu\text{g m}^{-3}$, respectively. Higher levels up to 92 $\mu\text{g m}^{-3}$ of hexanal were reported by Walgraeve *et al.* [18] in a study performed in 6 homes in Belgium. In this study, concentration of aromatic hydrocarbons was found to be up to 88 $\mu\text{g m}^{-3}$ corresponding to 25 % of the total VOC concentration. Significant levels of BTEX, hexanal and formaldehyde were also

detected in different environments worldwide, such as schools [13], [19], [20], universities [21], [22], coffee bars or farmer houses [23]. These results showed that regardless the country and the type of environment considered, VOC are always present.

In general, a multitude of emission sources can be found in indoor air (see Figure 1-3). The major source are the activities carried out by the occupants such as cooking or smoking [24], [25]. In general, all the activities involving combustion processes such as lighting the fireplace [26], candles [27] or incense [28] are significant sources of BTEX. Other primary BTEX sources in indoor air are cleaning products, furnishings and building materials such as flooring materials, wall coverings, particle boards, adhesives, varnishes or paints [15], [29]–[31]. In general, BTEX emissions from these materials are usually more intense just after the fabrication and decrease over time. In France, since 1st January 2012, building materials and furniture intended for indoor use must bear a label with information on the emission of volatile pollutants (Articles R221-22 to R221-28). For this label, the emissions of 10 different VOC substances and the total amount of VOC have to be measured and classified into four categories from A+ (low emissions) to C (high emissions). The resulting label is given by the worst results among the 11 results taken individually.

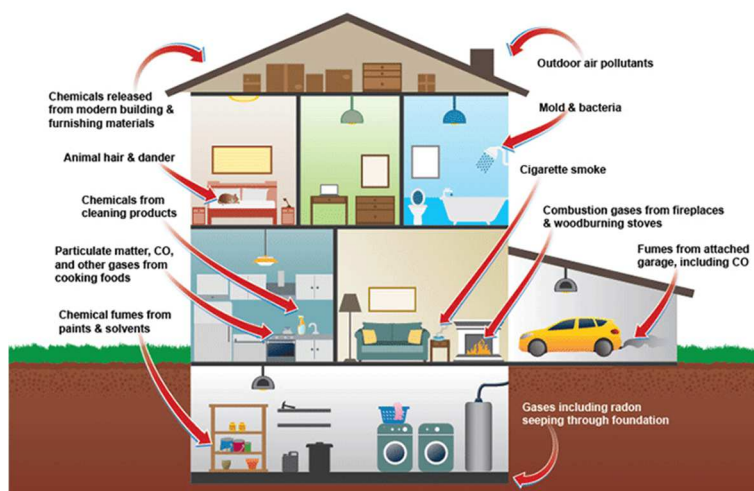


Figure 1-3. Main sources of indoor air pollution [32]

Finally, the other crucial factor affecting indoor air quality (IAQ) is the rate of air exchange. The type and frequency of ventilation plays indeed a critical role in indoor air pollution. A clear example can be found in the study of the seasonal variation of IAQ conducted by Walgraeve *et al.* [18]. In this study, VOC levels up to 10 times higher were found during winter compared to summer and autumn. This

difference can be attributed to the less frequent ventilation during wintertime. Generally, an increase in the rate of air exchange leads to a strong decrease in the pollutant concentration since their concentration indoors usually exceeds that of outdoors. However, the ambient air contains different pollutants that could be transferred through the ventilation, thus being an additional source of pollutants in indoor air.

1.1.3 Health effects

In the last decades, plenty of research studies have been conducted to elucidate the health effects caused by air pollution. An increasing amount of scientific evidence has demonstrated the relationship between the exposure to air pollutants and harmful effects on human health [33] like headache, eye and nose irritation or the development of much serious pathologies such as asthma [34], allergy [35] or even cancer [36]. These effects depend on the pollutant, its concentration and the exposure time. In addition, it is difficult to assess the risks associated to air pollution since outdoor as well as indoor air contain a mixture of diverse pollutants that can provoke a synergic effect often called “cocktail effect”. Different pollutants may interact indeed with each other, enhancing the adverse effects than the sum of the effects produced by each single pollutant. Besides, health effects are influenced by many factors such as gender or age, the most vulnerable being children, women and elderly people [37]. The presence of cardiovascular or respiratory diseases may worsen the adverse effects of air pollution. Some of the main harmful effects of the pollutants investigated in this work are briefly presented below.

Benzene

Among BTEX, benzene is considered the most dangerous since it is classified as human carcinogen (Group 1) by IARC (International Agency for Research on Cancer). For this type of compounds there is no safe level of exposure, therefore, only an estimate of the risk associated to different concentrations can be provided. For example, a concentration of airborne benzene of $1.7 \mu\text{g m}^{-3}$ is associated with an excess lifetime risk of 1/ 100 000 [38].

Different routes of exposure can be used for benzene adsorption such as inhalation, ingestion, skin and eye contact. Once adsorbed, it is quickly distributed throughout the human body, especially in tissues rich in lipids like the liver or the bone marrow where it is transformed into primary metabolites such as phenol, catechol et hydroquinone. These substances are extremely toxic and are directly linked

to the development of carcinogenic process [39]. Their accumulation provokes the deterioration of the tissues that makes blood cells in bone marrow leading to the development of different types of leukaemia in case of long-term exposure.

Toluene

Toluene is classified as not carcinogenic to humans (Group 3) by IARC. However, other less serious consequences have been associated to toluene exposure like irritation to the eyes, nose, throat and respiratory tract and in the case of acute inhalation, drowsiness, or respiratory depression [40]. Chronic exposure can lead to the damage of the central nervous system and kidneys. Additionally, many studies reported the harmful effects of toluene exposure on pregnant women [41]–[43]. Therefore, toluene is classified in the EU as a reproductive toxicant, category 2 (hazard statement H361: suspected of damaging the unborn child).

Ethylbenzene

The carcinogenic effects of ethylbenzene are not firmly demonstrated, and it is classified as probably carcinogenic to humans (Group 2B). The exposure to high concentration of ethylbenzene can cause eyes and throat irritation and in the case of exposure to very high levels, it can lead to vertigo and dizziness [44].

Xylenes

As toluene, xylenes are classified as not carcinogenic to humans (Group 3) by IARC. The principal health effects of xylene are related to the central nervous system and consist of headache, dizziness, nausea and vomiting [45]. Long-term exposure may lead to what is called "organic solvent syndrome" that involves irritability, insomnia, agitation, extreme tiredness, tremors and effects on short-term memory [46].

Formaldehyde

Formaldehyde has attracted increasing attention due its frequent presence in indoor air. This substance is considered as carcinogenic (Group 1) by IARC since 2006. Especially, formaldehyde has been associated with the development of nasopharyngeal cancer [47], [48], [48]. Short-term exposure can provoke throat, nose and eye irritation and headache. More serious effects such as decreased

pulmonary function, lachrymation, pneumonia and asthma have been associated with long term exposure [49].

Hexanal

Hexanal is a common pollutant encountered in indoor air. It is a colourless liquid with an intense odour that produces irritation of eyes, nose and throat when its concentration is above 10 ppm [50]. The most common exposure routes are *via* inhalation of ambient air, ingestion of food and drinking water, and dermal contact with consumer products containing this compound. Hexanal is not classified as carcinogenic by IARC.

1.1.4 Legislation

As illustrated in the above section, exposure to air pollution is associated to a multitude of pathologies in humans. Therefore, an extensive legislation concerning air quality has been developed in several countries to limit human exposure and protect public health.

At a global level, indoor air quality guidelines are published by the WHO [51] in which benzene and formaldehyde are part of the “known pollutants” affecting IAQ. For the former, the exposure to benzene levels of $1.7 \mu\text{g m}^{-3}$ (0.52 ppb) may increase the risk of leukaemia to 1/100 000. Thus, no safe level of exposure can be recommended, and their indoor exposure levels must be reduced as low as possible. Conversely, a short-term guideline of $100 \mu\text{g m}^{-3}$ is recommended for formaldehyde as preventing sensory irritation in the general population. This threshold should not be exceeded at any 30-minute interval during a day. The same value was adopted by the European Union for formaldehyde [38]. In Europe, however, a benzene threshold value of $5 \mu\text{g m}^{-3}$ has been established for long term exposure (1 year) [52].

In France, legislation concerning indoor air quality in public buildings has become stricter. According to the Decree no. 2011-1727 of 2nd December 2011 [53], a limit value of $5 \mu\text{g m}^{-3}$ long-term exposure was set for benzene from 1st January 2013 and it was decreased to $2 \mu\text{g m}^{-3}$ from 1st January 2016. In the case of formaldehyde, a limit value of $30 \mu\text{g m}^{-3}$ was fixed for long-term exposure to formaldehyde from 1st January 2015 and it will be decreased to $10 \mu\text{g m}^{-3}$ from 1st January 2023.

To check the compliance with this legislation, the measurements should be performed over two non-successive weeks of children attendance. Since the concentration of these compounds can vary greatly

from season to season, the air quality should be evaluated over two different periods: cold season (between November and February) and warm season (in September/October or April/May depending on institutions).

1.2 Methods for airborne VOC detection

VOC are a group of highly reactive gaseous pollutants frequently found in indoor as well as outdoor air. These compounds play a crucial role in physico-chemical processes in the atmosphere since they contribute to the formation of ozone and other photochemical oxidants [54]. Moreover, it is known that VOC exposure causes adverse effects on human health. Many VOC are either known, or suspected to be, irritants, neurotoxins, allergens or carcinogens [6]. Therefore, to limit human exposure and implement effective strategies for pollution control, the identification and quantification of VOC is of particular importance. To this purpose, several methods have been developed to quantify airborne VOC concentrations.

In this section, a review of the most common VOC analysis techniques is presented. These methods have been divided in two categories: chromatographic and spectroscopic methods. Most of these techniques require benchtop instruments whose features regarding, especially, sensitivity and reproducibility cannot be compared to those of their portable counterparts. Therefore, since one of the objectives of this research work is to develop a portable VOC analyser, a third category has been included to review the commercially available portable instruments for VOC detection.

1.2.1 Chromatographic methods (GC-TCD/PID/FID/MS)

Gas chromatography (GC) is an analytical separation technique widely employed in air quality analysis. The schematic diagram of a gas chromatograph is shown in Figure 1-4. The system is composed of three parts: an injector, a chromatography column placed inside an oven and a detector. In gas chromatography, a sample of a known volume is injected into a separation column where a carrier gas (usually an inert gas like helium, nitrogen or hydrogen) is continuously flowing through. The internal surface of the column is coated with a stationary phase that determines the separation properties of the column. Analytes contained in the sample interact with the stationary phase to a different extent depending on the strength of the interactions between them. The stronger the interaction, the more retained is the molecule and the longer is the time required for it to leave the

column, as illustrated in Figure 1-5. In this way, molecules are separated in the column arriving to the detector at different times, named retention times. Retention time is characteristic of each compound and it depends on the flow rate, the temperature and the characteristics (length, internal diameter and thickness) of the chromatography column. Once the analytes leave the column, they are quantified by means of a detector. Several detectors can be coupled to gas chromatography, and the choice will depend on the target compounds, the range of concentrations and the time resolution required. In air quality analysis, sensitive detectors with limit of detection (LOD) in the order of ppb or ppt are necessary. The most common detectors employed in gas chromatography are described below.

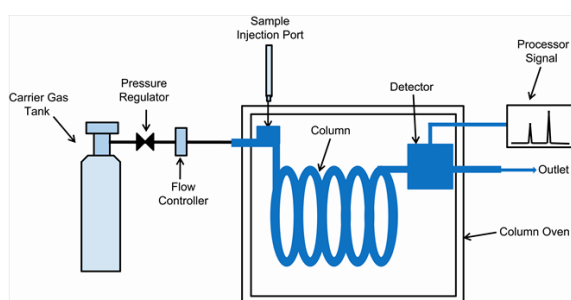


Figure 1-4. Schematic diagram of a gas chromatograph [55]

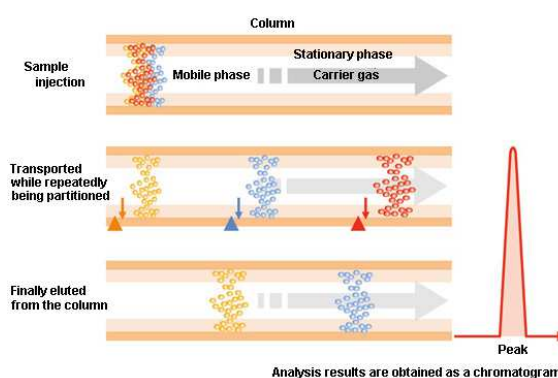


Figure 1-5. Analyte separation in a chromatography column [56]

Thermal conductivity detector (TCD)

The operating principle of a thermal conductivity detector (TCD) is based on the difference in thermal conductivity of a reference flow of carrier gas and the gas flow containing the sample. The presence of organic compounds usually reduces the total thermal conductivity of the sample gas flow, creating a difference between the conductivity of the reference and the sample flows that is measured and converted into a digital signal. Since most compounds produce a change in thermal conductivity, TCD is considered a universal detector. TCD is low cost, simple to use and has the advantage to be a non-destructive analytical technique. Its poor sensitivity (\sim ppm) compared to flame ionization detector (FID) or mass spectrometry (MS), however, limits its use in indoor air quality monitoring where the pollutant concentrations are generally in the range of ppb.

Flame ionization detector (FID)

The working principle of a FID resides in the ionization of molecules, and in this technique, the energy source employed is a flame. Compounds leaving the chromatography column are burnt in a flame resulting from the combustion of hydrogen in air. Only organic compounds, especially hydrocarbons, will be ionized by the flame producing ions. The produced electrical current is proportional to the concentration of the compounds in the sample gas flow. This current is collected by an electrometer, converted and sent to an output device. FID are known for their high sensitivity having LOD in the range of ppb and even tens or hundreds of ppt. Additionally, they have a large linearity interval and low maintenance requirements. The main issues of these detectors are the operation and safety hazards associated to the use of hydrogen as a burner, implying the use of either a hydrogen generator or a hydrogen gas cylinder of high purity.

Mass spectrometry (MS)

Mass spectrometry (MS) is an analytical technique widely employed in the analysis of airborne VOC, particularly of complex mixtures, since it allows not only the quantification, but also the identification of compounds. In MS, the molecules are ionized by means of an ion source causing the molecules to become charged or broken into charged fragments. These fragments are introduced in an analyser, accelerated in an electric or magnetic field and separated according to mass-to-charge ratio due to their different amount of deflection. Depending on the type of ion source, VOC molecules yield characteristic fragmentation patterns enabling the identification of the analysed molecule. Finally, the beam of ions is detected electrically and converted into a digital signal which is proportional to the concentration of the analyte in the sample. MS, along with FID, is one of the most sensitive techniques (LOD ~ ppt) but with the additional advantage of a wider spectrum of compounds that can be measured. In contrast, ultra-high vacuum is required in the analyser for ions separation, which implies the need of primary and secondary vacuum pumps and extremely pressure tight and leak-free systems.

Photoionization detector (PID)

A photoionization detector (PID) uses an ultraviolet (UV) lamp to ionize organic compounds. Generally, any compound with ionization energy (IE) lower than that of the lamp photons can be measured. The resulting electrons and ions are collected on the electrodes, generating an electrical

current that is proportional to the concentration of the ionized molecules in the sample. Usually, the commercial UV lamps are of 9.6, 10.0 or 10.6 eV, enabling the ionisation of several VOC compounds including aromatics and certain aldehydes. The main drawbacks of this technique are the regular maintenance of the UV lamp and the low selectivity due to the broad range of compounds with low IE. However, selectivity can be enhanced when the PID is coupled to a GC column, allowing the individual quantification of each compound. Moreover, PID are able to measure VOC over a wide range of concentrations (from ppb to ppm) and can be highly sensitive with LOD down to 0.5 ppb [57]. This type of detector is not destructive, enabling the coupling of other detectors to increase the range of VOC measured.

In this work, a miniPID was the detector selected for the compact BTEX analyser developed due to its reduced dimensions, simplicity of operation and suitability to detect the target compounds in the desired range of concentration.

1.2.2 Non-chromatographic methods

Other non-chromatographic methods such as spectroscopic methods are also used for VOC detection, but generally to a lesser extent than the techniques based on gas chromatography. Some of these techniques are based on the interaction of matter with electromagnetic radiation [58]. They have low LOD and relatively high time resolution; however, the large size and weight of most of these instruments limit their application for on-site measurements. Furthermore, their price is generally higher than those based on gas chromatography. The most commonly employed non-chromatographic techniques are briefly presented below.

Proton-Transfer-Reaction Mass Spectrometry (PTR-MS)

Proton-transfer-reaction mass spectrometry (PTR-MS) is a relatively new technique for VOC trace detection by combining chemical ionization and drift tube technologies. In this method, an ion source generates H_3O^+ ions that ionize VOC molecules by proton transfer reactions inside a drift tube. Subsequently, the ions are separated and detected by a mass spectrometer. It is considered a highly sensitive technique with LOD ranging from 10 to 100 ppt. Additionally, it provides a fast response time of nearly 1 s [59] allowing real-time measurements. Apart from the price, the principal technical limitation of this technique resides in the lack of discrimination between compounds having the same molecular weight, i.e. ethylbenzene and xylene isomers.

Differential Optical Absorption Spectroscopy (DOAS)

Differential optical absorption spectroscopy (DOAS) is a method frequently employed in atmospheric chemistry to measure concentrations of trace gases [60]. It is based on the analysis of the UV to visible absorption spectrum of a gas sample over a long path. As VOC molecules travel along this path, they leave a specific molecular absorption imprint that can be mathematically extracted and compared to a reference, enabling the determination of the VOC concentrations [61]. Optical paths are usually between several hundred meters up to 20 kilometres [62], [63] resulting in very low LOD for VOC ranging from ppb to ppt. Therefore, this technique is suitable for real time measurement of airborne pollutants at trace concentrations. Apart from the price and the size, their main limitations are the attenuation of UV light due to the absorption of oxygen, ozone or other VOC present in the ambient air [64] and the need of regular calibration to ensure reliability of the data owing to the sensitivity between pixels over time [65].

Infrared (IR) spectroscopy

Infrared (IR) spectroscopy is an analytical method based on the molecular absorption of IR radiation. IR light is passed through a gaseous sample and the difference between the emitted and the detected light is measured. The IR absorption spectrum of a molecule in the infrared range, i.e. from 0.7 μm (near-IR) to 1000 μm (far-IR), provides information about the concentration and the structural properties of the VOC molecules. In this spectrum, the existence of absorption bands at certain frequencies or wavelengths is associated with the presence of functional groups in the structure, and the intensity of the signal is related to the concentration of the molecules. The LOD for most VOC varies from 0.1 to 20 ppm [66]. Nevertheless, this sensitivity can be enhanced to the ppb range by integrating with Fourier transform technology (FT-IR) [67]. Difficulties have been encountered for the analysis of complex mixtures since overlapping of peaks belonging to different gaseous molecules can lead to non-negligible errors in the VOC quantification [68]. The other major limitation of this technique is the size and the high cost of the equipment due to the price of optical components, such as light sources, photo detectors, and lenses. In addition, liquid nitrogen is often needed to reduce the detector noise, implying a continuous and regular maintenance.

1.2.3 Portable devices for air quality monitoring

Due to the growing concern about air pollution, legislation in this area is becoming more restricted, leading to an increasing need of on-site measurements for air quality monitoring. To this purpose, several portable devices for VOC monitoring have been developed in the last years. In Table 1-1, a summary of the most relevant commercially available portable and transportable devices for VOC monitoring is presented.

As it is obvious from the table, most of the portable instruments for VOC detection are based on GC coupled to a PID. This technique is easy to implement, and components have a moderate cost in comparison with other techniques such as the spectroscopic methods. Additionally, these devices can achieve LOD in the order of ppb without preconcentration step, and can operate within a wide range of temperature and relative humidity conditions, making them a practical option for BTEX analysis although this kind of detector is quite specific to aromatic species and cannot detect all the VOC.

Current legislation set a threshold limit value of 1.6 ppb and 0.6 ppb for benzene in public buildings in the European Union and France, respectively. Only HAPSITE® ER, μ BTEX-1 and Pyxis GC are able to detect the concentration established by the European legislation and only two of them meet the requirements of the recent French regulation indicating that sensitive analysis with portable instruments still remains a challenging issue. On the other hand, the most portable instrument, i.e. VOC TRAQ II, only provides a total VOC measurement since no separation step is integrated in this system. Usually, higher sensitivity is associated to longer analysis times and bulky instruments, as in the case of HAPSITE® ER where the LOD is in the ppt range but its weight of 19 kg is at the limit of what can be considered portable. Pyxis GC and μ BTEX-1 are certainly the best compromises between reasonable weight and high sensitivity. Furthermore, their times of analysis vary between 10 to 15 min, allowing the elaboration of concentration-time profiles that are of vital importance in the identification of pollution sources and the quantification of the occupational exposure. The only disadvantage of these instruments is the limitation of target compounds to BTEX unlike other technologies based on MS or IR, which then are able to detect a broad spectrum of VOC. It is important to mention that significant progress has been made in recent years to reduce the gas consumption of the instruments. Currently, the trend in portable chromatography is the use of ambient air as carrier gas, eliminating the need of pressurized gas cylinders and increasing portability.

Table 1-1. Commercially available portable instruments for VOC detection

Reference	Analysis Technique	Carrier gas and consumption (mL/min)	LOD	Analysis time	Target compounds	Autonomy (h)	Dimensions h × w × d (cm)	Weight (kg)
MX908 [69, p. 908]	HPMS	n. r.	10 to 50 ppb ^a	s - min	Explosives, CWA, drugs	> 3	29.8 × 21.6 × 12.2	3.9
HAPSITE® ER [70]	GC/MS	N ₂	~ ppt (most analytes)	< 10 min	VOC, TIC, CWA, SVOC	2-3	46 × 43 × 18	19
GX-6000 [71, p. 6000]	PID	n. r.	10 ppb (benzene) 1 (TVOC)	n. a.	Benzene + VOC	14	20 × 6.8 × 5.2	0.4
PHA-100 [72]	FOCS		< 10 ppm (xylene)	~ min	C ₆ and higher MW	8	30 × 25 × 18	4.5
BTEX Mod. 530 [73]	GC- FID/PID	H ₂ : 30, Air: 300 N ₂ : 10	0.1 µg/m ³	15 min	BTEX	n. a.	25 × 48 × 56	15
VOC-TRAQ II [74]	PID	--	0.5 ppb	~ s	Total VOC	--	9.1 × 2.5 (length × diameter)	0.054
DX 4040 [75]	FT-IR	n. r.	100 ppb (BTEX) > 10 ppb (VOC)	1 min	Organic and inorganic gases	2.5	16.1 × 39 × 40.6	13.8
PID analyzer [76]	GC PID	n. r.	~ ppb	n. a.	BTEX and VOC	n. a.	n. a.	7
FROG 4000[77]	GC-PID	A. A	~ ppb	5 min	BTEX and VOC	6	25.4 × 19.1 × 36.8	2.2
µBTEX-1 [78]	GC-PID	N ₂ : 2.5	1 ppb (benzene)	10 min	BTEX	> 4	32 × 28 × 15	6
			0.05 ppb (benzene)	30 min				
PyxisGC [79]	GC-PID	A. A	0.3 ppb (benzene)	15 min	BTEX	n. a.	42.5 × 32.5 × 18	11.5

HPMS: High-pressure mass spectrometry; FOCS: fiber optic chemical sensor; CWA: chemical warfare agents; TIC: toxic industrial chemicals; SVOC: semi-volatile organic compounds; MW: molecular weight; n. a.: information not available; A.A.: ambient air; n. r.: not required; ^aReal time mode;

Nevertheless, there are still some portable GC devices using nitrogen, but the consumption has considerably decreased (\sim mL/min) compared with the previous generation of portable gas chromatographs (\sim 10 - 50 mL/min), increasing the autonomy of the current devices. This autonomy is, nowadays, limited by the energy consumption of such instruments. Most of current portable VOC analysers are battery-powered; however, the autonomy is generally limited from 2 to 6 h, preventing their use for long periods without power supply. Recent trends in portable devices to reduce energy consumption consist of eliminating the functionalities related to the data display and treatment from the instrument, resulting in less energy-consuming components such as screens or electronic cards. Instead, the devices are connected to a cloud where the data can be treated, stored and easily accessible via phone, tablet or PC.

In conclusion, great efforts have been made in the last decade to develop sensitive VOC portable analysers for air quality monitoring; however, there is still room for improvement, especially in terms of sensitivity, range of detected compounds, size and autonomy.

1.3 Gaseous VOC Preconcentrators: state-of-the-art

In the last decades, much research has been dedicated to shed light on the serious health effects caused by air pollution [4], [80]. As a consequence of these studies, most European countries have become aware of the importance of air quality and more stringent indoor air quality regulations are being established. In France, such regulations set the exposure limits for formaldehyde and benzene in indoor air of public buildings to $30 \mu\text{g m}^{-3}$ (24.4 ppb) and $5 \mu\text{g m}^{-3}$ (1.6 ppb), respectively. For benzene, even stricter limits of $2 \mu\text{g m}^{-3}$ (0.6 ppb) are set since 2018 (Decree No. 2011-1727 of 2 Dec. 2011). Therefore, a very sensitive analysis is required to check if IAQ in public buildings is in accordance with the new legislation. Miniaturized detectors or sensors are usually employed in transportable and portable analytical instruments but their LOD are in the order of 1 ppm. In these instruments, preconcentration devices are typically integrated to decrease the LOD to ppb levels required for on-site VOC monitoring.

1.3.1 Principle of thermal desorption

Preconcentration devices consist of a cavity filled or coated with an adsorbent to capture VOC molecules. The working principle of preconcentrators (PC) is based on the adsorption of VOC

followed by the thermal desorption of gaseous molecules from the adsorbent (see Figure 1-6). First, a given volume of sample flows through a solid adsorbent either by active flow using an air pump or through passive exposure. The analytes are then captured on the adsorbent. This step is typically conducted at room temperature or, in some cases, down to $-30\text{ }^{\circ}\text{C}$ to promote the analytes adsorption. The preconcentrator is then rapidly heated to relatively high temperatures ($200 - 350\text{ }^{\circ}\text{C}$) and the molecules are desorbed into a much smaller volume, thus increasing the analytes concentration in the sample prior to the analysis. Afterwards, a carrier gas directs the preconcentrated sample to the chromatography column for analytes separation.

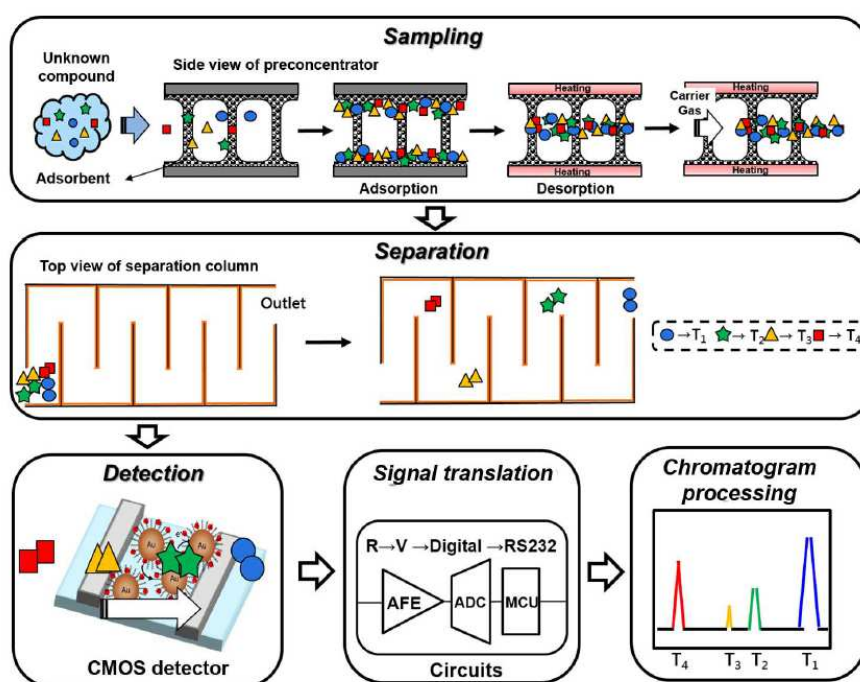


Figure 1-6. Working principle of a μGC [81]

In this regard, the efficiency of the preconcentration step depends on several factors:

- The physico-chemical properties of the adsorbent that determines the total amount of analyte adsorbed and the strength of adsorbate-adsorbent interactions: a well-chosen adsorbent is supposed to trap all the targeted gaseous molecules;
- The kinetics of the desorption process;
- The experimental conditions employed: the adsorption/desorption gas flow rates and the heating rate;
- The dead volume of the setup.

The experimental setup, the conditions and the preconcentrator itself are completely different in each study, rendering difficult the comparison of different PC in terms of preconcentration performances. The performance of any preconcentration technique is generally characterized by a figure of merit called preconcentration factor (PF). Several definitions are adopted for PF , as for example the ratio between the initial concentration of the sample and the concentration after the desorption [82]. PF can be also calculated as the ratio between the peak areas obtained with the empty PC and the PC filled with the adsorbent [83], [84]. Other authors determine PF as the ratio between the peak area obtained with and without PC [85], [86], which is close to the very first definition above. In this work, this method has been adopted since it allows comparing the analytical performances of a GC system without and with preconcentration step, and thus quantifying the improvement over the original GC version. However, although PF is frequently used to characterize the PC performance, it is not an intrinsic property of the preconcentrator itself [87]. Regardless the definition adopted, it depends on several factors such as analyte concentration, sampling time, flow rate, desorption temperature, heating rate and system dead volume. The preconcentration step is schematized in Figure 1-7.

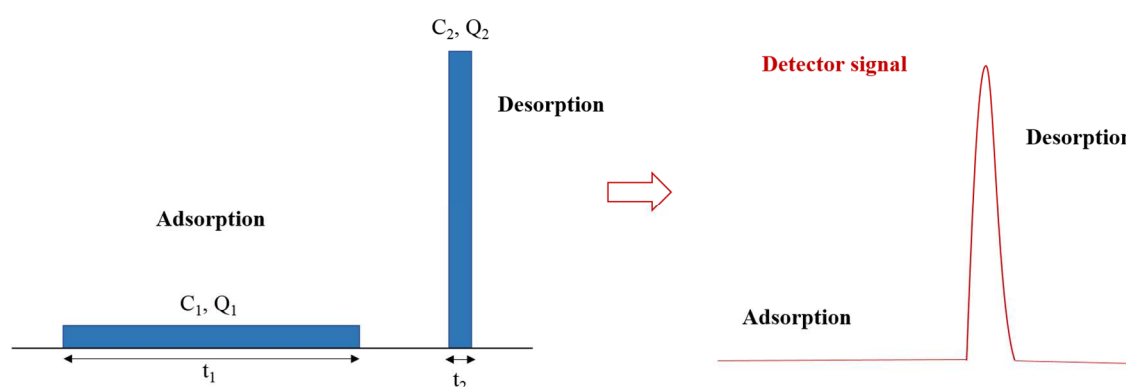


Figure 1-7. Diagram of adsorption-desorption cycle

Considering the diagram of an adsorption-desorption cycle and the conservation of mass, the preconcentration process can be roughly described by the following equation [88]:

$$C_1 t_1 Q_1 = C_2 t_2 Q_2 \quad \text{Eq. 1-1}$$

Where C_1 is the initial concentration, t_1 is the adsorption time, Q_1 is the flow rate during adsorption, C_2 is the average concentration after desorption, t_2 is the desorption time and Q_2 is the flow rate during

desorption. Since PF can be defined as the ratio between the initial concentration and the concentration after desorption, PF can be calculated as follows:

$$PF = \frac{C_2}{C_1} = \frac{t_1 Q_1}{t_2 Q_2} \quad \text{Eq. 1-2}$$

Since the objective of preconcentration is to increase the sensitivity of a method and therefore to maximize PF , the most favourable experimental conditions to improve this factor can be easily inferred from Eq. 1-2. For the adsorption, long sampling times and high flow rates are obviously preferred to inject the maximum amount of analytes. However, close attention should be paid to not exceed the breakthrough capacity of the adsorbent under the experimental conditions selected, to avoid non-quantitative sampling. For desorption, low flow rate and short time are desired to generate a very sharp analyte pulse ensuring a maximum concentration. To achieve a complete desorption in a very short time, the optimal temperature for desorption of analytes must be rapidly reached. Therefore, the faster the temperature ramp, the better.

In the GC system employed in this work, the desorption flow rate was fixed to 2.5 mL/min since the carrier gas of the GC column was used to inject the concentrated sample into the column. However, other aspects have been improved through this research work to increase the performances of the preconcentration step. For example, a reduction of heat capacity to speed up the temperature increase and, consequently, the time needed for a complete desorption. Several flow rates were tested to determine the maximum adsorption flow rate without analytes breakthrough. Finally, dead volumes of the setup were minimized as much as possible to avoid dilution before quantification.

1.3.2 Recent developments and trends in miniaturized gas preconcentrators

Because of the high demand of sensitive analytical instruments, several gas preconcentrators have been developed in the last decades for a wide variety of applications such as early cancer diagnosis [89]–[91], air quality monitoring [92]–[94], personal exposure [93], [95], [96], explosives and warfare agents detection [84], [97]–[99]. In this section, the most recent developments on VOC preconcentrators are reviewed in detail and their main characteristics, performances and future challenges are presented.

The first preconcentrators were developed in the 1980s. These tube-shaped devices were made of stainless steel or glass and usually filled with granular carbon or polymer-based adsorbents, i.e. Carbopack and Tenax®, whereas the heating system consisted of a metal wire coiled around the tube [100], [101]. Nowadays, similar models are commercialised for sampling applications (see Figure 1-8). These devices had large dead volumes and high heat capacity, which resulted in a limited heating efficiency and high-power consumption. To overcome these limitations, MEMS techniques began to be used for the fabrication of analytical devices. In 1999, the first MEMS-based PC was developed by Casalnuovo *et al.* [102] as a part of μ ChemLab™, a miniaturized GC for the detection of chemical warfare agents (CWA) and explosives. The PC consisted of a polymer-coated micro hotplate with Pt heaters, as displayed in Figure 1-9.



Figure 1-8. Sampling tubes commercialised by Sigma Aldrich [103]

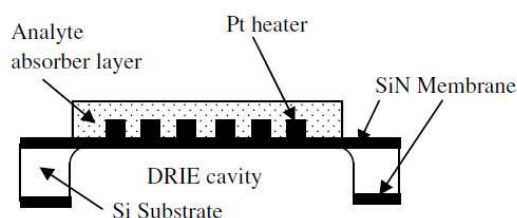


Figure 1-9. Schematic view of the first MEMS PC with a cavity etched by deep reactive ion etching (DRIE)

The use of MEMS technology opened new avenues concerning the development of analytical devices since they allowed to significantly reduce the size, the thermal mass and the power consumption of these devices. From that moment, multiple MEMS-based preconcentrators were developed with a wide variety of microstructures and geometries exhibiting great performance with very low power consumption. They were integrated into portable GC systems, leading to a considerable improvement of the sensitivity of these instruments. The use of these devices, however, presented also several drawbacks. For example, the materials typically employed for the fabrication, i.e. silicon and glass, are fragile and expensive. Due to their fragility and small dimensions, there are almost not commercially available fluidic and/or electrical connections, which often leads to leakages and renders difficult their integration in GC systems. In addition, the fabrication process requires suitable facilities (cleanroom) and high level of expertise, which results usually in an expensive and time-consuming process. All the foregoing, together with the difficulty to produce reliable and reproducible systems, has delayed their commercialisation. However, since demand for air quality monitoring is constantly increasing, the current trend is to fabricate more robust and low-cost devices able to demonstrate

satisfactory performance for a reasonable price. Although most of the preconcentrators reported in the literature are still fabricated using MEMS techniques, even if in the last years, some PC have been fabricated using other techniques. A summary of the most significant portable GC including a PC developed in the last 5 years is presented in Table 1-2.

1.3.2.1 *Materials used*

Ideally, the material employed for the fabrication of a PC should be thermally resistant to preserve its structure after several adsorption-desorption cycles. In addition, it should enable an effective heat transfer from the heating system to the adsorbent to promote a fast desorption of analytes. In this regard, a low heat capacity is also desired to allow a fast temperature ramp. MEMS technology has been widely used for the fabrication of PC; therefore, most of these devices are made of materials related to the electronics industry. So far, silicon has been the most employed material due to its relatively high thermal conductivity and the variety of techniques for its bulk micromachining. For example, wet etching using hydrofluoric acid or KOH serves to create microfluidic cavities and channels in silicon at a relatively low cost compared to other etching techniques [110], [115]. However, the most widespread technique is the deep reactive ion etching (DRIE) that offers the possibility to build high-aspect-ratio structures such as cavities, channels and pillars of different geometries as shown in Figure 1-10a. Although DRIE process is extremely slow for etching glass, this material has been nevertheless largely employed to fabricate preconcentration devices. Indeed, other techniques such as sandblasting [116] or wet etching with hydrofluoric acid [110] have been used for glass micromachining. Despite some PC entirely made of glass, in most cases, glass is used as a cover to seal the microfluidic cavity since it allows to see the inside of the device and can be bonded to silicon by an ordinary anodic bonding process. Besides, sandblasting enables to quickly create through-holes suitable for the integration of fluidic connections such as capillary tubes. Laser etching technology, milling or metal 3D printing techniques have been recently employed for PC fabrication. These techniques provide the possibility to use more robust materials such as copper [123] or stainless steel [105] at a lower cost (see Figure 1-10b and 1-10c). Furthermore, better gas tightness compared to MEMS-based devices is expected since their dimensions are generally larger and these materials can be machined to integrate standard fluidic connexions. However, larger dimensions involve higher heat capacity, resulting in high power requirements and slow temperature increase.

Table 1-2. Summary of micro preconcentrators developed in the last years

Reference	Target compounds	Adsorbents	PC Microstructure and dimensions l (mm) \times d (μ m) \times w (mm)	Materials	Heating system	Power cons. (W) / Heating rate ($^{\circ}$ C s $^{-1}$)	Detector and LOD (ppb)	Application field
[104]	BA, EB,p-X	Tenax-TA	Cavity filled with U-shaped micropillar array	Si-glass	-	-	FID	-
[96] PEMM-2	9 VOC	C-B 2.0 mg C-X 2.3 mg	2 Cavities ($V \sim 4.7 \mu$ L) 20 mm (l) \times 15 μ m (d) \times 9 cm (w) ^a	Si-glass	Pt	1 / -	μ CR array 16–600	Environmental monitoring
[105]	Toluene	HayeSep D 119.9 mg	Tube with cylindrical micro-pillars 38.68 mm (l) \times 7.69 mm (o. d.)	Stainless steel	NiCr wire	14.6 / 1.8	MS	-
[86]	Ethane	CNT Foam	Rectangular cavity 13 mm (l) \times 1.5 mm (d) \times 11 mm (w)	Si-glass	Pt	4.8 / 25	FID	Breath analysis
[85]	Isoprene	C-X 20 mg	Manifold-shaped with 4 μ channels of 12.6 mm (l) \times 2.5 μ m (d) \times 16 mm (w)	Copper	Ceramic	10.14 / 5.5	FID 0.016	Breath analysis
[89]	4 VOC	Zeolite DaY $\sim 13 \mu$ m	Cavity with micro-pillars 10 mm (l) \times 400 μ m (d) \times 5 mm (w)	Si-glass	-	-	MOS 5 – 2515	Breath analysis
[106]	BTEX	Tenax TA	Tapered cavity 21 mm (l) \times 400 μ m (d) \times 7.6 mm (w)	Si-glass	Pt	- / 19	MS	Breath analysis
[107]	Ethylene	CBS-II 1.187 g	Manifold shaped cavity 61 mm (l) \times 5.5 mm (d) \times 23 mm (w)	Ceramic	Tungsten	18 / 0.25	EC	Food industry, environmental monitoring
[108]	Benzene, toluene, styrene	SWCNT 0.15 mg	Four parallel channels of 350 μ m (d) 10 mm (l) with micropillars	Si-glass	-	-	PID	Environmental monitoring
[109]	BTEX	EtQxBox 10 mg	Parallel channels 25 mm (l) \times 1.3 mm (d) \times 12 mm (w)	Si-glass	Pt	- / 50	PID 1.25 ^b	Environmental monitoring
[110]	12 VOC	Tenax TA ~ 7 mg	Square cavity 2.54 cm (l) \times 2.54 cm (d) (whole chip)	Glass	2.8 / 17.6	-	FID 22	-
[83]	Toluene, m-xylene	Tenax-TA $\sim 3.7 \mu$ m	Tapered cavity with micropillars 9 mm (l) \times 400 μ m (d) \times 5 mm (w)	Si-glass	Gold	- / 75	FID	-

[111]	Ethylene	CBS-II 191.0 mg	8 parallel channels 40.0 mm (l) × 0.9 mm (d) × 2.0 mm (w)	Glass-Si- Glass	Tungsten	-	EC 3.8	Food industry
[81]	7 VOC including BTX	Carbon film	Cavity with micro-pillars 10 mm (l) × 250 mm (d) × 2 mm (w)	Si-glass	NiCr wire		CMOS 15 (1,3,5- TMB)	Breath analysis
[112]	Acetone	CBX 1012 ~ 4 mg	Spiral microchannel 120 mm (l) × 0.35 mm (d) × 0.35 mm (w)	Si-glass	Pt	4.52 / -	SCGSA 800	Breath analysis
[112][113] ¹¹³ (Michoń et al., 2016)(Micho ń et al., 2016)	Acetone	CBX 1018 0.95 - 11.3 mg	Tube 0.2 mm (i.d.) × 0.4 mm (o.d.) × 46.8 mm (l)	Glass	Ni-Cr wire	8.57 / -	SCGSA	Breath analysis
[112]	Acetone	CBX 1018 0.95 - 11.3 mg	Tube 0.7 mm (i.d.) × 1.2 mm (o.d.) × 38.2 mm (l)	Stainless steel	Ni-Cr wire	17.67 / -	SCGSA	Breath analysis
[92]	Benzene	HKUST-1 ~ 30 mg	Hotplate 3 mm (l) × 3 mm (w)	Alumina	Alumina	0.43 / -	MOX	Environmental monitoring
[114]	4 VOC	CB + Tenax	Tubular rolled plate 140 mm (l) × 600 (w)	Polyimide foil	Gold	1.7 / 40	PID	Explosives detection, security
[115]	Hexane	Silicalite 1 4.4 mg	Tapered cavity (A) ~54.0 mm (l) × 10 mm (w)	Si-glass	Gold	8 / -	MS	Occupational exposure
[115]	Hexane	Silicalite 1 4.1 mg	Tapered cavity (B) ~54.0 mm (l) × 10 mm (w)	Si-glass	Gold	8 / -	MS	Occupational exposure
[115]	Hexane	Silicalite 1 4.6 mg	Tapered cavity with pillars (C) ~54.0 mm (l) × 10 mm (w)	Si-glass	Gold	8 / -	MS	Occupational exposure
[115]	Hexane	Silicalite 1 4.7 mg	Tapered cavity with pillars (D) ~54.0 mm (l) × 10 mm (w)	Si-glass	Gold	8 / -	MS	Occupational exposure
[116]	19 VOC	C-B + C-X	U shape n.d. (l) × 300 mm (d) × 1350 mm (w)	Glass	Pt	10.5 / 46	Capacitive 10 – 2 (BTEX)	Environmental monitoring
[117]	50 VOC	C-B 1.135 mg	Tappered cavity 8.15 mm (l) × 250 mm (d) × 2.9 mm (w)	Si-glass	Pt	- / 314	PID	Environmental monitoring, food industry, biomedicine

[118]	Benzene	SWCNTs (0.15 mg)	4 microchannels 400 μm (d) \times 1000 μm (w)	Si-glass	Pt	- / 3.5	PID	Environmental monitoring
[119]	6 VOC	Tenax TA ~200nm	Square cavity pillars 10 mm (l) \times 240 mm (d) \times 10 mm (w)	Si-glass	Ni	16 / -	TCD ~ 1 ng	Environmental monitoring
[120]	17 VOC	C-X 1.4 mg C-B 2.0 mg	2 tapered cavities 380 μm deep	Si-glass	Pt	- / -	FID	Occupational exposure
[84]	ONT	Zeolite DaY 2.25 mg C-B 3 mg	Rectangular cavity with pillars 5 mm (l) \times 400 mm (d) \times 10 mm (w)	Si-glass	Pt	- / -	MOX 365	Explosives detection
[121]	10 VOC	C-X 2 mg C1000 1 mg	Tube 1.2 mm (i.d.) \times 8 cm (l)	Stainless Steel	NiCr wire	- / 75	PID 0.02 - 0.36	Environmental monitoring
[122]	TCE	C-X ~2.3 mg	Tapered cavity with pillars 3.2 mm (l) \times 3.5 mm (w)	Si-glass	Pt	- / 314	ECD 1.2	Environmental monitoring
[98]	2,4-DNT, 2,3- DMNB, 2,6- DNT	C-B 2.4 mg	Tapered cavity 3.2 mm (l) \times 3.5 mm	Si-glass	Gold	- / 314	0.067- 0.30	Explosive markers

C-B Carbopack™ B; C-X: Carbopack™ X; CBS-II: Carbosieve® II; CBX 1012: Carboxen® 1012; CBX 1018: Carboxen® 1018; C1000: Carboxen 1000; CNT Carbon nanotubes; QxCav: Quinoxaline bridged Cavitand; ^b: benzene; o.d.: outer diameter; i.d. inner diameter; CR: chemiresistor; MOS: Metal Oxide Semiconductor; CD: Capacitive Detector. CMOS: Complementary Metal Oxide MOX: Metal Oxide sensor; EC: electrochemical sensor; SCGSA: semiconductor gas sensor array; ECD: electron-capture detector; BA: butyl acetate; EB: ethylbenzene; p-X: p-xylene; 1,3,5 – TMB: 1,3,5-trimethylbenzene; ONT: orthonitrotoluene; TCE: trichloroethylene; 2,4-DNT: 2,4-dinitrotoluene; DMNB: 2,3-dimethyl-2,3-dinitrobutane; 2,6-DNT: 2,6-dinitrotoluene.

Other materials such as ceramics have been also employed for the fabrication of micro preconcentrators as displayed in Figure 1-10d [107], the use of ceramic technology reducing the manufacturing time and costs. Camara *et al.* [114] reported the use of more alternative materials such as polyimide foil for the fabrication of a PC (see Figure 1-10e). The main advantages of using this material are the low cost and easy processing since cleanroom facilities are not needed. Additionally, these PC are flexible, and the diameter of the inlet/outlet can be adjusted to work at higher flow rates, up to 1.5 L/min, much larger than in their silicon counterpart.

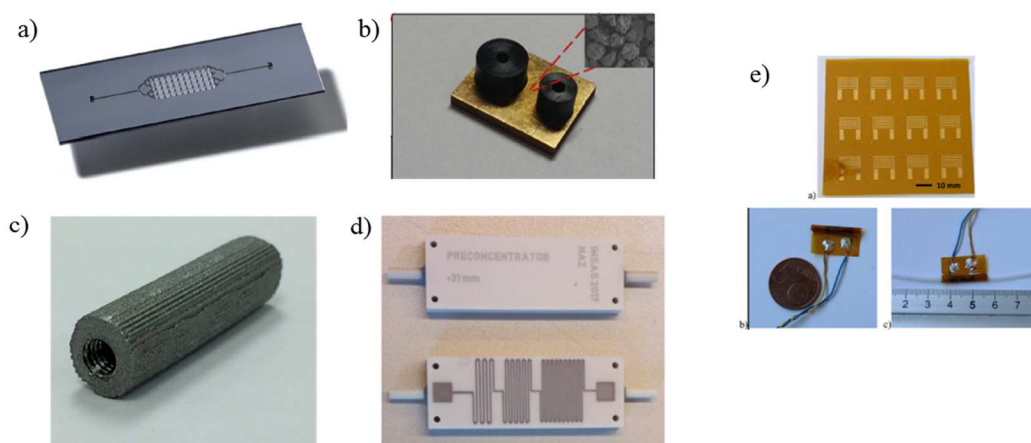


Figure 1-10. Micro preconcentrators made from diverse materials: (a) silicon-glass [89], (b) cooper [123], (c) stainless steel [105], (d) ceramics [107] and (e) polyimide foil [114]

1.3.2.2 Microstructures designs

According to their microstructure, preconcentrators can be divided into planar hotplates and three dimensional (3D) structures [124]. At first, most of PC consisted of a planar surface coated with an adsorbent selective to the target molecules, as shown in Figure 1-11. These devices had dead volume and the adsorption capacity was limited since only the surface of the adsorbent was exposed to the analytes. To overcome these limitations, 3D preconcentrators were later developed and currently, almost all the developed devices are 3D. To ensure a good performance of these 3D PC, several aspects should be considered for the design: uniform flow distribution inside the device, low pressure drops, large contact surface and long contact time between the adsorbate and the adsorbent to increase the probability of the molecules to be adsorbed and trapped.

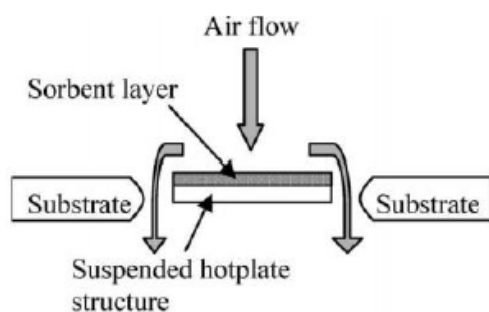


Figure 1-11. Schematic representation of a planar PC. Reprinted from [125]

In this regard, several geometries such as circular spiral [112], array of parallel channels [85], [94], U-shaped channel [116] have been reported for preconcentration devices, as shown in Figure 1-12.

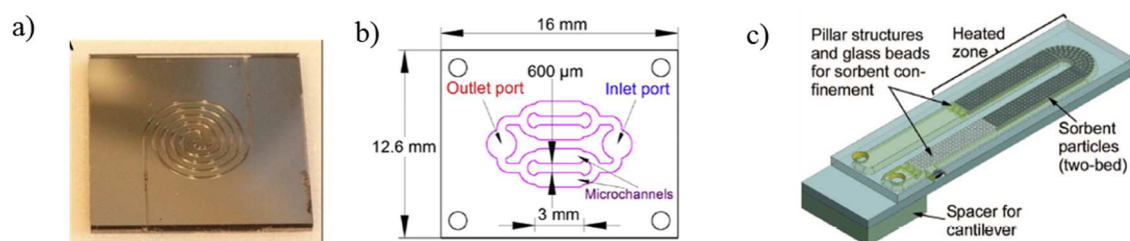


Figure 1-12. Preconcentrators with different geometries: circular spiral (a) [112], array of parallel channels (b) [85] and U-shape channel (c) [116].

Some of the one-single channel designs often shows relatively high pressure drops; hence, designs leading to lower pressure drop, such as a wide rectangular cavity connected to inlet and outlet channels [96], [107], [115], [126] are usually preferred. In these microdevices, prior to fabrication, flow simulations are frequently conducted to estimate the pressure drop and optimize the distribution of the gas flow. Li et al. [90] performed computational fluid dynamics (CFD) simulations and demonstrated the influence of the inlet angle on the flow field near the inlet (see Figure 1-13a). They reported that uniform gas flow velocity distribution can be achieved when the inlet and outlet triangular angles are smaller than 120° . Hence, it is very common to observe triangular inlets/outlets of these characteristics in micropreconcentrators [81], [83], as depicted in Figure 1-13b. Camara *et al.* [127] significantly improved the distribution of the gas flow in single channel preconcentrators by integrating a manifold fluidic system at the inlet/outlet of the device. Therefore, similar geometries have been later adopted by other authors [85], [89], [126], [128]. This type of system consists on the

split of the inlet/outlet channel in two channels and finally form a total of 16 narrow channels connected to a microfluidic cavity where the adsorbent is placed, as shown in Figure 1-13c.

Different microstructures are often found inside the adsorbent cavity. Their main function depends on the type of adsorbent employed. In PC filled with granular adsorbents, the presence of microstructures can improve the flow distribution without significantly reducing the amount of adsorbent that can be hosted [84].

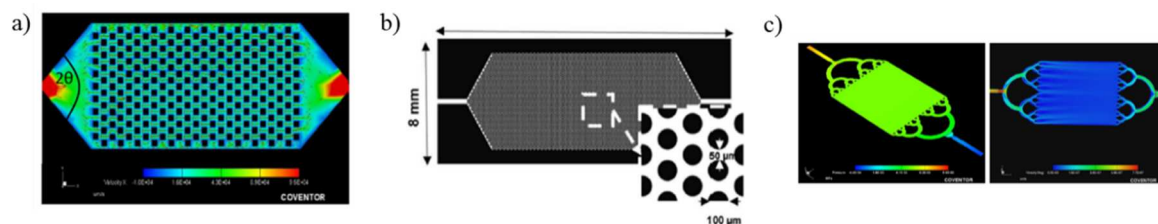


Figure 1-13. (a) Flow simulation in a PC with inlet/outlet angle $> 120^\circ$ [90]; (b) Preconcentrator containing micropillars and having inlet and outlet angles $> 120^\circ$ [81]; (c) Pressure (green) and flow velocity (blue) simulations in a PC with inlet/outlet manifold fluidic system [127]

Since most of the adsorbents have a low thermal conductivity, these structures serve to promote a more efficient heat transfer to the adsorbent bed [105]. In the case of thin films adsorbents, microstructures have a strong influence in preconcentration performance [129]. It is known that this type of adsorbents has a limited adsorption capacity due to the reduced surface exposed to the analytes. Therefore, the presence of microstructures inside the microfluidic cavity greatly increases the exposed surface, and additionally optimizes the path followed by the gas molecules, thus increasing their contact time with the adsorbent. Larger contact surface and longer residence time result in higher preconcentration performance due to the higher probability of the gas molecules to be adsorbed.

Alfeeli and Agah [129] studied the influence of the shape and the spacing of micropillars in preconcentration performance. Crisscross shaped pillars were found to be more efficient in terms of PF than ordered and staggered pillars. This PC contained more than 3500 micro pillars with dimensions of $30 \mu\text{m} \times 120 \mu\text{m} \times 240 \mu\text{m}$ and had a double inlet/outlet (see Figure 1-14a). The device was coated with 2,6-diphenylene oxide polymer (Tenax TA) and $PF > 10\,000$ was found for isopropanol. However, a great amount of 3D microstructures embedded within a microcavity can lead to high pressure drops. To minimize this increase, a low pressure drop design was proposed by Alfeeli

et al. [130]. This design consisted of an array of U-shaped pillars embedded within a 7 mm × 7 mm × 0.38 mm cavity. These pillars were arranged to divide the gas flow in the forward direction and combine the resulting two flows in the reverse direction, as displayed in Figure 1-14b. The spacing between the reflectors (side and middle spacing) was varied to investigate its effect on the device performance. The pressure drops of different pillars arrangements were investigated at a flow rate of 1.5 mL/min. The configuration with 300 and 150 μm of middle and side spacing, respectively, exhibited a pressure drop as small as 94 Pa. This configuration has been recently employed for the quantification of butyl acetate, ethylbenzene and p-xylene [104].

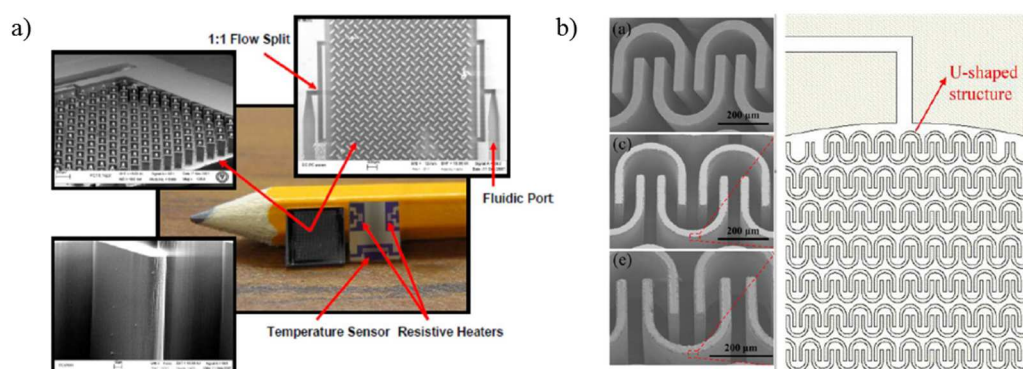


Figure 1-14. Preconcentrator containing crisscross shaped (a) [129] and U-shaped (b) [104] pillars

1.3.2.3 Heating system

During the preconcentration step, a very fast temperature ramp is needed for the flash desorption of analytes; therefore, the heating system is considered a key component of these devices. Faster is this rate, sharper the desorption peak and, thus, higher sensitivity and better chromatographic resolution can be achieved. However, since these devices are integrated in portable instruments and most of them are battery-powered, the energy required for a flash desorption of analytes should be limited to tens of watts. Hence, a compromise between heating performance and energy consumption is usually adopted. To this purpose, a wide variety of materials has been employed for the fabrication of these systems, as depicted in Figure 1-15.

Originally, the heating system of the first PC consisted of metal wires coiled around the devices [101]. Although some of these systems continue to be used today, the number of portable devices including this type of system is very small [81], [112], [121]. The material traditionally employed for these metal wires is Ni-Cr because of its high resistivity and almost constant temperature coefficient of resistance

(TCR) with temperature. These features render this alloy suitable for heating and temperature measurement applications [105]. Tzeng *et al.* [81] developed a micro gas chromatograph (μ GC) containing a MEMS PC coiled by a 6Ω Ni-Cr wire for the detection of seven VOC associated with lung cancer. Jian *et al.* [121] employed the same heating system for a stainless steel tubular PC integrated in a μ GC. This configuration required 12 V DC to reach $320 \text{ }^\circ\text{C}$ in less than 4 s. Nowadays, most of devices are fabricated by MEMS techniques integrating in-situ the heating systems. These systems consist of layers of resistive and conductive metals to form the resistive heater and the contact pads, respectively. Techniques such as e-beam evaporation [83] and sputtering [106], [110] are commonly used for metal deposition of a wide range of metals. Among them, platinum is one of the most used material in micro preconcentrator heating systems [84], [106], [116], [120], [131]–[133]. Similarly to Ni-Cr, platinum has a relatively high resistivity and constant TCR, rendering it suitable to act both as a heater and a temperature sensor. Heating rates from 3.5 to $314 \text{ }^\circ\text{C s}^{-1}$ have been reported in micro preconcentrators having heaters made of platinum. Although this metal presents better adherence to substrates than other metals, a metal layer such as titanium [106], [116], [122], [132] or chrome [134] is often employed to improve its adhesion to the substrate. Other less common metal combinations have been employed for the fabrication of heating systems like chromium-tungsten [110], chromium-nickel [119] and chromium-gold [98], [115]. Despite their widespread use, metal deposition processes by means of e-beam evaporation or sputtering are often tedious, and they involve the use of several photomasks. Kuo *et al.* [83] proposed to use electroless plating technology for the deposition of gold layers. This much simpler technique is based on the chemical reduction of gold and allows depositing high surface area gold layers on the surface of microchannels. Heating rates up to $75 \text{ }^\circ\text{C s}^{-1}$ were achieved in these devices.

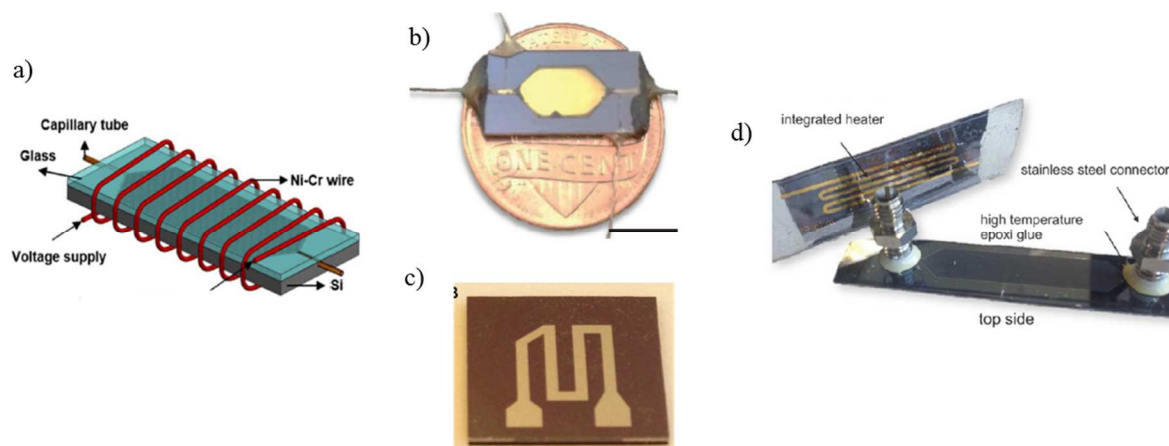


Figure 1-15. Diverse heating systems found in micropreconcentrators: (a) Ni-Cr wire [81], (b) gold layer deposited by electroless plating technology [83], (c) platinum heater [112] and (d) gold layer deposited by electron beam [115].

Heating systems consisting of metal layers are generally very effective for miniaturized devices; however, their fabrication requires cleanroom facilities and the resistances are relatively fragile. Since the layers are very thin, high voltages lead to a considerably deterioration of the heater due to high current density [119]. Furthermore, sometimes the adhesion to the substrate is not adequate and the metal layers can detach from the surface after several heating/cooling cycles. As alternative to the use of metal deposition, some groups have employed commercial ceramic heaters. Han *et al.* [85] reported the fabrication of a metal PC using ceramic heaters. This device reached 200 °C in 32 s with 10.14 W of supply power. These heaters provide reasonable heating power at a very low cost.

1.3.2.4 Adsorbent Materials

Apart from the previous specifications required and detailed above, a great part of the PC performance relies on the adsorbent employed. Their textural properties and chemical affinity to analytes will be determinant indeed for the efficiency of the adsorption/desorption process. In this regard, the desired features for an adsorbent are:

- Selectivity towards the target compounds. Ideally, the adsorbent should capture only the analyte of interest. In practice, the adsorption of a single compound is usually very challenging but during the preconcentration, some interfering species can be eliminated.
- High specific surface area. A large number of adsorption sites generally increases adsorption capacity and prevents early breakthrough.
- Moderate strength interactions with the adsorbate, enabling considerable adsorption and breakthrough capacity at room temperature and desorption at reasonable higher temperatures.
- Preservation of performances with regeneration cycles. A PC is expected to be continuously used; therefore, its performances must last throughout time.
- Low pressure drops and good thermal conductivity to minimize energy consumption and promote the fast desorption of analytes.

Traditionally, adsorbents have been distinguished in two categories: granular and thin films, although recently a new category of foam adsorbents is being developed. These three groups are displayed in Figure 1-16.

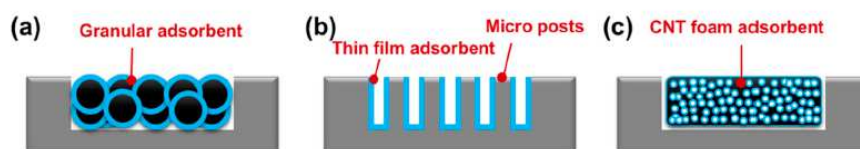


Figure 1-16. Schematic diagram of different categories of adsorbents employed in micro preconcentrators: (a) granular, (b) thin film and (c) foam adsorbents. Reprinted from [86]

Granular adsorbents have generally higher capacity than thin films since the grains are compactly packed, thus occupying almost all the volume available inside the PC. However, the complete filling of the microfluidic cavity usually results in high pressure drops. Most of these adsorbents are introduced inside the PC by suction [83], [110], [114], [128]. The other common method is to introduce a liquid dispersion [84], [134] in which adsorbent particles are suspended in a volatile solvent. The dispersion is inserted in the microfluidic cavity by depression and the solvent is then evaporated at room temperature. Graphitised carbon blacks are traditionally used for VOC preconcentration due to their hydrophobic character, which make them ideal candidates for VOC sampling in humid environments. Among them, the most common are Carbpac[®] B, which is recommended for the capture of C₅-C₁₂ molecules such as isoprene [123], and Carbpac[®] X, which is more suitable to trap C₃-C₉. Since these adsorbents are appropriate to trap compounds of intermediate volatility, they are considered to have medium strength. Most commonly, a combination of both adsorbents is employed to enlarge the range of analytes trapped [96], [116], [120]. Qin and Gianchandani [116] use this combination of adsorbents to preconcentrate a mixture of 19 VOC including aromatics, alkanes and halogenated compounds. Lee *et al.* [117] preconcentrate a gas mixture containing 50 VOC that is subsequently separated and detected by four independent GC columns and PID detectors. Carbon molecular sieves containing micropores are the adsorbents preferred for the trapping of very volatile compounds (C₂-C₅). These materials are considered as strong adsorbents. Carbosieve[®] II has been used for the preconcentration of ethylene [107], [111]. Rydosz *et al.* [112] used Carboxen 2012 for the preconcentration of acetone. A combination of molecular sieve with graphitised carbon blacks can be employed for the preconcentration of molecules differing in volatility. Jian *et al.* [121] developed a preconcentrator containing 3 mg of Carbpac[®] B, 2 mg of Carbpac[®] X, and 1 mg of Carboxen[®] 1000 for the analysis of 10 VOC mixture. In these cases, particular attention should be paid to the location of the adsorbents and the flow direction. Analytes of medium volatility are strongly adsorbed in molecular sieves, thus rendering difficult the subsequent desorption. Therefore, for sampling, adsorbents should be placed from the weaker to the stronger while the desorption should be carried

out in the opposite direction. Porous polymers as HayeSep® [135] and Tenax® [106], [110] are also commonly employed in preconcentration devices. Chappuis *et al.* [106] employed this latter polymer for the preconcentration of volatile tobacco markers. McCartney *et al.* [110] reported the preconcentration of a wide variety of VOC with a low cost PC filled with Tenax. Using this device, LOD down to 22 ppb were achieved with only 2 min of sampling. Metal organic frameworks such as HKUST-1 (commercially available as Basolite™ C300) have been used for the preconcentration of aromatic compounds [92], [126].

A general issue in gas preconcentration is the lack of selectivity of the employed adsorbents, which leads to the preconcentration of analytes but also interfering species. To tackle this issue, Zampolli *et al.* [94] synthesized in 2009 a quinoxaline based adsorbent named QxCav (see Figure 1-17a) for the selective preconcentration of aromatics compounds. This adsorbent has cavities of 8.3Å in which BTEX are adsorbed by means of weak CH- π interactions with the walls, whereas other non-aromatics molecules such as aliphatic compounds and water vapour are not retained. The same group recently developed an improved version of the adsorbent called EtQxBox [109], which structure is displayed in Figure 1-17b. In this complex, aromatics are selectively adsorbed and, additionally, toluene, ethylbenzene and xylene (TEX) are bind more strongly than benzene. The difference in the strength of interactions renders possible the benzene desorption at lower temperatures compared to TEX. This singularity allows the separation of analytes during the preconcentration step by control the temperature ramp and thus a GC column is no longer needed for the analysis.

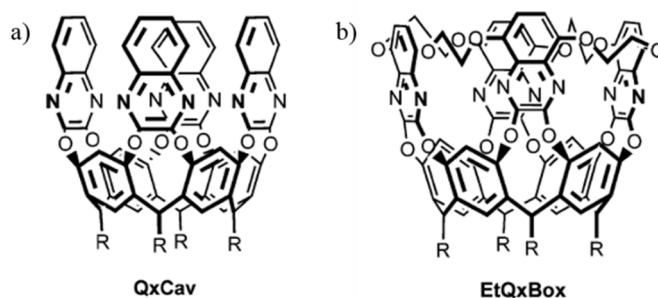


Figure 1-17. QxCav (a) and EtQxBox (b) cavitands employed for the selective preconcentration of aromatic compounds.
Reprinted from [109]

As it has been presented, granular adsorbents are widely employed in μ PC; however, their use is associated with high pressure drops. Additionally, heat transfer from the device to the adsorbent and between adsorbent particles is usually very poor, thus affecting the desorption rate. To decrease the pressure drop and improve the heat transfer, thin film adsorbents are thus employed. This type of

adsorbents is generally introduced into the microfluidic cavity in a suspension of a specific concentration followed by the evaporation of the solvent, leaving a film on the inner surface of the cavity [83]. Gregis *et al.* [89] employed a dispersion of a commercially available dealuminated zeolite (DaY) in ethanol to deposit a uniform 13 μm thick film. This system allowed the detection of toluene, o-xylene, propanol and cyclohexane at the low ppb levels, except for the cyclohexane. Other types of materials such as single-walled carbon nanotubes (SWCNT) have been deposited inside a micro PC for the quantification of VOC at trace levels [108], [118]. The use of this adsorbent is advantageous due to the large aspect ratio, high effective surface area, chemical and thermal stability and hydrophobicity. Other films have been synthesized inside the preconcentration device itself. For example, Tzeng *et al.* [81] and Wong *et al.* [136] presented in-situ-synthesized carbon adsorbent films for VOCs analysis. To this purpose, cellulose was inserted in a microfluidic cavity and then pyrolyzed at 600 °C under a nitrogen atmosphere to form the porous carbon film. This resulting adsorbent had a specific surface area of 308 $\text{m}^2 \text{g}^{-1}$ and the whole system exhibited a preconcentration factor of 13,637 for toluene. Almazán *et al.* [115] synthesized silicalite-1 inside of micro PC with diverse microstructures. These microstructures increased the inner surface of the PC and thus the amount of zeolite deposited compared to the empty PC. All PC filled with zeolite thin films showed higher preconcentration efficiency than their fixed bed counterpart, due to the uniform zeolite distribution along the inner surface. This homogeneity improved the gas–solid contact and thus adsorption/desorption processes and heat transfer. To increase the inner PC surface, Zhao *et al.* [104] proposed the formation of silicon nanowires as a surface template prior to the deposition of Tenax® inside the cavity. The use of this template increased the preconcentration performance of more than 188 % for butyl acetate compared to the PC only filled with Tenax®.

To improve the amount of adsorbent inside the cavity without greatly increasing the pressure drop, foam adsorbents have been recently developed. Lee and Lim [86] employed a carbon nanotube (CNT) foam for the preconcentration of gaseous ethane. For comparison purposes, the same PC was filled with Carbosieve™ SIII. Pressure drop was measured in both devices for flow rates from 1 to 5 mL min^{-1} . Pressure drops using the molecular sieve varied from 2,061 to 9,919 Pa whereas it was more limited with the CNT foam, where pressure drops ranged between 445 to 2,078 Pa. Therefore, the use of this adsorbent decreased of five times the pressure drops inside the PC.

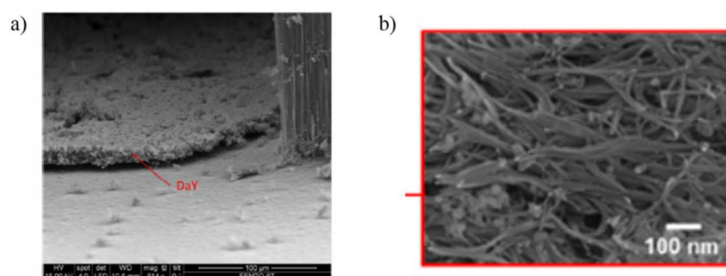


Figure 1-18. (a) Thin film layer of zeolite Day [89] and (b) CNT foam [86]

1.3.2.5 Applications

In the last decades, the quantification of a wide variety of VOC molecules has generated considerable research interest. These molecules are very often found at trace levels; therefore, μ GC integrating PC units have been developed for a broad spectrum of applications. One of the main applications is the air quality monitoring. Since it has been known that some gaseous compounds commonly present in indoor air have harmful effects on human health, diverse research groups have developed portable analytical systems for air quality monitoring. Wang *et al.* [96] developed a belt-mountable μ GC prototype to monitor personal exposure able to analyse a sample containing a mixture of 21 VOC in 3.5 min. This system has a LOD from 16 to 600 ppb depending on the compound. Trzciński *et al.* [109] reported the fabrication of a sensor prototype for environmental benzene monitoring. The PC integrated in this system contains an adsorbent that selectively desorbs benzene over other larger molecules, i.e. toluene, ethylbenzene and xylenes.

More recently, portable analytical systems for the detection of explosives or warfare agents have been also reported. Since these compounds easily degrade into a variety of species, the analysis is focused on these by-products instead of the explosive molecule itself. Mohsen *et al.* [84] designed a μ GC for the detection of an explosive-related compound, namely ortho-nitrotoluene. The system consisted of a silicon PC and a GC column coupled to a chemical gas sensor and allowed to detect up to 365 ppb of this compound in the presence of interfering compounds such as toluene and water. Collin *et al.* [98] presented a very compact GC for the quantification of 2,4,6-trinitrotoluene (TNT) derived products. For 1 L sample, LOD of 0.30, 0.067, and 0.12 ppb were achieved for 2,3-dimethyl-2,3-dinitrobutane (DMNB), 2,6-dinitrotoluene (2,6-DNT) and 2,4-dinitrotoluene (2,4-DNT), respectively.

Recent progress in medicine showed that some VOC are biomarkers of certain diseases [137]. These biomarkers are present in human breath at the ppb level; therefore, an accurate and sensitive analysis

in near real time may constitute a non-invasive method for early diagnosis of these serious diseases. To this purpose, several μ GC integrating PC units have been developed. Gregis *et al.* [89] reported a μ GC to monitor four biomarkers associated to lung cancer, namely propanol, toluene, o-xylene and cyclohexane. This system exhibited LOD of 24, 5, 21 and 112 ppb for toluene, o-xylene, propanol and cyclohexane, respectively. The LOD obtained for the first three compounds was maintained even in samples containing CO₂ and water levels similar to those found in real human breath samples.

Han *et al.* [123] reported a low cost PC for the preconcentration of isoprene which is one typical biomarker for the chronic liver disease found in human breath. Isoprene concentrations as low as 10 ppb can be achieved when this PC is coupled to a GC-FID. Despite the great advances made in the last years, high concentration of CO₂ (~ 40,000 ppm) and a relative humidity of 100 % at 25 °C present in human breath make that accurate analysis of human breath still a challenge.

1.4 Sorption/Desorption of VOCs

This section provides some scientific background about general adsorption process and, more specifically VOC adsorption, to help understanding the developed research work.

Sorption is a physical and/or chemical process of fixation of a substance (sorbate) by another substance in liquid or solid state (sorbent). Sorption describes two processes: adsorption, in which a substance is attached to the surface of another, and absorption, in which one substance enters within the bulk of another substance. Since in this work, only the adsorption of gaseous species on solid adsorbents has been studied, only the principles of the adsorption process for a solid-gas system are presented in this section. Additionally, the features of different adsorbents employed for VOC adsorption and the adsorption behaviour of the investigated VOC according to their structure and properties will be discussed.

1.4.1 Theoretical background

Adsorption is a phenomenon in which an adsorbate (gas, liquid or a dissolved solid) is attached to a surface (generally, a solid). This work is focused on the adsorption of gaseous organic compounds on solid surfaces. Obviously, this process is the result of the forces of attraction between the gas molecules and the atoms being part of the solid. According to the nature of these interactions, two types of adsorption can be distinguished: physisorption and chemisorption.

Physisorption (an abbreviation of “physical adsorption”) occurs when gas molecules are attached to a surface by means of Van der Waals interactions. These interactions are weak and the desorption energy when a particle is physisorbed is of the same order of magnitude as the enthalpy of condensation, typically in the range of 20 kJ/mol [138]. Such small interaction does not lead to a bond breaking, resulting in a rapid and reversible process in which the physisorbed molecule maintains its own structure.

By contrast, in **chemisorption** (an abbreviation of “chemical adsorption”) gas molecules are attached to the surface by chemical bonding causing changes in the structure of the adsorbate like in a chemical reaction. As chemical bonds must be formed, chemisorption is a highly specific process and it requires an activation energy. Consequently, the energy released when a chemisorbed molecule is desorbed is much greater than when it is physisorbed, exhibiting values around 200 kJ/mol. Due to these high binding energies, chemisorption is a non-reversible process.

In general, enthalpy of adsorption is the criterion employed to distinguish between the two types of adsorption. When enthalpy of adsorption is higher than -25 kJ/mol, it corresponds to a physical adsorption process whereas enthalpies lower than -40 kJ/mol are considered to represent chemisorption [138].

In most cases, adsorption is an exothermic process in which the amount of energy released depends on the adsorbate-adsorbent interactions, and in the case of high surface coverage, adsorbate-adsorbate interactions as well. Indeed, at high surface coverage, adsorbate molecules interact together, so that, if the particles repel each other, the adsorption process will be less thermodynamically favourable, and the enthalpy of adsorption will be less negative. Consequently, the adsorption will be less exothermic as the coverage increases [138].

Adsorption isotherms models

During the adsorption process, free gas and adsorbed gas are in dynamic equilibrium, as can be represented by the following equation:



where X is a free gaseous molecule, Z is an unoccupied site on the adsorbent surface and XZ represents the adsorbed gaseous molecule. According to Le Chatelier’s principle, when a system at equilibrium

is subjected to a change in concentration, temperature, volume, or pressure, the system changes to reach a new equilibrium. If pressure increases, the equilibrium changes to decrease the total number of gaseous molecules leading to an increase in the adsorption. To study the adsorption equilibrium, a representation of the surface coverage, which is the ratio between the occupied adsorption sites and the total number of adsorption sites, or the amount of gas adsorbed at equilibrium as a function of the gas partial pressure at a given temperature, called adsorption isotherm, is typically used.

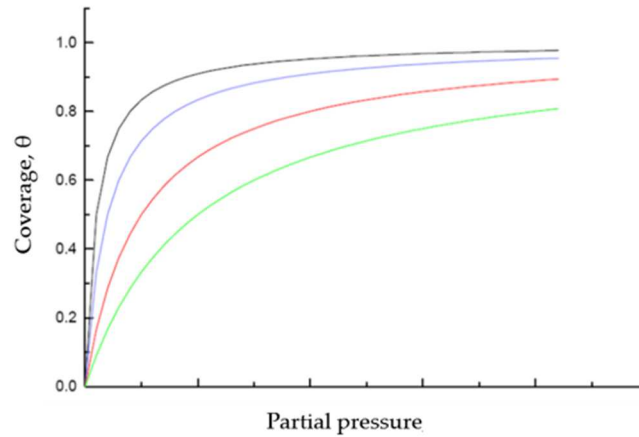


Figure 1-19. Example of adsorption isotherms at different temperatures from the lowest (black line) to the highest (green line).

An example of adsorption isotherms at different temperatures is presented in Figure 1-19. As can be observed, in all cases, surface coverage θ increases with increasing partial pressure P until saturation pressure P_0 is reached, which means that all the adsorption sites are occupied. From that point, no more adsorption occurs. The shape of the isotherm plot provides information about the porosity of the solid and the strength of adsorbate-adsorbent interactions. Several models based on different assumptions have been proposed to describe adsorption isotherms. The three most known models are described below.

Freundlich model

In 1909, Freundlich proposed an empirical equation describing the quantity of gas adsorbed by a solid with pressure at a constant temperature [139]. This equation is known as the Freundlich Adsorption Isotherm and it has the following form:

$$\frac{x}{m_a} = K_f P^{1/n_f} \quad \text{Eq. 1-4}$$

where x is the mass of the adsorbed gas, m_a is the mass of adsorbent, P is the partial pressure at equilibrium of the adsorbed gas and K_f and n_f are Freundlich constant and the exponent of non-linearity, respectively, whose values depend upon adsorbent and gas at a given temperature. It is important to mention that Freundlich isotherm is an empirical model and it does not have any theoretical basis. This model correctly describes the relationship of adsorption with pressure at low values but at higher pressures it shows significant deviations. The plot of this isotherm at different values of n_f is presented in Figure 1-20.

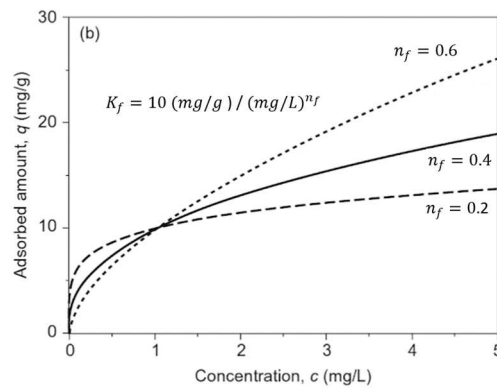


Figure 1-20. Freundlich isotherm at different n_f values [140]

Langmuir model

The Langmuir adsorption model is the most common model used to quantify the amount of adsorbate adsorbed on an adsorbent as a function of partial pressure at a given temperature. It is based on the following hypotheses:

- The adsorbent surface is homogeneous and consists of a certain number of active sites that are energetically identical.
- At maximum adsorption, only a monolayer is formed.
- There is no lateral interaction between the adsorbed molecules, thus the ability of a molecule to adsorb at a given site is independent of the coverage.

For the adsorption process presented in Equation Eq. 1-3, the equilibrium is reached when the rate of adsorption, k_a , equals the rate of desorption, k_d . Therefore, the rate of change of surface coverage θ due to adsorption is proportional to the partial pressure, P_B , of gas B and the number of active free sites, $N(1 - \theta)$, where N is the total number of sites, resulting in Eq. 1-5.

$$\frac{d\theta}{dt} = k_a P_B N(1 - \theta) \quad \text{Eq. 1-5}$$

On the other hand, the rate of change of θ due to the desorption is proportional to the number of adsorbed molecules, $N\theta$, as follows:

$$\frac{d\theta}{dt} = -k_d N\theta \quad \text{Eq. 1-6}$$

At equilibrium, surface coverage is constant and thus, both equations are equal to zero. Solving θ , Langmuir isotherm is obtained:

$$\theta = \frac{K}{1 + K} \quad \text{where } K = \frac{k_a}{k_d} \quad \text{Eq. 1-7}$$

An example of this equation is plotted in Figure 1-21. As it can be inferred from the representation, surface coverage increases when pressure increases until saturation pressure is reached, and all the available sites are occupied.

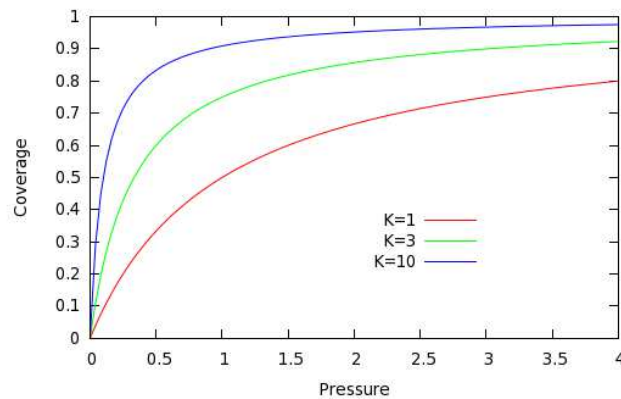


Figure 1-21. Example of Langmuir isotherm at different values of K [141]

Since in Langmuir model it is assumed that at maximum adsorption only a monolayer is formed, when the equilibrium is reached, the amount of adsorbed adsorbate corresponds to the monolayer capacity.

Brunauer, Emmet and Teller (BET) model.

The main limitation of Langmuir adsorption model was the assumption of the monolayer adsorption which is not realistic. To overcome this constraint, Stephen Brunauer, Paul Hugh Emmet and Edward Teller [142] proposed a multilayer adsorption theory based on the following assumptions:

- Gas molecules physically adsorb on a solid in layers infinitely
- There is no interaction between each adsorption layer
- The Langmuir theory can be applied to each layer

Basically, this theory establishes that Langmuir equation can be applied to each layer with the only difference that for the first layer the heat of adsorption may have a different value and for all consecutive layers it is equal to the heat of condensation of the liquid adsorbate. BET isotherm is represented by the following equation:

$$\frac{P}{V_P(P-P_0)} = \frac{1}{V_m c} + \frac{(c-1)}{V_m c} \left(\frac{P}{P_0} \right) \quad \text{Eq. 1-8}$$

where V_P is the volume of gas adsorbed at partial pressure P , V_m is the volume of gas required to form a monolayer, c is a constant related to the energy of adsorption of the first layer, P is the partial pressure at equilibrium and P_0 is the saturation pressure. The main characteristic of BET isotherms is that V_P rises indefinitely as the pressure increases because there is no limitation in the amount of adsorbed gas due to multilayer adsorption.

Type of adsorption isotherms

As explained before, adsorption isotherm is a representation of the gas adsorption on a material at a fixed temperature as a function of the adsorbate relative pressure ($\frac{P}{P_0}$), which corresponds to the ratio of partial pressure over its saturation pressure. The shape of this plot is, therefore, related to the porosity of the material since this feature defines the way in which the gas is adsorbed. Hence, IUPAC (International Union of Pure and Applied Chemistry) has proposed a general classification based on the shape of the isotherm (see Figure 1-22). The six types of isotherms proposed are typically associated to adsorbents that are microporous (type I), nonporous or macroporous (types II, III, and VI), or mesoporous (types IV and V).

Type I is the Langmuir type and it is usually found in **microporous solids**. These isotherms are concave and have a steep initial region due to very strong adsorption in the micropores. They are characterized by approaching a limit value when $\frac{P}{P_0} \sim 1$. This value corresponds to the complete adsorption of the monolayer (V_m).

Type II is characteristic of **non-porous or macroporous solids**. As can be observed in Figure 1-22, the isotherm tends to increase infinitely because of multilayers formation. There is an inflection point called "Point B" that corresponds to the total monolayer coverage (V_m); from this point multilayer adsorption begins.

Type III is exhibited by **non-porous solids**. This isotherm is convex over its entire range. Type III and V are characteristic of weak gas-solid interactions, this weakness leading to a limited adsorption at low pressures but once the first monolayer is adsorbed, the adsorbate-adsorbate forces encourage the adsorption of further molecules. Indeed, in this type of isotherm, lateral interactions between adsorbed gas molecules are stronger than the adsorbate-adsorbent interactions.

Type IV and **Type V** isotherms can be found in **mesoporous solids**. The difference between these two types is analogous to that observed between Types II and III. The first part of Type IV isotherm follows the same path as type II until the monolayer saturation (B point). After this point, capillary condensation begins in the narrowest pores and it continues until saturation pressure, at which the widest pores are filled, is reached. As explained above, Type V isotherm is indicative of weak gas-solid interactions, therefore, the initial part of the plot is similar to type III isotherm. As the relative pressure approaches 1, an abrupt rise indicates the condensation of adsorbate gas to liquid.

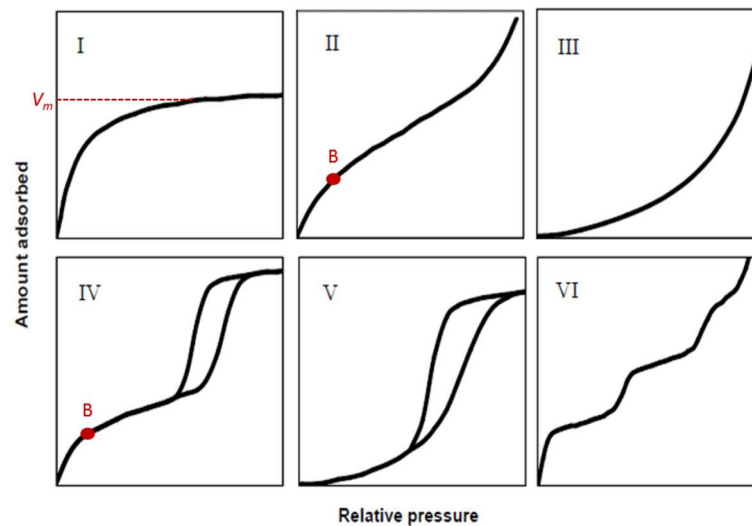


Figure 1-22. Types of adsorption isotherms according to the IUPAC classification [143]

In case of isotherms for mesoporous or macroporous materials, desorption curve does not follow the adsorption plot resulting in a hysteresis loop. This loop represents the capillary condensation of the adsorbate in the multilayer region.

Type VI isotherm is typically observed in **non-porous solids**. The plot exhibits several steps whose sharpness depends on the system and the temperature. This isotherm corresponds to a gradual adsorption by layers where monolayer capacity for each adsorbed layer can be determined by the height of each step.

1.4.2 VOC Adsorption on different materials

A broad range of materials of different nature has been employed for VOC adsorption. As mentioned before, adsorption is a surface process, therefore, the surface and textural properties of the solid such as the total specific surface, the pore volume, size and structure or the presence of functional groups play an essential role in this process. In this section, five groups of materials commonly used for VOC adsorption and the relationship between their diverse structures and adsorption properties are presented.

1.4.2.1 Carbon-based adsorbents

Carbon-based adsorbents have been typically used for VOC trapping. There is a large number of different types of carbon-based adsorbents but only the three most known categories are presented below.

1.4.2.1.1 Activated Carbon (AC)

Activated carbon (AC) is a type of carbon derived from charcoal that has been physically or chemically processed to have very small pores. This elevated degree of microporosity leads to an extremely high surface area available for adsorption or chemical reactions and thus, an outstanding adsorption capacity. Typical specific surface areas vary between 500 and 1000 m²/g, but reach up to 3,000 m²/g in some cases. Activated carbon fibres (ACF) have been widely employed for benzene and toluene adsorption [144], [145] since they present elevated specific surface areas, high micropores volumes and low pressure drops [146]. Generally, AC surface is hydrophobic; thus, these materials have commonly been used for the adsorption of molecules of similar polarity such as aromatics or long chain alkanes. For example, the adsorption of benzene and its derivatives is especially favoured due to the π -interactions between the aromatic rings and the graphene layers [147], [148]. AC adsorption capacity of aromatics can be enhanced by treating the surface with sulfuric acid due to an increment of the microporosity and low micropore volume resulting from this treatment.

Indeed, [149] reported an increase of 18% and 47% in toluene and benzene adsorption capacities on sulfuric treated AC compared with that on the standard AC. This increase in the adsorption was due to the increment of porosity of the AC and the number of surface oxygen groups available on the free surface, demonstrating that surface chemistry plays an important role in VOC adsorption on activated carbon [150], [151]. Besides, several studies reported also the use of activated carbons for adsorption of polar compounds such as aldehydes or ketones [152]. Generally, the adsorption of these compounds on AC is limited due to the different polarity between the adsorbate and the adsorbent. Therefore, surface functionalization is usually performed to increase the affinity of the AC surface to polar compounds. In general, the functionalization of AC results in a reduction of the specific surface area [153] but, in exchange, specific adsorption sites are created. Tang *et al.* (2016) observed a significant enhancement on AC adsorption capacity towards acetone and isopropanol when increasing of oxygen functional groups on the ACs surface [153]. Similar results were observed by Ortmann *et al.* [154] when they used AC and ordered mesoporous carbon-based adsorbents containing high amounts of surface oxygen groups for the adsorption of acetaldehyde and hexanal at low concentrations. Interestingly, AC modified by magnesium oxide have demonstrated extraordinary adsorption capacity of (432.7 mg/g) towards acetone due to strong chemisorption between MgO nanoparticles and acetone molecules. A recent study performed by molecular simulation evaluated the influence of pore size and functional groups on benzene, toluene, acetone and methanol adsorption on activated carbons [155]. It demonstrated that the addition of functional groups such as carboxyl or amino groups are a key parameter on acetone and methanol adsorption whereas they have little influence towards the adsorption of aromatics compounds on AC. In conclusion, AC are a group of adsorbents suitable for the adsorption of a wide range of VOC due to their high surface area and easily tuneable surface chemistry.

1.4.2.1.2 Graphitized Carbon Black (GCB)

Graphitized carbon blacks (GCB) are materials produced by the incomplete combustion of heavy petroleum products. The graphitization process results in a highly pure surface with great adsorption and desorption properties. GCB are hydrophobic, non-porous and non-specific adsorbents. The surface interactions with adsorbates are based on London forces; thus, they exhibit a medium adsorptive strength enable to trap VOC from C₃ to C₂₀. They are characterised by a specific surface between 10 and 100 m²/g and a relatively high thermal stability (up to 400°C). Among the commercially available GCB, the most commonly used are Carbotrap™ and Carbopack™ from

Supelco since they are employed in the EPA method TO-17 for the determination of VOC in ambient air using active sampling onto sorbent tubes. These carbons have been also employed in VOC preconcentration devices. Wang *et al.* [133] reported the integration of a preconcentrator containing Carbopack X and Carbopack B in a wearable GC for the detection of complex VOC mixtures at sub-ppm levels. Usually, GCB are combined with carbon molecular sieves to enlarge the range of VOC trapped to light VOC (C₂-C₅). Tian *et al.* [156] were able to quantify a mixture of 100 ppb of 30 common organic vapors containing alkanes, aromatics, and ketones by integrating a microfabricated preconcentrator-focuser filled with Carbopack B, Carbopack X, and Carboxen 1000 into a μ GC.

1.4.2.1.3 Carbon Molecular Sieves (CMS)

Carbon molecular sieves (CMS) are carbonaceous materials prepared by the controlled pyrolysis of a polymeric precursor. This process yields microporous materials with high specific surface area ranging between 200 and 1200 m²/g. CMS are considered as very strong adsorbents enabling to trap even the most volatile compounds (C₂ to C₅). As well as the other carbon-based adsorbents, CMS are hydrophobic, and they can be used for VOC removal in humid environments. The main application is the separation of C₁-C₃ hydrocarbons, small polar molecules and inorganic gases; the most known is the separation of nitrogen from air [157], [158]. Most known commercial CMS are Carboxen® and Carbosieve® with tapered pores and non-tapered pores, respectively.

Adsorption of less volatile compounds with more than 5 carbons is not recommended since they cannot be desorbed efficiently at reasonable temperatures. For this reason, CMS are commonly combined with GCB adsorbents in thermal desorption tubes widening the range of VOC adsorbed [159], [160]. In these tubes, the adsorbents are placed according to their adsorption strength, the weakest being placed in first position for the adsorption step (sampling) and CMS in the last position. The thermal desorption is always performed in the opposite sense of the sampling to prevent that the less volatile compounds are adsorbed irreversibly on CMS. Like GCB, CMS are usually employed in preconcentration devices [156].

1.4.2.2 Porous polymers

Porous polymers are very often used for VOC adsorption. In general, they have moderate specific surface areas and low maximum operating temperatures compared to other materials, as they usually

decompose at temperatures around 250°C. There are several commercially available porous polymers. A brief description of the most commonly used is given below.

Tenax™ is a hydrophobic porous polymer based on 2,6-diphenyl-p-phenyleneoxide. It is one of the most employed polymers for trapping medium to high boiling temperature VOC and is used in EPA Method TO-17. There are two main types: Tenax™ TA ~ 35 m²/g (350 °C temp limit) and Tenax™ GR which is a composite material with a slightly smaller specific surface (~ 25 m²/g) containing 70 % of Tenax™ TA and 30 % of graphite carbon. The addition of graphite to the traditional Tenax™ TA broadens the spectrum of adsorbed compounds possibly trapped including those with low boiling point.

HayeSep™ is a copolymer of divinylbenzene and ethylene glycol methacrylate, for which several series have been developed. Depending on the series (A, B, C, Q, T, R, N, DB), the specific surface area can vary from 250 to 795 m²/g. Since there are polymers, the maximum operating temperature is relatively low, ranging from 165 to 290 °C. It is why they are mainly used for chromatographic columns in gas chromatography in order to ensure the gaseous species separation.

Porapak™ adsorbents are mostly copolymers of polydivinylbenzene (DVB) like ethylvinylbenzene (Q series), vinyl pyrrolidone (R series), vinyl pyridine (S series) or ethylene glycol methacrylate (T series) presenting mesopores and/or micropores. They are similar to HayeSep™ in terms of specific surface area (150 – 550 m²/g) and maximum operating temperature (190 – 250 °C). They are commonly used for chromatographic separation of different groups of compounds such as acids, hydrocarbons, ethers, esters, alcohols and ketones, depending on the selected series.

1.4.2.3 *Mesoporous Silica*

Mesoporous silica are a relatively new group of materials with a wide range of applications including catalysis, drug delivery, waste water remediation [161] and indoor air cleaning [162], [163]. These materials show highly ordered pores and they are composed by a framework of silicon and oxygen atoms arranged in different structures forming a wide variety of pore geometries (hexagonal, cubic, cylindrical, etc.). By varying the synthesis conditions, several particles morphologies as rods or spheres can be achieved and functional groups can be incorporated onto the pore walls. Functionalization has been extensively used in mesoporous silica to increase their selectivity towards a broad variety of compounds of interest in numerous applications such as drug delivery [164]–[166],

water treatment [167], [168] or catalysis [169]–[171]. So far, a broad array of ordered mesoporous silica such as MCM, KIT, SBA or FDU has been developed; some of their structures are presented in Figure 1-23. Among these materials, SBA-15 and MCM-41 are the most commonly employed for VOC adsorption.

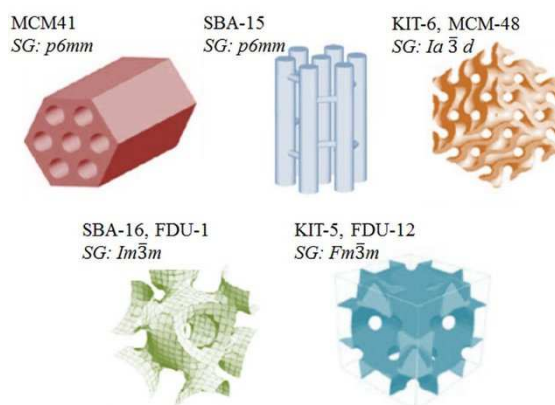


Figure 1-23. Different structures of mesoporous silica [172]. SG: Space Group

MCM-41 (Mobil Crystalline Materials 41) consists of a hexagonally ordered cylindrical pores (see Figure 1-23). The pore size can be easily tuneable by changing the synthesis conditions and their diameter can vary from 2 to 6.5 nm. The walls of the pores are thin (3-6 nm) [172] resulting in a relatively weak structure with limited hydrothermal stability.

SBA-15 (Santa Barbara Amorphous type 15) is another well-known type of mesoporous silica. Its structure is composed of a hexagonal system of cylindrical pores (see Figure 1-23) with a diameter between 5 and 15 nm [173]. In some cases, these mesopores are interconnected by micropores resulting in a high specific surface area typically in the range 400-900 m²/g [174, p. 15]. This material is hydrothermally more stable than MCM-41 [175], and is more robust when the microporosity increases [176].

1.4.2.4 Metal Organic Frameworks (MOF)

Metal organic frameworks (MOF) are a group of crystalline porous materials with large micropore volume and which structure is formed by metal ions coordinated to organic ligands. The nature of the metal and the ligand defines the three-dimensional structure of the network and, thus, the material properties. Several metals have been used in MOF synthesis such as Zn (IRMOF-1, IRMOF-3, MOF-177, ZIF-8), Mn, Cu (HKUST-1, NOTT-112), Zr (UiO-66), Cr (MIL-101), Fe (MIL-53). By varying the

metal and the organic linkers, a wide variety of surface properties and pore sizes can be achieved as shown in Figure 1-24. The high porosity of MOF results in a large pore volume and high specific surface area what makes these materials extremely valuable in the fields of catalysis [177]–[179] and gas storage [180], [181], gas separation [182], [183] and gas purification [184], [185].

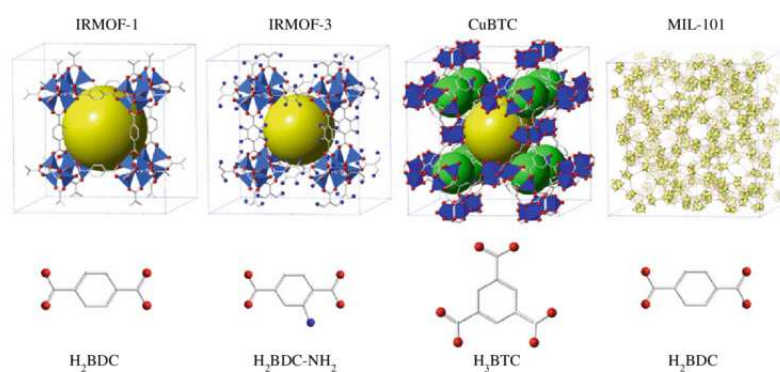


Figure 1-24. Structures of several MOF and their linkers. The yellow and green spheres represent the pore volume. [186]

IRMOF-1 ($Zn_4O(BDC)_3$) is a MOF made up of Zn_4O nodes with 1,4-benzenedicarboxylic (BDC) acid ligands between them. IR stands for isorecticular, which means it is a series of MOFs with the same topology, but different linkers and, thus, pore sizes (see Figure 1-24). In IRMOF-1, $[OZn_4]_6$ groups are linked to an octahedral array of $[O_2C-C_6H_4-CO_2]_2$ - (1,4-benzenedicarboxylate, BDC) groups whereas in **IRMOF-3**, $[OZn_4]_6$ groups are linked to 2-aminobenzenedicarboxylate (H_2N -BDCH₂) ligands. These structures create a very porous framework with an extremely high specific surface area ranging from 2,500 to 3,000 m^2/g [181] and a relatively high thermal stability [187]. Similarly to IRMOF-1, H_2BDC is the ligand in **MIL-101** (MIL, Matériel Institut Lavoisier). This MOF is made up of trimeric chromium (III) octahedral clusters interconnected by 1,4-BDC, resulting in a highly porous 3D structure with a specific surface area (SSA) higher than 3,000 m^2/g .

CuBTC, known as HKUST-1 (from Hong Kong University of Science and Technology) is another MOF widely employed in VOC adsorption. It is formed by copper nodes with 1,3,5-benzenetricarboxylic acid linkers between them. This MOF was investigated in this research work and its structure is described in detail in Chapter 2 in Section 2.1.1.2.

1.4.2.5 Zeolites

Zeolites are a large group of natural and synthetic porous aluminium silicates including more than 50 different types [188]. Each type of zeolite has a unique three-dimensional structure formed by SiO_4 and AlO_4 tetrahedra linked by oxygen atoms in the corners [189]. These crystalline nanoporous materials exhibit broad applications in many industrial processes such as catalysis, adsorption, and separation [190]. Natural zeolites present several drawbacks to be used in industrial applications such as heterogeneity in chemical composition or the presence of impurities; therefore, synthetic zeolites are preferred. The general formula of zeolite is $\text{M}_{x/n} [(\text{AlO}_2)_x(\text{SiO}_2)_y] \cdot m\text{H}_2\text{O}$ where M is the metal or hydrogen ion of valence n , balancing the negative charge of the zeolite framework [191]. The zeolite framework is similar to silica (SiO_2), but some Si (IV) are replaced by Al (III) atoms, and these tetrahedra constitute the primary building units of zeolites. These structures form rings of 4, 5, 6, 8, 10 or 12 members and the type of ring defines the pore size of the zeolite, one of the critical properties of these materials since pore size determines the molecules that can enter into the pore [192]. The most common structures have rings of 8, 10 and 12 members which are known as small-, medium- and large-pore zeolites, respectively. The different arrangements of these structures lead to numerous types of secondary building units. In Figure 1-25, some of the secondary building units, framework structure and pore size founded on zeolites are presented.

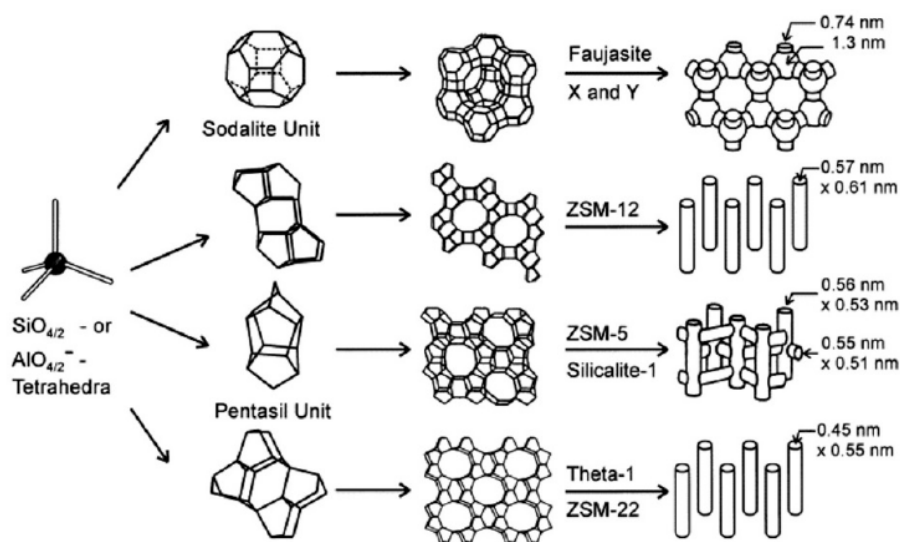


Figure 1-25. Structures of four commercial zeolites and their building units (reprinted from [193])

As mentioned before, zeolite structures are formed by SiO_4 and AlO_4 tetrahedra linked by oxygen atoms. In most cases, the proportion of silicon and aluminium is determined by the type of zeolite, but it can be modified by varying the synthesis conditions. During the synthesis, the Si (+IV) atoms are replaced by Al (+III) atoms increasing the negative charges in the framework and, hence, influencing the polarity. Therefore, the hydrophobicity in zeolites increases when less partial charges are present in the framework, i.e. when Al content decreases (higher Si/Al ratio). These negative partial charges are located at the oxygen atoms linked to Al atoms. Consequently, these oxygen atoms are more basic than the oxygen linked to two silicon atoms. In the zeolite framework, the negative charge is compensated with protons that are coordinated to one of these oxygen atoms, forming Brønsted acid sites [192] and, thus, increasing the acid properties of the material. These hydrogens can be replaced by other cations such Na^+ , Ca^{2+} , NH_4^+ , etc. increasing the hydrophilic character of the zeolite. A brief description of the most common used zeolites for VOC adsorption is given below:

Zeolite A, also known as LTA (Linde Type A), is the first industrially synthesized zeolite. Zeolite A is formed by the assembly of sodalite cages which are connected by four ring cages. In this structure, Si/Al ratio is equal to 1 and the negative charges are balanced by sodium cations.

Zeolites X and Y belong to the family of zeolites with faujasite-type structure. These structures are also formed by sodalite cages but they are linked by hexagonal prisms [194]. In this framework, a 12-membered ring forms the pores and they have a diameter of 7.4 Å. The main difference between these two zeolites are the Si/Al ratio, being from 1 to 1.5 for X-type and higher for the Y-type zeolite.

ZSM-5 (Zeolite Socony Mobil-5) is one of the synthetic zeolites with high silica content (Si/Al ratio from 1 to ∞). It was patented by Mobil Oil Company in 1975 and it is widely used in the petroleum industry as a heterogeneous catalyst for hydrocarbon isomerization reactions. It is composed by pentasil units bonded *via* oxygen bridges forming rings of 10 members. Further investigation of the influence of Si/Al ratio and structure of ZSM-5 zeolites on VOC adsorption has been carried out during this doctoral research.

1.4.3 General adsorption behaviour of aldehydes and aromatics compounds

In this section, a general description of the adsorption behaviour of the VOC investigated in this work is provided. The main properties of the studied compounds are summarised in Table 1-3. These compounds can be divided in two groups: BTEX and aldehydes. BTEX group is composed of benzene,

toluene, ethylbenzene and the three isomers of xylene. These compounds are hydrophobic, similar in size and all of them have an aromatic ring in their structure, therefore, it is expected that their adsorption behaviour is similar. On the other hand, the aldehydes group is formed by hexanal and formaldehyde. Both compounds have the same aldehyde functional group that gives them a more polar nature compared to aromatics. However, their different sizes and vapor pressures result in dissimilar adsorption behaviours.

Table 1-3. General properties of the investigated VOC

	Molar mass (g/mol)	Boiling point (°C) at 1 atm	Vapor pressure at 20°C (kPa)	Dipole moment (D)*	Kinetic diameter (nm)
Benzene	78.11	80.1	10.00	0	0.585
Toluene	92.14	110.6	2.90	0.375	0.585
Ethylbenzene	106.17	136.0	1.00	0.59	0.60
o-Xylene	106.16	144.4	0.93	0.64	0.68
m-Xylene	106.16	139.0	1.20	0.35	0.68
p-Xylene	106.16	138.4	1.20	0	0.585
Formaldehyde	30.03	-19.4	101.32	2.33	0.25
Hexanal	100.16	131.0	1.33	2.64	0.52

*[195]

1.4.3.1 BTEX adsorption behaviour

BTEX are a group of common gaseous pollutants in indoor as well as outdoor air. Due to their high toxicity and adverse effects on human health, their adsorption behaviour has been extensively studied for its applications as a removal technique. These compounds are hydrophobic and contain an aromatic ring; therefore, their adsorption behaviour is based on non-polar forces such as Van der Waals forces and π interactions. A summary of the parameters that strongly influence BTEX adsorption on diverse materials is described in this section.

Generally, the VOC adsorption capacity of a material is enhanced when its SSA is increased due to the presence of a higher number of available adsorption sites [196], [197]. Das *et al.* [198] studied the effect of this parameter on the adsorption of toluene on activated carbon fibres (ACF) and it was shown that an increase from 1000 m²/g to 1700 m²/g in the SSA of ACF can lead to a toluene breakthrough time four times longer. Serrano *et al.* [199] studied the adsorption of toluene in ordered mesoporous materials. They observed an increase of the adsorption capacity for the materials with elevated SSA but also highlighted the influence of the textural properties and pore size in the adsorption of aromatic compounds. Other studies on commercial ACF [200] also underlined the effect

of microporosity on toluene adsorption at low concentrations. It was shown that the available pore volume was more efficiently used in ultramicroporous (< 0.7 nm) material compared to supermicroporous (2 - 0.7 nm) counterpart due to stronger interactions of toluene with the pore walls of ACF, demonstrating that pore size plays a major role in toluene adsorption at low concentrations. In these conditions, contrary to the general trend, higher adsorption capacity was observed in ultramicroporous ACF compared to supermicroporous ACF despite their lower specific surface area. This observation pointed out the complexity of the adsorption process in which many factors must be taken into account.

Similar results regarding the importance of pore size on benzene and toluene adsorption on ACF were observed in other studies [201], [202]. Lillo-Ródenas *et al.* [202] found an extraordinary adsorption capacity of 31 g /100 g ACF and 53 g /100 g ACF, for benzene and toluene, respectively, at low concentrations due to the large volume of micropores with a size close to the size of adsorbate molecules (< 0.7 nm) and generated during the activation process of the materials. Russo *et al.* [203] investigated the adsorption of aliphatic and aromatic hydrocarbons at low concentrations on mesoporous materials. In agreement with previous studies on adsorption on ACF, they observed higher adsorption capacity of aromatics compared to aliphatic hydrocarbons due to strong adsorbate-adsorbent interactions inside the micropores with narrow pore openings.

In other microporous materials such as zeolites, both pore size and morphology also play a crucial role. Some zeolites (like ZSM-5, ZSM-12 and ZSM-22) exhibit very small micropores with pore diameter lower than 6 Å, avoiding the entrance of some molecules such as aromatics into the pores and, thus, preventing their adsorption [204], [205]. A study conducted by Ogata *et al.* [205] illustrates this behaviour for the adsorption of benzene in four different zeolites with 0.3, 0.4, 0.5 and 1 nm of micropore diameter. The dynamic diameter of benzene molecule is 0.59 nm, explaining why only the zeolite having micropores of 1 nm exhibited benzene adsorption. Similar observations were reported by Huang *et al.* [135] for the adsorption of toluene on 5A, HSZM-5, H β and HY zeolites having pore diameters of 5, 5.5, 6.6 and 7.4 Å, respectively. Since toluene dynamic size is 0.59 nm, this molecule cannot be adsorbed on the pores of 5A. Conversely to the trend found in carbonaceous materials, zeolites exhibited enhanced adsorption capacity of aromatic compounds when increasing pore size. Kim and Ahn [206] reported higher amount of BTEX adsorbed on faujasite than in modernite zeolites due to the larger pore opening.

Apart from SSA and pore morphology, the surface chemistry is a vital aspect in adsorption processes. To this purpose, different strategies depending on the type of material are employed to enhance the adsorbate-adsorbent interactions. In case of zeolites, a strategy commonly adopted to increase the adsorption of aromatics is the metal loading. Huang *et al.* [135] demonstrated that Ag loaded Y zeolites (Ag/HY) exhibited enhanced toluene adsorption than their not-loaded counterparts (HY) due to the formation of π complexation of Ag/HY with the aromatic ring of toluene. Indeed, the metals with empty s-orbital and available electrons in the d-orbital like Ag can form this type of interaction, promoting aromatics adsorption. In general, metal loading decreases the zeolite SSA due to the bigger size of metal cations. However, despite the lower SSA, metal substituted zeolites exhibit higher toluene adsorption capacity due to the ability to form π complexation [207].

Surface chemistry changes completely from one material to another. In MOFs, the main interactions adsorbate-adsorbent are π - π interactions and π complexation between the aromatics and the metallic centres or organic linkers of MOFs [208], [209]. These interactions all together with very high SSA make MOFs outstanding adsorbents for aromatic compounds [210]. In mesoporous silica, surface hydroxyl groups promote the adsorption of aromatic compounds due to the interaction with their π electrons. Russo *et al.* [203] reported higher affinity of toluene for pure silica surface than for organosilica or silica with chloromethyl groups due to the interaction of the π electrons with the hydroxyl groups present on the silica surface.

In conclusion, adsorption is an extremely complex process involving many factors such as specific surface area, pore size and morphology, strength of adsorbate-adsorbent and adsorbate-adsorbate interactions. Furthermore, the influence of each parameter on adsorption strongly depends on the adsorbent and adsorbate employed since the chemical structure and, thus, the molecular interactions can be completely different. Therefore, a special attention should be paid on the different aspects of the process when studying adsorption.

1.4.3.2 Aldehydes adsorption

In this work, formaldehyde and hexanal were selected as target aldehydes due to their occurrence in indoor air. As it can be seen in Table 1-3, formaldehyde and hexanal have higher dipole moments compare to the aromatics due to the C=O bond present in the aldehyde function. Dipole moment is the measure of the polarity of a molecule and it represents the sum of all dipole moments of covalent bonds. Therefore, formaldehyde and hexanal are considered as polar compounds and, thus, their

adsorption behaviour is quite different compared to the aromatics due to the different nature of the interactions with the adsorbent's surface. Rodriguez-Reinoso *et al.* [211] reported that the surface chemistry is one of the main factors influencing the adsorption of polar compounds whereas the adsorption of non-polar compounds is mostly influenced by the porous structure. Since formaldehyde and hexanal have the same functional group, the influence of the surface chemistry on the adsorption of these compounds is expected to be similar due to the same type of adsorbate-adsorbent interactions. However, lower efficiency in formaldehyde adsorption compared to hexanal is usually observed due to the smaller size and higher volatility of formaldehyde molecules. This difference has been also observed comparing hexanal and acetaldehyde adsorption on active carbons (AC) and ordered mesoporous carbon-based adsorbents (CMK) [154] indicating that molecule size is a key factor on formaldehyde adsorption.

As in the case of BTEX, carbon-based materials have been widely employed for aldehydes adsorption due to their low cost and high specific surface area [49]. As shown previously, AC exhibited exceptional performances for BTEX adsorption; however, they are not as efficient for polar compounds removal, especially formaldehyde [212]. This inefficiency can be explained by the weakness of HCHO-AC interactions due to the small size of formaldehyde molecules [213]. Furthermore, the presence of other pollutants can provoke the desorption of HCHO molecules due to the formation of stronger and thus, more favourable, interactions. For that reason, recent studies were focused on the functionalization of AC surfaces to enhance the strength of HCHO-AC interactions. Different types of functionalization for AC have been proposed in the last years. Nitrogen-containing groups have been shown to increase the formaldehyde adsorption capacity on AC and ACF. Song *et al.* [214] reported an enhancement of formaldehyde adsorption capacity in polyacrylonitrile based ACF resulting from the large number of nitrogen-containing groups on the surface, especially pyrrolic, pyridonic, and pyridinic. In this study, a linear correlation between the N/C ratio on the ACF and the formaldehyde adsorption capacity was observed. Lee *et al.* [215] also observed that ACF with high nitrogen content exhibited superior formaldehyde adsorption capacity than ACF with low nitrogen content suggesting that the amount of total nitrogen is a determining factor on formaldehyde adsorption on AC. They also reported that oxygen atoms close to nitrogen groups promoted formaldehyde adsorption ability by formation of hydrogen bonds.

The influence of oxygen containing groups on formaldehyde adsorption on active carbon ACF was investigated by Rong *et al.* [216]. They found an improvement in the adsorption capacity of

formaldehyde on oxidized AC compared to untreated AC owing to a large number of surface oxygen hydrophilic groups. Similar results were observed by Boonamnuyvitaya *et al.* [217] in formaldehyde adsorption capacity on coffee activated carbon prepared with $ZnCl_2$ impregnation and nitrogen activation. The enhancement of the adsorption capacity obtained with this AC was attributed to the creation of hydrophilic functional groups of O-H, C=O, C-O on the surface during the activation process. All these research works pointed out that formaldehyde adsorption on AC, contrary to what was observed for aromatics, is more influenced by surface chemistry than by textural and structural properties.

Adsorption capacity of aldehydes has been proved to be large in other porous adsorbents presenting nitrogen and oxygen containing groups on the surface like silica-based materials. A study of aldehydes adsorption on amino-functionalized porous silica was performed by Nomura *et al.* [218]. They observed that higher formaldehyde adsorption capacity was achieved with the primary aminosilica than the secondary and tertiary counterparts. This enhanced capacity was attributed to the ability of primary amines to react with carbonyl compounds forming imines and hemiaminals. Furthermore, the same trend was reported in the adsorption capacity of other aldehydes such as acetaldehyde, hexanal, and benzaldehyde. Drese *et al.* [219] studied the adsorption of formaldehyde in different amino functionalized silica materials. Aminosilica containing primary amines also exhibited the highest formaldehyde adsorption ability. These materials demonstrated the same behaviour in the adsorption capacity of C₅-C₉ aldehydes and ketones.

In amino functionalized materials, the adsorption of aldehydes is made by a chemisorption process; therefore, the reversibility of the adsorption is more complex than for physisorbed molecules. Technically, the reaction between aldehydes and primary amines can be reversible by means of acid hydrolysis [220]. Drese *et al.* [219] investigated the hexanal adsorption capacity of the regenerated aminosilica. After the adsorbent regeneration by acid hydrolysis, the adsorption capacity of hexanal was reduced to 24 % of the initial capacity indicating that more research should be done to optimize the regeneration process. At this stage, amino functionalized materials can be used for applications involving aldehydes removal, but the inefficiency of the regeneration process limits their use in aldehydes analysis.

Different strategies not involving amino groups have been adapted in zeolites for the improvement of the aldehydes' adsorption ability. Bellat *et al.* [221] reported an enhancement in formaldehyde adsorption capacity and affinity on zeolites having cations as Na⁺, K⁺ or Cu²⁺ in comparison to the

non-cationic DaY zeolite. Among them, sodium- and copper-faujasites (NaX, NaY, CuX) were more efficient adsorbents for formaldehyde at low concentration (< 1 ppm) than faujasites having K as ion (KY) suggesting that the interaction of formaldehyde with sodium or copper is stronger than with potassium. Moreover, since Na⁺ or Cu²⁺ are small metal cations, they do not greatly influence the specific surface area of the zeolite. Zhao *et al.* [222] studied formaldehyde adsorption in ZSM-5 zeolites demonstrating that the incorporation of Ag and/or other transition metal oxide can also enhance the formaldehyde adsorption. In this study, AgCu/HZSM-5 showed three times higher formaldehyde adsorption than H/HZSM-5, Ag/HZSM-5 and Cu/HZSM-5, indicating that a synergistic effect of Ag and Cu can increase the adsorption capacity.

Several methods to enhance the adsorbate-adsorbent interactions in aldehydes adsorption have been presented. However, most of them implies the grafting of hydrophilic functional groups such as hydroxyl or amines, resulting in an increase of the adsorbent's water affinity. Lee *et al.* [215] observed a significant reduction in the formaldehyde adsorption capacity of amino functionalized ACF compared to non-functionalized ACF under humid conditions caused by the water affinity of these nitrogen containing groups. Therefore, the performance of these functionalized adsorbents substantially decreases in humid environments. In contrast, when using metal substituted ZSM-5 zeolites, little influence of humidity on formaldehyde adsorption ability was observed. Zhao *et al.* [222] reported almost a constant formaldehyde adsorption capacity of AgCu/HZSM-5 zeolites in the relative humidity range from 20 to 93%, due to the hydrophobic properties of high-silica zeolite. These results pointed out the potential use of metal exchanged zeolites for aldehydes adsorption even in humid environments.

In conclusion, due to the different polarity of aldehydes, the main factors affecting their adsorption are different from the factors influencing aromatics adsorption. As shown, the presence of a carbonyl group able to form hydrogen bonds or to chemically react with hydrophilic groups on the surface of the adsorbent is the driven force in aldehydes adsorption. Therefore, SSA and pore morphology are not as critical as in aromatics adsorption.

1.4.4 VOC removal methods for air pollution control

VOC are a group of air pollutants generated in process industries and other types of factories [223]. Exposure to VOC has been related to the development of serious pathologies such as asthma, allergy

and some types of cancer [3]. In consequence, in the last decades, air quality regulations have been introduced to reduce and control their emissions into the atmosphere [224].

In order to comply with these regulations, several techniques based on physicochemical or biological processes have been developed for VOC removal. The most common methods for VOC removal are divided in two categories: destructive techniques and recovery techniques.

Destructive techniques involve the chemical transformation of the VOC molecules into harmless inorganic molecules such as CO₂ and H₂O. Among these techniques, thermal, catalytic or photocatalytic oxidation, plasma or biological methods are the most popular [225]. Thermal oxidation is commonly used to remove contaminants in air streams at concentrations ranging from 100 to 200 ppm [224]. The oxidation is carried out at temperatures typically between 800 and 1400 °C and the pollutant removal can achieve a rate of 95-99%. It is a cost-effective and highly efficient method for VOC removal at these concentrations; however, for more diluted streams the efficiency is significantly decreased [200]. This technique is usually employed when the working conditions do not allow using catalytic oxidation. Catalytic oxidation is employed in the same concentration conditions as thermal oxidation. In this technique, a catalyst is used to accelerate the decomposition reaction or reduce the needed temperature to 700–900 °C, leading to lower energy requirements, and thus reducing costs. The major disadvantage of this method is the potential poisoning of the catalyst by non-VOC materials such as sulphur, chlorides and silicon [226] and the selectivity of some catalysts to certain VOC [227],[228]. To widen the range of targeted pollutants, non-selective methods such as plasma oxidation or photocatalysis are often employed. A more ecological and inexpensive method compared to the physicochemical treatments is the biofiltration. This technique is one of the most commonly used biological method for VOC abatement and it has proven to be an efficient technique at low concentrations at laboratory scale [229], [230]. Nevertheless, their industrial applications are still limited since the efficiency of these systems varies with VOC concentration [231]. In addition, specific conditions of humidity and pH and a frequent replacement of the biological substrate are required.

Other abatement techniques, the so-called recovery techniques, allow the reuse of VOC molecules. Condensation is one of the industrial methods for VOC recovery. It is usually employed in highly polluted streams (> 500 ppm) containing VOC with boiling point above 35°C at atmospheric pressure, since the condensation of VOC with lower boiling points requires intensive cooling or pressurization, resulting in a significant increase of costs. The efficiency of this method usually does not exceed 80 % [225]. Membrane separation is another technique employed to separate the pollutants from the air

stream by means of a permeable membrane. It is generally utilized to clean highly contaminated streams (1000 - 10000 ppm). The efficiency of VOC removal depends on the membrane features but recovery rates up to 95% have been reported [232]. Despite the satisfactory results obtained in terms of efficiency, membrane separation method is not used on an industrial scale due to the costs of the membrane and the necessity to adapt the membrane to the targeted VOC. For industrial applications, it is more suitable to employ absorption methods. This technique allows VOC removal from very polluted streams (500 – 5000 ppm) by solving the pollutants in a liquid solvent. The air stream and the liquid solvent are put in contact in specific absorber towers designed to increase the mass transfer. VOC removal efficiencies between 90 to 98% are generally achieved [226].

A similar recovery method is adsorption where the VOC molecules are transferred from the gas phase to a solid surface. A large part of the efficiency is based on the contact between the gas and the solid; hence, microporous adsorbents with high specific surface areas like activated carbons, zeolites and silica gels are preferred. The affinity of the adsorbent to the targeted VOC is also a crucial factor in the efficiency. Among the presented VOC abatement techniques, adsorption is the only one that allows an effective VOC recovery from diluted streams (< 100 ppm) at a low-moderate cost. Therefore, the use of this method can be extended from industrial to the household applications.

1.5 Objectives of this work

The present doctoral research work continues the work performed by Rouba Nasreddine [233] during her thesis focused on the development of a portable GC for near real-time low level detection of BTEX. At the end of her thesis, a pre-industrial prototype of the portable GC was manufactured. Starting from this point, the main objectives of the present work are:

- Evaluation of pre-industrial GC prototype developed by Nasreddine *et al.* [234] under real conditions in a field campaign and determination of BTEX concentrations and main sources in indoor air.
- Design, conception and fabrication of a BTEX preconcentrator to be part of the GC prototype and decrease the LOD for benzene to less than the threshold value set by the French government, i.e. $2 \mu\text{g m}^{-3}$ (0.6 ppb). The final prototype should maintain similar characteristics in terms of carrier gas and energy consumption and temporal resolution.

- Provide experimental data of VOC adsorption on different materials at realistic concentrations (low ppm - ppb). Assessment of these materials for gas analysis and pollutant removal applications.

This thesis is organized in 6 chapters. In Chapter 1, a general introduction about the air quality and the methods employed for VOC detection followed by the current state of the art in the development of VOC preconcentrators were presented. Finally, a theoretical background of the adsorption process was described. Chapter 2 provides a description of the investigated adsorbents and the techniques employed for their characterization. In addition, the three different setups employed in dynamic adsorption experiments and the preconcentrator prototypes developed throughout this work are described in detail. Chapter 3 presents the results obtained in field campaign of indoor air quality conducted in two French primary schools for 5 weeks. Chapter 4 summarizes the characterization in terms of heating performance and BTEX preconcentration of the different BTEX preconcentrator prototypes developed throughout this work. In Chapter 5, a study of BTEX, formaldehyde and hexanal on different materials is presented and the influence of the different textural and chemical properties on adsorption is discussed. Finally, in the last section, the general conclusions and future perspectives are presented.

References

- [1] "9 out of 10 people worldwide breathe polluted air, but more countries are taking action." [Online]. Available: <https://www.who.int/news-room/detail/02-05-2018-9-out-of-10-people-worldwide-breathe-polluted-air-but-more-countries-are-taking-action>. [Accessed: 19-Oct-2019].
- [2] K. R. Smith et al., "Millions Dead: How Do We Know and What Does It Mean? Methods Used in the Comparative Risk Assessment of Household Air Pollution," *Annual Review of Public Health*, vol. 35, no. 1, pp. 185–206, Mar. 2014.
- [3] G. D'Amato, G. Liccardi, M. D'Amato, and M. Cazzola, "Outdoor air pollution, climatic changes and allergic bronchial asthma," *European Respiratory Journal*, vol. 20, no. 3, pp. 763–776, Sep. 2002.
- [4] G. Hoek et al., "Long-term air pollution exposure and cardio- respiratory mortality: a review," *Environmental Health*, vol. 12, no. 1, p. 43, May 2013.
- [5] R. A. Rinsky et al., "Benzene and Leukemia," *New England Journal of Medicine*, vol. 316, no. 17, pp. 1044–1050, Apr. 1987.
- [6] M. P. Tsakas, A. P. Siskos, and P. Siskos, "Indoor Air Pollutants and the Impact on Human Health," *Chemistry, Emission Control, Radioactive Pollution and Indoor Air Quality*, Jul. 2011.
- [7] J. Samet and D. Krewski, "Health Effects Associated With Exposure to Ambient Air Pollution," *Journal of Toxicology and Environmental Health, Part A*, vol. 70, no. 3–4, pp. 227–242, Feb. 2007.
- [8] "Where Does Air Pollution Come From? - Air (U.S. National Park Service)." [Online]. Available: <https://www.nps.gov/subjects/air/sources.htm>. [Accessed: 19-Oct-2019].
- [9] Bell Michelle L, Davis Devra L, and Fletcher Tony, "A retrospective assessment of mortality from the London smog episode of 1952: the role of influenza and pollution.," *Environmental Health Perspectives*, vol. 112, no. 1, pp. 6–8, Jan. 2004.
- [10] R. Stone, "Counting the Cost of London's Killer Smog," *Science*, vol. 298, no. 5601, pp. 2106–2107, Dec. 2002.
- [11] M. C. McCormack et al., "Common household activities are associated with elevated particulate matter concentrations in bedrooms of inner-city Baltimore pre-school children," *Environmental Research*, vol. 106, no. 2, pp. 148–155, Feb. 2008.

- [12] J. Madureira et al., "Source apportionment of CO₂, PM₁₀ and VOCs levels and health risk assessment in naturally ventilated primary schools in Porto, Portugal," *Building and Environment*, vol. 96, pp. 198–205, Feb. 2016.
- [13] L. Zhong, F.-C. Su, and S. Batterman, "Volatile Organic Compounds (VOCs) in Conventional and High Performance School Buildings in the U.S.," *International Journal of Environmental Research and Public Health*, vol. 14, no. 1, p. 100, Jan. 2017.
- [14] P. Wolkoff and G. D. Nielsen, "Organic compounds in indoor air—their relevance for perceived indoor air quality?," *Atmospheric Environment*, vol. 35, no. 26, pp. 4407–4417, 2001.
- [15] D. Campagnolo et al., "VOCs and aldehydes source identification in European office buildings - The OFFICAIR study," *Building and Environment*, vol. 115, pp. 18–24, Apr. 2017.
- [16] O. Geiss, G. Giannopoulos, S. Tirendi, J. Barrero-Moreno, B. R. Larsen, and D. Kotzias, "The AIRMEX study - VOC measurements in public buildings and schools/kindergartens in eleven European cities: Statistical analysis of the data," *Atmospheric Environment*, vol. 45, no. 22, pp. 3676–3684, Jul. 2011.
- [17] C. Mandin et al., "Assessment of indoor air quality in office buildings across Europe – The OFFICAIR study," *Science of The Total Environment*, vol. 579, pp. 169–178, Feb. 2017.
- [18] C. Walgraeve, K. Demeestere, J. Dewulf, K. Van Huffel, and H. Van Langenhove, "Diffusive sampling of 25 volatile organic compounds in indoor air: Uptake rate determination and application in Flemish homes for the elderly," *Atmospheric environment*, vol. 45, no. 32, pp. 5828–5836, 2011.
- [19] J. Madureira et al., "Source apportionment of CO₂, PM₁₀ and VOCs levels and health risk assessment in naturally ventilated primary schools in Porto, Portugal," *Building and Environment*, vol. 96, pp. 198–205, Feb. 2016.
- [20] D. Norbäck, J. H. Hashim, Z. Hashim, and F. Ali, "Volatile organic compounds (VOC), formaldehyde and nitrogen dioxide (NO₂) in schools in Johor Bahru, Malaysia: Associations with rhinitis, ocular, throat and dermal symptoms, headache and fatigue," *Science of The Total Environment*, vol. 592, pp. 153–160, Aug. 2017.
- [21] E. Can, Ö. Özden Üzmez, T. Döğeroğlu, and E. O. Gaga, "Indoor air quality assessment in painting and printmaking department of a fine arts faculty building," *Atmospheric Pollution Research*, vol. 6, no. 6, pp. 1035–1045, Nov. 2015.

- [22] S. Yurdakul, M. Civan, Ö. Özden, E. Gaga, T. Döğeroğlu, and G. Tuncel, "Spatial variation of VOCs and inorganic pollutants in a university building," *Atmospheric Pollution Research*, vol. 8, no. 1, pp. 1–12, Jan. 2017.
- [23] K. Liu et al., "Serious BTEX pollution in rural area of the North China Plain during winter season," *Journal of Environmental Sciences*, vol. 30, pp. 186–190, Apr. 2015.
- [24] Md. A. Bari, W. B. Kindzierski, A. J. Wheeler, M.-È. Héroux, and L. A. Wallace, "Source apportionment of indoor and outdoor volatile organic compounds at homes in Edmonton, Canada," *Building and Environment*, vol. 90, pp. 114–124, Aug. 2015.
- [25] P. Romagnoli, C. Balducci, M. Perilli, F. Vichi, A. Imperiali, and A. Cecinato, "Indoor air quality at life and work environments in Rome, Italy," *Environ Sci Pollut Res Int*, vol. 23, no. 4, pp. 3503–3516, Feb. 2016.
- [26] P. Gustafson, L. Barregard, B. Strandberg, and G. Sällsten, "The impact of domestic wood burning on personal, indoor and outdoor levels of 1,3-butadiene, benzene, formaldehyde and acetaldehyde," *Journal of Environmental Monitoring*, vol. 9, no. 1, pp. 23–32, 2007.
- [27] M. Derudi et al., "Emissions of air pollutants from scented candles burning in a test chamber," *Atmospheric environment*, vol. 55, pp. 257–262, 2012.
- [28] S.-C. Lee and B. Wang, "Characteristics of emissions of air pollutants from burning of incense in a large environmental chamber," *Atmospheric Environment*, vol. 38, no. 7, pp. 941–951, Mar. 2004.
- [29] Y.-H. Cheng, C.-C. Lin, and S.-C. Hsu, "Comparison of conventional and green building materials in respect of VOC emissions and ozone impact on secondary carbonyl emissions," *Building and Environment*, vol. 87, pp. 274–282, May 2015.
- [30] E. M. Martins, P. F. de S. Borba, N. E. dos Santos, P. T. B. dos Reis, R. S. Silveira, and S. M. Corrêa, "The relationship between solvent use and BTEX concentrations in occupational environments," *Environ Monit Assess*, vol. 188, no. 11, p. 608, Oct. 2016.
- [31] M. Verrièle et al., "The MERMAID study: indoor and outdoor average pollutant concentrations in 10 low-energy school buildings in France," *Indoor Air*, vol. 26, no. 5, pp. 702–713, Oct. 2016.
- [32] "LA Mold and VOC Testing Services in Los Angeles, CA," *Mold Inspection | Common Sense Inspections*. .

- [33] I. Buka, S. Koranteng, and A. R. Osornio-Vargas, "The effects of air pollution on the health of children," *Paediatr Child Health*, vol. 11, no. 8, pp. 513–516, Oct. 2006.
- [34] A. A. Arif and S. M. Shah, "Association between personal exposure to volatile organic compounds and asthma among US adult population," *Int Arch Occup Environ Health*, vol. 80, no. 8, pp. 711–719, Aug. 2007.
- [35] G. D'Amato, L. Cecchi, M. D'Amato, and G. Liccardi, "Urban Air Pollution and Climate Change as Environmental Risk Factors of Respiratory Allergy: An Update," *J Investig Allergol Clin Immunol*, vol. 20, p. 8, 2010.
- [36] D. Pyatt and S. Hays, "A review of the potential association between childhood leukemia and benzene," *Chemico-Biological Interactions*, vol. 184, no. 1, pp. 151–164, Mar. 2010.
- [37] M. J. Mendell and G. A. Heath, "Do indoor pollutants and thermal conditions in schools influence student performance? A critical review of the literature," *Indoor Air*, vol. 15, no. 1, pp. 27–52, Jan. 2005.
- [38] World Health Organization, Ed., *Air quality guidelines for Europe*, 2nd ed. Copenhagen: World Health Organization, Regional Office for Europe, 2000.
- [39] T. J. Atkinson, "A review of the role of benzene metabolites and mechanisms in malignant transformation: summative evidence for a lack of research in nonmyelogenous cancer types," *Int J Hyg Environ Health*, vol. 212, no. 1, pp. 1–10, Jan. 2009.
- [40] "Toluène (FT 74). Généralités - Fiche toxicologique - INRS." [Online]. Available: http://www.inrs.fr/publications/bdd/fichetox/fiche.html?refINRS=FICHETOX_74. [Accessed: 10-May-2019].
- [41] S. E. Bowen and J. H. Hannigan, "Developmental toxicity of prenatal exposure to toluene," *AAPS J*, vol. 8, no. 2, pp. E419–E424, Jun. 2006.
- [42] Donald J M, Hooper K, and Hopenhayn-Rich C, "Reproductive and developmental toxicity of toluene: a review.," *Environmental Health Perspectives*, vol. 94, pp. 237–244, Aug. 1991.
- [43] L. Wilkins-Haug and P. A. Gabow, "Toluene abuse during pregnancy: obstetric complications and perinatal outcomes.," *Obstet Gynecol*, vol. 77, no. 4, pp. 504–509, Apr. 1991.
- [44] "ATSDR - Public Health Statement: Ethylbenzene." [Online]. Available: <https://www.atsdr.cdc.gov/phs/phs.asp?id=381&tid=66>. [Accessed: 10-May-2019].

- [45] "ATSDR - Public Health Statement: Xylenes." [Online]. Available: <https://www.atsdr.cdc.gov/phs/phs.asp?id=293&tid=53>. [Accessed: 10-May-2019].
- [46] R. Kandyala, S. P. C. Raghavendra, and S. T. Rajasekharan, "Xylene: An overview of its health hazards and preventive measures," *J Oral Maxillofac Pathol*, vol. 14, no. 1, pp. 1–5, Jan. 2010.
- [47] M. Hauptmann, J. H. Lubin, P. A. Stewart, R. B. Hayes, and A. Blair, "Mortality from Solid Cancers among Workers in Formaldehyde Industries," *Am J Epidemiol*, vol. 159, no. 12, pp. 1117–1130, Jun. 2004.
- [48] G. M. Marsh, A. O. Youk, J. M. Buchanich, S. Erdal, and N. A. Esmen, "Work in the metal industry and nasopharyngeal cancer mortality among formaldehyde-exposed workers," *Regulatory Toxicology and Pharmacology*, vol. 48, no. 3, pp. 308–319, Aug. 2007.
- [49] S. Suresh and T. J. Badosz, "Removal of formaldehyde on carbon -based materials: A review of the recent approaches and findings," *Carbon*, vol. 137, pp. 207–221, Oct. 2018.
- [50] L. Ernstgård, A. Iregren, B. Sjögren, U. Svedberg, and G. Johanson, "Acute effects of exposure to hexanal vapors in humans," *J. Occup. Environ. Med.*, vol. 48, no. 6, pp. 573–580, Jun. 2006.
- [51] World Health Organization, Ed., *Who guidelines for indoor air quality: selected pollutants*. Copenhagen: WHO, 2010.
- [52] Directive 2008/50/EC of the European Parliament and of the Council of 21 May 2008 on ambient air quality and cleaner air for Europe, vol. OJ L. 2008.
- [53] Décret n° 2011-1727 du 2 décembre 2011 relatif aux valeurs-guides pour l'air intérieur pour le formaldéhyde et le benzène. 2011.
- [54] A. Kumar and I. Viden, "Volatile Organic Compounds: Sampling Methods and Their Worldwide Profile in Ambient Air," *Environ Monit Assess*, vol. 131, no. 1, pp. 301–321, Aug. 2007.
- [55] "(1) (PDF) Development of a Liquid Chromatography Ion Trap Mass Spectrometer Method for Clinical Drugs of Abuse Testing with Automated On-Line Extraction Using Turbulent Flow Chromatography." [Online]. Available: https://www.researchgate.net/publication/273134301_Development_of_a_Liquid_Chromatography_Ion_Trap_Mass_Spectrometer_Method_for_Clinical_Drugs_of_Abuse_Testing_with_Automated_On-Line_Extraction_Using_Turbulent_Flow_Chromatography. [Accessed: 08-Jul-2019].
- [56] "Gas Chromatography(GC): SHIMADZU (Shimadzu Corporation)." [Online]. Available: <https://www.shimadzu.com/an/gc/support/fundamentals/gc.html>. [Accessed: 08-Jul-2019].

- [57] “piD-TECH® eVx Photoionization Detector On Ametek Mocon - Baseline.” [Online]. Available: <http://products.baseline-mocon.com/viewitems/oem-sensors-detectors/rs-detectors-pid-tech-evx-photoionization-detector>. [Accessed: 08-Jul-2019].
- [58] R. Herrmann and C. Onkelinx, “Quantities and units in clinical chemistry: Nebulizer and flame properties in flame emission and absorption spectrometry (Recommendations 1986),” *Pure and Applied Chemistry*, vol. 58, no. 12, pp. 1737–1742, Jan. 1986.
- [59] A. Jordan et al., “A high resolution and high sensitivity proton-transfer-reaction time-of-flight mass spectrometer (PTR-TOF-MS),” *International Journal of Mass Spectrometry*, vol. 286, pp. 122–128, 2009.
- [60] J. M. Plane and A. Saiz-Lopez, “UV-Visible Differential Optical Absorption Spectroscopy (DOAS),” in *Analytical Techniques for Atmospheric Measurement*, John Wiley & Sons, Ltd, 2007, pp. 147–188.
- [61] R. Jiménez, H. Van den Bergh, and B. Calpini, DOAS as an Analytical Tool for Effective Air Pollution Management. Air Pollution Laboratory Report (LPAS), Swiss Federal Institute of ..., 1999.
- [62] G. Hönninger, C. von Friedeburg, and U. Platt, “Multi axis differential optical absorption spectroscopy (MAX-DOAS),” *Atmospheric Chemistry and Physics*, vol. 4, no. 1, pp. 231–254, Feb. 2004.
- [63] J.-M. Nasse, P. G. Eger, D. Pöhler, S. Schmitt, U. Frieß, and U. Platt, “Recent improvements of Long-Path DOAS measurements: impact on accuracy and stability of short-term and automated long-term observations,” *Atmospheric Measurement Techniques Discussions*, pp. 1–36, Mar. 2019.
- [64] M. T. Parsons et al., “Real-time monitoring of benzene, toluene, and p-xylene in a photoreaction chamber with a tunable mid-infrared laser and ultraviolet differential optical absorption spectroscopy,” *Appl. Opt., AO*, vol. 50, no. 4, pp. A90–A99, Feb. 2011.
- [65] H. Edner, P. Ragnarson, S. Spännare, and S. Svanberg, “Differential optical absorption spectroscopy (DOAS) system for urban atmospheric pollution monitoring,” *Appl. Opt.*, vol. 32, no. 3, p. 327, Jan. 1993.
- [66] Z. Hashisho, G. Morshed, and C. C. Small, “Review of Technologies for the Characterization and Monitoring of VOCs, Reduced Sulphur Compounds and CH₄,” 2012.
- [67] T. Visser, “Infrared Spectroscopy in Environmental Analysis,” in *Encyclopedia of Analytical Chemistry*, R. A. Meyers, Ed. Chichester, UK: John Wiley & Sons, Ltd, 2000, p. a0832.

- [68] H. J. McDermott, *Air Monitoring for Toxic Exposures*, 2 edition. Hoboken, N.J: Wiley-Interscience, 2004.
- [69] "MX908," 908 Devices. [Online]. Available: <https://908devices.com/products/mx908/>. [Accessed: 11-Jul-2019].
- [70] www.inficon.com, "HAPSITE® ER Chemical Identification System - INFICON." [Online]. Available: <https://products.inficon.com/en-us/nav-products/product/detail/hapsite-er-identification-system/>. [Accessed: 11-Jul-2019].
- [71] "Benzene Detector - GX-6000 PID gas monitor," Gas Detectors - Portable Gas Monitors - Gas Sensors by RKI. .
- [72] "Portable Hydrocarbon Analyzer - PHA-100 by PetroSense. Portable hydrocarbon detector. The world's first patented fiber optic chemical sensor (FOCS®." [Online]. Available: <https://www.petrosense.com/PHA-100.html>. [Accessed: 11-Jul-2019].
- [73] "PID / FID detector Mod. BTEX 530," PCF Elettronica. [Online]. Available: <http://www.pcfelettronica.it/en/products/air-quality-monitoring-analyzers/mod-530-btex-pid-fid-detector>. [Accessed: 11-Jul-2019].
- [74] "VOC-TRAQ II USB Toxic Gas Detector & Data Logger," Ametek Mocon - Baseline. [Online]. Available: <http://products.baseline-mocon.com/item/portable-detectors/voc-traq-usb-toxic-gas-detector-data-logger/voc-traq>. [Accessed: 11-Jul-2019].
- [75] "Portable Gas Analyzer, DX4040, manufactured by Gasmeter Technologies," Gasmeter.com. [Online]. Available: <https://www.gasmeter.com/products/category/portable-gas-analyzers/dx4040/>. [Accessed: 11-Jul-2019].
- [76] "PID-Analyzer – IUT Technologies." .
- [77] "FROG-4000 Chemical Detector Chemical Sensor Portable GC PID Gas Chromatograph Environmental Testing Mobile Lab Vapor Intrusion Soil Vapor Extraction BTEX - Defiant Technologies." [Online]. Available: <http://www.defiant-tech.com/frog-4000.php>. [Accessed: 11-Jul-2019].
- [78] "BTEX Analyzer - Indoor Air Quality," In'air Solutions. .
- [79] "PyxisGC BTEX," Pollution Analytical Equipment. .
- [80] F. Ahmed et al., "Impact of household air pollution on human health: source identification and systematic management approach," *SN Appl. Sci.*, vol. 1, no. 5, p. 418, Apr. 2019.

- [81] T.-H. Tzeng et al., "A Portable Micro Gas Chromatography System for Lung Cancer Associated Volatile Organic Compound Detection," *IEEE Journal of Solid-State Circuits*, vol. 51, no. 1, pp. 259–272, Jan. 2016.
- [82] E. H. M. Camara, "Développement d'un micro-préconcentrateur pour la détection de substances chimiques à l'état de trace en phase gaz," Dec. 2009.
- [83] C.-Y. Kuo, P.-S. Chen, H.-T. Chen, C.-J. Lu, and W.-C. Tian, "Development of micromachined preconcentrators and gas chromatographic separation columns by an electroless gold plating technology," *J. Micromech. Microeng.*, vol. 27, no. 3, p. 035012, 2017.
- [84] Y. Mohsen et al., "Development of a micro-analytical prototype for selective trace detection of orthonitrotoluene," *Microchemical Journal*, vol. 114, pp. 48–52, May 2014.
- [85] B. Han, H. Wang, H. Huang, T. Liu, G. Wu, and J. Wang, "Micro-fabricated packed metal gas preconcentrator for enhanced monitoring of ultralow concentration of isoprene," *Journal of Chromatography A*, Aug. 2018.
- [86] J. Lee and S.-H. Lim, "CNT Foam-Embedded Micro Gas Preconcentrator for Low-Concentration Ethane Measurements," *Sensors (Basel)*, vol. 18, no. 5, May 2018.
- [87] B. Alfeeli, "Chemical Micro Preconcentrators Development for Micro Gas Chromatography Systems," p. 168.
- [88] M. Camara, P. Breuil, D. Briand, J.-P. Viricelle, C. Pijolat, and N. F. de Rooij, "Preconcentration Modeling for the Optimization of a Micro Gas Preconcentrator Applied to Environmental Monitoring," *Analytical Chemistry*, vol. 87, no. 8, pp. 4455–4463, Apr. 2015.
- [89] G. Gregis et al., "Detection and quantification of lung cancer biomarkers by a micro-analytical device using a single metal oxide-based gas sensor," *Sensors and Actuators B: Chemical*, vol. 255, pp. 391–400, Feb. 2018.
- [90] M. Li, S. Biswas, M. H. Nantz, R. M. Higashi, and X.-A. Fu, "A microfabricated preconcentration device for breath analysis," *Sensors and Actuators B: Chemical*, vol. 180, pp. 130–136, Apr. 2013.
- [91] J. Sun, D. Cui, F. Guan, L. Zhang, X. Chen, and H. Li, "Detection biomarkers of lung cancer using mini-GC-PID system integrated with micro GC column and micro pre-concentrator," *Nanoscale Res Lett*, vol. 9, no. 1, p. 576, Oct. 2014.

- [92] M. Leidinger, M. Rieger, T. Sauerwald, C. Alépée, and A. Schütze, "Integrated pre-concentrator gas sensor microsystem for ppb level benzene detection," *Sensors and Actuators B: Chemical*, vol. 236, pp. 988–996, Nov. 2016.
- [93] J. Wang et al., "Compact prototype microfabricated gas chromatographic analyzer for autonomous determinations of VOC mixtures at typical workplace concentrations," *Microsystems & Nanoengineering*, vol. 4, p. 17101, Apr. 2018.
- [94] S. Zampolli et al., "Real-time monitoring of sub-ppb concentrations of aromatic volatiles with a MEMS-enabled miniaturized gas-chromatograph," *Sensors and Actuators B: Chemical*, vol. 141, no. 1, pp. 322–328, Aug. 2009.
- [95] A. G. Fung et al., "Wearable Environmental Monitor To Quantify Personal Ambient Volatile Organic Compound Exposures," *ACS Sens.*, vol. 4, no. 5, pp. 1358–1364, May 2019.
- [96] J. Wang et al., "Belt-Mounted Micro-Gas-Chromatograph Prototype for Determining Personal Exposures to Volatile-Organic-Compound Mixture Components," *Anal. Chem.*, vol. 91, no. 7, pp. 4747–4754, Apr. 2019.
- [97] M. Camara, F. James, P. Breuil, C. Pijolat, D. Briand, and N. F. de Rooij, "MEMS-based Porous Silicon Preconcentrators Filled with Carbopack-B for Explosives Detection," *Procedia Engineering*, vol. 87, pp. 84–87, 2014.
- [98] W. R. Collin, G. Serrano, L. K. Wright, H. Chang, N. Nuñoверо, and E. T. Zellers, "Microfabricated Gas Chromatograph for Rapid, Trace-Level Determinations of Gas-Phase Explosive Marker Compounds," *Anal. Chem.*, vol. 86, no. 1, pp. 655–663, Jan. 2014.
- [99] S. Reidy, G. Lambertus, J. Reece, and R. Sacks, "High-Performance, Static-Coated Silicon Microfabricated Columns for Gas Chromatography," *Anal. Chem.*, vol. 78, no. 8, pp. 2623–2630, Apr. 2006.
- [100] C. J. Lu and E. T. Zellers, "Multi-adsorbent preconcentration/focusing module for portable-GC/microsensor-array analysis of complex vapor mixtures," *Analyst*, vol. 127, no. 8, pp. 1061–1068, 2002.
- [101] C.-J. Lu and E. T. Zellers, "A dual-adsorbent preconcentrator for a portable indoor-VOC microsensor system," *Analytical chemistry*, vol. 73, no. 14, pp. 3449–3457, 2001.
- [102] S. A. Casalnuovo et al., "Gas phase chemical detection with an integrated chemical analysis system," in *Proceedings of the 1999 Joint Meeting of the European Frequency and Time Forum and*

the IEEE International Frequency Control Symposium (Cat. No.99CH36313), Besancon, France, 1999, vol. 2, pp. 991–996.

[103] “Carbotrap[®] 217 30137U,” Sigma-Aldrich. [Online]. Available: <https://www.sigmaaldrich.com/catalog/product/supelco/30137u>. [Accessed: 22-Oct-2019].

[104] B. Zhao, F. Feng, X. Yang, F. Luo, H. Zhou, and X. Li, “Improved Performance of Micro-Preconcentrator Using Silicon Nanowires as a Surface Template,” in 2019 20th International Conference on Solid-State Sensors, Actuators and Microsystems Eurosensors XXXIII (TRANSDUCERS EUROSENSORS XXXIII), 2019, pp. 1281–1284.

[105] X. Huang et al., “A Binder Jet Printed, Stainless Steel Preconcentrator as an In-Line Injector of Volatile Organic Compounds,” *Sensors*, vol. 19, no. 12, p. 2748, Jan. 2019.

[106] T. H. Chappuis et al., “Miniaturization of breath sampling with silicon chip: application to volatile tobacco markers tracking,” *J. Breath Res.*, 2018.

[107] N. A. Zaidi, M. W. Tahir, M. J. Vellekoop, and W. Lang, “Design of Novel Ceramic Preconcentrator and Integration in Gas Chromatographic System for Detection of Ethylene Gas from Ripening Bananas,” *Sensors*, vol. 18, no. 8, p. 2589, Aug. 2018.

[108] Y. Zhang, J. Sun, X. Zhu, J. Liu, and Z. Ning, “Mini pretreatment system integrated with micro pre-concentrator and micro GC column,” *Sensor Review*, vol. 37, no. 2, pp. 137–141, Mar. 2017.

[109] J. W. Trzciński et al., “In Search of the Ultimate Benzene Sensor: The EtQxBox Solution,” *ACS Sensors*, vol. 2, no. 4, pp. 590–598, Apr. 2017.

[110] M. M. McCartney et al., “An Easy to Manufacture Micro Gas Preconcentrator for Chemical Sensing Applications,” *ACS Sensors*, vol. 2, no. 8, pp. 1167–1174, Aug. 2017.

[111] S. Janssen, T. Tessmann, and W. Lang, “High sensitive and selective ethylene measurement by using a large-capacity-on-chip preconcentrator device,” *Sensors and Actuators B: Chemical*, vol. 197, pp. 405–413, Jul. 2014.

[112] A. M. Rydosz, D. Michon, K. Domanski, W. Maziarz, and T. Pisarkiewicz, “Various Preconcentrator Structures For Determination of Acetone in a Wide Range of Concentration,” *Advances in Electrical and Electronic Engineering*, vol. 14, no. 1, pp. 59–65–65, Mar. 2016.

[113] D. Michoń, A. Rydosz, K. Domański, W. Maziarz, and T. Pisarkiewicz, “Detection of acetone in exhaled breath with the use of micropreconcentrator and a commercial gas sensor,” 2016, p. 1017511.

- [114] M. Camara, P. Breuil, C. Pijolat, J. P. Viricelle, N. F. de Rooij, and D. Briand, "Tubular gas preconcentrators based on inkjet printed micro-hotplates on foil," *Sensors and Actuators B: Chemical*, vol. 236, pp. 1111–1117, Nov. 2016.
- [115] F. Almazán et al., "Zeolite based microconcentrators for volatile organic compounds sensing at trace-level: fabrication and performance," *J. Micromech. Microeng.*, vol. 26, no. 8, p. 084010, 2016.
- [116] Y. Qin and Y. B. Gianchandani, "A fully electronic microfabricated gas chromatograph with complementary capacitive detectors for indoor pollutants," *Microsystems & Nanoengineering*, vol. 2, p. 15049, Feb. 2016.
- [117] J. Lee, M. Zhou, H. Zhu, R. Nidetz, K. Kurabayashi, and X. Fan, "Fully Automated Portable Comprehensive 2-Dimensional Gas Chromatography Device," 06-Oct-2016. [Online]. Available: <http://pubs.acs.org/doi/abs/10.1021/acs.analchem.6b03000>. [Accessed: 14-Jan-2019].
- [118] X. F. Zhu, Z. W. Ning, J. H. Sun, T. J. Ma, Y. N. Zhang, and J. H. Liu, "Micro-Fabricated Pre-Concentrator Filled with Single-Walled Carbon Nanotubes as Adsorbent Material," *Key Engineering Materials*, vol. 645–646, pp. 681–686, May 2015.
- [119] A. Garg et al., "Zebra GC: A mini gas chromatography system for trace-level determination of hazardous air pollutants," *Sensors and Actuators B: Chemical*, vol. 212, pp. 145–154, Jun. 2015.
- [120] J. Bryant-Genevier and E. T. Zellers, "Toward a microfabricated preconcentrator-focuser for a wearable micro-scale gas chromatograph," *Journal of Chromatography A*, vol. 1422, pp. 299–309, Nov. 2015.
- [121] R.-S. Jian, Y.-S. Huang, S.-L. Lai, L.-Y. Sung, and C.-J. Lu, "Compact instrumentation of a μ -GC for real time analysis of sub-ppb VOC mixtures," *Microchemical Journal*, vol. 108, pp. 161–167, May 2013.
- [122] T. Sukaew, H. Chang, G. Serrano, and E. T. Zellers, "Multi-stage preconcentrator/focuser module designed to enable trace level determinations of trichloroethylene in indoor air with a microfabricated gas chromatograph," *Analyst*, vol. 136, no. 8, pp. 1664–1674, Mar. 2011.
- [123] B. Han, H. Wang, H. Huang, T. Liu, G. Wu, and J. Wang, "Micro-fabricated packed metal gas preconcentrator for enhanced monitoring of ultralow concentration of isoprene," *Journal of Chromatography A*, Aug. 2018.
- [124] H. Lahlou, X. Vilanova, and X. Correig, "Gas phase micro-preconcentrators for benzene monitoring: A review," *Sensors and Actuators B: Chemical*, vol. 176, pp. 198–210, Jan. 2013.

- [125] I. Voiculescu et al., "Micropreconcentrator for enhanced trace detection of explosives and chemical agents," *IEEE Sensors Journal*, vol. 6, no. 5, pp. 1094–1104, 2006.
- [126] I. Lara-Ibeas et al., "Sub-ppb Level Detection of BTEX Gaseous Mixtures with a Compact Prototype GC Equipped with a Preconcentration Unit," *Micromachines*, vol. 10, no. 3, p. 187, Mar. 2019.
- [127] E. H. M. Camara, P. Breuil, D. Briand, N. F. de Rooij, and C. Pijolat, "A micro gas preconcentrator with improved performance for pollution monitoring and explosives detection," *Analytica Chimica Acta*, vol. 688, no. 2, pp. 175–182, Mar. 2011.
- [128] N. A. Zaidi, M. W. Tahir, M. J. Vellekoop, and W. Lang, "A Gas Chromatographic System for the Detection of Ethylene Gas Using Ambient Air as a Carrier Gas," *Sensors*, vol. 17, no. 10, p. 2283, Oct. 2017.
- [129] B. Alfeeli and M. Agah, "MEMS-Based Selective Preconcentration of Trace Level Breath Analytes," *IEEE Sensors Journal*, vol. 9, no. 9, pp. 1068–1075, Sep. 2009.
- [130] B. Alfeeli, H. Vereb, A. Dietrich, and M. Agah, "Low pressure drop micro preconcentrators with cobweb Tenax-TA film for analysis of human breath," in *2011 IEEE 24th International Conference on Micro Electro Mechanical Systems*, 2011, pp. 916–919.
- [131] B. Han, G. Wu, H. Wang, and J. Wang, "Micro-fabricated packed metal gas preconcentrator for low detection limit exhaled VOC gas measurements," 2017, pp. 269–273.
- [132] J. Lee, M. Jung, S. Barthwal, S. Lee, and S.-H. Lim, "MEMS gas preconcentrator filled with CNT foam for exhaled VOC gas detection," *BioChip Journal*, vol. 9, no. 1, pp. 44–49, Mar. 2015.
- [133] J. Wang, N. Nuñovero, Z. Lin, R. Nidetz, S. Buggaveeti, C. Zhan, K. Kurabayashi, W.H. Steinecker, E.T. Zellers, "A Wearable MEMS Gas Chromatograph for Multi-Vapor Determinations," *Procedia Engineering*, vol. 168, pp. 1398–1401, 2016.
- [134] X. F. Zhu, Z. W. Ning, J. H. Sun, T. J. Ma, Y. N. Zhang, and J. H. Liu, "Micro-Fabricated Pre-Concentrator Filled with Single-Walled Carbon Nanotubes as Adsorbent Material," *Key Engineering Materials*, vol. 645–646, pp. 681–686, May 2015.
- [135] R. Huang, M. Lu, P. Wang, Y. Chen, J. Wu, M. Fu, L. Chen, D. Ye, "Enhancement of the non-thermal plasma-catalytic system with different zeolites for toluene removal," *RSC Adv.*, vol. 5, no. 88, pp. 72113–72120, Aug. 2015.

- [136] M.-Y. Wong, W.-R. Cheng, M.-H. Liu, W.-C. Tian, and C.-J. Lu, "A preconcentrator chip employing μ -SPME array coated with in-situ-synthesized carbon adsorbent film for VOCs analysis," *Talanta*, vol. 101, pp. 307–313, Nov. 2012.
- [137] B. Buszewski, M. Kęsy, T. Ligor, and A. Amann, "Human exhaled air analytics: biomarkers of diseases," *Biomedical Chromatography*, vol. 21, no. 6, pp. 553–566, 2007.
- [138] P. Atkins and J. de Paula, *Atkins' Physical Chemistry*. OUP Oxford, 2010.
- [139] H. Freundlich, *Kapillarchemie, eine Darstellung der Chemie der Kolloide und verwandter Gebiete*, von Dr. Herbert Freundlich, ... Akademische Verlagsgesellschaft, 1909.
- [140] E. Worch, *Adsorption Technology in Water Treatment: Fundamentals, Processes, and Modeling*. Walter de Gruyter, 2012.
- [141] "Adsorption:Langmuir - Wiketomica." [Online]. Available: <http://rheneas.eng.buffalo.edu/wiki/Adsorption:Langmuir>. [Accessed: 25-Jul-2019].
- [142] S. Brunauer, P. H. Emmett, and E. Teller, "Adsorption of Gases in Multimolecular Layers," *J. Am. Chem. Soc.*, vol. 60, no. 2, pp. 309–319, Feb. 1938.
- [143] C. R. Clarkson and B. Haghshenas, "Modeling of Supercritical Fluid Adsorption on Organic-Rich Shales and Coal," in *SPE Unconventional Resources Conference-USA*, The Woodlands, Texas, USA, 2013.
- [144] J. A. G. Balanay, S. A. Crawford, and C. T. Lungu, "Comparison of Toluene Adsorption Among Granular Activated Carbon and Different Types of Activated Carbon Fibers (ACFs)," *Journal of Occupational and Environmental Hygiene*, vol. 8, no. 10, pp. 573–579, Oct. 2011.
- [145] V. Gaur, A. Sharma, and N. Verma, "Preparation and characterization of ACF for the adsorption of BTX and SO₂," *Chemical Engineering and Processing: Process Intensification*, vol. 45, no. 1, pp. 1–13, Jan. 2006.
- [146] X. Zhang, S. Chen, and H. T. Bi, "Application of wave propagation theory to adsorption breakthrough studies of toluene on activated carbon fiber beds," *Carbon*, vol. 48, no. 8, pp. 2317–2326, Jul. 2010.
- [147] T. García, R. Murillo, D. Cazorla-Amorós, A. M. Mastral, and A. Linares-Solano, "Role of the activated carbon surface chemistry in the adsorption of phenanthrene," *Carbon*, vol. 42, no. 8, pp. 1683–1689, Jan. 2004.

- [148] C. Moreno-Castilla, "Adsorption of organic molecules from aqueous solutions on carbon materials," *Carbon*, vol. 42, no. 1, pp. 83–94, Jan. 2004.
- [149] S.-H. Pak, M.-J. Jeon, and Y.-W. Jeon, "Study of sulfuric acid treatment of activated carbon used to enhance mixed VOC removal," *International Biodeterioration & Biodegradation*, vol. 113, pp. 195–200, Sep. 2016.
- [150] Y.-C. Chiang, P.-C. Chiang, and C.-P. Huang, "Effects of pore structure and temperature on VOC adsorption on activated carbon," *Carbon*, vol. 39, no. 4, pp. 523–534, Apr. 2001.
- [151] J. Rivera-Utrilla, M. Sánchez-Polo, V. Gómez-Serrano, P. M. Álvarez, M. C. M. Alvim-Ferraz, and J. M. Dias, "Activated carbon modifications to enhance its water treatment applications. An overview," *Journal of Hazardous Materials*, vol. 187, no. 1, pp. 1–23, Mar. 2011.
- [152] E. M. Carter, L. E. Katz, G. E. Speitel, and D. Ramirez, "Gas-Phase Formaldehyde Adsorption Isotherm Studies on Activated Carbon: Correlations of Adsorption Capacity to Surface Functional Group Density," *Environ. Sci. Technol.*, vol. 45, no. 15, pp. 6498–6503, Aug. 2011.
- [153] L. Tang, L. Li, R. Chen, C. Wang, W. Ma, and X. Ma, "Adsorption of acetone and isopropanol on organic acid modified activated carbons," *Journal of Environmental Chemical Engineering*, vol. 4, no. 2, pp. 2045–2051, Jun. 2016.
- [154] R. Ortmann, C. Pasel, M. Luckas, S. Kraas, M. Fröba, and D. Bathen, "Sorption of Acetaldehyde and Hexanal in Trace Concentrations on Carbon-Based Adsorbents," *Chemical Engineering & Technology*, vol. 38, no. 1, pp. 125–130, 2015.
- [155] Y. An, Q. Fu, D. Zhang, Y. Wang, and Z. Tang, "Performance evaluation of activated carbon with different pore sizes and functional groups for VOC adsorption by molecular simulation," *Chemosphere*, vol. 227, pp. 9–16, Jul. 2019.
- [156] W.-C. Tian, H. K. L. Chan, C.-J. Lu, S. W. Pang, and E. T. Zellers, "Multiple-stage microfabricated preconcentrator-focuser for micro gas chromatography system," *Journal of Microelectromechanical Systems*, vol. 14, no. 3, pp. 498–507, Jun. 2005.
- [157] T. R. Gaffney, "Porous solids for air separation," *Current Opinion in Solid State and Materials Science*, vol. 1, no. 1, pp. 69–75, Feb. 1996.
- [158] H. Jüntgen, K. Knoblauch, and K. Harder, "Carbon molecular sieves: production from coal and application in gas separation," *Fuel*, vol. 60, no. 9, pp. 817–822, Sep. 1981.

- [159] "Thermal Desorption Tubes: Unconditioned, Conditioned & Capped / Sample Handling / Chromatography Products at Restek.com." [Online]. Available: <https://www.restek.com/catalog/view/7837>. [Accessed: 30-Jun-2019].
- [160] US EPA, "Air Toxics Monitoring Methods | Ambient Monitoring Technology Information Center | US EPA Stations." [Online]. Available: <https://www3.epa.gov/ttn/amtic/airtox.html#compendium>. [Accessed: 24-Apr-2018].
- [161] A. M. Burke, J. P. Hanrahan, D. A. Healy, J. R. Sodeau, J. D. Holmes, and M. A. Morris, "Large pore bi-functionalised mesoporous silica for metal ion pollution treatment," *J. Hazard. Mater.*, vol. 164, no. 1, pp. 229–234, May 2009.
- [162] P. Delaney et al., "Porous silica spheres as indoor air pollutant scavengers," *J. Environ. Monit.*, vol. 12, no. 12, pp. 2244–2251, Dec. 2010.
- [163] A. Kumar et al., "Direct Air Capture of CO₂ by Physisorbent Materials," *Angewandte Chemie International Edition*, vol. 54, no. 48, pp. 14372–14377, Nov. 2015.
- [164] S.-W. Song, K. Hidajat, and S. Kawi, "Functionalized SBA-15 Materials as Carriers for Controlled Drug Delivery: Influence of Surface Properties on Matrix–Drug Interactions," *Langmuir*, vol. 21, no. 21, pp. 9568–9575, Oct. 2005.
- [165] A. Szewczyk, M. Prokopowicz, W. Sawicki, D. Majda, and G. Walker, "Aminopropyl-functionalized mesoporous silica SBA-15 as drug carrier for cefazolin: adsorption profiles, release studies, and mineralization potential," *Microporous and Mesoporous Materials*, vol. 274, pp. 113–126, Jan. 2019.
- [166] Y. Wang et al., "Mesoporous silica nanoparticles in drug delivery and biomedical applications," *Nanomedicine: Nanotechnology, Biology and Medicine*, vol. 11, no. 2, pp. 313–327, Feb. 2015.
- [167] A. Shahbazi, H. Younesi, and A. Badieli, "Functionalized SBA-15 mesoporous silica by melamine-based dendrimer amines for adsorptive characteristics of Pb(II), Cu(II) and Cd(II) heavy metal ions in batch and fixed bed column," *Chemical Engineering Journal*, vol. 168, no. 2, pp. 505–518, Apr. 2011.
- [168] J. Toufaily et al., "Functionalization of SBA-15 materials for the adsorption of phenols from aqueous solution," *Cent. Eur. J. Eng.*, vol. 3, no. 1, pp. 126–134, Mar. 2013.

- [169] A. J. Crisci, M. H. Tucker, M.-Y. Lee, S. G. Jang, J. A. Dumesic, and S. L. Scott, "Acid-Functionalized SBA-15-Type Silica Catalysts for Carbohydrate Dehydration," *ACS Catal.*, vol. 1, no. 7, pp. 719–728, Jul. 2011.
- [170] N. Hao, F. Tang, and L. Li, "MCM-41 mesoporous silica sheet with ordered perpendicular nanochannels for protein delivery and the assembly of Ag nanoparticles in catalytic applications," *Microporous and Mesoporous Materials*, vol. 218, pp. 223–227, Dec. 2015.
- [171] D. Srinivas and L. Saikia, "Functionalized SBA-15 and its Catalytic Applications in Selective Organic Transformations," *Catal Surv Asia*, vol. 12, no. 2, p. 114, Apr. 2008.
- [172] S. Savic, K. Vojisavljevic, M. Počuča-Nešić, K. Zivojevic, M. Mladenovic, and N. Knezevic, "Hard Template Synthesis of Nanomaterials Based on Mesoporous Silica," *Metallurgical and Materials Engineering*, vol. 24, no. 4, Dec. 2018.
- [173] D. Zhao et al., "Triblock Copolymer Syntheses of Mesoporous Silica with Periodic 50 to 300 Angstrom Pores," *Science*, vol. 279, no. 5350, pp. 548–552, Jan. 1998.
- [174] J. P. Thielemann, F. Girgsdies, R. Schlögl, and C. Hess, "Pore structure and surface area of silica SBA-15: influence of washing and scale-up," *Beilstein Journal of Nanotechnology*, vol. 2, no. 1, pp. 110–118, Feb. 2011.
- [175] K. Cassiers et al., "A Detailed Study of Thermal, Hydrothermal, and Mechanical Stabilities of a Wide Range of Surfactant Assembled Mesoporous Silicas," *Chem. Mater.*, vol. 14, no. 5, pp. 2317–2324, May 2002.
- [176] F. Zhang et al., "Understanding Effect of Wall Structure on the Hydrothermal Stability of Mesostructured Silica SBA-15," *J. Phys. Chem. B*, vol. 109, no. 18, pp. 8723–8732, May 2005.
- [177] A. Corma, H. García, and F. X. Llabrés i Xamena, "Engineering Metal Organic Frameworks for Heterogeneous Catalysis," *Chem. Rev.*, vol. 110, no. 8, pp. 4606–4655, Aug. 2010.
- [178] J. Lee, O. K. Farha, J. Roberts, K. A. Scheidt, S. T. Nguyen, and J. T. Hupp, "Metal–organic framework materials as catalysts," *Chem. Soc. Rev.*, vol. 38, no. 5, pp. 1450–1459, Apr. 2009.
- [179] X. Xu, Z. Zhang, and X. Wang, "Well-Defined Metal–Organic-Framework Hollow Nanostructures for Catalytic Reactions Involving Gases," *Advanced Materials*, vol. 27, no. 36, pp. 5365–5371, 2015.

- [180] K.-S. Lin, A. K. Adhikari, C.-N. Ku, C.-L. Chiang, and H. Kuo, "Synthesis and characterization of porous HKUST-1 metal organic frameworks for hydrogen storage," *International Journal of Hydrogen Energy*, vol. 37, no. 18, pp. 13865–13871, Sep. 2012.
- [181] N. L. Rosi et al., "Hydrogen Storage in Microporous Metal-Organic Frameworks," *Science*, vol. 300, no. 5622, pp. 1127–1129, May 2003.
- [182] J.-R. Li, J. Sculley, and H.-C. Zhou, "Metal–Organic Frameworks for Separations," *Chem. Rev.*, vol. 112, no. 2, pp. 869–932, Feb. 2012.
- [183] S. R. Venna and M. A. Carreon, "Metal organic framework membranes for carbon dioxide separation," *Chemical Engineering Science*, vol. 124, pp. 3–19, Mar. 2015.
- [184] L. Li et al., "Flexible–Robust Metal–Organic Framework for Efficient Removal of Propyne from Propylene," *J. Am. Chem. Soc.*, vol. 139, no. 23, pp. 7733–7736, Jun. 2017.
- [185] G. W. Peterson et al., "Multifunctional Purification and Sensing of Toxic Hydride Gases by CuBTC Metal–Organic Framework," *Ind. Eng. Chem. Res.*, vol. 54, no. 14, pp. 3626–3633, Apr. 2015.
- [186] J. Kim, H.-Y. Cho, and W.-S. Ahn, "Synthesis and Adsorption/Catalytic Properties of the Metal Organic Framework CuBTC," *Catal Surv Asia*, vol. 16, no. 2, pp. 106–119, Jun. 2012.
- [187] J.-M. Yang, Q. Liu, Y.-S. Kang, and W.-Y. Sun, "Controlled growth and gas sorption properties of IRMOF-3 nano/microcrystals," *Dalton Trans.*, vol. 43, no. 44, pp. 16707–16712, Sep. 2014.
- [188] "Zeolite structure and types - Lenntech." [Online]. Available: <https://www.lenntech.pl/zeolites-structure-types.htm>. [Accessed: 24-Jun-2019].
- [189] J. Weitkamp, *Catalysis and Zeolites: Fundamentals and Applications*. Springer Science & Business Media, 1999.
- [190] B. Sels, *Zeolites and Zeolite-like Materials*. Elsevier Science, 2016.
- [191] B. Jha and D. N. Singh, "A Review on Synthesis, Characterization and Industrial Applications of Flyash Zeolites," *JOURNAL OF MATERIALS EDUCATION*, vol. 33, no. 1/2, pp. 65–132, 2011.
- [192] S. M. Auerbach, K. A. Carrado, and P. K. Dutta, *Handbook of Zeolite Science and Technology*. CRC Press, 2003.
- [193] J. Weitkamp, "Zeolites and catalysis," *Solid State Ionics*, vol. 131, no. 1, pp. 175–188, Jun. 2000.
- [194] A. Julbe and M. Drobek, "Zeolite X: Type," in *Encyclopedia of Membranes*, E. Drioli and L. Giorno, Eds. Berlin, Heidelberg: Springer Berlin Heidelberg, 2014, pp. 1–2.

- [195] D. R. Lide, *CRC Handbook of Chemistry and Physics*, 84th Edition. CRC Press, 2003.
- [196] S. K. P. Veerapandian, N. De Geyter, J.-M. Giraudon, J.-F. Lamonier, and R. Morent, "The Use of Zeolites for VOCs Abatement by Combining Non-Thermal Plasma, Adsorption, and/or Catalysis: A Review," *Catalysts*, vol. 9, no. 1, p. 98, Jan. 2019.
- [197] A. Walcarius and L. Mercier, "Mesoporous organosilica adsorbents: nanoengineered materials for removal of organic and inorganic pollutants," *Journal of Materials Chemistry*, vol. 20, p. 4478, 2010.
- [198] D. Das, V. Gaur, and N. Verma, "Removal of volatile organic compound by activated carbon fiber," *Carbon*, vol. 42, no. 14, pp. 2949–2962, Jan. 2004.
- [199] D. P. Serrano, G. Calleja, J. A. Botas, and F. J. Gutierrez, "Adsorption and Hydrophobic Properties of Mesostructured MCM-41 and SBA-15 Materials for Volatile Organic Compound Removal," *Ind. Eng. Chem. Res.*, vol. 43, no. 22, pp. 7010–7018, Oct. 2004.
- [200] G. B. Baur, "Development of Adsorbents for Selective Volatile Organic Compounds Removal from Diluted Gas Streams," *Infoscience*, 2015. [Online]. Available: <https://infoscience.epfl.ch/record/212805>. [Accessed: 30-Jun-2019].
- [201] K. L. Foster, R. G. Fuerman, J. Economy, S. M. Larson, and M. J. Rood, "Adsorption characteristics of trace volatile organic compounds in gas streams onto activated carbon fibers," *Chem. Mater.*, vol. 4, no. 5, pp. 1068–1073, Sep. 1992.
- [202] M. A. Lillo-Ródenas, D. Cazorla-Amorós, and A. Linares-Solano, "Benzene and toluene adsorption at low concentration on activated carbon fibres," *Adsorption*, vol. 17, no. 3, pp. 473–481, Jun. 2011.
- [203] P. A. Russo, M. M. L. R. Carrott, and P. J. M. Carrott, "Hydrocarbons adsorption on templated mesoporous materials: effect of the pore size, geometry and surface chemistry," *New J. Chem.*, vol. 35, no. 2, pp. 407–416, Feb. 2011.
- [204] B. Dou et al., "Enhanced removal of toluene by dielectric barrier discharge coupling with Cu-Ce-Zr supported ZSM-5/TiO₂/Al₂O₃," *Catalysis Communications*, vol. 92, pp. 15–18, Mar. 2017.
- [205] A. Ogata, D. Ito, K. Mizuno, S. Kushiyama, and T. Yamamoto, "Removal of dilute benzene using a zeolite-hybrid plasma reactor," *IEEE Transactions on Industry Applications*, vol. 37, no. 4, pp. 959–964, Jul. 2001.

- [206] K.-J. Kim and H.-G. Ahn, "The effect of pore structure of zeolite on the adsorption of VOCs and their desorption properties by microwave heating," *Microporous and Mesoporous Materials*, vol. 152, pp. 78–83, Apr. 2012.
- [207] W. Wang, H. Wang, T. Zhu, and X. Fan, "Removal of gas phase low-concentration toluene over Mn, Ag and Ce modified HZSM-5 catalysts by periodical operation of adsorption and non-thermal plasma regeneration," *Journal of Hazardous Materials*, vol. 292, pp. 70–78, Jul. 2015.
- [208] C. Liu, L.-Q. Yu, Y.-T. Zhao, and Y.-K. Lv, "Recent advances in metal-organic frameworks for adsorption of common aromatic pollutants," *Microchim Acta*, vol. 185, no. 7, p. 342, Jun. 2018.
- [209] S.-W. Lv et al., "Recent advances on porous organic frameworks for the adsorptive removal of hazardous materials," *Journal of Environmental Sciences*, vol. 80, pp. 169–185, Jun. 2019.
- [210] S. H. Jhung, J.-H. Lee, J. W. Yoon, C. Serre, G. Férey, and J.-S. Chang, "Microwave Synthesis of Chromium Terephthalate MIL-101 and Its Benzene Sorption Ability," *Advanced Materials*, vol. 19, no. 1, pp. 121–124, 2007.
- [211] F. Rodriguez-Reinoso, M. Molina-Sabio, and M. A. Munecas, "Effect of microporosity and oxygen surface groups of activated carbon in the adsorption of molecules of different polarity," *J. Phys. Chem.*, vol. 96, no. 6, pp. 2707–2713, Mar. 1992.
- [212] H. B. An et al., "Indoor formaldehyde removal over CMK-3," *Nanoscale Res Lett*, vol. 7, no. 1, p. 7, Jan. 2012.
- [213] S. Shin and J. Song, "Modeling and simulations of the removal of formaldehyde using silver nano-particles attached to granular activated carbon," *Journal of Hazardous Materials*, vol. 194, pp. 385–392, Oct. 2011.
- [214] Y. Song, W. Qiao, S.-H. Yoon, I. Mochida, Q. Guo, and L. Liu, "Removal of formaldehyde at low concentration using various activated carbon fibers," *Journal of Applied Polymer Science*, vol. 106, no. 4, pp. 2151–2157, 2007.
- [215] K. J. Lee, J. Miyawaki, N. Shiratori, S.-H. Yoon, and J. Jang, "Toward an effective adsorbent for polar pollutants: Formaldehyde adsorption by activated carbon," *Journal of Hazardous Materials*, vol. 260, pp. 82–88, Sep. 2013.
- [216] H. Rong, Z. Ryu, J. Zheng, and Y. Zhang, "Effect of air oxidation of Rayon-based activated carbon fibers on the adsorption behavior for formaldehyde," *Carbon*, vol. 40, no. 13, pp. 2291–2300, Jan. 2002.

- [217] V. Boonamnuayvitaya, S. Sae-ung, and W. Tanthapanichakoon, "Preparation of activated carbons from coffee residue for the adsorption of formaldehyde," *Separation and Purification Technology*, vol. 42, no. 2, pp. 159–168, Mar. 2005.
- [218] A. Nomura and C. W. Jones, "Amine-Functionalized Porous Silicas as Adsorbents for Aldehyde Abatement," *ACS Appl. Mater. Interfaces*, vol. 5, no. 12, pp. 5569–5577, Jun. 2013.
- [219] J. H. Drese, A. D. Talley, and C. W. Jones, "Aminosilica Materials as Adsorbents for the Selective Removal of Aldehydes and Ketones from Simulated Bio-Oil," *ChemSusChem*, vol. 4, no. 3, pp. 379–385, 2011.
- [220] W. P. Jencks, "Studies on the Mechanism of Oxime and Semicarbazone Formation 1," *J. Am. Chem. Soc.*, vol. 81, no. 2, pp. 475–481, Jan. 1959.
- [221] J.-P. Bellat et al., "Capture of formaldehyde by adsorption on nanoporous materials," *Journal of Hazardous Materials*, vol. 300, pp. 711–717, Dec. 2015.
- [222] D.-Z. Zhao, X.-S. Li, C. Shi, H.-Y. Fan, and A.-M. Zhu, "Low-concentration formaldehyde removal from air using a cycled storage–discharge (CSD) plasma catalytic process," *Chemical Engineering Science*, vol. 66, no. 17, pp. 3922–3929, Sep. 2011.
- [223] S. Revah and J. M. Morgan-Sagastume, "Methods of Odor and VOC Control," in *Biotechnology for Odor and Air Pollution Control*, Z. Shareefdeen and A. Singh, Eds. Berlin, Heidelberg: Springer Berlin Heidelberg, 2005, pp. 29–63.
- [224] M. Słomińska, S. Król, and J. Namieśnik, "Removal of BTEX Compounds From Waste Gases; Destruction and Recovery Techniques," *Critical Reviews in Environmental Science and Technology*, vol. 43, no. 14, pp. 1417–1445, Jan. 2013.
- [225] G. R. Parmar and N. N. Rao, "Emerging Control Technologies for Volatile Organic Compounds," *Critical Reviews in Environmental Science and Technology*, vol. 39, no. 1, pp. 41–78, Dec. 2008.
- [226] F. I. Khan and A. Kr. Ghoshal, "Removal of Volatile Organic Compounds from polluted air," *Journal of Loss Prevention in the Process Industries*, vol. 13, no. 6, pp. 527–545, Nov. 2000.
- [227] V. I. Parvulescu, M. Magureanu, and P. Lukes, Eds., *Plasma Chemistry and Catalysis in Gases and Liquids*. Weinheim, Germany: Wiley-VCH Verlag GmbH & Co. KGaA, 2012.
- [228] "Plasma Chemistry and Catalysis in Gases and Liquids - Google Books." [Online]. Available: https://books.google.fr/books?id=UG_Tsd2UBQ8C&pg=PA133&lpg=PA133&dq=plasma+oxidation+r

emoval+voc+cost&source=bl&ots=2kW_Q58EKr&sig=ACfU3U0x1aiHa0cpXqC6W8nod0pqcRiXBg&hl=en&sa=X&ved=2ahUKEwjLqcmk05XjAhUh3OAKHeExBRcQ6AEwBnoECAkQAQ#v=onepage&q=plasma%20oxidation%20removal%20voc%20cost&f=false. [Accessed: 02-Jul-2019].

[229] H. Cox, "Co-treatment of H₂S and toluene in a biotrickling filter," *Chemical Engineering Journal*, vol. 87, no. 1, pp. 101–110, May 2002.

[230] B. Guieysse, C. Hort, V. Platel, R. Munoz, M. Ondarts, and S. Revah, "Biological treatment of indoor air for VOC removal: Potential and challenges," *Biotechnology Advances*, vol. 26, no. 5, pp. 398–410, Sep. 2008.

[231] M. M. Galera, E. Cho, E. Tuuguu, S.-J. Park, C. Lee, and W.-J. Chung, "Effects of pollutant concentration ratio on the simultaneous removal of NH₃, H₂S and toluene gases using rock wool-compost biofilter," *Journal of Hazardous Materials*, vol. 152, no. 2, pp. 624–631, Apr. 2008.

[232] M. Yeow, "Preparation of divinyl-PDMS/PVDF composite hollow fibre membranes for BTX removal," *Journal of Membrane Science*, vol. 203, no. 1–2, pp. 137–143, Jun. 2002.

[233] R. Nasreddine, "Développement d'une méthode analytique et d'un microanalyseur miniaturisé pour la détection des BTEX dans l'air," thesis, Strasbourg, 2016.

[234] R. Nasreddine, V. Person, C. A. Serra, and S. Le Calvé, "Development of a novel portable miniaturized GC for near real-time low level detection of BTEX," *Sensors and Actuators B: Chemical*, vol. 224, pp. 159–169, 2016.

Chapter 2. Materials and Methods

In this chapter, the materials used during this thesis project are introduced and the techniques employed for their characterization are also described. Afterwards, the different experimental setups used for dynamic adsorption experiments and the calculation methods employed are presented. Finally, design and fabrication of several prototypes of a BTEX preconcentrator are detailed.

2.1 Study of VOC adsorption/desorption behaviour

VOC adsorption and desorption behaviours were investigated on different types of commercial materials: a graphitized carbon black (Carbopack® B), a metal organic framework (Basolite® C300), a mesoporous silica (SBA-16) and ZSM-5 zeolite (CBV-3020E). Furthermore, this behaviour was also studied in a series of ZSM-5 zeolites with different Si/Al ratios that were synthesized by the Group of Energy and Fuels for a Sustainable Environment Team at ICPEES led by Benoît Louis. This section is organised as follows: first, the main characteristics of these solids are presented in section 2.1.1. Afterwards, the techniques used for the characterization of these materials and the experimental conditions employed in this study are described in section 2.1.2. Finally, the theoretical basis of dynamic adsorption experiments and the different experimental setups employed during this research work are detailed in section 2.1.3.

2.1.1 Selected adsorbents

Many sorbents have been used for VOC trapping and preconcentration depending on the type of compound of interest. This work was mainly focused on two different groups of compounds: BTEX and aldehydes. The first group called BTEX consists of non-polar aromatic compounds with relatively high volatility and kinetic diameters between 5.8 and 6.8 Å. The second group includes a large variety of molecules but only formaldehyde and hexanal have been investigated regarding their occurrence and high levels in indoor environments. Since these two aldehydes have the same functional group, the dipole moments are similar (see chapter 1 in section 1.4.3); however, their boiling points are very different, being -19.4 and 131 °C for formaldehyde and hexanal, respectively. This significant difference is due to the size of the molecules: formaldehyde is a small molecule with a single carbon whereas hexanal has an alkyl chain of 6 carbon atoms which results in stronger intramolecular forces. Due to the diverse nature of the targeted compounds, four types of sorbents with different polarities,

chemical surfaces and pore sizes were selected to evaluate their adsorption/desorption behaviours. Among them, they are four commercially available adsorbents and several *in-situ* synthesized zeolites with different Si/Al ratios and acidities. The main features of the commercial adsorbents provided by the suppliers are listed in Table 2-1. In this work, a more exhaustive characterisation of the materials was conducted and it will be presented in Chapter 5.

Table 2-1. Main characteristics of commercially available adsorbents selected for the study

Name	Supplier	Material type	Specific surface area (m ² /g)	Particle size (µm)	Porosity
Carbopack™ B	Supelco	GCB	100	180 - 250	Non-porous
SBA-16	ACS Materials	Mesoporous silica	500 - 700	50 - 120	Mesoporous
Basolite™ C300	Sigma Aldrich	MOF	1500 – 2100	15.96*	Microporous
CBV-3020E	Zeolyst	Zeolite	403	-	Microporous

GCB = graphitized carbon black, MOF = metal organic framework. *This value corresponds to D50 in particle size distribution

2.1.1.1 Carbopack™ B

Carbopack™ B is a non-porous graphitized carbon black (GCB) used as a reference material for VOC trapping in the EPA (Environmental Protection Agency) method TO-17 and has been widely used for VOC sampling and analysis [1]–[4]. This material is considered to have a medium strength, which means that it is suitable for trapping relatively high volatile compounds ranging from n-C₆ to n-C₂₀. Hence, it is expected to have a better adsorption of BTEX and hexanal than formaldehyde. Furthermore, Carbopack™ B is hydrophobic resulting in a high VOC adsorption even in extremely humid environments. In this study, Carbopack™ B has been employed as a reference material to compare the results obtained with other sorbents.

2.1.1.2 Basolite™ C300

Basolite™ C300 (Cu₃(BTC)₂(H₂O)₃), called also Cu-BTC, HKUST-1 or MOF-199, is a metal organic framework formed by multiple links of paddle-wheel-like coordination between two Cu²⁺ ions and four 1,3,5-benzenetricarboxylate (BTC) ligands [5]. This arrangement leads to the three-dimensional structure displayed in Figure 2-1a, containing three different types of pores represented by coloured

spheres, two of similar size (green and orange spheres) and a smaller pore (pink sphere). The detailed structures and the window sizes of these cages are presented in Figure 2-1b. These pores can host small molecules making this material exceptional for multiple applications such as gas storage [6] and separation, catalysis and pollutants removal from gas effluents [7]. It should be noted that, in this structure, Cu^{2+} ions are exposed to the open spaces of the larger cages, being easily accessible for the interaction with the guest molecules. These Cu^{2+} ions are open coordination sites (OCS) that are usually coordinated to water molecules, but these latter can be replaced by other Lewis bases such as carbon dioxide, amines, etc. The porous structure with several OCS of Basolite™ C300 altogether with a very high specific surface area ranging from 1500-2100 m^2/g , constitutes an extraordinary adsorbent for numerous VOCs. It is why this material was selected in this study.

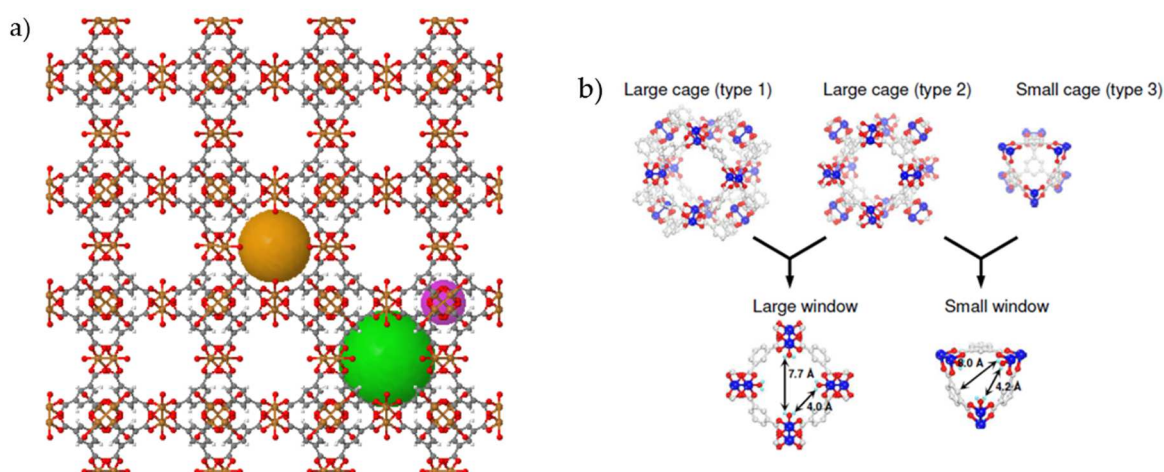


Figure 2-1. a) Schematic view of Basolite™ C300 three-dimensional structure. The spheres represent the pore volume. Atoms are displayed in the following colours: Carbon (grey), Hydrogen (white), Oxygen (red) and Copper (brown) and b) Representation of different cages and windows in Basolite™ C300. Atoms are displayed in the following colours: Carbon (white), Oxygen (red) and Copper (blue). For simplicity, hydrogen atoms are not displayed [8].

2.1.1.3 SBA-16

SBA-16 (Santa Barbara No. 16) is a mesoporous silica with cubic $Im\bar{3}m$ pore morphology formed by silicon atoms bonded by oxygen bridges. Specific surface, porosity, and particle shape may vary depending on the synthesis conditions. SBA-16 provided by ACS materials was synthesized using tetraethoxysilane (TEOS) as a silicon source and a ternary combination of surfactant (F127 (EO106PO70EO106)), water, and butanol [9]. According to the supplier, employing this synthetic route, micron-sized spheres and amorphous aggregated particles, with pores ranging from 3 to 5 nm,

are obtained. These pores are large enough to host BTEX or formaldehyde molecules since their kinetic diameters range from 0.25 to 0.58 nm. As shown previously in Figure 1-23, SBA-16 presents 3D cubic arrangement of pores corresponding to $Im\bar{3}m$ crystallographic group, which provides a high specific surface area up to 700 m²/g available for adsorption. Since silica surface is covered with OH groups [10], it is envisaged that the main adsorbate-adsorbent forces will be of hydrogen bond-type, which means that this material will not be very selective as it can interact almost with every compound containing hydrogen. On the other hand, hydrogen bond is one of the strongest intermolecular forces, but weaker than covalent or ionic bonds which can be very advantageous for a reversible adsorption process. This aspect could be interesting in terms of gas preconcentration if the desorption can operate at a moderate temperature, so that, this material was selected for more detailed study. Furthermore, the pore size in SBA-16 is bigger than Basolite® C300, hence, the comparison of both materials allows us to evaluate the influence of the pore size on the adsorption properties.

2.1.1.4 ZSM-5 zeolites

As mentioned in chapter 1 in section 1.1.1.5, zeolites are formed by silicon and aluminium atoms linked by oxygen bridges. This configuration can be arranged in several ways, resulting in different types of zeolites. In this study, ZSM-5 was selected over other zeolites due to its high hydrophobicity and small pore size, which is very similar to the size of BTEX. As can be seen in Figure 2-2, ZSM-5 is formed by a network of straight and zigzag channels of similar diameters. Ideally, in zigzag channels, the pore opening is 5.1 Å × 5.5 Å whereas for straight channels it is equal to 5.3 Å × 5.6 Å [11]. These small dimensions determine the diffusivity of gas molecules through the network leading to a differentiation of molecules by size and shape. This discrimination has been widely exploited in catalysis, where the pore opening of the catalyst plays a key role as it determines the size of the reactant, the product or the transition intermediate that participates in the reaction [12], [13]. This shape-selectivity could be very interesting on VOC adsorption, where the zeolite could act as a molecular sieve by selectively adsorbing VOC molecules that could diffuse into the channel system. Among the aromatic compounds investigated in this study, it is expected to selectively adsorb benzene, toluene, ethylbenzene and p-xylene due to their smaller kinetic diameters compared to ortho- and meta-xylenes. The exclusion of these compounds could be beneficial as separation step in an analytical or an industrial process; therefore, to better understand the adsorption of BTEX mixtures on ZSM-5, several dynamic adsorption experiments were carried out in this research work.

For these experiments, ZSM-5 zeolites with different aluminium contents were employed. In fact, VOC adsorption is not only defined by pore size. The aluminium content, represented by Si/Al ratio, has a significant impact on sorption behaviour since it influences the hydrophobicity and the acidity of the zeolite [14], [15]. Typically, this type of zeolites is characterized by high Si/Al ratio; however, by varying the synthesis conditions, low Si/Al ratio ZSM-5 zeolites can be also synthesized [16]. Generally, hydrophobicity increases with Si/Al ratio due to the distribution of the charge in the zeolite network. Indeed, the substitution of Si^{4+} by Al^{3+} results in total negative charge in the network, which is partially located on the oxygen close to Al^{3+} of the Si-O-Al bond. Thus, this oxygen, partially negatively charged, is more probable to form hydrogen bonds with water molecules than the oxygens located between two silicon atoms in Si-O-Si bonds, leading to a decrease in the hydrophobicity of the zeolite. The total negative charge of the network is usually compensated by hydrogens giving to the zeolite an acidic nature (Brønsted acidity). The zeolite acidity not only derives from the hydrogens that compensate the negative charge of the network; the Al^{3+} atoms, which have a free orbital, are Lewis acids that can interact with Lewis bases such as NH_3 or with aromatic compounds by means of cation- π interactions. As it is expected, many studies reported an increase of the adsorption capacity of aromatic compounds as the number of Al^{3+} atoms increases, i.e. at low Si/Al ratio. However, most studies concern the adsorption of a single compound, which is unusual in real environments and, to our knowledge, there are no previous studies on the adsorption of gaseous BTEX mixtures on zeolites ZSM-5. Therefore, in this work, the influence of the Si/Al ratio on the multicomponent vapor-phase adsorption of BTEX was also investigated.

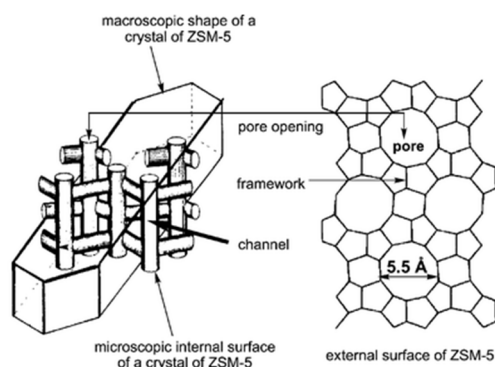


Figure 2-2. Pore structure and geometry of ZSM-5 [17].

Zeolite synthesis

ZSM-5 zeolites were synthesized *via* fluoride-mediated route adapted from previous studies [18], [19]. Typically, the aluminium source (different amounts to achieve 300, 200, 150, 100 and 50 Si/Al molar

ratios, respectively) was placed in a 150 mL-Erlenmeyer flask where 50 mL of distilled water were added under vigorous stirring (700 rpm, room temperature). Once they were dissolved, tetrapropylammonium bromide (TPABr) (0.498 g) and NH_4F (1.103 g) were sequentially added. Finally, 1.607 g of SiO_2 (Aeroperl 300/30, Evonik) was gradually added during 5 min. The gel was aged 2 h under vigorous stirring and finally autoclaved at 443 K for 144 h. H-zeolite form was obtained after a single calcination at 823 K during 15 h in static air. The samples were named as ZSM-5_1 to ZSM-5_5, respectively, where the number 1 to 5 increases according to the Si/Al molar ratio decrease, i.e. from 300 to 50.

Mg-ZSM-5 zeolite

Mg ZSM-5 zeolite was synthesized from commercial H-ZSM-5 zeolite (CBV3020E) following a procedure adapted from [20], [21]. To this purpose, 2 g of commercial ZSM-5 zeolite were dispersed in 100 mL of distilled water and stirred vigorously. Then, $\text{Mg}(\text{NO}_3)_2$ was added to the mixture was stirred at 70 °C for 1 h. Afterwards, the solution was dried in a rotavapor at 50 °C under vacuum until total evaporation of water. The solid was then dried at 110 °C overnight. Finally, the sample was calcined at 550 °C for 5 h. The amount of Mg introduced was calculated by weight difference between the original and the doped sample.

2.1.2 Characterization Techniques

Sorption is a physical and chemical process of fixation of a substance in the gas phase (sorbate) by another substance in liquid or solid state (sorbent). The nature of this phenomenon depends on the sorbate-sorbent interactions as well as on the sorbent properties. In this work, numerous techniques have been used to characterize the sorbent surface since it represents an interface between the gas and the sorbent itself; thus, the study of its properties is of great interest to understand the sorption mechanism of the targeted molecules. The characterization techniques and the experiment conditions employed in this work are detailed in this section.

2.1.2.1 *Scanning Electron Microscopy (SEM)*

Scanning Electron Microscopy (SEM) is a useful tool employed to obtain information about the particle size distribution and morphology, composition and surface topography of a sample. It is widely used in scientific- and industry-related fields as a valuable tool for material characterization.

In SEM, the sample is placed inside a chamber operated at ultra-high vacuum. Then, a high energy beam of electrons is controlled to hit part of the sample surface. The electrons interact with atoms in the sample producing secondary electrons, backscattered electrons and characteristic X-rays [22]. The generated scatter patterns provide information about the morphology and composition of the sample. All these signals are collected by different detectors and converted into black and white images. The maximum resolution obtained with this technique depends on multiple factors, but current SEM provides a maximum resolution between 1 and 20 nm.

SEM micrographs presented in this work were acquired on ZEISS GEMINI SEM 500 microscope equipped with in-lens backscatter electron (BSE) and secondary electron (SE) detectors. In this work, only the SE detector placed at the bottom lens was employed, so that most of the recovered electrons were secondary electrons although some backscatter electrons can be also recovered. This type of detector consists of a scintillator inside a Faraday cage where a low positive voltage is applied attracting secondary electrons. Then, the scintillator is employed to accelerate these electrons and convert them into photons. Finally, these photons arrive to a photomultiplier for amplification and the signal is transformed in an image.

Experimental conditions

In this work, a double face carbon tape was employed to fix the sample to the stub. Then, the stub was positioned on a sample holder with up to 9 stub positions. All the samples were examined using an electron high tension (EHT) voltage from 2 to 6 kV and a working distance of 6.6 mm for Basolite® C300 and 5.5 mm for other samples.

2.1.2.2 *N₂ physisorption: specific surface area (BET method)*

Adsorption is a surface process, therefore the characterization of the sorbent surface in terms of the specific surface area and porosity is necessary to understand the sorption mechanism of the targeted molecules on the selected sorbents. To this end, the most employed technique is N₂ physisorption at its boiling point (77 K). Nitrogen is used as the standard adsorptive since it is relatively inert, and the size of the molecule is very well known. Moreover, it forms well-defined monolayers on many non-porous and mesoporous adsorbents [23].

In this work, the specific surface area of the material was calculated from BET equation where the amount of adsorbate gas corresponding to a monomolecular layer adsorbed on the surface was determined by multi-point method. Since the BET equation (see Eq. 1-8) does not fit the entire isotherm, only measurements in the range of relative pressures near completed monolayers ($0.05 < P/P_0 < 0.3$) are used to determine the monolayer capacity. In multi-point method, at least three measurements must be conducted in this range. Then, $\frac{P}{V_p(P-P_0)}$ is plotted against P/P_0 according to equations 1-6 and the volume V_m of gas required to form a monolayer can be calculated from the slope and the intercept of the obtained curve, and thus, the monolayer capacity. Afterwards, the total surface area is calculated by the following equation:

$$S_t = n_m A_m N \quad \text{Eq. 2-1}$$

where S_t is the total surface area, n_m is the monolayer capacity, A_m is the area occupied by one molecule and N is the Avogadro's number. Finally, the total surface area divided by the weight of the sample is equal to the specific surface area.

Experimental conditions

In this study, gas sorption experiments were performed using a Micromeritics ASAP 2420. Prior to analysis, all samples were outgassed at 180 °C for 5 h under vacuum excepting zeolites, for which the outgassing was performed at 250 °C to ensure the complete desorption of water and other gas molecules. Nitrogen gas was used as the adsorbate at 77 K and the specific surface area was calculated as explained above. Total pore volume was estimated by single point method from the amount of adsorbed N₂ at $P/P_0 = 0.99$.

2.1.2.3 *Thermogravimetric Analysis – Differential Scanning Calorimetry (TGA-DSC)*

Prior to adsorption/desorption experiments, thermal stability was evaluated in order to define the range of operating temperatures for each adsorbent. For this purpose, simultaneous thermogravimetric analysis and differential scanning calorimetry were conducted.

Thermogravimetric analysis is a method of thermal analysis where sample mass is continuously monitored over time while the temperature changes. A typical thermogravimetric analyser is made up of a sample pan that is supported by a precision microbalance placed inside a furnace. Generally,

during the experiment, the temperature is increased at a fixed rate under a selected atmosphere. Most commonly used atmospheres are vacuum, inert gases, ambient air and oxidizing/reducing gases. Monitoring of sample weight enables to determine thermal events such as adsorption/desorption processes, decomposition or degradation that takes place at certain temperatures.

In this work, thermogravimetric analysis was performed simultaneously with differential scanning calorimetry. This latter is extensively used in materials characterization and consists of measuring the difference between the amount of heat required to increase the temperature of a sample and a reference as a function of temperature [24]. In this technique, the investigated sample and the reference are always maintained at the same temperature that increases with time at a constant rate. The heat fluxes provided to rise the temperature are measured and plotted as a function of temperature or time [25]. In case of endothermic or exothermic phenomena taking place in the sample, variations in the supplied heat flux are observed. This technique is widely employed in the study of polymeric materials in order to determine glass transition, crystallisation and decomposition temperatures.

Experimental conditions

In this study, thermogravimetric analyses were mainly used to evaluate the adsorbent's thermal stability and affinity to water. This latter was evaluated by measuring the physisorbed water in the sample. To this end, weight change of the sample was determined at temperatures close to 100 °C, the boiling point of water at ambient pressure. Experiments were conducted with a thermogravimetric analyser coupled to differential scanning calorimetry apparatus (SDT 650, TA Instruments) with a constant temperature ramp of 10 °C/min in N₂ atmosphere with a purge rate of 100 mL/min. Samples of about 5 mg of Carbopack™ B, SBA-16 and Basolite™ C300 were analysed using a temperature range of 500, 1000 and 400 °C, respectively.

2.1.2.4 *Temperature-Programmed Desorption (TPD)*

Temperature programmed desorption is an analysis technique in which the compounds released by the sample are monitored over time as the temperature increases, by means of a detector like a thermal conductivity detector (TCD) or a mass spectrometer (MS). This method is usually employed in the field of catalysis to study the interactions of reaction gases with solid surfaces and determine the number of active sites on catalyst surface. In adsorption/desorption studies, this technique has been

used to determine the desorption temperature of the investigated adsorbate and the presence of different adsorption sites at the solid surface.

Typically, about 100 mg of adsorbent is placed in a reactor. Prior to adsorption, the adsorbent is outgassed at relatively high temperatures (200-400 °C) under an inert gas flow. After a period of some hours, the adsorbent is cooled down to ambient temperature or the desired temperature for the adsorption study. Then, the adsorption starts so that the target compound flows through the adsorbent at a known concentration and flow rate for a given time period. Then, the desorption takes place by heating the adsorbent at a constant rate under a carrier gas flow. The difference between the composition of the desorbed gas and the carrier gas is monitored with a downstream detector as a function of temperature. Finally, a three-axis plot representing temperature variation and detector response as a function of time is obtained and the desorption temperatures (T_p) can be determined from the maximum of the obtained peaks. For single-component adsorption studies, it is expected to observe only one peak, but more peaks can be observed if there are energetically different adsorption sites at the solid surface.

Additionally, TPD desorption curves provide information about the kinetics of desorption such as the reaction order, pre-exponential factor, activation energy for desorption in the desorption rate constant, and variation of each of these factors with adsorbate coverage [26]. After a series of TPD experiments at different heating rates, the activation energy E_d for the desorption can be estimated according to the following calculations [27, p. 2], [28], [29]. The Polanyi–Wigner equation (Eq. 2-2) describes desorption phenomena:

$$-\frac{d\theta}{dT} = \frac{A}{\beta} \theta^n \exp(-E_d/RT) \quad \text{Eq. 2-2}$$

where θ is the surface coverage, T is the temperature (K), A is the desorption rate coefficient, β is the heating rate, n is the order of the reaction, E_d is the activation energy of the desorption, and R is the ideal gas constant. During the desorption, the temperature is at a maximum (T_p) when:

$$-\frac{d\theta^2}{dT^2} = 0 \quad \text{Eq. 2-3}$$

T_p corresponds to the temperature of the desorption peak maximum observed during the TPD experiment. Using this derivative relationship, the Polanyi-Wigner equation becomes:

$$\frac{E_d}{RT_p^2} = \frac{A}{\beta} n \theta^{n-1} \exp(-E_d/RT_p) \quad \text{Eq. 2-4}$$

Assuming that desorption follows first order kinetics, Eq. 2-4 yields:

$$\frac{E_d}{RT_p^2} = \frac{A}{\beta} \exp(-E_d/RT_p) \quad \text{Eq. 2-5}$$

Rearranging and taking logarithm of Eq. 2-5 gives:

$$\ln\left(\frac{RT_p^2}{\beta}\right) = \ln\left(\frac{E_d}{A}\right) + \frac{E_d}{RT_p} \quad \text{Eq. 2-6}$$

Once the TPD experiments were conducted and, thus, T_p at different heating rates determined, E_d can be calculated by plotting $\ln\left(\frac{RT_p^2}{\beta}\right)$ versus $1/T$. According to Eq. 2-10, the desorption rate coefficient can be extracted from the intercept of the line. It is important to note that the activation energy of desorption may significantly vary when coverage increases due to the influences of the adsorbate-adsorbate interactions; therefore, to use this method for activation energy calculation, the series of TPD experiments must be conducted at the same coverage.

TPD technique can also be used to measure acidity in porous materials such as zeolites [30] or mesoporous silica [31] by using ammonia as adsorbate. Indeed, NH_3 -TPD (temperature programmed ammonia desorption) is widely employed since it constitutes a simple, cost-effective and accurate method to determine the number of acid sites in a solid. The experimental procedure is very similar to the one described previously. In this case, about 100 mg of the adsorbent is placed in a reactor and a diluted NH_3 flow passes through until complete saturation of the material. Then, a flow of inert gas is used to remove the physisorbed NH_3 and, after that, the temperature is gradually increased until the total desorption of NH_3 molecules. In zeolites, ammonia can be fixed on two different acid sites: Brønsted and Lewis acid sites. Brønsted sites are formed by the protons that compensate the negative charge of the zeolite network. These protons are coordinated to an oxygen located between silicon and aluminium atoms in the network and they can form hydrogen bonds with basic molecules such as NH_3 [32]. Lewis acid sites are located on Al^{3+} atoms with low coordination or Si^+ ions resulting from dehydroxylation in the thermal treatment [14]. The presence of these two energetically different acid sites for NH_3 results in two desorption peaks in NH_3 -TPD curves of zeolites. By integrating those

peak areas and assuming a stoichiometry of one NH_3 molecule adsorbed per acid site, it is possible to calculate the total NH_3 adsorbed by the sample. Furthermore, by dividing the total acidity by the BET surface area, the values for acid site density can be thus calculated.

Experimental conditions

During this thesis, toluene-TPD analysis of the investigated commercial adsorbents was performed using a Micromeritics AutoChem II 2920 equipped with a TCD detector. Prior to the analysis, samples of 134.6 mg of Carbopack™ B and 113 mg of SBA-16 were dried at 350 °C for 1 h, and a sample of 110 mg de Basolite™ was dried at 230 °C for 1 h. All samples were dried under a flow of 50 mL/min of helium. Then, a gas stream of 50 mL/min of toluene diluted in synthetic air (100 ppm, Air Products, USA) was passed through every sample for 30 min. The samples were analysed using a temperature ramp of 10, 15, 20, 25 and 30 °C/min and helium as a carrier gas at a flow rate of 5 mL/min. The final temperature was 350 °C for Carbopack™ and SBA-16, and 250 °C for Basolite™ C300.

NH_3 -TPD was employed to determine the acid site density in zeolites. In this experiment, the samples were pre-treated *in-situ* at 550 °C during 1 h. Then, they were cooled down to room temperature and a 5 % NH_3/He flow was passed through the reactor until sorbent saturation. Afterwards, physisorbed ammonia was removed by passing a helium flow and, finally, the temperature was gradually increased up to 550 °C. The desorption peaks obtained in the NH_3 -TPD curves were integrated and the peak areas interpolated in the calibration equation of the instrument. In this way, the total amount of acid sites was determined and the acid site density could be calculated by dividing this value by the BET surface area.

2.1.3 Dynamic VOC adsorption experiments

Dynamic adsorption experiments of BTEX, formaldehyde and hexanal were carried out on the adsorbents presented in 2.1.1. These experiments provided the necessary data to plot the corresponding breakthrough curves and, thus, to study the adsorption behaviour of target pollutants on the selected adsorbents in terms of adsorption capacity, adsorption rates and kinetics of each adsorbate-adsorbent couple. Indeed, breakthrough curves represent the evolution of the adsorbate concentration in the effluent leaving the adsorbent bed as a function of time. In Figure 2-3, a typical breakthrough curve is presented. In this type of curve, two characteristic points are highlighted: breakthrough time (t_b) and saturation time (t_s). The breakthrough time is usually defined as the time

needed to reach 1 % or 5 % of the initial injected concentration. In this work, t_b is defined as the time at which 5 % of the molecules are leaving the adsorbent bed so that when 5 % of the injected concentration (C_0) is passing through the adsorbent and, thus, the measured concentration at the outlet (C) is equal to $0.05 C_0$. Up to this point, the adsorption can be considered complete. Once t_b is reached ($C/C_0 = 0.05$), the analyte concentration at the outlet of the tube starts to rise until the saturation point. The steepness of the concentration profile provides information about the mass transfer from gas phase to the sorption sites inside the sorbent particles. Once saturation time is reached ($C/C_0 = 1$), all the adsorption sites are occupied. At this point, sorbent is completely saturated and sorption in the bed does not occur. Consequently, the outlet concentration is constant and equal to the initial concentration injected.

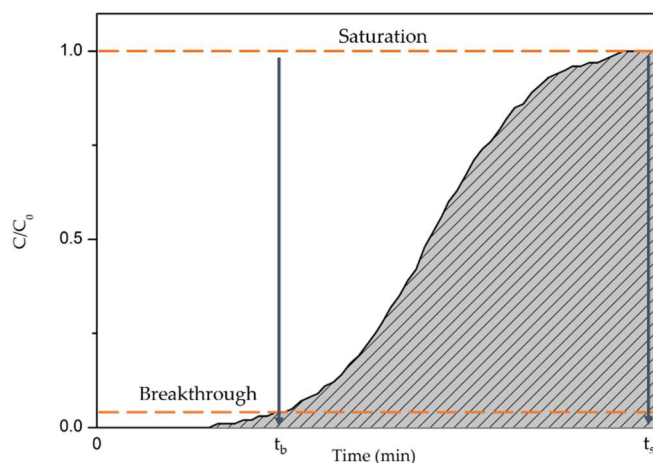


Figure 2-3. Example of breakthrough curve.

The dynamic adsorption capacity of an adsorbent can be calculated from its breakthrough curve using the following equation:

$$q = \frac{F C_0}{m} \int_{t_0}^{t_s} \left(1 - \frac{C}{C_0}\right) dt \quad \text{Eq. 2-7}$$

where q is the dynamic adsorption capacity per gram of adsorbent, Q is the gas flow rate, m is the mass of adsorbent, t_0 is the initial time, t_s is the saturation time, C_0 is the initial concentration, and C is the outlet concentration at a given time.

In this work, to carry out the dynamic adsorption experiments, the selected sorbents were packed separately in thermal desorption tubes (Sigma Aldrich, USA) between two glass wool plugs as shown in Figure 2-4.

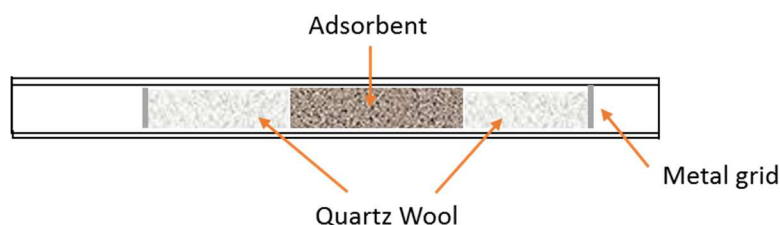


Figure 2-4. Schematic representation of thermal desorption tube employed in breakthrough tests.

Glass wool plugs and metal grids prevent the sorbent to escape from the tube. Afterwards, adsorbents were conditioned using a thermal desorber (TurboMatrix 350, Perkin Elmer, USA) to remove water and other adsorbed molecules. The conditions varied depending on the adsorbent and more details are provided later in this chapter. Once adsorbents were conditioned, the tubes were mounted in the corresponding dynamic adsorption setup in which a quantity of pollutant at a constant flow rate and concentration was passing through the adsorbent until it reached the saturation. During the experiment, the pollutant concentration at the outlet of the tube was continuously monitored.

2.1.3.1 Experimental setup for dynamic adsorption experiments of aromatics compounds

Dynamic adsorption of toluene and a BTEX mixture were conducted during this research work. The setup employed in these experiments is displayed in Figure 2-5. Target compounds were flowed through the adsorbent tube using a cylinder filled with toluene diluted in synthetic air (100 ppm, Air Products, France) or a mixture of BTEX diluted in nitrogen (10 ppm, Air Products, France), for toluene and BTEX experiments, respectively. In this system, the gas cylinder was connected to a mass flow controller (MFC1) in which the flow rate was set to 5 mL/min for both experiments. Then, the gas flow passed through the adsorption tube and, prior to the analysis, it was diluted with nitrogen (99.999% purity, Messer, Germany) by means of MFC2 to avoid the possible saturation of the chromatograph detector. Due to the different concentrations employed in toluene (100 ppm) and BTEX (10 ppm) mixtures, the effluent gas stream was diluted using a flow of 995 and 95 mL/min of nitrogen, respectively. After dilution, the gas flow was continuously analysed by a gas chromatograph (μ BTEX-1 In'Air Solutions, France). In this instrument, the gas was constantly flowing through a 200 μ L

sampling loop. Every 10 min, the content of the loop was injected into the chromatography column by means of a six-port valve. Then, the different compounds were separated and quantified by using a PID detector.

Prior to each adsorption experiment, the gas from the cylinder was flowed through the bypass, diluted and analysed. The peak area obtained corresponds to the initial concentration and, therefore, it was used as a reference of the concentration at the saturation point during the experiments.

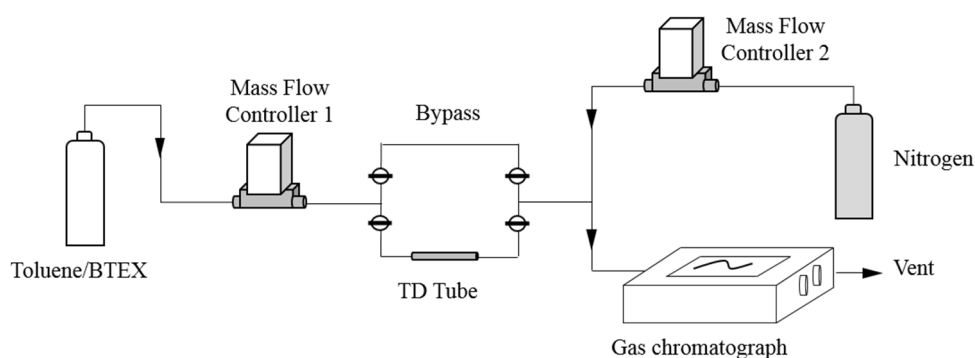


Figure 2-5. Schematic drawing of experimental setup for Toluene or BTEX breakthrough experiments

Experimental conditions

As the concentrations of toluene and BTEX mixtures were relatively elevated from the indoor air quality point of view, 15 mg of each adsorbent were employed on dynamic adsorption tests. The samples were packed separately in thermal desorption tubes (Sigma Aldrich, USA) and conditioned for 2 h at 230 °C for Basolite™ and 350 °C for Carbopack™ B, SBA-16 and zeolites under a helium flow of 50 mL/min using thermal desorber (TurboMatrix 350, Perkin Elmer, USA) to remove the possibly adsorbed molecules.

2.1.3.2 Experimental setup for dynamic adsorption experiments of formaldehyde

The second experimental setup (see Figure 2-6) was employed for formaldehyde dynamic adsorption tests. For these experiments, a formaldehyde generator developed by our research group was employed to generate a constant concentration of 164 ppb. The operating principle of the formaldehyde generator is based on the permeation principle. The device consists of two gas flows: a formaldehyde gas flow generated from a formaldehyde aqueous solution of a known concentration and a synthetic air flow used for dilution. By keeping the formaldehyde solution at a constant

temperature, typically 10 or 20 °C, and varying the flow rates of both gases, concentrations from 15 to 164 ppb can be generated. The overall setup employed for formaldehyde breakthrough tests was similar to the one described above for toluene and BTEX. In this case, MFC 1 was set at a flow rate of 15 mL/min and the dilution prior to the analysis was made using synthetic air at a flow rate of 30 mL/min (MFC 2). Afterwards, the effluent gas was continuously sampled and analysed using a formaldehyde analyser (μ F-1 In'Air Solutions, France).

Using this instrument, formaldehyde analysis is conducted on three steps [33], [34]. First, the uptake of gaseous formaldehyde is performed into an aqueous solution of Fluoral-p at room temperature. Then, the solution flows through a temperature regulated oven at 65 °C where the reaction between formaldehyde and Fluoral-p takes place, yielding a fluorescent product, i.e. 3,5-diacetyl-1,4-dihydrolutidine (DDL). Afterwards, the solution containing DDL flows through a detection cell where DDL is excited by a LED with a wavelength centered at 415 nm. Finally, the generated fluorescence is collected by a photomultiplier calibrated beforehand for quantification.

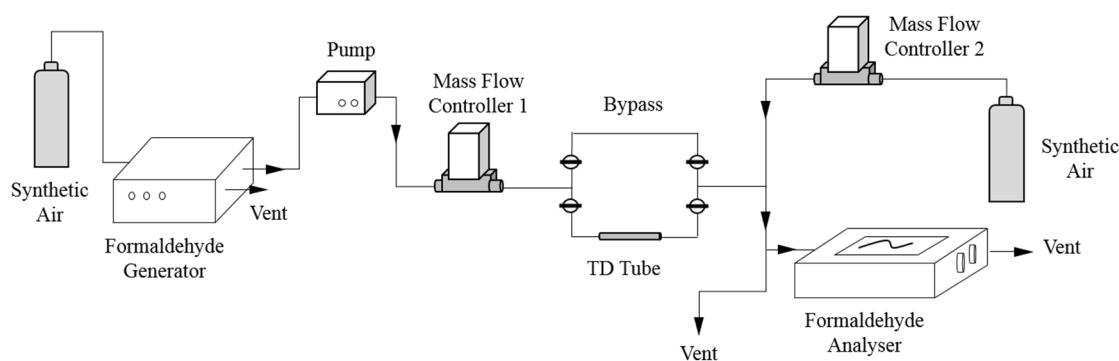


Figure 2-6. Schematic drawing of experimental setup for formaldehyde breakthrough experiments.

Experimental conditions

Formaldehyde adsorption experiments were performed by using the highest known formaldehyde concentration usually generated with the generator, i.e. 164 ppb. The adsorbent mass employed in each experiment varied from 2 to 6 mg depending on the adsorption capacity of the investigated adsorbent. Then, the samples were packed separately in copper tubes of 1/8" diameter and conditioned for 2 h at 180 °C for Basolite™ and 350 °C for Carbopack™ B, SBA-16 and zeolites under a helium flow of 50 mL/min. Dynamic adsorption tests were carried out immediately after conditioning.

2.1.3.3 Experimental setup for dynamic adsorption experiments of hexanal

The dynamic adsorption of hexanal was conducted on the experimental setup displayed in Figure 2-7. This system consists of two parts, for gaseous hexanal generation and gas stream analysis. Due to high cost and availability of the gas cylinders, gaseous hexanal was generated by using the principle of permeation, similar to the working principle of the formaldehyde generator. In this setup, a constant gas concentration of hexanal was generated by flowing nitrogen at a rate of 20 mL/min (MFC1) through a saturator containing liquid pure hexanal (98%, Sigma Aldrich). The saturator was kept at 0 °C by means of an ice bath to provide a constant hexanal partial pressure. Then, gaseous hexanal flew either through the adsorption tube (TD tube) or Bypass 2, and it was continuously analysed by means of a thermal desorber coupled to a gas chromatograph and a FID detector (TurboMatrix 350, Perkin Elmer, USA). In this way, prior to the experiment, it was possible to measure the generated concentration by selecting Bypass 2, and during the adsorption experiment, the concentration of the effluent leaving the adsorption tube could be continuously monitored.

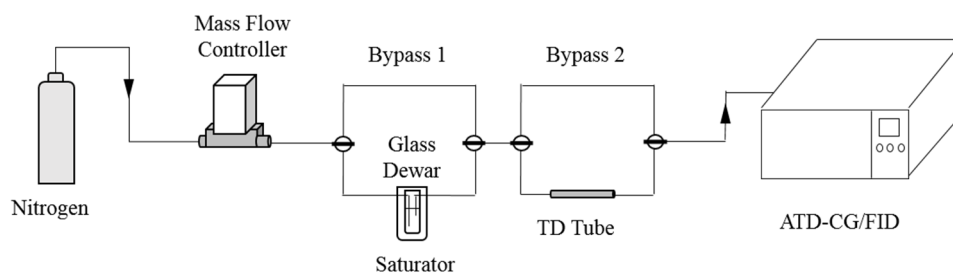


Figure 2-7. Schematic drawing of experimental setup for hexanal breakthrough experiments

For hexanal analysis, a quick analysis method was developed. As the objective was to analyse the hexanal content in the gas flow, an online mode was selected in ATD-GC/FID. This mode enables to analyse a gas flow without the need of using desorption tubes by pumping the sample directly from the gas flow to the cold trap. Once the desired volume was sampled, the trap was rapidly heated and the trapped hexanal was released. Then, it was injected into the chromatography column and, subsequently, quantified by a FID detector. The optimal parameters employed in this method are summarized in Table 2-2 and they enable hexanal quantification in about 15 min.

Table 2-2. Parameters employed in hexanal analysis method by ATD-GC-FID

	Parameter	Setpoint
ATD	Sample flow rate	5 mL/min
	Sampling time	1 min
	Outlet split	150:1
	Inlet split	50:1
	Trap adsorption/desorption temp.	-30 / 300 °C
	Trap hold	1 min
GC	Temperature program	120 → 200 °C at 30 °C/min
		200 → 240 °C at 10 °C/min
	Type of column	PerkinElmer Phase Elite 1 (100 % PDMS, 60 m, 0.25 mm ID, 0.25 mm film thickness)
	Column flow rate	1.2 mL/min
	Total analysis time	6.7 min
FID	Temperature	250 °C
	Air flow rate	400 mL/min
	Hydrogen flow rate	40 mL/min

Estimation of generated hexanal concentration

To estimate the generated hexanal concentration, the relation between vapour pressure and temperature for pure components, known as Antoine equation, was employed. This equation has the following form:

$$\log \frac{P_0}{P_{ref}} = A_A - \frac{B_A}{T + C_A} \quad \text{Eq. 2-8}$$

where P_0 is the saturation pressure of the pure component, P_{ref} is the reference pressure, T is the temperature and $A_A = 7.34663$, $B_A = 1588.31$ K and $C_A = -45.791$ K are the coefficients of Antoine equation. These coefficients are valid for hexanal at temperatures between -56 and 308.85 °C. From P_0 it is possible to calculate the concentration using the following equation:

$$C = \frac{P_0 \cdot M}{R \cdot T} \quad \text{Eq. 2-9}$$

where C is the concentration of the compound in the gas phase, M is its molecular weight, R is the ideal gas constant and T is the temperature.

2.2 Development of microfluidic devices for BTEX preconcentration

2.2.1 Analyser operating principle

The gas chromatograph (GC) laboratory prototype employed in this study is presented in Figure 2-8 and very similar to the commercial portable GC proposed by In'Air Solutions (μ BTEX-1 In'Air Solutions, France). The system is based on the GC laboratory prototype developed by Nasreddine et al. [35]. The system operates according to three steps: sampling, separation and detection. Sampling is performed by means of a SP 570 EC-BL micropump (Schwarzer Precision, Germany) connected to an EL-FLOW flow controller (Bronkhorst, Ruurlo, Netherlands). Air samples are pumped and introduced in a PEEK (Polyether ether ketone) 200 μ L sampling loop (CHEMINERT, Inter-chim, France) connected to a solenoid 6-port valve (MTV-6LL-N32UF-1, Takasago, Japan). Once the sampling loop is filled, the 6-port valve switched for 20 s, and the sample is injected into the chromatography column. Separation step is carried out using a commercial 20-m long capillary column (internal diameter (ID) 0.18 mm, Rxi-624 stationary phase, 1 μ m film thickness, Restek, Bellefonte, PA, USA) with nitrogen as a carrier gas. Polydimethylsiloxane (PDMS) is a non-polar stationary phase typically employed for BTEX separation. It provides high resolution but since the interaction of PDMS with aromatic compounds is relatively strong, separation times are long. In environmental monitoring, a compromise between short analysis time and reasonable resolution is required, therefore, a slightly more polar column (Rxi-624Sil MS) was selected to be used in this prototype. Detection is conducted employing an eVx Blue mini photoionization detector (PID) (Baseline MOCON, Lyons, CO, USA) equipped with a 10.6 eV ultra-violet lamp. This GC laboratory prototype was controlled by a computer using a homemade software.

In a previous study [35], a nitrogen flow rate of 2.5 mL min⁻¹ and a constant temperature of 80 °C were selected as the optimal conditions for BTEX separation. Using these conditions, BTEX analysis was performed in 10 min and detection limits between 1–3 ppb were found for the different compounds. Analytical performances of this device were validated under controlled laboratory conditions [35] and in real environments [36], [37].

The main objectives of this work were to improve the sensitivity of this instrument and to widen the range of detected compounds. For this purpose, the development of a micro gas chromatograph

(μ GC) column and a micro preconcentrator and their integration in the GC system shown above were investigated.

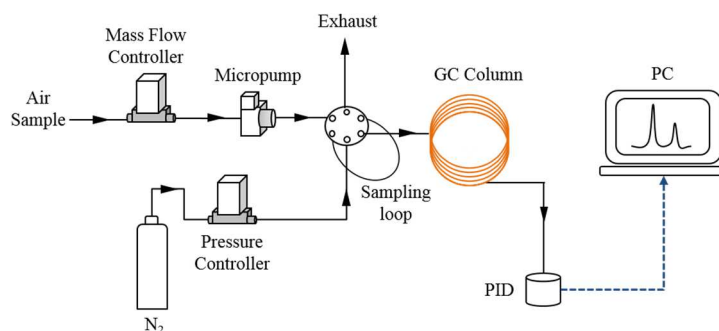


Figure 2-8. Schematic drawing of GC laboratory prototype

2.2.2 Development of a BTEX preconcentrator

During this thesis, several preconcentration devices have been developed to improve the sensitivity of the BTEX analyser previously developed by our research group. The design and fabrication of these devices are described in detail in this section.

2.2.2.1 Macro Aluminium Preconcentrator (MAP)

The first prototype is an aluminium preconcentrator, herein called Macro Aluminium Preconcentrator (MAP) with dimensions of 40 mm \times 40 mm \times 12.3 mm and weight of 54.9 g (see Figure 2-9). The manufacturing of MAP was performed by PIT SAS (Meyzieu, France) by using micro milling techniques. The design of the microfluidic cavity was based on the preconcentrator proposed by Camara *et al.* [38] in which a symmetrical manifold fluidic system was fabricated at the inlet and outlet of the adsorbent cavity to promote a uniform flow distribution. However, there are some differences between both designs. In this preconcentrator two metal porous filters (GKN Sinter Metals, Bonn, Germany) were located between the manifold system and the adsorbent cavity to ensure that the adsorbent remains in the cavity and to prevent clogging of the microchannels. The manifold consists of one inlet channel (400 μ m width, 300 μ m depth) split in two channels of 350 μ m which were also split to obtain finally four channels of 300 μ m connected to a square cavity of 4.6 mm length \times 7.4 mm width \times 300 μ m depth where the adsorbent was placed.

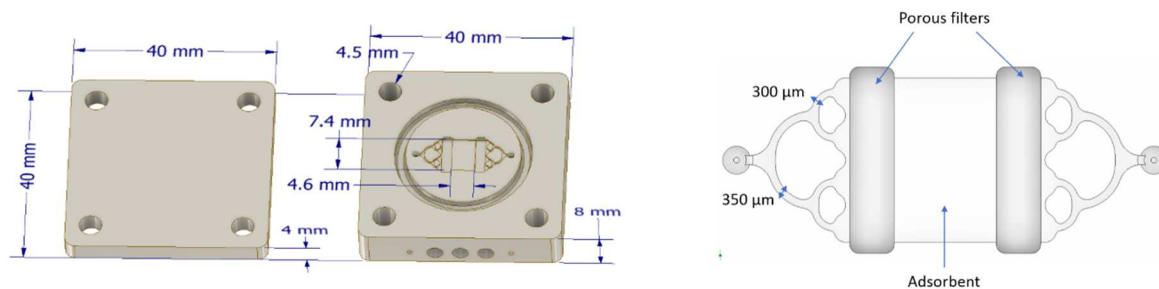


Figure 2-9. Macro Aluminium Preconcentrator (MAP).

As displayed in Figure 2-9, the device is composed of two independent parts. The top part has only two holes for positioning the fluidic connections and four other holes to host the screws that join both pieces. The bottom part contains the microfluidic cavity, a groove in which an O-ring is placed to ensure the sealing and four holes aligned with the previous ones for joining both parts. Furthermore, this bottom part has three cylindrical holes crossing the bulk of the preconcentrator where the heating cartridges were located. Temperature was measured with a type K thermocouple (RS Pro, France). The performance of this device in terms of BTEX preconcentration was assessed (see chapter 4 section 4.1.3) and very low limits of detection in the order of hundreds of ppt were achieved for all compounds excepting o-xylene. Despite this remarkably sensitivity, many features of this prototype could be significantly improved. Indeed, the high-energy consumption of the heating system prevents the device to be powered by battery and, thus, conditions its use to places where power supply is available. Furthermore, the heavy weight of the device leads to a slow heating rate which resulted in a long desorption and, therefore, in large chromatographic peaks. By miniaturizing the preconcentrator, a significant reduction in weight could be achieved and, moreover, much less energy would be required to supply the heating system making the device more autonomous and opening the possibility to be battery powered. For these reasons, other miniaturized preconcentration units were developed.

2.2.2.2 MEMS Preconcentrator (MEMS-P)

To solve the main drawbacks mentioned above related to the energy consumption and relatively low heating rate of the first preconcentrator, a second prototype, herein called MEMS-P, was developed based on microfabrication techniques. It is important to note that the use of microfabrication techniques requires special facilities. STnano Platform is the only cleanroom available at University of

Strasbourg and only certain microfabrication techniques were available including photolithography, metal deposition, wet etching, reactive ion etching, optical microscopy and profilometry. In cleanrooms, the level of contamination is controlled, and they are classified according to the number and size of particles permitted per volume of air. ST Platform is a cleanroom classified as ISO 5, which allows no more than 3 520 particles equal to or larger than 0.5 microns per cubic meter of air. Preliminary tests were made in this platform to find a suitable design for the heating system and to understand the set of issues derived from the required fabrication techniques. Afterwards, the final design was conceived, and it was sent to a more equipped microfabrication platform in Toulouse (LAAS) for manufacturing.

The general structure of this new preconcentrator is presented in Figure 2-10. The device consists of two parts: a silicon wafer (bottom part) and a glass plate (top part). The silicon wafer has a heating system integrated on the bottom side, and a 500 μm layer of SU-8 patterned on the top side to form the microfluidic cavity where the adsorbent is deposited. This cavity is sealed by a glass plate bonded to the SU-8 layer. On the top side of the glass plate, two holes are drilled to insert the microfluidic connections.

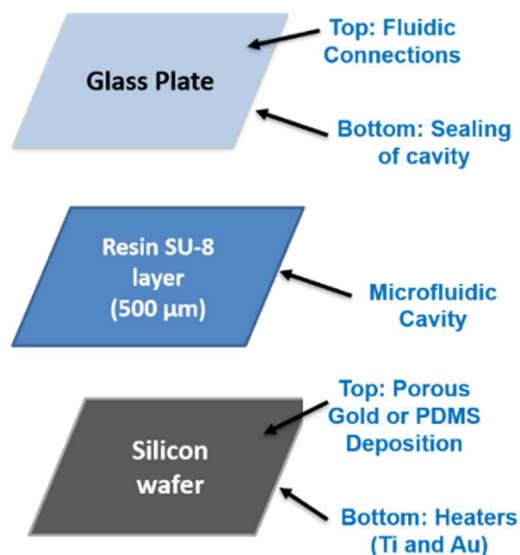


Figure 2-10. Structure of MEMS-based Preconcentrator

2.2.2.2.1 Silicon wafer top part: microfluidic design

Two different patterns were proposed for the microfluidic chip: a square shape (based on the previous preconcentrator version) and a serpentine configuration (see Figure 2-11). Inside these cavities, a thin layer or granular sorbent materials has been placed to investigate their adsorption properties. Thin layers of adsorbents like porous gold or PDMS were deposited during the device manufacturing process whereas granular adsorbents, such as Carbo-pack® B or Basolite® C300, have been introduced inside the cavity once the device was sealed.

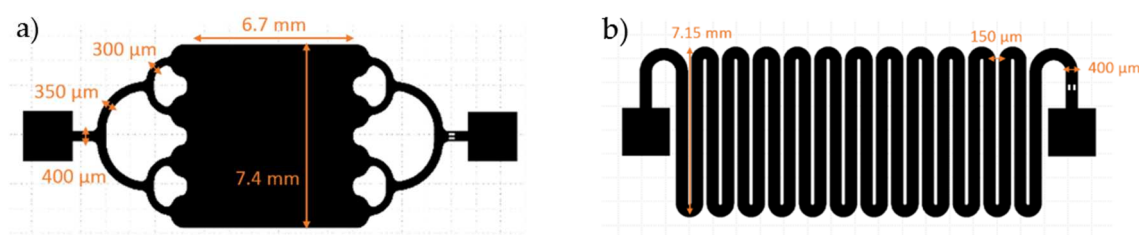


Figure 2-11. Designs proposed for the microfluidic cavity: a) square shape and b) serpentine.

Prior to the fabrication of MEMS-based microdevices, flow simulations were performed using ANSYS Fluent to estimate the pressure drop and verify the uniformity of the flow distribution in the proposed configurations (Figure 2-11). In the model employed, as low pressure drops and low Mach numbers were expected, air was considered as an incompressible gas. The first step consisted of determining the flow regime inside the microdevice. Two different flow rates of 2.5 mL/min and 5 mL/min were proposed for the simulations, based on the real flow rates expected during the sampling step in the BTEX analyser. Then, the Reynolds number was calculated at the inlet for both flow rates following the procedure described below. First, inlet hydraulic diameter was calculated for both configurations as follows:

$$D_h = \frac{4 S_i}{P_w} \quad \text{Eq. 2-10}$$

where D_h is the hydraulic diameter, S_i is the inlet cross section area and P_w is its wetted perimeter. Then, the inlet mean velocity was calculated by using the following equation:

$$v = \frac{Q_i}{S_i} \quad \text{Eq. 2-11}$$

where v is the inlet mean velocity and Q_i is the inlet volume flow rate. Once hydraulic diameter and inlet linear velocity were determined, the Reynolds number Re can be determined as follows:

$$Re = \frac{v D_h}{\nu_{air}} \quad \text{Eq. 2-12}$$

where ν_{air} is the kinematic viscosity of air. Reynolds numbers are 6 and 12 for 2.5 and 5 mL/min, respectively. Since the Reynolds number is lower than 2300 in both cases, the flow is laminar and as the hydrodynamic entrance length ($0.05 Re D_h$) is here negligible, the hydraulic resistance is independent of the device wall roughness. The boundary conditions set for simulation were an inlet velocity calculated in Eq. 2-11 and a pressure outlet fixed to atmospheric pressure. Operating and boundary conditions are summarised in Table 2-3.

Table 2-3. Parameters employed in flow simulations for both designs of MEMS Preconcentrator

Boundary conditions and flow regime		
Inlet flow rate (mL/min)	2.5	5
Inlet velocity magnitude (m/s)	0.415	0.2075
Outlet gauge pressure (Pa)*	0	0
Reynolds number	6	12
Regime	Laminar	Laminar

*operating pressure = atmospheric pressure (101325 Pa)

The accuracy of the simulation depends on the numerical scheme and the quality of the mesh: total number and shape of cells. In all conducted simulations, least squares cell-based gradient, pressure-based solver and second-order upwind scheme were selected in order to achieve high accuracy in the calculations. Concerning the number and shape of the cells, an increase in their number leads to better accuracy but also increases the computational effort; therefore, a compromise between accuracy and simulation time should be adopted. In this work, two meshes with different levels of refinement were investigated for each configuration in order to verify the accuracy of the results. It is expected to obtain similar results if the less refined mesh is already accurate enough.

- Serpentine configuration

In serpentine configuration, a structured mesh composed of hexahedrons cells was selected. Since variations of pressure and velocity are expected along the channel, it is better to use this type of grid that provides the highest accuracy for the proposed solutions. In order to save computation time, a plane of symmetry (XZ) was employed. In this geometry, the first mesh (M1) contained 276 426 cells

while in the more refined mesh (M2), the number of cells was increased to 2 211 408. A zoom of both meshes at the inlet of the microdevice is presented in Figure 2-12. In M1 the cross section contained 9×10 cells (see Figure 2-12a) whereas in M2, the cross section contained 18×20 cells (see Figure 2-12b).

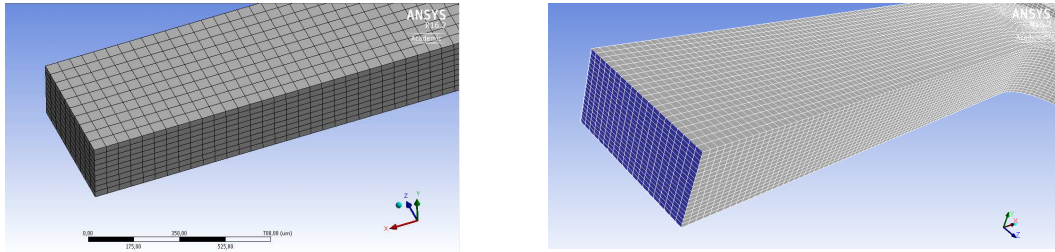


Figure 2-12. Schematic view of mesh 1 (a) and mesh 2 (b) at the inlet of the microdevice with serpentine configuration.

- Square configuration

In square configuration, two meshes were also proposed. Prior to mesh definition, two planes of symmetry (XY and XZ) were established to reduce the number of cells by a factor of 4. For this geometry, the first mesh (M1) contained 529 809 cells. Then, this mesh was refined only in areas of interest where pressure and velocity gradients are higher, i.e. at the inlet and outlet, resulting in a mesh of 2 136 092 cells (M2). Data of both meshes are summarized in Table 2-4.

Table 2-4. Summary of mesh parameters employed in flow simulations for MEMS Preconcentrator

		Mesh 1	Mesh 2
Serpentine Configuration	Number of cells	276 426	2 211 408
	Cell geometry	Hexahedra	Hexahedra
	Number of cells per cross-section	10×9	20×18
Square Configuration	Number of cells	529 809	2 136 092
	Cell geometry	Triangular prism	Triangular prism
	Number of cells per cross-section	6×4	12×8

Results obtained in flow simulations (see chapter 4 section 4.2.1) were very satisfactory in terms of pressure losses showing pressure drops lower than 110 Pa. The flow distribution was much more homogeneous in the case of the square configuration since the velocity along the microfluidic cavity was almost constant whereas in the serpentine configuration larger variations were observed. Flow simulations allowed to validate the proposed geometries, so that the next step was the design and validation of the heating system.

2.2.2.2.2 Silicon wafer bottom part: heating system

i. Design

The preconcentrator heating system was made by metal deposition of silver/gold and titanium. These metals were selected for their conductive properties according to their relatively high (titanium) and low (silver and gold) electrical resistivity. The specific dimensions and geometry of resistances, which serve as heaters and temperature sensors, were chosen in accordance with the desired performance of the elements. Initially, the heating system was conceived with the goal to achieve 250 °C in 10 s. As resistance depends on the geometry of a conductor as well as on what the conductor is made of, theoretical calculations were made prior to design and microfabrication as described below. Firstly, the mass, m , of the silicon plate was calculated by taking into account the dimensions of the chip and the silicon density as follows:

$$m = L \cdot w \cdot h \cdot \rho \quad \text{Eq. 2-13}$$

where L is the length, w is the width, h is the height of the silicon chip and ρ is the density of silicon at 25 °C. Then, the heat Q_H required to achieve the defined heating performance was calculated by the following equation:

$$Q_H = m \cdot c_{Si} \cdot \Delta T \quad \text{Eq. 2-14}$$

where c_{Si} is the specific heat of Si, and ΔT is the temperature increase of the wafer. Then, the total power Π needed to achieve the defined performance can be calculated as follows:

$$\Pi = \frac{Q_H}{t} \quad \text{Eq. 2-15}$$

where t is the time required to reach the temperature increase ΔT . The heating system was made up of several heaters, specifically 2 or 4 heating elements. Therefore, the required power per heater (Π_i) was calculated by dividing the total power Π by the number of heaters. Afterwards, the current and the resistance required per heater were calculated by Eq. 2-16 and Eq. 2-17, taking into consideration a voltage supply (U) and the fact that the resistances will be connected in parallel:

$$\Pi_i = U \cdot I \quad \text{Eq. 2-16}$$

$$\Pi_i = R_i \cdot I^2 \quad \text{Eq. 2-17}$$

where U is the voltage, I is the current and R_i is the resistance per element. The resulting power value was corrected to take into account heat lost by convection by using Eq. 2-18 and Eq. 2-19:

$$\Pi_{lost} = h_c \cdot S_w \cdot \Delta T \quad \text{Eq. 2-18}$$

$$\Pi_{useful} = \Pi - \Pi_{lost} \quad \text{Eq. 2-19}$$

where Π_{lost} is the lost heat flux, h_c is an estimated value of convective heat transfer coefficient assuming free convection, S_w is the wafer section area, Π_{useful} is the useful power. Finally, the required dimensions of each heating element were calculated according to the following equation:

$$R_i = \rho_e \frac{L_e}{S_e} \quad \text{Eq. 2-20}$$

where ρ_e is the electrical resistivity of the metal, L_e and S_e are the length and the cross section of the metal heating element.

For the design of temperature sensors, the relationship between the electrical resistivity and the temperature was used (see Eq. 2-21).

$$\rho_e(T) = \rho_{e0}[1 + \alpha_0(T - T_0)] \quad \text{Eq. 2-21}$$

where T_0 is the initial temperature, T is the temperature, ρ_{e0} is the electrical resistivity at T_0 and α_0 is the temperature coefficient of resistance at T_0 . If it assumed that the change in length and area with temperature is negligible, Eq. 2-21 can be written in terms of resistance as follows:

$$R_i(T) = R_{i0}[1 + \alpha_0(T - T_0)] \quad \text{Eq. 2-22}$$

As can be inferred from Eq. 2-22, the greater the initial resistance, the larger the change produced in the resistance by temperature variation, leading to a better sensitivity in the temperature measurement. For this reason, high values of resistance and, thus, long metal layers are preferred for

the design of temperature sensors. Dimensions for these elements will be chosen as the best compromise between sensitivity and available space on the silicon wafer.

ii. First set of heating systems

The first set of heating systems was conceived with the goal to achieve 250 °C in 10 s. The metals used in this version were silver for connectors and titanium for heating resistances. In this first attempt, four different designs with linear and serpentine geometries and different dimensions were proposed. Their features are listed in Table 2-5 and the masks employed in their fabrication are shown in Figure 2-13. The orange and black lines correspond to heating elements and temperature sensors, respectively. Due to manufacturing constraints, the thickness of Ti and Ag layers were chosen to be 100 nm in all systems.

Table 2-5. Features of each heating system design.

Design no.	Device dimensions (mm ²)	Heating elements				Temperature sensors			
		Number	Resistances (Ω)	Width (mm)	Length (mm)	Number	Resistances (Ω)	Width (mm)	Length (mm)
1	25 × 15	4	74	1	7.5	2	188	1	19
2	20 × 12	2	50	1	5	1	555	0.250	10
3	20 × 12	2	50	1	5	2	188	1	19
4	20 × 12	4	84	1	8.5	2	117	0.250	7

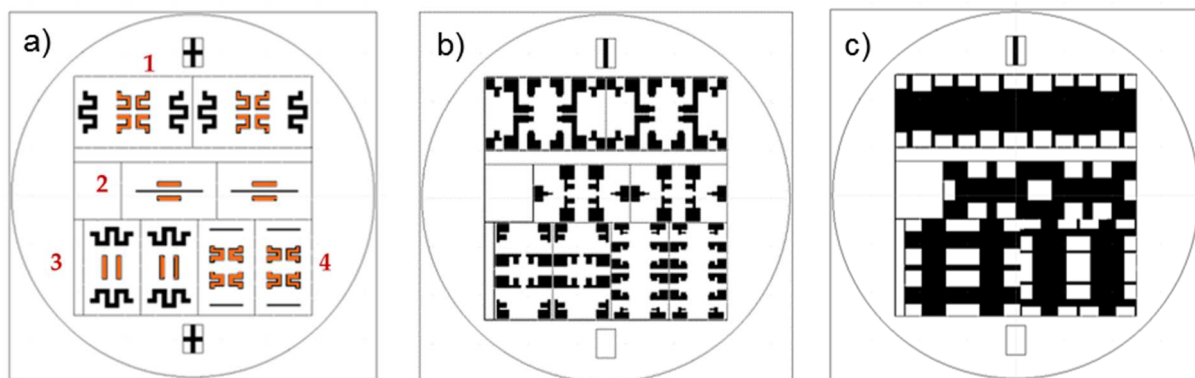


Figure 2-13. Design of thin film masks employed for Ti deposition (heating elements in orange and temperature sensors in black) (a); Ag deposition (b) and SiO₂ sputtering (c) for the first heating system

Once the design of heating elements and sensors was completed, microfabrication of the systems was carried out by means of UV photolithography followed by metal deposition of Ti and Ag in a silicon

wafer (orientation: $\langle 100 \rangle$, conductivity type: P, Dopant: Boron) of 3-inch diameter. A schematic view of the whole microfabrication process is displayed in Figure 2-14.

As a first step, the silicon wafer was rinsed with acetone, ethanol and isopropanol. Afterwards, a 1.40 μm layer of reversible photoresist AZ 5214 was spin-coated and the wafer was baked at 105 $^{\circ}\text{C}$ for 1 min 40 s. A thin film mask was used to transfer the pattern of Ti resistances (see Figure 2-13a) to the photoresist with UV photolithography (Süss MJB3). This procedure includes two extra steps, a reversal bake at 120 $^{\circ}\text{C}$ for 1 min 30 s and an extra UV irradiation, so that the photoresist was transformed from positive to negative. The photoresist was developed by a specific developer, known as MIF 726, rinsed with deionized water and 100 nm of Ti were deposited by e-beam evaporation (Plassys MEB550S). Photoresist lift-off was performed in an acetone bath and the wafer was then rinsed once more with acetone, ethanol and isopropanol, so that the procedure described was repeated using a second mask with the design of electrodes (see Figure 2-13b). In the first set of heating systems, 100 nm of Ag were deposited along with 5 nm of Cr as adhesion layer by resistive thermal evaporation (Plassys MEB 300). The addition of a chromium layer enhanced the adhesion of the Ag layer to the wafer. Finally, the wafer was insulated with a SiO_2 layer 150 nm thick using the film mask displayed in Figure 2-13c. This protective layer was deposited by sputtering (Alliance Concept EVA300+) and it covered all heating systems excepting square areas of $2 \times 2 \text{ mm}^2$ that were excluded from isolation at the points where electrical current or voltage was meant to be supplied. Finally, chips were diced by means of a diamond saw.

For every heating system, characterization of the metal layers was performed using a profilometer (3D Dektak, Veeco) to assess the thickness of the metal layer and the deposition quality. The resistance of heaters and temperature sensors was measured by means of a four-point probe station (Karl Suss PM8). Characterization of temperature ramps achieved with these systems is presented in detail in Chapter 4.

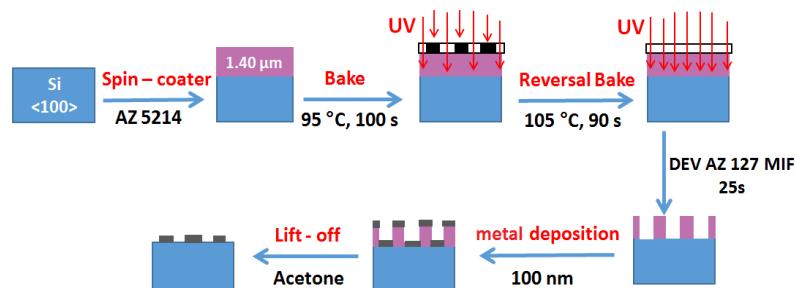


Figure 2-14. Overview of the fabrication protocol of heating systems by photolithography followed by metal deposition

iii. Second set of heating systems

In the second set of heating systems, the film masks presented in Figure 2-13 were also employed so that the heaters and temperature sensors had the same geometries and dimensions, but the connectors were made in gold instead of silver. The manufacturing process was essentially identical except the deposition of a 60 nm thick gold layer along with a 10 nm thick titanium adhesion layer during the second metal deposition step. In this case, gold was deposited by e-beam evaporation (Plassys MEB550S). The performances obtained with these systems were considerably better than the ones obtained with the previous version (see chapter 4 section 4.2.2). Temperature measurements as a function of time at different voltage supplies allowed to estimate the difference between the theoretical values calculated for the power and the experimental results obtained. This difference was used as a “correction factor” to improve the accuracy of the calculations in the heating system design of the final MEMS preconcentrator.

2.2.2.2.3 *Design and fabrication of the final MEMS preconcentrator*

Once the performances of the investigated heating systems and the geometry of the microfluidic cavity were validated, a version including all the elements was fabricated.

Two 400 μm thick double-sided polished silicon wafers (4 in., orientation $\langle 100 \rangle$, conductivity type P) were used for the fabrication. The size of each prototype was $27 \times 12 \text{ mm}^2$ so that 10 devices could be fabricated in a single wafer. As shown in Figure 2-17a, five prototypes of each microfluidic configuration were created per wafer. The dimensions of the chips were selected to leave enough space between the drilled inlet/outlet holes to glue two Nanoport® connectors (Idex Health and Science, LLC; USA) to the glass plate.

After the tests performed with the previous heating systems, it was concluded that a heating system with 2 heaters was more appropriate in terms of electrical connections since the small electrode contacts made difficult to connect more than 4 wires in a single device. The dimensions and geometry of the heating resistances were the same as in designs number 2 and 3 (linear, $5 \times 1 \text{ mm}^2$), except by the thickness that was increased to 300 μm . Based on the results obtained in previous tests and according to our calculations, two heating resistances with these characteristics should achieve a temperature of about 225 °C in 10 s.

In this final version, temperature sensors were removed due to the problems arose from the electrical connections and the measurement of the resistance. Instead, two square contact pads were deposited in each chip to facilitate the attaching of an external type K thermocouple. The final design of the heating system is presented in Figure 2-17a and Figure 2-17b.

The manufacturing of MEMS-P was performed in several stages:

1) Porous gold deposition as adsorbent

An overview of the whole porous gold deposition process is displayed in Figure 2-15.

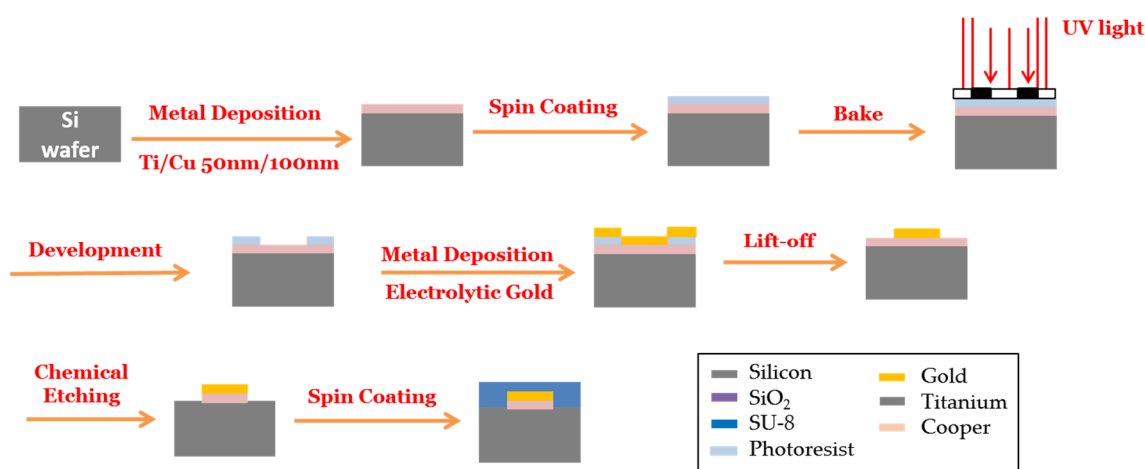


Figure 2-15. Process flow of porous gold deposition

The first step of the microfabrication process was the deposition of the porous gold layer. These pores were created by supplying a high voltage current to a deposited thin gold layer. Since silicon is a semiconductor, prior to gold deposition, it was necessary to create a conductive path. In order to do this, a 50 nm thick titanium layer was deposited on the surface of the silicon wafer followed by the deposition of a 100 nm thick copper layer by means of physical vapor deposition (PVD). After that, a dry film mask containing the patterns where the gold layer should be deposited (see Figure 2-16a) was employed to deposit a protective resin by photolithography. As mentioned before, to create the porosity into the gold layer, high voltage supply must be used which limited the total surface of deposited gold to 2 cm² per wafer. Considering this limitation and in order to have a reasonable adsorption surface (0.5 cm²), only 4 devices per wafer could receive porous gold as adsorbent.

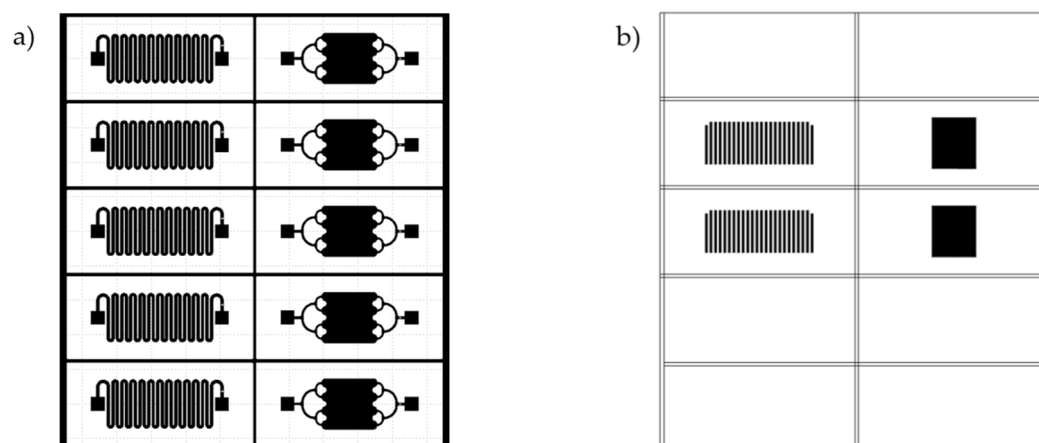


Figure 2-16. Patterns for the fabrication of masks for: (a) SU-8 deposition and (b) gold deposition to form the porous layer

As illustrated in Figure 2-16b, one pattern for the gold layer was proposed for each configuration: in the serpentine configuration, the porous gold was deposited only at the central part of the channels whereas in the square design, the gold was deposited only at the centre of the microfluidic cavity. Then, a 100 μm thick gold layer was supposed to be deposited by electrochemical deposition but, due to manufacturing constraints regarding the gold growing and the desired geometry, only 10 and 40 μm thick layers could be deposited on the channels and the square, respectively. After that, the resin protective layer was removed, and the formed porous gold was protected with other resin by using the same dry film mask. Finally, the Ti/Cu layer deposited at the beginning was removed by chemical etching followed by protective resin removal by lift-off.

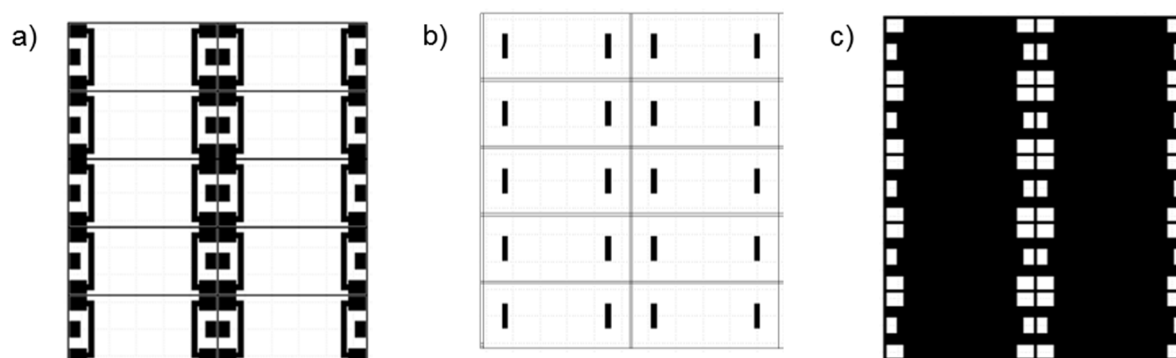


Figure 2-17. Patterns for the fabrication of chromium masks for: (a) titanium and gold deposition, (b) gold etching and (c) SiO_2 deposition

Finally, a 500 μm thick SU-8 layer was deposited by spin coating to protect the porous gold during the next steps of the microfabrication process.

2) Titanium and gold deposition for heating system

The second step of the fabrication was the titanium and gold deposition to form the heating system. An overview of the whole titanium and gold deposition process is displayed in Figure 2-18.

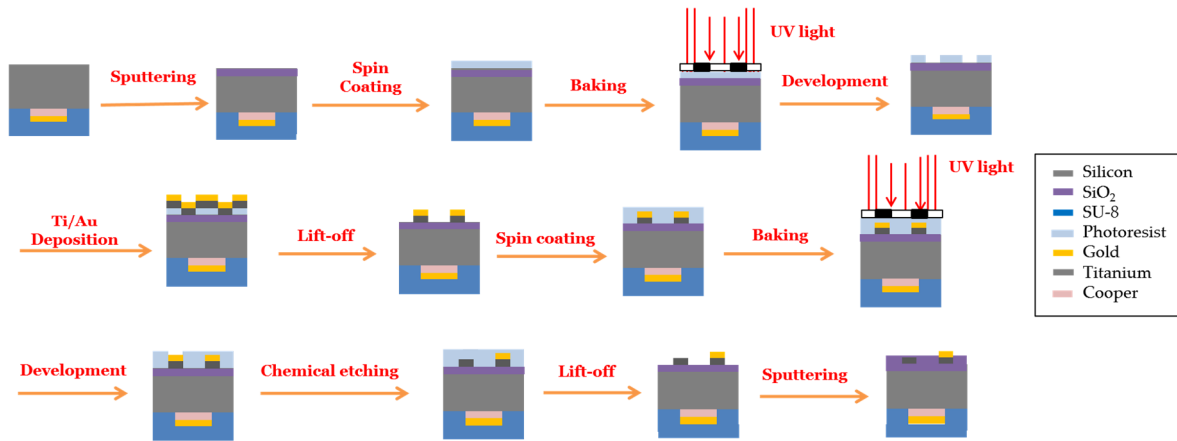


Figure 2-18. Process flow of the fabrication of titanium and gold resistances

First, a 150 nm thick SiO₂ layer was sputtered over the whole wafer for electrical isolation purposes. Then, a 300 nm thick titanium layer followed by 150 nm thick gold layer were patterned by photolithography using the mask displayed in Figure 2-17a. Then, part of the gold deposited was removed by chemical etching using the mask presented in Figure 2-17b. At this point, the heaters were finished and a 150 nm thick SiO₂ layer was sputtered using the mask shown in Figure 2-17c to protect them from impacts.

3) SU-8 patterning

Once the heating system was fabricated, the previously deposited SU-8 layer was patterned by photolithography using the mask presented in Figure 2-16a and, thus, creating the microfluidic cavities as shown in Figure 2-19. SU-8 is an epoxy-based photoresist widely employed in microfabrication to create high aspect ratio structures. Traditionally, DRIE is the selected technique to create the microfluidic cavity in preconcentrators [39]–[41]. However, this technique is very expensive and its cost increases with the desired depth. In this work, an alternative and cheaper approach was proposed using SU-8 to pattern the 3D structures on the silicon surface, thus creating the microfluidic cavity.

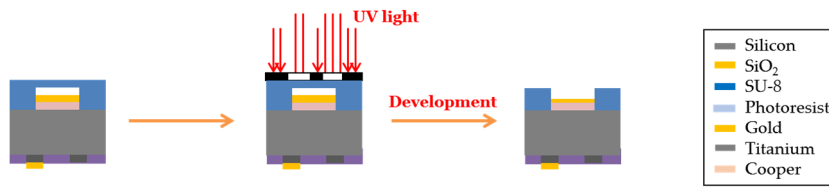


Figure 2-19. Manufacturing the microfluidic cavity by SU-8 patterning

4) Drilling of inlet/outlet holes and SU-8 deposition

The microfluidic cavities were sealed using a glass plate by adhesive bonding using SU-8. Prior to the bonding, inlet and outlet holes were drilled using a sand blasting technique. Sand blasting is a cost-effective technique for drilling holes in microdevices where a particle jet is directed towards the glass plate for removing the material [42]. As illustrated in Figure 2-20, the micromachining process is very simple. First, a photoresistant layer was deposited on the glass plate and the holes pattern was transferred to the photoresistant by photolithography. Then, two holes were drilled by sandblasting and the photoresistant was removed by lift-off.

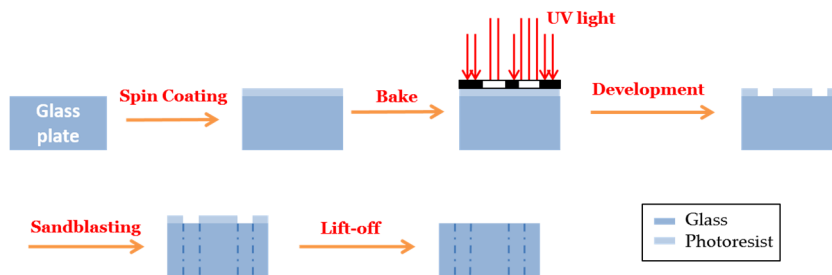


Figure 2-20. Overview of sandblasting process and SU-8 deposition

5) Adhesive bonding

Once the glass plate was drilled, it was flipped, and a 15 μm thick SU-8 layer was deposited on the glass surface. Once again, the holes pattern was transferred to the photoresist using photolithography. This SU-8 layer was used as glue to perform an adhesive bonding between the glass plate and micro-patterned structures deposited on the silicon wafer. To enable adhesive bonding, the SU-8 surface was activated previously with oxygen plasma. Then, both workpieces were put in contact, the temperature rose up to 100 $^{\circ}\text{C}$ for the SU-8 to polymerise and high pressure was applied to improve the surface contact. After the completion of the bonding, the wafer was diced by means of a diamond saw to release the devices.

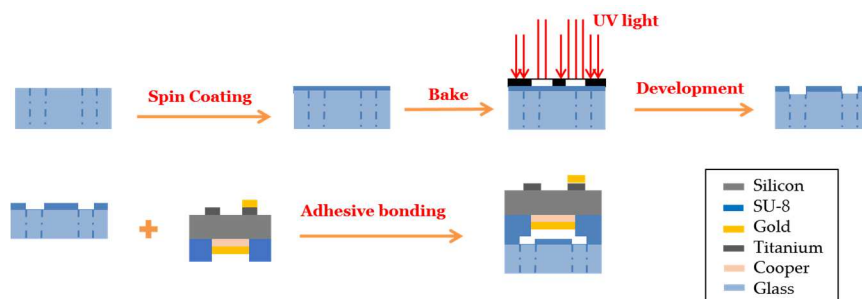


Figure 2-21. Process flow of adhesive bonding

2.2.2.3 Mixed Aluminium/Polymer Preconcentrator

With the goal to solve the problems encountered on the previous version of the preconcentrator, it was concluded that micromilling technology could be one of the most viable options for the manufacturing of the preconcentrator. This technique allows to fabricate microfluidic devices with relative high precision at a reasonable price.

The design of the mixed aluminium/polymer preconcentrator (MAPP) was different from the others when it comes to the overall structure but very similar to the MAP in terms of the microfluidic cavity. In fact, the geometry of the cavity was the same excepting a long channel arriving to the manifold located at each side of the cavity (see Figure 2-22a). For the preconcentration tests carried out with this device, 5 mg of Carpack™ B were manually packed inside the cavity.

In order to increase the heating rate with regard to the first prototype (MAP), the heating system was substituted by a ceramic resistance of 10 Ω with a maximum power of 100 W (Model XH-RJ157012) and a maximum operating temperature of 600 °C, which was expected to heat faster with less power consumption. This resistance was located below the adsorbent cavity (see Figure 2-22b) and had dimensions of 15 × 70 × 1.2 mm³, covering all the aluminium board surface and, thus, avoiding temperature gradients along the board.

The main idea behind this design was to use the same design and working principle than the MAPP but with an energy consumption significantly reduced. This reduction is achieved by decreasing the weight of aluminium parts and replacing some of them by others made of insulating materials, specifically PEEK and ABS (acrylonitrile butadiene styrene). PEEK was employed to fabricate the board that provides the sealing for the microfluidic cavity and in which the fluidic connections were placed. This board was in contact with the aluminium part and the ceramic resistance; for this reason,

a relatively high thermoresistant polymer such as PEEK (maximum operating temperature = 345 °C) was chosen. The housing that keeps in place the whole assembly was 3D printed using ABS. This material is a very cheap polymer that allows to quickly manufacture customized parts, reducing the time consumption as well as the cost of the fabrication process.

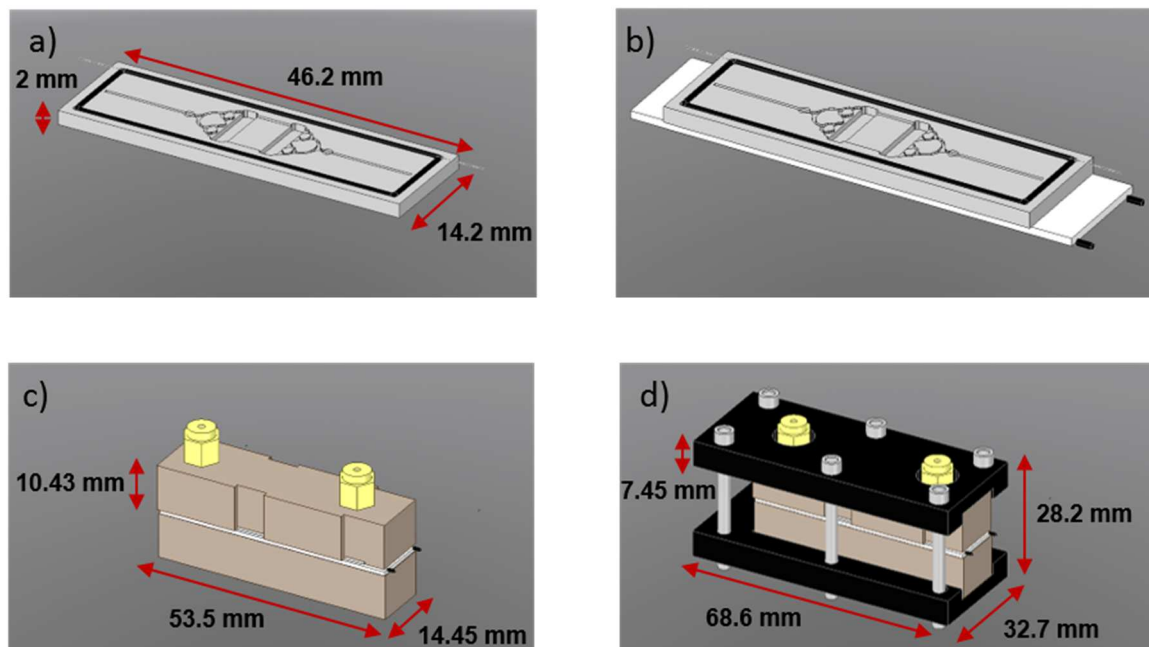


Figure 2-22. 3D design of MAPP preconcentrator: (a) aluminium board with the cavity and the O-ring microfluidic cavity and (b) aluminium board with ceramic resistance; (c) fluidic connections were integrated in a PEEK block and (d) the overall structure was fixed using a housing made of two polymer pieces joined by screws

Heating and cooling rates were characterized for this new prototype (see chapter 4 section 4.3.1) exhibiting better performance than the one achieved with MAP device, but there is still substantial room for improvement. Furthermore, preconcentration tests conducted for a BTEX mixture revealed some problems arising from the adsorbent packing, the flow distribution inside the microfluidic cavity and the closing of the device. These problems were critical for the repeatability of the results, preventing its use in industrial applications. Therefore, other alternatives were proposed for the preconcentrator design.

2.2.2.4 Micro Aluminium Preconcentrator (μ AP1)

In order to simplify the manufacturing process and reduce the costs, the micro aluminium preconcentrator (μ AP1) was conceived. This device consists of a 1/8-inch outer diameter copper tube

(see Figure 2-23a) in which centre the adsorbent is placed held by two glass wool plugs. The geometry was completely changed to avoid the problems related to the fact that some molecules were not adsorbed during the sampling due to the difficulty to pack the adsorbent. In this configuration, the solid covers the whole cross section of the cylinder, so that the air sample must flow through the adsorbent bed and the probability of the molecules to be adsorbed is greatly increased. This copper tube was placed inside a small aluminium cube of $6 \times 10 \times 10 \text{ mm}^3$ (see Figure 2-23b) that served as contact surface for the heating system. Between the aluminium cube and the copper tube, thermal paste was added to improve the thermal transfer. The heating system was made of two flat ceramic resistances ($10 \times 10 \times 2 \text{ mm}^3$) of $10 \ \Omega$ with a maximum power of 50 W (Model XH-RJ101012) and a maximum operating temperature of $600 \text{ }^\circ\text{C}$. The device was connected to the GC system using two standard stainless steel and two brass Swagelok fittings of 1/4 and 1/16-inch, respectively, as shown in Figure 2-23c. Both fittings were connected by means of a stainless-steel adapter. The dimensions of the whole module including the connectors were 80.7 mm in length and 12.5 mm in diameter while the weight was 36 g.

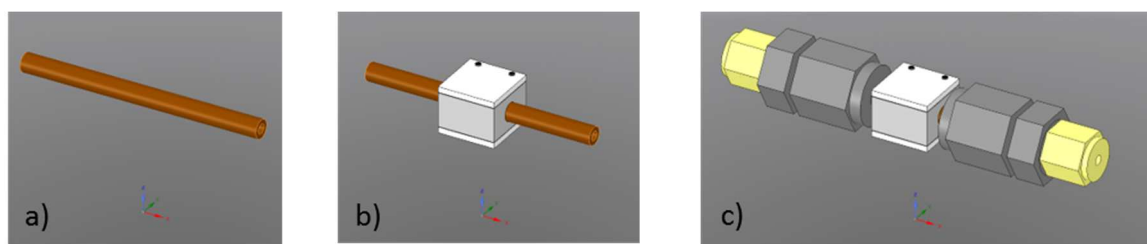


Figure 2-23. μPA 3D design: (a) copper tube, (b) copper tube, aluminium cube and ceramic resistances and (c) whole assembly including the fluidic connections.

In this prototype, the use of standard fluidic connectors provided an excellent gas tightness; however, due to the heaviness of the assembly and the use of heat-conducting materials for Swagelok connectors, the thermal performance was unsatisfactory. Furthermore, the heat transfer was not uniform along the device caused by the interface between two different materials (copper and aluminium). To overcome this poor heat transfer, another preconcentrator design was proposed in which the tube and the cube were made of one single-piece, so that heat transfer was significantly improved.

2.2.2.5 Micro Aluminium Preconcentrator (μAP2)

As mentioned before, another preconcentrator prototype similar in shape but more compact than the previous one was conceived, herein called μAP2 . The μAP1 prototype exhibited an extraordinary gas

tightness but the poor thermal transfer arising from the different materials employed and its heavy weight, limited its performance concerning the BTEX preconcentration. Therefore, the design of this new version aimed to improve the performance of the heating system while maintaining the gas tightness. For that, the tube and the cube presented in the last version were made of one aluminium piece (see Figure 2-24a) reducing the total weight of the device to 29.6 g (connectors included). The μ AP2 has dimensions of $26 \times 12 \times 3.2 \text{ mm}^3$ and a cylindrical hole of 1.6 mm of internal diameter crossed through the length of the device. These cylindrical parts were polished to fit very tight inside the Swagelok connectors (6 mm) as shown in Figure 2-24b. This device was fabricated using traditional milling techniques that imply the use of cutting oils to cool and lubricate the material during the machining process. Therefore, once the device fabricated, it was washed with acetone in an ultrasounds bath for 2 h and then rinsed with deionised water. Afterwards, it was heated to $200 \text{ }^\circ\text{C}$ and a 20 NmL/min nitrogen flow was passing through it for 1h. Finally, 5 mg of adsorbent were packed manually inside the cylindrical cavity and held using two glass wool plugs.

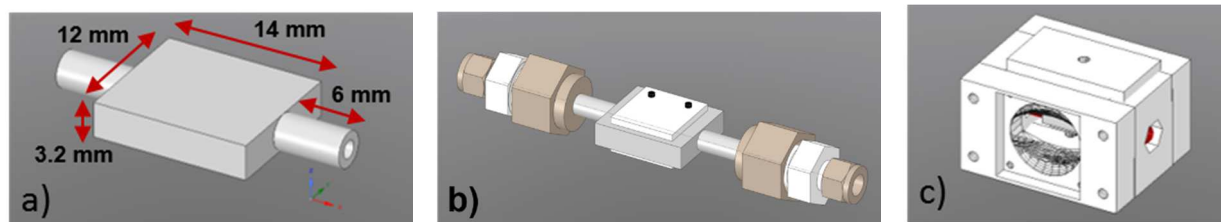


Figure 2-24. μ AP2 3D design: (a) aluminium block; (b) aluminum block, Swagelok standard connectors and ceramic resistances; (c) first draft of the housing of μ AP2 prototype including two fans for rapid cooling.

The heating system of μ AP2 was the same as the one employed in μ AP1: two ceramic resistances ($10 \times 10 \times 2 \text{ mm}^3$) of $10 \ \Omega$ (Model XH-RJ101012). Since the weight of μ AP2 was slightly reduced and the whole device was made of the same material, the heating power of this device was exceptionally improved. The results corresponding to the performances of the heating system are presented in detail in chapter 4 in section 4.5.1. Preconcentration tests were also conducted injecting a BTEX mixture at different concentrations and using several sample volumes. The results showed an outstanding linearity of the signal with the injected concentration and sample volume. Furthermore, the fast heating ramp allowed to have sharper chromatographic peaks and, thus, better sensitivity than the one obtained with MAP (Lara-Ibeas et al., 2019). For this prototype, the design of a specific housing integrating two fans is in progress in order to accelerate the cooling process of the device.

2.3 Conclusions

In the first part of this chapter, the materials employed in this research work as well as the analytical techniques employed for their characterization have been presented. These techniques provided valuable information concerning the morphology, specific surface area, porosity, thermal stability and water affinity of these materials necessary prior to the interpretation of the adsorption data. A detailed description of the different setups employed for VOC dynamic adsorption experiments was presented and the methods to determinate the adsorption capacity of the investigated materials were also detailed.

In the second part, the working principle of the compact GC employed throughout this thesis has been described. Since one of the main objectives of this work was to increase the sensitivity of this instrument, five different versions of a preconcentrator were conceived and fabricated. The advantages and drawbacks of the decisions made concerning materials, geometries and heating systems have been presented in this section. The great efforts made to develop an operational device illustrate the complexity and interdisciplinarity of the design process of an analytical instrument. Finally, the last PC version (μ AP2) complies with the requirements established in the objectives of this project in terms of sensitivity, energy consumption and costs.

References

- [1] "Air Toxics Monitoring Methods | Ambient Monitoring Technology Information Center | US EPA Stations." [Online]. Available: <https://www3.epa.gov/ttn/amtic/airtox.html>. [Accessed: 10-Jun-2019].
- [2] S. Król, B. Zabiegała, and J. Namieśnik, "Monitoring VOCs in atmospheric air II. Sample collection and preparation," *TrAC Trends in Analytical Chemistry*, vol. 29, no. 9, pp. 1101–1112, Oct. 2010.
- [3] H.-W. Liu et al., "Process sampling module coupled with purge and trap–GC–FID for in situ auto-monitoring of volatile organic compounds in wastewater," *Talanta*, vol. 80, no. 2, pp. 903–908, Dec. 2009.
- [4] A. Borbon, N. Locoge, T. Léonardis, J.-C. Galloo, and C. Badol, "An automated monitoring system for VOC ozone precursors in ambient air: development, implementation and data analysis," *Analytical and Bioanalytical Chemistry*, vol. 378, no. 7, pp. 1815–1827, Apr. 2004.
- [5] J. Bae et al., "Multiple Coordination Exchanges for Room-Temperature Activation of Open-Metal Sites in Metal–Organic Frameworks," *ACS Appl. Mater. Interfaces*, vol. 9, no. 29, pp. 24743–24752, Jul. 2017.
- [6] K.-S. Lin, A. K. Adhikari, C.-N. Ku, C.-L. Chiang, and H. Kuo, "Synthesis and characterization of porous HKUST-1 metal organic frameworks for hydrogen storage," *International Journal of Hydrogen Energy*, vol. 37, no. 18, pp. 13865–13871, Sep. 2012.
- [7] B. Sun, S. Kayal, and A. Chakraborty, "Study of HKUST (Copper benzene-1,3,5-tricarboxylate, Cu-BTC MOF)-1 metal organic frameworks for CH₄ adsorption: An experimental Investigation with GCMC (grand canonical Monte-carlo) simulation," *Energy*, vol. 76, pp. 419–427, Nov. 2014.
- [8] H. K. Kim et al., "A Chemical Route to Activation of Open Metal Sites in the Copper-Based Metal–Organic Framework Materials HKUST-1 and Cu-MOF-2," *J. Am. Chem. Soc.*, vol. 137, no. 31, pp. 10009–10015, Aug. 2015.
- [9] "SBA-16 - Mesoporous Silica | ACS Material." [Online]. Available: <https://www.acsmaterial.com/sba-354.html>. [Accessed: 03-May-2019].
- [10] M. Niculaua, B. I. Cioroiu, A. M. Tomoiag, M. E. Cioroiu, and M. I. Lazar, "Assessment of SBA-16 Adsorption Capacity Towards Active Substances with Different Chemical Structures," *Cellulose Chem. Technol*, vol. 51, p. 10, 2017.

- [11] "Atlas of Zeolite Framework Types - Ch. Baerlocher, Lynne B. McCusker, D.H. Olson - Google Books." [Online]. Available: https://books.google.fr/books/about/Atlas_of_Zeolite_Framework_Types.html?id=66z0m59omwC&printsec=frontcover&source=kp_read_button&redir_esc=y#v=onepage&q&f=false. [Accessed: 02-May-2019].
- [12] M. Moshoeshoe, M. S. Nadiye-Tabbiruka, and V. Obuseng, "A Review of the Chemistry, Structure, Properties and Applications of Zeolites," *American Journal of Materials Science*, vol. 7, no. 5, pp. 196–221, 2017.
- [13] C. Perego and P. Pollesel, "Chapter 2 - Advances in Aromatics Processing Using Zeolite Catalysts," in *Advances in Nanoporous Materials*, vol. 1, S. Ernst, Ed. Elsevier, 2010, pp. 97–149.
- [14] L. Rodríguez-González, F. Hermes, M. Bertmer, E. Rodríguez-Castellón, A. Jiménez-López, and U. Simon, "The acid properties of H-ZSM-5 as studied by NH₃-TPD and ²⁷Al-MAS-NMR spectroscopy," *Applied Catalysis A: General*, vol. 328, no. 2, pp. 174–182, Sep. 2007.
- [15] M. W. Munthali, M. A. Elsheikh, E. Johan, and N. Matsue, "Proton Adsorption Selectivity of Zeolites in Aqueous Media: Effect of Si/Al Ratio of Zeolites," *Molecules*, vol. 19, no. 12, pp. 20468–20481, Dec. 2014.
- [16] P. Losch, "Synthesis and characterisation of zeolites, their application in catalysis and subsequent rationalisation: methanol-to-olefins (MTO) process with designed ZSM-5 zeolites," p. 173, 2016.
- [17] X. Lei, S. Jockusch, M. F. Ottaviani, and N. J. Turro, "In situ EPR investigation of the addition of persistent benzyl radicals to acrylates on ZSM-5 zeolites. Direct spectroscopic detection of the initial steps in a supramolecular photopolymerization," *Photochem. Photobiol. Sci.*, vol. 2, no. 11, pp. 1095–1100, Nov. 2003.
- [18] F. L. Bleken, S. Chavan, U. Olsbye, M. Boltz, F. Ocampo, and B. Louis, "Conversion of methanol into light olefins over ZSM-5 zeolite: Strategy to enhance propene selectivity," *Applied Catalysis A: General*, vol. 447–448, pp. 178–185, Dec. 2012.
- [19] P. Losch et al., "H-ZSM-5 zeolite model crystals: Structure-diffusion-activity relationship in methanol-to-olefins catalysis," *Journal of Catalysis*, vol. 345, pp. 11–23, Jan. 2017.
- [20] A. J. Maia, B. Louis, Y. L. Lam, and M. M. Pereira, "Ni-ZSM-5 catalysts: Detailed characterization of metal sites for proper catalyst design," *Journal of Catalysis*, vol. 269, no. 1, pp. 103–109, Jan. 2010.

- [21] V. Kazansky and A. Serykh, "A new charge alternating model of localization of bivalent cations in high silica zeolites with distantly placed aluminum atoms in the framework," *Microporous and Mesoporous Materials*, vol. 70, no. 1–3, pp. 151–154, May 2004.
- [22] J. Goldstein et al., *Scanning Electron Microscopy and X-Ray Microanalysis: Third Edition*. Springer US, 2003.
- [23] K. Sing, "The use of nitrogen adsorption for the characterisation of porous materials," *Colloids and Surfaces A: Physicochemical and Engineering Aspects*, vol. 187–188, pp. 3–9, Aug. 2001.
- [24] R. Sindhu, P. Binod, and A. Pandey, "Chapter 17 - Microbial Poly-3-Hydroxybutyrate and Related Copolymers," in *Industrial Biorefineries & White Biotechnology*, A. Pandey, R. Höfer, M. Taherzadeh, K. M. Nampoothiri, and C. Larroche, Eds. Amsterdam: Elsevier, 2015, pp. 575–605.
- [25] P. Gill, T. T. Moghadam, and B. Ranjbar, "Differential Scanning Calorimetry Techniques: Applications in Biology and Nanoscience," *J Biomol Tech*, vol. 21, no. 4, pp. 167–193, Dec. 2010.
- [26] D. Holmes Parker, M. E. Jones, and B. E. Koel, "Determination of the reaction order and activation energy for desorption kinetics using TPD spectra: Application to D₂ desorption from Ag(111)," *Surface Science*, vol. 233, no. 1, pp. 65–73, Jul. 1990.
- [27] Z. Zhang, S. Xian, H. Xi, H. Wang, and Z. Li, "Improvement of CO₂ adsorption on ZIF-8 crystals modified by enhancing basicity of surface," *Chemical Engineering Science*, vol. 66, no. 20, pp. 4878–4888, Oct. 2011.
- [28] P. A. Redhead, "Thermal desorption of gases," *Vacuum*, vol. 12, no. 4, pp. 203–211, Jul. 1962.
- [29] F. Xu, S. Xian, Q. Xia, Y. Li, and Z. Li, "Effect of Textural Properties on the Adsorption and Desorption of Toluene on the Metal-Organic Frameworks HKUST-1 and MIL-101," *Adsorption Science & Technology*, vol. 31, no. 4, pp. 325–339, Apr. 2013.
- [30] N. Katada, H. Igi, and J.-H. Kim, "Determination of the Acidic Properties of Zeolite by Theoretical Analysis of Temperature-Programmed Desorption of Ammonia Based on Adsorption Equilibrium," *J. Phys. Chem. B*, vol. 101, no. 31, pp. 5969–5977, Jul. 1997.
- [31] E. Rodríguez-Castellón et al., "Textural and structural properties and surface acidity characterization of mesoporous silica-zirconia molecular sieves," *Journal of Solid State Chemistry France*, vol. 175, pp. 159–169, Nov. 2003.
- [32] F. Lónyi and J. Valyon, "On the interpretation of the NH₃-TPD patterns of H-ZSM-5 and H-mordenite," *Microporous and Mesoporous Materials*, vol. 47, no. 2–3, pp. 293–301, Oct. 2001.

- [33] M. Guglielmino, A. Allouch, C. A. Serra, and S. L. Calvé, "Development of microfluidic analytical method for on-line gaseous Formaldehyde detection," *Sensors and Actuators B: Chemical*, vol. 243, pp. 963–970, May 2017.
- [34] M. Guglielmino, P. Bernhardt, C. Trocquet, C. A. Serra, and S. Le Calvé, "On-line gaseous formaldehyde detection by a microfluidic analytical method based on simultaneous uptake and derivatization in a temperature controlled annular flow," *Talanta*, vol. 172, pp. 102–108, Sep. 2017.
- [35] R. Nasreddine, V. Person, C. A. Serra, and S. Le Calvé, "Development of a novel portable miniaturized GC for near real-time low level detection of BTEX," *Sensors and Actuators B: Chemical*, vol. 224, pp. 159–169, 2016.
- [36] I. Lara-Ibeas et al., "BTEX near real-time monitoring in two primary schools in La Rochelle, France," *Air Quality, Atmosphere & Health*, vol. 11, pp. 1091–1107, Aug. 2018.
- [37] R. Nasreddine, V. Person, C. A. Serra, C. Schoemaeker, and S. Le Calvé, "Portable novel micro-device for BTEX real-time monitoring: Assessment during a field campaign in a low consumption energy junior high school classroom," *Atmospheric Environment*, vol. 126, pp. 211–217, Feb. 2016.
- [38] E. H. M. Camara, P. Breuil, D. Briand, N. F. de Rooij, and C. Pijolat, "A micro gas preconcentrator with improved performance for pollution monitoring and explosives detection," *Analytica Chimica Acta*, vol. 688, no. 2, pp. 175–182, Mar. 2011.
- [39] Y. Zhang, J. Sun, X. Zhu, J. Liu, and Z. Ning, "Mini pretreatment system integrated with micro pre-concentrator and micro GC column," *Sensor Review*, vol. 37, no. 2, pp. 137–141, Mar. 2017.
- [40] G. Gregis et al., "Detection and quantification of lung cancer biomarkers by a micro-analytical device using a single metal oxide-based gas sensor," *Sensors and Actuators B: Chemical*, vol. 255, pp. 391–400, Feb. 2018.
- [41] D. Michoń, A. Rydosz, K. Domański, W. Maziarz, and T. Pisarkiewicz, "Detection of acetone in exhaled breath with the use of micropreconcentrator and a commercial gas sensor," 2016, p. 1017511.
- [42] L. A. Hof and J. Abou Ziki, "Micro-Hole Drilling on Glass Substrates—A Review," *Micromachines*, vol. 8, no. 2, p. 53, Feb. 2017.

Chapter 3. Field Measurements: BTEX near real-time monitoring in two primary schools in La Rochelle, France

3.1 Impact'Air Project

In recent years, indoor air quality (IAQ) has gained attention due to the adverse effects of pollutants on human health. These effects are even more serious for children due to their higher inhalation rates, the continuing development of their tissues and organs and their immature immune system [1]. Besides, children spend long time indoors where levels of pollutants are usually from 2 to 10 times higher than outdoors. Daisey *et al.* reported that nearly 30 % of the time indoors is spent at school [2]. In this context, the Impact'Air project aimed at quantifying the concentrations-time profiles in order to better characterize the indoor air pollution in schools and to provide some useful recommendations for improving their air quality. In the framework of this project, a field campaign was carried out in a kindergarten and two primary schools of La Rochelle (France) for five weeks. The main objectives of this project were:

- to monitor French indoor regulated air pollutants (formaldehyde, benzene, and CO₂)
- identify the main emissions sources of air pollutants
- estimate the efficiency of various ventilation scenarios on IAQ
- draft of general good practices guidelines in IAQ in schools

Although formaldehyde and benzene are the only regulated VOC, toluene, ethylbenzene and xylenes were also monitored since the continuous exposure can lead to health problems and physical discomfort [3]. Additionally, CO₂ concentration was continuously measured and was adopted as an indicator of ventilation rates inside the building.

In order to identify the main pollution sources and the efficiency of the different ventilation scenarios, air quality measurements were conducted in different conditions each week. During the first week, the investigated classrooms were always closed, not ventilated and occupied neither by students nor by teachers. Thus, the contribution of the building materials to the indoor air pollution could be estimated. At the beginning of the second week, the furniture was added, and the classrooms remained closed for the whole week. This scenario enabled to quantify the additional pollution


potentially emitted by the furniture. Finally, the last three weeks, normal school activities were carried out in the classrooms and different ventilation practices were performed each week.

Our real-time measurements, contrary to traditional passive sampling, allowed us to establish BTEX concentration-time profiles and to identify exactly when higher concentrations of BTEX were emitted, which allowed us to determine the origin of the main pollution sources. A detailed description of the development of this field campaign and the results obtained are presented in the following publication.

3.2 Article 1 published in *Air Quality, Atmosphere & Health*: “BTEX near real-time monitoring in two primary schools in La Rochelle, France



BTEX near real-time monitoring in two primary schools in La Rochelle, France

Irene Lara-Ibeas^{1,2} · Claire Trocquet² · Rouba Nasreddine² · Christina Andrikopoulou¹ · Vincent Person¹ · Béatrice Cormerais³ · Stéphanette Englaro² · Stéphane Le Calvé^{1,2} 

Received: 12 April 2018 / Accepted: 29 July 2018
© Springer Nature B.V. 2018

Abstract

The present field campaign was conducted in two French primary schools for 5 weeks, where the experimental conditions were modified every week. During the first week, the classrooms were empty and not occupied, whereas the furniture was added the second week. For the three last weeks, the classrooms were normally occupied by students and various scenarios of ventilation were applied. BTEX concentrations were monitored by using novel portable pre-industrial prototypes with low gas and energy consumption, which worked continuously and operated in near real time with a time resolution of 10 min. The BTEX concentrations were compared to CO₂ measurements since the latter is commonly considered as a confinement indicator. In both schools, BTEX were not detected during the absence of students indicating that neither building materials nor furniture emit such compounds. Once the schools occupied by students, BTEX have been detected from time to time, and their concentrations ranged as follows: 0–12 ppb (benzene); 0–29 ppb (toluene), 0–4 ppb (ethylbenzene), 0–11 ppb (m/p-xylenes), and 0–10 ppb (o-xylene) excluding huge values due to paint emissions in one of the schools. Toluene was found to be strongly correlated to high levels of CO₂, showing that it was emitted by internal students activities scheduled at the end of mornings. On the contrary, benzene peak was not correlated to high values of CO₂, suggesting that it comes from external sources.

Keywords BTEX · Toluene · Indoor air schools · CO₂ levels · Real time · Portable device

Highlights

- BTEX levels were monitored in near real time in 2 primary schools for 5 weeks.
- BTEX concentrations were discussed according to the various weekly ventilation scenarios.
- Strong correlations between concentration time profiles of BTEX and CO₂ were highlighted.
- The BTEX analyzer demonstrated its ability for real-time monitoring and detection of rapid changes in the range 1–30 ppb.

Electronic supplementary material The online version of this article (<https://doi.org/10.1007/s11869-018-0611-3>) contains supplementary material, which is available to authorized users.

✉ Stéphane Le Calvé
slecalve@unistra.fr

¹ Institut de Chimie et Procédés pour l’Energie, l’Environnement et la Santé (ICPEES, UMR 7515 CNRS/Unistra), groupe physico-chimie de l’atmosphère, 25 rue Becquerel, 67087 Strasbourg Cedex 02, France

² In’Air Solutions, 25 rue Becquerel, 67000 Strasbourg, France

³ Direction Santé Publique de la Ville de La Rochelle, 1 rue Nicolas Venette, 17000 La Rochelle, France

Introduction

During the last decades, indoor air quality (IAQ) is a growing concern in the scientific community due to the harmful effects of airborne pollutants on human health. According to the World Health Organization (WHO), household air pollution led to more than 4 million premature deaths annually, among which the large majority concerns children. Children are more vulnerable than adults to the adverse health effects of air pollution due to their higher inhalation rates, the continuing development of their tissues and organs, their immature immune system, and the longer periods of time they spend indoors (Mendell and Heath 2005). A large number of epidemiological studies have reported an association between exposure to criteria air pollutants and several morbidity and mortality outcomes in children (Buka et al. 2006).

Between the age of 3 and 16, schools are the most common places where children spend almost 30% of their day, 70% of which inside classrooms (Daisey et al. 2003). Therefore, IAQ in schools is very critical for children’s health. Indeed, an increasing amount of scientific evidence has demonstrated

that the physical environments in which children spend their time have a profound impact not only on their health but also on their ability to learn (Mendell and Heath 2005; Simoni et al. 2010). IAQ in schools is assessed generally by its comfort parameters (such as relative humidity, temperature, and CO₂ levels), ventilation rates, and particulate matter levels and by gaseous pollutants concentrations.

Even if CO₂ is not defined as an air pollutant by the WHO, its concentration level is commonly adopted as an indicator of ventilation rates inside the building (Satish et al. 2012) or in other words, a confinement indicator. According to the American Society of Heating, Refrigerating, and Air-Conditioning Engineers (ASHRAE), if CO₂ is controlled to less than 700 ppm, then it is generally thought that indoor environment receives sufficient quantities of outdoor air to dilute human metabolic odors (and some other odors) to acceptable levels. A number of researches have shown that CO₂ concentrations above 1000 ppm can affect students' performance (Apte et al. 2000; Twardella et al. 2012; Muscatiello et al. 2015). Many studies of IAQ in classrooms reported CO₂ levels between 500 and 4000 ppm (Alves et al. 2016) and most frequently above 3000 ppm, especially in naturally ventilated schools. These high levels of CO₂ exceed the ASHREA recommended threshold value, demonstrating inadequate ventilation for the majority of schools (Griffiths and Eftekhari 2008; Turanjanin et al. 2014; Bari et al. 2015; Hänninen et al. 2017).

Numerous studies have been carried out in order to monitor the indoor/outdoor levels of volatile organic compounds (VOCs) in schools (see Table 1). Among the indoor air contaminants, BTEX (benzene, toluene, ethylbenzene, and xylenes isomers) have been founded to be the most abundant in school indoor air (Kotzias et al. 2009; Geiss et al. 2011). The presence of BTEX in indoor air presents harmful effects for children's health leading to the development of serious pathologies such as asthma (Arif and Shah 2007). Among BTEX, benzene is the most dangerous since it was classified as human carcinogenic according to the WHO and International Agency for Research on Cancer (IARC) in 1986. Therefore, the European Union has established guidelines for benzene in indoor air, where a threshold level is fixed to 5 µg m⁻³ (1.6 ppb) in public buildings, requiring sensitive analytical methods.

Table 1 presents some studies carried out during the last few years focused on IAQ in schools. All reported studies except for one were carried out using classical methods: Indoor/outdoor air was sampled on commercial cartridges for a duration time varying between few hours to few days depending on the type of sampling method, i.e., active or passive. In both cases, once sampling was achieved, the commercial cartridges were thermally desorbed or extracted with the appropriate solvent and then analyzed using a gas chromatograph equipped with a flame ionization detector (FID) or a mass spectrometer (MS). Even if these techniques are very

sensitive and can analyze tens of molecules at a single run, the obtained results represent only an average concentration of the detected molecules over the considered sampling time.

Therefore, these offline analysis are not adapted for real-time monitoring and concentration-time profiles determination, which can be a key information to identify the sources of pollutants in a given indoor environment. In the literature, only one study was performed using real-time devices aimed to monitor BTEX in indoor air of schools over a long period. This study, conducted by our research group, reported toluene levels for two consecutive weeks in an unoccupied classroom using a laboratory prototype of a miniaturized GC (Nasreddine et al. 2015), whereas other BTEX were not detected.

In addition, simultaneous passive measurements in indoor and outdoor air are often performed in order to identify if the studied pollutants are emitted inside or outside the investigated building by determining commonly the ratio between indoor and outdoor concentrations (Madureira et al. 2016; Romagnoli et al. 2016; Zhong et al. 2017; Marzocca et al. 2017). Nevertheless, this type of passive sampling provides only an average value (usually one measurement per week in the case of schools), which does not allow highlighting the temporal phenomena that are demonstrated by inducing peaks of pollution.

In this work, we report for the first time the accurate temporal variation of all BTEX concentrations in two primary schools and one kindergarten over 5 weeks and 1 week respectively, using pre-industrial BTEX analyzers based on the miniaturized GC/PID reported previously by Nasreddine et al. (2015). This field campaign was performed in the city of La Rochelle, in the framework of Impact'Air project aiming at monitoring French indoor regulated air pollutants (formaldehyde, benzene, and carbon dioxide), at quantifying the relative emissions sources of air pollutants (building materials vs furniture for example) and at identifying the efficiency of various ventilation scenarios on IAQ. Note that formaldehyde measurements will be published in a separate paper.

One of the interesting aspects of this study lies in the fact that the real-time measurement of BTEX combined with the measurement of CO₂ serves the same purpose as an additional measurement of outdoor air pollution. Indeed, the continuous measurement of CO₂ permits to precisely identify the windows' opening periods of the classroom, which are visible when the CO₂ concentration rapidly decreases to values close to 400–500 ppm. As a result, during this study, parallel outdoor pollution monitoring was not conducted, but the correlation of pollutants concentrations with outdoor or indoor sources was possible. As soon as the windows were open (as indicated by CO₂ values), an increase in the pollutants' concentration in the room can be attributed to external pollution in the absence of controlled mechanical ventilation. On the other hand, when the windows were closed, an increase in the concentration in the room can be imputed to indoor pollution.

Table 1 Comparison of BTEX levels found in indoor air of schools

Reference/location	Sampling time and method	Analysis method	Concentration (ppb)	Benzene	Toluene	Ethylbenzene	m/p-Xylenes	o-Xylene
Norback et al. 2017 8 Junior high schools Malaysia	Active for 4 h (Charcoal tubes)	CS ₂ Desorption GC-MS	Max	9.92	7.54	2.1	188.4	
	Passive for 1 week (Dräger ORSA 5)	CS ₂ Desorption GC-MS	Max	n.d.	10.16	0.88	32.47	
Zhong et al. 2017 37 Elementary schools USA	Passive for 2 days (Tenax GR)	ATD-GC-MS	Max	1.37	22.19	0.46	1.70	0.51
Marzocca et al. 2017 Primary school Italy	Passive for 2 weeks (Radiello)	TD-GC-MS	Max	0.14	0.39	0.27	0.51	0.60
Madureira et al. 2016 20 Primary schools in Portugal	Passive for 5 days (Tenax TA)	GC-MS	Max	0.86	53.62	NM	95.98	
Romagnoli et al. 2016A primary school Italy			Max	0.28	0.86	0.13	0.69	
Nasreddine et al. 2016A junior high school in France	Active for 2 weeks	GC-PID	Max	0.5	18	0.5	0.5	0.5
Verrielle et al. 2016 10 Schools LCB France	Passive for 4.5 days (Radiello code 145)	ATD-GC-FID	Mean occupation	0.3	11.54	0.25	0.57	0.20
			Mean inoccupation	0.18	11.59	0.32	0.27	0.18
Canha et al. 2016 17 Schools France	Passive for 5.3 days (Radiello code 145)	ATD-GC-FID and ATD-GC-MS	Min	0.46	0.42	0.41	0.27	0.25
			Max	0.82	0.73	45.78	82.56	11.85
Madureira et al. 2015 20 Schools Portugal	Passive (Tenax GR)	ATD-GC-MS	Min	0.46	0.47	n.d.	0.27	0.25
			Max	0.82	52.75	n.d.	82.56	11.85
Godoi et al. 2013 25 Schools Brazil	Passive for 1 week (Radiello)	CS ₂ Desorption GC-FID	Min	0.06	0.10	0.04	0.04	0.03
			Max	0.98	2.11	0.70	1.58	1.18
Pegas et al. 2011 14 Schools Portugal	Passive for 14 days (Radiello code 130)	Solvent desorption GC-FID	Min	0.06	0.36	0.07	0.16	0.07
			Max	0.27	1.90	3.21	9.04	3.05
Godwin and Betterman 2007 9 Schools USA	Passive (Tenax GR)	GC-MS	Max	0.49	19.43	0.63	14.24	0.86
Guo et al. 2003 7 Schools	Active for 8 h (Canister)	GC-MS	Min	0.20	1.45	0.23	0.20	0.23
			Max	3.74	12.77	3.94	2.69	0.58

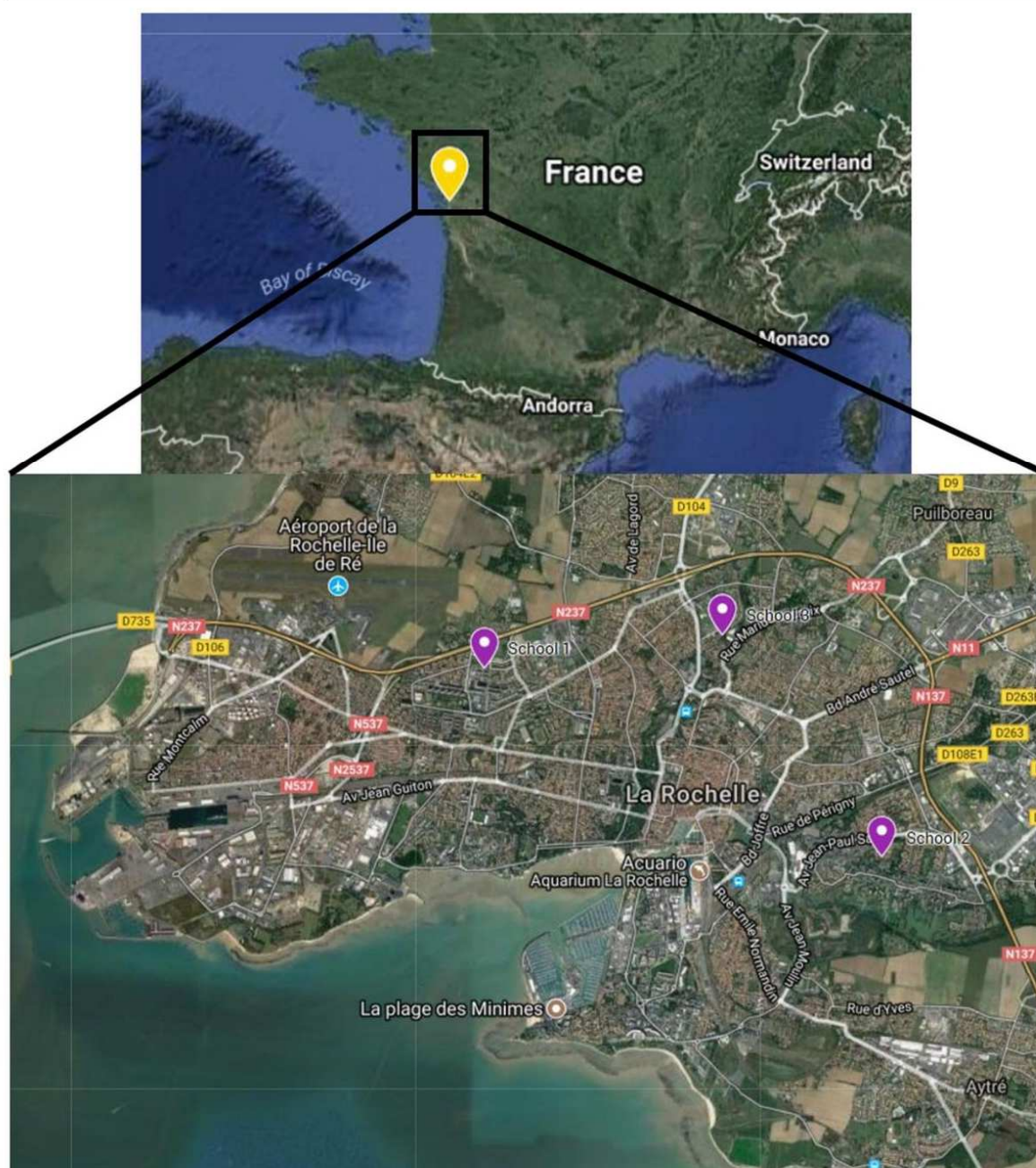


Fig. 1 Location of La Rochelle city in France and the selected schools for the field study

Methodology

Site description

The study was conducted in La Rochelle city (east of France $46^{\circ} 09' 33.9''$ North $1^{\circ} 09' 21.6''$ West). Two public primary

schools hereinafter school 1 (S1) and school 2 (S2) and one kindergarten hereinafter school 3 (S3) were selected considering as representative schools of the city. Figure 1 shows the sites of the three selected schools. S1 is a primary school built in 1965 and located at a residential suburban area at about 150 m from the highway and at 1.2 km far from La Rochelle

airport. S2 was constructed in 1974, and it is also located at a residential suburban area next to the city park. The kindergarten S3 was also built in the 1970s and was located about 300 m from the same highway as S1.

One classroom was chosen on each site according to the possibility (1) to install the analytical materials inside an adjacent room to limit noise as much as possible and thus avoid disturbing the courses and (2) to limit the sampling line length. In the first one (S1), the classroom occupied 187 m³ and presented four west-facing windows and two doors: One was connected to an adjoining office and the second to a hallway. During the activity period, the classroom was occupied by 25 students aged between 9 and 11 years. In S2, the classroom volume was equal to 198 m³ and also equipped with four windows west sides and three doors. This classroom was occupied by 16 students of 7–9 years. In S3, the classroom volume was similar to the other schools (180 m³) and had four large south-east facing bay windows and three doors connecting the classroom with the corridor, the playground, and the library. During school days, the classroom was occupied by 23 students between the age of 3 and 6 years.

The investigated rooms in S1 and S2 had similar characteristics, i.e., tiled floor, wallpaper, a blackboard, and two corkboards. The only differences were the type of the ceiling, covered by ceiling plates in S1, while it was painted in S2 and the presence of a whiteboard in S1.

On the other hand, the classroom studied in S3 had a linoleum floor, painted walls, ceiling covered of ceiling plates, a blackboard, and a corkboard.

All the investigated classrooms were naturally ventilated and equipped with heating radiators operating from 7 a.m. to 5 p.m. in weekdays to keep an average temperature of 20 °C during the day and 16 °C during the night.

Analytical instruments

In order to monitor in real time the three French regulated pollutants, different analytical instruments were used: home-made HCHO analyzers, pre-industrial BTEX analyzers, and CO₂ detectors, i.e., LUM'Air (Cairpol) or Q-Trak™ IAQ monitor (TSI Incorporated, St. Paul, Minnesota, USA). During the whole campaign, temperature, relative humidity, and carbon dioxide were measured using Q-Trak™ IAQ in all schools. In addition, LUM'Air was used to alert when threshold levels were exceeded.

LUM'Air CO₂ detector

In both S1 and S2, the LUM'Air CO₂ detector was used. This later is equipped with three different LED (green, orange, and red), which are switched on depending on the CO₂ concentration. For concentrations below 1000 ppm, the green LED is on, meaning atmosphere is not confined. When levels are

higher than 1000 ppm (first alert threshold), light is switched to orange indicating windows and/or doors should be opened. If concentration exceeds 1700 ppm (second alert threshold), light is switched to red and windows and/or doors must be open quickly to renew indoor air.

In the kindergarten (S3), temperature, humidity, and CO₂ levels were also measured continuously every 10 min with Q-Trak™ IAQ monitor (TSI Incorporated, St. Paul, Minnesota, USA). The BTEX results were correlated to CO₂ values to determine exactly when indoor air was renewed by opening windows and/or doors.

Pre-industrial BTEX analyzer

Gaseous BTEX in schools' indoor air were continuously analyzed by two novel pre-industrial BTEX analyzers (see Fig. 1). These devices were constructed based on the laboratory prototype μ GC developed by Nasreddine et al. (2015) and used for real-time toluene monitoring in a previous study Nasreddine et al. (2016). The pre-industrial μ GC operates according to three steps: (i) sampling, (ii) separation, and (iii) detection as shown in Fig. 2. The detailed operating principle is described elsewhere (Nasreddine et al. 2015), so that only a brief description is given below.

In a previous study (Nasreddine et al. 2015), the optimal experimental conditions of BTEX separation were determined according to the calculated height equivalent to the theoretical plate (HETP) and the total analysis time for a single run, which was set to a maximum of 10 min. Using the optimal conditions, the detection limit, stability, and repeatability of the analytical system were assessed. A detection limit of 1 ppb was found for benzene and toluene, whereas it was less than 3 ppb for other monoaromatic compounds.

The pre-industrial BTEX analyzer was standalone and fully controlled by an embedded software running on Linux which provides visualization of real-time chromatograms, automatic integration of obtained BTEX peaks, and calculation of the corresponding concentrations. The pre-industrial BTEX analyzer system shown in Fig. 3 can fit into a plastic case that measures 32.4 (l) \times 28.9 (w) \times 14.5 (h) cm and weights around 5.5 kg (e.g., battery and screen included). The micro-device can be powered either by a 12 V DC external adapter or a 12 V battery pack. A built-in 7-in. touch panel screen is used to control all GC parameters (sampling time, oven temperature, number and frequency of analysis, and integration parameters). This powerful instrument provides a full BTEX analysis within only 10 min.

The laboratory prototype of this micro-device was also deployed in a junior high school for 2 weeks during a previous indoor field campaign (Nasreddine et al. 2016). The obtained results validated and demonstrated its ability to highlight rapid changes of atmospheric BTEX concentrations in the range between 1 and 20 ppb. In addition, the toluene concentrations

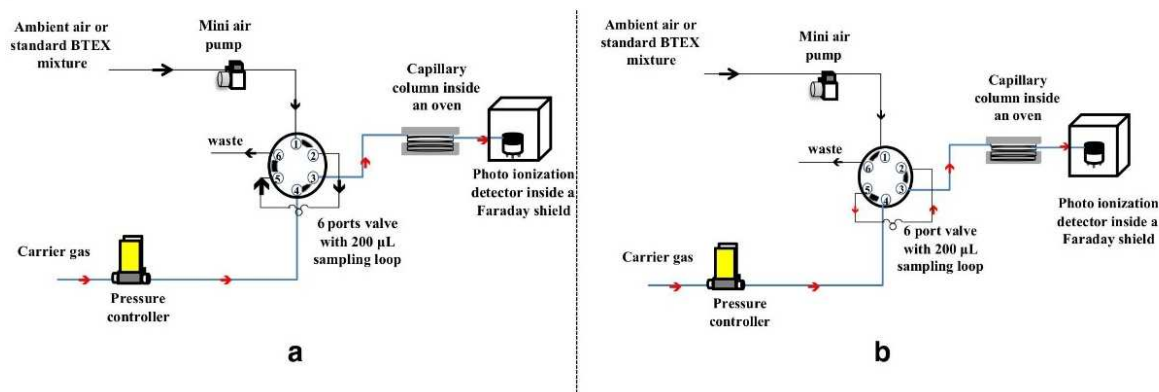


Fig. 2 Schematic representation of the BTEX micro-device operating principle either in sampling mode (a) or in analysis mode (b) (injection and detection)

measured with our new micro-device were in very good agreement with those provided by another commercial BTEX analyzer (GC8900, Baseline).

Calibration and detection limits of BTEX analyzer During this previous campaign, it was highlighted that all devices equipped with a photoionization detector may need to be recalibrated during field campaign occurring several weeks. A long interruption due to a long transport also implies to make in situ a full calibration or at least a partial one to check the previous calibration curves made under laboratory conditions.

For these reasons, in the present study, both pre-industrial portable BTEX analyzers were in situ calibrated at the beginning and during the field campaign using the calibration procedure detailed below.

Stainless steel canisters were previously cleaned in our laboratory within a standard cycle of three steps using Model 3100A canister cleaner (Entech Instruments, Inc.). Cleaned canisters were then filled with a standard mixture of BTEX purchased from Messer (France). The initial concentration of

every compound was equal to 100 ppb with a 10% of uncertainty.

Once the instruments were installed in the schools, the aforementioned canisters were connected to calibration setup described elsewhere (Nasreddine et al. 2015), this later being connected to the sampling inlet of the BTEX analyzer. The different BTEX concentrations were obtained by dilution in nitrogen (99.999%, Messer). Each generated BTEX concentration and its corresponding analysis was repeated twice. This setup allowed us to calibrate easily the system during field campaign. For both pre-industrial devices, BTEX concentrations ranged from 0 to 50 ppb, and calibration curves were obtained by plotting the peak area for each species versus the corresponding gaseous concentrations. The equations of the calibration curves and limits of detection are presented in Table 2.

Every week, a single-point calibration with a BTEX mixture at 20 ppb was performed for each instrument. This allowed the detection of any significant change of the response factor of the BTEX analyzer. Finally, these pre-industrial micro-devices were recalibrated twice during the course of our field campaign and deviations between 3 and 15% compared to the initial calibration were recorded depending on the gaseous compound and on the BTEX analyzer, excepting for ethylbenzene in the pre-industrial micro-device 1 that reached a deviation of 26%.



Fig. 3 Photograph of pre-industrial BTEX analyzer used during the field campaign

Sampling conditions and ventilation scenarios

The field campaign was conducted during winter for five consecutive weeks from 15th of February 2016 to 20th of March 2016 for schools 1 and 2, whereas the school 3 was only investigated for the week 4.

All instruments excepting CO₂ probes were installed in an adjacent room, and indoor air was continuously sampled through 6 mm Teflon tube. This sampling tube measured 4

Table 2 Equations of calibration curves and detection limits (LOD) of BTEX obtained with both instruments at the beginning of the field campaign

Compound	Pre-industrial device (1)			Pre-industrial device (2)		
	Equation	R^2	LOD* (ppb)	Equation	R^2	LOD* (ppb)
Benzene	$y = 670 \times$	0.9976	1.08	$y = 503 \times$	0.9993	1.33
Toluene	$y = 374 \times$	0.9988	2.06	$y = 406 \times$	0.9997	1.87
Ethylbenzene	$y = 167 \times$	0.9723	4.53	$y = 194 \times$	0.9912	3.37
m- and p-Xylene	$y = 148 \times$	0.9944	9.36	$y = 213 \times$	0.9961	6.26
o-Xylene	$y = 110 \times$	0.9404	8.43	$y = 148 \times$	0.9985	6.15

*LOD (ppb) is determined from $S/N = 3$

Pre-industrial device (1); 3 concentrations of 20 ppb

Pre-industrial device (2); 2 concentrations of 20 ppb and 5 ppb

to 6 m, and its inlet reached approximately the middle of the classroom at 50 to 100 cm under the classroom ceiling. Each instrument had its own sampling line. The sampling flow rate used for the portable analyzers was fixed at 20 mL min^{-1} , which is a sufficient rate to ensure the air renewal in the sampling line in less than 3 min. Each analysis was completed in only 10 min, the next sampling starting 3 min before the end of the previous analysis, and the pre-industrial BTEX analyzer was programmed to work continuously for a full week. Simultaneous indoor and outdoor BTEX measurements in real time were not feasible in this case because of the number of analytical devices available and the number of schools investigated. Nevertheless, CO_2 concentrations were continuously monitored thus providing information on the windows status (open or closed) and enabling the investigation of possible correlation of indoor BTEX concentrations with outdoor sources.

The various ventilation scenarios used in this field campaign have been summarized in Table 3. For the first 2 weeks of the campaign, the two investigated classrooms of schools S1 and S2 were not ventilated and occupied neither by students nor by teachers. The windows were always closed, whereas the doors were maintained closed as much as possible, and nobody was allowed to enter inside the investigated classroom. During the first week from 15th to 21st of February 2016, the chosen classrooms were also fully empty without any furniture in order to estimate the concentration levels, which could be attributed to emissions from building materials.

The second week, the furniture was added to the classrooms at the very beginning of the second week, and the pollutants' concentrations were measured from 22nd to 28th of February 2016. Note that in S1, the ramp of the stairs leading to the hallway was repainted at the beginning of the second week, which distorted a part of the results.

For the weeks 3 to 5, students and their teachers were also present in the classrooms, and they followed different ventilation instructions each week. In S1, during the third week (from 1st to 6th of March 2016), usual ventilation was followed,

where no specific instructions were given to the teachers, so they followed its subjective criteria for ventilation. During the fourth week (from 7th to 13th of March 2016), ventilation was made according to the CO_2 level reached in the room, inducing the lighting of LED on the CO_2 detector, and the fifth week (from 14th to 20th of March 2016) ventilation instructions given by the French Indoor Air Quality Observatory were followed. According to these latter instructions, windows were opened an average of 30 min in the following cases: before and after the classes, every 2 h of class, and after the cleaning events. All the doors of the classroom remained open during the night. The time schedules for both usual ventilation and the ventilation made according to the instructions given by the French OQAI are detailed in Table S1.

In S2, the ventilation scenario previously explained was also applied but in a different order because of the availability of a single-LUM'Air CO_2 detector. Consequently, ventilation following the recommendations given by the French OQAI was carried out during the fourth week (from 7th to 13th of March 2016), whereas the occupants used the lighting of LED on the CO_2 detector during the fifth week (from 14th to 20th of March 2016), in opposite to S1.

In S3, measurements were conducted only over the fourth week, i.e., from 7th to 13th of March 2016, during the presence of students and when no specific ventilation constraints were followed, so that teachers and children can open doors/windows as usual.

Results and discussion

The data obtained in this work are summarized in Table 4. Results obtained for school 3 are not included in this table since no BTEX were detected. The temperature inside the studied room varied between 14.9 and $24.4 \text{ }^\circ\text{C}$ and 17.4 and $23.5 \text{ }^\circ\text{C}$ for S1 and S2, respectively. The relative humidity ranged from 41.8 to 69.6% in S1 and from 35.3 to 67.3% in S2.

Table 3 Summary of the scenario performed in 2016 during 5 weeks of field campaign in three schools

	Week 1	Week 2	Week 3	Week 4	Week 5
	15–21 February 2016	22–28 February 2016	1–6 March 2016	7–13 March 2016	14–20 March 2016
School 1	Empty room ¹	Furniture ²	Usual ventilation ³	Ventilation based on CO ₂ measurements ⁴	Ventilation according to French recommendations ⁵
School 2	Empty room ¹	Furniture ²	Usual ventilation ³	Ventilation according to French recommendations ⁵	Ventilation based on CO ₂ measurements ⁴
School 3	–	–	–	Usual ventilation ³	–

¹ The classroom was fully empty without any furniture, the students being absent, and the room being closed

² Furniture was added into the room, the student being absent, and the room being closed

³ This correspond to the usual ventilation given by the school authority

⁴ Ventilation according to the CO₂ level reached in the room which induces the lighting of LED on the CO₂ detector (see Analytical Instruments in Methodology section)

⁵ Ventilation following the recommendations given by the French Observatory of Indoor Air Quality

CO₂ concentration

During week 1, the weekly average concentrations of CO₂ were found to be 576 and 460 ppm for S1 and S2 respectively with the maximum concentrations of 972 and 661 ppm recorded during the sampling lines installation. After the addition of furniture in the classroom but in absence of people, the maximum CO₂ concentrations reached 918 and 958 ppm respectively, and the weekly mean levels of CO₂ were 444 and 418 ppm.

As expected, significant higher values of carbon dioxide were recorded in both S1 and S2, when the occupants were present in weeks 3 to 5. The highest concentrations were monitored, when the occupants followed the usual ventilation with average values equal to 1296 and 1221 ppm and maximum levels up to 3743 and 3565 ppm for S1 and S2 respectively. The lowest values recorded in presence of occupants correspond to the week, where the occupants opened the windows and doors according to the CO₂ level reached in the room, which induced the lighting of LED on the CO₂ detector. During this week, average CO₂ values of 820 and of 682 ppm were recorded for S1 and S2 respectively limiting at the same time the corresponding maximum CO₂ concentrations equal to 2211 and 1805 ppm.

Intermediate average levels of CO₂ were finally monitored during the week, where occupants complied with ventilation instructions given by the French OQAI: 1066 ppm (S1) and 756 ppm (S2). The corresponding maximum concentrations were then 3752 and 2974 ppm, which are close to those recorded during week 3.

As expected, our recorded CO₂ levels were higher in the occupation period than those detected in the previous weeks in absence of people. Our CO₂ concentrations were often above 1000 ppm, when children were present confirming the results of many studies in classrooms reporting CO₂ levels between 500 and 4000 ppm and most frequently above 3000 ppm, especially in naturally ventilated schools, demonstrating

inadequate ventilation for majority of schools (Griffiths and Eftekhari 2008; Turanjanin et al. 2014; Bari et al. 2015).

In S3, average CO₂ level was equal to 459 ppm, significantly lower than those found in primary schools during the occupation periods. In this school, the maximum CO₂ concentration recorded was 1406 ppm.

BTEX monitoring in both schools

General results

Once all instruments are installed and calibrated, indoor air sampling began for five consecutive weeks and instruments worked continuously, except when they were stopped for calibration or moved to another school as in the case of the pre-industrial micro-device 2 (moved from S2 to S3 during the fourth week).

Data collected were analyzed daily since our novel BTEX analyzer operates in near real-time with a time resolution of 10 min. The BTEX concentration ranges obtained during the whole campaign are given in Table 4. Results obtained in S3 are not presented in the table because none of BTEX were detected in the chosen classroom of the kindergarten.

Empty room The results reported in Table 4 show the absence of BTEX in indoor air in both schools S1 and S2 during the first week, where classrooms were empty, except traces of toluene in S1 lower than 1.6 ppb. This fact demonstrates that building materials in both schools do not emit any benzene, ethylbenzene, and xylenes. Very low emissions of toluene from building materials were only recorded in S1.

Addition of furniture When the furniture was added into the classroom at the beginning of the second week, the BTEX concentrations were again below their corresponding detection limits in S2 for the whole week and in S1 at the very beginning (see Table 4). Later on, in school 1, benzene and

Table 4 Summary of BTEX concentrations ranges obtained during 5 weeks in both schools

	Week 1			Week 2			Week 3			Week 4			Week 5			
	S1 ^a		S2 ^a		S1 ^b		S2 ^b		S1 ^c		S2 ^c		S1 ^c		S2 ^d	
	Max	Mean	Max	Mean	Max	Mean	Max	Mean	Max	Mean	Max	Mean	Max	Mean	Max	Mean
Benzene (ppb)	n. d.	n. d.	n. d.	n. d.	n. d. ^f n. d. ^g	n. d. ^f n. d. ^g	n. d.	n. d.	1.1	0.01	n. d.	n. d.	12.1	0.04	n. d.	n. d.
Toluene (ppb)	1.6	0.01	n. d.	n. d.	1.1 3.2 ^g	0.01 ^f 1.2 ^g	n. d.	n. d.	29.5	0.62	3.5	0.23	5.5	0.25	17.6	0.58
Ethylbenzene (ppb)	n. d.	n. d.	n. d.	n. d.	1.5 ^h n. d. ^g	0.8 ^h n. d. ^g	n. d.	n. d.	n. d.	n. d.	4.4	0.29	n. d.	n. d.	n. d.	2.7
m/p-Xylenes (ppb)	n. d.	n. d.	n. d.	n. d.	n. d. ^f 59.5 ^g	n. d. ^f 33.8 ^g	n. d.	n. d.	10.9	0.12	10.4	1.35	n. d.	n. d.	n. d.	6.7
o-Xylene (ppb)	n. d.	n. d.	n. d.	n. d.	21.5 ^h 41.4 ^g	14.9 ^h 24.9 ^g	n. d.	n. d.	10.5	0.26	6.6	0.24	n. d.	n. d.	n. d.	n. d.
CO ₂ (ppm)	658 ^j	557 ^j	661 ^j	416 ^j	918	444	958	418	3743	1296	3565	1221	2211	820	2974	756
Temperature (°C)	20.8	18.8	20.8	19.1	23.1	19.4	21.5	19.6	24.4	18.1	21.55	19.8	21.5	17.1	21.5	20.0
Relative humidity (%)	69.6	57.7	63.2	49.9	62.9	52.4	58.75	53.1	65.9	59.0	67.2	53.6	62.6	55.5	57.9	48.8

^aThe classroom was fully empty without any furniture, the students being absent, and the room being closed

^bFurniture was added into the room, the students being absent, and the room being closed

^cThis correspond to the usual ventilation given by the school authority

^dVentilation according to the CO₂ level reached in the room which induces the lighting of LED on the CO₂ detector (see Analytical Instruments in Methodology section)

^eVentilation following the recommendations given by the French Observatory of Indoor Air Quality

^fBefore painting from 22nd of February 2016 at midnight to 23rd of February 2016 at 9:15

^gAfter painting from 26th of February at 11:30 to 27th of February 2016 at 23:56

^hLast day, i.e., 28th of February 2016

ⁱNot measured this week, since the instrument was moved to school 3 from 4th of March at 15:10 to 14th of March at 19:30

^jExcluding the data corresponding to the installation of the sampling lines in the classroom

ethylbenzene were all the time absent or below the detection limit; however, higher xylenes levels were recorded at the same specific period as an unplanned repainting of the ramp of the stairs leading to the floor, where the classroom was located. Concentrations of xylenes suddenly increased up to 59.5 and 41.4 ppb for m/p-xylenes and o-xylene respectively, and then slowly decreased from 59.5 ppb on February 26th at 11 a.m. to 27.5 ppb on February 27th and down to 15.6 ppb on February 28th. Finally, on February 29th at 6 a.m., the levels of xylenes were below the detection limit of the instrument or equal to zero. This may be related to the fact that at 6 a.m., the cleaning of the classroom was usually performed, maintaining the windows opened, and renewing the air inside the classroom. Toluene levels ranged between 0 and 3.2 ppb. The latter were recorded in the same period as xylenes, and they followed the same decreasing trend from February 26th until February 29th suggesting that the toluene may also be originated by the use of paints near the classroom. To support this observation, correlation analysis was performed between toluene and o-xylene concentration versus m/p-xylenes concentration. Correlation coefficients ranging between 0.62 and 0.97 indicate that all of them were emitted by the same source, i.e., paints application in this case.

Moreover, the increase of VOC concentration due to the use of paints has also been reported in other studies (Srivastava et al. 2000). To evaluate if the toluene concentrations before and after the painting were statistically different, *p* values using standard Student's test were calculated between the first week and the three groups of measurements conducted the second week. As expected, for the series of measurements performed in week 2 before the painting, there was no statistical difference with the concentrations measured during the first week ($p = 0.866$). On the contrary, *p* values calculated for the two next series of measurements obtained after the painting were lower than 0.0001 indicating that the painting strongly influenced toluene concentration in the investigated classroom.

In conclusion, the furniture equipping the classroom does not constitute a significant emission source of BTEX in S2; whereas, for S1, no certain conclusions could be made about the furniture emission since results were distorted by the unplanned painting. However, the absence of BTEX in S1 just after the installation of furniture, at the very beginning of week 2, can be considered as an indication of no significant emission from furniture.

Presence of occupants The results obtained during school occupation by students and teachers showed considerable variations of BTEX levels.

During the third week, when children followed the usual ventilation procedure, most of BTEX were detected at different levels in both schools, except benzene in S2, and ethylbenzene in S1. If we do not consider xylenes concentrations

recorded in S1 during the second week due to the paint emission, the values recorded during this third week were always higher than those found for weeks 1 and 2.

During the fourth week in S1, corresponding to ventilation according to the CO₂ level, benzene and toluene were detected in ranges 0–12.1 and 0–5.5 ppb respectively, although other BTEX were not present. All xylenes emitted during the paint episode were not detected from week 4 indicating the corresponding emissions were significantly reduced. Note that no measurements were conducted in S2 during week 4 because the instrument was moved to S3, the choice to move this instrument instead of the other installed in S1 being motivated by the presence of hazardous benzene level in S1.

During the fifth week in S1, corresponding to ventilation instructions given by the French OQAI, only benzene and toluene were found to be present similar to week 4 and varied in ranges 0–5.7 and 0–17.6, respectively. In S2, where they followed ventilation according to the CO₂ level, the BTEX concentrations were slightly lower than those found during week 3 suggesting that this ventilation mode could be more efficient.

Contrary to the results obtained by Verrielle et al. (2016) showing no significant difference in BTEX levels between absence and presence of occupants in schools, the BTEX concentrations measured in this work were higher, when the students and the teachers were present in both schools, except for all xylenes isomers in S1, whose elevated levels during week 2 were related to the fresh painting of the hallway nearby.

For both schools S1 and S2, Student's test was conducted between the BTEX concentrations measured in weeks 3, 4, and 5, where different ventilation scenarios were applied, week 3 being considered as the reference since the standard ventilation mode was used. The results will be presented below.

Benzene concentration time profiles

During this field campaign, benzene was only present in S1 which is close to the airport of La Rochelle and near to a busy road which may lead to high VOCs concentrations in the area, as suggested in other studies (Madhoun et al. 2011; Rad et al. 2014; Liu et al. 2016b). During the first and the second week when people were absent, benzene concentrations in both schools were zero or below the detection limit of our instruments (see Table 4) indicating that building construction materials and school furniture do not constitute an emission source of benzene.

During the 3 weeks of children occupation, benzene was not detected in S2. These results are in agreement with those encountered in other studies of air quality in schools, where benzene concentrations varied between 0.06 and 1 ppb (see Table 1), levels that are below the detection limit of our devices. In school 1, on the contrary to S2, benzene was always

present, but its concentration was not constant and varied between 0 and 12.1 ppb. Most of the time benzene concentration was below our detection limit of 1.1 ppb and then considered equal to zero but sometimes exhibited some maximum peaks in specific periods. In S1, benzene concentrations during week 5 were significantly different ($p < 0.001$) when compared to those of week 3, although this was not the case when compared data of weeks 3 and 4 ($p = 0.24$).

For example, Fig. 4 highlights benzene and CO₂ concentration time profiles inside the studied classroom in S1 during the fifth week. On March 15, a benzene peak up to almost 5 ppb can be clearly identified during the night. Other scattered values up to 6 ppb were recorded on March 16 and 17 around 12:00. It should be underlined that these upper values are higher than the threshold of 1.6 ppb set as an annual average value by the European Union.

Comparison of benzene concentrations and CO₂ levels shows that they are not correlated. Indeed, the main peak of benzene concentration was recorded on March 15, when CO₂ level decreased, indicating the window opening. Benzene started to disappear, when CO₂ concentration started to increase, once the windows are closed as shown in Fig. 4. This observation indicates that the main emission source of benzene was not related to the students' activities, but was more probably due to the road resurfacing work occurred in close proximity of school 1 in the same period. Despite the windows are closed during the night, an unusual event of great pollution influenced significantly the indoor air quality of the classroom. Nevertheless, the other scattered concentrations recorded on March 16 and 17 around 15:00 were correlated to CO₂ peaks indicating that this compound may be emitted inside the classroom by a non-continuous source such as related to students activities.

Toluene concentration time profiles

During the first 2 weeks, toluene was detected only in S1, and its concentrations ranged from 0 to 3.2 ppb showing that the building materials and maybe the furniture constitute an indoor emission source of toluene in this school. Both schools have similar characteristics except for the presence of a whiteboard in S1. This may constitute a source of toluene since markers release toluene as it was demonstrated in other studies (Liu et al. 2016; Madureira et al. 2015; Pegas et al. 2010). The ceiling was also different in both schools, but the ceiling plate of S1 is not known to be a source of toluene.

When occupants were present (weeks 3 to 5), toluene was present in both schools, unlike benzene, and its concentrations varied in ranges 0–29.5 and 0–3.5 ppb in Schools 1 and 2, respectively.

In S1, contrary to benzene, toluene concentration was found to be significantly different in week 4, where ventilation was done according to the CO₂ level ($p < 0.001$), when

compared to those of week 3 (standard ventilation); whereas, this was not the case when compared weeks 3 and 5 ($p = 0.77$). In S2, the difference was also significant ($p < 0.001$) between week 5 (ventilation based on CO₂ level) and week 3 (standard ventilation).

Concentration time profiles of toluene and CO₂ are presented in Fig. 5 for measurements performed in S1 during the fifth week (Fig. 5a) and in S2 during the third week (Fig. 5b). In S1, toluene concentrations ranged from 0 to 17.6 ppb during the fifth week (Fig. 5a). Similar to benzene during the same week as discussed above, most of the time toluene concentration was below our detection limit of 1.1 ppb and then considered equal to zero but sometimes exhibited some maximum peaks, more or less at the same time (around noon) every day from Monday 14th to Friday 18th.

Figure 5 shows that benzene and CO₂ concentration time profiles inside the studied classroom in S1 during the fifth week were strongly correlated. Indeed, the toluene concentration was low (2 to 4 ppb) or equal to zero when CO₂ levels were around 1000 ppm. Higher concentrations of toluene were recorded (8–17.6 ppb), when the levels of CO₂ were higher than 1500 ppm. The decrease of CO₂ level from 3500 ppm to less than 1000 ppm indicates that air inside the classroom was renewed, either by opening of windows and/or doors. Interestingly, the same observation was noted in School 2 on March 1st and 4th (see Fig. 5b). This obvious correlation tends to prove that toluene emission is related to students' activities such as arts and craft, or the use of glue and paints as it was noticed in other previous studies (Pegas et al. 2010; Madureira et al. 2015; Liu et al. 2016a).

In order to confirm if the variation of toluene levels is related to students' activities, the measured concentrations during the occupation condition in S1, i.e., the third, fourth, and fifth weeks were overlapped and presented in Fig. 6. This figure shows clearly that concentration time profiles of toluene over 3 weeks present a similar behavior from 1 week to another with maximum concentrations always recorded between 11:30 and 12:00. Such observation reinforces the idea that toluene emission is directly related to students' activities. Furthermore, in both schools, toluene levels were lower during the week, where the CO₂ indicator was used, following the same trend as CO₂ concentration. As it was discussed above, the use of this device may limit the confinement of the classroom and may be also a way to reduce the presence of pollutants issued from an internal source.

Ethylbenzene and xylenes concentration time profiles

In school 1, ethylbenzene was never detected. Except during and after the paint event (weeks 2 and 3), xylenes were also absent in S1. Indeed, once the painting was finished and classroom was ventilated, their concentrations decrease to reach

zero in the beginning of the third week, and they were totally absent in the last 2 weeks.

In S2, the presence of ethylbenzene and xylenes was limited to few days. Their concentrations varied between 0 and 10 ppb and from 0 to 4 ppb for xylenes and ethylbenzene, respectively. In S2, for ethylbenzene and m/p-xylenes, the difference was significant ($p < 0.001$, Student's test) between week 5 (ventilation according to CO₂ level) and week 3 used as reference (standard ventilation).

Figure 7 represents the variations of ethylbenzene and xylenes concentrations obtained in school 2 during the third week, i.e., 29th of February to 5th of March. Figure 7 highlights that both compounds were rarely detected in the investigated classroom and that increase of their concentrations were not correlated to high-CO₂ levels. Indeed, Fig. 7a shows an increase of ethylbenzene concentration from 2 to 4.5 ppb, when CO₂ level decreases from 3500 to 1000 ppm, and then, its concentration decreases from its maximum to reach its initial value around 1.5 ppb and at the same time, the CO₂ level increases from 1000 ppm to 2500 ppm. Similar behavior was observed with m/p-xylenes, where its concentration increases from 2 to 10 ppb, when CO₂ level decreases from 2700 to 1000 ppm, and then, the m/p-xylenes concentration decreases from its maximum to reach 1.5 ppb, when CO₂ level increases and reaches 2500 ppm as shown in Fig. 7b. These two concentration time profiles indicate clearly that ethylbenzene and xylenes were only present when CO₂ levels decrease, which is related to air exchange inside the classroom by opening of windows and/or doors. This behavior suggests that the main emission source is located outside the investigated classroom in S2 and more probably outdoor.

Comparison with literature data

Benzene Indoor benzene with a maximum level of 12.7 ppb measured in this study is higher than those reported in most of the previous studies of air quality in schools (see Table 1).

As mentioned in “Benzene concentration time profiles,” outdoor air pollution can influence significantly the indoor air quality of the classroom. It was the case in school 1 on March 15th, where benzene peak up to almost 5 ppb was recorded during the night. This observation is consistent with other studies, where benzene concentration in indoor air depends strongly of outdoor concentration (Godoi et al. 2013; Guo et al. 2003). High levels of benzene were measured in a recent study carried out in eight well-ventilated high schools in Johor Bahru, Malaysia (Norbäck et al. 2017). In this study, where the windows of the studied classrooms were always opened, the average concentration of benzene found in indoor air was 2.3 ppb, the same concentration was measured in outdoor air, and the maximum measured indoor was 9.9 ppb. The I/O ratio of benzene was equal to 0.93, indicating

that the main benzene source was the external environment as suggested in our present study.

Similar to schools, the ratio I/O for benzene was often below one for other indoor environments (see Table 5), indicating that the main source is frequently the outdoor environment. Consequently, indoor benzene concentrations followed similar trends as the outdoor levels. This observation can be noticed in several recent studies (Bari et al. 2015; Madureira et al. 2016; Romagnoli et al. 2016; Hazrati et al. 2016; Yurdakul et al. 2017; Zhong et al. 2017; Marzocca et al. 2017).

Toluene If we do not consider the high concentrations recorded during the second week in S1 and generated by the fresh paint applied to the steps ramp, toluene was the major benzene derivative found in the investigated classroom of school 1. This is consistent with most of school measurements reported in the literature (see Table 1) (Guo et al. 2003; Godwin and Batterman 2007; Stranger et al. 2007; Phatrabuddha 2013; Godoi et al. 2013; Nasreddine et al. 2016; Romagnoli et al. 2016; Verrielle et al. 2016; Yurdakul et al. 2017; Zhong et al. 2017) and with results obtained in other type of indoor environments (see Table 5) such as residential buildings (Bari et al. 2015; Romagnoli et al. 2016; Hazrati et al. 2016).

Similar to benzene, indoor toluene with a maximum level of 29.5 ppb measured in this study is higher than those reported in most of the previous studies of air quality in schools (see Table 1). However, toluene concentration was lower than the values ranging between 0 and 106.3 ppb found in other indoor environments such as universities (Can et al. 2015; Yurdakul et al. 2017), or urban and rural dwellings (Liu et al. 2015; Bari et al. 2015).

Most of studies indicate that main sources of toluene are indoor ones (Ilgen et al. 2001; Kotzias et al. 2009). For example, Can et al. (2015) reported toluene concentrations close to 80 ppb in the Faculty of Fine Arts of Anadolu University due to the use of oil-based paintings, varnish, and adhesives related to art activities. As mentioned in “Toluene concentration time profiles,” toluene emission was found to be related to people's activities such as arts and craft, or the use of glue or paints as it was noticed in other previous studies (Pegas et al. 2010; Madureira et al. 2015; Liu et al. 2016a). In addition, in dwellings, toluene can be present at high concentrations varying between 0.10 and 99.79 ppb, but the sources are typically household products, combustion processes, or wall coverings (Bari et al. 2015).

Ethylbenzene and xylenes For ethylbenzene and xylenes, our results are consistent with those obtained by previous studies reported in Table 1, excepting those found for xylenes in several studies (Madureira et al. 2016; Canha et al. 2016; Norbäck et al. 2017). Norbäck et al. (2017) have reported very high levels of xylenes, reaching 118 ppb for the three isomers which may be explained by the infiltration of outdoor air. In

Fig. 4 Benzene and CO₂ variation in school 1 during week 5 of the campaign

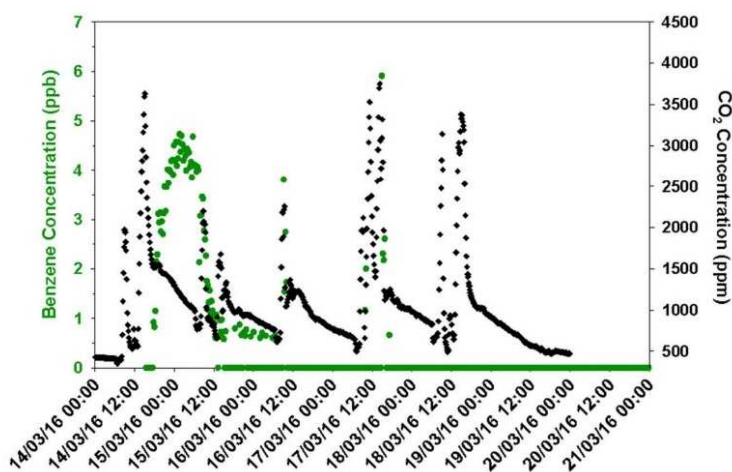


Fig. 5 Toluene and CO₂ variations in studied classrooms during occupation in school 1 during fifth week (a) and in school 2 during the third week (b)

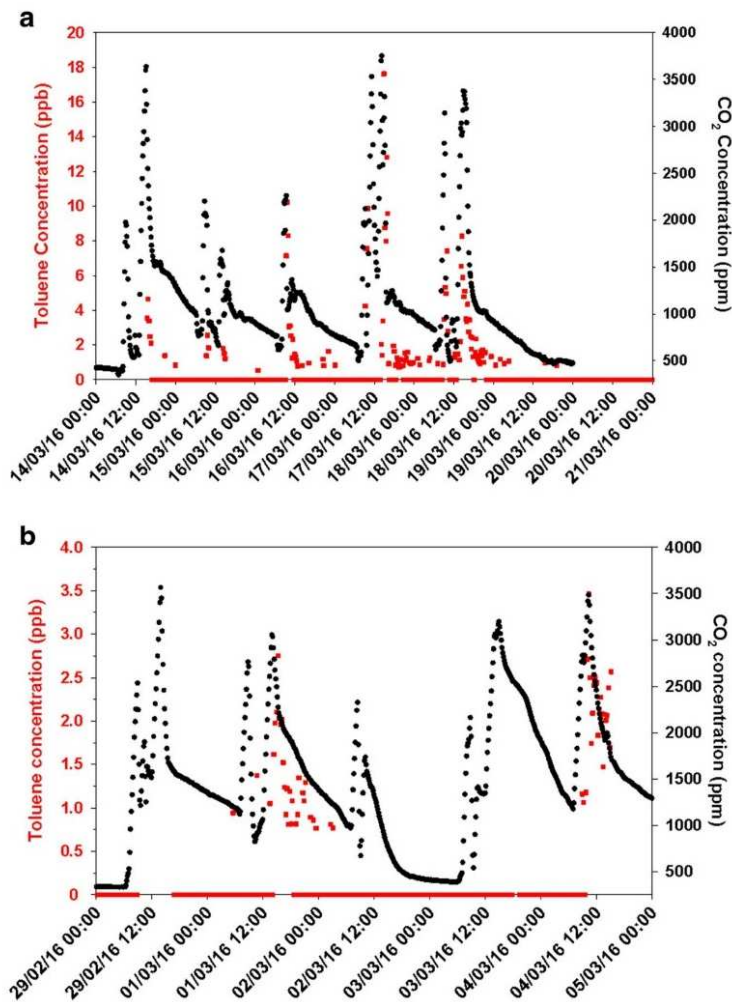


Fig. 6 Overlapping of Toluene concentrations over three occupation weeks obtained with the pre-industrial device (♦) third week (•) fourth week (x) fifth week in school 1

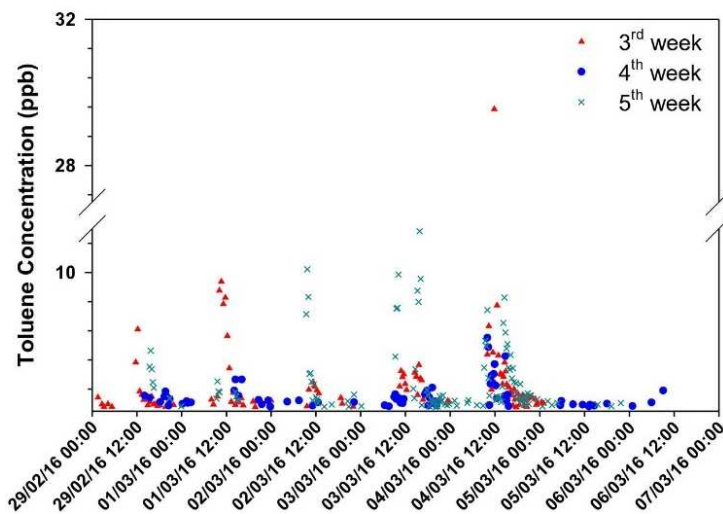


Fig. 7 Variations of ethylbenzene (a) and m/p-xylenes (b) obtained in school 2 during the third week. Both obtained concentrations were correlated to CO₂ levels measured at the same time in the investigated classroom

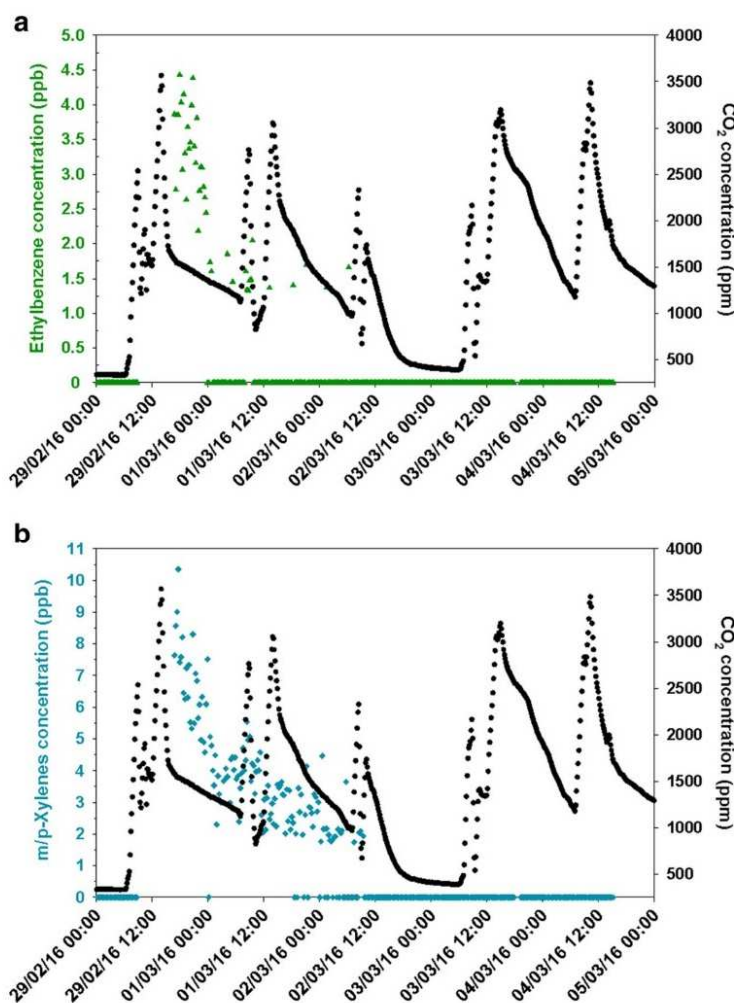


Table 5 BTEX concentrations ranges measured indoor and outdoor of various environments

Reference	Location	Concentration (ppb)															
		Benzene		Toluene		Ethylbenzene		Xylenes isomers		Benzene		Toluene		Ethylbenzene		Xylenes isomers	
		In	Out	In	Out	In	Out	In	Out	In	Out	In	Out	In	Out	In	Out
Zhong et al. 2017	37 Elementary schools USA (2015–2016) ^a	0–1.37	0–0.66	0–22.19	0–1.85	0–0.46	0–0.21	0–0.21	0–1.13								
Marzocca et al. 2017	Primary school near to an industrial area in Toronto City, Italy (2017) ^a	0.13–0.26	0.18–0.26	0.34–0.46	0.41–0.49	0.11–0.27	0.08–0.28	0.20–0.82	0.27–0.81								
Hazrati et al. 2016	50 Residential buildings in Iran (2016) ^b	0–4.85	0–2.77	0–18.18	0–10.58	0–2.73	0–1.11	0–10.87	0–1.68								
Madureira et al. 2016	20 Public primary schools in Portugal (2011–2013) ^a	0.48–0.86	0.51–0.90	0.48–53.62	0.32–2.75	n. m.	n. m.	0.53–95.98	0.5–8.54								
Bari et al. 2015	26 Homes in Canada during winter (2010) ^b	0.12–3.07	0.82–1.19	0.10–99.79	0.01–16.68	0.04–124.85	0–33.24	0.05–354.43	0–112.18								
Yurdakul et al., 2017	University building in Turkey (2016) ^a	0.34–8.91	0.23–4.63	2.61–106.3	1.45–23.18	0–3.84	0.01–0.59	0.88–28.72	0.61–2.67								
Romagnoli et al. 2016	Rome, Italy (2013) ^a	0–0.45	0–0.43	0–1.22	0–1.31	0–0.20	0–0.15	0–0.89	0–0.85								
	Coffee bar	0–0.28	0–0.33	0–0.86	0–0.77	0–0.13	0–0.11	0–0.69	0–0.52								
	Primary school	0–0.76	0–0.34	0–1.28	0–0.77	0–0.17	0–0.12	0–0.89	0–0.51								
	Dwelling near to a busy road	3.37–27.71	2.06–21.52	3.42–48.75	1.69–21.21	1.24–24.32	1.10–9.49	5.01–53.30	1.84–22.78								
Liu et al. 2015	A farmer house in China (2013) ^b	0–0.46	0–0.48	0–78.76	0–0.95	0–3.33	0–0.04	0–8.98	0–0.14								
Can et al. 2015	Faculty of Fine Arts Turkey (2012) ^a	0–0.78	0–0.48	0–39.70	0–0.95	0–1.36	0–0.04	0–0.36	0–0.14								
	Painting workshop																
	Office																

Type of sampling: ^a Passive and ^b Active

fact, during the study, the windows of the investigated classroom were always opened, in addition to the presence of high levels of xylenes outdoors. Results for m/p-xylenes concentrations found by Canha et al. (2016) and Madureira et al. (2016) ranged between 0.27–82.56 and 0–95.98, respectively, did not agree with our results. This difference can be due to the presence of additional internal sources of xylenes, since an I/O ratio of 1.25 and 1.8, respectively by Madureira and Canha was determined.

Conclusion

In this study, our pre-industrial portable devices were able to detect all BTEX compounds in both primary school classrooms. The devices provided measurements at the same temporal variations of 10 min, while working continuously for five consecutive weeks. The simultaneous continuous monitoring of CO₂ level was found to be very useful to indicate if the windows were open or closed in presence of students. The comparison between CO₂ and BTEX concentrations permits us to highlight correlation or anti-correlation, which was proven very helpful to identify the origin of their main emission source, whether it was internal or external.

All BTEX were present in the investigated classrooms at different levels excepting in the kindergarten, where all BTEX levels were lower than the detection limit of the device. Benzene was only present in S1, where its concentration reached up 6 ppb, which is almost four times higher than the threshold value fixed by the European Union. The comparison with the CO₂ measurements showed that its main emission source is the outdoor environment. The same conclusion was obtained for ethylbenzene and xylenes, which were rarely present in both schools, and their concentrations were limited to few tens of ppb. However, toluene was the most abundant compound in both schools, and its concentrations were very variable. The higher measured toluene concentration was 30 ppb. In addition, its comparison with CO₂ levels measured in both schools has shown a clear correlation indicating that it was emitted inside the classroom. More precisely, our real-time measurements contrary to traditional passive sampling on Radiello cartridges allowed us to observe the repetitive patterns in toluene temporal variation related to students' activities.

This study showed that naturally ventilated schools present high-confinement index as shown the CO₂ measurements, where its concentration reached 3500 ppm, when windows and doors are closed. This high value of CO₂ could have side effects on occupants' health. During the occupation period over 3 weeks, CO₂ concentration was lower in both schools during the week, where the CO₂ indicator was used, indicating that this device may be an efficient method to limit the confinement of the classroom. In addition, the external

environment of the school presents a significant effect on indoor air quality. On the one hand, opening of windows or doors could dramatically decrease the CO₂ level, improving afterwards the air quality by reducing the confinement. On the other hand, the outdoor air may constitute an additional source of pollutants, as in the case for benzene, ethylbenzene, and xylenes leading to degrade further the indoor air quality.

This field campaign showed the significance of a portable device able to provide in situ answers in near real-time. Our devices were able to detect the BTEX temporal variations in two schools in different occupation conditions and during the presence of students and teachers. We succeed to detect every single variation and determine how the BTEX concentrations varied during school days as well as to identify exactly when higher concentrations of BTEX are emitted, which allow us to determine the origin of their sources. This result could not be obtained with classical methods because of the sampling duration. In the case of schools occupied by children, the comparison and correlations with CO₂ real-time monitoring were found to be an alternative solution to the widely used quantification of indoor/outdoor air ratio for a given pollutant, in order to determine its origin, i.e., indoor or outdoor one.

Acknowledgments This work has been conducted in the framework of Impact'Air project financially supported by ADEME (Agence De l'Environnement et de la Maîtrise de l'Energie), the city of La Rochelle, and the Ligue contre le cancer.

References

- Alves C, Duarte M, Ferreira M, Alves A, Almeida A, Cunha Â (2016) Air quality in a school with dampness and mould problems. *Air Qual Atmosphere Health* 9:107–115. <https://doi.org/10.1007/s11869-015-0319-6>
- Apte MG, Fisk WJ, Daisey JM (2000) Associations between indoor CO₂ concentrations and sick building syndrome symptoms in U.S. office buildings: an analysis of the 1994–1996 BASE study data. *Indoor Air* 10:246–257. <https://doi.org/10.1034/j.1600-0668.2000.010004246.x>
- Arif AA, Shah SM (2007) Association between personal exposure to volatile organic compounds and asthma among US adult population. *Int Arch Occup Environ Health* 80:711–719. <https://doi.org/10.1007/s00420-007-0183-2>
- Bari MA, Kindziarski WB, Wheeler AJ, Héroux M-È, Wallace LA (2015) Source apportionment of indoor and outdoor volatile organic compounds at homes in Edmonton, Canada. *Build Environ* 90:114–124. <https://doi.org/10.1016/j.buildenv.2015.03.023>
- Buka I, Koranteng S, Osornio-Vargas AR (2006) The effects of air pollution on the health of children. *Paediatr Child Health* 11:513–516
- Can E, Özden Üzmez Ö, Döğeroğlu T, Gaga EO (2015) Indoor air quality assessment in painting and printmaking department of a fine arts faculty building. *Atmospheric Pollut Res* 6:1035–1045. <https://doi.org/10.1016/j.apr.2015.05.008>
- Canha N, Mandin C, Ramalho O, Wyart G, Ribéron J, Dassonville C, Hänninen O, Almeida SM, Derbez M (2016) Assessment of ventilation and indoor air pollutants in nursery and elementary schools in France. *Indoor Air* 26:350–365. <https://doi.org/10.1111/ina.12222>
- Daisey JM, Angell WJ, Apte MG (2003) Indoor air quality, ventilation and health symptoms in schools: an analysis of existing information. *Indoor Air* 13:53–64. <https://doi.org/10.1034/j.1600-0668.2003.00153.x>
- Geiss O, Giannopoulos G, Tirendi S, Barrero-Moreno J, Larsen BR, Kotzias D (2011) The AIRMEX study - VOC measurements in public buildings and schools/kindergartens in eleven European cities: statistical analysis of the data. *Atmos Environ* 45:3676–3684. <https://doi.org/10.1016/j.atmosenv.2011.04.037>
- Godoi RHM, Godoi AFL, Gonçalves Junior SJ, Paralovo SL, Borillo GC, Gonçalves Gregório Barbosa C, Arantes MG, Charello RC, Rosário Filho NA, Grassi MT, Yamamoto CI, Potgieter-Vermaak S, Rotondo GG, De Wael K, van Grieken R (2013) Healthy environment — indoor air quality of Brazilian elementary schools nearby petrochemical industry. *Sci Total Environ* 463–464:639–646. <https://doi.org/10.1016/j.scitotenv.2013.06.043>
- Godwin C, Batterman S (2007) Indoor air quality in Michigan schools. *Indoor Air* 17:109–121. <https://doi.org/10.1111/j.1600-0668.2006.00459.x>
- Griffiths M, Eftekhari M (2008) Control of CO₂ in a naturally ventilated classroom. *Energy Build* 40:556–560. <https://doi.org/10.1016/j.enbuild.2007.04.013>
- Guo H, Lee SC, Li WM, Cao JJ (2003) Source characterization of BTEX in indoor microenvironments in Hong Kong. *Atmos Environ* 37:73–82. [https://doi.org/10.1016/S1352-2310\(02\)00724-0](https://doi.org/10.1016/S1352-2310(02)00724-0)
- Hänninen O, Canha N, Kulinkina AV, Dume I, Deliu A, Mataj E, Lusati A, Krzyzanowski M, Egorov AI (2017) Analysis of CO₂ monitoring data demonstrates poor ventilation rates in Albanian schools during the cold season. *Air Qual Atmos Health* 10:773–782. <https://doi.org/10.1007/s11869-017-0469-9>
- Hazrati S, Rostami R, Farjaminezhad M, Fazlzadeh M (2016) Preliminary assessment of BTEX concentrations in indoor air of residential buildings and atmospheric ambient air in Ardabil, Iran. *Atmos Environ* 132:91–97. <https://doi.org/10.1016/j.atmosenv.2016.02.042>
- Ilgén E, Karfich N, Levsen K, Angerer J, Schneider P, Heinrich J, Wichmann H-E, Dunemann L, Begerow J (2001) Aromatic hydrocarbons in the atmospheric environment: part I. Indoor versus outdoor sources, the influence of traffic. *Atmos Environ* 35:1235–1252. [https://doi.org/10.1016/S1352-2310\(00\)00388-5](https://doi.org/10.1016/S1352-2310(00)00388-5)
- Kotzias D, Geiss O, Tirendi S, Barrero J, Reina V, Gotti A, Cimino Reale G, Marafante E, Sarigiannis D, Casati B (2009) Exposure to multiple air contaminants in public buildings, schools and kindergartens - the European indoor air monitoring and exposure assessment (AIRMEX) study. *Fresenius Environ Bull* 18:670–681
- Liu K, Zhang C, Cheng Y, Liu C, Zhang H, Zhang G, Sun X, Mu Y (2015) Serious BTEX pollution in rural area of the North China Plain during winter season. *J Environ Sci* 30:186–190. <https://doi.org/10.1016/j.jes.2014.05.056>
- Liu S, Li R, Wild RJ, Warneke C, de Gouw JA, Brown SS, Miller SL, Luongo JC, Jimenez JL, Ziemann PJ (2016a) Contribution of human-related sources to indoor volatile organic compounds in a university classroom. *Indoor Air* 26:925–938. <https://doi.org/10.1111/ina.12272>
- Liu Z, Li N, Wang N (2016b) Characterization and source identification of ambient VOCs in Jinan, China. *Air Qual Atmos Health* 9:285–291. <https://doi.org/10.1007/s11869-015-0339-2>
- Madhoun WAA, Ramli NA, Yahaya AS, Yusuf NFFM, Ghazali NA, Sansuddin N (2011) Levels of benzene concentrations emitted from motor vehicles in various sites in Nibong Tebal, Malaysia. *Air Qual Atmos Health* 4:103–109. <https://doi.org/10.1007/s11869-010-0083-6>
- Madureira J, Paciência I, Rufo J, Ramos E, Barros H, Teixeira JP, de Oliveira FE (2015) Indoor air quality in schools and its relationship with children's respiratory symptoms. *Atmos Environ* 118:145–156. <https://doi.org/10.1016/j.atmosenv.2015.07.028>

- Madureira J, Paciência I, Rufo J, Severo M, Ramos E, Barros H, de Oliveira FE (2016) Source apportionment of CO₂, PM₁₀ and VOCs levels and health risk assessment in naturally ventilated primary schools in Porto, Portugal. *Build Environ* 96:198–205. <https://doi.org/10.1016/j.buildenv.2015.11.031>
- Marzocca A, Di Gilio A, Farella G, Giua R, de Gennaro G (2017) Indoor air quality assessment and study of different VOC contributions within a school in Taranto City, south of Italy. *Environments* 4:23. <https://doi.org/10.3390/environments4010023>
- Mendell MJ, Heath GA (2005) Do indoor pollutants and thermal conditions in schools influence student performance? A critical review of the literature. *Indoor Air* 15:27–52. <https://doi.org/10.1111/j.1600-0668.2004.00320.x>
- Muscatiello N, McCarthy A, Kiel C, Hsu W-H, Hwang S-A, Lin S (2015) Classroom conditions and CO₂ concentrations and teacher health symptom reporting in 10 New York State Schools. *Indoor Air* 25:157–167. <https://doi.org/10.1111/ina.12136>
- Nasreddine R, Person V, Serra CA, Le Calvé S (2015) Development of a novel portable miniaturized GC for near real-time low level detection of BTEX. *Sens Actuators B Chem* 224:159–169. <https://doi.org/10.1016/j.snb.2015.09.077>
- Nasreddine R, Person V, Serra CA, Schoemaeker C, Le Calvé S (2016) Portable novel micro-device for BTEX real-time monitoring: assessment during a field campaign in a low consumption energy junior high school classroom. *Atmos Environ* 126:211–217. <https://doi.org/10.1016/j.atmosenv.2015.11.005>
- Norbäck D, Hashim JH, Hashim Z, Ali F (2017) Volatile organic compounds (VOC), formaldehyde and nitrogen dioxide (NO₂) in schools in Johor Bahru, Malaysia: associations with rhinitis, ocular, throat and dermal symptoms, headache and fatigue. *Sci Total Environ* 592:153–160. <https://doi.org/10.1016/j.scitotenv.2017.02.215>
- Pegas PN, Evtugina MG, Alves CA, Nunes T, Cerqueira M, Franchi M, Pio C, Almeida SM, Freitas M, Do C (2010) Outdoor/indoor air quality in primary schools in Lisbon: a preliminary study. *Quím Nova* 33:1145–1149. <https://doi.org/10.1590/S0100-40422010000500027>
- Pegas PN, Alves CA, Evtugina MG, et al (2011) Indoor air quality in elementary schools of Lisbon in spring. *Environ Geochem Health* 33:455–468. <https://doi.org/10.1007/s10653-010-9345-3>
- Phatrabuddha N (2013) Ambient and personal exposure levels of BTEX among school children residing near the oil refineries in Chonburi Province. *Appl Environ Res* 35:57–73
- Rad HD, Babaei AA, Goudarzi G, Angali KA, Ramezani Z, Mohammadi MM (2014) Levels and sources of BTEX in ambient air of Ahvaz metropolitan city. *Air Qual Atmos Health* 7:515–524. <https://doi.org/10.1007/s11869-014-0254-y>
- Romagnoli P, Balducci C, Perilli M, Vichi F, Imperiali A, Cecinato A (2016) Indoor air quality at life and work environments in Rome, Italy. *Environ Sci Pollut Res Int* 23:3503–3516. <https://doi.org/10.1007/s11356-015-5558-4>
- Satish U, Mendell MJ, Shekhar K, Hotchi T, Sullivan D, Streufert S, Fisk WJ (2012) Is CO₂ an indoor pollutant? Direct effects of low-to-moderate CO₂ concentrations on human decision-making performance. *Environ Health Perspect* 120:1671–1677. <https://doi.org/10.1289/ehp.1104789>
- Simoni M, Annesi-Maesano I, Sigsgaard T, Norback D, Wieslander G, Nystad W, Canciani M, Sestini P, Viegi G (2010) School air quality related to dry cough, rhinitis and nasal patency in children. *Eur Respir J* 35:742–749. <https://doi.org/10.1183/09031936.00016309>
- Srivastava PK, Pandit GG, Sharma S, Mohan Rao AM (2000) Volatile organic compounds in indoor environments in Mumbai, India. *Sci Total Environ* 255:161–168. [https://doi.org/10.1016/S0048-9697\(00\)00465-4](https://doi.org/10.1016/S0048-9697(00)00465-4)
- Stranger M, Potgieter-Vermaak SS, Van Grieken R (2007) Comparative overview of indoor air quality in Antwerp, Belgium. *Environ Int* 33:789–797. <https://doi.org/10.1016/j.envint.2007.02.014>
- Turanjanin V, Vučićević B, Jovanović M, Mirkov N, Lazović I (2014) Indoor CO₂ measurements in Serbian schools and ventilation rate calculation. *Energy* 77:290–296
- Twardella D, Matzen W, Lahrz T, Burghardt R, Spiegel H, Hendrowarsito L, Frenzel AC, Fromme H (2012) Effect of classroom air quality on students' concentration: results of a cluster-randomized cross-over experimental study. *Indoor Air* 22:378–387. <https://doi.org/10.1111/j.1600-0668.2012.00774.x>
- Verrielle M, Schoemaeker C, Hanoune B, Leclerc N, Germain S, Gaudion V, Locoge N (2016) The MERMAID study: indoor and outdoor average pollutant concentrations in 10 low-energy school buildings in France. *Indoor Air* 26:702–713. <https://doi.org/10.1111/ina.12258>
- Yurdakul S, Civan M, Özden Ö, Gaga E, Döğeroğlu T, Tuncel G (2017) Spatial variation of VOCs and inorganic pollutants in a university building. *Atmos Pollut Res* 8:1–12. <https://doi.org/10.1016/j.apr.2016.07.001>
- Zhong L, Su F-C, Batterman S (2017) Volatile organic compounds (VOCs) in conventional and high performance school buildings in the U.S. *Int J Environ Res Public Health* 14:100. <https://doi.org/10.3390/ijerph14010100>

3.3 Conclusions

This chapter presents a field campaign of indoor air quality conducted in two French primary schools where BTEX concentrations were continuously monitored by using portable pre-industrial prototypes for 5 weeks. Various scenarios of occupation and ventilation were studied to determine the potential pollutant sources and to evaluate the efficiency of the different ventilation methods.

The near-real time measurements performed with GC prototypes allowed to record temporal variation of BTEX levels during the 5 weeks. CO₂ levels were simultaneously monitored during the field campaign and they were used as a ventilation indicator. The comparison between CO₂ and BTEX concentrations allowed us to identify the origin of their main emission source, whether it was internal or external. All the BTEX were present in the investigated classrooms at different levels excepting in the kindergarten, where all BTEX levels were lower than the detection limit of the device. Among BTEX, toluene was the most abundant compound in both schools. Its concentration was strongly correlated to CO₂ concentration suggesting that the main emission source was internal. Furthermore, repetitive patterns were observed during the last three weeks indicating that these high levels were related to children activities.

This study highlights the importance of near-real time measurements compared to traditional passive sampling. Indeed, this type of measurements provides high temporal resolution enabling to identify the specific periods of time where a rise in BTEX concentrations is produced and thus identify the potential pollution sources. It has been demonstrated that the comparison and correlations of BTEX and CO₂ concentrations were very useful to determine the origin of such sources.

In conclusion, our compact highly portable GC has shown its ability to monitor BTEX continuously over long periods of time and to record small changes in its concentration related to children activities or ventilation, which is not possible with classical passive sampling methods. Nevertheless, a more sensitive instrument is needed to quantify benzene concentrations lower than 1 ppb as established by the recent French IAQ legislation. In this regard, the development and integration of a preconcentration unit has been performed to address this issue and is detailed in chapter 4.

References

- [1] M. J. Mendell and G. A. Heath, "Do indoor pollutants and thermal conditions in schools influence student performance? A critical review of the literature," *Indoor Air*, vol. 15, no. 1, pp. 27–52, Jan. 2005.
- [2] J. M. Daisey, W. J. Angell, and M. G. Apte, "Indoor air quality, ventilation and health symptoms in schools: an analysis of existing information," *Indoor Air*, vol. 13, no. 1, pp. 53–64, Mar. 2003.
- [3] M. P. Tsakas, A. P. Siskos, and P. Siskos, "Indoor Air Pollutants and the Impact on Human Health," *Chemistry, Emission Control, Radioactive Pollution and Indoor Air Quality*, Jul. 2011.

Chapter 4. Development of a preconcentrator for BTEX quantification

One of the main objectives of this research work was the development of a preconcentrator to increase the sensitivity of the GC prototype presented in chapter 2 in section 2.2.1. The new version of the GC prototype should improve significantly its sensitivity and exhibit a detection limit lower than 0.6 ppb for benzene, to meet with the new French legislation concerning indoor air quality in public buildings. Furthermore, it must maintain similar features of the previous GC prototype concerning:

- Energy consumption: the increase in the energy consumption due to the integration of the preconcentrator (PC) should be limited since the overall GC system should be battery powered;
- Analysis time: addition of a preconcentration step should not significantly increase the total analysis time.

In this chapter, the microfluidic-based preconcentrators prototypes presented in chapter 2 section 2.2.2 are evaluated in terms of temperature increase and BTEX preconcentration performance and the obtained results are discussed. The methodology followed to determine the optimal operating conditions is also described. Finally, the performances of the different developed preconcentration units are compared with those available in the literature and discussed in terms of advantages and drawbacks.

4.1 Macro Aluminium Preconcentrator (MAP)

MAP was the first version of the preconcentrator. This version allows to understand how complex it is to design an analytical device due to the problems encountered during the development and testing of this prototype.

4.1.1 Leakage test

The first test was always related to the leakage. To this purpose, leakage was tested in adsorption and desorption conditions using the setup presented in Figure 4-1. In Figure 4-1a, controlled flow rates between 5 and 20 NmL/min were flowing through the preconcentrator (red line) to simulate the flow rates that could be employed during adsorption. The mass flow controller (MFC) setpoint was compared to the reading of the reference flow meter placed at the exhaust. Once the absence of leakage

was checked in these conditions, desorption conditions were tested. For this purpose, the six-port valve was switched and the PC was then connected to the GC column and subjected to a pressure of 4 bar (see Figure 4-1b, blue line). The flow rate was measured after the PID and should be the same as when the carrier gas is directly connected to the GC column (i.e. ~ 2.5 NmL/min). The PC was then heated up to desorption temperature (~ 200 °C) and cooled down to the room temperature, the leakage being evaluated according to the above-mentioned procedure after the adsorption/desorption cycle where the PC was under pressure at high temperature. This procedure was followed for each PC prototype. If no leakage was observed in these conditions, characterization of the temperature ramp and preconcentration tests were then conducted.

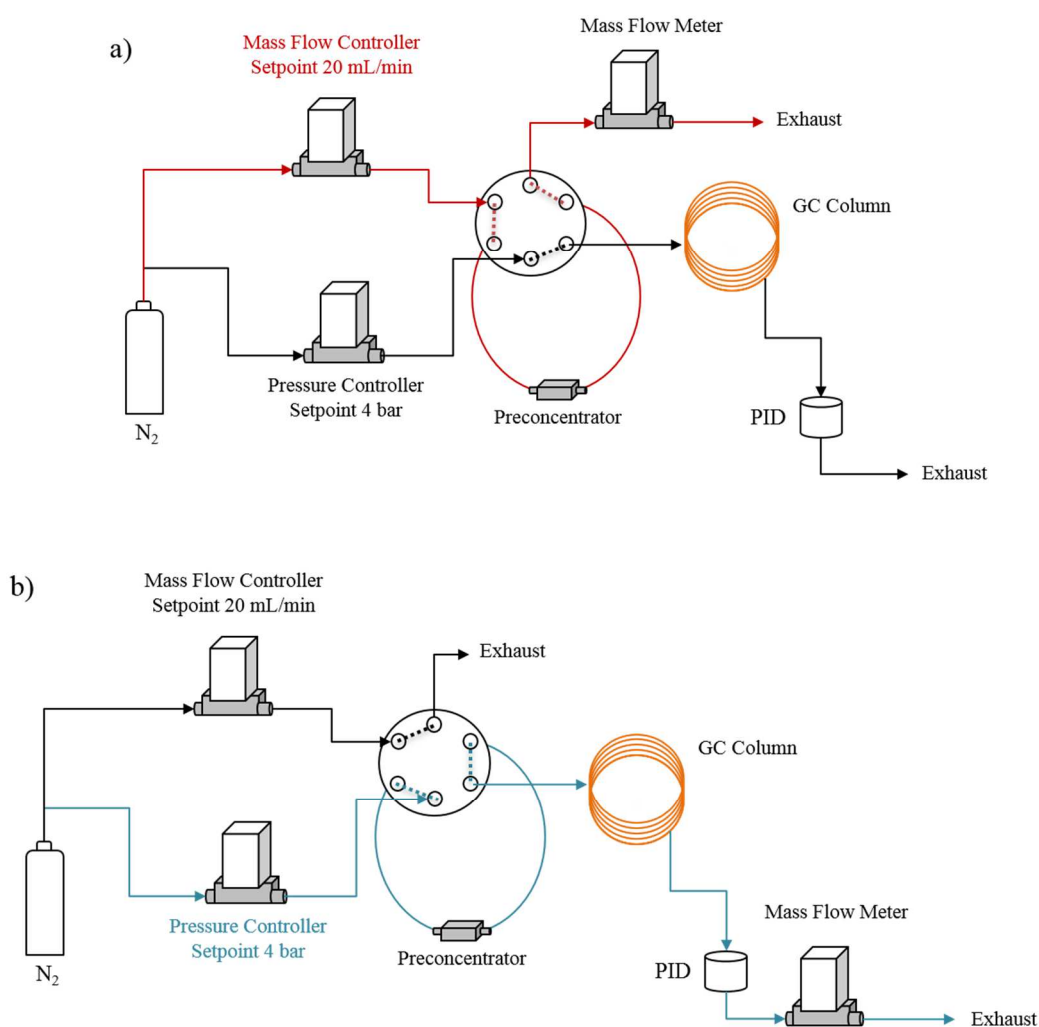


Figure 4-1. Setup employed in PC gas leakage testing simulating adsorption (a) and desorption (b) operating modes

The described procedure for leakage testing was followed with MAP. During the test in adsorption mode, no flow was observed at the exhaust suggesting that the gas flow was blocked somewhere. In desorption mode, there was no flow after the detector and an increase in the pressure up to 5.5 bar was noticed in the pressure controller that was set at 4 bar, indicating that something was blocking the air flow. After checking the fluidic connections, an error in the design of the PC was observed, the depth of the screw holes was not enough and the thread of the connector exceeded the screw hole, causing the blocking of the air flow as shown in Figure 4-2. The solution was to not completely tighten the screw to avoid the blocking of the air passage, add some Teflon tape around the thread and some epoxy resin around the connector to seal the connection and prevent any leakage. After this, the device was tested in the aforementioned conditions and no more leakage was observed.

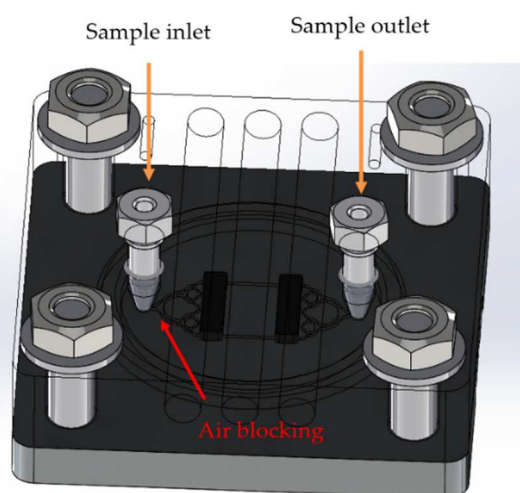


Figure 4-2. Blocking of air passage in MAP due to a design error. To visualize the inner part of MAP, the top part was shown as transparent

4.1.2 Temperature tests

The heating performance of a PC is a critical factor in analyte quantification since it plays a key role on the peak resolution. If the temperature ramp during the desorption is very slow, indeed, the resulting chromatographic peaks will be large promoting the coelution of some of them. On the contrary, an efficient heating system provides a fast desorption of the analytes resulting in sharp and well-defined chromatographic peaks. In MAP, the heating system consisted of three heating cartridges (Watlow, St. Louis, MO, USA) of 70 W each controlled by a PID controller (CAL Controls, UK) and the temperature was measured with a type K thermocouple (RS Components SAS, France).

The temperature ramp obtained using this heating system with a nominal voltage supply of 24 V and a current of 14.7 A is displayed in Figure 4-3. As it can be observed, 250 °C were reached in 90 s. Taking as a reference the desorption temperature of BTEX from Carbopack® B, which is usually between 200 and 250 °C [1], the minimum time to reach this temperature was 70 s and, thus, the injection time should be at least 70 s.

Another vital issue for the preconcentrator development is the cooling time, i.e. the time needed to return to the adsorption temperature. After desorption, temperature should drop rapidly to reach the room temperature before initiating the sampling of the next analysis. Since BTEX analysis is conducted every 10 min, ideally, the time needed to reach room temperature should not exceed 5 min. In this way, the sampling of the next analysis could start when the separation of the first analysis is still in progress and the gaseous sample injection could be performed right after the end of the first analysis.

Initially, the time to reach room temperature from 200°C by natural convection cooling was measured. As it is observed in Figure 4-4, this device required 30 min to return to the room temperature due to its relative high mass of 54.9 g and thermal inertia. This time is even longer than the total analysis time and, therefore, was not compatible with near real-time measurements. In consequence, a total of three fans were added in order to accelerate the device cooling. This change produced a considerable improvement in the cooling rate and the cooling was achieved in less than 6 min instead of 30 min.

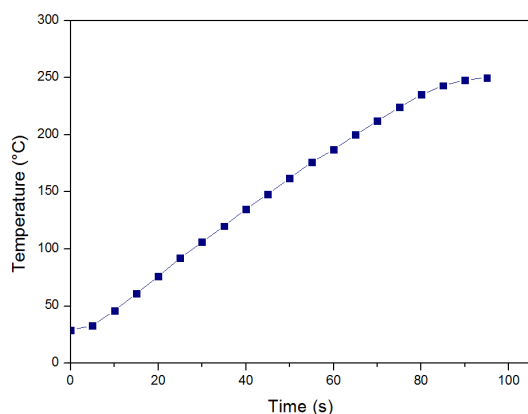


Figure 4-3. Temperature ramp obtained in MAP with a voltage supply of 24 V and a current of 3 A

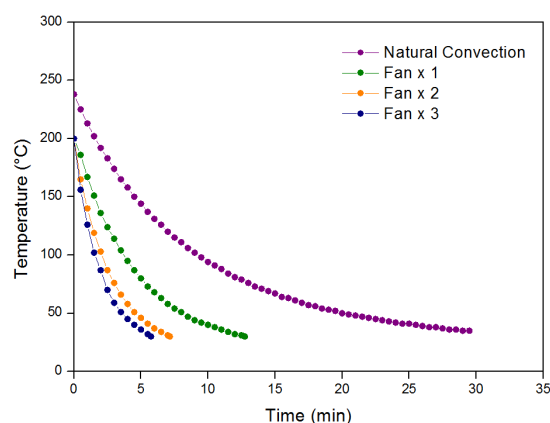


Figure 4-4. Device cooling by natural convection cooling (purple), one fan (green), two fans (orange) and three fans (blue)

Once heating and cooling procedures were validated, MAP preconcentration performance was investigated by using three different adsorbents.

4.1.3 Main results obtained

Since Carbopack® B is a reference material and it is known from literature that BTEX are well desorbed at temperatures between 200 and 250 °C [1], the first experiments were carried out using this material as adsorbent.

Initially, MAP was filled with 5.7 mg of Carbopack® B and conditioned at 200 °C for 1 h. Once the device was at room temperature, preconcentration performance was evaluated by injecting 100 ppb BTEX samples of 40 mL. In the first experiment, the desorption temperature was set at 220 °C. Right after each sample, a desorption at the same temperature was conducted to verify that all BTEX molecules were desorbed. The second desorption resulted in BTEX chromatographic peaks of much less intensity indicating that the first BTEX desorption was not fully complete. Therefore, a cleaning step was added between consecutive analysis to ensure the total desorption of the analytes. This step consisted of raising the temperature of MAP to 220 °C while a nitrogen flow of 20 NmL/min was passing through. To achieve the total cleaning of the adsorbent, several cleaning durations were tested and, finally, it was concluded that the duration should be adapted to the amount of BTEX injected because the residues were proportional to the concentration injected. Depending on the injected concentration, cleaning steps from 30 to 60 min were sometimes required to remove 95 % of residues. Obviously, this duration is far from ideal, since our objective was to perform the whole analysis within a maximum of 20 min. Despite this problem, several preconcentration tests were performed in order to validate the proof of concept of this device.

For this purpose, 40 mL samples of BTEX at several concentrations ranging from 10 to 100 ppb were injected in duplicate. A cleaning step between 30 and 60 min was performed between two consecutive analysis. After each cleaning, a blank was conducted to verify that the adsorbent was totally clean. Chromatograms were integrated and the average of peak areas obtained from duplicates versus the injected concentration of each compound are plotted in Figure 4-5a and Figure 4-5b.

As it can be seen, the peak areas increased linearly with the injected concentration demonstrating that the MAP device is functional. This linearity was confirmed by the R^2 coefficients of the linear fitting that varied from 0.9772 to 0.9951 (see Table 4- 1) depending on the species.

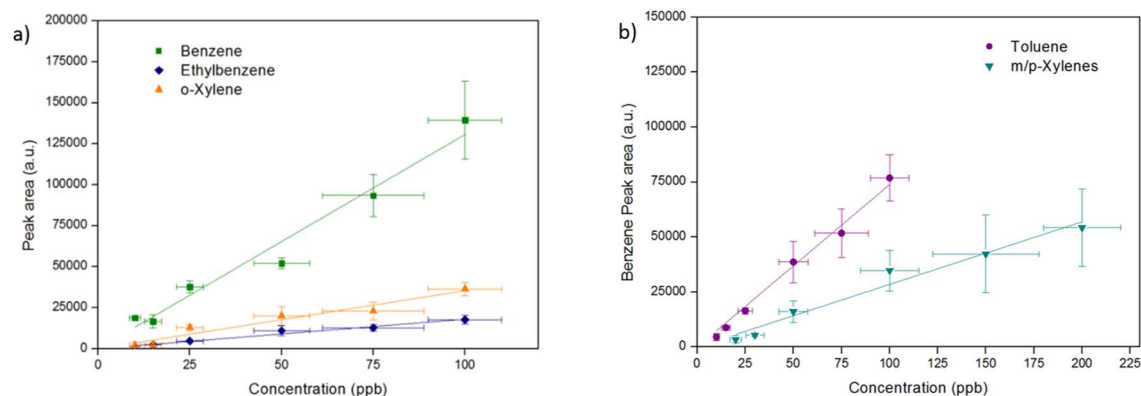


Figure 4-5. Average peak areas versus the injected concentrations of a) benzene, ethylbenzene and o-xylene and b) toluene and m/p-xylenes for 40 mL BTEX samples. Horizontal error bars correspond to the uncertainty obtained during BTEX generation calculated as explained in Appendix and vertical error bars are the standard deviation of duplicates.

Table 4- 1. Calibration equations and coefficients of determination obtained from the linear fittings forced through zero

Compound	Calibration equation	R ²
Benzene	$y = 1306.5 x$	0.9876
Toluene	$y = 738.5 x$	0.9951
Ethylbenzene	$y = 180.0 x$	0.9903
m/p-Xylenes	$y = 284.6 x$	0.9874
o-Xylene	$y = 353.8 x$	0.9772

Despite the incomplete desorption of BTEX, the molecules were desorbed in a reproducible way. To improve BTEX desorption, the best option would be to increase the desorption temperature but, during the heating-cooling cycles and preconcentration tests, a considerably deterioration of the epoxy resin employed to prevent leakage was observed. As a result, some peaks appeared in the chromatogram corresponding to compounds released from the resin and a leakage was detected at the fluidic connectors. Due to these thermal limitations, Carboxpack® B cannot be used as adsorbent in this preconcentrator prototype because it requires high desorption temperatures causing damage of the preconcentration unit. However, the device was fully operational, and it could be useful if filled with a different adsorbent enabling low temperature desorption of BTEX.

Some studies reported desorption temperatures of 150 °C for toluene from mesoporous silica [2]. This is why a mesoporous silica, i.e. SBA-16, was tested as an alternative adsorbent. This material was already used for the preconcentration of BTEX [3] in its microporous form. Since the interactions of

molecules in the micropores are usually stronger, we thought that the desorption temperature could be lower on the mesoporous counterpart.

The first part of the experiments was related to the optimization of the desorption temperature. Since high temperatures such as 200°C could potentially damage the connectors leading to leakage, the highest temperature tested was therefore 180 °C. For the optimization, two replicates of 20 mL samples of BTEX at 100 ppb were injected and desorbed at 135, 150 and 180 °C. The average peak areas obtained for each compound are displayed in Figure 4-6. As can be seen in the figure, peak areas were lower at 135 °C indicating that, at this temperature, the desorption was not complete. On the other hand, the areas of the desorption peaks at 150 and 180 °C were nearly similar suggesting that the same quantity of molecules was desorbed whatever the compound. Therefore, 150°C was chosen as the appropriate desorption temperature to prevent the deterioration of this PC prototype.

Desorption was performed right after each injection, to evaluate the residuals remaining on the adsorbent. Residues of considerably intensity were found after each desorption indicating that desorption was not fully satisfactory in any of the cases. Therefore, a cleaning experimental protocol was developed as described for Carbopack® B, adapting the duration depending on the injected concentration and using a temperature of 180 °C considered as the usable maximum temperature.

Despite the incomplete desorption, a series of 20 mL BTEX samples of different concentrations ranging from 10 to 200 ppb were injected into the system to verify the linearity of the detector response. Unfortunately, using this adsorbent and due to the effect of preconcentration, the peaks corresponding to ethylbenzene and xylenes were significantly enlarged and, thus, too coeluted for an accurate integration; therefore, these peaks were integrated together. The resulting peak areas were plotted versus the concentration (see Figure 4-7). Even if the desorption was not fully accomplished, the obtained peak areas increased linearly with the concentration and preconcentration factors of 11 were achieved for benzene and toluene.

The last tested adsorbent was Basolite® C300. To this purpose, a MAP preconcentrator prototype was filled with 5.8 mg of Basolite® C300. Since the temperature was the critical point in previous tests, the first step was the optimization of the desorption temperature. For this purpose, three replicates of 20 mL BTEX samples of 100 ppb were injected and they were desorbed at different temperatures, i.e. 125, 135 and 150 °C, which is considerably lower than the maximum temperature of 200 °C usable without any damage.

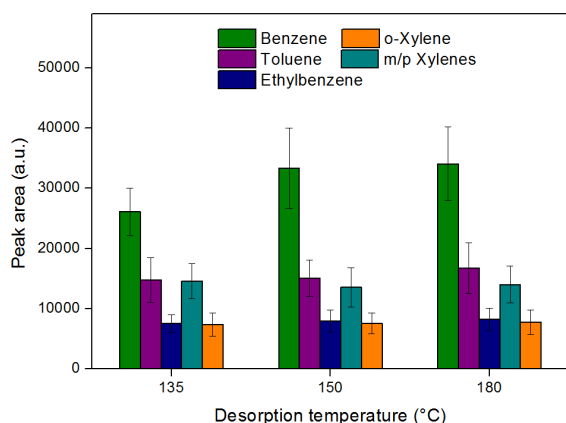


Figure 4-6. Optimization of the desorption temperature (100 ppb 20 mL) between 135 and 180 °C.

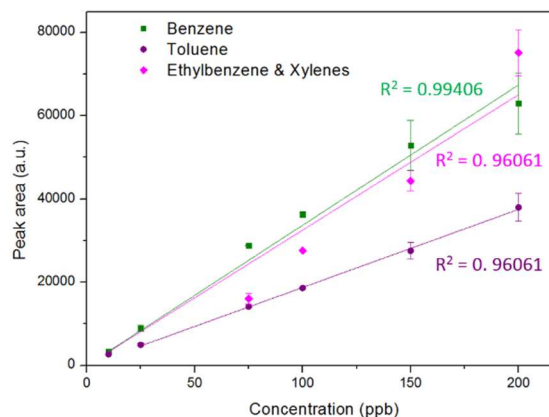


Figure 4-7. Peak areas obtained for the injections of different BTEX concentrations ranging from 10 to 200 ppb. Vertical error bars correspond to the standard deviation of duplicates. Linear fitting was forced through zero.

As illustrated in Figure 4-8, there was no big difference between the peak areas obtained at different temperatures. The peak areas obtained at a desorption temperature of 150 °C were slightly higher; hence, this temperature was set for further experiments.

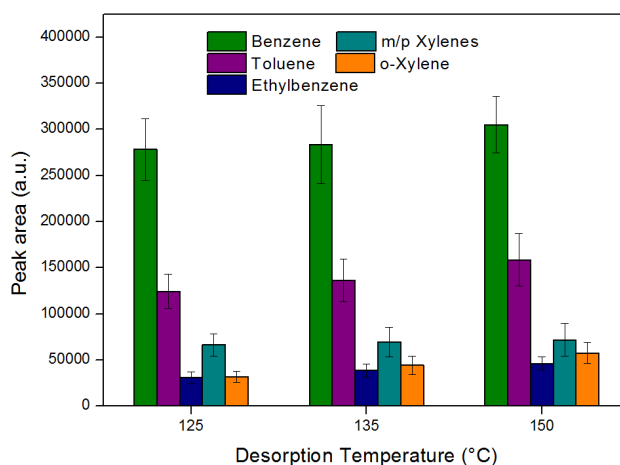


Figure 4-8. BTEX peak area as a function of desorption temperature (20 mL, 100 ppb). Vertical error bars represent the standard deviation of triplicates.

Once desorption temperature was optimized, the residues after the first desorption were evaluated by conducting a second desorption right after the first one. Even if the residues peaks were much less intense than in the case of Carboxpack® B or SBA-16, some of them were still present, and therefore, a cleaning step was required. Different cleaning durations were tested at a temperature of 180 °C and 10 min was found to be an efficient cleaning step even in the case of highly concentrated samples such

as 100 ppb. As can be seen in Figure 4-9, the residues measured after the cleaning step were barely visible, they were quantified and they represented lower than 3% of the injected concentration. It means that the error made in quantification of highly concentrated samples is less than 3 ppb and it decreases as the injected concentration decreases. Actually, these tests were made by using a concentration of 100 ppb that mimics an extremely polluted environment where the use of preconcentrator is not necessary. The idea behind this test was to put the device under extreme conditions to estimate the measurement error and ensure that, even in the extreme cases, the device could provide accurate results.

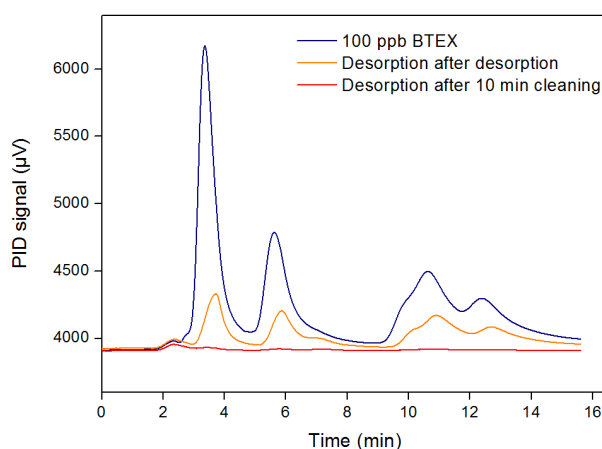


Figure 4-9. Chromatograms obtained after the injection of 100 ppb BTEX sample (blue), desorption right after the first desorption (orange) and desorption after a cleaning step of 10 min (red)

After desorption temperature and cleaning duration, other operating conditions were optimized. First, different sampling flow rates were evaluated to verify that all molecules were trapped during the adsorption step. For this purpose, flow rates of 2, 5, 10 and 15 NmL/min were tested in duplicate to sample a total volume of 40 mL. The measured peak areas for each compound are presented in Figure 4-10. As it is obvious from this figure, at flow rates higher than 5 NmL/min, the amount of trapped BTEX decreased suggesting that some of the molecules are not adsorbed. This fact can be explained by the velocity of the flow and also by a mistake in the device design. In fact, since the adsorbent had to be packed manually, it was noticed that sometimes the cavity was not perfectly filled, leaving some free paths for gas molecules to pass through the cavity without crossing the adsorbent bed. Similar results were obtained for lower flows, i.e. 2 and 5 NmL/min indicating that the same amount of BTEX was trapped at both flow rates. Therefore, 5 NmL/min was chosen as the optimal

sampling flow rate as the best compromise between a quantitative sampling and a short sampling time.

The injection time was the next parameter optimized in this work. From the heating tests performed in the first part of the study, it was demonstrated that the device achieved 150 °C in 60 s. Since the optimized desorption temperature was 150 °C, it was decided to arbitrarily set 80 s as injection time, which included 60 s for the device to reach 150 °C and kept this temperature for 20 s. To evaluate the influence of this parameter, injection times of 65 and 95 s were also tested. The peak areas obtained for each compound in all experiments were very similar (see Figure 4-11), demonstrating that this parameter has a minor influence in desorption compared to other parameters investigated in this study. Similar peak areas were observed for injection times of 80 and 95 s whereas they were slightly lower for 65 s; therefore, 80 s was chosen as the optimal injection time.

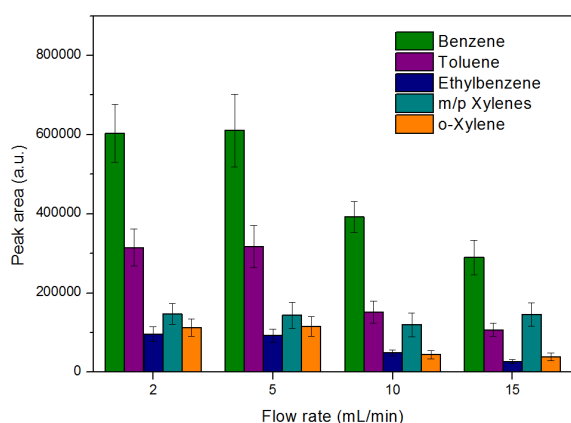


Figure 4-10. Benzene and toluene peak areas as a function of flow rate for 40 mL of 100 ppb BTEX samples. Vertical error bars represent the standard deviation of duplicates.

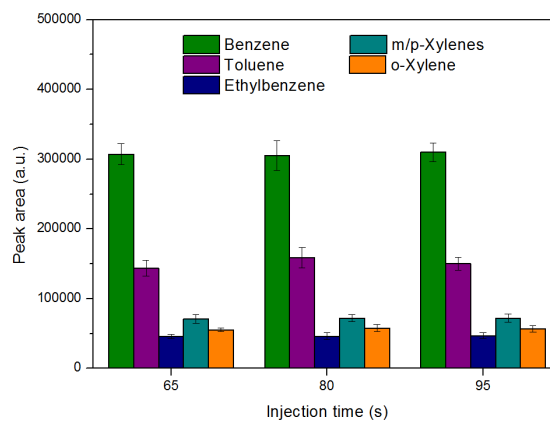


Figure 4-11. Benzene and toluene peak areas as a function of injection time (20 mL, 100 ppb). Vertical error bars represent the standard deviation of duplicates.

Using the optimal operating conditions determined in the aforementioned experiments, a detailed characterization and calibration of the system using Basolite® C300 as adsorbent was performed. The results obtained are described in detail in the publication untitled “Sub-ppb level detection of BTEX gaseous mixtures with a compact prototype GC equipped with a preconcentration unit” presented in the next section.

Although this system is far from ideal, the results obtained in the preconcentration tests were satisfactory in terms of sensitivity. By integrating MAP in the prototype GC presented in Section 2.2.1,


detection limits of 0.20, 0.26, 0.49, 0.80 and 1.70 ppb were achieved for benzene, toluene, ethylbenzene, m/p-xylenes and o-xylene, respectively.

4.1.4 Article 2 published in Micromachines “Sub-ppb Level Detection of BTEX Gaseous Mixtures with a Compact Prototype GC Equipped with a Preconcentration Unit “



Article

Sub-ppb Level Detection of BTEX Gaseous Mixtures with a Compact Prototype GC Equipped with a Preconcentration Unit

Irene Lara-Ibeas ^{1,2}, Alberto Rodríguez-Cuevas ³, Christina Andrikopoulou ¹, Vincent Person ³, Lucien Baldas ², Stéphane Colin ²  and Stéphane Le Calvé ^{1,3,*}

¹ ICPEES UMR 7515, Université de Strasbourg/CNRS, F-67000 Strasbourg, France; ilaraibeas@unistra.fr (I.L.-I.); candrikopoulou@unistra.fr (C.A.)

² Institut Clément Ader (ICA), Université de Toulouse/CNRS, INSA, ISAE-SUPAERO, Mines-Albi, UPS, 31400 Toulouse, France; baldas@insa-toulouse.fr (L.B.); stephane.colin@insa-toulouse.fr (S.C.)

³ In'Air Solutions, 25 rue Becquerel, 67087 Strasbourg, France; arodriguez@inairsolutions.com (A.R.-C.); vperson@inairsolutions.fr (V.P.)

* Correspondence: slecalve@unistra.fr; Tel.: +33-3-6885-0368

Received: 8 February 2019; Accepted: 7 March 2019; Published: 13 March 2019



Abstract: In this work, a compact gas chromatograph prototype for near real-time benzene, toluene, ethylbenzene and xylenes (BTEX) detection at sub-ppb levels has been developed. The system is composed of an aluminium preconcentrator (PC) filled with Basolite C300, a 20 m long Rxi-624 capillary column and a photoionization detector. The performance of the device has been evaluated in terms of adsorption capacity, linearity and sensitivity. Initially, PC breakthrough time for an equimolar 1 ppm BTEX mixture has been determined showing a remarkable capacity of the adsorbent to quantitatively trap BTEX even at high concentrations. Then, a highly linear relationship between sample volume and peak area has been obtained for all compounds by injecting 100-ppb samples with volumes ranging from 5–80 mL. Linear plots were also observed when calibration was conducted in the range 0–100 ppb using a 20 mL sampling volume implying a total analysis time of 19 min. Corresponding detection limits of 0.20, 0.26, 0.49, 0.80 and 1.70 ppb have been determined for benzene, toluene, ethylbenzene, m/p-xylenes and o-xylene, respectively. These experimental results highlight the potential applications of our device to monitor indoor or outdoor air quality.

Keywords: preconcentrator; microfluidics; miniaturized gas chromatograph; BTEX; PID detector

1. Introduction

In recent years, there has been an increasing interest in air pollution since numerous studies have demonstrated its impact on human health [1–3]. Among the broad variety of identified air contaminants, benzene, toluene, ethylbenzene and xylenes (BTEX) require particular attention not only for their toxic, mutagenic, and/or carcinogenic effects but also for their key role in photochemical reactions. These compounds can be emitted by several indoor as well as outdoor sources. In outdoor air, the main sources are related to fuel storage or combustion processes such as road traffic, petrol stations or industrial activities [4–7]. In closed environments, most of BTEX are emitted by cleaning products, furnishings as well as building materials like flooring materials, wall coverings, adhesives, varnishes or paints [8–10]. Smoking and cooking are also considered as other major sources of BTEX in indoor air [11,12]. Numerous investigations have demonstrated the harmful effects of BTEX on human health even at low concentrations [13]. Fatigue, loss of coordination, memory problems, headache, skin and eyes irritation as well as other more severe effects like asthma, kidney damage or neurological problems have been linked to BTEX exposure [14,15]. In addition, benzene is a known carcinogen

compound, with long-term exposure being associated with the development of leukaemia [16]. Thus, in 2013, a threshold limit value of $5 \mu\text{g m}^{-3}$ (1.6 ppb) for benzene was set by the European Union in public buildings. In France, this limit was decreased to $2 \mu\text{g m}^{-3}$ (0.6 ppb) in 2016. Therefore, to check if indoor air quality (IAQ) is in accordance with the new legislation, on-site rapid and sensitive analysis is required.

So far, methods based on gas chromatography have typically been the techniques employed for BTEX analysis in indoor and outdoor air. Benchtop chromatographs are sensitive and accurate instruments enabling BTEX detection in the order of parts per trillion (ppt). However, their large size, heavy weight and high energy consumption limit their use for in-situ measurements. Consequently, many air quality measurement campaigns have been conducted using commercial sampling cartridges [8,17–21] that were subsequently analyzed in a laboratory increasing not only the total analysis time but also the risk of sample degradation during storage or transport. Furthermore, these off-line analyses do not provide concentration-time profiles since each measurement represents an average value of pollutant concentration over the selected sampling time.

During the past two decades, great efforts have been made to develop real-time sensitive miniaturized gas chromatographs. Portable instruments containing micro-electro-mechanical systems (MEMS)-based components have grown in popularity due to their small dimensions, low energy consumption and short time of analysis. Table 1 summarizes the most remarkable commercially available and laboratory prototypes of miniaturized gas chromatographs (GC) developed in the last decade. All devices presented are highly portable (weight < 5 kg) enabling on-site measurements. Most of these instruments perform BTEX analysis in less than 15 min providing high-resolution concentration-time profiles. Nevertheless, these analyzers have a detection limit of a few ppb, which is not enough to comply with the requirements of the new regulation. So far, only the GC-metal oxide semiconductor (MOS) reported by Zampolli et al. [22] and the GC- photoionization detector (PID) developed by Skog et al. [23] were able to detect concentrations below 1 ppb. High sensitivities are usually correlated with long sampling times. In the first case, 55 min of sampling and around 12 min for separation were needed to achieve sub-ppb detection of BTEX [22]. Shorter sampling (20 min) and similar separation (15 min) times were required by Skog et al. [23] to reach limits of detection (LOD) in the order of ppt. Both devices imply a considerable long total analysis time, hindering the possibility to provide near real-time BTEX concentrations. Regarding the MEMS-based instruments available in the literature, a sensitive and rapid BTEX analysis remains a challenging issue.

The present work reports the development of a compact GC prototype for near real-time BTEX detection at sub-ppb levels and its validation under controlled laboratory conditions. The device is based on the miniaturized GC developed by Nasreddine et al. [24] where a preconcentration unit has been added in order to significantly improve its sensitivity. An improvement ratio between 1.55 and 4.46 in detection limit was achieved for the different compounds compared to the previous version. To our knowledge, this is the first work to report a GC prototype able to perform sub-ppb BTEX levels detection in such a short analysis time.

The paper is organized as follows: Section 2 describes the GC working principle and presents the experimental setup for BTEX generation employed in this project. Section 3 presents the performances of the GC prototype in reference to adsorption capacity, linearity and sensitivity. Section 4 summarizes the conclusions and proposes several improvements for the future work.

Table 1. Most representative compact gas chromatographs (GC) for BTEX analysis over last decade.

Ref.	Size (cm)	Weight (kg)	Sampling Time (min)	Analysis Time (min)	Preconcentrator l (mm) \times d (μ m) \times w (mm)	Adsorbent	GC Column l (m) \times d (μ m) \times w (μ m)	Stationary Phase and Thickness	Carrier Gas Flow Rate (mL/min)	Detector	LOD (ppb)
This work	32 \times 29 \times 14	~5	4	15	Cavity 4.6 \times 350 \times 7.4	Basolite C300 5.8 mg	Capillary 20 \times 180 (i.d.)	Rxi 624 SH MS 1 μ m	N ₂ 2.5	PID	0.1–1.6 (BTEX)
GC-PID [23]	31 \times 30 \times 20	32	20	~15	Tube 0.165 cm i.d.	ResSil-B 75 mg	Capillary 15 \times 530 (i.d.)	MXT-1 3 μ m	A.A. 0.8–2.2	PID	0.002–0.011 (BTEX)
GC-MOS [25]	n. d.	n. d.	5	4	Cavity with micro-pillars 10 \times 400 \times 5	Zeolite Day-13 1 μ m	Circular spiral 5 \times 100 \times 100	PDMs 100 nm	7	MOS	24 (toluene) 5 (o-xylene)
GC-PID [26]	n. d.	n. d.	1	5 (5 comp.)	4 Parallel channels n.d. \times 400 \times 0.6	SWNTs 0.15 mg	Serpentine with micropillars 4 \times 350 \times 320	OV-101 0.2 μ m	A.A. 5	PID	<1 (benzene)
GC-MOS [27]	n. d.	n. d.	n. d.	60 (3 comp.)	n. p.	n. p.	Serpentine 1.6 \times 1200 \times 600	Porapak Q	A.A.	MOS	5 (benzene)
PEMMA-1 [28]	19 \times 30 \times 14	3.5	1	4 (17 comp.)	2 Cavities (V ~ 9.4 μ L) 380 (d)	C-B 2.0 mg C-X 2.3 mg	Square spiral 0.20 μ m	PDMs 0.20 μ m	He 3	5 μ CR	420–890 (BTEX)
Frog-4000 [29]	25 \times 19 \times 37	<2.2	0.5	5	n. d.	Silica gel aerogel	4.8*	PDMs 0.8 μ m	A.A.	PID	–ppb
GC-PID [30]	n. d.	n. d.	50	13	n. d.	EQBox 10 mg	n. p.	n. p.	A.A. 30	PID	1.25 (benzene)
GC-PID [31]	60 \times 50 \times 10	<5	2	14.2 (50 comp.)	Cavity 8.15 \times 250 \times 2.9	C-B 1.135 mg	1D: 10 \times 250 (i.d.) 2D: 3 \times 250 (i.d.)	1D: Rtx-SMS 2D: Rtx-200 0.25 μ m	He 2	μ PID	n. d.
GC-CR [32]	20 \times 15 \times 9	2.1	2.5 min (9 comp.)	5	2 Cavities (V ~ 9.4 μ L)	C-B 2.0 mg C-X 2.3 mg	6*	PDMs 0.2 μ m	n. d.	μ CR	n. d.
GC-CMOS [33]	16 \times 11 \times 11	n. d.	n. d.	n. d.	Cavity with micro-pillars 10 \times 250 \times 2	Carbon film	Square spiral 3 \times 250 \times 100	DB-1	n. d.	CMOS	15 (1,3,5-TMB)
iGC3.2 [34]	8 \times 10	n. d.	120	10	U-shape n.d. \times 300 \times 1350	C-B + C-X	2-Serpentines 0.30 \times 230 (i.d.)	OV-1 0.2 μ m	A.A. 0.2	2 CD	10–2 (BTEX)
Zebra GC [35]	15 \times 30 \times 10	~1.8	10	<2	Cavity with micro-pillars 13 \times 240 \times 13	Tenax TA ~ 200 nm	Serpentine 2 \times 70 \times 240 ~250 nm	OV-1 ~250 nm	He 1	TCD	~25 (TEX)
GC-PID [24]	32 \times 29 \times 14	~4	1	10	n. p.	n. p.	Capillary 20 \times 180 (i.d.)	Rxi 624 SH MS 1 μ m	N ₂ 2.5	PID	0.8–3.2 (BTEX)
GC-MOX [22]	n. d.	n. d.	55	~12	Ten parallel channels 800 μ m depth	QxCav	Square spiral 0.5 \times 900 \times 900	Carbograph 2.0.2% Carbowax	A.A. 15	MOS	0.1 (benzene)

i.d.: internal diameter, comp.: compounds, n. d.: not defined, n. p.: not present,* only column length is reported, A.A.: ambient air, MOS: metal oxide semiconductor, CR: chemiresistor detector, CD: capacitive detector, CMOS: complementary metal oxide sensor, MOX: metal oxide sensor, QxCav: quinoxaline bridged cavitand.

2. Materials and Methods

2.1. Prototype of Micro Gas Chromatograph (GC)

The GC laboratory prototype employed in this study is presented in Figure 1. The system is based on the GC laboratory prototype developed by Nasreddine et al. [24]. In the present work, a preconcentration module has been integrated into the system enabling an improvement in sensitivity. The detailed operating principle of the GC is described in [24] so that only a brief description of the overall system is given below while the preconcentration module developed in the present work is highly detailed in the next section. The system operates according to four steps: sampling, preconcentration, separation and detection. Samples are collected and introduced in the preconcentrator (PC) by means of a SP 570 EC-BL micropump (Schwarzer Precision, Germany) and a EL-FLOW flow controller (Bronkhorst, Ruurlo, Netherlands). Separation step is carried out using a commercial 20-m long capillary column (i.d. 0.18 mm, Rxi-624 stationary phase, 1 μm film thickness, Restek, Bellefonte, PA, USA). Polydimethylsiloxane (PDMS) columns are typically used for BTEX separation because as they are non-polar, they provide high resolution but long separation times as well. In environmental monitoring, a compromise between short analysis time and reasonable resolution is required, therefore, a slightly more polar column (Rxi-624Sil MS) was selected. Detection is conducted employing an eVx Blue mini photoionization detector (PID) (Baseline MOCON, Lyons, CO, USA) equipped with a 10.6 eV ultra-violet lamp. This GC laboratory prototype was controlled by a computer using a homemade software.

In a previous study [24], injection time was set to 20 s to transfer the sampling loop content to the column. In this new version, injection time of 80 s has been fixed according to the temperature ramp of the heating system, where 150 $^{\circ}\text{C}$ were reached in 60 s and were maintained for 20 s. After desorption, the six port-valve returned to the initial position to start the next sampling.

In the aforementioned work [24], flow rate of 2.5 mL min^{-1} and 80 $^{\circ}\text{C}$ were selected as the optimal conditions for BTEX separation. Using these conditions, BTEX analysis was performed in 10 min and detection limits between 1–3 ppb were found for the different compounds. Analytical performances of this device were validated under controlled laboratory conditions and in real environments [36,37]. In the present version, as the enriched peaks are larger, temperature of the column had to be reduced of 10 $^{\circ}\text{C}$ to avoid coelution between ethylbenzene and m/p-xylenes peaks; therefore, the total analysis time was increased to 15 min.

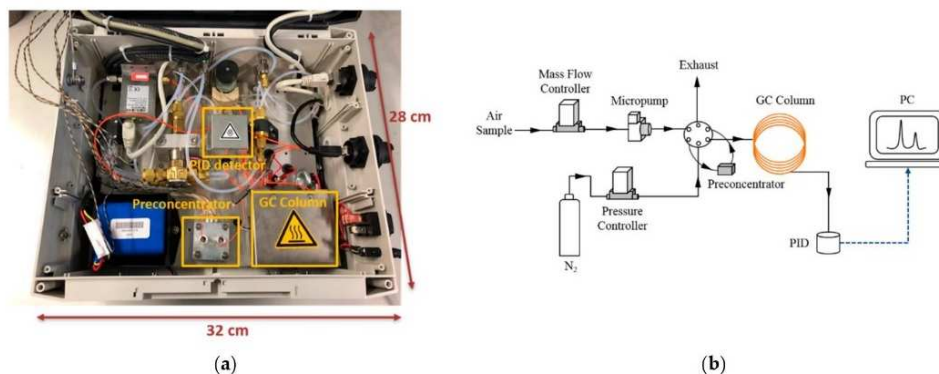


Figure 1. (a) Photograph of the compact gas chromatographs (GC) prototype and (b) schematic view of the device updated with a preconcentration unit.

2.2. Preconcentration Module

An aluminium PC with dimensions of 40 mm \times 40 mm \times 12.3 mm and weight of 54.9 g was manufactured and integrated into the GC laboratory prototype. The device is presented in Figure 2.

The design is based on the preconcentrator proposed by Camara et al. [38] in which a symmetrical manifold fluidic system was fabricated at the inlet and outlet of the adsorbent cavity to promote a uniform flow distribution. However, there are some differences between both designs. In this PC, two metal porous filters (GKN Sinter Metals, Bonn, Germany) are located between the channel system and the microfluidic cavity to ensure that the adsorbent remains in the cavity and to prevent clogging of the microchannels. The manifold consists of one inlet channel split in two channels of $350\ \mu\text{m}$ which are also split to obtain finally four channels of $300\ \mu\text{m}$ connected to a microfluidic cavity of $4.6\ \text{mm} \times 7.4\ \text{mm}$ (see Figure 2b) where the adsorbent is placed. In this cavity, 5.8 mg of Basolite was packed manually. Heating system consists of three heating cartridges (Watlow, St. Louis, MO, USA) of 70 W each. The system allows to reach a temperature ramp of about $150\ ^\circ\text{C}/\text{min}$. In the experiments, desorption was performed at $150\ ^\circ\text{C}$ and this temperature was maintained for 20 s. Temperature is measured with a type K thermocouple (RS Components SAS, Beauvais, France). Prior to the beginning of the experiments, the adsorbent was conditioned at $180\ ^\circ\text{C}$ under a nitrogen flow of $10\ \text{mL}/\text{min}$ during 2 h.

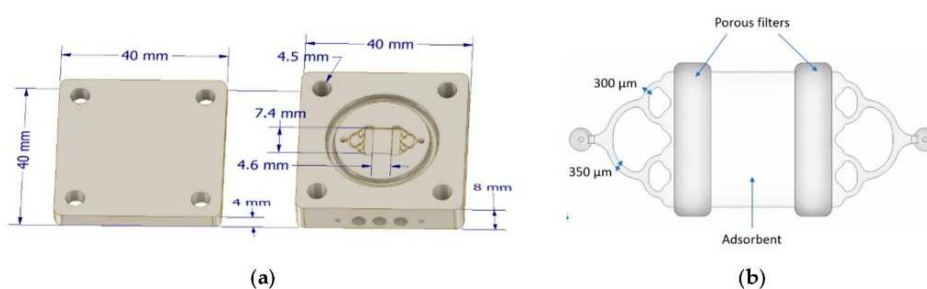


Figure 2. (a) Design of the preconcentrator and (b) zoom on the microfluidic system and the adsorbent cavity.

2.3. Experimental Setup for BTEX Generation

Different BTEX concentrations were generated using the experimental device shown in Figure 3. A standard mixture of BTEX purchased from Messer (Folschviller, France) was diluted with nitrogen (99.999% purity) using mass flow controllers 1 and 2. The initial concentration of every compound was equal to 100 ppb with a 10% uncertainty. This setup allows generating different concentrations in the range 2–100 ppb. Mass flow controller 3 was used to select the sampling flow rate which was set to $5\ \text{mL}/\text{min}$ for all the experiments.

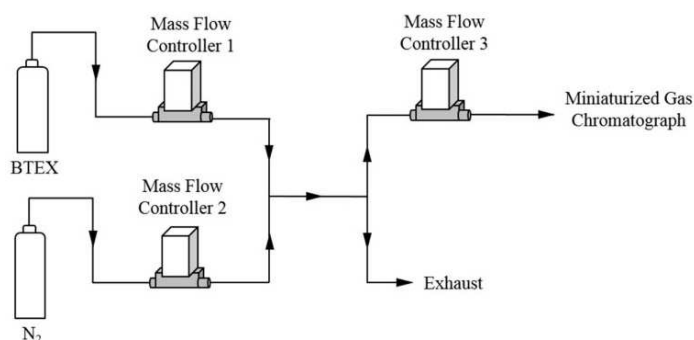


Figure 3. Experimental setup for BTEX generation.

2.4. Breakthrough Test

The above described preconcentrator was mounted on the set-up showed in Figure 4. The 5 mL/min of an equimolar 1 ppm BTEX mixture diluted in nitrogen (Air Products SAS, Aubervilliers, France) flowed through the preconcentration unit. This concentration was too high to be analyzed by a standard gas chromatograph (μ BTEX-1 In'Air Solutions, Strasbourg, France) equipped with a 200 μ L sampling loop. Therefore, the gas stream from the preconcentrator outlet was diluted prior to the analysis using an additional flow of 95 mL/min of nitrogen (99.999% purity, Messer, Folschviller, France) to avoid saturation of the gas chromatograph detector. The whole diluted gas stream was connected directly to the chromatograph sampling loop which was constantly renewed. Every 11 min, the content of the sampling loop was injected into the separation column and analyzed.

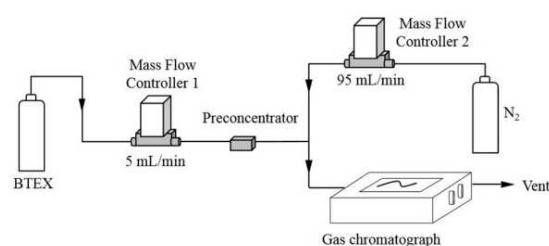


Figure 4. Schematic drawing of set-up used for breakthrough experiments.

3. Results and Discussion

Numerous experiments were conducted to evaluate the performances of the GC prototype: (1) A breakthrough experiment was carried out with a high BTEX concentration of 1 ppm in order to determine the adsorption capacity of the preconcentrator in the studied conditions; (2) repeatability was investigated; (3) the sample volume varied in the range 0–80 mL for a fixed gaseous concentration of BTEX; and (4) the gaseous BTEX concentration varied between 0–100 ppb for a given sample volume.

3.1. Adsorption Capacity

The adsorption capacity is dependent on the preconcentrator geometry, the adsorbent itself and the gas flow rate. The breakthrough time is defined as the time at which 5% of the molecules are leaving the adsorbent bed [39] so that it indicates the maximum sampling time to conduct a quantitative analysis at this concentration. Consequently, the breakthrough point is reached when 5% of the injected concentration (C_0) is passing through the adsorbent and, thus, the measured concentration at the outlet (C) is equal to $0.05 C_0$. It should be noted that the breakthrough time will depend on the injected gas concentration, the flow rate and on the molecule in the case of a competitive adsorption.

Basolite C300 was selected as adsorbent as it has been already employed for benzene preconcentration in other analytical devices [40], demonstrating better preconcentration performance than Tenax TA, one of the most common materials for BTEX preconcentration.

In order to assess the adsorption capacity of the preconcentrator, a breakthrough experiment was performed. In this experiment, an equimolar 1 ppm (C_0) mixture of BTEX flowed through the preconcentrator at a flow rate of 5 mL/min. Usually, BTEX concentrations in indoor air are lower than 10 ppb and do not exceed 100 ppb, so that 1 ppm BTEX mixture simulates a highly polluted environment. The effluent concentration (C) at the preconcentrator outlet was continuously analyzed by a BTEX analyzer provided by In'Air Solutions (μ BTEX-1 In'Air Solutions, Strasbourg, France) and the relative BTEX concentrations (C/C_0) were plotted versus time (see Figure 5a).

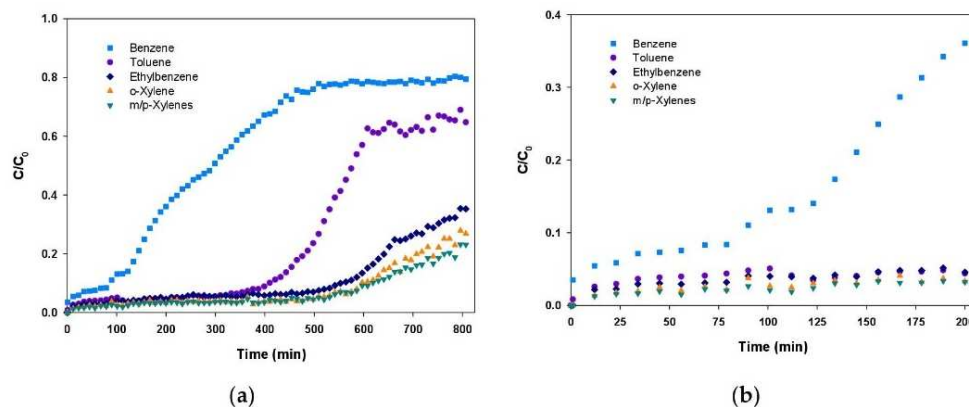


Figure 5. (a) C/C_0 vs. time during a breakthrough experiment performed with an equimolar 1 ppm mixture of BTEX over Basolite-filled preconcentrator and (b) enlarged view of the first 200 min of the experiment.

As it can be observed in Figure 5a, breakthrough curves have two different parts. The first part is almost a flat line indicating that the concentration at the outlet is close to zero and, thus, all the molecules are being adsorbed. Once the breakthrough time is reached ($C/C_0 = 0.05$), the second step begins. In this interval, the adsorbent starts to be overloaded and some of the molecules are not being adsorbed, leading to an increase of concentration at the PC outlet. This concentration rise is sharp at the beginning and starts to be less pronounced as the preconcentrator is close to the total saturation. In our experiment, only benzene and toluene have reached this point with relative concentrations of 0.7–0.8. As the objective of this test was to determine the breakthrough time, the experiment was stopped before achieving the total saturation of the adsorbent ($C/C_0 = 1$).

It is visible in Figure 5 that the adsorption capacity is remarkably different depending on the compound. Breakthrough times were determined as follows: 12 min (benzene), 156 min (toluene and ethylbenzene), 454 min (m/p-xylenes) and 457 min (o-xylene). The remarkable adsorption obtained for most of the compounds can be attributed to the large micropore volume of Basolite C300 as reported in other studies [41]. This noticeable adsorption capacity enables the collection of large sample volumes.

To illustrate the differences between benzene and the other compounds, Figure 5b presents an enlarged view of the first 200 min of the experiment where benzene clearly started to leave the adsorbent bed before the others. However, our results suggest that a sampling time of 12 min at 5 mL/min, corresponding to a sample volume of 60 mL, can be performed in a considerably polluted environment without any sample loss due to breakthrough, which would lead to an underestimation of the real gas concentration in air.

3.2. Repeatability

To evaluate the repeatability of the device, ten 20-mL samples containing 100 ppb of BTEX were consecutively injected. Between two consecutive injections, a cleaning step was conducted. During the separation step and once the sample was injected, the preconcentrator was maintained at 180 °C for 10 min to ensure there were no residues of the previous injection. After each cleaning step, a blank was conducted to verify that all BTEX were desorbed before starting the next injection. Peak area and retention time were determined for every replicate. Relative standard deviations (RSD) of peak area and retention time were calculated to verify the stability of the measurements. The corresponding RSD for the peak areas were 3.8, 6.3, 11.0, 14.7 and 13.4% for benzene, toluene, ethylbenzene, m/p-xylenes and o-xylene, respectively. The greater dispersion of ethylbenzene and m/p xylenes peak areas is probably due to the peak integration itself; as these species are coeluted, the error in the integration could be higher than in the case of benzene and toluene. Furthermore, in the current prototype, sample

injection and desorption as well as the cleaning step were conducted manually because these functions were not yet integrated in the software although they can obviously impact the repeatability of the measurements. Indeed, it is expected to substantially improve the repeatability of the measurements when all the steps will be operated automatically by the software. Despite the lack of automatization, retention times were remarkably stable with RSD of 0.5, 0.7, 1.7, 1.4 and 1.4% for benzene, toluene, ethylbenzene, m/p-xylenes and o-xylene, respectively. Peak area of each blank was also determined, showing that after the cleaning step, the residues are less than 3% even after the injection of 100 ppb samples. It must be noted that a concentration of 100 ppb BTEX mimics a highly polluted environment where a preconcentrator is usually not required for analysis. Even if these results are far from ideal, the repeatability tests demonstrated that desorption is repeatable and, consequently, the aforementioned results show that the integration of the preconcentration unit into the previous GC version has not significantly influenced the repeatability of the device.

3.3. GC Signal Versus Sample Volume

After validation of the high adsorption capacity of BTEX on Basolite at high concentrations of 1 ppm and the stability of the measurements, the influence of sample volume passing through the preconcentrator was evaluated. For this, different volumes varying from 5–80 mL of a 100-ppb standard gaseous mixture of BTEX were injected in duplicate at a fixed flow rate of 5 mL/min. As it is described above, a cleaning step was performed after each analysis to ensure all BTEX have been desorbed. As illustrated in Figure 6, peak areas calculated from the chromatograms increase proportionally with the corresponding sampling volumes with correlation coefficients (R^2) of 0.9946, 0.9892, 0.9824, 0.9608 and 0.9838 for benzene, toluene, ethylbenzene, m/p-xylenes and o-xylene, respectively. Therefore, different sample volumes can be used for the analysis in the studied range without modifying the performances of the experimental device. However, longer sampling improves the sensitivity but decreases the temporal resolution, i.e., the time needed for sampling and analysis increases. Therefore, a sample volume of 20 mL was selected as a compromise between sampling volume and time resolution, the flow rate being fixed at 5 mL/min to avoid any breakthrough.

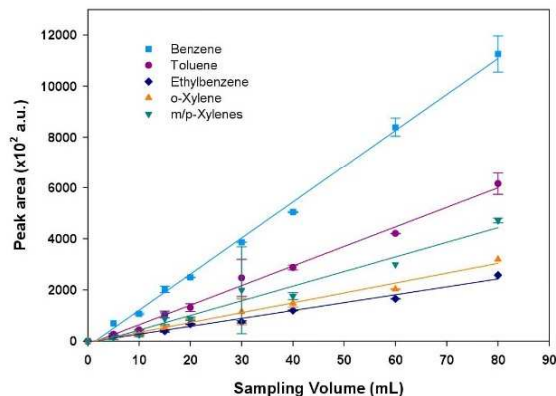


Figure 6. Peak area variation with sampling volume (BTEX concentration of 100 ppb). The vertical error bars show the standard deviation for duplicate injections.

3.4. Calibration Curves and Detection Limit

Once adsorption capacity validated and sample volume fixed to 20 mL at a flow rate of 5 mL/min, a calibration was performed using different gaseous concentrations of the targeted compounds ranging from 2.5–100 ppb. Each concentration was injected in duplicate. As mentioned before, a cleaning step after each analysis was performed. The mean peak area was then calculated and plotted versus

the injected concentration for each compound. Note that m- and p-xylenes were not separated. The obtained calibration curves are displayed in Figure 7 for each species.

The peak area increases linearly with the injected concentrations, demonstrating that the preconcentrator operates in a very satisfactory way as confirmed by the obtained correlation coefficients in the range 0.9777–0.9959 (see Table 2). The calibration slopes decrease with the molecular weight of the compound, being steeper for benzene (C_6H_6) and toluene (C_7H_8) than for the other compounds (C_8H_{10}) and, thus, leading to a greater sensitivity for the weakest compounds as already observed by Nasreddine et al. [24].

Detection limits were calculated from a signal-to-noise ratio of 3 for the two lowest injected concentrations (2.5 and 5 ppb). Using a sample volume of 20 mL, detection limits of the order of a few hundred ppt were obtained for all compounds, excepting o-xylene (see Table 2).

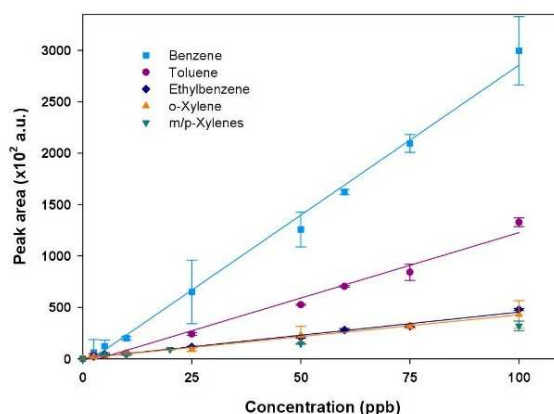


Figure 7. Calibration curves of BTEX performed at 5 mL/min and with a sampling volume of 20 mL. The vertical error bars show the standard deviation for duplicate injections.

Table 2. Calibration equations and limits of detection (LOD) obtained for BTEX with and without the preconcentration module (this work, Nasreddine et al. [24]).

Compound	Calibration Equation	R ²	LOD 1 (ppb) * (This Work)	LOD 2 (ppb) Nasreddine et al. [24]	Ratio LOD 2/LOD 1
Benzene	$y = 2828.2 x$	0.9913	0.20	0.72	3.6
Toluene	$y = 1206.3 x$	0.9777	0.26	1.16	4.46
Ethylbenzene	$y = 454.2 x$	0.9895	0.49	2.10	4.40
m/p-Xylenes	$y = 311.9 x$	0.9959	0.80	1.40	1.75
o-Xylene	$y = 427.0 x$	0.9949	1.70	2.63	1.55

* LOD (ppb) = $(3 \times \text{lowest injected concentration}) / (S/N \text{ of the lowest injected concentration})$.

These results show a considerable sensitivity enhancement compared to the previous development made by Nasreddine et al. [24] with an improvement ratio ranging between 1.55–4.46. To illustrate this improvement, a chromatogram of 100 ppb BTEX with and without the preconcentration stage is displayed in Figure 8. As evidenced by the figure, peak intensities are significantly greater in the new version, with the noise also increasing, but to a lesser extent.

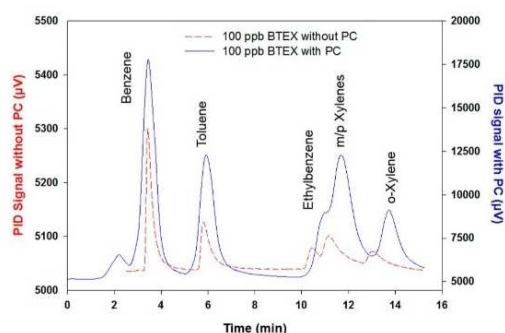


Figure 8. Red dashed line: Chromatogram of 100 ppb BTEX without preconcentration step (sample volume of 200 μL). Blue solid line: Chromatogram of 100 ppb BTEX with preconcentration step (sample volume of 20 mL).

It should be noted that lower detection limits can be achieved with this new prototype by increasing the sample volume passing through the preconcentration unit. In addition, the benzene limit of detection of 0.2 ppb obtained with the novel miniaturized GC integrating a preconcentration module is now consistent with the threshold limit value of 0.6 ppb imposed by the French regulation.

Apart from peak intensities, peak areas have been significantly enhanced. To quantify this improvement, a preconcentration factor (PF) has been defined as the ratio between peak areas with and without the preconcentration step. This factor is expected to be 100 as the sampling volume is increased by a factor of 100 (20 mL/200 μL) in the new prototype version. For the chromatogram presented in Figure 8, PF were 63.2, 82.4, 81.3, 89.3 and 77.9 for benzene, toluene, ethylbenzene, m/p xylenes and o-xylene, respectively. The difference between the obtained PF and the expected PF of 100 could be explained by two facts. Firstly, as it was demonstrated by the blanks performed in the repeatability test, some BTEX residues were not desorbed during the first desorption and, secondly, as the microfluidic cavity was manually packed with the adsorbent, it is probable that it was not completely filled and, thus, some BTEX molecules can pass through the cavity without being in contact with the adsorbent. For example, as illustrated in Figure 5b for the breakthrough experiments, some benzene molecules left the cavity without being adsorbed, even from the beginning of the experiments. This lower benzene trapping yield of 96% can explain the lower benzene PF of 63 observed. Nevertheless, satisfactory and repeatable results were obtained when varying the injected volume or concentration, showing that the trapping yield of BTEX and the preconcentrator factor are reproducible and have little significance in the accuracy of the analysis once the device is properly calibrated.

By sampling a volume of 20 mL, one full analysis cycle is performed in 19 min. Since preconcentrator cleaning and cooling down operated during the separation step, the resulting total analysis time was 19 min, which is acceptable to establish concentration–time profiles. Even if these results are successful, there are still significant scopes for improvements in terms of analysis time and peak resolution. It is expected to decrease the time of analysis by replacing the current separation column by a MEMS-based column enabling BTEX separation in 5 min, as it was reported in other studies [26,29]. Peak resolution can be enhanced by improving the performance of the PC heating system and/or reducing the detector response time. More compact devices with an integrated heating system can achieve a faster temperature ramp, which would result in shorter injection time and narrower desorption peaks. Additionally, a most powerful heating system could achieve higher temperatures in shorter times decreasing the amount of non-desorbed BTEX and, therefore, increasing the PF. Further work is planned to investigate alternative adsorbents that could potentially improve the trapping yield for benzene. On the other hand, a μPID detector with small detection chamber could also improve the peak resolution since the sample renewal inside the chamber would be faster and, thus, peak broadening would be reduced.

4. Conclusions

We reported the development of a compact GC prototype for near-real time BTEX analysis in sub-ppb range. Using a 20 mL sampling volume, BTEX analysis was conducted in 19 min and corresponding detection limits of 0.20, 0.26, 0.49, 0.80 and 1.70 ppb were calculated for benzene, toluene, ethylbenzene, m/p-xylenes and o-xylene, respectively. Considering the extremely low detection limit achieved by this prototype, it becomes possible to extend its use to other fields of application such as the food industry, early cancer diagnosis or explosives detection, by measuring other VOCs families and/or by changing the nature of adsorbent.

Several improvements can be proposed for future versions of the compact GC. First, the preconcentrator mass should be reduced in order to achieve faster heating, which would lead to more rapid temperature transfer to the adsorbent and, thus, faster desorption and then to thinner chromatographic peaks. Secondly, a shorter separation column based on MEMS technology could potentially reduce the total analysis time. In addition, the miniaturization of both components will reduce the energy consumption of the prototype, increasing its autonomy and improving its portability.

Finally, the automation of the device should integrate the cleaning step of adsorbent during pollutants chromatographic separation between two adsorption/desorption cycles, in order to improve the analysis quality.

Author Contributions: Conceptualization, V.P.; Methodology, I.L.-I., A.R.-C. and S.L.C.; Investigation, I.L.-I., A.R.C. and C.A; writing—original draft preparation, I.L.-I.; writing—review and editing, L.B., S.C. and S.L.C.; supervision, S.L.C., S.C. and L.B.

Funding: This work has received funding from the Clean Sky 2 Joint Undertaking under the European Union's Horizon 2020 research and innovation program under grant agreement No 687014. This project was also supported through the ELCOD project which was implemented as a part of the INTERREG V Oberrhein/Rhin Supérieur program and was supported by the European Regional Development Fund (ERDF) and the co-financed project partners Region Grand Est in France and the countries of Baden-Württemberg and Rhineland-Palatinate. This project has also received funding from the European Union's Framework Programme for Research and Innovation Horizon 2020 (2014–2020) under the Marie Skłodowska-Curie Grant Agreement No. 643095. This ITN Research Project is supported by European Community H2020 Framework under the Grant Agreement No. 643095 (H2020-MSCA-INT-2014).

Acknowledgments: This study was supported by the founders aforementioned cited and by CNRS and University of Strasbourg.

Conflicts of Interest: The authors declare no conflict of interest.

References

1. Bruce, N.; Perez-Padilla, R.; Albalak, R.; Organization, W.H. The health effects of indoor air pollution exposure in developing countries. *World Health Organ.* **2002**, *78*, 1078–1092.
2. Buka, I.; Koranteng, S.; Osornio-Vargas, A.R. The effects of air pollution on the health of children. *Paediatr. Child Health* **2006**, *11*, 513–516.
3. Kampa, M.; Castanas, E. Human health effects of air pollution. *Environ. Pollut.* **2008**, *151*, 362–367. [[CrossRef](#)]
4. Esmaelnejad, F.; Hajizadeh, Y.; Pourzamani, H.; Amin, M. Monitoring of benzene, toluene, ethyl benzene, and xylene isomers emission from Shahreza gas stations in 2013. *Int. J. Environ. Health Eng.* **2015**, *4*, 17.
5. Li, J.; Xie, S.D.; Zeng, L.M.; Li, L.Y.; Li, Y.Q.; Wu, R.R. Characterization of ambient volatile organic compounds and their sources in Beijing, before, during, and after Asia-Pacific Economic Cooperation China 2014. *Atmos. Chem. Phys.* **2015**, *15*, 7945–7959. [[CrossRef](#)]
6. Madhoun, W.A.A.; Ramli, N.A.; Yahaya, A.S.; Yusuf, N.F.F.M.; Ghazali, N.A.; Sansuddin, N. Levels of benzene concentrations emitted from motor vehicles in various sites in Nibong Tebal, Malaysia. *Air Qual. Atmos. Health* **2011**, *4*, 103–109. [[CrossRef](#)]
7. Miri, M.; Rostami Aghdam Shendi, M.; Ghaffari, H.R.; Ebrahimi Aval, H.; Ahmadi, E.; Taban, E.; Gholizadeh, A.; Yazdani Aval, M.; Mohammadi, A.; Azari, A. Investigation of outdoor BTEX: Concentration, variations, sources, spatial distribution, and risk assessment. *Chemosphere* **2016**, *163*, 601–609. [[CrossRef](#)]

8. Campagnolo, D.; Saraga, D.E.; Cattaneo, A.; Spinazzè, A.; Mandin, C.; Mabilia, R.; Perreca, E.; Sakellaris, I.; Canha, N.; Mihucz, V.G.; et al. VOCs and aldehydes source identification in European office buildings—The OFFICAIR study. *Build. Environ.* **2017**, *115*, 18–24. [[CrossRef](#)]
9. Cheng, Y.-H.; Lin, C.-C.; Hsu, S.-C. Comparison of conventional and green building materials in respect of VOC emissions and ozone impact on secondary carbonyl emissions. *Build. Environ.* **2015**, *87*, 274–282. [[CrossRef](#)]
10. Martins, E.M.; de Sá Borba, P.F.; dos Santos, N.E.; dos Reis, P.T.B.; Silveira, R.S.; Corrêa, S.M. The relationship between solvent use and BTEX concentrations in occupational environments. *Environ. Monit. Assess.* **2016**, *188*, 608. [[CrossRef](#)]
11. Bari, M.A.; Kindziński, W.B.; Wheeler, A.J.; Héroux, M.-È.; Wallace, L.A. Source apportionment of indoor and outdoor volatile organic compounds at homes in Edmonton, Canada. *Build. Environ.* **2015**, *90*, 114–124. [[CrossRef](#)]
12. Romagnoli, P.; Balducci, C.; Perilli, M.; Vichi, F.; Imperiali, A.; Cecinato, A. Indoor air quality at life and work environments in Rome, Italy. *Environ. Sci. Pollut. Res. Int.* **2016**, *23*, 3503–3516. [[CrossRef](#)]
13. Ueno, Y.; Horiuchi, T.; Morimoto, T.; Niwa, O. Microfluidic Device for Airborne BTEX Detection. *Anal. Chem.* **2001**, *73*, 4688–4693. [[CrossRef](#)]
14. Hazrati, S.; Rostami, R.; Farjaminezhad, M.; Fazlzadeh, M. Preliminary assessment of BTEX concentrations in indoor air of residential buildings and atmospheric ambient air in Ardabil, Iran. *Atmos. Environ.* **2016**, *132*, 91–97. [[CrossRef](#)]
15. Kandyala, R.; Raghavendra, S.P.C.; Rajasekharan, S.T. Xylene: An overview of its health hazards and preventive measures. *J. Oral Maxillofac. Pathol. JOMFP* **2010**, *14*, 1–5. [[CrossRef](#)]
16. Rinsky, R.A.; Smith, A.B.; Hornung, R.; Filloon, T.G.; Young, R.J.; Okun, A.H.; Landrigan, P.J. Benzene and Leukemia. *N. Engl. J. Med.* **1987**, *316*, 1044–1050. [[CrossRef](#)]
17. Mandin, C.; Trantallidi, M.; Cattaneo, A.; Canha, N.; Mihucz, V.G.; Szigeti, T.; Mabilia, R.; Perreca, E.; Spinazzè, A.; Fossati, S.; et al. Assessment of indoor air quality in office buildings across Europe—The OFFICAIR study. *Sci. Total Environ.* **2017**, *579*, 169–178. [[CrossRef](#)]
18. Norbäck, D.; Hashim, J.H.; Hashim, Z.; Ali, F. Volatile organic compounds (VOC), formaldehyde and nitrogen dioxide (NO₂) in schools in Johor Bahru, Malaysia: Associations with rhinitis, ocular, throat and dermal symptoms, headache and fatigue. *Sci. Total Environ.* **2017**, *592*, 153–160. [[CrossRef](#)]
19. Xu, J.; Szyszkwicz, M.; Jovic, B.; Cakmak, S.; Austin, C.C.; Zhu, J. Estimation of indoor and outdoor ratios of selected volatile organic compounds in Canada. *Atmos. Environ.* **2016**, *141*, 523–531. [[CrossRef](#)]
20. Yurdakul, S.; Civan, M.; Özden, Ö.; Gaga, E.; Döğeroğlu, T.; Tuncel, G. Spatial variation of VOCs and inorganic pollutants in a university building. *Atmos. Pollut. Res.* **2017**, *8*, 1–12. [[CrossRef](#)]
21. Zhong, L.; Su, F.-C.; Batterman, S. Volatile Organic Compounds (VOCs) in Conventional and High Performance School Buildings in the U.S. *Int. J. Environ. Res. Public Health* **2017**, *14*, 100. [[CrossRef](#)]
22. Zampolli, S.; Elmi, I.; Mancarella, F.; Betti, P.; Dalcanale, E.; Cardinali, G.C.; Severi, M. Real-time monitoring of sub-ppb concentrations of aromatic volatiles with a MEMS-enabled miniaturized gas-chromatograph. *Sens. Actuators B Chem.* **2009**, *141*, 322–328. [[CrossRef](#)]
23. Skog, K.M.; Xiong, F.; Kawashima, H.; Doyle, E.; Soto, R.; Gentner, D.R. Compact, Automated, Inexpensive, and Field-Deployable Vacuum-Outlet Gas Chromatograph for Trace-Concentration Gas-Phase Organic Compounds. *Anal. Chem.* **2019**, *91*, 1318–1327. [[CrossRef](#)]
24. Nasreddine, R.; Person, V.; Serra, C.A.; Le Calvé, S. Development of a novel portable miniaturized GC for near real-time low level detection of BTEX. *Sens. Actuators B Chem.* **2016**, *224*, 159–169. [[CrossRef](#)]
25. Gregis, G.; Sanchez, J.-B.; Bezverkhyy, I.; Guy, W.; Berger, F.; Fierro, V.; Bellat, J.-P.; Celzard, A. Detection and quantification of lung cancer biomarkers by a micro-analytical device using a single metal oxide-based gas sensor. *Sens. Actuators B Chem.* **2018**, *255*, 391–400. [[CrossRef](#)]
26. Sun, J.; Xue, N.; Wang, W.; Wang, H.; Liu, C.; Ma, T.; Li, T. Compact Prototype GC-PID System integrated with Micro-PC and Micro GC Column. *J. Micromech. Microeng.* **2019**, *29*, 1–6. [[CrossRef](#)]
27. Sun, J.; Geng, Z.; Xue, N.; Liu, C.; Ma, T. A Mini-System Integrated with Metal-Oxide-Semiconductor Sensor and Micro-Packed Gas Chromatographic Column. *Micromachines* **2018**, *9*, 408. [[CrossRef](#)]

28. Wang, J.; Bryant-Genevier, J.; Nuñoovero, N.; Zhang, C.; Kraay, B.; Zhan, C.; Scholten, K.; Nidetz, R.; Buggaveeti, S.; Zellers, E.T. Compact prototype microfabricated gas chromatographic analyzer for autonomous determinations of VOC mixtures at typical workplace concentrations. *Microsyst. Nanoeng.* **2018**, *4*, 17101. [CrossRef]
29. Soo, J.-C.; Lee, E.G.; LeBouf, R.F.; Kashon, M.L.; Chisholm, W.; Harper, M. Evaluation of a portable gas chromatograph with photoionization detector under variations of VOC concentration, temperature, and relative humidity. *J. Occup. Environ. Hyg.* **2018**, *15*, 351–360. [CrossRef]
30. Trzciński, J.W.; Pinalli, R.; Riboni, N.; Pedrini, A.; Bianchi, F.; Zampolli, S.; Elmi, I.; Massera, C.; Ugozzoli, F.; Dalcanale, E. In Search of the Ultimate Benzene Sensor: The EtQxBox Solution. *ACS Sens.* **2017**, *2*, 590–598. [CrossRef]
31. Lee, J.; Zhou, M.; Zhu, H.; Nidetz, R.; Kurabayashi, K.; Fan, X. Fully Automated Portable Comprehensive 2-Dimensional Gas Chromatography Device. Available online: <http://pubs.acs.org/doi/abs/10.1021/acs.analchem.6b03000> (accessed on 14 January 2019).
32. Wang, J.; Nuñoovero, N.; Lin, Z.; Nidetz, R.; Buggaveeti, S.; Zhan, C.; Kurabayashi, K.; Steinecker, W.H.; Zellers, E.T. A Wearable MEMS Gas Chromatograph for Multi-Vapor Determinations. *Procedia Eng.* **2016**, *168*, 1398–1401. [CrossRef]
33. Tzeng, T.-H.; Kuo, C.-Y.; Wang, S.-Y.; Huang, P.-K.; Huang, Y.-M.; Huang, Y.-M.; Hsieh, W.-C.; Huang, Y.-J.; Kuo, P.-H.; Yu, S.-A.; et al. A Portable Micro Gas Chromatography System for Lung Cancer Associated Volatile Organic Compound Detection. *IEEE J. Solid-State Circuits* **2016**, *51*, 259–272.
34. Qin, Y.; Gianchandani, Y.B. A fully electronic microfabricated gas chromatograph with complementary capacitive detectors for indoor pollutants. *Microsyst. Nanoeng.* **2016**, *2*, 15049. [CrossRef]
35. Garg, A.; Akbar, M.; Vejerano, E.; Narayanan, S.; Nazhandali, L.; Marr, L.C.; Agah, M. Zebra GC: A mini gas chromatography system for trace-level determination of hazardous air pollutants. *Sens. Actuators B Chem.* **2015**, *212*, 145–154. [CrossRef]
36. Nasreddine, R.; Person, V.; Serra, C.A.; Schoemaeker, C.; Le Calvé, S. Portable novel micro-device for BTEX real-time monitoring: Assessment during a field campaign in a low consumption energy junior high school classroom. *Atmos. Environ.* **2016**, *126*, 211–217. [CrossRef]
37. Lara-Ibeas, I.; Trocquet, C.; Nasreddine, R.; Andrikopoulou, C.; Person, V.; Cormerais, B.; Englaro, S.; Le Calvé, S. BTEX near real-time monitoring in two primary schools in La Rochelle, France. *Air Qual. Atmos. Health* **2018**, *11*, 1091–1107. [CrossRef]
38. Camara, E.H.M.; Breuil, P.; Briand, D.; de Rooij, N.F.; Pijolat, C. A micro gas preconcentrator with improved performance for pollution monitoring and explosives detection. *Anal. Chim. Acta* **2011**, *688*, 175–182. [CrossRef]
39. Dettmer, K.; Engewald, W. Adsorbent materials commonly used in air analysis for adsorptive enrichment and thermal desorption of volatile organic compounds. *Anal. Bioanal. Chem.* **2002**, *373*, 490–500. [CrossRef]
40. Leidinger, M.; Rieger, M.; Sauerwald, T.; Alépée, C.; Schütze, A. Integrated pre-concentrator gas sensor microsystem for ppb level benzene detection. *Sens. Actuators B Chem.* **2016**, *236*, 988–996. [CrossRef]
41. Vellingiri, K.; Kumar, P.; Deep, A.; Kim, K.-H. Metal-organic frameworks for the adsorption of gaseous toluene under ambient temperature and pressure. *Chem. Eng. J.* **2017**, *307*, 1116–1126. [CrossRef]



© 2019 by the authors. Licensee MDPI, Basel, Switzerland. This article is an open access article distributed under the terms and conditions of the Creative Commons Attribution (CC BY) license (<http://creativecommons.org/licenses/by/4.0/>).

4.2 MEMS Preconcentrator (MMP)

Although the results obtained with MAP exhibited a significant enhancement of the GC prototype performance in terms of sensitivity, the high energy consumption required by the preconcentrator and the peak widening were some aspects to be improved. Our objective was to develop a very sensitive portable analyser, which implies that the energy consumption should be minimal to enable its use powered by battery. To achieve this goal, this new preconcentrator version was fabricated by using microfabrication techniques. The deployment of these techniques allowed fabricating a miniaturised device with an integrated powerful and low-consuming heating system. This device weighted 0.86 g, which resulted in not only a reduction in the energy consumption, but also a much faster temperature ramp and a more rapid cooling due to the decrease of the thermal inertia compared to MAP. The fabricated prototypes are displayed in Figure 4-12. The results obtained in the performed flow simulations, as well as the optimization of the heating system and the performances of the final device are presented below.

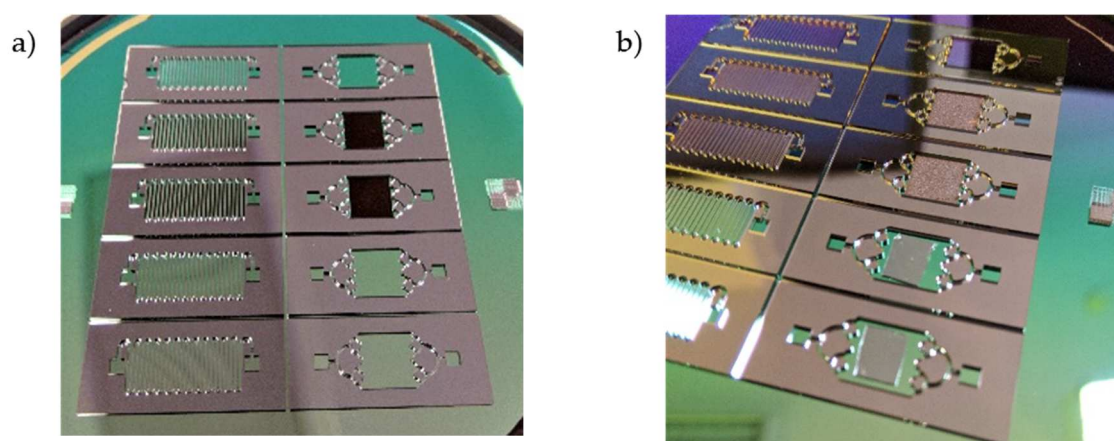


Figure 4-12. MMP Prototypes a) empty and filled with porous gold (black shape) and b) filled with PDMS and porous gold

4.2.1 Flow Simulations

As explained in chapter 2 section 2.2.2.2.2, flow simulations were conducted using flow rates of 2.5 and 5 mL/min to evaluate the flow distribution and pressure drop in the proposed configurations in the absence of granular adsorbent. Ideally, if simulations data are accurate, they should not change by increasing the density of the mesh in the model. As observed in Table 4-2, the refinement of the mesh influences very slightly the results obtained for pressure drop and maximum velocity, indicating

that the values calculated using M1 were accurate in all cases excepted at a flow rate of 2.5 mL/min in the square configuration.

Table 4-2. Pressure drop and maximum velocity obtained at different flow rates in absence of granular adsorbent

Configuration	Flow rate (mL/min)	Mesh	Pressure drop (Pa)	Maximum velocity (m/s)
Serpentine	5	1	104.7	0.899
		2	107.4	0.910
	2.5	1	50.3	0.439
		2	51.6	0.442
Square	5	1	10.0	0.825
		2	9.3	0.840
	2.5	1	4.6	0.421
		2	6.1	0.333

In all cases, the serpentine configuration exhibited much higher pressure drop than the square counterpart due to the higher length and shorter width of the channel. This behaviour is illustrated in Figure 4-13a. In square configuration the pressure variation is far lower and pressure is almost constant along the microfluidic cavity (Figure 4-13b). Both pressure drops were almost negligible and, thus, they were considered satisfactory for our application. At this point, it is important to note that these pressure drops were estimated for an empty device and, thus, they are expected to increase when the adsorbent is added. However, these results can be a relatively acceptable estimation for the pressure drop when thin film adsorbent ($\sim 100 \mu\text{m}$) is deposited inside the device. On the contrary, this value can totally change if a granular adsorbent is employed. In this case, more complex simulations considering the adsorbent particle size and porosity are needed to estimate the pressure drop. However, these simulations are not within the scope of this work.

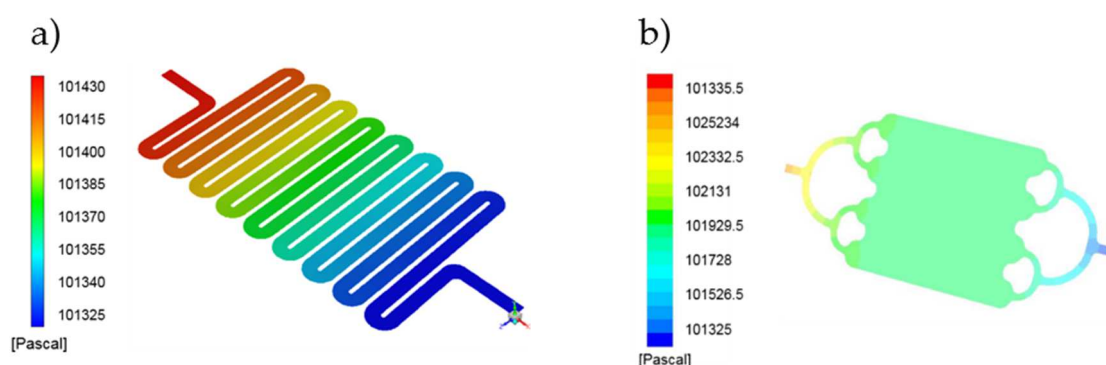


Figure 4-13. Pressure cartographies obtained after a CFD simulation for a flow rate of 5 mL/min in (a) serpentine and (b) square designs

The velocity distribution in both designs was also simulated, and the results obtained for the velocity field in the XZ plan of symmetry are presented in Figure 4-14. As can be observed in the figure, the velocity field was much more homogeneous in the square configuration where, as it was previously observed in pressure distribution, velocity was almost constant over the whole microfluidic cavity. Consequently, in a XZ plan, a uniform residence time distribution of the molecules is expected for this configuration.

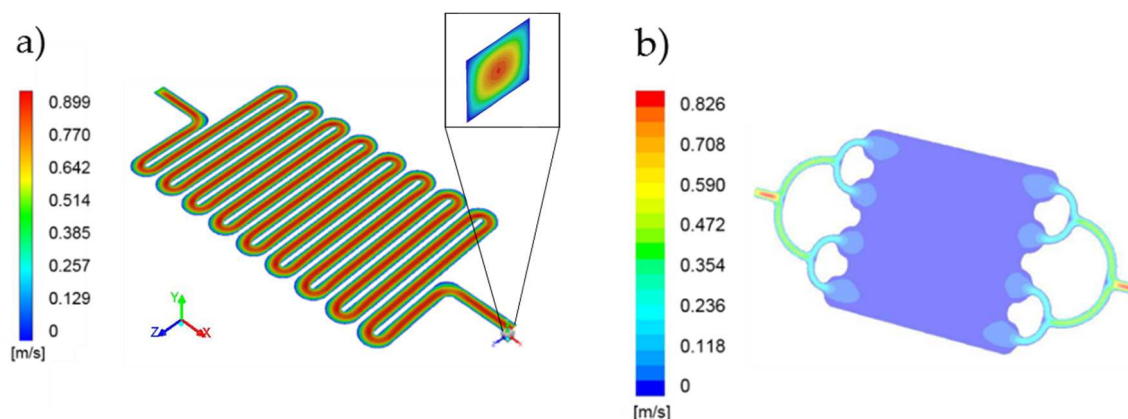


Figure 4-14. Velocity distribution in serpentine (a) and square (b) configurations obtained after a CFD simulation for a flow rate of 5 mL/min

In both designs, velocity significantly varies across the channel depth in the Y-direction, naturally reaching its maximum value in the symmetry plane. In the case of serpentine design, however, this gradient is also very significant along the width, due to the small width of the channel. In order to illustrate this variation, a plot of velocity along the X-axis is represented in Figure 4-15a, in which the velocity is equal to 0.83 m/s at the points near the centre of the channel whereas it is zero at the walls. Similar effects are naturally observed along the Y-axis as it is shown in the inset of Figure 4-15b but in this direction gradients are similar for both designs. The gradients of velocity in the XZ plane, however, certainly lead to a less homogeneous residence time distribution of the molecules compared to the square design, where the velocity gradient is only significant along the depth, in the Y-direction.

Finally, pressure drops in both designs were considered satisfactory and the two proposed configurations were fabricated. Even if the velocity distribution was not optimal in the case of serpentine, this device was fabricated to evaluate the influence of this parameter on the preconcentrator performance that can provide useful recommendations for future device design.

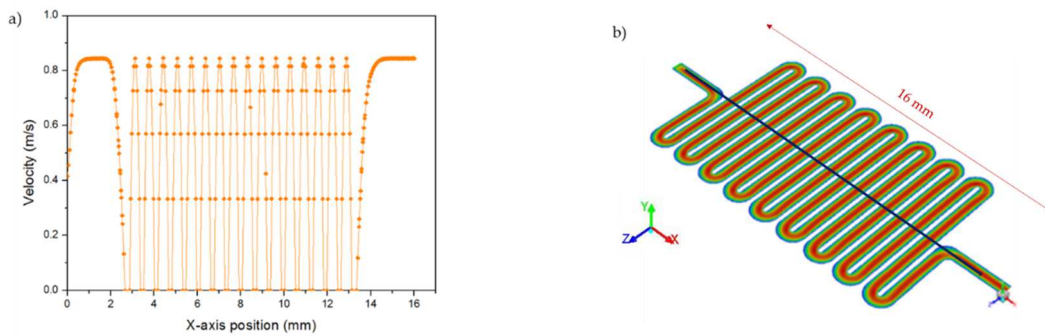


Figure 4-15. a) Velocity variation along the blue line (X-axis) shown in b)

4.2.2 Temperature tests

Prior to the final device, two sets of heating systems were fabricated and tested to find the optimal features for the design. Results of this optimization are detailed in this section.

- First set of heating systems

The first set of heating systems was made by metal deposition of silver and titanium in Strasbourg nanotechnology facilities (ST nano Platform). The masks presented in section 2.2.2.2 were employed in the microfabrication process. As shown in Figure 4-16, four different configurations were proposed and each one was fabricated in duplicate.

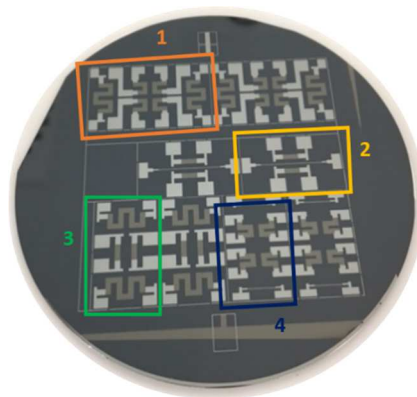


Figure 4-16. Silicon wafer prior to dicing containing the first set of heating systems. Four different designs (1, 2, 3 and 4) were fabricated in duplicate.

Designs 1 and 4 were composed of four heating resistances, so that eight wires were required to provide the energy supply. After some attempts, it was impossible to connect so many wires in such a small device with the techniques available. Therefore, only designs with two heating resistances

(designs 2 and 3) could be tested. During the experiments, a type K thermocouple (RS Pro, France) was employed to measure the temperature. The temperature ramps obtained at different voltage supplies are presented in Figure 4-17a and Figure 4-17b.

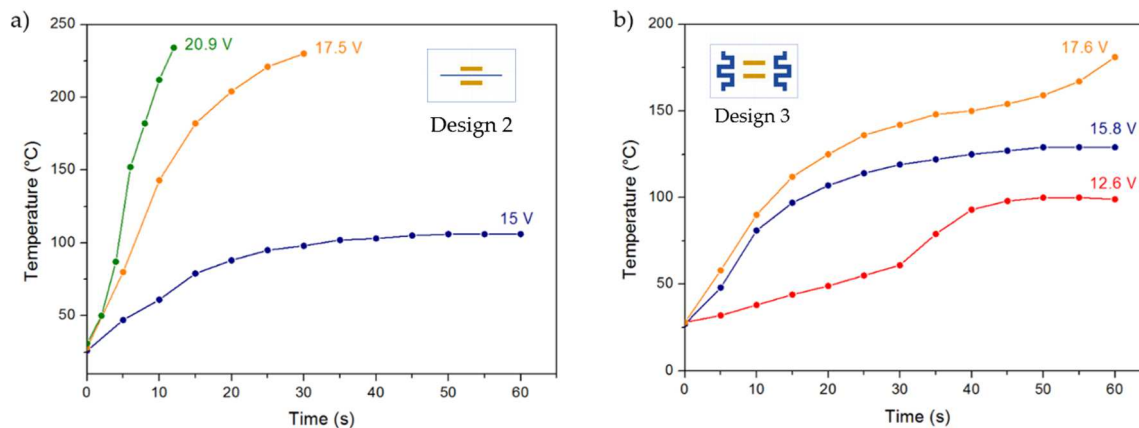


Figure 4-17. Temperature curves obtained with heating system designs (a) 2 and (b) 3 with silver-titanium resistances

As can be observed from the plots, even if the silver layer geometry was the same in both designs and, thus, the same heating power was delivered, design 2 was found more efficient than design 3. In the second configuration, 230 °C were reached in 30 s by using a voltage of 17.5 V whereas in the third configuration, 181 °C were achieved in 60 s at almost the same voltage (17.6 V). The only difference between these two prototypes was the connection to the power supply. The first idea was indeed to weld the wires to the electrodes, but it was not possible because the welding could not join both pieces, so a silver conductive paste was employed instead. Since the application method of this glue was completely manual, it was impossible to connect the wires in exactly the same way. It was observed that the better the wires were attached, the better the electrical transfer and the faster the heating, so that the difference between both systems was probably due to the superior electrical conductivity on the electrodes. Furthermore, the paste enabled to attach the wires, but they were detached easily when applying high voltages or the temperature reached more than 230 °C. Even if this glue was thermally resistant, a considerable deterioration was observed on the glue and on the electrodes, where the silver layers gradually became dark grey when exposed to high temperatures. For this reason, during the experiments, the temperature was limited to this value even though the initially desired performance was to heat the device up to 250 °C in 20 s.

This objective of reaching 230 °C was achieved in 30 s by using design 2 at a voltage of 17.5 V. Actually, the heating systems were conceived to operate at 12 V instead of 17.5 V but some parameters were not

considered in the calculations. First, as explained before, the connection between the wires and the electrodes play a crucial role in the performance of the heating system. These connections generated additional resistance to the current flow that were not considered in the calculations, and that is probably one of the reasons why there was a considerable difference between the voltage employed for the calculations and the real voltage required. The other reason that could explain this difference could be the resistivity; in fact, this value is different in a bulk material or a thin film due to the differences in their microstructures [4]. As the resistivity of 100 μm thin film of titanium was not found in the literature, the resistivity employed in the calculations was the bulk resistivity of titanium ($41.7 \times 10^{-8} \Omega \text{ m}$ [5]). In general, the resistivity of thin films is higher than the one of the bulk materials, so that the estimated resistance of the layer was underestimated implying lower heating power.

- *Second set of heating systems*

In order to improve the electrical connections, a second set of heating systems was fabricated using the same designs but this time gold, instead of silver, was employed for the electrodes. Gold has higher resistivity ($2.0510 \times 10^{-8} \Omega \text{ m}$ at 273 K [5]) than silver ($1.467 \times 10^{-8} \Omega \text{ m}$ at 273 K) but it is less susceptible to be damaged and oxidized.

In this set, similarly to silver-titanium resistances, designs 1 and 4 could not be tested and, in addition, design 2 was damaged during the fabrication process and it was not possible to be tested. Therefore, only design 3 was tested at different voltage supplies. As it is obvious from Figure 4-18, the temperature ramps achieved with this system need much less voltage to achieve similar performance. Using this system, indeed, 205 $^{\circ}\text{C}$ were reached in 22 s by using 12 V. Considering that temperatures higher than 230 $^{\circ}\text{C}$ may damage the conductive paste, it can be considered as an acceptable result and, therefore, gold was selected to fabricate the electrodes in the final device.

Taking into consideration the results obtained with this heating system, a correction factor was calculated by comparing the expected and the real performances of the heating resistances. This factor was applied in the calculations to design the heating system of the final prototype.

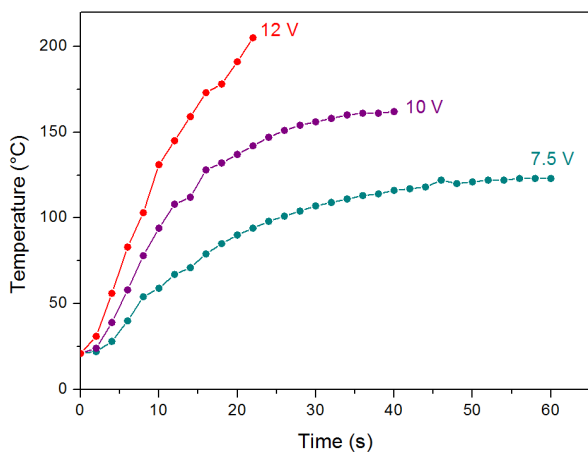


Figure 4-18. Temperature plots obtained with the heating system, design 3, with gold-titanium resistances (nominal current of 1.5 A)

- Final heating system of MMP

The heating system integrated in MMP was composed of two resistances as in the design presented in the previous paragraph. Since the performance of these resistances was characterized, the same geometry was maintained in the final prototype. In this version, the heating resistances were placed at opposing ends of the device to limit temperature gradients along the chip. Furthermore, the thickness of the titanium layer was increased to 300 μm enabling theoretically to reach 225 $^{\circ}\text{C}$ in 10 s at a voltage of 12 V. The final heating systems of the 10 chips fabricated at LAAS nanotechnology facilities (Toulouse, France) are presented in Figure 4-19a.

As in the other versions, electrical wires were connected to the electrodes by using silver conductive glue. In Figure 4-19b, the results of the increase of temperature in MMP using different voltage supplies are presented. This design perfectly meets the objectives set out during the designing step, since 220 $^{\circ}\text{C}$ were experimentally achieved in 10 s using a voltage supply of 12 V and current of 1 A. This fast temperature ramp guarantees a flash desorption and represents a considerable enhancement compared to the previous preconcentrator version (MAP) that achieved 200 $^{\circ}\text{C}$ in 70 s.

Unfortunately, during the heating tests some of the chips cracked. The difference in the thermal expansion of the SU-8 resin and the glass caused the glass cracking when the temperature changed rapidly, i.e. when heating or cooling. Due to this critical defect in the design of the device, MMP was unable to stand temperatures higher than 100 $^{\circ}\text{C}$. After the cracks, the chips were leaking and, therefore, in most cases, the preconcentration cycle was impossible to perform.

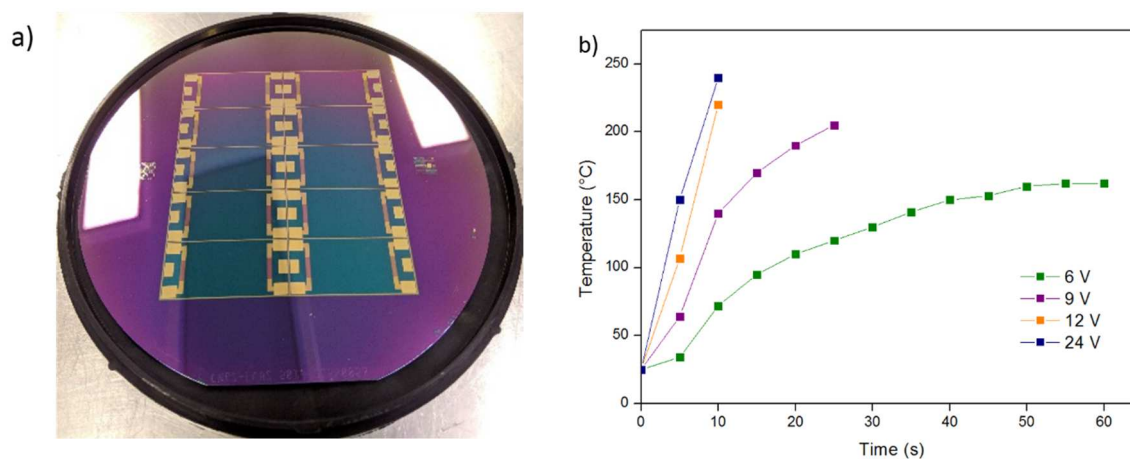


Figure 4-19. a) Bottom part of silicon wafer containing the heating system of 10 chips; b) Temperature increase at different levels of voltage supply with current intensity fixed at 1 A.

4.2.3 Preconcentration tests

Despite a great number of devices broken during the heating tests, one preconcentrator with square microfluidic cavity filled with porous gold could be tested for adsorption at room temperature and desorption at moderate temperature.

In order to carry out the tests, a housing was fabricated by 3D printing. It consists of two plastics parts joined by four screws. At the top of the housing (see Figure 4-20a), two holes served to hold the fluidic connectors (Nanoport®, IDEX Health and Science, LLC; USA). Inside the housing, at the bottom part, two metal rods were placed to be in contact with the electrodes of the heating resistances. The contact between the rods and the electrodes was reinforced by using silver conductive paste and wires were used to connect these rods to the voltage supply. The holes displayed in Figure 4-20b served to pass through the wires and place the temperature sensor employed in the tests.

The integration of the electrical and fluidic connectors in MEMS-based devices was not easy, and many efforts were devoted to the development of this housing. Finally, this configuration allowed to have a gas-tight device that could be electrically supplied. However, the assembly was not robust and after some tests leakage was observed, or the heating resistances were disconnected from the housing, making impossible the use of the device. Nevertheless, despite all the problems encountered, some preconcentration tests could be done.

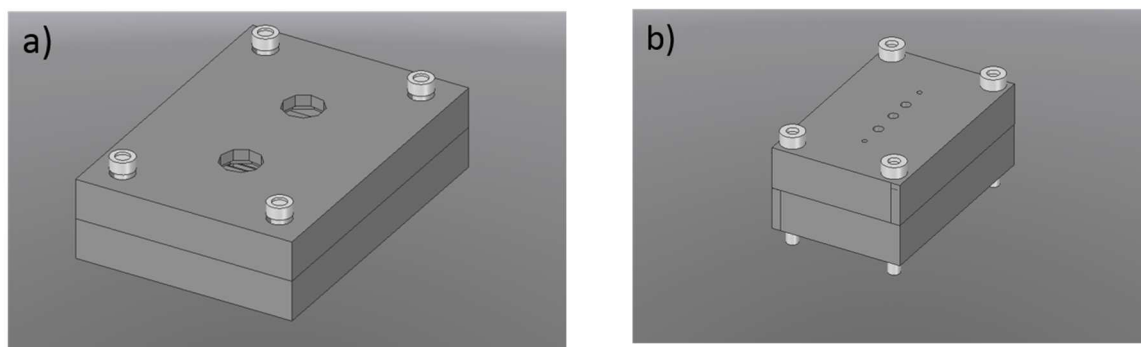


Figure 4-20. Housing of MMP integrating fluidic and electrical connections: (a) top and (b) bottom views

Prior to these tests, the device was conditioned at 80 °C for 30 min under a nitrogen flow of 10 NmL/min. After that, two injections of 100 ppb BTEX samples of 50 mL at a flow rate of 5 NmL/min were performed. The device was gently heated to 80 °C in 60 s to limit the risk of cracks and this temperature was kept for 20 s. In these two samples, BTEX peaks were almost indistinguishable from the baseline of the chromatogram suggesting that a minimal amount of BTEX was trapped on the porous gold. Therefore, the sampling volume was increased to 300 mL. The obtained chromatogram is presented in Figure 4-21. In order to compare the performance with the previous preconcentrator version, preconcentration factors were calculated for each compound by dividing the peak area obtained using the preconcentrator and the peak area obtained using the sampling loop. Preconcentration factors were calculated to be 1.2, 2.1, 4.0, 3.5 and 2.3 for benzene, toluene, ethylbenzene, m/p-xylenes and o-xylene, respectively, indicating a very limited performance in terms of preconcentration. This poor result was probably due to limitations in the adsorption and desorption of BTEX. On the one hand, one of the drawbacks of thin film adsorbents is the low adsorption capacity since the amount of material deposited is, in general, very small compared to the granular counterparts [6]. Furthermore, the contact surface between the sample and the adsorbent is limited to the surface of the layer, reducing the probability of the molecules to be adsorbed during the sampling. On the other hand, due to the defects in designing, the temperature could not be increased to typical desorption temperatures of 200 – 300 °C that have been used in other studies [7] and, thus, it is probable that the molecules were not all released at the temperature employed during the test, resulting in very low preconcentration factors.

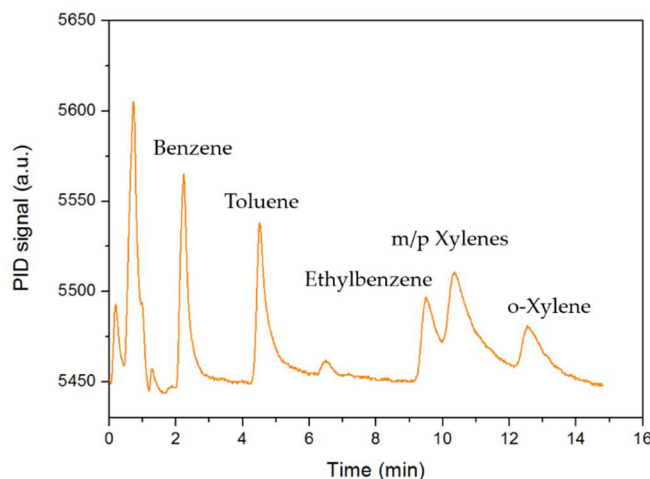


Figure 4-21. Chromatogram obtained for the injection of 100 ppb BTEX sample of 300 mL in MMP

Finally, it was decided to completely change the design of the device and use other simpler and cost-effective techniques. Microfabrication techniques can be very interesting, but they are expensive and time-consuming. Thus, no more versions were designed using these techniques because of the extremely long time between the order and the delivery of the prototypes that risked to exceed the estimated time for this doctoral research work. Additionally, the packaging and integration of MEMS devices was not evident; in fact, the extremely reduced size of these devices limits the choice of connectors and very few electrical and fluidic appropriate connections are commercially available. For all these reasons, another preconcentrator version was fabricated by combining alternative techniques such as micromilling and 3D printing.

4.3 Mixed Aluminium/Polymer Preconcentrator (MAAP)

Due to the drawbacks of the microfabrication process concerning its costs, delivery time and complexity of design and the problems issued from the integration of these microdevices within the whole system, it was decided to simplify the design as well as to reduce the fabrication cost by using techniques available in our laboratory. Consequently, most of the parts of this new prototype were fabricated at ICPEES by using micromilling and 3D printing.

MAAP design was based on MAP, but the metallic parts were reduced to a single board containing the microfluidic cavity, decreasing significantly the mass to be heated to 3.31 g and, thus, the power required for a fast desorption. All other parts were made of insulating materials like PEEK or ABS

that are relatively temperature resistant polymers (melting temperature of 345 and 100 °C, respectively) limiting the heat losses from the metallic board (see chapter 2 for the detailed description). The results obtained with this prototype in terms of heating and preconcentration performances are detailed below.

4.3.1 Temperature tests

In this prototype, the heating system was composed of a ceramic with a resistance of 10 Ω . Initially, the device was tested using 12 V and 3 A of nominal power supply and it reached 200 °C in 140 s. This result was surprisingly slow considering that most parts of the prototype were thermal insulators (see Figure 2-22). Afterwards, the contact surface between the resistance and the housing was reduced by modifying the design of the PEEK board. Instead of a flat surface, the piece had two edges where the aluminium board was supported, hence, limiting the heat transfer to the polymer part. As it is displayed in Figure 4-22, the new configuration led to a considerable improvement in the heating performance and the device was able to reach 200 °C in 48 s at the same power supply as the previous test ($U = 12$ V and $I = 3$ A). Even if this result was far from ideal, it was an improvement compared to MAP and, therefore, it was expected to obtain higher resolution desorption peaks than with this initial version.

On the other hand, the cooling process was also evaluated. Obviously, in this case, the use of insulating materials was disadvantageous since they prevent the heat evacuation from the metal board. This hypothesis was confirmed by the results obtained during the cooling tests. Device cooling was carried out by natural convection cooling and the temperature decrease is illustrated in Figure 4-22. As expected, natural cooling was slow, taking almost 13 min to return from 200 °C to the room temperature. In this version, the fan was not integrated in the housing to facilitate the heat removal, but an external fan was employed to speed up the cooling process during the preconcentration tests.

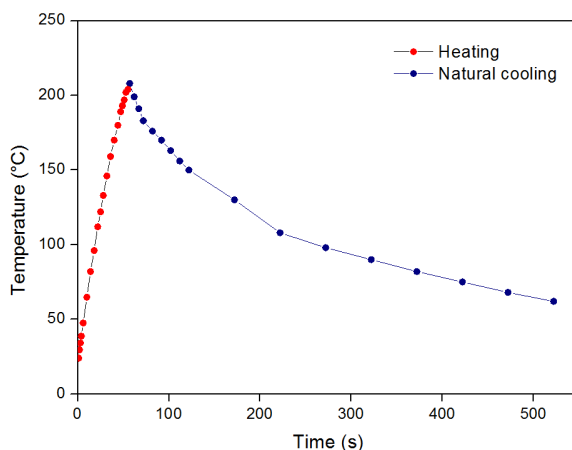


Figure 4-22. Heating performance at a power supply of 12 V and 3 A (red) and natural cooling (blue) of MAP

4.3.2 Preconcentration tests

Once the heating system was validated, the device was filled with 5.2 mg of Carboxpack® B. Since Carboxpack® B is a reference material in VOC sampling and has been widely used in VOC preconcentration, the following PC versions were all filled with this adsorbent.

To assess the preconcentration performance of MAP, a series of 100 ppb BTEX samples of different volumes were injected: 10, 20, 40 and 100 mL. The resulting peak areas for each compound were plotted versus the injected volumes. As can be observed in Figure 4-23, the signal provided when MAAP was used was significantly higher than the one obtained using the 200 μ L sampling loop of the GC prototype confirming that the preconcentration was efficient.

To quantify the preconcentration of the sample, peaks were integrated, and the resulting areas were plotted versus the injected volumes as shown in Figure 4-24a and Figure 4-24b. It is obvious from the correlation coefficients that there was a highly linear relationship between the peak area and the sampling volume in all the range of volumes, except for benzene. In fact, the peak area of benzene for the 100 mL sample was almost the same as the area obtained for the 40 mL sample. This phenomenon could be explained by the fact that the eVx PID detector employed in this study is designed to operate in a concentration range from 0 to 2 ppm, and out of that range, the response is not linear. Therefore, it is possible that this limit was exceeded when a 100 mL sample was injected and, thus, the detector response was not linear at this concentration level.

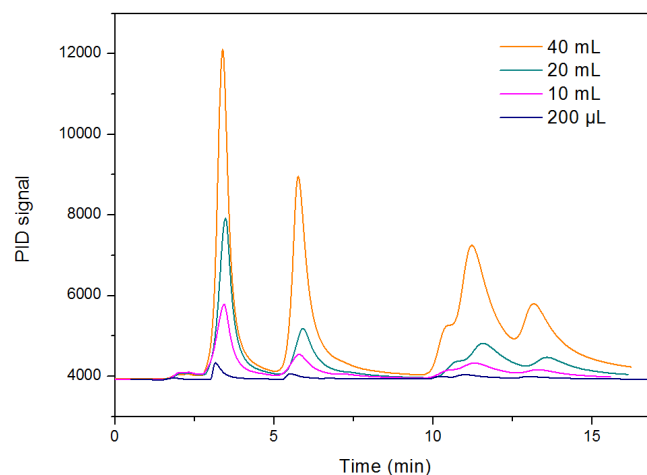


Figure 4-23. Chromatograms obtained by injecting different volumes of 100 ppb BTEX mixtures in MAP (100 mL sample was not included for reasons of scale)

Furthermore, the detector gives a different response for each analyte, being more intense in the case of benzene. That is why this fact could explain that the non-linearity was observed only for benzene peak area. As the benzene peak area for 100 mL sample was a complete outlier, this point was not considered in the linear fitting.

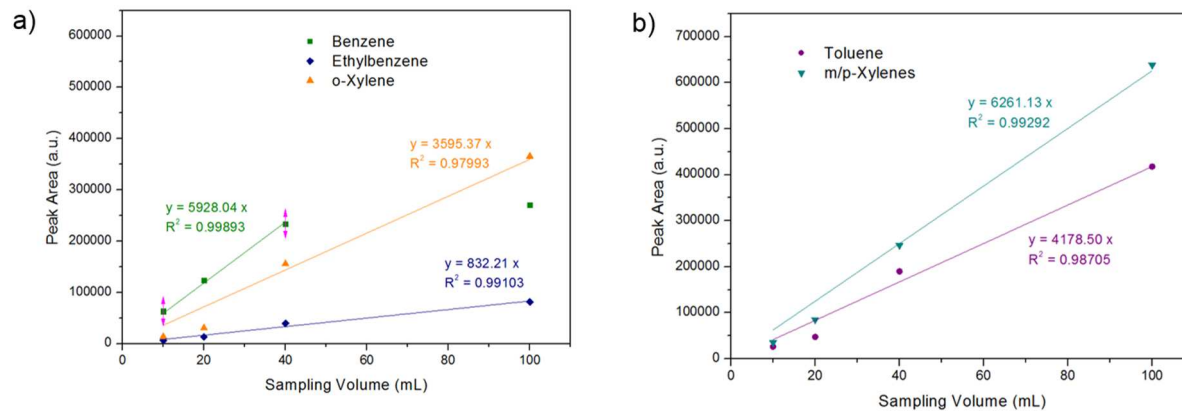


Figure 4-24. (a) Benzene, ethylbenzene and o-xylene and (b) toluene and m/p-xylenes peak areas obtained after injecting 100 ppb samples of different volumes.

Unfortunately, after some adsorption-desorption cycles, the plastic parts of the design started to be damaged and leakage was observed. PEEK is a relatively good thermal insulator with a thermal conductivity of the order of 0.3 W/m/K. However, if this material is continuously exposed to heat, the heat is of course slowly transferred to and stored inside the material. Therefore, after some cycles, the heat finally reached ABS, which is not thermally resistant, causing the degradation of the polymer

and, thus, screw-loosening. Since ABS housing was deteriorated, the entire structure was not properly hold resulting in leakage from the microfluidic cavity. Some attempts were made to solve this problem by adding supplementary screws or increasing the thickness of the PEEK parts but when the device was operated under working conditions employed in the GC system (pressure = 4 bar, temperature = 200 °C) for a long time, leakage was observed once again. Consequently, the injections could not be replicated. Because of these problems, another preconcentration version was designed.

For this new version, the main objectives were to decrease even more the device size to achieve a faster temperature increase, and to simplify the whole structure by having less separated parts.

4.4 Micro Aluminium Preconcentrator (μ AP1)

In order to drastically minimize the size of the preconcentrator by keeping an affordable cost, μ AP1 was conceived. The design of this preconcentrator was simple: a 1/8" copper tube was filled with 5.0 mg of CarboPack B and two plugs of glass wool were placed on each side of the tube to hold the solid adsorbent (see Figure 2-23). An aluminium cube with a 1/8" hole, fitting perfectly with the outer diameter of the copper tube, was located at the same level of the adsorbent and the ceramic resistances were placed on two opposite sides of this cube (see chapter 2 for the detailed description). The main results obtained with this prototype are presented below.

4.4.1 Temperature tests

Firstly, the heating performance of this device was tested at the maximum operating conditions of resistive elements, i.e. a nominal voltage of 28 V and a current of 3 A. The temperature ramp obtained during this experiment is represented by the red line in Figure 4-25. In this device, 250 °C were reached in 62 s, a faster temperature ramp than the previous PC versions except the one fabricated by microfabrication techniques. This implies a considerable decrease on the desorption time and thus a shorter injection. Furthermore, cooling down to the room temperature was achieved by natural convection in 8 min, and this time was decreased to only 150 s when using an external fan. Therefore, this version met the requirement concerning the cooling time fixed to less than 5 min. This short cooling time enables to keep the time for an analysis cycle in the range 10-15 min and, thus, monitor the BTEX concentration in near real-time.

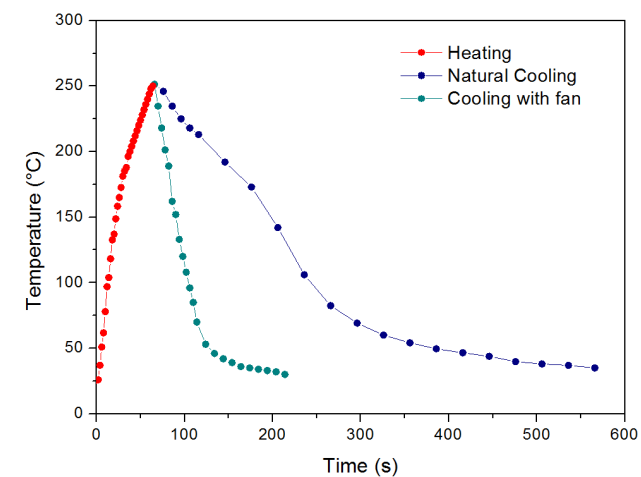


Figure 4-25. Temperature ramps obtained with μ AP1: heating at nominal voltage of 20 V and current of 2.15 A (red), natural cooling (dark blue) and cooling with fan (light blue)

Additionally, μ AP1 exhibited an acceptable heating performance allowing to reach the target temperature in less than 1 min. Taking into account the manufacturing price, these results were considered very satisfactory in terms of heating-cooling duration, so that preconcentration tests were conducted.

4.4.2 Preconcentration tests

Once the leakage tests were performed successfully, a series of experiments were performed by injecting 100 ppb BTEX samples of different volumes (5 – 100 mL) in duplicate to assess the preconcentration ability of μ AP1. The calculated mean peak area was plotted versus sample volume as shown in Figure 4-26. As can be seen, there is a linear relation between peak area and sample volume; however, the coefficients of determination, R^2 , are not very satisfactory (see Table 4-3), especially for ethylbenzene ($R^2 = 0.96$) and xylenes ($R^2 = 0.93$ - 0.96). Moreover, the calculated slopes for the curves do not follow the expected order (benzene > toluene ~ m/p-xylenes > ethylbenzene > o-xylene) since the m/p-xylenes one is the highest and the one of ethylbenzene the lowest. These results can be explained by the inaccurate integration of peaks. As evidenced from Figure 4-27, ethylbenzene and xylenes peaks are too coeluted to allow an accurate integration, leading to major errors in the peak area estimation. Even benzene and toluene peaks seem to be slightly coeluted, suggesting a too long desorption.

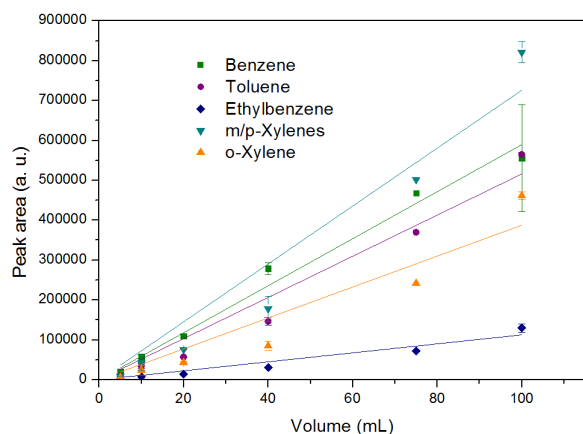


Figure 4-26. Mean peak areas obtained for different sample volumes. BTEX concentration = 100 ppb, flow rate = 5 NmL/min, desorption temperature = 250 °C, injection time = 75 s. Vertical error bars give the standard deviation of duplicates.

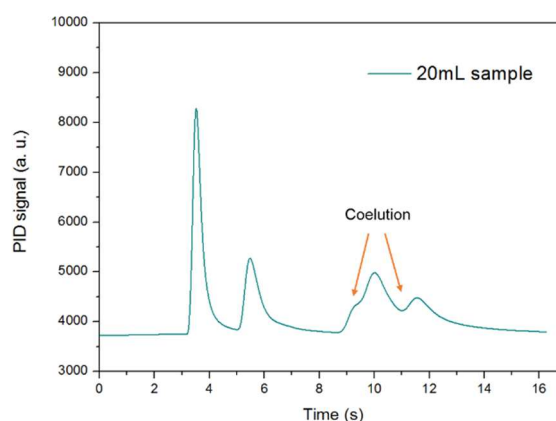


Figure 4-27. Chromatogram of 20 mL sample using μ AP1. BTEX concentration = 100 ppb, flow rate = 5 NmL/min, desorption temperature = 250 °C, injection time = 75 s.

Indeed, this peak broadening was produced by a slow heating ramp that prevented the desorption in a short pulse. In fact, despite the 250 °C measured in the aluminium cube, a great temperature difference could be expected between this latter and the adsorbent bed. Even if the copper tube fitted perfectly into the hole of the metallic cube and some thermal paste was added in between, the heat transfer between layers of different materials was supposed to be not optimal. To overcome this relatively poor thermal transfer, another more compact PC version, called μ AP2, was then designed.

Table 4-3. Equations from the volume calibration curves

Compound	Equation	R ²
Benzene	$y = 5896.8x$	0.99249
Toluene	$y = 5162.9x$	0.97770
Ethylbenzene	$y = 1126.4x$	0.96209
m/p-Xylenes	$y = 7262.4x$	0.96275
o-Xylene	$y = 3877.2x$	0.93909

4.5 Micro Aluminium Preconcentrator (μ AP2)

μ AP1 version met many requirements concerning fabrication costs and preconcentration ability; however, the design consisting of two independent parts resulted in a poor heat transfer. In this context, a single-piece PC version was designed integrating the cylindrical part into the cube (see Figure 2-24). In this way, the whole structure was made of aluminium and heat transfer between the

heating resistance and the adsorbent bed was greatly enhanced. The experimental results obtained with this PC version, called μ AP2, are presented below.

4.5.1 Temperature tests

The heating performance was tested in the same operating conditions as the previous version (a nominal voltage of 28 V and a current of 3 A). A thermocouple was located at one side of the central part of μ AP2, as shown in Figure 4-28. As can be observed, 330°C were reached in 68 s demonstrating a considerably improvement in heat transfer. Taking into account the results of the last version, 330°C were fixed as the desired desorption temperature to ensure a suitable temperature in the adsorbent bed and thus, a sharp desorption pulse. Once 330°C were reached, cooling down to the room temperature was performed in 10 min by using a fan (see Figure 4-28). During the experiments, an external fan was temporarily placed close to μ AP2 to speed up the tests but, as evidenced from the figure, it was not very efficient. Indeed, the design of a housing integrating two fans is still in progress; therefore, for the moment, the tests had to be conducted in these conditions. Similarly to the previous version, a substantial reduction of cooling time is expected when the PC will be integrated in the housing allowing to reach room temperature in less than 5 min, the maximum cooling time established in the objectives.

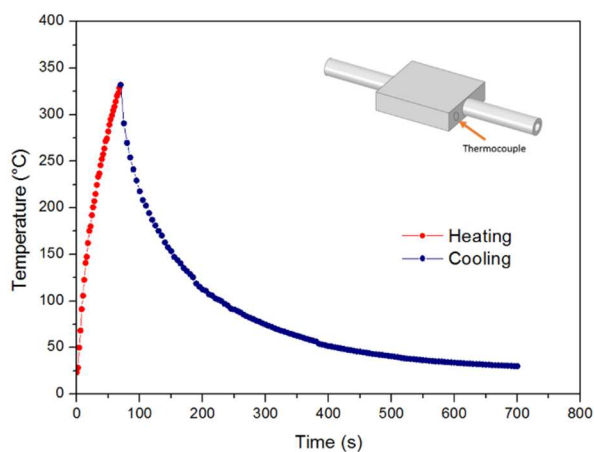


Figure 4-28. Temperature variation in a heating-cooling cycle in μ AP2 with and external fan was temporarily placed close to the device.

4.5.2 Preconcentration tests

Once the heating system performance was validated, the preconcentration ability of this new device was evaluated using two different adsorbents: SBA-16 and Carbo-pack® B. It is important to note that,

for this version, all the experiments were conducted using a commercial analyser (μ BTEX-1, In'Air Solutions) instead of the laboratory prototype. The use of the commercial analyser enabled an improved control over the injection time and oven temperature, thus increasing the repeatability of the results. The experimental conditions employed in all tests performed in this section are presented in Table 4-4.

Table 4-4. Summary of the experimental conditions employed in a series of tests with μ AP2.

Parameter	Setpoint	Parameter	Setpoint
Temperature GC column ($^{\circ}$ C)	45	Sampling flow rate (NmL/min)	5
Pressure GC column (bar)	4.2	Adsorption temperature ($^{\circ}$ C)	R.T.
Injection time (s)	75	Desorption temperature ($^{\circ}$ C)	330 $^{\circ}$ C

R.T.: room temperature.

4.5.2.1 SBA-16

Since SBA-16 exhibited significant adsorption ability for BTEX (see Chapter 5), it was interesting to test its suitability for gas analysis applications. For that, μ AP2 was filled with 5 mg of SBA-16 and conditioned at 220 $^{\circ}$ C under a 20 NmL/min nitrogen flow overnight to eliminate the possible adsorbed molecules. Then, it was mounted in the GC system and a series of 20 mL samples of different concentrations ranging from 2 to 50 ppb were injected in triplicate. The peak areas obtained were plotted against the injected concentration and the resulting calibration curves are presented in Figure 4-29. As can be seen, there is a linear relationship between the peak area and the concentration in all cases, as confirmed by the coefficients of determination $R^2 \geq 0.97$ (see Table 4-5). These coefficients are considerably better than those obtained for μ AP1 but not as good as with the MAP version, especially for toluene. The calibration slopes decrease with the volatility of the compound, being considerably steeper for the most volatile compounds, i.e. benzene and toluene, compared to the less volatile ones (ethylbenzene and xylenes), as expected. Between injections, a blank was performed to verify the complete desorption of BTEX. These tests showed that less than 1 % of residuals were observed in those blanks, confirming a quantitative desorption of BTEX for 20 mL samples in the range 2 – 50 ppb. Anyway, a cleaning step was performed between each analysis to ensure that μ AP2 was perfectly clean before the next sampling/analysis cycle.

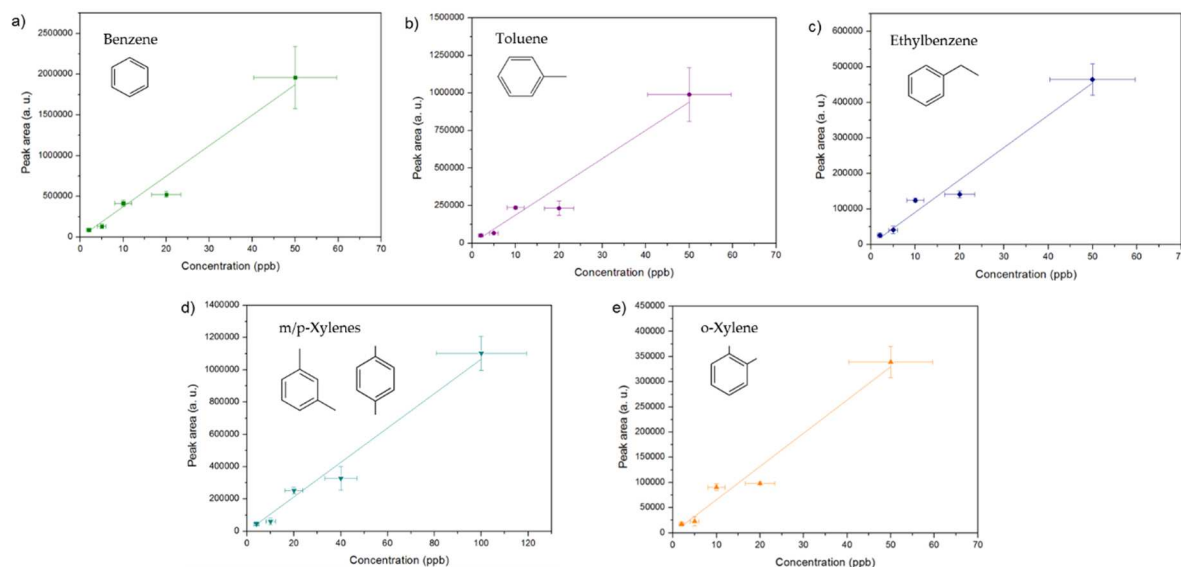


Figure 4-29. Calibration curves of benzene (a), toluene (b), ethylbenzene (c), m/p-xylenes (d) and o-xylene (e) using μ AP2 filled with SBA-16. Sample volume = 20 mL, sampling flow rate = 5 NmL/min, desorption temperature = 330 °C, injection time = 75 s. Horizontal error bars are the errors on the generated concentrations whereas the vertical ones represent the standard deviation of triplicates.

Detection and quantification limits were calculated from a signal-to-noise ratio of 3 and 10, respectively, from the lowest injected concentration, i.e. 2 ppb. As shown in Table 4-5, detection and quantification limits of the order of a few hundred ppt can be achieved for all compounds using a sample volume of only 20 mL. By increasing the sampling time, larger volumes can be sampled, thus reaching even lower detection and quantification limits.

Table 4-5. Performances obtained for the GC prototype integrating μ AP2 filled with SBA-16

Compound	Calibration Equation	R ²	LOD (ppb)	LOQ (ppb)
Benzene	$y = 37442.6 x$	0.9818	0.016	0.054
Toluene	$y = 18797.5 x$	0.96994	0.027	0.091
Ethylbenzene	$y = 9098.4 x$	0.98541	0.076	0.252
m/p Xylenes	$y = 10667.8 x$	0.98678	0.099	0.329
o-Xylene	$y = 6599.2 x$	0.98159	0.120	0.400

LOD: limit of detection; LOQ: limit of quantification.

To verify the linearity of the detector response for larger volumes, 10 ppb BTEX samples of different volumes ranging from 20 to 80 mL were injected. Similarly to the previous tests, the mean of the obtained peak areas was plotted against the sample volume (see Figure 4-30).

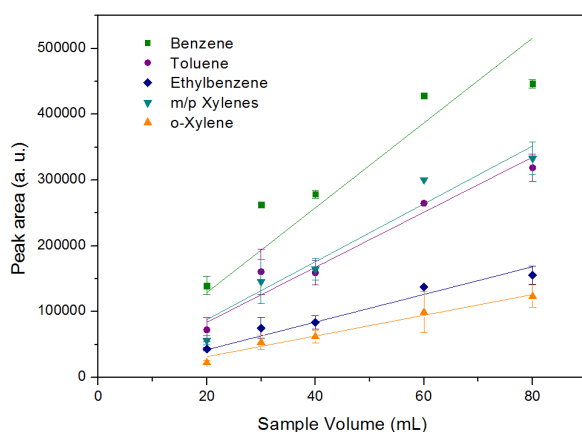


Figure 4-30. Mean peak areas obtained for the different sample volume injected in μ AP2 filled with SBA-16. BTEX concentration = 10 ppb, sampling flow rate = 5 NmL/min, desorption temperature = 330 °C, injection time = 75 s. Vertical error bars represent the standard deviation of duplicates.

Table 4-6. Data from calibration (volume) obtained for the GC prototype integrating μ AP2 filled with SBA-16

Compound	Equation	R ²
Benzene	$y = 6449.98 x$	0.9730
Toluene	$y = 4187.04 x$	0.9897
Ethylbenzene	$y = 2103.96 x$	0.9904
m/p-Xylenes	$y = 4398.35 x$	0.9851
o-Xylene	$y = 1575.68 x$	0.9943

As observed in Figure 4-30, peak area increases linearly with the injected volume. Determination coefficients are satisfactory except for benzene (see Table 4-6) where $R^2 = 0.973$. Indeed, a relatively high dispersion was observed in the peak areas obtained for this compound. Additionally, at the beginning of this series of tests a considerable decrease in the intensity of the peaks was observed compared to the concentration, especially for benzene. Indeed, in the previous series of tests, a 20 ppb sample of 20 mL yielded a peak area of ~500 000 a.u. whereas, in the last experiments, for a 10 ppb sample of 40 mL (sample with an equivalent amount of BTEX) a peak area of ~275 000 a.u. was observed. It is known from the literature that PID detectors have a non-negligible drift [8] but this huge intensity decrease cannot be only attributed to the detector. Therefore, it appears to be associated to a decrease in the adsorption-desorption ability of SBA-16 after some heating-cooling cycles. Since this material has not been previously used for gas analysis, there is no available data on regeneration after adsorption-desorption cycles. Hence, a priori, this material seems to be not highly suitable for gas analysis applications and further investigations should be conducted to elucidate the causes of such adsorption-desorption performance decrease.

Therefore, to achieve a very satisfactory and lasting adsorption-desorption performance, μ AP2 was filled with the reference material Carboxen[®] B, which is known to maintain its adsorption-desorption performance after a large number of cycles [9].

4.5.2.2 Carbo-pack® B

μ AP2 was then filled with 5 mg of Carbo-pack® B and conditioned at 220 °C under a 20 NmL/min nitrogen flow overnight. Afterwards, it was connected to the GC system to perform the preconcentration tests.

GC calibration as a function of gaseous concentrations

Calibration of the GC prototype integrating μ AP2 was conducted by injecting a series of 20 mL samples of different concentrations ranging from 2 to 50 ppb in triplicate. A chromatogram of a 50 mL BTEX sample of 20 ppb is displayed in Figure 4-31. As observed, BTEX peaks are well-defined and much less peak broadening is observed compared with the previous PC version (μ AP1). This improvement in peak shape is due to the faster temperature ramp that allows the desorption of analytes in less time, thus producing a narrower peak compared to the previous version. The mean peak areas of the analysed samples were plotted against the injected concentration and the resulting calibration curves as shown in Figure 4-32. The peak areas increase linearly with the injected concentration for all the compounds. Determination coefficients $R^2 \geq 0.99$ (see Table 4-7) show a considerably improvement of the linearity of the results compared to all previous PC versions.

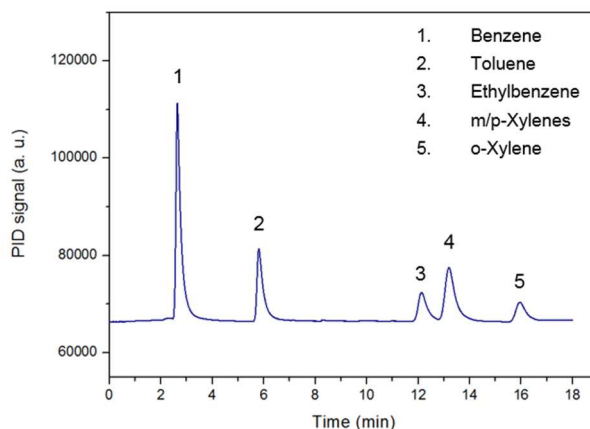


Figure 4-31. Chromatogram of BTEX obtained with μ AP2-GC-PID. $V_{\text{sample}} = 50 \text{ mL}$, $C_{\text{BTEX}} = 20 \text{ ppb}$, desorption temperature = 330 °C, injection time = 75 s.

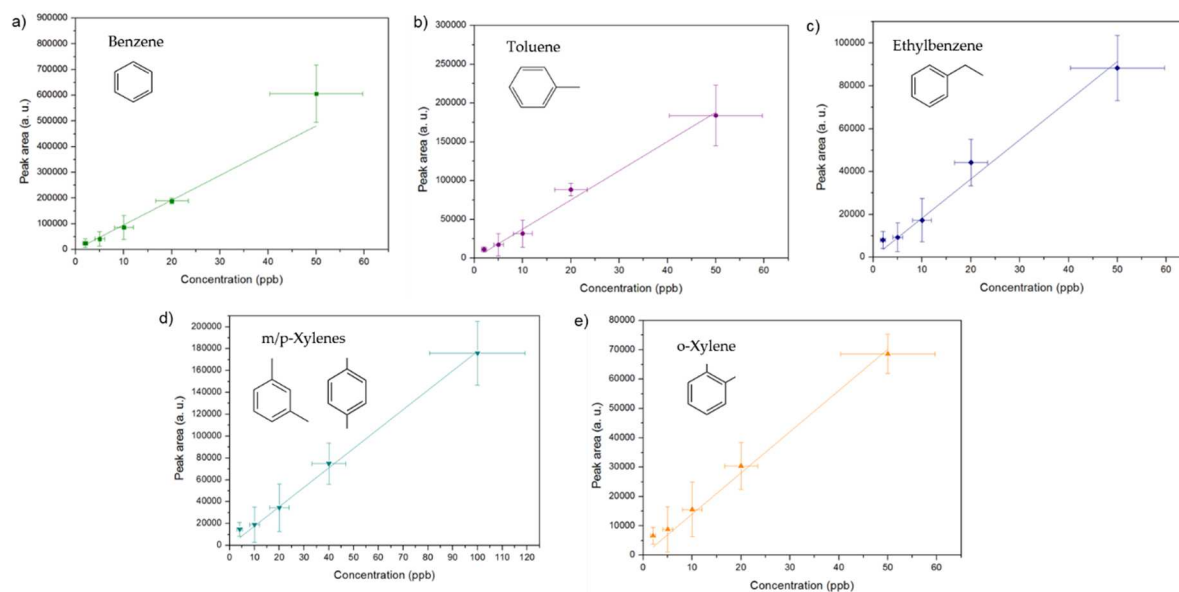


Figure 4-32. Calibration curves of benzene (a), toluene (b), ethylbenzene (c), m/p-xylenes (d) and o-xylene (e) using μ AP2 filled with Carboxpack® B. Sample volume = 20 mL, sampling flow rate = 5 NmL/min, desorption temperature = 330 °C, injection time = 75 s. Horizontal error bars are the errors on the generated concentrations whereas the vertical ones represent the standard deviation of triplicates.

As expected, calibration slopes decrease with the volatility of the compound, being considerably steeper for the most volatile compounds, i.e. benzene and toluene. Between injections, a cleaning step consisting of rising the temperature from 250 to 350 °C five times was performed to ensure the complete desorption of BTEX before the next analysis (more details on the residuals analysis are given below). It should be noted that this was done manually but could be automated and driven by the software in the future, when this preconcentrator will be integrated into the industrial device.

Detection and quantification limits of the GC system were calculated from a signal-to-noise ratio of 3 and 10, respectively, from the lowest injected concentration, i.e. 2 ppb. Detection limits are in the hundreds of ppt order with only 20 mL of sample for all compounds whereas quantification limits exceeded the ppb in the case of ethylbenzene and xylenes (see Table 4-7). It is important to note that this extraordinary sensitivity meets the requirements of the indoor air quality French legislation that establishes a benzene threshold value of 0.6 ppb in public buildings.

Table 4-7. Performances obtained for the GC prototype integrating μ AP2 filled with Carboxpack® B

Compound	Calibration Equation	R ²	LOD (ppb)	LOQ (ppb)
Benzene	$y = 9618.8 x$	0.9940	0.057	0.191
Toluene	$y = 3761.5 x$	0.9930	0.150	0.499
Ethylbenzene	$y = 1828.7 x$	0.9891	0.368	1.226
m/p Xylenes	$y = 1776.2 x$	0.9974	0.396	1.319
o-Xylene	$y = 1403.7 x$	0.9941	0.418	1.393

GC calibration as a function of sample volume

As in previous preconcentrator versions, GC linearity was evaluated when varying the injected sample volume from 5 to 50 mL for a fixed gaseous BTEX concentration of 20 ppb in duplicates. Mean peak areas obtained are plotted versus the sample volume as illustrated in Figure 4-33. Peak area increases perfectly linearly with the sample volume for all species, as highlighted by the calculated determination coefficients $R^2 \geq 0.99$ (see Table 4-8).

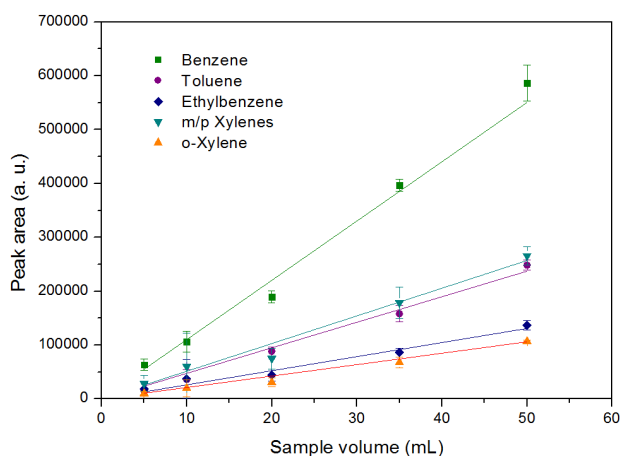


Table 4-8. Equation and determination coefficients obtained in sample volume variation tests.

Compound	Equation	R ²
Benzene	$y = 11009.7 x$	0.9930
Toluene	$y = 4743.3 x$	0.9942
Ethylbenzene	$y = 2616.3 x$	0.9940
m/p-Xylenes	$y = 5139.6 x$	0.9896
o-Xylene	$y = 2120.1 x$	0.9978

Figure 4-33. Mean peak areas vs the sample volume injected in μ AP2 filled with Carboxpack® B. BTEX concentration = 20 ppb, sampling flow rate = 5 NmL/min, desorption temperature = 330 °C, injection time = 75 s. Vertical error bars represent the standard deviation of duplicates

During the series of sample volume variation tests, the residual amount of BTEX inside the preconcentrator adsorbent was evaluated after each analysis by performing a blank right after desorption. Similar residuals percentage was observed after the injection of different sample volumes, indicating that the residuals were proportional to the injected BTEX amount. These average

percentages were found to be 1.6, 2.6, 9.2, 7.1 and 6.8 % for benzene, toluene, ethylbenzene, m/p-xylenes and o-xylene, respectively, being higher for the less volatile compounds since, logically, they need higher temperature to be fully desorbed. Again, this issue could be improved by increasing the desorption time with a precise control of the target desorption temperature.

Repeatability and reproducibility

As any analytical device, repeatability and reproducibility of the GC should be evaluated to ensure reliable results in the long run. To assess repeatability, seven 20 mL samples containing 20 ppb of BTEX were consecutively analysed in the same day using the same experimental conditions (desorption temperature = 330 °C, injection time = 75 s). Between two consecutive samples, a cleaning step was conducted. Peak areas and retention time obtained are presented in Figure 4-34a and Figure 4-34b, respectively. Slight variability was observed in peak areas of different samples whereas the variation in the retention time of different samples was almost negligible. Relative standard deviation (% RSD) of peak area was calculated to be 4.9, 3.7, 4.3, 8.0 and 5.6 % for benzene, toluene, ethylbenzene, m/p – xylenes and o-xylene, respectively. These values below 10 % for all the compounds demonstrate that the analyses performed with the GC prototype integrating μ AP2 were highly repeatable even in manual injection mode. The corresponding % RSD was also calculated for the obtained retention times, being equal to 0.1 % for all the analytes. Due to the inadequate isolation of the GC oven, retention times are often shifted in portable GC; however, this parameter appears to be very stable in our prototype GC. In this prototype version integrating μ AP2, both sample injection and data acquisition were automatized; therefore, although the sampling time was manually controlled, these obtained results were very satisfactory and the measurements repeatability in terms of peak area and retention time was considerably improved compared to the previous PC version, i.e. MAP.

Reproducibility was evaluated according to the following method: three 20 mL samples containing 20 ppb of BTEX were consecutively analysed over three different days. Figure 4-35a and Figure 4-35b displayed the results obtained for the peak areas and the retention time of each sample, respectively. Peak areas obtained in three different days were comparable and % RSD was calculated to be 3.2, 10.1, 21.8, 13.8, 13.9 % for benzene, toluene, ethylbenzene, m/p – xylenes and o-xylene, respectively. The variation obtained in this case was obviously higher than the one obtained for the analysis performed in a single day; however, all the % RSD, except the one of ethylbenzene, were less than 15 %.

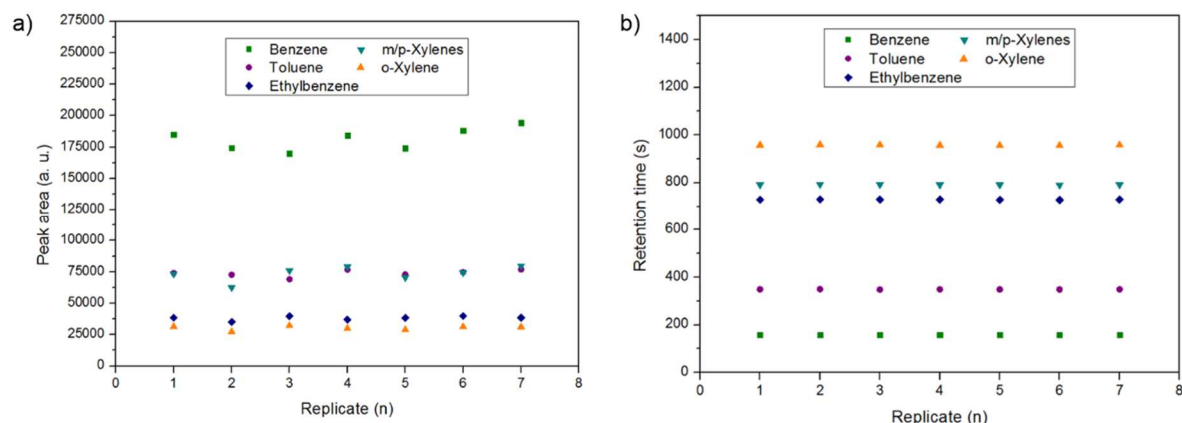


Figure 4-34. Repeatability test results obtained for 7 consecutive BTEX samples analysed in the same day: (a) peak areas and (b) retention time. $V = 20$ mL, $C = 20$ ppb

Higher % RSD were also observed for the retention time compared to the previous test, being 1.0, 0.7, 0.5, 0.5 and 0.4 % for benzene, toluene, ethylbenzene, m/p – xylenes and o-xylene, respectively. Despite this small increase, the variation observed in the retention times was minimal and the values can be considered as highly reproducible over time.

The results obtained in the repeatability and reproducibility tests highlight the stability of the measurements conducted with this prototype over time, even with relatively low BTEX concentrations of 20 ppb.

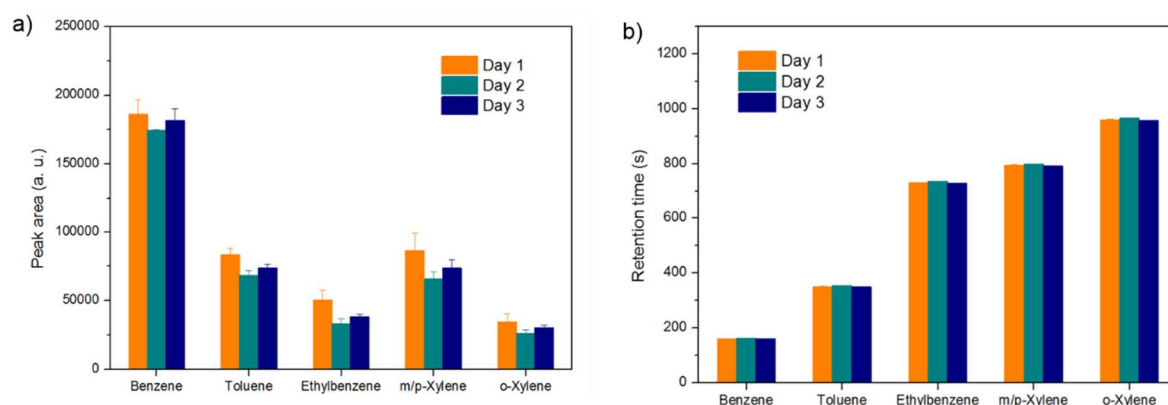


Figure 4-35. Reproducibility test results obtained for 3 BTEX samples analysed over three different days: (a) peak areas and (b) retention time. $V = 20$ mL, $C = 20$ ppb, desorption temperature = 330 °C, injection time = 75 s. Vertical error bars represent the standard deviation of the triplicates.

4.6 Comparison with existing instruments

In the last years, great efforts have been made to develop real-time sensitive miniaturized gas chromatographs for a broad spectrum of applications. Most of them include a preconcentration device enabling to achieve very low detection limits. These devices differ in their features (dimensions, manufacturing materials, used adsorbents, power consumption, etc.) and their analytical performances. However, a simple and direct comparison between them in terms of preconcentration performance is not possible since these results depends on other elements such as the type of detector. Therefore, a comparison between the miniaturized GC existing in the literature with a special focus on preconcentrator features is presented in this section.

Table 4-9 summarizes the most significant miniaturized GC with integrated PC developed for VOC quantification in the last decade. All devices presented are highly portable (weight < 5 kg) and have relatively small dimensions, which makes them suitable for on-site measurements. PID is the most commonly employed detector for VOC quantification in μ GC. Indeed, this detector is easy to integrate in the GC system and is more selective and sensitive than most of metal oxide and chemical sensors. However, these sensors are generally less expensive than PID and enable to detect a larger screening of organic compounds.

These miniaturized GC were conceived for a wide variety of applications requiring very sensitive instruments such as environmental monitoring [10], [11], early cancer diagnosis [12], [13] or food quality control [14]. Therefore, all GC systems include a preconcentrator that improves the detector sensitivity to tens or hundreds of ppb in the case of sensors and, to ppb or hundreds of ppt in the case of PID detectors. These preconcentrators are very different from one another. After the fabrication of the first microsystem including a micromachined PC in 1999 [15], great efforts were addressed to develop MEMS-based preconcentrators devices. MEMS technology offered indeed the possibility to create miniaturized devices exhibiting great performance with very low power consumption. Therefore, in the last decades, most of these preconcentrators were made from silicon and glass [11], [16], [17], materials typically used in electronics. However, there are several drawbacks associated with the use of MEMS-based devices. For example, the materials usually employed are fragile and expensive and there are almost not commercially available fluidic and/or electrical connections, leading frequently to leakage problems. In addition, the fabrication process needs suitable facilities (cleanroom) and high level of expertise that results very often in an expensive and time-consuming process. Lately, new fabrication technologies have been developed and those already existing have been improved to reduce the fabrication costs. Laser etching technology, milling or metal 3D printing techniques provide the possibility to use more robust materials such as copper [18], stainless steel [19]

or aluminium (this work). Furthermore, standard fluidic connections can be usually integrated since these materials can be micromachined with traditional techniques and their dimensions are generally larger than the MEMS-based counterparts, ensuring better gas tightness. However, these dimensions involve higher thermal mass, leading to high power requirements and slow temperature ramps compared to MEMS-based PC. As illustrated in Table 4-9, power consumption in MEMS PC varies between 1 and 16 W whereas in metal PC it ranges from 10 to 70 W, except MAP (210 W) that was the first PC developed by our team. Despite the considerable difference of energy consumption required, the consumption of metal PC is still compatible with their integration in battery-powered devices. Nevertheless, the autonomy will be significantly reduced. In this regard, MEMS-based PC are preferred in applications where great autonomy is required. Due to the greater thermal mass, heating rates in metal PC (0.25 – 5.5 °C/s) are very low compared to MEMS-based PC (25 – 314 °C/s), while a fast temperature ramp is preferred to generate sharp chromatographic peaks. However, in this study, it was demonstrated that well-defined peaks could be achieved with a heating rate of 5.5 °C/s.

Considering the LOD achieved with these miniaturized GC, it appears that this feature depends more on the type of detector itself than on the preconcentration unit employed, since the instruments having PID detectors are much more sensitive.

Until the present work, only three instruments had LOD in the ppt range. Zampolli *et al.* [11] proposed a miniaturized GC-PID with a PC filled of an innovative quinoxaline-based adsorbent. LOD down to 0.1 ppb for benzene was reached; however, 55 min of sampling were needed to collect the 2750 mL required to achieve such a sensitivity. This very long sampling time prevents to establish concentration time profiles that can help to determine occupational exposure or identify pollutant sources [8]. Shorter sampling time of 20 min was employed by Skog *et al.* [20] to collect a sample of 4 L and achieve LOD from 2 to 11 ppt for BTEX. Sun *et al.* [21] reported LOD below 1 ppb with a sampling time of only 1 min but the sample volume employed was not mentioned. Since LOD strongly depends on the sample volume, the sensitivity of each system was calculated for the lowest detectable mass of analyte for better comparison. Indeed, it is not necessarily relevant to reason in terms of sensitivity because, as we have shown, the areas of the chromatographic peaks increase linearly when the volume of the sample increases, indicating that this volume can be easily modulated. A relatively small sample volume will provide better temporal resolution while a large volume will provide a lower LOD. To calculate sensitivity, the lowest LOD achieved for each method was multiplied by the

sample volume. For example, in our case, benzene LOD ($0.18 \mu\text{g m}^{-3}$ at $P = 1 \text{ atm}$ and $T = 25 \text{ }^\circ\text{C}$) was multiplied by the sample volume ($2 \times 10^{-5} \text{ m}^3$), giving a sensitivity of 3.6 pg.

To our knowledge, the analytical system developed in this work showed the highest sensitivity reported to date for BTEX analysis exhibited by a portable GC. This instrument achieved LOD from 0.06 to 0.4 ppb ($0.18 - 1.82 \mu\text{g m}^{-3}$ at $P = 1 \text{ atm}$ and $T = 25 \text{ }^\circ\text{C}$) using a sample volume of only 20 mL ($2 \times 10^{-5} \text{ m}^3$). It means that the lowest detectable amount with this compact GC was 3.6, 11.3, 32.0, 34.4 and 36.3 pg for benzene, toluene, ethylbenzene, m/p-xylenes and o-xylene, respectively.

The portable GC developed by Zampolli *et al.* [11] had a low benzene LOD of 0.1 ppb ($0.32 \mu\text{g m}^{-3}$ at $P = 1 \text{ atm}$ and $T = 25 \text{ }^\circ\text{C}$) but it required a large sample volume of 2750 mL ($2.75 \times 10^{-3} \text{ m}^3$) resulting in a sensitivity 878.5 pg for this compound. A lower detection limit was found with the compact GC developed by Skog *et al.* [20] where a benzene LOD of 0.01 ppb ($0.03 \mu\text{g m}^{-3}$ at $P = 1 \text{ atm}$ and $T = 25 \text{ }^\circ\text{C}$) was achieved with a 4 L ($4 \times 10^{-3} \text{ m}^3$) sample giving a sensitivity of 140.6 pg. Therefore, the sensitivity obtained with the portable GC developed in this work differed by 2 - 3 orders of magnitude from most of the values reported in the literature, even those reporting very low detection limits. For the analysis of BTEX, only the first preconcentrator version (MAP) developed in this work yielded similar results [8]. Despite of the outstanding benzene sensitivity of 6.4 pg achieved with MAP, this new version has improved this feature by a ratio of 1.8. Han *et al.* [22] reported a sensitivity comparable for the analysis of isoprene. However, this sensitivity does not correspond to a portable GC since the developed preconcentrator in this case was connected to a benchtop GC-FID. These results suggest that the performance achieved by our prototype in terms of sensitivity is close to those typically exhibited by benchtop instruments.

Another crucial aspect of analytical performance is the stability of the measurements. Among the studies presented in Table 4-9, repeatability was only evaluated for 10 instruments [12], [14], [16]–[18], [20], [21], [23], [24]. Despite the importance of repeatability, in some cases this parameter was characterized only graphically by showing the peak shape of triplicates [14], [18], which is not useful for comparison purposes. In other studies, repeatability was characterized in terms of % RSD, but the different experimental conditions employed, such as sample concentration and number of replicates, make difficult an objective comparison. Sun *et al.* [21] evaluate the repeatability by consecutively analysing 8 benzene samples at a concentration of 1 ppm. They found a very low % RSD of 0.42 % for the peak area. However, this high repeatability may decrease when stability is evaluated in more realistic conditions such as low ppb concentrations. Garg *et al.* [16] evaluated the repeatability of the

Table 4-9. Summary of miniaturized GC with integrated PC developed in the last years.

Ref.	Size (cm ³)	Weight (kg)	Analysis time (min)	Sample Volume (mL)	Preconcentrator					Target compounds	Det.	LOD (ppb)	Sensitivity (pg)
					<i>l</i> (mm) × <i>d</i> (μm) × <i>w</i> (mm)	Material	Adsorbent	Heating system	Power cons. (W) / heating rate (°C/s)				
This work	32 × 29 × 14	~ 5	19	20	Cavity 4.6 × 350 × 7.4	Al	C-B 5 mg	Ceramic heaters	~70 / 4.8	BTEX	PID	0.06-0.4 (BTEX)	3.6 ^b
PEMM-2 [17]	20 × 15 × 9	~2.1	3	5	2 Cavities (V~4.7 μL)	Si-glass	C-B 2.0 mg C-X 2.3 mg	Ti/Pt	1 / -	9 VOC	μCR array	16-600 (150 ^b)	2396 ^b
SS PC* [19]	-	-	-	10	Tube with micro-pillars 38.68 (l) × 7.69 mm (o.d.)	S.S.	HayeSep D 119.9 mg	NiCr wire	14.6 / 1.8	Toluene	MS	-	-
MAP [23]	32 × 29 × 14	~ 5	19	20	Manifold-shaped cavity 4.6 × 350 × 7.4	Al	Basolite C300 5.8 mg	Cartridge	210 / 2.5	BTEX	PID	0.1-1.6 (BTEX)	6.4 ^b
GC-PID [20]	31 × 30 × 20	32	~35	4000	Tube 0.165 cm i.d.	-	ResSil-B 75 mg	-	-	34 VOC	PID	0.002 - 0.011 (BTEX)	140.6 ^b
MGP* [22]	-	-	~6	18	Manifold-shaped with 4 μchannels 12.6 × 2.5 mm × 16	Copper	C-X 20 mg	Ceramic heater	10.14 / 5.5	Isoprene	FID	0.016	0.8
Ceramic PC [14]	-	-	~50	200	Manifold shaped cavity 61 × 5.5 mm × 23 mm	Ceramic	C-SII 1.187 g	Tungsten	18 / 0.25	Ethylene	EC	25	5736
GC-MOS [12]	n. d.	n. d.	9	250	Cavity with micro-pillars 10 × 400 × 5	Si-glass	Zeolite DaY ~13 μm	-	-	4 VOC	MOS	24 ^t	22611 ^t
GC-PID [25]	n. d.	n. d.	6	-	4 Parallel channels n.d × 400 × 0.6 μm	Si-glass	SWNTs 0.15 mg	Cr/Pt	-	5 VOC	PID	< 1 ^b	-
Frog 4000 [24]	25 × 19 × 37	< 2.2	5.5	-	n. d.	Si-glass	Silica gel aerogel	-	-	-	PID	~ ppb	-

GC-PID [26]	n. d.	n. d.	63	600	Parallel channels 25 × 1.3 mm × 12	Si-glass	EtQxBx 10 mg	Pt	- / 50	Benzene	PID	1.25 ^b	2396 ^b
GC-PID [27]	60 × 50 × 10	< 5	16.2	50	Tapered cavity 8.15 × 250 × 2.9	Si-glass	C-B 1.135 mg	Pt	- / 314	50 VOC	μPID	n. d.	-
GC-CMOS [13]	16 × 11 × 11	n. d.	n. d.	-	Cavity with micro- pillars 10 × 250 × 2	Si-glass	Carbon film	Ni-Cr wire	-	7 VOC	CMOS	15 (1,3,5- TMB)	-
iGC3.2 [28]	8 × 10	n. d.	130	24	U shape n.d. × 300 × 1350	Glass	C-B + C-X	Ti/Pt	10.5 / 46	19 VOC	2 CD	10 – 2 (BTEX)	766.7 ^b
Zebra GC [16]	15 × 30 × 10	~1.8	< 12	10	Cavity with micro- pillars 13 × 240 × 13	Si-glass	Tenax TA ~200 nm	Cr/Ni	16 / 25	6 VOC	TCD	~25 (TEX)	942.1 ^b
GC-MOX [11]	n. d.	n. d.	~67	2750	Ten parallel channels 800 *m depth	Si-glass	QxCav	Pt	- / 50	Benzene	MOS	0.1	878.5 ^b

^b: benzene; ^t: toluene; CR: chemiresistor; S.S.: stainless steel; O.D.: outer diameter; MOS: Metal Oxide Semiconductor; CD: Capacitive Detector. CMOS: Complementary Metal Oxide Sensor. MOX: Metal Oxide sensor. QxCav: Quinoxaline bridged Cavitand; EC: electrochemical sensor; *this PC is not integrated in a miniaturized GC.

Zebra GC using 10 mL samples of a 5 VOC mixture at 100 ppb (1 – 3.2 ng). The peak areas and retention times showed average % RSD for all analytes less than 1.3 and 4.7 %, respectively, demonstrating the high stability of this compact GC-TCD. Skog *et al.* [20] found % RSD between 9 and 30 % for peak areas of BTEX. These high % RSD can be explained by the very low concentrations employed in these experiments, in the order of pg. Wang *et al.* [17] reported also an outstanding stability for the belt-mounted GC for samples up to 9 µg of a 9 VOC mixture. Peak area and retention time stability were assessed in short-term (i.e., 30 min), intraday (i.e., 8 h) for samples collected from the same test atmosphere. % RSD values lower than 2.5 and 5.0 % were found, respectively. Additionally, reproducibility was also evaluated in samples analysed in five different days and % RSD of 7.7 % was reported. It is worthy to mention that no more results of reproducibility tests were found in the literature. In this context, our system seems to have a comparable repeatability in terms of peak area (< 10 %) and very satisfactory in terms of retention time (< 0.1 %) compared to those reported in the literature.

In conclusion, this compact GC exhibited an excellent sensitivity as well as very satisfactory stability of the measurements. In addition, an analysis cycle is performed in a reasonable time of 19 min, enabling to establish accurate concentration time profiles. In the future, this time can be reduced once it will be fully automatized, the next sampling being collected during the analysis step of the current analysis cycle.

4.7 Conclusions

In this chapter, the performance of every PC prototype version (see Figure 4-36) developed during this research work has been presented and discussed. The first prototype, named MAP, was functional but with a major drawback concerning energy consumption, that prevents its use in a commercial portable analyser. In this regard, several improvements have been proposed by changing the materials employed in the fabrication, the adsorbent and the type of heating system.

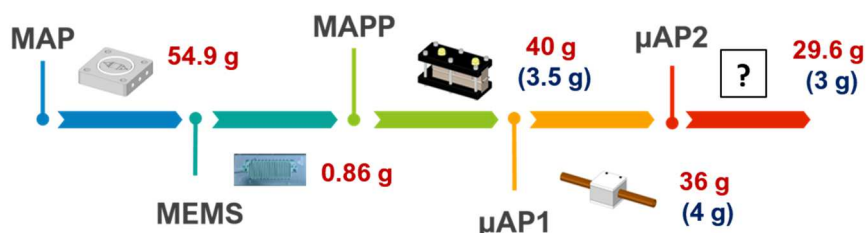


Figure 4-36. Preconcentrator prototypes developed in this work and their thermal mass including connectors (red) and without connectors (blue)

However, as shown in Table 4-10 most of these devices were not fully functional and suitable for industrialization, except the last one, called μ AP2. This device was tested under controlled conditions, demonstrating that it meets the requirements established in the objectives of this project in terms of:

- Sensitivity: the benzene LOQ achieved (0.191 ppb) with an air sample of only 20 mL is lower than the threshold value established in the recent French legislation concerning indoor air quality (0.6 ppb). This sensitivity could be easily improved by increasing the sample volume considered, the benzene LOQ becoming 0.076 ppb with 50 mL of sample, requiring 10 min at 5 NmL/min.
- Energy consumption: the additional power consumption of \sim 70 W needed on a very short duration estimated to 70 s (time needed to reach the desorption temperature) associated to the preconcentration step is compatible with a portable analytical system.
- Analysis time: the addition of a preconcentration step has not substantially increased the total analysis time, enabling BTEX monitoring in near real-time. In addition, in the case of consecutive analyses, the sampling of the next sample can start and fully occur during the separation and analysis in progress.

Prototype	Heating system	Energy consumption	System integration	Robustness	Manufacturing process	Cost
MAP	✗	✗	✓	✓	✓	✓
MEMS	✓	✓	✗	✗	✗	✗
MAPP	✗	✓	✓	✗	✓	✓
μ AP1	✗	✓	✓	✓	✓	✓
μ AP2	✓	✓	✓	✓	✓	✓

Table 4-10. Summary of performances of each preconcentrator prototype developed in this work.

Additionally, contrary to other portable GC found in the literature, the prototype developed in this work was evaluated in terms of repeatability and reproducibility. The relatively low % RSD (< 10 % and < 15 %, respectively) obtained in these two tests indicates that measurements conducted are stable over time.

The stability of the measurements altogether with the remarkable sensitivity and an acceptable analysis time make this GC prototype a good candidate for air quality monitoring applications. Nevertheless, this instrument should be tested in real conditions to evaluate the possible influence of interfering compounds and other issues derived from the use in real environments. Other adsorbents

could be used and tested in the near future in order to try to decrease the desorption temperature needed and consequently the energy consumption.

Furthermore, this preconcentration device can be standalone for possible coupling with other GC systems and be used for other applications requiring high sensitivity, such as warfare agents and explosives detection, early cancer diagnosis or quality food control. Since its proper functioning has been demonstrated, its use for those applications can be achieved by changing the adsorbent and/or replacing the PID detector by others more suitable to the target compounds, i.e. TCD, MOS.

References

- [1] C. Liaud, N. T. Nguyen, R. Nasreddine, and S. Le Calvé, "Experimental performances study of a transportable GC-PID and two thermo-desorption based methods coupled to FID and MS detection to assess BTEX exposure at sub-ppb level in air," *Talanta*, vol. 127, pp. 33–42, Sep. 2014.
- [2] W. Zhang, Z. Qu, X. Li, Y. Wang, D. Ma, and J. Wu, "Comparison of dynamic adsorption/desorption characteristics of toluene on different porous materials," *Journal of Environmental Sciences*, vol. 24, no. 3, pp. 520–528, Mar. 2012.
- [3] Y. Ueno, A. Tate, O. Niwa, H.-S. Zhou, T. Yamada, and I. Honma, "High benzene selectivity of mesoporous silicate for BTX gas sensing microfluidic devices," *Anal Bioanal Chem*, vol. 382, no. 3, pp. 804–809, Jun. 2005.
- [4] K. L. Zhang, S. K. Chou, and S. S. Ang, "Fabrication, modeling and testing of a thin film Au/Ti microheater," *International Journal of Thermal Sciences*, vol. 46, no. 6, pp. 580–588, Jun. 2007.
- [5] D. R. Lide, *CRC Handbook of Chemistry and Physics*, 84th Edition. CRC Press, 2003.
- [6] B. Alfeeli, "Chemical Micro Preconcentrators Development for Micro Gas Chromatography Systems," Oct. 2010.
- [7] B. Alfeeli, M. A. Zareian-Jahromi, and M. Agah, "Micro preconcentrator with seedless electroplated gold as self-heating adsorbent," in *2009 IEEE Sensors*, 2009, pp. 1947–1950.
- [8] I. Lara-Ibeas et al., "BTEX near real-time monitoring in two primary schools in La Rochelle, France," *Air Qual Atmos Health*, vol. 11, no. 9, pp. 1091–1107, Nov. 2018.
- [9] C. Liaud, "Développement de méthodes d'échantillonnage rapides et d'analyses différées au laboratoire: détermination de l'évolution temporelle des concentrations des COVs et COSVs et compréhension des processus physico-chimiques en air intérieur," thesis, Strasbourg, 2014.
- [10] J. Wang et al., "Compact prototype microfabricated gas chromatographic analyzer for autonomous determinations of VOC mixtures at typical workplace concentrations," *Microsystems & Nanoengineering*, vol. 4, p. 17101, Apr. 2018.
- [11] S. Zampolli et al., "Real-time monitoring of sub-ppb concentrations of aromatic volatiles with a MEMS-enabled miniaturized gas-chromatograph," *Sensors and Actuators B: Chemical*, vol. 141, no. 1, pp. 322–328, Aug. 2009.
- [12] G. Gregis et al., "Detection and quantification of lung cancer biomarkers by a micro-analytical device using a single metal oxide-based gas sensor," *Sensors and Actuators B: Chemical*, vol. 255, pp. 391–400, Feb. 2018.

- [13] T.-H. Tzeng et al., "A Portable Micro Gas Chromatography System for Lung Cancer Associated Volatile Organic Compound Detection," *IEEE Journal of Solid-State Circuits*, vol. 51, no. 1, pp. 259–272, Jan. 2016.
- [14] N. A. Zaidi, M. W. Tahir, M. J. Vellekoop, and W. Lang, "Design of Novel Ceramic Preconcentrator and Integration in Gas Chromatographic System for Detection of Ethylene Gas from Ripening Bananas," *Sensors*, vol. 18, no. 8, p. 2589, Aug. 2018.
- [15] S. A. Casalnuovo et al., "Gas phase chemical detection with an integrated chemical analysis system," in *Proceedings of the 1999 Joint Meeting of the European Frequency and Time Forum and the IEEE International Frequency Control Symposium (Cat. No.99CH36313)*, Besancon, France, 1999, vol. 2, pp. 991–996.
- [16] A. Garg et al., "Zebra GC: A mini gas chromatography system for trace-level determination of hazardous air pollutants," *Sensors and Actuators B: Chemical*, vol. 212, pp. 145–154, Jun. 2015.
- [17] J. Wang et al., "Belt-Mounted Micro-Gas-Chromatograph Prototype for Determining Personal Exposures to Volatile-Organic-Compound Mixture Components," *Anal. Chem.*, vol. 91, no. 7, pp. 4747–4754, Apr. 2019.
- [18] B. Han, H. Wang, H. Huang, T. Liu, G. Wu, and J. Wang, "Micro-fabricated packed metal gas preconcentrator for enhanced monitoring of ultralow concentration of isoprene," *Journal of Chromatography A*, Aug. 2018.
- [19] X. Huang et al., "A Binder Jet Printed, Stainless Steel Preconcentrator as an In-Line Injector of Volatile Organic Compounds," *Sensors*, vol. 19, no. 12, p. 2748, Jan. 2019.
- [20] K. M. Skog, F. Xiong, H. Kawashima, E. Doyle, R. Soto, and D. R. Gentner, "Compact, Automated, Inexpensive, and Field-Deployable Vacuum-Outlet Gas Chromatograph for Trace-Concentration Gas-Phase Organic Compounds," *Anal. Chem.*, vol. 91, no. 2, pp. 1318–1327, Jan. 2019.
- [21] J. Sun et al., "Compact prototype GC-PID system integrated with micro PC and micro GC column," *Journal of Micromechanics and Microengineering*, vol. 29, no. 3, p. 29, 2018.
- [22] B. Han, H. Wang, H. Huang, T. Liu, G. Wu, and J. Wang, "Micro-fabricated packed metal gas preconcentrator for enhanced monitoring of ultralow concentration of isoprene," *Journal of Chromatography A*, Aug. 2018.
- [23] I. Lara-Ibeas et al., "Sub-ppb Level Detection of BTEX Gaseous Mixtures with a Compact Prototype GC Equipped with a Preconcentration Unit," *Micromachines*, vol. 10, no. 3, p. 187, Mar. 2019.
- [24] J.-C. Soo, E. G. Lee, R. F. LeBouf, M. L. Kashon, W. Chisholm, and M. Harper, "Evaluation of a portable gas chromatograph with photoionization detector under variations of VOC concentration,

temperature, and relative humidity,” *Journal of Occupational and Environmental Hygiene*, vol. 15, pp. 351–360, Jan. 2018.

[25] J. Sun et al., “Compact Prototype GC-PID System integrated with Micro-PC and Micro GC Column,” *J. Micromech. Microeng.*, 2018.

[26] J. W. Trzciński et al., “In Search of the Ultimate Benzene Sensor: The EtQxBox Solution,” *ACS Sensors*, vol. 2, no. 4, pp. 590–598, Apr. 2017.

[27] J. Lee, M. Zhou, H. Zhu, R. Nidetz, K. Kurabayashi, and X. Fan, “Fully Automated Portable Comprehensive 2-Dimensional Gas Chromatography Device,” 06-Oct-2016. [Online]. Available: <http://pubs.acs.org/doi/abs/10.1021/acs.analchem.6b03000>. [Accessed: 14-Jan-2019].

[28] Y. Qin and Y. B. Gianchandani, “A fully electronic microfabricated gas chromatograph with complementary capacitive detectors for indoor pollutants,” *Microsystems & Nanoengineering*, vol. 2, p. 15049, Feb. 2016.

Chapter 5. VOC adsorption on different materials

In this chapter, the adsorption of diverse VOC at low concentrations on adsorbents of different nature was investigated to evaluate their suitability for VOC analysis and removal. These adsorbents were characterized in terms of specific surface area, pore size and volume, thermal stability, and affinity to water. Afterwards, single component dynamic adsorption experiments were performed to determine the adsorption capacity of each material toward various organic species. Besides, since in indoor air a broad spectrum of gaseous pollutants usually coexists, multicomponent dynamic adsorption experiments were performed to determine adsorption capacity in a more realistic environment. The results obtained are discussed considering the textural properties and surface chemistry of each adsorbent and compared with similar studies available in the literature.

5.1 BTEX adsorption on commercial adsorbents

5.1.1 Introduction

As presented in Chapter 1, a wide spectrum of gaseous pollutants can be encountered in the air we breathe. Among them, BTEX are frequently found in indoor [1]–[3] and outdoor [4], [5] air. These compounds represent a major threat to public health since they are associated to the development of serious diseases such as allergy, asthma or cancer [6], [7]. Besides, in the atmosphere, photochemical reactions of BTEX can generate secondary pollutants, such as ozone [8] and secondary aerosols [9] leading to a further degradation of the air quality. Therefore, air pollution control is necessary to limit human exposure and prevent the environment degradation. Adsorption is a very simple technique for VOC removal, enabling an effective VOC recovery from diluted streams (< 100 ppm) at a low-moderate cost [10]. The efficiency of this technique and air quality monitoring in general is usually performed by means of gas chromatographs. However, the LOD of these instruments is very often not low enough to detect ppb levels, and preconcentration units are frequently coupled to increase the sensitivity. Adsorbents employed for VOC removal or preconcentration prior to analysis should have some common features such as long breakthrough time, large adsorption capacity, thermal stability and selectivity to the targeted pollutants. Therefore, the adsorption study performed in this work can be useful to evaluate the investigated materials for both applications.

In this study, three commercially available materials, namely Carbopack® B, SBA-16 and HKUST-1 were characterized with regard to their textural properties, and their adsorption capacity was assessed

by means of dynamic adsorption experiments at low concentrations. In these experiments, single component adsorption was investigated using toluene as probe molecule and the obtained results were compared to those obtained in multicomponent adsorption experiments. This comparison shed light on the competitive adsorption phenomena that occur in real environments where a mixture of pollutants is present. Since for both applications adsorbents should be regenerated, in the last part of the study, temperature programmed desorption measurements were performed to get insights into the desorption activation energy.

5.1.2 Article 3 published in Journal of Environmental Chemical Engineering



Contents lists available at ScienceDirect

Journal of Environmental Chemical Engineering

journal homepage: www.elsevier.com/locate/jece

Adsorbent screening for airborne BTEX analysis and removal

Irene Lara-Ibeas^{a,b}, Cristina Megías-Sayago^c, Alberto Rodríguez-Cuevas^d, Rubén Ocampo-Torres^a, Benoît Louis^c, Stéphane Colin^b, Stéphane Le Calvé^{a,d,*}

^a ICPEES – Institut de Chimie et Procédés pour l’Energie, l’Environnement et la Santé, Atmospheric Physical Chemistry Team, UMR 7515 CNRS – Université de Strasbourg – ECPM, 25 rue Becquerel F-67087 Strasbourg cedex 2, France

^b Institut Clément Ader (ICA), Université de Toulouse/CNRS, INSA, ISAE-SUPAERO, Mines-Albi, UPS, 31400 Toulouse, France

^c ICPEES – Institut de Chimie et Procédés pour l’Energie, l’Environnement et la Santé, Energy and Fuels for a Sustainable Environment Team, UMR 7515 CNRS – Université de Strasbourg – ECPM, 25 rue Becquerel F-67087 Strasbourg cedex 2, France

^d In’Air Solutions, 25 rue Becquerel, 67087 Strasbourg, France

ARTICLE INFO

Keywords:

Adsorption
BTEX
Air pollution
Desorption
Air treatment

ABSTRACT

Adsorption is a commonly used technique for removal and analysis of gaseous pollutants due to its cost efficiency at low concentrations. In this work, single and competitive BTEX adsorptions were studied on three non-porous, mesoporous and microporous commercial adsorbents, namely Carbopack® B, SBA-16 and HKUST-1, respectively. For all these materials, C₆ aromatics were preferentially adsorbed, preventing in some cases the adsorption of the most volatile species, i.e. benzene and toluene. This behavior indicates that the competition phenomenon is closely related to the strength of adsorbate-adsorbent interactions. Activation energies for the desorption process were determined to be 33.8 and 33.7 and 35.9 kJ/mol for Carbopack® B, SBA-16 and HKUST-1, respectively, demonstrating that stronger interactions are present in microporous materials. Among the investigated adsorbents, SBA-16 seems to be the best candidate for air treatment and analysis since it exhibited high adsorption capacity, moderate hydrophobicity, minimal roll-up and low activation energy for the desorption. The experimental results obtained illustrate the complexity of multicomponent adsorption process on materials with different porosity and surface chemistry.

1. Introduction

Benzene, Toluene, Ethylbenzene and Xylenes isomers (BTEX) are a group of highly volatile gaseous pollutants frequently found in indoor [1–4] and outdoor air [5,6]. It is known from the literature that these compounds have a negative impact on the environment since they contribute to the formation of ozone and other photochemical oxidants [7]. Moreover, BTEX are either known for being, or suspected to be, irritants, neurotoxins, allergens or carcinogens [8] and their exposure on a long term basis presents a serious threat to the human health [9,10]. Therefore, implementing effective strategies for pollution control is of paramount importance to limit human exposure and prevent the environment degradation.

Nowadays, numerous techniques based on physicochemical or biological processes have been developed for gaseous pollutant’s removal such as thermal, plasma, catalytic or photocatalytic oxidation, condensation, membrane separation, biological degradation, absorption and adsorption [11–13]. However, the pollutant concentration in indoor air or industrial environments is relatively low, ranging from sub

ppb level to a hundred of ppm. It is worthy to mention that not all removal techniques can be effective at such low concentration ranges [14]. Furthermore, some of these methods are expensive or require regular maintenance limiting their use at domestic scale. Among them, adsorption has been demonstrated to be a technique that exhibits a good compromise between cost and efficiency for BTEX removal at low concentrations.

At the same time, analytical methods such as gas chromatography are required to monitor air quality and/or control the efficiency of the aforementioned depollution techniques. Since BTEX concentrations are usually very low, the integration of preconcentration devices is generally needed to increase the sensitivity of these methods. Thus, in the mentioned preconcentration unit, an adsorbent is used to trap pollutant molecules and concentrate the sample that will be, subsequently, analysed by conventional gas chromatography. The adsorbent requirements in pollutant removal as well as gas analysis include a minimal breakthrough, large adsorption capacity, thermal stability and selectivity to the targeted pollutants. Additionally, the desorption temperature should be moderate to enable an effective, inexpensive and

* Corresponding author.

E-mail address: slecalve@unistra.fr (S. Le Calvé).

<https://doi.org/10.1016/j.jece.2019.103563>

Received 18 October 2019; Received in revised form 20 November 2019; Accepted 22 November 2019
2213-3437/ © 2019 Elsevier Ltd. All rights reserved.

Table 1
Summary of former studies on benzene and toluene adsorption on various types of silicas.

Silica type	S_{BET} (m^2/g)	V_{total} (mL/g)	V_{micro} (mL/g)	D_{meso} (\AA)	Compound	Concentration (ppm)	Temperature ($^{\circ}\text{C}$)	Adsorption Capacity (mg/g ads)	Reference
SBA-16	572	0.72	–	3.4 and 6.0	Toluene	100	23	24.88	This work
SBA-15	698	1.2	0.07	6.3	Benzene	1000	–	71.08	[29]
MCM-41	1088	0.92	–	2.9	Benzene	1000	–	79.67	[29]
MCM-48	1210	1.02	–	2.4	Benzene	1000	–	76.55	[29]
KIT-6	912	1.29	0.13	6.3	Benzene	1000	–	98.42	[29]
SBA-15-1	612	1.00	0.05	5.6	Toluene	71.65	30	147.39*	[28]
SBA-15-2	596	0.84	0.06	6.55	Toluene	71.65	30	190.74*	[28]
MCM-41	538	0.64	–	2.38	Toluene	71.65	30	130.05*	[28]
SiO_2	558	0.8	–	4.33	Toluene	71.65	30	86.70*	[28]
SBA-15	501	1.143	–	8.15	Benzene	1000	20	15.78	[30]
SBA-15 A	495	0.54	0.089	5.58	Toluene	n. a.	25	167.42	[31]
SBA-15 B	715	0.77	0.122	6.47	Toluene	n. a.	25	187.27	[31]
SBA-15 C	496	0.45	0.083	3.82	Toluene	n. a.	25	415.39	[31]
SBA-15 D	644	0.81	0.094	7.72	Toluene	n. a.	25	321.58	[31]
MCM-41	539	0.64	–	2.43	Toluene	n. a.	25	151.95	[31]

n. a.: not available data; * equilibrium adsorption capacity extracted from isotherm data; D_{meso} : mesopore diameter.

rapid adsorbent regeneration.

In this regard, several materials differing in structure, porosity and surface chemistry have been lately investigated. Among these materials, carbon-based materials have been addressed as BTEX adsorbents including activated carbons [15,16], ordered mesoporous carbons [17] or carbon nanotubes [18]. However, graphitised carbon blacks, typically employed for sampling [19] and gas analysis [20] applications, have been scarcely evaluated in terms of adsorption capacity. In contrast, BTEX adsorption capacity of a wide variety of silicas have been extensively studied as shown in Table 1. Multiple silica structures such as SBA-15, MCM-41, MCM-48, KIT-6 or SiO_2 exhibited significant adsorption abilities ranging from 15.78 to 415.39 mg/g towards benzene and toluene. Several MOF have been also employed for VOC adsorption studies [21–24]. More precisely, HKUST-1 have been widely investigated for the adsorption of various aromatic compounds such as benzene, toluene, p-xylene and o-xylene (see Table 2).

Despite the huge number of BTEX adsorption related studies to date, most of them have been conducted at very high concentrations (5300–800000 ppm) as recently reported by Szulejko *et al.* [25]. Nevertheless, there is a lack of studies employing more realistic BTEX concentrations, ranging from 0.5 to 99 ppm [26–28].

On the other hand, a considerable number of compounds (pollutants) with different polarities and molecular sizes are commonly co-existing in real environments [36], which may lead to competitive adsorption on available adsorption sites, thus resulting in preferential adsorption. Therefore, the study of multicomponent adsorption is a crucial issue to take into account when a material is assessed for pollutant removal or gas analysis. In this sense, only few studies have simulated the adsorption of gas mixtures including BTEX [26,33,37].

In this work, three commercially available materials differing in

their composition, porosity and surface chemistry have been selected to perform single and multicomponent adsorption of low concentrated BTEX mixtures (10–100 ppm). Carbone® B is a non-porous graphitised carbon black traditionally used as a reference material in sorbent tubes for environmental monitoring [38,39] and preconcentration devices [40–42]. SBA-16 is a mesoporous silica with relatively high specific surface area employed especially in catalytic applications [43–45], and, to a lesser extent, in gas analysis [46–48]. Finally, HKUST-1 ($\text{Cu}_3(\text{BTC})_2$) is a microporous MOF formed by copper nodes with 1,3,5-benzenetricarboxylic acid linkers between them. This material has been widely employed in catalysis [49,50], gas analysis [51] as well as in VOC adsorption [52,53]. These three adsorbents were characterized and evaluated in terms of adsorption capacity in single and multicomponent dynamic adsorption experiments. Furthermore, toluene desorption activation energy was determined and compared between the three materials. The present study provides, therefore, new experimental data concerning the multicomponent adsorption of low concentrated BTEX mixtures, highlighting the importance of adsorbate-adsorbent interactions on the competitive adsorption of aromatics compounds.

2. Materials and methods

2.1. Materials

Commercially available Carbone® B (60–80 mesh, SUPELCO), HKUST-1 (Basolite® C300, Sigma-Aldrich), and SBA-16 (ACS Materials) were used as received for adsorption tests. Toluene diluted in synthetic air (100 ppm, Air Products, France) and BTEX mixture diluted in nitrogen (10 ppm, Air Products, France) were employed in temperature

Table 2
Summary of BTEX adsorption studies on HKUST-1.

Reference	S_{BET} (m^2/g)	V_{total} (mL/g)	V_{micro} (mL/g)	Pore diameter (\AA)	Compound	Concentration (ppm)	Temperature ($^{\circ}\text{C}$)	Adsorption Capacity (mg/g ads)
This work	1733	0.89	0.68	5.4 and 6.9	Toluene	100	23	7
[26]	1122.4	0.47	n. a.	7.5	Toluene	2.5	23	238
[26]	1122.4	0.47	n. a.	7.5	o-xylene	2.5	23	147
[27]	1237	0.47	n. a.	10.51	Toluene	99	25	150
[32]	907.2	0.46	n. a.	n.a.	Toluene	920000	25	516*
[33]	1718	0.68	n. a.	n. a.	o-xylene	5925	125	297*
[33]	1718	0.68	n. a.	n. a.	m-xylene	5925	125	255*
[33]	1718	0.68	n. a.	n. a.	p-xylene	5925	125	297*
[34]	1188.3	0.77	0.41	n. a.	Toluene	950000	25	571*
[35]	1568.5	0.75	0.61	6.51 and 8.25	Benzene	64187	15	794*

n. a.: not available data; * equilibrium adsorption capacity extracted from isotherm data.

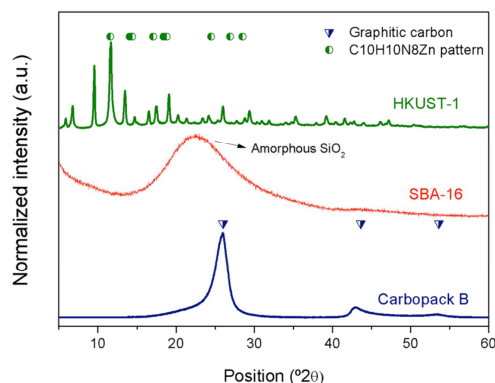


Fig. 1. X-Ray diffraction patterns of commercial adsorbents.

programmed desorption (TPD) and dynamic adsorption experiments.

2.2. Characterization of adsorbents

X-ray diffraction patterns were recorded on a Bruker D8 Advance diffractometer, with a Ni detector side filtered Cu K α radiation (1.5406 Å) over a 2θ range of 5–60°.

Scanning electron microscopy (SEM) images were acquired in a ZEISS GEMINI SEM 500 microscope using an electron high tension (EHT) voltage ranging from 2 to 6 kV.

The textural properties were analysed by means of nitrogen physisorption using a Micromeritics ASAP 2420 equipment. Prior to analysis, the samples were outgassed at 180 °C for 5 h under vacuum. The specific surface area was calculated using the Brunauer–Emmett–Teller (BET) method. The total pore volume was estimated by the single point method from the amount of adsorbed N₂ at a relative pressure (P/P_0) of 0.99. Pore size distributions (PSD) were determined using Barrett, Joyner, and Halenda (BJH) method from the adsorption branch of the isotherm. The micropore volume and micropore surface area were calculated by a t-plot method. Micropore size distribution was calculated by Saito and Foley method [54].

Thermogravimetric analyses (ATG) were performed in a thermobalance coupled with a differential scanning calorimetry apparatus (SDT 650, TA Instruments). The samples were analysed in inert (N₂) atmosphere from room temperature to 500 °C by using a 10 K/min heating rate.

Temperature Programmed Desorption (TPD) experiments were used to calculate the toluene desorption energy from the adsorbent surfaces. TPD analyses were carried out in a Micromeritics AutoChem II 2920 equipped with a TCD detector. Samples were outgassed *in-situ* at 280 °C during 1 h. Afterwards, they were cooled down to room temperature and a gas stream of 50 mL/min of toluene diluted in synthetic air (100 ppm, Air Products, USA) was passed through the adsorbent bed for 15 min. Subsequently, samples were analysed using a helium flow rate of 30 mL/min at several temperature ramps between 10 and 30 K/min for Carpack® B and SBA-16. Lower heating rates from 4 to 12 K/min were used on HKUST-1 samples to prevent adsorbent decomposition before toluene desorption.

2.3. Dynamic adsorption experiments

Carpack® B, SBA-16 and HKUST-1 (15 mg) were packed separately in thermal desorption tubes (Sigma Aldrich, USA) using two glass wool plugs. Prior to analysis, the samples were conditioned for 2 h at 280 °C under a helium flow of 50 mL/min using thermal desorber (TurboMatrix 350, Perkin Elmer, USA) in order to ensure a clean surface. Then, the tubes were mounted on a self-made experimental device

showed in Figure S1 (Supporting Information). For a single component breakthrough test, toluene diluted in synthetic air (100 ppm, Air Products, France) was flowed through each tube under ambient conditions (room temperature, $T = 23 \text{ °C} \pm 2 \text{ °C}$). As for the multi-component adsorption, BTEX mixture diluted in nitrogen (10 ppm, Air Products, France) was employed and flowed at the same temperature, with a 5 mL/min flow rate in both experiments (Mass flow controller 1). The effluent gas stream was continuously analysed by a gas chromatograph (μ BTEX-1 In'Air Solutions, France). Before the analysis and in order to avoid the detector saturation, the effluent was diluted using a second mass flow controller operating at 995 mL/min and 95 mL/min nitrogen flow (99.999 % purity, Messer, Germany) for single and multi-component experiments, respectively, to obtain a concentration of 500 ppb at the analytical instrument inlet. Prior to each adsorption experiment, the peak area corresponding to the initial concentration (C_0) was measured. To this purpose, the gas stream was flowed through a bypass, diluted and analysed. For a given compound, the obtained bypass peak area was used as reference to determine the time at which the adsorbent saturation is reached ($C = C_0$).

The dynamic adsorption capacity (q) for given concentration and flow rate can be calculated as the area above the breakthrough curve using the following equation:

$$q = \frac{F C_0}{m} \int_{t_0}^{t_s} \left(1 - \frac{C}{C_0}\right) dt \quad (1)$$

where q is the dynamic adsorption capacity per gram of adsorbent (mg/g ads), F is the volume gas flow rate ($\text{m}^3/\text{min}^{-1}$), m is the mass of adsorbent (g), t_0 is the initial time (min), t_s is the saturation time (min), C_0 is the initial concentration (mg/m^{-3}), C is the outlet concentration (mg/m^{-3}) at a given time.

3. Results and discussion

3.1. Characterization of the adsorbents

XRD analysis of commercial adsorbents was carried out to assess the crystal structure (Fig. 1). Briefly, Carpack® B exhibits the characteristic diffractions of graphitic carbon (ICDD #00-023-0064), HKUST-1 corresponds to those of C₁₀H₁₀N₈Zn composite (ICDD #00-023-1971) while a broad peak is observed in the case of SBA-16, which is ascribed to amorphous silica, usually appearing in the XRD patterns of ordered mesoporous silicas. Related to the latter, the highest diffractions are observed at small angles, not detectable with the present method. Nevertheless, XRD profiles allow confirming the existing phases.

Representative SEM micrographs of the studied materials are shown in Fig. 2. Both Carpack® B and SBA-16 samples (Figs. 2a and b, respectively) are characterized by different sized agglomerates (ranging from 10 to 180 μm) with highly grainy surface. In contrast, HKUST-1 (Fig. 2c) exhibits a homogeneous morphology constituted by smooth surface octahedral crystals having uniform sizes between 10 and 25 μm . The latter is congruent with previous literature reports [26], [35], [55] [56], or was purchased as commercial material [57].

The corresponding N₂ adsorption-desorption isotherms are presented in Fig. 3. Carpack® B (Fig. 3a) exhibits a type III isotherm according to the IUPAC classification, which is characteristic of non-porous materials. The significant increase in adsorbed N₂ observed at $P/P_0 = 0.8-0.95$ suggests that, at this point, all the layers were saturated, and the adsorbate molecules are filling the interparticle space. Thus, the estimated total pore volume may not correspond only to the pores present on the adsorbent but also to the space between particles. As displayed in Fig. 3b, SBA-16 exhibits a type IV isotherm, characteristic of mesoporous materials. A hysteresis loop can be noticed at intermediate P/P_0 associated to capillary condensation occurring in mesopores [58]. The form of the hysteresis curve, with two different widths, reveals the presence of two different types of pores. This evidence was

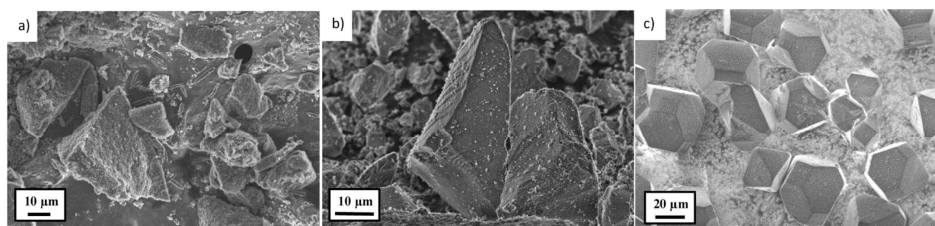


Fig. 2. SEM micrographs of (a) Carbpacck® B, (b) SBA-16 and (c) HKUST-1.

confirmed by the pore size distribution (see Fig. S2) with pore diameters of nearly 3.4 and 6.0 nm. The high quantity absorbed by HKUST-1 at low pressures (Fig. 3c) followed by a long horizontal plateau at higher pressures is typical of type I adsorption isotherms and can be associated to a very strong adsorption within the micropores [37,56,59]. Most probable pore diameter were determined by Saito and Foley method (see Figure S3) resulting to be 5.4 and 6.9 Å, similar to the diameters of the small (4.5 Å) and large cages (9 Å) theoretically presented in the MOF structure [53]. These diameters imply that, although the dynamic diameters of BTEX molecules are larger (from 0.59 to 0.68 nm; see Table S1) than the size of the small cages, they may enter inside the larger pores thus interacting by means of π - π stacking with the organic linkers.

The textural properties of all studied samples are summarized in Table 3. As expected, the specific surface area increases with the porosity (112, 572, 1734 m² g⁻¹ for Carbpacck® B, SBA-16 and HKUST-1, respectively) with the highest value for the microporous adsorbent. Concerning the pore volume, SBA-16 presents a total volume of 0.72 cm³ g⁻¹, barely lower than that observed for HKUST-1, 0.89 cm³ g⁻¹. These adsorbents exhibit therefore similar pore volumes but different pore diameters. According to the pore size distribution, 95 % of the total pore volume in SBA-16 corresponds to pores having 3.4 or 6.0 nm diameter (V_{meso}). In contrast, most of the pores in HKUST-1 have diameters around 0.54 and 0.69 nm. The micropore volume of HKUST-1 sample was calculated to be 0.68 cm³ g⁻¹ which corresponds to 77 % of the total volume, thus assessing a highly microporous nature.

In order to evaluate both the thermal stability and water affinity of the adsorbents, a thermogravimetric study was carried out over the samples after 2 h of exposure to ambient air (Figure S4). All samples have in common a first weight loss situated around 100 °C, usually ascribed to physisorbed water. As deduced from the thermal profiles, Carbpacck B is the most hydrophobic adsorbent (showing less than 2 % weight loss at 100 °C) followed by SBA-16 (6 %) and HKUST-1 (exhibiting 32 % weight loss between 80 and 150 °C). It is well known from the literature that HKUST-1 exhibits a high affinity towards water [26] [35,55], since water molecules can coordinate to the free copper sites [60]. These results are in agreement with those observed by Seo *et al.* [61] reporting a weight loss of 30 % at ~110 °C associated to a presumed loss of 15 water molecules (29.7 %) per Cu₃ unit present in HKUST-1 structure. This great affinity to water prevents the use of

Table 3

Textural properties of investigated adsorbents.

Sample	S_{BET} (m ² g ⁻¹)	V_{total} (cm ³ g ⁻¹)	V_{meso} (cm ³ g ⁻¹)	V_{micro} (cm ³ g ⁻¹)	D_{pore} (nm)
Carbpacck® B	112	–	–	–	–
SBA-16	572	0.72	0.68	–	3.4/6.0
HKUST-1	1733	0.89	0.14	0.68	0.54/0.69

S_{BET} : BET surface area; V_{total} : total pore volume; V_{meso} : mesoporous volume; V_{micro} : microporous volume; D_{pore} : pore diameter.

HKUST-1 as an effective adsorbent in moist environments since water molecules may occupy adsorption sites resulting in a considerable decrease in the adsorption capacity. Nevertheless, this adsorbent can be employed for VOC removal in dry environments such as aircraft cabins where the relative humidity ranges between 2 and 23 % [62].

HKUST-1 decomposition takes place at around 320 °C as evidenced by a dramatic weight loss of ~30 % accompanied by a heat release (exothermic peak), which is usually ascribed to the MOF decomposition into Cu₂O and CuO [55,61] and the subsequent benzene di-carboxylic group oxidation [63]. The material decomposition involves the loss of its chemical structure and, thus, its adsorption properties. Consequently, this temperature must not be exceeded during the activation/desorption process. No remarkable thermal events were observed at higher temperatures. As depicted in Figure S4a and S4b, Carbpacck® B and SBA-16 suffered a total weight loss of 3 and 7 %, respectively, up to 400 °C, demonstrating high thermal stability.

3.2. Single component adsorption experiments

Single aromatic adsorption experiments were carried out using toluene as probe molecule (Fig. 4). The breakthrough curves represent the evolution of the pollutant concentration in the effluent leaving the adsorbent bed as a function of time. They provide information about the bed adsorption capacity and the kinetics of the adsorption process. Three different zones can be distinguished in these consecutive curves: the unsaturated zone, mass transfer zone and saturated zone. The first zone ranges from the beginning of the experiment (t_0) to the breakthrough time (t_b). Usually, in air treatment, even a very low amount of pollutant in the effluent is not allowable; therefore, the breakthrough

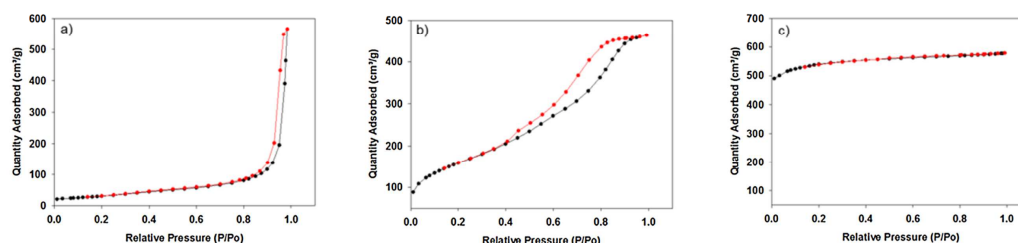


Fig. 3. Nitrogen adsorption (black) and desorption (red) isotherms at 77 K of (a) Carbpacck® B, (b) SBA-16, (c) HKUST-1. (For interpretation of the references to colour in this figure legend, the reader is referred to the web version of this article).

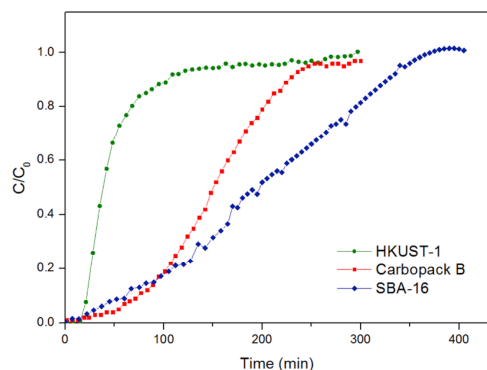


Fig. 4. Breakthrough curves of toluene over SBA-16 (blue), Carbo-pack® B (red) and HKUST-1 (green). Toluene concentration = 100 ppm, flow rate 5 mL/min. (For interpretation of the references to colour in this figure legend, the reader is referred to the web version of this article).

time is reached when 5 % of the concentration of the feed (C_0) is leaving the adsorbent bed. Prior to the breakthrough, adsorption can be considered complete. Industrially, the quantity of pollutant adsorbed during this stage represents the usable capacity of the reactor. From the breakthrough point, the concentration measured at the outlet progressively increases until the saturation time (t_s) is reached ($C/C_0 = 1$). The steepness of the concentration profile between t_b and t_s represents the mass transfer zone. The profile of this zone provides insights about the mass transfer from gas phase to the adsorption sites inside the sorbent particles. From an industrial point of view, a short mass transfer zone is preferred considering that from t_b the adsorption is considered ineffective. From t_s , all the adsorption sites are occupied, and no further adsorption takes place. Therefore, the measured concentration of the effluent at the outlet is equal to the concentration of the feed. At this point, the dynamic adsorption capacity of the adsorbent under the operating conditions can be determined.

Table 4 shows the obtained breakthrough times and the calculated dynamic adsorption capacities. Although the duration of the unsaturated zone is similar for the three adsorbents, HKUST-1 exhibits the shortest breakthrough time. It could be somehow related with the adsorbent density, which is different in each case. Certainly, HKUST-1 density (bulk density of 0.35 g/cm^3) was higher compared to Carbo-pack® B and SBA-16, which implies that the adsorbent bed length was slightly shorter and, thus, toluene molecules might pass through faster.

As evidenced by the breakthrough curves, the mass transfer zones have different shapes depending on the adsorbent, being the steepness of the concentration front related to the kinetics of the adsorption process. In this way, the breakthrough curve of HKUST-1 increases sharply from the breakthrough point to the saturation suggesting fast toluene adsorption kinetics. It might be related both to the particle size, as smaller sizes should enable higher intraparticle mass transfer rates, and with the presence of micropores. HKUST-1 consists of smaller particles (10–25 μm , see Fig. 2), compared with the other two adsorbents (10–180 μm), which may lead to shorten the mass transfer zone.

Table 4

Breakthrough times and adsorption capacities obtained in toluene adsorption experiments.

Adsorbent	Breakthrough time (min)	Adsorption Capacity (mg/ g ads)
Carbo-pack® B	54	18.74
SBA-16	32	24.87
HKUST-1	20	6.96

The adsorbent adsorption capacities were calculated from the area below the respective breakthrough curves (Fig. 4). Surprisingly, the adsorbent with higher specific surface area (HKUST-1) led to the lowest adsorption capacity, suggesting that toluene adsorption may be influenced by different factors. Theoretically, in HKUST-1, the structure is composed by two large cages with a pore diameter of 9 Å and internal diameters of 13.2 and 11.1 Å connected to 6 Å sized smaller cages with 4.5 Å diameter. These values are slightly different from those obtained experimentally (5.4 and 6.9 Å), however, in both cases, toluene molecules (kinetic diameter = 5.8 Å) are not expected to enter in the smaller cages, but they can be adsorbed in the larger ones. Nevertheless, if HKUST-1 is slightly hydrated, the water molecules may reduce the opening diameter of pores thus preventing the entrance of toluene molecules [26,64]. Despite the existence of adsorbed water molecules is highly unlikely after the adsorbent outgassing at 280 °C, it has been demonstrated that the powder pre-treatment at temperatures above 250 °C may cause a drastic decrease in porosity [53], hence reducing the available surface area.

In contrast to HKUST-1, SBA-16 presents the highest adsorption capacity compared to other adsorbents. The results suggest that the presence of large pores (3.4–6.0 nm) can lead to an increase in the adsorption capacity, as demonstrated by Zhang *et al.* for the toluene adsorption over UiO-66 MOF [65]. They reported an enhancement of toluene dynamic adsorption capacity of the micro-mesoporous UiO-66 compared to the microporous counterpart, due to an increase in the molecular transfer rate that allows toluene molecules to diffuse in the material further thus increasing the residence time of the adsorbate molecules in the adsorbent bed. Moreover, it seems that the adsorption of toluene molecules in larger pores can promote the adsorption of new toluene molecules by π - π stacking within the mesopores, which may lead to higher adsorption capacity. Carbo-pack® B exhibited lower adsorption capacity than SBA-16 probably due to its lower specific surface area and, thus, less available adsorption sites.

3.3. Comparison with the literature

The adsorption of aromatics has been widely studied in the last years. However, the variability of the conditions used in the experiments render difficult the comparison of the results. Table 2 summarizes the results for aromatics adsorption previously reported over HKUST-1 [26,27,32–35]. Since most of the studies were performed at very high concentrations (5925–950000 ppm) compared to ours (10 ppm), the measured adsorption capacities in these studies were (in comparison) rather high. Only the results reported by Vellingiri *et al.* [27] were conducted under similar conditions (initial concentration of 99 ppm and 25 °C) and can be compared to the adsorption capacity determined herein. In this regard, our measured toluene adsorption capacity over HKUST-1 sample (6.96 mg/g) was significantly lower than the value of 150 mg/g obtained by Vellingiri *et al.* The difference could be associated to the temperature employed during the outgassing process, 170 °C (Vellingiri *et al.*) instead of 280 °C (this study), which would further confirm that HKUST-1 is very sensitive to the temperature, starting its structural degradation at $T < 280 \text{ °C}$.

Similarly, Table 1 summarizes the obtained results for both benzene and toluene adsorption over micro- and mesoporous silicas. As noted above, most of the experiments were conducted at very high initial concentrations, which do not provide representative data for realistic environments. Mesoporous silicas with diverse structures have been tested for aromatics adsorption, some of them combining meso- and micropores. The latter ones exhibited higher adsorption performance due to the stronger interactions of the molecules in the narrow pores that promotes their adsorption. Indeed, considering only the mesoporous silicas, the pore volume did not seem to be a key parameter influencing the adsorption, whilst a linear increase in adsorption capacity appears to be related to the decrease in the pore diameter, as shown in Figure S5 for toluene. This may explain the low toluene

adsorption capacity of SBA-16 compared to other silicas with narrower mesopores.

As for graphitised carbon blacks solids, few data addressing BTEX total adsorption capacity have been found in literature. In contrast, these materials have been traditionally used for VOC sampling; the studies dealing mainly with its regeneration [40], uptake rates [39] and samples stability [66]. Furthermore, Carbopack® B has been lately replaced by Carbopack® X due to its higher specific surface area (240 m²/g to be compared with 112 m²/g for Carbopack® B). The adsorption capacity of this material was investigated by Khan *et al.* that reported a benzene adsorption capacity of 6.79 mg/g (50 ppm, 25 °C) [67]. This value, relatively lower than the toluene adsorption capacity found for Carbopack® B in the present work, could be explained by the lower volatility of toluene, as it will be highlighted during the multi-component experiments.

3.4. Multicomponent adsorption experiments

Single component adsorption experiments allowed determining the adsorption capacity of each material, illustrating the differences on toluene adsorption among them. In indoor air, however, a broad spectrum of gaseous pollutants usually coexists, resulting in competitive adsorption phenomena. Therefore, the capacity of an adsorbent for pollutant removal or analysis cannot be based solely on the adsorption of a single compound. To determine this capacity in a more realistic environment, a mixture of aromatic compounds was employed for dynamic adsorption experiments.

Fig. 5 illustrates the obtained breakthrough curves for BTEX under ambient conditions ($T = 296 \text{ K} \pm 2 \text{ K}$), using a feed of 5 mL/min containing 10 ppm of each pollutant. For each adsorbent, the plot is composed of five breakthrough curves corresponding to each single compound in the mixture, excepting coeluted m- and p-xylenes that are represented by the same curve. In general, the obtained plots are somewhat comparable, and higher boiling point compounds are

Table 5

Breakthrough times and adsorption capacities obtained in multicomponent adsorption experiments.

Compound	Breakthrough time (min)			Adsorption Capacity (mg/g ads)		
	CB	SB	HK	CB	SB	HK
Benzene	1	11	28	0	0.6	0.16
Toluene	23	40	44	1.47	2.81	0.82
Ethylbenzene	51	99	70	3.31	8.16	3.25
m/p - Xylenes	116	129	76	6.13	8.96	3.45
o - Xylene	190	159	73	7.32	9.67	3.59
Total	-	-	-	18.22	30.2	11.28

CB: Carbopack® B; SB: SBA-16; HK: HKUST-1.

preferentially adsorbed following the order benzene > toluene > ethylbenzene > m/p-xylenes > o-xylene. Nevertheless, the concentration profiles and the calculated adsorption capacities (see Table 5) for each compound vary from one adsorbent to another suggesting that slightly different adsorbate-adsorbent interactions/diffusional processes are co-existing.

Initially, all compounds were completely adsorbed, excepting benzene over Carbopack® B that passed through the adsorbent bed from the beginning. Afterwards, the other species start to break through in accordance with their increasing boiling point. In this way, the outlet adsorbate concentrations start to rise, reaching, in the case of benzene and toluene, higher values than the inlet concentration ($C/C_0 > 1$). This phenomenon, called roll-up, appears when the thermodynamic effects govern the adsorption process [68] i.e. the adsorbate with weaker interactions is replaced by other species with more favourable adsorbate-adsorbent interactions. Roll-up was observed over all materials in different degrees, resulting in the desorption of the most volatile compounds in favour of the adsorption of the less volatile compounds.

SBA-16 and Carbopack® B present minimum benzene/toluene roll-up whereas over HKUST-1 the effect is more pronounced.

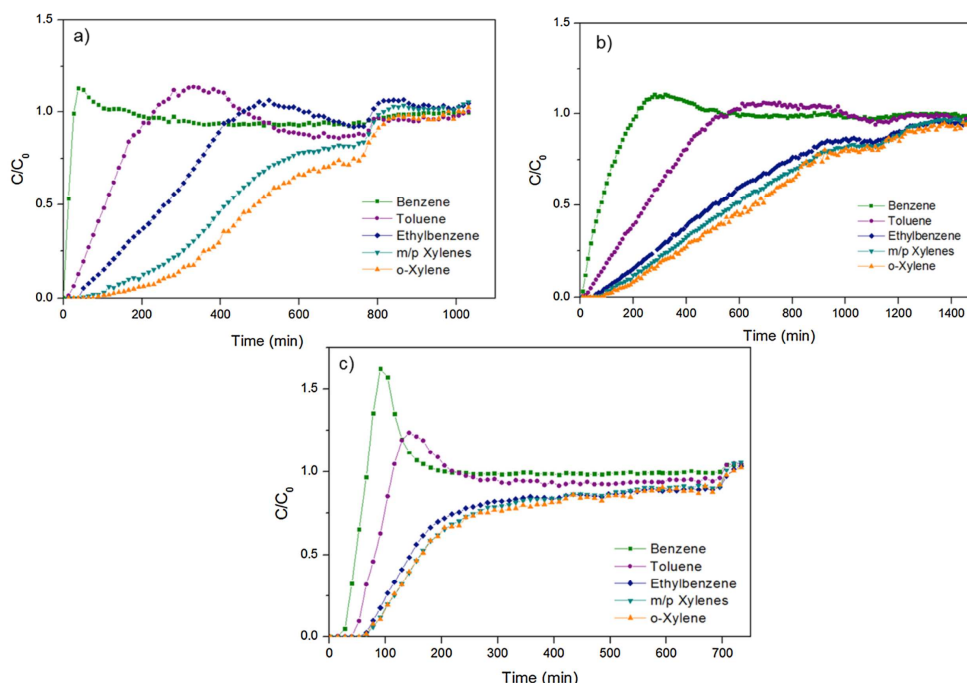


Fig. 5. Breakthrough curves for BTEX over Carbopack® B (a), SBA-16 (b), and HKUST-1 (c). BTEX concentration = 10 ppm, flow rate 5 mL/min.

Consequently, the adsorption capacities of each compound were strongly related to adsorbate-adsorbent interactions as well as to the presence of micropores.

In Carbpac[®] B, London interactions are the prevailing adsorbate-adsorbent forces that govern the adsorption process due to the non-polar surface of this material. Consequently, the adsorption capacity for each compound is considerably different due to the different strength of these interactions and, logically, follows the order of the boiling points (o-xylene > m/p-xylenes > ethylbenzene > toluene > benzene) provided in Table S1. It should be noted that the effect of the competitive sorption between the different species in this material is remarkable, resulting in the total desorption of the most volatile compound, *i.e.* benzene. Therefore, special attention should be paid when this material is used to remove/analyze benzene or similar boiling points pollutants in presence of less volatile compounds.

Even when interactions of different nature can be established, London forces are usually the driving force in the adsorption of high boiling point molecules, having also high molecular mass. It is known from the literature that in mesoporous silicas, the hydroxyl groups located at the surface may behave as weak acid sites interacting with the π -electrons of the aromatic rings [69,70]. Hence, in SBA-16, adsorption can take place via London forces and weak π -system – hydrogen bonding of the aromatic ring with silanols. For these dipole forces, the strength increases with the polarizability of the molecule, which explains the low adsorption capacity obtained for benzene and toluene compared to ethylbenzene and m/p-xylenes. As in the previous case, the adsorption capacity follows the order of the boiling points (o-xylene > m/p-xylenes > ethylbenzene > toluene > benzene). Obviously, o-xylene, with its highest boiling point and high polarizability, demonstrated the highest adsorption capacity.

Similarly to SBA-16, BTEX adsorption in HKUST-1 occurs through London forces as well as π -interactions but, in this case, these interactions are between the aromatic ring of the adsorbate and those presented in the HKUST-1 structure [71] formed with benzene 1,3,5-tricarboxylate linkers. Once again, the adsorption capacity follows the order: o-xylene > m/p-xylenes > ethylbenzene > toluene > benzene. However, the roll-up observed in the breakthrough curve for benzene and toluene is considerably more pronounced than in the mesoporous silica. This difference is probably due to the fact that in HKUST-1, BTEX molecules are adsorbed within the micropores instead of mesopores, and the BTEX molecules size is very close to that of micropores. Since London forces are distance sensitive, they are expected to play an important role in the adsorption within the micropores resulting in a huge difference between the adsorption capacities of smaller molecules, *i.e.* benzene and toluene, compared to the larger molecules.

These results are in line with those reported in other studies. Chevalier *et al.* performed breakthrough experiments of 1.25 ppm binary mixtures of toluene and o-xylene on HKUST-1 [26]. They observed a pronounced roll-up effect of toluene indicating highly selective adsorption of o-xylene over toluene. Peralta *et al.* investigated the single and competitive adsorption of xylene isomers on HKUST-1 [33]. In single experiments, they found similar adsorption capacities for the three isomers, with a slightly higher value for o-xylene. Nevertheless, in multicomponent experiments, a preferential adsorption of o-xylene over m- and p-xylenes was reported.

As a *priori* expected, the results regarding total adsorption capacity in the multicomponent adsorption study are consistent with those obtained in single component experiments. Total adsorption capacity followed the order SBA-16 > Carbpac[®] B > HKUST-1. It is clear from our results that multicomponent adsorption is a complex process in which polarizability, molecular size, surface chemistry and porosity play a crucial role. In this context, the multicomponent breakthrough curves can provide valuable information about the key aspects in competitive adsorption of pollutants according to their characteristics. SBA-16 has demonstrated the highest adsorption capacity for aromatics in both single and multicomponent experiments. Moreover, among the

investigated materials, the mesoporous silica exhibited the minimum roll-up, thus avoiding the release of compounds previously adsorbed, which can be dangerous since benzene is the most hazardous one. Therefore, SBA-16 can be a promising candidate for applications to pollutant removal and analysis. Nevertheless, for its use in adsorbents at industrial scale, enough length should be expected to prevent early breakthroughs.

3.5. Desorption activation energy of toluene

In gas analysis as well as in pollutant removal, the activation energy of the desorption process of contaminants is a crucial parameter for a sound selection of an adsorbent. This energy should be relatively high to enable the trapping of pollutants at room temperature but low enough to permit its desorption at moderate temperatures, typically in the range 150–350 °C. In this context, TPD is powerful surface analysis technique providing valuable information regarding desorption kinetics, reaction order or desorption activation energy, as well as the variation of each of these factors with respect to the adsorbate coverage [72].

In this work, toluene TPD experiments were carried out at different heating rates, between 10–30 K/min, over Carbpac[®] B and SBA-16 samples. Lower heating rates from 4 to 12 K/min were used over HKUST-1 to prevent adsorbent decomposition before toluene desorption. The obtained desorption curves are displayed in Fig. 6.

Whatever the adsorbent, only one desorption peak was detected, thus indicating that the adsorption of toluene took place from a single adsorption site. As illustrated in Fig. 6, an increment in the heating rate led to an increase in the peak desorption temperature (T_p). SBA-16 and Carbpac[®] B exhibited similar desorption temperatures at the same heating rates, whilst higher temperatures were required for HKUST-1. This implies that higher energies are required to desorb toluene from this material and, consequently, either the toluene-adsorbent interactions are stronger or the diffusional limitations higher compared to those of SBA-16 and Carbpac[®] B. Relating this to the obtained results during the competitive adsorption experiments, where toluene was released from HKUST-1 (Fig. 5c), it might be expected that the adsorbate-adsorbent interactions of C8 aromatics could be even stronger.

The desorption activation energy (E_d) of toluene can be estimated using the data from TPD experiments [71,73,74] according to the Polanyi-Wigner equation [76]:

$$-\frac{d\theta}{dT} = \frac{A}{\beta} \theta^n \exp(-E_d/RT) \quad (2)$$

where θ is the surface coverage, T (K) is the temperature, A (s^{-1}) is the desorption rate coefficient, β ($K s^{-1}$) is the heating rate, n is the order of the reaction, E_d ($J mol^{-1}$) is the activation energy of the desorption and R ($J mol^{-1} K^{-1}$) is the ideal gas constant. During the desorption, the desorption peak temperature T_p is reached when $\frac{d^2\theta}{dT^2} = 0$. Taking this into account and assuming that desorption follows first order kinetics, Eq. (2) yields:

$$\ln\left(\frac{RT_p^2}{\beta}\right) = \ln\left(\frac{E_d}{A}\right) + \frac{E_d}{RT_p} \quad (3)$$

In this way, by plotting $\ln\left(\frac{RT_p^2}{\beta}\right)$ versus $1/T_p$, the toluene desorption activation energy over the different materials can be calculated (Fig. 7). The obtained desorption activation energies are 33.7, 33.8 and 35.9 kJ/mol for SBA-16, Carbpac[®] B and HKUST-1, respectively. These values are very close, indicating that the strength of the adsorbate-adsorbent interactions is similar in all investigated materials. Among them, HKUST-1 exhibited a barely higher desorption activation energy probably due to both the stronger toluene electrostatic interactions within the micropores and the expected lower diffusional coefficient. In addition, the presence of benzyl groups in HKUST-1 structure allows forming π - π interactions with toluene, hence enhancing the energy

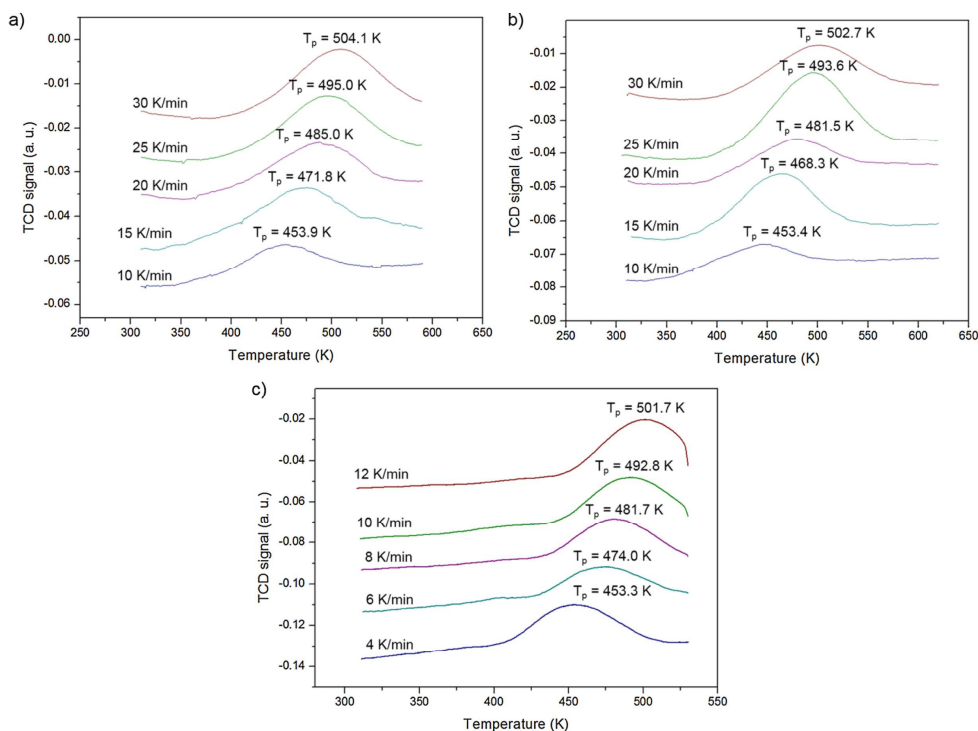


Fig. 6. Toluene desorption TPD curves over Carbopack® B (a), SBA-16 (b) and HKUST-1 (c) samples at different heating rates.

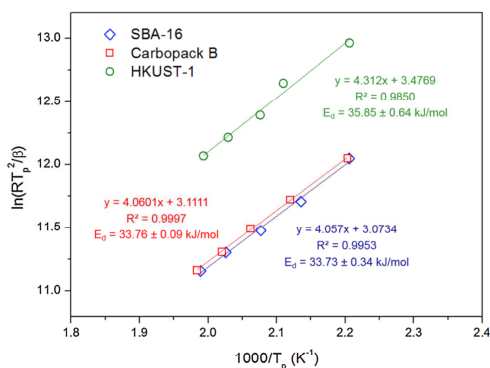


Fig. 7. Linear dependence between $\ln(RT_p^2/\beta)$ and $1/T_p$ for TPD of toluene on SBA-16 (blue), Carbopack® B (red) and HKUST-1 (green). The desorption activation energies are derived from the slope according to Eq. (3). (For interpretation of the references to colour in this figure legend, the reader is referred to the web version of this article).

required for the desorption. In the case of mesoporous and non-porous materials such as SBA-16 and Carbopack® B, the molecule diffusion should not be limited, thus leading to a lower desorption activation energy. Nevertheless, the activation energy was found to be almost identical on SBA-16 and Carbopack® B, suggesting that the presence of pores much larger than the size of the adsorbate molecule did not significantly influence the adsorbate-adsorbent interactions.

The activation energy of the desorption process was 35.9 kJ/mol for HKUST-1, being barely lower than 43.8 kJ/mol reported by Xu *et al.* [75] for toluene and slightly higher than the value of 33.8 kJ/mol

determined by Zhao *et al.* for the desorption of benzene [35]. This difference might be mostly related to the lower benzene cross-sectional area, which allows a better diffusion within the micropores.

From an industrial point of view, a lower desorption energy is preferred since less energy is required for the adsorbent regeneration, thus resulting in more cost-effective processes. Therefore, considering only the energy aspect, SBA-16 seems again to be the best candidate for pollutant removal and analysis among the studied adsorbents.

4. Conclusions

In this study, three commercial adsorbents with different porosities and surface chemistries were characterized and their BTEX adsorption was assessed in terms of breakthrough time and adsorption capacity. Firstly, single component dynamic adsorption studies were carried out using toluene as a probe molecule. Those results suggest that breakthrough time is closely related to both particle size, being shorter for smaller particles, and the micropores presence. From the breakthrough curves, adsorption capacity values of those materials were calculated to be 18.7, 24.9 and 7.0 mg/g for Carbopack® B, SBA-16 and HKUST-1, respectively. It was expected to find an increasing adsorption capacity as specific surface area increases. However, the material with larger specific surface area (HKUST-1) exhibited the lowest adsorption capacity, pointing out possible diffusional limitations related to the microporous structure. The same trend in adsorption capacity was found during multicomponent adsorption experiments. Furthermore, roll up effect was observed to some extent with all adsorbents. The intensity of this phenomenon was related to adsorbate-adsorbent interactions in each case, indicating that the strength of these interactions plays a major role in competitive adsorption. Roll-up effect is of great importance when using adsorbents in air treatment, since hazardous compounds can be released even when the adsorbent is far from

saturation. Finally, the activation energy for toluene desorption determined by TPD technique was 33.8, 33.7 and 35.9 kJ/mol for Carbopack® B, SBA-16 and HKUST-1, respectively. The microporous material (HKUST-1) exhibited the highest desorption activation energy due most probably to both stronger molecule interactions and diffusional limitations within the micropores. Non-porous (Carbopack® B) and mesoporous solids (SBA-16) exhibited almost identical energies suggesting comparable adsorbate-adsorbent interactions and diffusional coefficients. Among the investigated adsorbents, SBA-16 seems to be the most appropriate for air treatment due to its superior adsorption capacity, minimal roll-up and low desorption temperature. Nevertheless, a detailed study of the adsorption capacity of this material after several regeneration cycles should be performed to fully evaluate its suitability for air treatment and gas analysis.

CRedit authorship contribution statement

Irene Lara-Ibeas: Conceptualization, Methodology, Data curation, Formal analysis, Visualization, Investigation, Writing - original draft, Writing - review & editing. **Cristina Megías-Sayago:** Methodology, Data curation, Formal analysis, Visualization, Writing - original draft. **Alberto Rodríguez-Cuevas:** Conceptualization, Investigation. **Rubén Ocampo-Torres:** Supervision, Validation, Writing - original draft. **Benoît Louis:** Supervision, Validation, Writing - original draft. **Stéphane Colin:** Funding acquisition, Supervision, Writing - original draft. **Stéphane Le Calvé:** Conceptualization, Methodology, Supervision, Validation, Funding acquisition, Project administration, Writing - original draft, Writing - review & editing.

Declaration of Competing Interest

The authors declare that they have no known competing financial interests or personal relationships that could have appeared to influence the work reported in this paper.

Acknowledgements

This work has received funding from the Clean Sky 2 Joint Undertaking under the European Union's Horizon 2020 research and innovation program under grant agreement No. 687014(MACAO project) and under the Marie Skłodowska-Curie Grant Agreement No. 643095(MIGRATE project) [H2020-MSCA-ITN-2014]. This project has also been supported by the European Union's through the LIFE SMART IN'AIR – Smart indoor air monitoring network to reduce the impacts of pollutants on environment and health – under grant number LIFE17 ENV/FR/000330.

Appendix A. Supplementary data

Supplementary material related to this article can be found, in the online version, at doi:<https://doi.org/10.1016/j.jece.2019.103563>.

References

- I. Lara-Ibeas, et al., BTEX near real-time monitoring in two primary schools in La Rochelle, France, *Air Qual. Atmos. Health* 11 (November (9)) (2018) 1091–1107.
- C. Mandin, et al., Assessment of indoor air quality in office buildings across Europe – the OFFICAIR study, *Sci. Total Environ.* 579 (February) (2017) 169–178.
- R. Nasreddine, V. Person, C.A. Serra, C. Schoemaeker, S. Le Calvé, Portable novel micro-device for BTEX real-time monitoring: assessment during a field campaign in a low consumption energy junior high school classroom, *Atmos. Environ.* 126 (February) (2016) 211–217.
- M. Śmielowska, M. Marć, B. Zabiegała, Indoor air quality in public utility environments—a review, *Environ. Sci. Pollut. Res. Int.* 24 (12) (2017) 11166–11176.
- R. Montero-Montoya, R. López-Vargas, O. Arellano-Aguilar, Volatile organic compounds in air: sources, distribution, exposure and associated illnesses in children, *Ann. Glob. Health* 84 (July (2)) (2018).
- M. Verrielle, et al., The MERMAID study: indoor and outdoor average pollutant concentrations in 10 low-energy school buildings in France, *Indoor Air* 26 (October (5)) (2016) 702–713.
- A. Kumar, I. Viden, Volatile organic compounds: sampling methods and their worldwide profile in ambient air, *Environ. Monit. Assess.* 131 (August (1)) (2007) 301–321.
- M.P. Tsakas, A.P. Siskos, P. Siskos, Indoor air pollutants and the impact on human health, *Chem. Emission Control* (July) (2011).
- F. Ahmed, et al., Impact of household air pollution on human health: source identification and systematic management approach, *SN Appl. Sci.* 1 (April (5)) (2019) 418.
- G. Hoek, et al., Long-term air pollution exposure and cardio-respiratory mortality: a review, *Environ. Health* 12 (May (1)) (2013) 43.
- B. Guieu, C. Hort, V. Platel, R. Munoz, M. Ondarts, S. Revah, Biological treatment of indoor air for VOC removal: potential and challenges, *Biotechnol. Adv.* 26 (September (5)) (2008) 398–410.
- G.R. Parmar, N.N. Rao, Emerging control technologies for volatile organic compounds, *Crit. Rev. Environ. Sci. Technol.* 39 (December (1)) (2008) 41–78.
- M. Slomińska, S. Król, J. Namieśnik, Removal of BTEX compounds from waste gases; destruction and recovery techniques, *Crit. Rev. Environ. Sci. Technol.* 43 (January (14)) (2013) 1417–1445.
- G.B. Baur, Development of Adsorbents for Selective Volatile Organic Compounds Removal from Diluted Gas Streams, *Infoscience*, 2015 [Online]. Available: <https://infoscience.epfl.ch/record/212805>. [Accessed: 30-Jun-2019].
- K. Zhou, et al., Activated carbons modified by magnesium oxide as highly efficient sorbents for acetone, *RSC Adv.* 8 (6) (2018) 2922–2932.
- A. Khan, S.J. Mandokhail, N. Mohammad, Z. Baloch, M. Siddique, M. Akram, Comparative analysis of pressure regions of gaseous benzene using ground activated carbon sorbents under ambient conditions, *J. Appl. Emerg. Sci.* 8 (April (2)) (2019) pp. 160–167–167.
- B. Rubahamya, K.S.K. Reddy, A. Prabhu, A.A. Shoaibi, C. Srinivasakannan, Porous carbon screening for benzene sorption, *Environ. Prog. Sustain. Energy* 38 (s1) (2019) S93–S99.
- H.Q.A. Le, D.T. Phan, Investigation of BTEX adsorption on carbon nanotubes cartridges from air samples, *AMM* 889 (March) (2019) 216–222.
- J. Senthilnathan, K.-H. Kim, J.-C. Kim, J.-H. Lee, H.N. Song, Indoor air pollution, sorbent selection, and analytical techniques for volatile organic compounds, *Asian J. Atmos. Environ. (AJAE)* 12 (4) (2018).
- J. Wang, et al., Compact prototype microfabricated gas chromatographic analyzer for autonomous determinations of VOC mixtures at typical workplace concentrations, *Microsyst. Nanoeng.* 4 (April) (2018) 17101.
- M. Bahri, F. Haghghat, H. Kazemian, S. Rohani, A comparative study on metal organic frameworks for indoor environment application: adsorption evaluation, *Chem. Eng. J.* 313 (April) (2017) 711–723.
- X. Zhang, Y. Yang, L. Song, J. Chen, Y. Yang, Y. Wang, Enhanced adsorption performance of gaseous toluene on defective UiO-66 metal organic framework: equilibrium and kinetic studies, *J. Hazard. Mater.* 365 (March) (2019) 597–605.
- L.-H. Xie, X.-M. Liu, T. He, J.-R. Li, Metal-organic frameworks for the capture of trace aromatic volatile organic compounds, *Chemistry* 4 (August (8)) (2018) 1911–1927.
- C. Liu, L.-Q. Yu, Y.-T. Zhao, Y.-K. Lv, Recent advances in metal-organic frameworks for adsorption of common aromatic pollutants, *Microchim. Acta* 185 (June (7)) (2018) 342.
- J.E. Szulejko, K.-H. Kim, J. Parise, Seeking the most powerful and practical real-world sorbents for gaseous benzene as a representative volatile organic compound based on performance metrics, *Sep. Purif. Technol.* 212 (April) (2019) 980–985.
- V. Chevalier, J. Martin, D. Peralta, A. Roussey, F. Tardif, Performance of HKUST-1Metal-Organic Framework for a VOCs mixture adsorption at realistic concentrations ranging from 0.5 to 2.5 ppmv under different humidity conditions, *J. Environ. Chem. Eng.* (April) (2019) 103131.
- K. Vellingiri, P. Kumar, A. Deep, K.-H. Kim, Metal-organic frameworks for the adsorption of gaseous toluene under ambient temperature and pressure, *Chem. Eng. J.* 307 (January) (2017) 1116–1126.
- W. Zhang, Z. Qu, X. Li, Y. Wang, D. Ma, J. Wu, Comparison of dynamic adsorption/desorption characteristics of toluene on different porous materials, *J. Environ. Sci.* 24 (March 3) (2012) 520–528.
- B. Dou, Q. Hu, J. Li, S. Qiao, Z. Hao, Adsorption performance of VOCs in ordered mesoporous silicas with different pore structures and surface chemistry, *J. Hazard. Mater.* 186 (February 2) (2011) 1615–1624.
- Q. Hu, J.J. Li, Z.P. Hao, L.D. Li, S.Z. Qiao, Dynamic adsorption of volatile organic compounds on organofunctionalized SBA-15 materials, *Chem. Eng. J.* 149 (July (1)) (2009) 281–288.
- Y. Qin, Y. Wang, H. Wang, J. Gao, Z. Qu, Effect of morphology and pore structure of SBA-15 on toluene dynamic Adsorption/Desorption performance, *Procedia Environ. Sci.* 18 (January) (2013) 366–371.
- F. Xu, S. Xian, Q. Xia, Y. Li, Z. Li, Effect of textural properties on the adsorption and desorption of toluene on the metal-organic frameworks HKUST-1 and MIL-101, effect of textural properties on the adsorption and desorption of toluene on the metal-organic frameworks HKUST-1 and MIL-101, *Adsorpt. Sci. Technol.* 31 (April (4)) (2013) 325–339.
- D. Peralta, et al., Adsorption and separation of xylene isomers: CPO-27-Ni vs HKUST-1 vs NaY, *J. Phys. Chem. C* 116 (October (41)) (2012) 21844–21855.
- Y. Li, et al., Mechanochemical synthesis of Cu-BTC@GO with enhanced water stability and toluene adsorption capacity, *Chem. Eng. J.* 298 (August) (2016) 191–197.
- Z. Zhao, S. Wang, Y. Yang, X. Li, J. Li, Z. Li, Competitive adsorption and selectivity of benzene and water vapor on the microporous metal organic frameworks (HKUST-1), *Chem. Eng. J.* 259 (January) (2015) 79–89.
- D.A. Sarigiannis, S.P. Karakitsios, A. Gotti, I.L. Liakos, A. Katsoyiannis, Exposure to

- major volatile organic compounds and carbonyls in European indoor environments and associated health risk, *Environ. Int.* 37 (May 4) (2011) 743–765.
- [37] K. Vellingiri, et al., Metal organic frameworks as sorption media for volatile and semi-volatile organic compounds at ambient conditions, *Sci. Rep.* 6 (21) (2016) 27813.
- [38] K.-H. Kim, M.-H. Lee, J.E. Szulejko, Simulation of the breakthrough behavior of volatile organic compounds against sorbent tube sampler as a function of concentration level and sampling volume, *Anal. Chim. Acta* 835 (July) (2014) 46–55.
- [39] B. Tolnai, G. Barkó, J. Hlavay, A. Gelencsér, Evaluation of Carbopack B adsorbent for the tube-type diffusive sampling of volatile organic compounds at ambient concentration, *Analyst* 124 (12) (1999) 1859–1863.
- [40] P. Ciccio, E. Brancaleoni, A. Ceginato, C. di Palo, A. Brachetti, A. Liberti, Gas chromatographic evaluation of the organic components present in the atmosphere at trace levels with the aid of carbopack b for pre-concentration of the sample, *J. Chromatogr. A* 351 (January) (1986) 433–449.
- [41] I. Voiculescu, M. Zaghloul, N. Narasimhan, Microfabricated chemical pre-concentrators for gas-phase microanalytical detection systems, *Trac Trends Anal. Chem.* 27 (April 4) (2008) 327–343.
- [42] J. Wang, et al., Belt-mounted micro-gas-Chromatograph prototype for determining personal exposures to volatile-organic-Compound mixture components, *Anal. Chem.* 91 (April 7) (2019) 4747–4754.
- [43] Z. Gao, et al., Synthesis of mesoporous materials SBA-16 with different morphologies and their application in dibenzothiophene hydrodesulfurization, *Chem. Eng. Sci.* 155 (November) (2016) 141–152.
- [44] M. Jourshabani, A. Badiei, Z. Shariatnia, N. Lashgari, G. Mohammadi Ziarani, Fe-supported SBA-16 type cage-like mesoporous silica with enhanced catalytic activity for direct hydroxylation of benzene to phenol, *Ind. Eng. Chem. Res.* 55 (April 14) (2016) 3900–3908.
- [45] L. Kong, et al., Oxidative dehydrogenation of ethane to ethylene over Mo-incorporated mesoporous SBA-16 catalysts: the effect of MoO_x dispersion, *Appl. Catal. A Gen.* 510 (January) (2016) 84–97.
- [46] K. Hamdi, M. Hébrant, P. Martin, B. Galland, M. Etienne, Mesoporous silica nanoparticle film as sorbent for in situ and real-time monitoring of volatile BTX (benzene, toluene and xylenes), *Sens. Actuators B Chem.* 223 (February) (2016) 904–913.
- [47] Y. Ueno, A. Tate, O. Niwa, H.-S. Zhou, T. Yamada, I. Honma, High benzene selectivity of mesoporous silica for BTX gas sensing microfluidic devices, *Anal. Bioanal. Chem.* 382 (June 3) (2005) 804–809.
- [48] F. Luo, et al., Improved separation of micro gas chromatographic column using mesoporous silica as a stationary phase support, *Talanta* 188 (October) (2018) 546–551.
- [49] T. Granato, F. Testa, R. Olivo, Catalytic activity of HKUST-1 coated on ceramic foam, *Microporous Mesoporous Mater.* 153 (May) (2012) 236–246.
- [50] J. Lee, O.K. Farha, J. Roberts, K.A. Scheidt, S.T. Nguyen, J.T. Hupp, Metal-organic framework materials as catalysts, *Chem. Soc. Rev.* 38 (April 5) (2009) 1450–1459.
- [51] I. Lara-Ibeas, et al., Sub-ppb level detection of BTEX gaseous mixtures with a compact prototype GC equipped with a preconcentration unit, *Micromachines* 10 (March 3) (2019) 187.
- [52] J. Moellmer, A. Moeller, F. Dreisbach, R. Glaeser, R. Staudt, High pressure adsorption of hydrogen, nitrogen, carbon dioxide and methane on the metal-organic framework HKUST-1, *Microporous Mesoporous Mater.* 138 (February 1–3) (2011) 140–148.
- [53] F. Raganati, V. Gargiulo, P. Ammendola, M. Alfe, R. Chirone, CO₂ capture performance of HKUST-1 in a sound assisted fluidized bed, *Chem. Eng. J.* 239 (March) (2014) 75–86.
- [54] A. Saito, H.C. Foley, Argon porosimetry of selected molecular sieves: experiments and examination of the adapted Horvath-Kawazoe model, *Microporous Mater.* 3 (January 4–5) (1995) 531–542.
- [55] N. Al-Janabi, et al., Mapping the Cu-BTC metal-organic framework (HKUST-1) stability envelope in the presence of water vapour for CO₂ adsorption from flue gases, *Chem. Eng. J.* 281 (December) (2015) 669–677.
- [56] K.-S. Lin, A.K. Adhikari, C.-N. Ku, C.-L. Chiang, H. Kuo, Synthesis and characterization of porous HKUST-1 metal organic frameworks for hydrogen storage, *Int. J. Hydrogen Energy* 37 (September 18) (2012) 13865–13871.
- [57] N. Lamia, M. Jorge, M.A. Granato, F.A. Almeida Paz, H. Chevreau, A.E. Rodrigues, Adsorption of propane, propylene and isobutane on a metal-organic framework: molecular simulation and experiment, *Chem. Eng. Sci.* 64 (July 14) (2009) 3246–3259.
- [58] Y. Zhai, B. Tu, D. Zhao, Organosilane-assisted synthesis of ordered mesoporous poly (furfuryl alcohol) composites, *J. Mater. Chem.* 19 (December 1) (2008) 131–140.
- [59] G. Autie-Castro, M.A. Autie, E. Rodríguez-Castellón, C. Aguirre, E. Reguera, Cu-BTC and Fe-BTC metal-organic frameworks: role of the materials structural features on their performance for volatile hydrocarbons separation, *Colloids Surf. A Physicochem. Eng. Asp.* 481 (September) (2015) 351–357.
- [60] P. Küsgens, et al., Characterization of metal-organic frameworks by water adsorption, *Microporous Mesoporous Mater.* 120 (April 3) (2009) 325–330.
- [61] Y.-K. Seo, G. Hundal, I.T. Jang, Y.K. Hwang, C.-H. Jun, J.-S. Chang, Microwave synthesis of hybrid inorganic-organic materials including porous Cu₃(BTC)₂ from Cu(II)-trimesate mixture, *Microporous Mesoporous Mater.* 119 (March 1) (2009) 331–337.
- [62] N.L. Nagda, M. Hodgson, Low relative humidity and aircraft cabin air quality, *Indoor Air* 11 (September 3) (2001) 200–214.
- [63] A. Banerjee, U. Singh, V. Aravindan, M. Srinivasan, S. Ogale, Synthesis of CuO nanostructures from Cu-based metal organic framework (MOF-199) for application as anode for Li-ion batteries, *Nano Energy* 2 (November 6) (2013) 1158–1163.
- [64] D. Farrusseng, et al., Heats of adsorption for seven gases in three metal-Organic frameworks: systematic comparison of experiment and simulation, *Langmuir* 25 (July 13) (2009) 7383–7388.
- [65] X. Zhang, et al., Adsorption/desorption kinetics and breakthrough of gaseous toluene for modified microporous-mesoporous UiO-66 metal organic framework, *J. Hazard. Mater.* 366 (March) (2019) 140–150.
- [66] J.H. Lee, S.A. Batterman, C. Jia, S. Chernyak, Ozone artifacts and carbonyl measurements using tenax GR, Tenax TA, carbopack B, and carbopack X adsorbents, *J. Air Waste Manage. Assoc.* 56 (November 11) (2006) 1503–1517.
- [67] A. Khan, et al., A comparison of figure of merit (FOM) for various materials in adsorptive removal of benzene under ambient temperature and pressure, *Environ. Res.* 168 (January) (2019) 96–108.
- [68] D. Peralta, et al., Comparison of the behavior of metal-Organic frameworks and zeolites for hydrocarbon separations, *J. Am. Chem. Soc.* 134 (May 19) (2012) 8115–8126.
- [69] R. Serna-Guerrero, A. Sayari, Applications of pore-expanded mesoporous silica. 7. Adsorption of volatile organic compounds, *Environ. Sci. Technol.* 41 (July 13) (2007) 4761–4766.
- [70] X.S. Zhao, G.Q. Lu, X. Hu, Organophilicity of MCM-41 adsorbents studied by adsorption and temperature-programmed desorption, *Colloids Surf. A Physicochem. Eng. Asp.* 179 (January 2–3) (2001) 261–269.
- [71] D. Peralta, et al., Comparison of the behavior of metal-Organic frameworks and zeolites for hydrocarbon separations, *J. Am. Chem. Soc.* 134 (May 19) (2012) 8115–8126.
- [72] D. Holmes Parker, M.E. Jones, B.E. Koel, Determination of the reaction order and activation energy for desorption kinetics using TPD spectra: application to D₂ desorption from Ag(111), *Surf. Sci.* 233 (July 1) (1990) 65–73.
- [73] Z. Zhang, S. Xian, H. Xi, H. Wang, Z. Li, Improvement of CO₂ adsorption on ZIF-8 crystals modified by enhancing basicity of surface, *Chem. Eng. Sci.* 66 (October 20) (2011) 4878–4888.
- [74] P.A. Redhead, Thermal desorption of gases, *Vacuum* 12 (July 4) (1962) 203–211.
- [75] F. Xu, S. Xian, Q. Xia, Y. Li, Z. Li, Effect of textural properties on the adsorption and desorption of toluene on the metal-organic frameworks HKUST-1 and MIL-101, effect of textural properties on the adsorption and desorption of toluene on the metal-organic frameworks HKUST-1 and MIL-101, *Adsorp. Sci. Technol.* 31 (April 4) (2013) 325–339.
- [76] H. Pan, M. Xu, Z. Li, S. Huang, C. He, Catalytic combustion of styrene over copper-based catalyst: inhibitory effect of water vapor, *Chemosphere* 76 (July 5) (2009) 721–726.

Supplementary information

ADSORBENT SCREENING FOR AIRBORNE BTEX ANALYSIS AND REMOVAL

Irene Lara-Ibeas^{1,2}, Cristina Megías-Sayago³, Alberto Rodriguez-Cuevas⁴, Rubén Ocampo¹, Benoît Louis³, Stéphane Colin², Stéphane Le Calvé^{1,4,*}

¹ ICPEES – Institut de Chimie et Procédés pour l’Energie, l’Environnement et la Santé, Atmospheric Physical Chemistry Team, UMR 7515 CNRS – Université de Strasbourg – ECPM, 25 rue Becquerel F-67087 Strasbourg cedex 2, France

² Institut Clément Ader (ICA), Université de Toulouse/CNRS, INSA, ISAE-SUPAERO, Mines-Albi, UPS, 31400 Toulouse, France

³ ICPEES – Institut de Chimie et Procédés pour l’Energie, l’Environnement et la Santé, Energy and Fuels for a Sustainable Environment Team, UMR 7515 CNRS – Université de Strasbourg – ECPM, 25 rue Becquerel F-67087 Strasbourg cedex 2, France

⁴ In’Air Solutions, 25 rue Becquerel, 67087 Strasbourg, France

* slecalve@unistra.fr; Tel.: +33-3-6885-0368

Table of contents

Figure S1. Schematic representation of thermal desorption tube employed in breakthrough tests

Figure S2. Schematic drawing of experimental set-up for dynamic adsorption experiments

Figure S3. Pore size distribution of SBA-16

Table S1. BTEX physicochemical properties

Figure S4. Pore size distribution of HKUST-1

Figure S5. ATG analysis of Carbopack® B (a), SBA-16 (b) and HKUST-1 (c) after 2 hours of exposure to ambient air

Figure S6. Linear relationship between benzene (a) and toluene (b) adsorption capacity with mesopore size

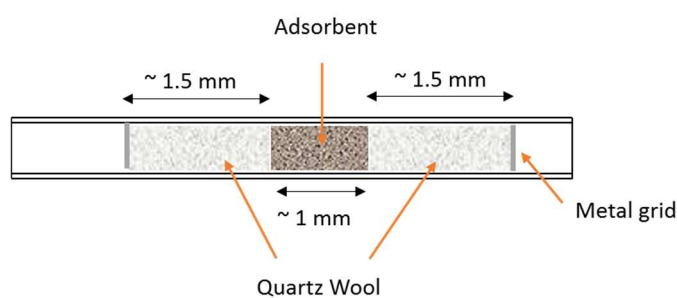


Figure S1. Schematic representation of a stainless-steel thermal desorption tube employed in breakthrough tests. Dimensions: 89 mm (length) × 6.4 mm (outside diameter) × 5 mm (internal diameter)

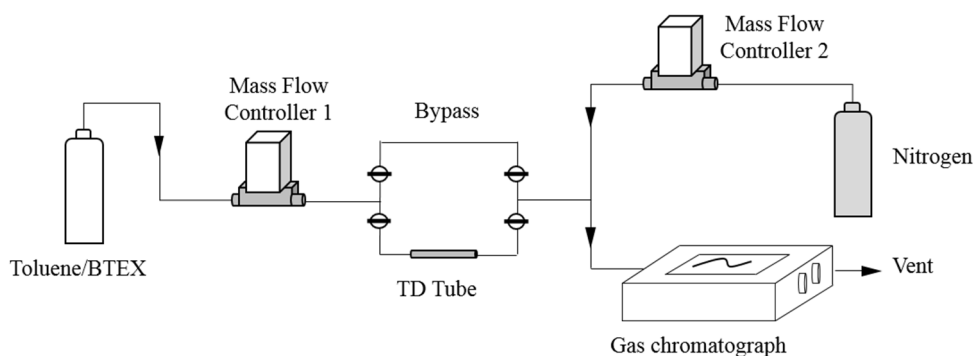


Figure S2. Schematic drawing of experimental set-up for dynamic adsorption experiments

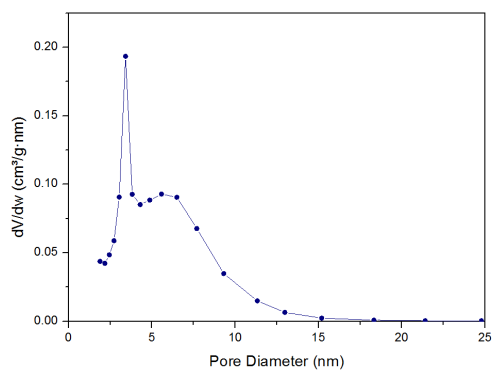


Figure S3. Pore size distribution of SBA-16

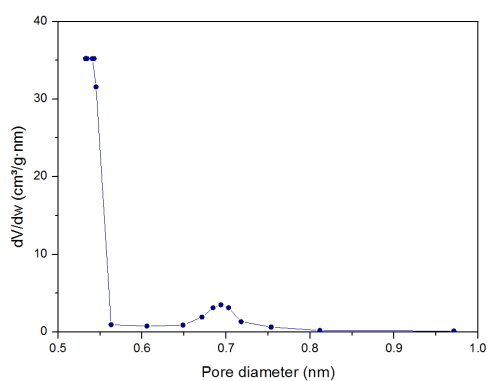


Figure S4. Pore size distribution of HKUST-1

Table S1. BTEX physicochemical properties

Compound	Molar mass (g/mol)	Boiling point (°C)	Vapor pressure at 20°C (kPa)	Dipole moment (D)*	Polarizability (Å ³)	Kinetic diameter (nm)
Benzene	78.11	80.1	10	0	10.44	0.585
Toluene	92.14	110.6	2.9	0.37	12.40	0.585
Ethylbenzene	106.17	136	1.00	0.59	14.24	0.6
o-Xylene	106.16	144.4	0.93	0.640	14.25	0.68
m-Xylene	106.16	139	1.20	0.35	14.33	0.68
p-Xylene	106.16	138.4	1.20	0	14.35	0.585

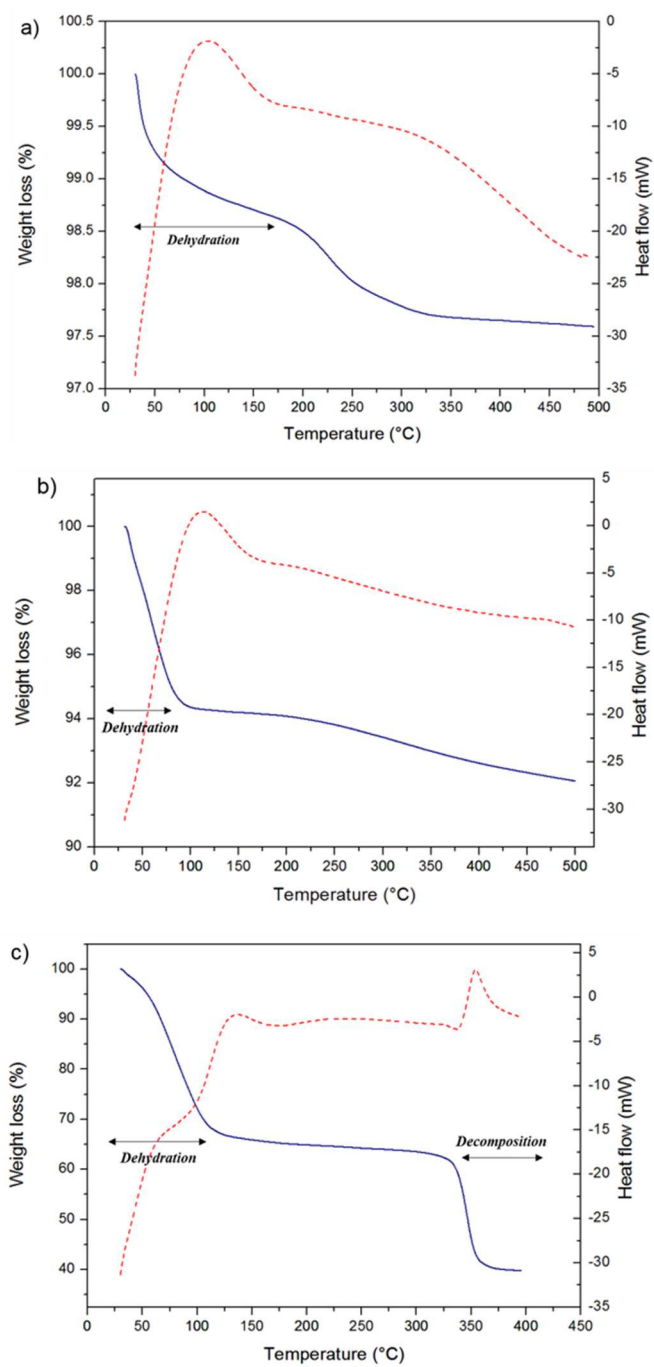


Figure S5. ATG analysis of Carbopack® B (a), SBA-16 (b) and HKUST-1 (c) after 2 hours of exposure to ambient air. Weight loss (blue line), heat flow (red dashed line).

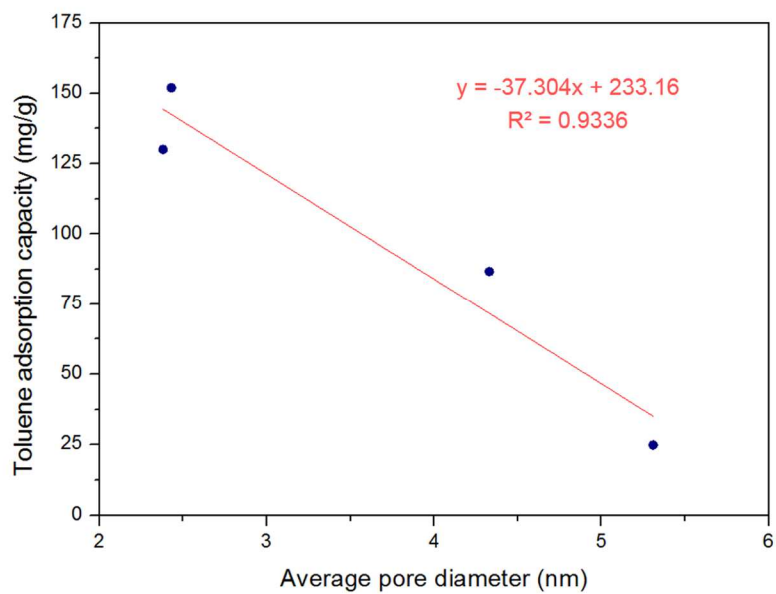


Figure S6. Linear relationship between toluene adsorption capacity and mesopore size. Data from refs: (Qin et al., 2013; Zhang et al., 2012) and the average pore diameter of SBA-16 (this work)

5.1.3 Conclusions

Three commercially available materials namely Carbopack® B, SBA-16 and HKUST-1 have been investigated to evaluate their performance for gaseous BTEX adsorption at low concentrations (10 - 100 ppm). These materials were selected for their diverse specific surface area, porosity and surface chemistry, which presumably lead to different adsorbate-adsorbent interactions. Single and multicomponent dynamic adsorption experiments were conducted to determine the adsorption capacity of those materials. In these experiments, SBA-16 exhibited the higher adsorption capacity in both single and multicomponent tests, followed by Carbopack® B and HKUST-1. Results obtained from the breakthrough curves suggested that adsorption capacities of each compound were strongly related to adsorbate-adsorbent interactions as well as to the presence of micropores. The strength of these interactions seems to be also associated to the intensity of the roll-up effect observed in multicomponent adsorption experiments. In these tests, roll-up phenomenon may result in the total desorption of the most volatile compound, i.e. benzene on Carbopack® B. Therefore, it is of significant interest to characterize this effect, which could happen when using these adsorbents for analysis and/or removal of gaseous pollutant mixtures.

Finally, toluene was selected as a representative molecule of BTEX and temperature programmed desorption (TPD) analyses were conducted to evaluate the activation energy of desorption. The results revealed that toluene is more strongly adsorbed in the microporous material, i.e. HKUST-1, whereas the strength adsorbate-adsorbent interactions appear to be comparable for Carbopack® B and SBA-16.

Among the investigated adsorbents, SBA-16 exhibited the highest adsorption capacity, a minimum roll-up and a reasonable activation energy for desorption; therefore, it appears to be the most suitable for gaseous BTEX analysis and removal.

5.2 BTEX adsorption on zeolites

5.2.1 Introduction

After the assessment of BTEX adsorption performance of three different types of adsorbents, it was decided to investigate their sorption on zeolites differing in their chemical composition to properly evaluate the influence of surface chemistry on BTEX adsorption. For this study, a material having an easily tailorable surface chemistry was selected: ZSM-5 zeolite. The chemical composition in zeolites

can be modified by varying the amount of aluminium employed during synthesis. Furthermore, zeolites have high specific surface area, are thermally stable up to very high temperatures and present well-defined microporous structures with a pore size of ~ 0.55 nm. A pore size similar to the kinetic diameter of BTEX molecules may result in the steric exclusion of larger molecules, leading to preferential adsorption of BTEX. This selectivity can be very advantageous for BTEX analysis applications since the preconcentration step, apart from increasing sensitivity, may serve to eliminate interfering compounds.

In this work, several ZSM-5 zeolites with Si/Al ratios ranging from 79 to 310 were synthesized *via* fluoride route and characterized in terms of textural properties and acidity. As in the previous section, dynamic adsorption experiments of a mixture of BTEX were performed to evaluate the adsorption performance of the different zeolites. Afterwards, toluene was selected as a probe molecule and thermogravimetric adsorption experiments were conducted to estimate the diffusion on each zeolite. Finally, the influence of zeolite properties on the adsorption capacity is discussed and the most suitable characteristics for selective adsorption of BTEX are presented.

5.2.2 Article 4 published in Journal of Environmental Chemical Engineering



Contents lists available at ScienceDirect

Journal of Environmental Chemical Engineering

journal homepage: www.elsevier.com/locate/jece

Volatile organic compounds (VOCs) removal capacity of ZSM-5 zeolite adsorbents for near real-time BTEX detection

Cristina Megías-Sayago^{a,*}, Irene Lara-Ibeas^b, Qiang Wang^c, Stephane Le Calvé^{b,d}, Benoît Louis^a^a ICPEES – Institut de Chimie et Procédés pour l’Energie, l’Environnement et la Santé, Energy and Fuels for a Sustainable Environment Team, UMR 7515 CNRS – Université de Strasbourg – ECPM, 25 Rue Becquerel F-67087 Strasbourg Cedex 2, France^b ICPEES – Institut de Chimie et Procédés pour l’Energie, l’Environnement et la Santé, Group of Atmospheric Physical Chemistry, UMR 7515 CNRS – Université de Strasbourg – ECPM, 25 Rue Becquerel F-67087 Strasbourg Cedex 2, France^c Environmental Functional Nanomaterials (EFN) Laboratory, College of Environmental Science and Engineering, Beijing Forestry University, Beijing 100083, China^d In’Air Solutions, 25 Rue Becquerel, 67000 Strasbourg, France

ARTICLE INFO

Keywords:

BTEX abatement
ZSM-5 zeolite
Adsorbent design
Real-time detection

ABSTRACT

The environmental impact of air pollution along with the registered detrimental effects on human health due to BTEX exposure have forced most countries to set limit values in public spaces and buildings, requiring the development of *in situ* devices able to quantify in (near)-real time the pollutants concentration, even at ppb levels. In this work, several ZSM-5 zeolites with $79 < \text{Si} / \text{Al} < 316$ have been synthesized and used as part of a pre-concentration unit connected to a miniaturized GC prototype, needed to drop the detection limit according to current legislation. The most important parameters influencing the multicomponent gas-phase adsorption of BTEX over ZSM-5 zeolites have been found to be the number of available acid sites (Al content), the zeolite pore size and its hydrophobicity. The experimental results demonstrate that a compromise between the hydrophobic character and the number of Al atoms should be found in order to properly design an adsorbent for near-real time BTEX detection.

1. Introduction

The uncontrolled pollutant emissions mainly derived from the transport sector and several industrial processes have turned air pollution as one of the most notorious worldwide problem nowadays. Climate change evidence along with the numerous publications dealing with air pollution impact in human health [1–3] have forced most developing countries to apply severe laws aiming its depletion. Volatile organic compounds (VOCs) usually denote organic compounds mainly originated during engine combustion and industrial emissions but they can be also released, to a minor extent, from building materials or domestic products. Amid the wide variety of VOCs, special interest has been paid to benzene, toluene, ethylbenzene and xylenes (BTEX) due to their toxic, mutagenic and/or carcinogenic effects even at low concentrations [4]. Indeed, several effects in human health as skin and eyes irritation, headache, memory problems and loss of coordination have been linked to BTEX exposure [5,6] along with more detrimental effects as the development of leukemia, ascribed to the highest carcinogenic compound, *i.e.*, benzene [7]. These severe problems drove the European Union in 2013 to set a limit value of 1.6 ppb for benzene in public

buildings, value that was further decreased to 0.6 ppb in 2016 in France [8]. Therefore, the adopted legislation forces somehow the development of new, *in-situ* fast and highly sensitive analytical devices.

Gas chromatography (GC) has been the most powerful technique to detect BTEX in air, having detection limits down to ppt levels. The main problem associated to classical chromatographs, however, has been their huge size and weight as well as the high-energy consumption, factor that limit their application for *in-situ* measurements. Therefore, most of the time the air is sampled on site on adsorbents tubes which are then analyzed in the laboratory after thermal or chemical desorption. As a consequence, the development of miniaturized systems for real-time BTEX analysis has attracted much attention in the last years. Lately, low-size GC prototypes have been successfully developed. However, the detection limit in the ppt range remains a challenge in most of these small devices. Recently, Lara-Ibeas [8] have designed a compact GC prototype equipped with a pre-concentration unit which lowered the detection limit down to sub-ppb level. This unit is filled with an adsorbent that allows the BTEX pre-concentration during *in-situ* measurements in a way that the gaseous samples are taken during a given time, adsorbed (concentrated) in the solid adsorbent and, finally,

* Corresponding author.

E-mail address: megiassayago@unistra.fr (C. Megías-Sayago).<https://doi.org/10.1016/j.jece.2020.103724>

Received 29 October 2019; Received in revised form 21 January 2020; Accepted 27 January 2020

Available online 27 January 2020

2213-3437/ © 2020 Published by Elsevier Ltd.

desorbed (by increasing the temperature in the unit) to be analyzed by the miniaturized GC. Hence, low-polluted environments can be studied; being possible to tune the sampling time in order to increase BTEX injected amount as much as needed.

Activated carbons are the most useful adsorbents for VOCs uptake [9–11], nevertheless the practical problems linked to their use such as the difficulty for regeneration [12] and flammability [13] limit their implementation in the mentioned application. An adsorbent with high specific surface area, non-toxic character, high thermal stability and easy to regenerate (able to bear charge / discharge cycles) is highly warranted. In this sense, zeolite-type materials exhibit all these features as well as tailorable surface hydrophobicity, which turn them perfect candidates to be used as adsorbents in the aforementioned pre-concentration unit. Another important factor is the zeolite pore size which differs among the different zeolitic frameworks, becoming a tunable and interesting property. Indeed, properly tuning the size of the pores allows selective adsorption, thus diminishing the interferences due to the presence of other atmospheric organic pollutants during the analysis. The latter became necessary in high-polluted environments, as is the case of airports, where the concentration of VOCs can reach high concentrations [14,15]. Hence, to ensure a wider application of the GC prototype, a zeolite with pore size close to the BTEX cross-sectional areas [16] is highly desired. In this context, ZSM-5 zeolite having a pore size of roughly 0.55 nm appears to be a suitable candidate.

In this work, several ZSM-5 zeolites differing in their Si/Al molar ratio are synthesized *via* fluoride route and characterized by different techniques. Multicomponent gas-phase BTEX breakthrough experiments have been carried out over all as-prepared zeolites, packed separately in thermal desorption tubes connected to the miniaturized GC prototype. The impact of the zeolite properties on the adsorption performance has been deeply studied and discussed, aiming to establish the key parameters affecting the process which will help us to accurately design an adsorbent for near real-time BTEX detection.

2. Experimental

2.1. H-ZSM-5 synthesis

ZSM-5 zeolites were synthesized *via* fluoride-mediated route adapted from our previous studies [17,18]. Typically, the aluminum source (different amounts to achieve Si/Al = 300, 200, 150, 100 and 50 mol ratios, respectively) was placed in a 150 mL-Erlenmeyer flask where 50 mL of distilled water was added under vigorous stirring (700 rpm, r.t.). Once dissolved, TPABr (0.498 g) and NH_4F (1.103 g) were sequentially added. Finally, 1.607 g SiO_2 (Aeroperl 300/30, Evonik) was gradually added during 5 min. The gel was then aged 2 h under vigorous stirring and finally autoclaved at 443 K for 144 h. H-zeolite form was obtained after a single calcination at 823 K during 15 h in static air. The samples were named as ZSM-5_1 to ZSM-5_5, respectively, being the number increase related with the Si/Al molar ratio (abbreviated as SAR) decrease.

2.2. Characterization

X-ray diffraction (XRD) analysis was performed in a Bruker D8 (Cu $\text{K}\alpha$) diffractometer operated at 40 kV and 40 mA. XRD patterns were recorded in the $2\theta = 5 - 60^\circ$ range with a step size of 0.05° .

SEM micrographs were acquired in a JEOL FEG-6700 F microscope working at a 9 kV accelerating voltage.

Zeolite chemical compositions were determined by X-ray fluorescence (XRF) using a XEPOS (AMETEK) device equipped with a Rh radiation tube.

Surface areas (BET method) and pore volumes were determined by nitrogen physisorption using a Micromeritics ASAP 2420 equipment. Samples were pre-treated *in-situ* at 250 °C under vacuum prior to the analyses.

The acid site density was evaluated by NH_3 -TPD (temperature programmed ammonia desorption) by using a Micromeritics AutoChem II chemisorption analyzer equipped with a TCD detector. Samples were pre-treated *in-situ* at 550 °C during 1 h. Afterwards, samples were cooled down to room temperature and a 5 % NH_3/He flow was passed through the reactor. Once physisorbed ammonia was removed, the temperature gradually increased to 550 °C.

^{27}Al ($I = 5/2$) MAS NMR was carried out with a Bruker Avance II 400 spectrometer operating at $B_0 = 9.4 \text{ T}$ (Larmor frequency = 104.2 MHz) equipped with a Bruker 2.5 mm double channel probe. Measurements were carried out with $[\text{Al}(\text{H}_2\text{O})_6]^{3+}$ as external standard reference.

The hydrophilicity of the zeolites has been determined by contact angle measurements. For this purpose, 20 mg of powder was placed under a hydraulic press and let under 12 bar for 30 s to obtain a compact pellet. Wetting properties of the samples were determined by static contact angle using an optical tensiometer (Attension theta, Biolin Scientific). A 2 μL drop of purified water (milli Q) was deposited on the pellet surface and the angle was recorded by the camera mounted on the device.

Thermogravimetric analysis (TGA) was employed to monitor toluene uptake measurements. Prior to analysis, the samples were sieved in order to have a particle diameter between 0.074 and 0.100 mm. After that, they were placed in the sample holder and pre-treated *in-situ* at 550 °C for 30 min with a heating ramp of $10^\circ\text{C}/\text{min}$ under a 40 mL/min nitrogen flow. Once conditioned, the temperature was diminished to 40 °C, and gas switched for 0.28 mg/min toluene concentration. The mass variation during all the experiment was monitored until saturation. In some cases, toluene desorption was also recorded.

2.3. Breakthrough experiments

Single dynamic adsorption experiments were carried out for each adsorbent in a homemade set-up schematized in Fig. S1 (Supporting Information, SI). For these tests, $15.0 \pm 0.2 \text{ mg}$ (Mettler Toledo AG204, USA) of the as-prepared zeolites were packed separately in thermal desorption (TD) tubes (Sigma Aldrich, USA) using two quartz wool plugs to fix the adsorbent bed. These tubes were placed in the aforementioned setup through which $5.00 \pm 0.05 \text{ mL}/\text{min}$ (F-201CV-020, Bronkhorst, Netherlands) constant flow of an equimolar mixture of BTEX diluted in nitrogen ($10 \pm 1 \text{ ppm}$, Air Products, France) was passed. Prior to analysis, the tube outlet flow was diluted with pure nitrogen (5 mL/min diluted with 95 mL/min pure N_2 flow, being 500 ppb the final concentration) to end up in the linear calibration range of the instrument and to avoid possible detector saturation. The gaseous effluent was then continuously analyzed by a gas chromatograph ($\mu\text{BTEX-1}$ In'Air Solutions, France). This instrument operates according to three steps: sampling, separation and detection. A gaseous sample is collected and introduced in a 200 μL sampling loop by means of a SP 570 EC-BL micropump (Schwarzer Precision, Germany). It is subsequently injected into the GC column (i.d. 0.18 mm, RXI-624 stationary phase, 1 μm film thickness, Restek, Bellefonte, PA, USA) for compounds separation and the detection is conducted employing an eVx Blue mini photoionization detector (PID) (Baseline MOCOCN, Lyons, CO, USA) [19–21].

Prior to each adsorption experiment, the gas stream was flowed through a bypass, directly diluted as previously mentioned and then analyzed to determine the peak area corresponding to the initial concentration. The zeolite samples were conditioned at 350 °C for 2 h under a helium flow of 50 mL/min using thermal desorber (TurboMatrix 350, Perkin Elmer, USA) to remove the possible adsorbed molecules.

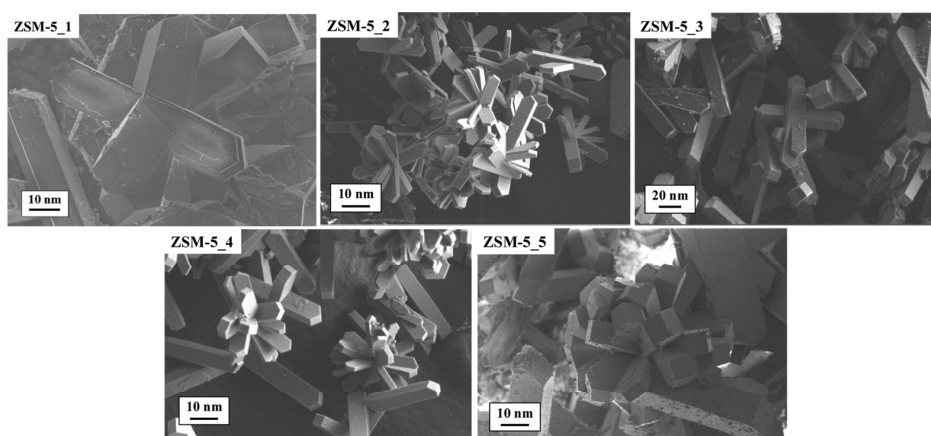


Fig. 1. SEM micrographs of as-synthesized ZSM-5 zeolites.

3. Results and discussion

3.1. Samples characterization

The diffraction patterns of all synthesized ZSM-5 zeolites confirm the sole presence of the MFI structure (Fig. S2) [18,22] together with high crystallinity degree in all cases. The latter is usually related with the fluoride medium used during the zeolite synthesis which provides milder conditions in comparison with alkaline medium, thus facilitating the formation of few nuclei under diluted conditions as consequence of a slow release of SiO_xF_y^- species [17,23]. This, along with high Si/Al ratios, leads to the formation of zeolites with fewer defects and more open structures than in alkaline medium [24]. The formation of highly crystalline zeolites is further evidenced by SEM (Fig. 1). In all cases, large coffin-shaped crystals having between 30–60 μm in size are formed.

The chemical composition, textural properties and the total number of Brønsted acid sites of fresh samples are summarized in Table 1. The targeted variation of acid properties is successfully accomplished as confirmed by XRF results and further contrasted after NH_3 -TPD experiments. SAR (Si/Al molar ratio) values ranging from 316 to 79 decrease within the series, hence providing a suitable acid site density variation ($\text{mmol}(\text{H}^+)/\text{g}$ zeolite) range. This approach is very useful to evaluate the Al content (indirectly the acidity) effect on the zeolites adsorptive properties. Likewise for textural properties, similar values regarding both specific surface area and pore volumes are obtained, thus facilitating the sole evaluation of acid site density during the multicomponent vapor-phase adsorption of BTEX.

3.2. BTEX adsorption

Breakthrough curves represent the evolution of the adsorbate

Table 1
Chemical composition, acid site density and textural properties of as-prepared H-ZSM-5 zeolites.

Sample	SAR (XRF)	Acid site density ($\text{mmol}(\text{H}^+)/\text{g}$ zeolite) ^a	S_{BET} [m^2/g]	V_{pore} (cm^3/g)	Mean pore diameter (nm)
ZSM-5_1	316	0.044	386	0.19	0.55 ± 0.01
ZSM-5_2	198	0.132	367	0.17	0.55 ± 0.01
ZSM-5_3	132	0.133	352	0.18	0.55 ± 0.01
ZSM-5_4	113	0.172	375	0.18	0.55 ± 0.01
ZSM-5_5	79	0.249	348	0.18	0.55 ± 0.01

concentration in the gaseous effluent leaving the adsorbent bed as a function of time. In this type of curves, two important features are obtained: breakthrough time (t_b) and saturation time (t_s). The definition of breakthrough time may vary depending on the application, but the typical values are 1 % or 5 % of the initial concentration. In this work, t_b is defined as the time at which 5 % of the molecules are leaving the adsorbent bed so that when 5 % of the injected concentration (C_0) is passing through the adsorbent and, thus, the measured concentration at the outlet (C) is equal to $0.05 C_0$. Up to this point, the adsorption can be considered complete. Once t_b is reached ($C/C_0 = 0.05$), the analyte concentration at the outlet starts to rise until the saturation point. The steepness of the concentration profile provides useful information about the mass transfer from gas phase to the sorption sites inside the sorbent particles. Once saturation time is reached ($C/C_0 = 1$), all the adsorption sites are occupied. At this point, sorbent is completely saturated and sorption in the bed does not occur. Consequently, the outlet concentration is constant and equal to the initial concentration injected upstream of the adsorbent.

Fig. 2 shows the results obtained after the breakthrough tests over all synthesized ZSM-5 zeolites. For each sample, five breakthrough curves can be distinguished which correspond to each single adsorbate interaction with the zeolite. It should be noted that, due to the long breakthrough times registered, the room temperature was subjected to variations that finally affected the breakthrough curve. As an example the first sample, ZSM-5_1, between 1600–2400 min corresponding to nighttime when room temperature diminished till its lowest value.

Apparently, the obtained results seem comparable, as the general behavior remains quite similar. Generally speaking, a clear exclusion of *o*-xylene during sorption experiments is observed as well as a C/C_0 constant value of around 0.4–0.5 for *m/p*-xylene mixture suggesting the exclusion of one of the isomers. Related to this observation, it should be considered that adsorbate molecules within the zeolite framework are exposed to different possible interactions among which acid-base ones must be taken into account [25]. When comparing the relative basicities of benzene, toluene and *p*-xylene (0.61, 0.92 and 1.26, respectively) one may expect that the three considered VOCs exhibit different level of interactions toward Brønsted acid sites, being xylenes the ones interacting strongly due to their highest relative basicity. However, the obtained results show that xylenes present the lowest abatement. This adsorption reduction with respect to xylenes isomers could be linked to the small micropores of ZSM-5 – 0.55×0.51 nm and 0.56×0.53 nm for [100] and [010] planes (Fig. 3), respectively, and the differences between the cross-sectional areas of adsorbates. Indeed, *m/o*-xylene molecules cross-sectional areas are



Fig. 2. Breakthrough curves obtained during BTEX adsorption experiments with 10 ppm mixture.

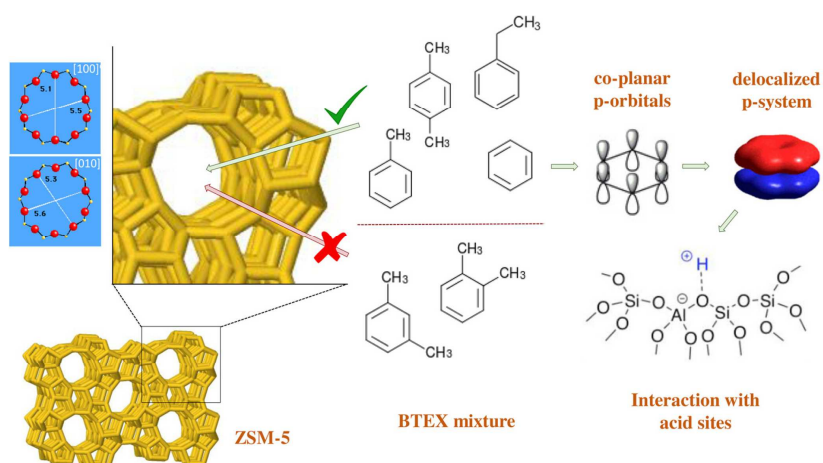


Fig. 3. Schematic representation of BTEX adsorption process over ZSM-5 zeolites.

0.56 nm [16], higher than those of ethylbenzene (0.55 nm), p-xylene (0.54 nm), toluene (0.47 nm) and benzene (0.43 nm) [16]. The latter explains the steric exclusion of m/o-xylene molecules in zeolite micropores [26] thus supporting the observed experimental data. It should be underlined that, despite this steric exclusion of m/o-xylene prevents their adsorption, it allows the separation of m/p-xylene isomers, usually a difficult task in gas chromatography which could be reached by coupling a gas chromatograph to a preconcentration unit filled with this adsorbent. Indeed, the chromatographic analysis method used during this work does not allow the separated quantification of m/p-xylenes since they are coeluted. Therefore, the steric exclusion over ZSM-5 zeolites could be an effective strategy to separate both isomers without the need for a very specific chromatographic column.

Concerning benzene, toluene and ethylbenzene breakthrough curves, there are mainly two aspects that should be taken into account. Firstly, the phenomenon known as roll-up, consisting in desorption of a molecule by competitive adsorption of a more strongly adsorbed molecule (C/C_0 values over 1) and, secondly, the uptake curve slope. Attending to the first one, benzene trends always to desorb whatever the zeolite composition, toluene is largely desorbed after interaction with samples 1, 2 and 3, respectively, but the desorption occurs to a much lesser extent in samples 4 and 5 and ethylbenzene stays trapped into the zeolite framework in all the experiments. As mentioned before, adsorbate molecules are exposed to different possible interactions among which Brønsted acid-base ones seem to be the key interactions controlling the process as demonstrated by Alejandro et al. [25]. They confirmed by means of FTIR that benzene, toluene and xylene molecules are adsorbed within the ZSM-5 framework due to a direct interaction between acid sites and the delocalized π -system of benzene ring (see Fig. 3). Logically the interaction strength may change between all molecules due to slight variations in the π -cloud as a consequence of the (m)ethyl substituents in the ring. Methyl group (toluene) is an electron donor which leads to an electron-rich π -system thus enabling stronger interaction with H^+ sites in the zeolite. The π -donor character of methyl and ethyl groups may be assumed the same.

Considering now the two aforementioned aspects, *i.e.* the desorption process and the slope of uptake curve, not only the π -interaction should be kept in mind but also the diffusion process of each molecule within zeolite channels. Benzene is the smallest interacting molecule (0.43 nm), followed by toluene (0.47 nm) and ethylbenzene (0.55 nm). One may therefore *a priori* expect the same diffusion trend through the zeolite cavities. Indeed, the curve slopes verify this trend, the greatest is observed for benzene, followed by toluene and ethylbenzene.

As for the desorption process, benzene is the molecule diffusing faster which is also characterized by a “weaker” interaction with the acid sites. The latter may explain its behavior during the breakthrough tests together with a certain degree of adsorptive competition with toluene and ethylbenzene. Toluene, for its part, has both bigger cross-sectional area and “stronger” interaction with zeolite. It is desorbed in the samples with low aluminum content (1, 2 and 3) but remains adsorbed in those with higher Al content (4 and 5). The latter confirms somehow that the interaction is directly related to the number of available Brønsted acid sites. It seems that the toluene molecules that diffuse along high SAR zeolite channels face problems to find available active sites, then being desorbed. The same effect could be expected for ethylbenzene, however, as its cross-sectional area is comparable to zeolite pore size, its diffusion along the channels is limited (see its uptake slope), thus hindering its possible desorption. This phenomenon is also observed for adsorbed p-xylene.

In order to properly evaluate the effect of ZSM-5 chemical composition in BTEX abatement, the breakthrough times and adsorption capacities over the five as-prepared samples have been evaluated for each compound separately. Table S1 summarizes the obtained breakthrough times, presented as a function of the Si/Al molar ratio in Fig. 4. As it can be seen, there is a correlation between the breakthrough time values and the Al content in the zeolite, different for each adsorbed compound.

In all cases, the lowest SAR sample (ZSM-5.5, SAR 79) is excluded from the trend, which may give us some insights about the physical and/or chemical parameters involved during the adsorption process.

Regarding the rest of zeolite samples (ZSM-5.1 to ZSM-5.4) a clear maximum is situated around SAR 220 ± 10 (ZSM-5.2, SAR 198) for Benzene, Toluene and Ethyl Benzene. Conversely, p-Xylene exhibits a minimum value at SAR value of 250 and reaches its maximum value over ZSM-5.4 (SAR 113). It appears that a proper explanation of the observed results is far from being simple and not directly related to simply the aluminum content in the zeolite framework. Certainly, the Al percentage is directly related with the total number of Brønsted acid sites but also with the zeolite hydrophilic character [27], even higher when some Al species are in an octahedral environment. This is considered as a defect in the zeolite network, usually denoted as EFAL species (extra-framework Al species). In this case and due to the hydrophobic character of the adsorbates, the higher the zeolite hydrophobic character, the stronger the interaction between them. In addition, the Al content (number of active sites, possible presence of EFAL) also affects the molecules diffusion thus altering the obtained breakthrough times and sorption capacities. Therefore, a compromise between all factors should lead to an optimized system.

In order to evaluate the EFAL percentage and hydrophobic character of the samples with respect to their Al content, ZSM-5.2 (SAR 198) and ZSM-5.5 (SAR 79) samples were chosen to perform both ^{27}Al MAS NMR and contact angles measurements (Fig. S3). As *a priori* expected, EFAL species percentage increases with higher Al content (1 and 3 % for ZSM-5.2 and ZSM-5.5, respectively). The latter suggests that the hydrophilic character also increases from SAR 198 to 79 due to an increment in both framework Al and EFAL species. Contact angle measurements confirm these results, sample 2 exhibited the highest angle meaning that the hydrophobic character of high SAR zeolites is superior to lower SAR zeolites.

From these results, the obtained breakthrough time dependence with Si/Al ratio can be understood as a compromise between the number of acid sites needed for allowing the adsorption process and the hydrophobic character of the adsorbent. For benzene, toluene and ethylbenzene that compromise (optimum) is attained when SAR is 198. Nevertheless, the following two questions arise: why is systematically sample 5 excluded from all the correlations shown in Fig. 4? Are those differences related to molecules diffusion paths?

In order to evaluate the effective diffusivity, toluene was chosen as representative probe molecule. Uptake measurements were carried out in a thermobalance under non-equilibrium isothermal conditions (40 °C), in a way that the mass variation was monitored during the experiment as shown in Fig. S4. The toluene adsorption capacity is directly obtained from the measured variations while for the effective diffusivity calculation some specific initial and boundary conditions should be fixed as presented in our recent work [28]. Derived from this, the effective diffusivity can be calculated from the linear part of the uptake curves that can be expressed as follows (Eq. 1):

$$\frac{q - q_0}{q_\infty - q_0} = \frac{6}{\sqrt{\pi}} \left(\frac{D_{eff}}{r^2} \right)^{1/2} \sqrt{t} \quad (1)$$

where q is the sample weight at a given time, q_0 the initial mass sample, q_∞ the saturation weight, D_{eff} the effective diffusivity, r the particles diameter and t the time.

The toluene uptake curves are presented in Fig. 5 where the y-axis represents catalyst mass percentage as a function of time. In general, two stages concerning the sorption process can be differentiated depending on the sample. Initially, a faster uptake reaction that occurs at the initial stage of toluene absorption and, secondly, a later long-period stage where it is possible to distinguish a continuous (but considerably slower) increase in the sample weight (sample 5). Zeolites with SAR over 100 (samples 2, 3 and 4) present similar behavior being the saturation time t_s ($Q/Q_\infty = 1$) directly related with Al content in a way

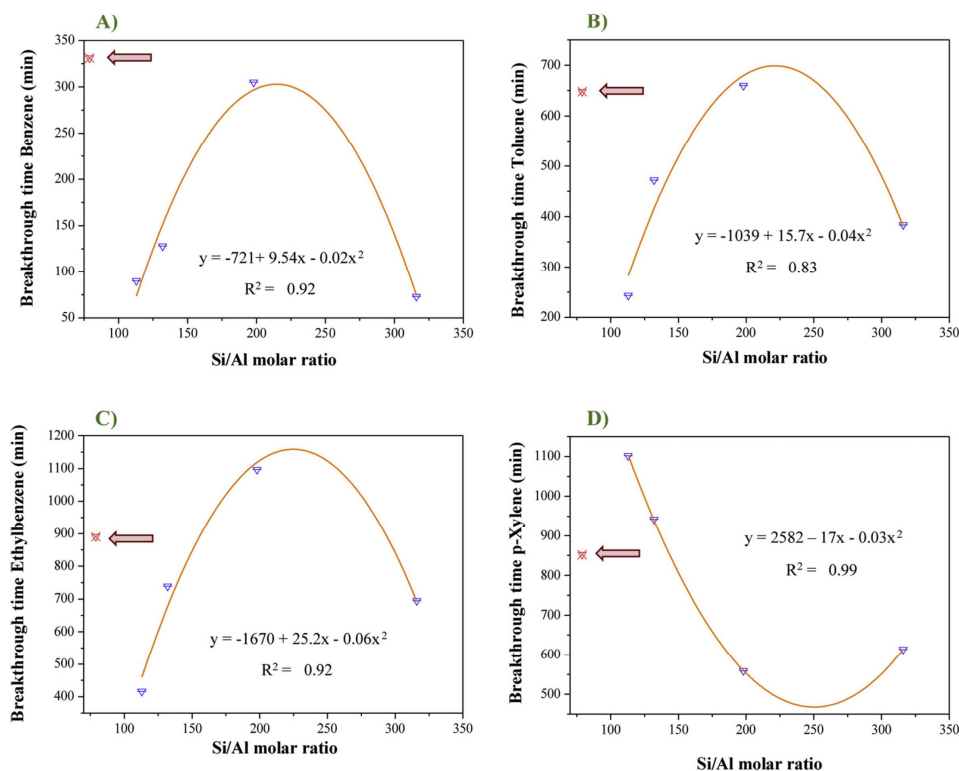


Fig. 4. Breakthrough time dependence on zeolite Si/Al molar ratio. A) Benzene, B) Toluene, C) Ethylbenzene and D) p-Xylene.

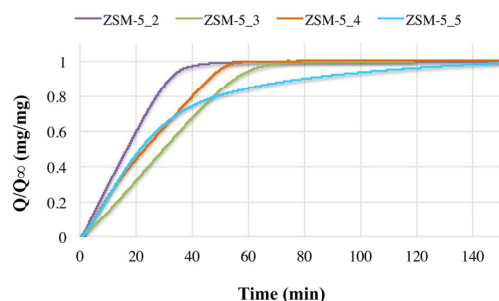


Fig. 5. Toluene uptake curves (TGA experiments).

that the higher the SAR, the lower the t_b . These results demonstrate, once again, that the active sites for toluene adsorption are the acid sites and, therefore, the lower the Al amount the lower the adsorption time.

Again, sample 5 behaves differently, showing the above-mentioned second step, the slower but continuous toluene sorption. Nevertheless, it is noted that for ZSM-5_2 the linear part of the curve possesses slightly higher slope value compared to samples 3 and 4, which means that higher effective diffusivity could be envisaged in this sample. The calculated diffusivity coefficients are presented in Table 2 together with the registered toluene capacities ($\mu\text{mol/g}$). D_{eff} values follow this trend $ZSM-5_2 > ZSM-5_5 > ZSM-5_4 \approx ZSM-5_3$ which is similar to those appearing in Fig. 4B. Actually, the highest diffusivity values coincide with the longest breakthrough times. The latter highlights the importance and effect of diffusivity in the sorption process. The differences regarding the uptake curves of both samples (2 and 5) can be associated also to the Al atoms in the zeolite framework. ZSM-

Table 2

Toluene adsorption capacities and effective diffusional coefficients obtained from TGA experiments.

Sample	Q ($\mu\text{mol toluene/g zeolite}$)	Deff (m^2/s)
ZSM-5_2	581	1.6E-12
ZSM-5_3	640	6.0E-13
ZSM-5_4	667	6.5E-13
ZSM-5_5	728	1.1E-12

5_2 having low Al atoms and defects exhibits higher diffusion coefficient and faster saturation in comparison with ZSM-5_5, which seems to suffer from diffusional limitations. In this sample, the probability of encountering the next active site considerably raises as Al content is higher which means that a larger amount of toluene molecules diffuse and absorb within the pores, thus hindering the next toluene molecules diffusion along the cavities. This can be somehow contrasted by the observed toluene capacities, higher when Al content increases. These results suggest that the breakthrough time dependence with Si/Al ratio is mainly governed by the number of acid sites which directly influences both the hydrophobic character of the adsorbent and the effective diffusivity of the molecules along the channels.

The effect of the ZSM-5 chemical composition in BTEX abatement (Fig. 2) has also been evaluated in term of adsorption capacities for each compound. The dynamic adsorption capacity can be calculated from the breakthrough curve using the following equation (Eq. 2):

$$q = \frac{F C_0}{m} \int_{t_0}^{t_b} \left(1 - \frac{C}{C_0}\right) dt \quad (2)$$

where q is the dynamic adsorption capacity per gram of adsorbent ($\text{mg}/$

Table 3
Obtained adsorption capacities over prepared samples.

Sample	Adsorption capacity ($\mu\text{mol/g}$)				
	Benzene	Toluene	Ethylbenzene	P-Xylene	m/o-Xylene
ZSM-5_1	0	62.3 ± 2.1	232.9 ± 7.7	174.4 ± 5.8	0
ZSM-5_2	0	53.7 ± 1.8	247 ± 8.2	175.5 ± 5.8	0
ZSM-5_3	10.9 ± 0.4	76.1 ± 2.5	196 ± 6.5	155.1 ± 5.1	0
ZSM-5_4	0	75.1 ± 2.5	235.3 ± 7.8	170.4 ± 5.6	0
ZSM-5_5	20 ± 0.7	119.5 ± 3.9	249.7 ± 8.2	188.4 ± 6.2	0

g_{ads} , F is the gas flow rate (m^3/min), m is the mass of adsorbent (g), t_0 is the initial time (min), t_s is the saturation time (min), C_0 is the initial concentration (mg/m^3), C is the outlet concentration (mg/m^3) at a given time. The error on the calculation of the dynamic adsorption capacity has been estimated as follows:

$$\frac{\Delta q}{q} = \frac{\Delta F}{F} + \frac{\Delta C_0}{C_0} + \frac{\Delta t}{t} + \frac{\Delta m}{m}$$

where Δq is the error on the adsorption capacity. ΔF is the error on the flow rate, ΔC_0 is the error on the initial concentration and Δm is the error on the adsorbent mass.

The capacity values are presented in Table 3 and plotted vs. Si/Al molar ratio in Fig. 6.

In contrast to the breakthrough time dependence, the capacity variation does not follow a clear trend, except for toluene. Benzene remains adsorbed only in low SAR samples, thus suggesting that when the number of acid sites is limited, the most volatile compounds such as benzene are desorbed in favor of more strongly adsorbing species. Ethylbenzene and p-xylene adsorption capacities are comparable, not being affected by the Al content. The latter could be attributed to their

hindered diffusion along the cavities. Finally, toluene exhibits the same capacity as observed during TGA experiments for ZSM-5_2 to ZSM-5_5 samples, i.e., toluene capacity increases with Al content. It is clear then that, in terms of capacity values, the optimal system is that with lower SAR.

In order to evaluate the possible regeneration of the adsorbent, needed to employ it in realistic conditions, the total desorption of BTEX was evaluated by means of thermogravimetric measurements. In all cases, the final zeolite mass corresponds to that placed at the beginning of the experiment pointing out a successful regeneration of the adsorbent.

In summary, a proper adsorbent design involves the control of many factors dealing with both zeolite and adsorbate properties. The most important parameters influencing BTEX adsorption over ZSM-5 zeolites have been found to be the number of available acid sites (Al content), the zeolite pore size and the hydrophobicity. An optimum value regarding Al atoms and framework hydrophobic character is desirable to favor any pollutant adsorption. As mentioned in the characterization part, the used fluoride route leads to obtain zeolites with fewer defects compared to the classical alkaline route which, as a consequence, diminishes the adsorbent hydrophilicity. In fact, only 2 % extra-framework Al atoms (EFAl species) variation was observed when ZSM-5_2 (SAR 198) and ZSM-5_5 (SAR 79) were analyzed by ^{27}Al MAS NMR. The latter renders possible the utilization of lower SAR zeolites, which remarkably increment the adsorbate uptake due to the direct interaction adsorbate-Brønsted sites.

4. Conclusions

Several ZSM-5 zeolites with $79 < \text{Si} / \text{Al} < 316$ have been successfully synthesized and used in the multicomponent gas-phase adsorption of BTEX. The samples were packed separately in thermal desorption tubes connected to a miniaturized GC prototype, as a

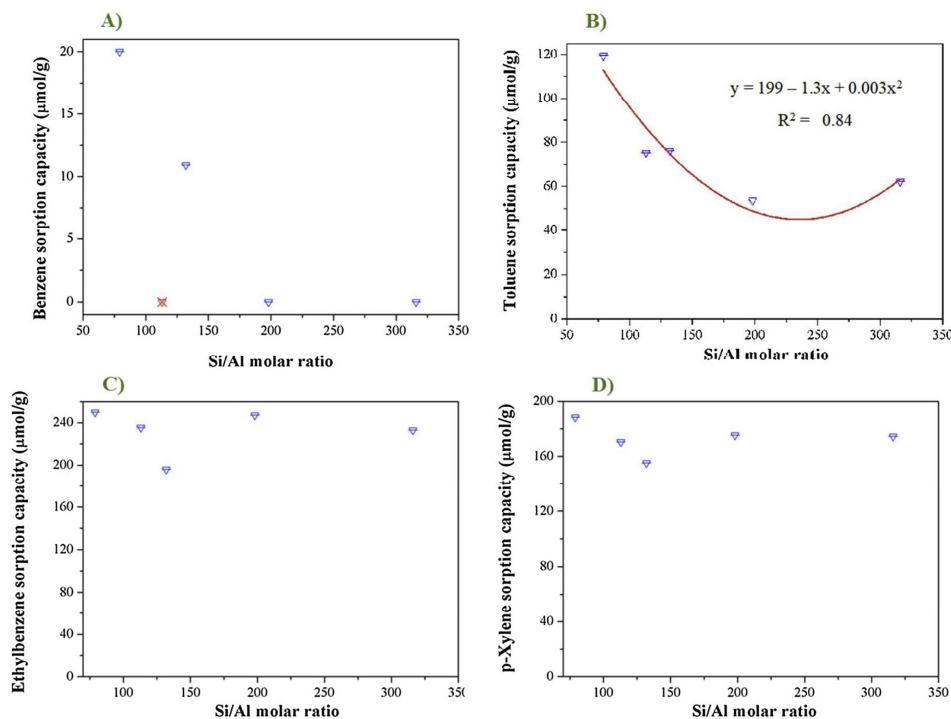


Fig. 6. Si/Al molar ratio effect on adsorption capacity for A) Benzene, B) Toluene, C) Ethylbenzene and D) p-Xylene.

representative approach to the pre-concentration unit needed to drop the detection limit according to current legislation. The design of an adsorbent for near real-time BTEX detection involves the control of several factors including both zeolite and adsorbate properties. The most important parameters influencing BTEX adsorption over ZSM-5 zeolites have been demonstrated to be the number of available acid sites (Al content), the hydrophobicity and the zeolite pore size. An optimum value regarding Al atoms and framework hydrophobic character is desirable to favor the pollutant adsorption. In this context, the fluoride-mediated synthesis of ZSM-5 zeolite appears as an excellent strategy. Indeed, zeolites with fewer defects and more open structures are obtained, compared to the classical alkaline route. In addition, this effect leads to higher hydrophobic materials even at low SAR, rendering possible the utilization of lower SAR zeolites, which remarkably raised the BTEX uptake due to the direct interaction adsorbate-Brønsted sites.

These experimental results demonstrate that a compromise between the hydrophobic character and the number of Al atoms should be tailored in order to properly design an adsorbent for near-real time BTEX detection, compromise that can be easily reached when zeolite-mediated fluoride route is used. In addition, such zeolites can be selective to p-Xylene whereas m-, and o-Xylenes are not trapped. This promising result suggests that it will be possible to synthesize in the future, a zeolite specific for benzene, which does not trap the other BTEX, since benzene is the only regulated aromatic compound in indoor air because of its very high toxicity. This could permit to avoid the long separation chromatographic step by injecting directly the desorbed benzene molecule into a detector.

CRedit authorship contribution statement

Cristina Megías-Sayago: Conceptualization, Methodology, Data curation, Formal analysis, Visualization, Investigation, Writing - original draft, Writing - review & editing. **Irene Lara-Ibeas:** Methodology, Data curation, Formal analysis, Visualization, Writing - original draft. **Qiang Wang:** Supervision, Validation, Funding acquisition. **Stephane Le Calvé:** Conceptualization, Methodology, Supervision, Validation, Funding acquisition, Project administration, Writing - original draft, Writing - review & editing. **Benoît Louis:** Conceptualization, Methodology, Supervision, Validation, Funding acquisition, Project administration, Writing - original draft, Writing - review & editing.

Declaration of Competing Interest

The authors declare that there are no conflicts of interest.

Acknowledgments

This work has received funding from the Clean Sky 2 Joint Undertaking under the European Union's Horizon 2020 research and innovation program under grant agreement No 687014 (MACAO Project). This work was also funded by the European Commission through the LIFE program (SMART'IN AIR, LIFE17 ENV/FR/000330).

Appendix A. Supplementary data

Supplementary material related to this article can be found, in the online version, at doi:<https://doi.org/10.1016/j.jece.2020.103724>.

References

- [1] N. Bruce, R. Perez-Padilla, R. Albalak, The health effects of indoor air pollution

- exposure in developing countries, *World Health Organ.* 78 (2002) 1078–1092.
- [2] I. Buka, S. Koranteng, A.R. Osornio-Vargas, The effects of air pollution on the health of children, *Paediatr. Child Health* 11 (2006) 513–516.
- [3] M. Kampa, E. Castanas, Human health effects of air pollution, *Environ. Pollut.* 151 (2008) 362–367.
- [4] Y. Ueno, T. Horiuchi, T. Morimoto, O. Niwa, Microfluidic device for airborne BTEX detection, *Anal. Chem.* 73 (2001) 4688–4693.
- [5] S. Hazrati, R. Rostami, M. Farjaminezhad, M. Fazlzadeh, Preliminary assessment of BTEX concentrations in indoor air of residential buildings and atmospheric ambient air in Ardabil, Iran, *Atmos. Environ.* 132 (2016) 91–97.
- [6] R. Kandyala, S.P.C. Raghavendra, S.T. Rajasekharan, Xylene: An overview of its health hazards and preventive measures, *J. Oral Maxillofac. Pathol.* 14 (2010) 1–5.
- [7] R.A. Rinsky, A.B. Smith, R. Hornung, T.G. Filloon, R.J. Young, A.H. Okun, P.J. Landrigan, Benzene and leukemia, *N. Engl. J. Med.* 316 (1987) 1044–1050.
- [8] I. Lara-Ibeas, A. Rodríguez-Cuevas, C. Andrikopoulou, V. Person, L. Baldas, S. Colin, S. Le Calvé, Sub-ppb level detection of BTEX gaseous mixtures with a compact prototype GC equipped with a preconcentration unit, *Micromachines* 10 (2019) 187.
- [9] S.W. Lee, J.K. Cheon, H.J. Park, M.G. Lee, Adsorption characteristics of binary vapors among acetone, MEK, benzene, and toluene, *Korean J. Chem. Eng.* 25 (2008) 1154–1159.
- [10] H.K. Son, S. Sivakumar, M.J. Rood, B.J. Kim, Electrothermal adsorption and desorption of volatile organic compounds on activated carbon fiber cloth, *J. Hazard. Mater.* 301 (2006) 27–34.
- [11] J. Choma, M. Marszewski, L. Osuchowski, J. Jagiello, A. Dziura, M. Jaroniec, Adsorption properties of activated carbons prepared from waste CDs and DVDs, *ACS Sustain. Chem. Eng.* 3 (2015) 733–742.
- [12] B. Dragoi, V. Rakic, E. Dumitriu, A. Auroux, Adsorption of organic pollutants on microporous solids investigated by microcalorimetry techniques, *J. Therm. Anal. Calorim.* 99 (2010) 733–740.
- [13] L. Zhang, Y. Peng, J. Zhang, L. Chen, X. Meng, F.S. Xiao, Adsorption and catalytic properties in the removal of volatile organic compounds over zeolite-based materials, *Cuihua Xuebao/Chin. J. Catal.* 37 (2016) 800–809.
- [14] T. Mokalled, J. Adjizian-Gérard, M. Abboud, C. Trocquet, R. Nasreddine, V. Person, S. Le Calvé, VOC tracers from aircraft activities at Beirut Rafic Hariri International Airport, *Atmos. Pollut. Res.* 10 (2019) 537–553.
- [15] T. Mokalled, J.A. Gérard, M. Abboud, C. Liaud, R. Nasreddine, S. Le Calvé, An assessment of indoor air quality in the Maintenance Room at Beirut-Rafic Hariri International Airport, *Atmos. Pollut. Res.* 10 (2019) 701–711.
- [16] H.F.H.A.L. Mc Clellan, Cross-sectional areas of molecules adsorbed on solid surfaces, *J. Colloid Interface Sci.* 23 (1967) 577–599.
- [17] P. Losch, A.B. Pinar, M.G. Willinger, K. Soukup, S. Chavan, B. Vincent, P. Pale, B. Louis, H ZSM 5 zeolite model crystals: structure - diffusion activity relationship in methanol- to-olefins catalysis, *J. Catal.* 345 (2017) 11–23.
- [18] F. Ocampo, J.A. Cunha, M.R. de L. Santos, J.P. Tessonnier, M.M. Pereira, B. Louis, Synthesis of zeolite crystals with unusual morphology: application in acid catalysis, *Appl. Catal. A Gen.* 390 (2010) 102–109.
- [19] R. Nasreddine, V. Person, C.A. Serra, S. Le Calvé, Development of a novel portable miniaturized GC for near real-time low level detection of BTEX, *Sens. Actuators B Chem.* 224 (2016) 159–169.
- [20] R. Nasreddine, V. Person, C.A. Serra, C. Schoemaeker, S. Le Calvé, Portable novel micro-device for BTEX real-time monitoring: assessment during a field campaign in a low consumption energy junior high school classroom, *Atmos. Environ.* 126 (2016) 211–217.
- [21] I. Lara-Ibeas, C. Trocquet, R. Nasreddine, C. Andrikopoulou, V. Person, B. Cormerais, S. Englaro, S. Le Calvé, BTEX near real-time monitoring in two primary schools in La Rochelle, France, *Air Qual. Atmos. Health* 11 (2018) 1091–1107.
- [22] F. Ocampo, H.S. Yun, M.M. Pereira, J.P. Tessonnier, B. Louis, Design of MFI zeolite-based composites with hierarchical pore structure: a new generation of structured catalysts, *Cryst. Growth Des.* 9 (2009) 3721–3729.
- [23] E.M. Flanigen, B.M. Lok, R.L. Patton, S.T. Wilson, Y. Murakami, A. Iijima, *New Developments in Zeolite Science and Technology*, (1986).
- [24] Y. Xu, P.J. Maddox, J.W. Couves, The synthesis of SAPO-34 and CoSAPO-34 from a triethylamine-hydrofluoric acid-water system, *J. Chem. Soc. Faraday Trans.* 86 (1990) 425–429.
- [25] S. Alejandro, H. Valdés, M.H. Manero, C.A. Zoror, BTX abatement using Chilean natural zeolite: the role of Brønsted acid sites, *Water Sci. Technol.* 66 (2012) 1759–1765.
- [26] A. Kurganov, St. Marmé, K. Unger, Effect of size of solvent molecule on the adsorption of p- and o-xylene on ZSM-5 type zeolites and mechanism of adsorption, *Studies in Surface Science and Catalysis*, Elsevier, 1994, pp. 1299–1306.
- [27] T. Kawai, K. Tsutsumi, Evaluation of hydrophilic-hydrophobic character of zeolites by measurements of their immersional heats in water, *Colloid Polym. Sci.* 270 (1992) 711–715.
- [28] R. Bingre, B. Vincent, Q. Wang, P. Nguyen, B. Louis, Assessment of the improvement of effective diffusivity over technical zeolite bodies by different techniques, *J. Phys. Chem. C* 123 (2019) 637–643.

Supporting Information

Volatile Organic Compounds (VOCs) Removal Capacity of ZSM-5 Zeolite Adsorbents for Near Real-Time BTEX detection

Cristina Megías-Sayago^{1,*}, Irene Lara-Ibeas², Qiang Wang³, Stephane Le Calvé^{2,4} and Benoît
Louis¹

¹ ICPEES – Institut de Chimie et Procédés pour l’Energie, l’Environnement et la Santé, Energy and Fuels for a Sustainable Environment Team, UMR 7515 CNRS – Université de Strasbourg – ECPM, 25 rue Becquerel F-67087 Strasbourg cedex 2, France

² ICPEES – Institut de Chimie et Procédés pour l’Energie, l’Environnement et la Santé, Group of Atmospheric Physical Chemistry, UMR 7515 CNRS – Université de Strasbourg – ECPM, 25 rue Becquerel F-67087 Strasbourg cedex 2, France

³ Environmental Functional Nanomaterials (EFN) Laboratory, College of Environmental Science and Engineering, Beijing Forestry University, Beijing 100083, China

⁴ In’Air Solutions, 25 rue Becquerel, 67000 Strasbourg, France

*corresponding author: megiasayago@unistra.fr

Table of contents

Figure S1. Experimental set-up used for BTEX breakthrough experiments.

Figure S2. XRD patterns of prepared ZSM-5 zeolites.

Table S1. Obtained breakthrough times over prepared samples.

Figure S3. ^{27}Al MAS NMR and contact angle measurements over ZSM-5_2 and ZSM-5_5 samples

Figure S4. Mass variation during toluene adsorption/desorption experiments.

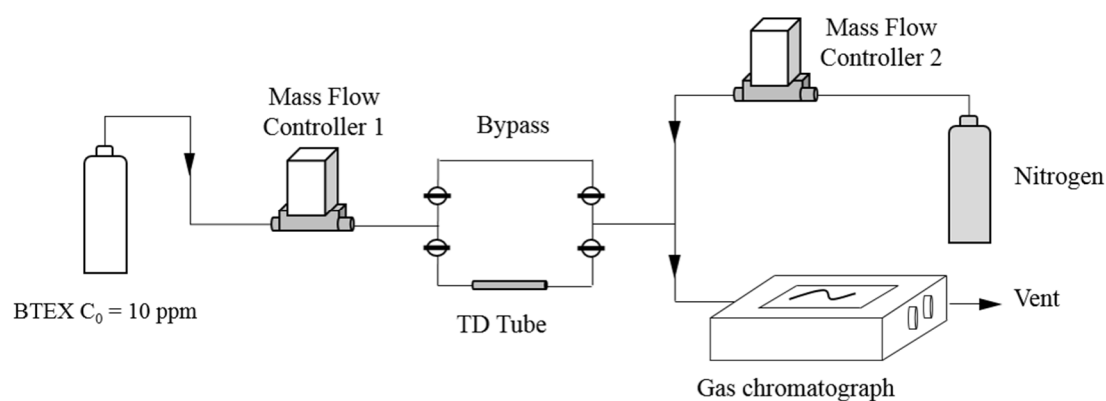


Figure S1. Experimental set-up used for BTEX breakthrough experiments.

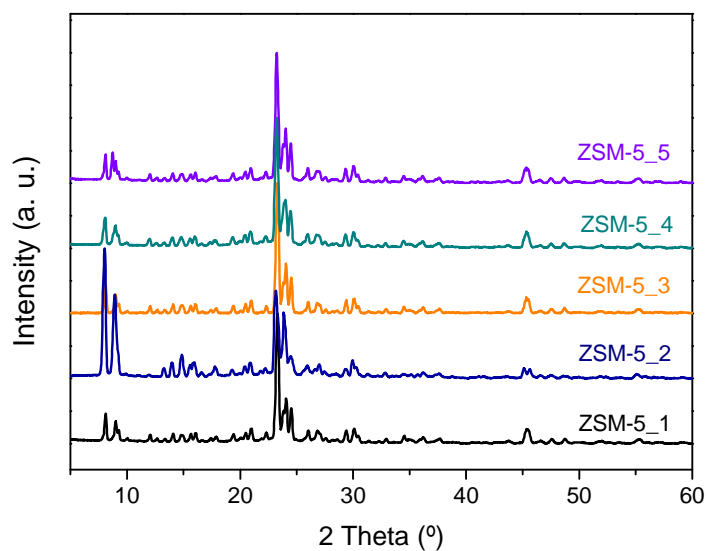
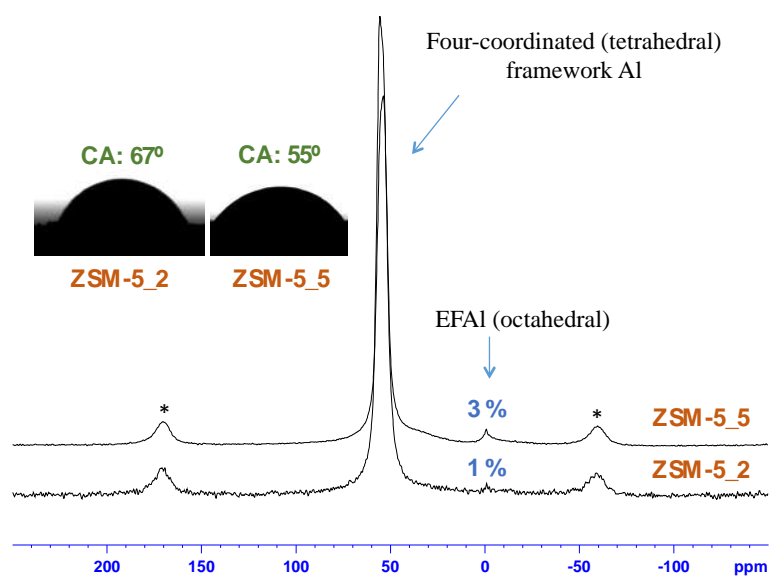


Figure S2. XRD patterns of prepared ZSM-5 zeolites.

Table S1. Obtained breakthrough times over prepared samples.

Sample	Breakthrough time (min)				
	Benzene	Toluene	Ethylbenzene	p-Xylene	m/o-Xylene
ZSM-5_1	73	384	695	614	0
ZSM-5_2	305	660	1097	559	0
ZSM-5_3	128	472	739	942	0
ZSM-5_4	90	243	416	1102	0
ZSM-5_5	331	648	890	852	0

**Figure S3.** ^{27}Al MAS NMR and contact angle measurements over ZSM-5_2 and ZSM-5_5 samples

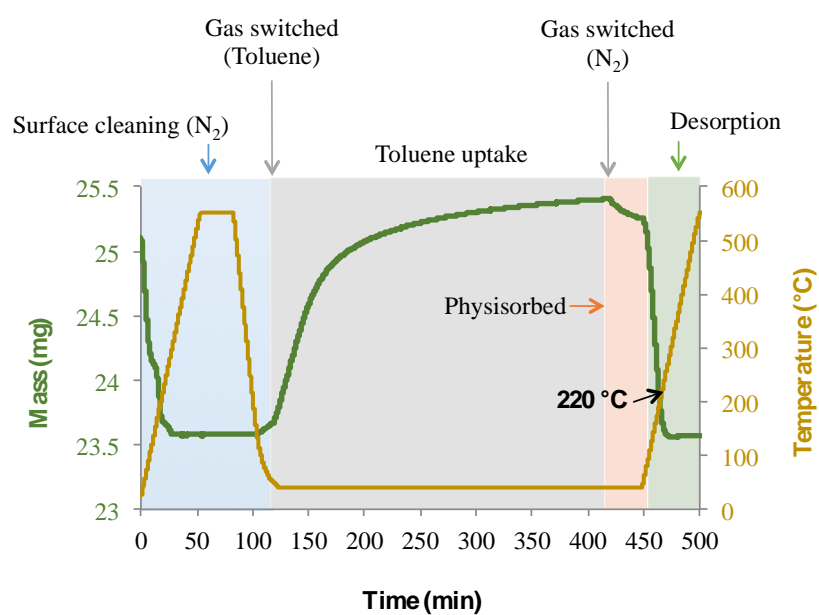


Figure S4. Mass variation during toluene adsorption/desorption experiments.

5.2.3 Conclusions

Several ZSM-5 zeolites with Si/Al ratio (SAR) ranging from 79 to 316 have been successfully synthesized and characterized. The results obtained in dynamic adsorption experiments shed light on the critical factors driving BTEX adsorption on zeolites. These results suggest that aluminium content, hydrophobicity and pore size are the driving parameters in BTEX adsorption. The adsorption capacity was strongly related to the number of acid sites available for adsorption: it is higher as the amount of acid sites increases. Besides, when the number of acid sites is limited, the most volatile compounds such as benzene are desorbed in favour of more strongly adsorbing species. However, when considering breakthrough times, it was demonstrated that not only SAR but also hydrophobicity of the adsorbent plays a major role. The optimum breakthrough time was indeed achieved as a compromise between the number of acid sites required for adsorption and the hydrophobicity of the adsorbent. In this regard, the fluoride-mediated synthesis of ZSM-5 zeolite employed in this work seems to be an advantageous strategy compared to the traditional alkaline route. This synthesis allows to obtain highly hydrophobic materials even with low SAR, resulting in high adsorption capacities due to BTEX interaction with acid sites. Additionally, ZSM-5 zeolites selectively adsorb p-xylene over m- and o-xylenes, due to steric hindrance. This exclusion may be tailored in the future to synthesize a zeolite for selective adsorption of benzene, thus avoiding the need of long separation chromatographic step and rendering possible a real-time analysis. In this sense, ZSM-5 zeolites seem to be promising candidates as selective adsorbents for BTEX gas analysis applications.

5.3 Aldehydes adsorption on different materials

In this chapter, hexanal and formaldehyde adsorption on materials of diverse nature is presented. As previously mentioned in Section 1.1.2, these two compounds are among the most frequently found aldehydes in indoor air [2], [11], [12] and they have adverse effects on human health. These potential effects can vary from simple eyes and nose irritation when exposed to hexanal, to more serious pathologies such as cancer in the case of formaldehyde. Therefore, it is of great interest to monitor the levels of these aldehydes in indoor air and, in the case of significant levels measured, to remove them. Adsorption is one of the methods typically used for gaseous pollutant removal; however, few studies [13] reported the adsorption behaviour of these compounds at low concentrations relevant in confined environments. To provide more information about the aldehydes adsorption in these conditions, a set

of dynamic adsorption experiments of formaldehyde and hexanal on different types of adsorbents were carried out.

In this section, the results obtained in these experiments are presented and the influence of different factors such as specific surface area, pore size and surface chemistry on adsorption capacity of several materials is discussed. The better understanding of the adsorption behaviour of aldehydes at low concentrations and the features playing a major role in this process can contribute to the development of specific materials for indoor air purification applications.

5.3.1 Hexanal adsorption

At the beginning, the idea was to test the adsorption at concentrations of the same order as those found in indoor air (0-106 $\mu\text{g}/\text{m}^3$ [14]) but some problems were encountered to get such low concentrations. Ideally, a gas cylinder containing diluted hexanal would be the best option to generate low concentrations, but hexanal mixture is only available on special order, resulting in expensive price and long lead times of manufacture and delivery, this later point being not compatible with this thesis schedule. Therefore, a method to generate gaseous hexanal from the pure liquid hexanal was employed instead. This method was based on the permeation of a nitrogen gas flow into the liquid hexanal by using a gas bubbler. There is an equilibrium between the gas and the liquid phase of hexanal, therefore, when the nitrogen flow passes through the liquid phase, it displaces the same volume of the gas phase contained in the bubbler, generating a gaseous flow of diluted hexanal. Obviously, the equilibrium of the liquid and gas phases depends on the temperature: the colder the solution, the lower the concentration of gaseous hexanal. Since the objective was to generate a concentration in the range of ppb, the bubbler should be kept at temperatures lower than -80°C , which is not an easy task. There are some cooling bath mixtures such as dry ice-acetone or liquid nitrogen-acetone enabling to achieve temperatures of -77 and -94.6°C , respectively [15]. Nevertheless, the main problem consists in keeping this temperature constant to generate a constant and stable hexanal concentration. Indeed, despite the use of dewars and other materials to isolate the gas bubbler, temperature variations of few degrees can easily occur, resulting in a high uncertainty in the generated concentration. For simplicity and to allow a better control of the concentration, an ice bath was selected as the cooling method for the gas bubbler. During the experiments, the bubbler was completely buried in ice that was continuously added to maintain a constant temperature of 0°C . The principal drawback of using this method was that the temperature was equal to 0°C and, thus, the generated

concentration was calculated to be 3,298.3 ppm, which was far from the desired ppb range, and consequently, a dilution would be necessary. The first attempt to carry out the hexanal dynamic adsorption experiment was conducted in the setup shown in Figure 5-1. The system was composed of a flow controller to provide the inert gas flow (argon). After that, the line was split in two lines, the first one conducting to the glass reactor containing the adsorbent bed and the other one to the bypass. Both lines arrived at a T junction from where it was possible to take a sample of the gas effluent (sampling point) by using a round flask. The content of this flask was manually injected in a GC/FID and analysed. An additional line could be added to this setup to make a dilution but, unfortunately, the first set of measurements conducted were not satisfactory: strong fluctuations on the measured concentrations were observed, mainly due to the errors accumulated in the different steps of the analysis. Actually, in this setup, sampling and sample injection into the GC were performed manually, resulting in large variations between the analysis from one sample to another. To limit the errors during the measurements, an alternative setup able to perform automatically most of the steps was mounted (see Figure 2-7). As in the previous setup, this system was composed of a mass flow controller, a gas bubbler and a split separating the line into a bypass and the tube containing the adsorbent bed. Then, two lines were connected to a T junction linked to the online sampler of an automated thermal desorption (ATD) coupled with gas chromatography (GC) and flame ionization detector (FID). This instrument automatically pumped a sample at a flow of 5 mL/min for 1 min from the gas effluent. The sample was directly injected in the cold trap of the instrument and desorbed at 300 °C in a very reproducible way. Therefore, the errors made in the analysis using this technique were considerably lower than with the previous setup and the study of hexanal adsorption could be carried out. However, due to restricted space to mount this setup, an additional line for dilution could not be included and the experiments were conducted at a concentration of 3,298.3 ppm.

Once the setup was mounted, the first step was to measure the dead volume of the system. Dead volume corresponds to the volume between the point of injection and the point of detection. In fact, in this work, dead time instead of dead volume was measured; it corresponds to the duration between the time of sample injection and the time of sample detection [16]. Dead time can be measured by replacing the tube containing the adsorbent bed by an empty tube. Hence, in this setup, the bypass line was employed to measure the dead time. Then, a sample was injected in the same conditions of temperature and flow rate that the ones employed during the experiments, and the duration between

the time of injection and the time at which the compound reached the detector was measured. This dead time could be estimated to be 52 min and it was subtracted from the breakthrough curves.

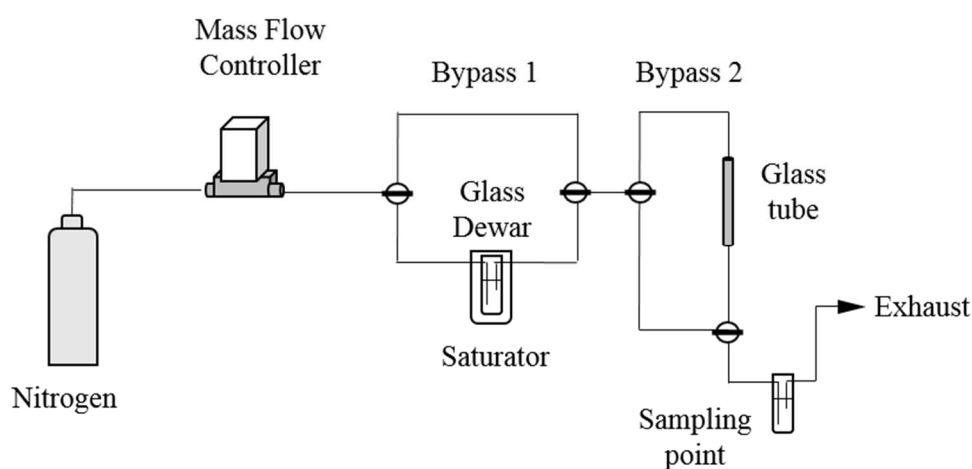


Figure 5-1. Schematic diagram of the first setup employed for hexanal dynamic adsorption experiments

5.3.1.1 Dynamic adsorption experiments

Hexanal dynamic adsorption experiments were conducted by using four different adsorbents, *i.e.* Carbopack® B, SBA-16, HKUST-1 and ZSM-5, and the obtained breakthrough curves are plotted in Figure 5-2. As can be seen, Carbopack® B as well as SBA-16 breakthrough occurred at the beginning of the experiment; in contrast, longer breakthrough times of 55 and 72 min (see Table 5-1) were observed for ZSM-5 and HKUST-1, respectively. Moreover, the saturation point is rapidly reached in Carbopack® B. This behaviour may result from the low specific surface area of 112 m²/g and weak adsorbate-adsorbent interactions owe to the aldehyde function of hexanal.

Table 5-1. Textural properties and adsorption capacities of studied materials towards gaseous hexanal

Adsorbent	S_{BET} (m ² /g)	V_{pore} (mL/g)	Pore size (Å)	Breakthrough time (min)	Adsorption Capacity (mg/g ads)*
Carbopack® B	112	-	-	0	39.4 ± 5.6
SBA-16	572	0.72	3.4 / 6.0	10	341.5 ± 48.6
HKUST-1	1,733	0.89	0.54 / 0.69	72	816.2 ± 116.1
ZSM-5	367	0.17	0.55	55	451.5 ± 64.2

*Errors associated to the generated concentration by taking into account a variation of ± 2°C in the saturator

Concerning the mass transfer zone, it is usually related to the particle size, smaller sizes enabling higher intraparticle mass transfer rates, and also to the presence of micropores. ZSM-5 as well as HKUST-1 showed smaller particle size (10 – 30 μm) compared to SBA-16 (10 – 180 μm), which may lead to shorter mass transfer zone. Nevertheless, hexanal seems to suffer from diffusional limitations in HKUST-1 since the kinetics of the adsorption process appears to be lower than in ZSM-5. For each adsorbent, the total adsorption capacity was calculated as the area above the breakthrough curve, following the procedure detailed in Section 2.1.3. As shown in Table 5-1, HKUST-1 exhibited the largest adsorption capacity (816.2 mg/g adsorbent) followed by ZSM-5 (451.5 mg/g adsorbent), SBA-16 (341.5 mg/g adsorbent) and, finally, Carbopack® B (39.4 mg/g adsorbent). The lower adsorption capacity of Carbopack® B could be explained by its lower specific surface area compared to other materials, thus limiting the amount of adsorption sites and leading to more rapid saturation. Moreover, the interactions between the hydrophobic surface of Carbopack® B and the hexanal molecule may be presumably weak due to the permanent dipole moment of the aldehyde function. SBA-16 and ZSM-5 showed comparable adsorption capacities. Indeed, the structure of silica is quite similar to that of zeolite since both 3D framework structures are built of SiO_4 tetrahedra. However, while silica is essentially a covalent structure with low polarity due to some free hydroxyl groups on the surface [17], ZSM-5 includes also AlO_4 tetrahedra creating negative charges along the framework. These charges are compensated by positive cations, increasing the polarity of the framework. In the studied zeolite, the negative charges are compensated by hydrogens, forming hydroxyl groups bonded to aluminium atoms. These Si-(OH)-Al groups act as rather strong up to very strong Brønsted acids whereas Si-OH groups in mesoporous silica exhibit a weak acid strength [18]. Therefore, both groups can interact with hexanal molecules *via* hydrogen bonds but to a different extent, the interactions being stronger as the acid strength increases, which may explain the higher adsorption capacity of ZSM-5 compared to SBA-16. Moreover, hexanal molecules size (5.2 Å) being very close to that of ZSM-5 micropores (5.5 Å), strong electrostatic interactions are expected within these micropores that may also promote hexanal adsorption at low concentrations, as reported by Ortmann *et al.* [13].

HKUST-1 showed the higher adsorption capacity among the studied materials. This superior capacity could be attributed to a very high specific surface area that provides a large amount of adsorption sites but also to favorable adsorbate-adsorbent interactions. Similarly to the case of ZSM-5, strong electrostatic interactions are expected between hexanal molecules and micropore walls due to their

similar size. Additionally, polar or polarizable molecules can strongly interact with copper ions of HKUST-1 [19]. These interactions between the carbonyl group and the copper ions are expected to be stronger compared to the hydrogen bonds due to the higher charge of the cation, thus leading to an enhanced adsorption capacity. A remarkable adsorption performance of HKUST-1 for molecules containing polar functions such as alcohols, ketones, aldehydes, phenolic or indolic compounds, presumably due to its elevated surface area and the presence of unsaturated copper centres, was reported in other studies [20]–[22].

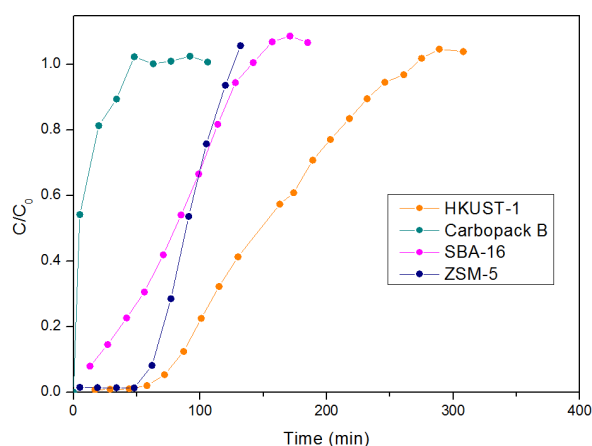


Figure 5-2. Breakthrough curves of gaseous hexanal on different materials (flow rate = 20mL/min, $C_0 = 3289.3$ ppm)

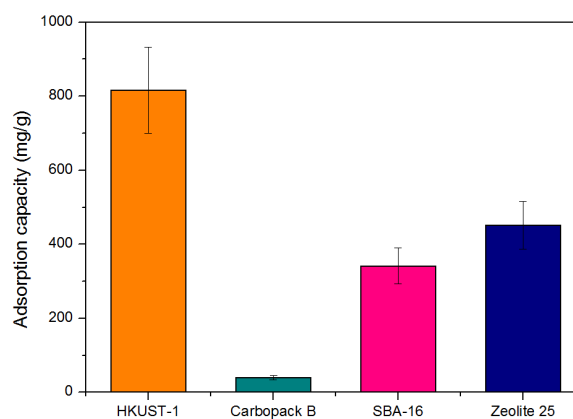


Figure 5-3. Hexanal adsorption capacity of each adsorbent (mg/g adsorbent)

5.3.1.2 Comparison with the literature

Adsorption of a broad spectrum of pollutants has been widely studied to evaluate the suitability of certain materials for air pollution control. However, few experimental data on adsorption of gaseous hexanal were found in the literature [13], [23], [24]. These results are summarized in Table 5-2. It is apparent from the results that a pore size close to the hexanal molecule mean diameter and a favourable surface chemistry seem to be the two key factors promoting hexanal adsorption. Since hexanal is a relatively polar molecule compared to other hydrocarbons, the interactions with hydrophobic surfaces are generally weak. To increase the affinity of certain materials to hexanal, a commonly employed technique has been the surface functionalization with amines. Amine functions can strongly interact with the aldehyde function, leading to an enhancement of the hexanal adsorption compared to the non-functionalized materials [23], [24]. An accurate comparison of those materials with those employed in this study is difficult due to the different experimental conditions employed,

Table 5-2. Literature review of gaseous hexanal adsorption on various materials

Adsorbent	S_{BET} (m ² /g)	V_{total} (mL/g)	V_{micro} (mL/g)	Pore size (nm)	Concentration (ppm)	Temperature (°C)	Adsorption Capacity (mg/g ads)	Reference
Carbopack® B	112	-	-	-	3,289	22	39.4*	This work
SBA-16	572	0.72	-	3.4 / 6.0	3,289	22	341.5*	This work
HKUST-1	1,733	0.89	0.68	0.54 / 0.69	3,289	22	816.2*	This work
ZSM-5	348	0.18	-	0.55	3,289	22	451.5*	This work
SBA-15	922	1.14	-	7.6	106	r. t.	50.1	[24]
S-AP	422	0.72	-	7.0	106	r. t.	180.3	[24]
S- MAP	401	0.69	-	6.6	106	r. t.	150.2	[24]
D47-3 Extra (AC)	980	-	-	0.4 - 1	1,000	25	~ 284.7	[13]
CMK-3	1,561	-	-	4.37	1,000	25	~ 422.1	[13]
AP-BTEVA PMO	992	-	-	4.1	1,000	25	~ 410	[23]
BTEVA PMO	1,360	-	-	4.4	1,150	25	~ 480	[23]
AC D47-3 Extra	1,000	-	-	1.0	1,000	25	~ 300	[23]
BTEVB PMO	895	-	-	4.2	1,320	25	~ 225	[23]

*dynamic adsorption capacity; S-AP: primary aminosilica; S- MAP: secondary aminosilica; BTEVA: bis(triethoxysilyl)vinyl]aniline; BTEVB: [bis(triethoxysilyl)vinyl]benzene; PMO: Periodic mesoporous organosilica

i.e. the gas concentrations ranges used and the adsorbent nature itself. However, it is evident from the results that Carbopack® B is not an appropriate adsorbent for hexanal removal due to its limited adsorption capacity even at very high concentrations. In contrast, HKUST-1 showed an outstanding adsorption performance. Even if this performance was measured at considerably high hexanal levels, significant adsorption capacity at lower gas hexanal concentrations could be expected and should be comparable with those of the amino functionalized materials. Therefore, HKUST-1 could be a suitable candidate for pollutant removal without the need for functionalization.

5.3.1.3 Conclusions

The adsorption capacity is a key feature of a potential material for air pollutant removal and gas analysis applications [25]. Among the investigated adsorbents, HKUST-1 has demonstrated the highest hexanal adsorption capacity (816.2 mg/g adsorbent) followed by ZSM-5 (451.5 mg/g adsorbent), SBA-16 (341.5 mg/g adsorbent) and, finally, Carbopack® B (39.4 mg/g adsorbent). From this point of view, HKUST-1 could be the most appropriate adsorbent for hexanal removal. Nevertheless, it is known that metallic centres of HKUST-1 can also strongly interact with water resulting in a dramatic decrease in the adsorption capacity in humid environments [26]. To our knowledge, there is no studies on competitive adsorption of hexanal-water mixtures on HKUST-1; therefore, further investigation must be conducted to evaluate the adsorption performance of these adsorbents under more realistic conditions (moderate humidity and low concentrations).

5.3.2 Formaldehyde adsorption

Formaldehyde is one of the most common toxic pollutants found in indoor air [27]. At domestic scale, adsorptive methods are usually employed for gaseous pollutant removal. These methods are also employed for sample preconcentration in gas analysis. However, common adsorbents are very often not effective for formaldehyde adsorption due to its high polarity and small size. For these reasons, in the last years, a significant number of studies has been conducted on formaldehyde adsorption on different materials. Nevertheless, most of these works are performed at unrealistic formaldehyde levels (1 to 150 ppm) [24], [28]–[30], presumably due to the difficulties associated to accurately generate a formaldehyde gas flow at ppb levels and also, ascribed to the online accurate measurement required to monitor the adsorption process.

In domestic indoor environments, formaldehyde levels range typically between 10 and 100 ppb [31], [32] and in workplaces, the concentrations can usually vary in the range 100-1000 ppb [33], [34]. Therefore, the experimental results obtained at ppm levels are not fully representative of the performances of these materials in real environments. Indeed, adsorption capacity depends on the partial pressure of the gaseous compound and this relationship is not linear in all the pressure ranges. To illustrate the influence of the experimental conditions selected, two examples are given below. Carter *et al.* [29] studied formaldehyde adsorption in three different forms of activated carbon in the ppm range. As can be observed in Figure 5-4, in the high-pressure region (formaldehyde concentration ~ 25 ppm), ACF (activated carbon fibers) exhibited the highest adsorption capacity followed by GAC1 (all-purpose granular AC) and GACF (commercial granular AC for HCHO gas-phase removal). However, at lower concentrations such as 3.5 ppm, the behaviour of the adsorbents changes completely, GACF showing the highest adsorption capacity followed by ACF and GAC1. These results reveal the importance of using concentrations as close as possible to the real ones to accurately assess the adsorption performance for real-world applications. Similar results were reported by Bellat *et al.* [28] when studying formaldehyde adsorption on AC, MIL-53 and SBA-15, as shown in Figure 5-5. In this case, AC showed a poor adsorption capacity compared to MIL-53 at formaldehyde partial pressure of 2 hPa (~ 2000 ppm). However, the adsorption capacity of these adsorbents was almost identical when formaldehyde partial pressure approached more realistic levels. These results demonstrate that performances obtained at high concentrations do not necessarily correspond to the ones obtained at very low levels. In this regard, there is an obvious lack of experimental data in the literature on formaldehyde adsorption at ppb levels, which are necessary to properly evaluate the materials for either pollutant removal or potential gas analysis applications.

The objective of this study is to provide accurate information on the adsorption performance of a series of materials at realistic formaldehyde concentrations. To this purpose, dynamic adsorption experiments have been conducted, employing the setup presented in Figure 2-6. For the experiments, a formaldehyde concentration of 164 ppb was provided by the home-made formaldehyde generator presented in Section 2.1.3.3. This instrument was previously calibrated by using the conventional sampling method on DNPH cartridges followed by HPLC/UV analysis.

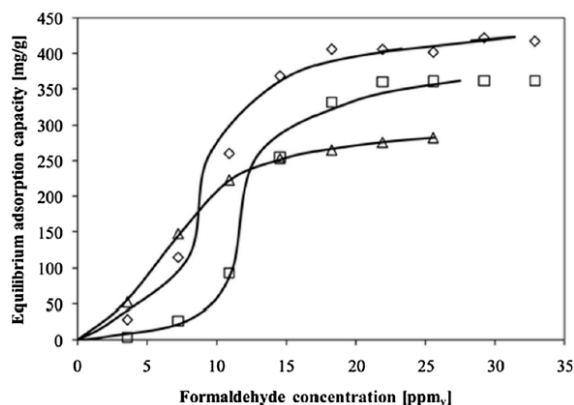


Figure 5-4. Formaldehyde adsorption isotherms for ACF (\diamond), GAC1 (\square), and GACF (\triangle) representing the adsorption capacity at different formaldehyde concentrations ($T = 299$ K) [29].

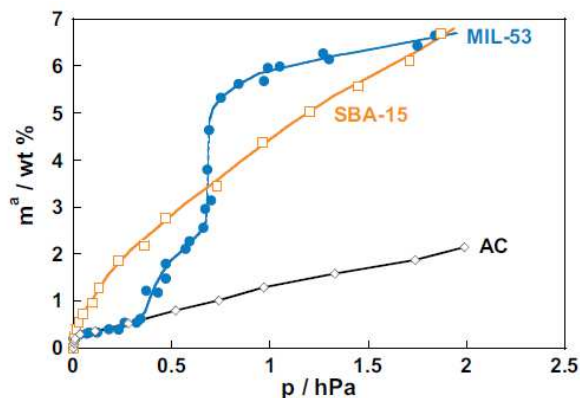


Figure 5-5. Formaldehyde adsorption isotherms on AC (black), SBA-15 (orange) and MIL-53 (blue) representing the adsorption capacity of these materials at different formaldehyde partial pressures ($T = 298$ K) [28].

The overall relative uncertainties of the generated gaseous concentrations were calculated and are in the range 9-11%. Dynamic adsorption experiments were carried out at a flow rate of 15 mL/min and formaldehyde concentration of 164 ppb. Since the formaldehyde analyser (μ F-1, In'Air Solutions, France) employed to monitor the gaseous effluent was very sensitive (LOD \sim 1 ppb), prior to the analysis, this latter was diluted with 30 mL/min of synthetic air to avoid the detector saturation. An average of 13 min was subtracted from the calculated breakthrough and saturation times due to the response time of this instrument (10 min) and the setup dead time (3 min).

Firstly, formaldehyde adsorption on three commercial adsorbents previously employed in BTEX adsorption experiments was investigated. Afterwards, the adsorption was studied on the series of HZSM-5 zeolites presented in Section 5.2. Additionally, the adsorption was tested on two other ZSM-5 zeolites: the commercially available CBV3020E (SAR = 15) and CBV3020E exchanged with Mg as a compensating cation. Finally, a comparison with experimental data of the literature is presented.

5.3.2.1 Formaldehyde adsorption on commercial adsorbents

The commercial adsorbents, *i.e.* Carbopack® B, SBA-16 and HKUST-1 studied previously for toluene and BTEX adsorption, were also investigated for formaldehyde adsorption. Dynamic adsorption experiments were performed to obtain the corresponding breakthrough curves. For each material, formaldehyde adsorption capacity was calculated as the area above the curve according to Equation 2-7. Adsorption capacities and breakthrough times are presented in Table 5-3. It is important to note

that, to enable better graphical comparison of the breakthrough curves, 5.5 mg of Carbopack® B and SBA-16 were employed whereas only 3 mg were used in the case of HKUST-1. As observed in Figure 5-6a, Carbopack® B and SBA-16 exhibit a comparable adsorption behaviour while HKUST-1 shows an outstanding adsorption performance despite the smaller adsorbent quantity used. Figure 5-6b provides a detailed view of the first 150 min of the experiment in which an appreciable difference can be observed between Carbopack® B and SBA-16 curves. Carbopack® B shows immediate breakthrough and the outlet concentration sharply increases until the saturation point is reached after 26 min of adsorption. This behaviour can be explained by the surface chemistry of the graphitised carbon black. Indeed, due to the hydrophobic surface of the carbon, the adsorbate-adsorbent interactions depend solely on London forces. For a small molecule such as formaldehyde, these forces are very weak; in consequence, the adsorption of this compound on Carbopack® B is almost negligible (see Figure 5.6). In contrast, SBA-16 curve needs 34 min to reach the breakthrough due to a higher specific surface area as well as more favourable adsorbate-adsorbent interactions. As previously explained in Section 2.1.1.3, SBA-16 contains a large number of silanol groups (Si–OH) at the inner surface of its mesopores. The aldehyde function of formaldehyde molecules can interact with these groups *via* hydrogen bonding [24], thus, promoting the adsorption of formaldehyde molecules. As a result, the adsorption capacity of SBA-16 is much higher than that obtained for Carbopack® B.

Table 5-3. Textural properties and adsorption capacities of studied materials towards gaseous formaldehyde

Adsorbent	S_{BET} (m^2/g)	V_{pore} (mL/g)	Pore size (nm)	Breakthrough time (min)	Adsorption Capacity ($\mu g/g$ ads)
Carbopack® B	112	-	-	2 ¹	4.5 ¹
SBA-16	572	0.72	3.4 / 6.0	32 ¹	29.0 ¹
HKUST-1	1,733	0.89	0.54 / 0.69	67 ²	503.7 ²

¹5.5mg sample; ²3 mg sample;

HKUST-1 showed the best adsorption performance among the investigated commercial adsorbents. Despite the mass of HKUST-1 employed in the experiment lower than the mass of the other adsorbents, the breakthrough and the saturation points were reached much later. This remarkable capacity obtained can be explained by several factors. HKUST-1 has a very high specific surface area that provides a large amount of adsorption sites. Additionally, this material presents pores with diameters of 5.4 and 6.9 Å. These pores are suitable for formaldehyde adsorption since they are sufficiently large to enable the entrance of the formaldehyde molecule (kinetic diameter = 2.5 Å) and

narrow enough for the molecules to establish significant interactions with the linkers of the pore walls. Moreover, it is expected that copper atoms present in the metal organic framework structure establish a coordination bond with the oxygen from formaldehyde carbonyl group as reported by Dutta *et al.* [35]. Therefore, it is evident that surface area influences the formaldehyde adsorption, but it seems that the remarkable adsorption capacity is mainly attributed to very favourable adsorbate-adsorbent interactions and, thus, the surface chemistry. This observation is in line with the results reported in previous studies. Rong *et al.* found an enhancement of the adsorption capacity related to the amount of oxygen-containing functional groups on the surface of AC due to the formation of strong adsorbate-adsorbent interactions [36]. Similar correlation between formaldehyde adsorption capacity and nitrogen-containing groups, especially pyrrolic, pyridonic, pyridinic, and quaternary on the surface of AC was observed by Song *et al.* [37]. Despite the decrease in the specific surface area that is typically observed after surface functionalization, these materials exhibited higher adsorption capacity than their bare counterparts, demonstrating that surface chemistry is the driven parameter in the adsorption of polar molecules.

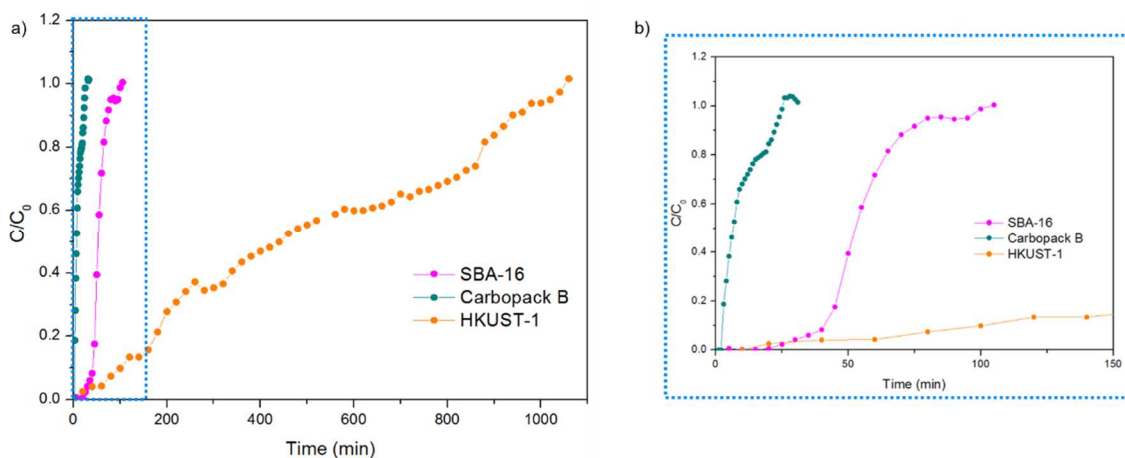


Figure 5-6. (a) Breakthrough curves of gaseous formaldehyde on Carbopack® B, SBA-16 and HKUST-1 (formaldehyde concentration = 201 ppb, flow rate = 15 mL/min) and (b) enlarged view of the first 150 min of the experiment

Among the adsorbents studied in this work, HKUST-1 could be the most appropriate candidate for airborne formaldehyde removal. However, as formaldehyde molecules, water molecules can be easily coordinated on the unsaturated copper sites of HKUST-1 [38]. If this interaction is more favourable than the interaction with formaldehyde, a significant decrease of the formaldehyde adsorption capacity in humid environments could be expected, limiting its use in these conditions. In gas analysis, this disadvantage can be partially overcome by adding a device to trap the water molecules prior to

the gas sampling on the adsorbent bed, as for example a Nafion tube. To avoid the need to integrate devices for water trapping, more hydrophobic adsorbents such as ZSM-5 zeolites were also investigated.

5.3.2.2 Formaldehyde adsorption on zeolites

Due to the decrease expected in the formaldehyde adsorption capacity of HKUST-1 in humid environments, more hydrophobic materials such as ZSM-5 zeolites have been selected for study. This type of zeolites is mainly hydrophobic, but its polarity is tunable by modifying the aluminium content in the framework. This content can be easily controlled by varying the conditions employed during the synthesis. When aluminium content increases, Al (+III) atoms replace Si (+IV) atoms, resulting in larger amount of negative charges in the framework and, hence, influencing the polarity. Therefore, the hydrophobicity in zeolites increases when less partial charges are present in the framework, *i.e.* when Al content decreases (high SAR) [39]. In these structures, negative charges are compensated with protons that are coordinated to one of these oxygen atoms, forming Brønsted acid sites [40]. In consequence, higher acidity is expected in zeolites with high aluminium content. Zeolites surface chemistry can also be modified by replacing these hydrogens by other cations such as Na⁺, Ca²⁺, NH₄⁺, *etc.* resulting in an increase of zeolite hydrophilicity.

Firstly, three zeolites were synthesized with SAR of 198, 132 and 79 to evaluate the influence of the aluminium content and, thus, the acidity on zeolite adsorptive properties. The chemical composition, textural properties and the total number of Brønsted acid sites of investigated zeolites are listed in Table 5-4. As expected, zeolites with low SAR had higher acid site density. The three materials have comparable specific surface areas and pore volumes, enabling a comparison of the adsorptive properties exclusively based on the acidity. To determine the corresponding adsorption capacities, dynamic adsorption experiments were carried out using a formaldehyde concentration of 164 ppb at a flow rate of 15 mL/min. The breakthrough curves obtained are presented in Figure 5-7.

For all zeolites, the obtained curves are fairly similar in shape. During the first minutes of the experiment, the adsorption of formaldehyde was complete and breakthrough point was reached at 11, 12 and 21 min for ZSM-5_198, ZSM-5_132 and ZSM-5_79, respectively. Zeolites with higher SAR exhibited earlier breakthrough probably due to the difficulty of formaldehyde molecules to find adsorption sites.

Table 5-4. Chemical composition, acid site density, textural and adsorption properties of as-prepared H-ZSM-5 zeolites.

Sample	SAR	Acid site density (mmol H ⁺ /g zeolite)	S_{BET} (m ² /g)	V_{pore} (cm ³ /g)	Breakthrough time (min)	Adsorption Capacity (µg/g ads)
ZSM-5_198	198	0.132	367	0.17	21 ¹	10.18 ¹
ZSM-5_132	132	0.133	352	0.18	12 ¹	14.80 ¹
ZSM-5_79	79	0.249	348	0.18	11 ¹	21.61 ¹
CBV3020E	15	0.361	369	0.13	7	25.99 ²
CBV3020E - Mg	15	0.280	296	0.11	4	34.86 ²

¹5.5mg sample; ²1.7 mg sample;

By contrast, ZSM-5_79 possessing almost twice more acid sites showed a later breakthrough. After the breakthrough point, two different slopes can be distinguished. Firstly, a sharp concentration increase in the outlet effluent is observed indicating fast kinetics and, afterwards, outlet concentration slowly increases until the initial concentration is reached, suggesting that the adsorption kinetics close to the adsorbent saturation is much slower. Adsorption capacity was assessed by numerical integration of the area above the breakthrough curve, following the procedure already described in Section 2.1.3.

As can be observed in Figure 5-7, zeolites with higher acid density, *i.e.* lower Si/Al ratio, exhibited greater adsorption capacity. It appears from this evidence that the adsorption of formaldehyde molecules is directly related to the aluminium content and, thus, the amount of Brønsted acid sites. In order to illustrate this relationship, adsorption capacities of the investigated ZSM-5 zeolites, including another ZSM-5 commercial zeolite (Si/Al = 15) were plotted versus SAR (see Figure 5-8). A highly linear correlation is observed in all the SAR range suggesting that formaldehyde adsorption could be attributed to the interactions between the carbonyl function and zeolitic Si-(OH)-Al groups, as reported previously by Kukulska-Zajac and Datka [41].

Moreover, the reduction of the specific surface area observed when SAR decreases appears to have a negligible effect on formaldehyde adsorption. This observation reinforces the idea that formaldehyde adsorption is primarily dominated by surface chemistry.

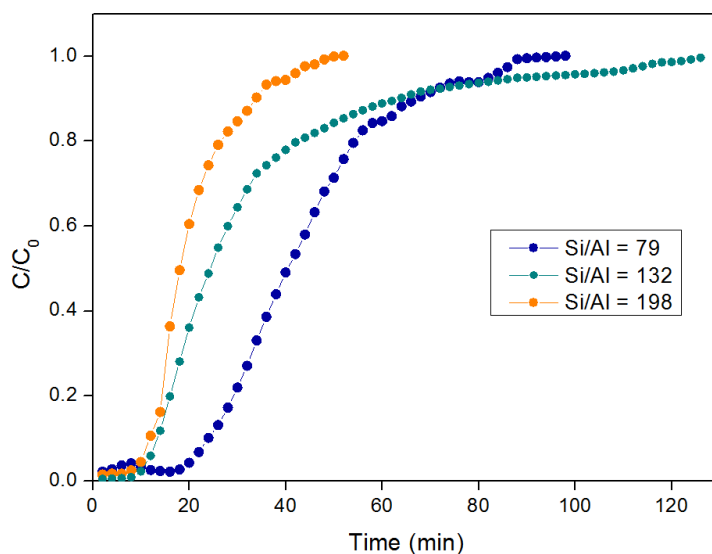


Figure 5-7. Breakthrough curves of gaseous formaldehyde over ZSM-5 zeolites with different Si/Al ratios (formaldehyde concentration = 164 ppb, flow rate = 15 mL/min)

Therefore, it can be concluded that, at low concentrations, a more effective formaldehyde adsorption can be achieved by using zeolites with high aluminium content.

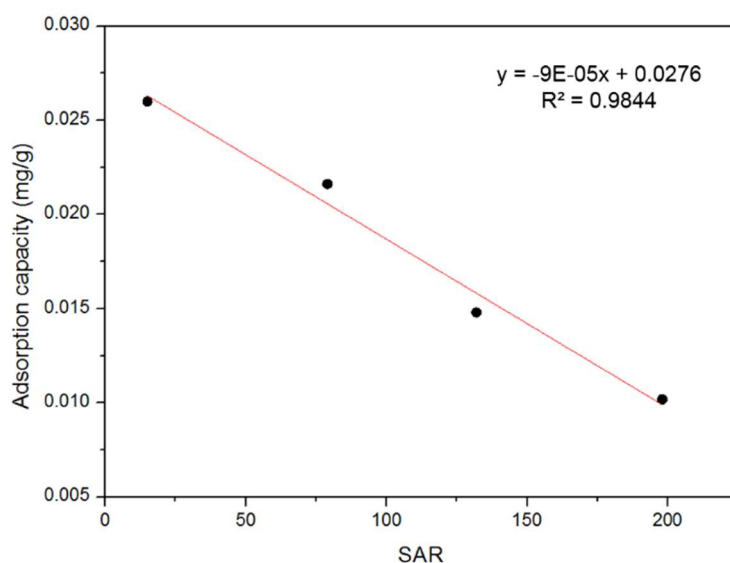


Figure 5-8. Formaldehyde adsorption capacities of ZSM-5 with different Si/Al ratios

The second part of the study deals with the influence of the compensating cation of the zeolite network on formaldehyde adsorption. The commercial ZSM-5 zeolite (CBV3020E, Zeolyst) was loaded with Mg following the procedure described in Section 2.1.14. Textural properties and acidity of the pristine and metal loaded zeolites are presented in Table 5-4. As reported in other studies, a decrease in the

specific surface area between the metal and the hydrogen substituted zeolites was observed [28], [42]. This reduction can be explained by the larger size of Mg atom with respect to hydrogen atom. The metal loading was successfully accomplished as suggested by the reduction of the acidity in the metal loaded zeolite, indicating that some of the hydrogens of the network were replaced, and further confirmed by the presence of Mg in EDX (Energy Dispersive X-Ray) micrographs (see Figure 5-9). Once metal loading was verified, the dynamic adsorption capacities of CBV3020E and CBV3020E-Mg were investigated. Breakthrough curves obtained are displayed in Figure 5-10. Apparently, both curves are very similar; however, the masses employed for the tests were 1.8 and 1.6 mg for CBV3020E and CBV3020E-Mg, respectively. Therefore, a slight difference between the curves could represent a great variation, for example, in the adsorption capacity. Breakthrough times obtained for pristine and metal loaded zeolite were 7 and 4 min, respectively. The shorter breakthrough time of CBV3020E-Mg could be attributed to the lower mass of the sample and lower specific surface of this material. With regard to kinetics, both zeolites showed similar kinetics until C/C_0 reached ~ 0.5 . From this point to the saturation, CBV3020E-Mg exhibited slower kinetics, presumably due to diffusional limitations caused by Mg^{2+} cations.

Adsorption capacity of zeolite increased 34% from the bare to the metal loaded counterpart due to the addition of Mg^{2+} (4 wt%). This enhancement in the adsorption capacity suggests that formaldehyde establishes stronger interactions with Mg^{2+} than hydrogen. These results are in line with those reported by Bellat *et al.* [28]. They observed indeed that the presence of cations such as Na^+ , K^+ or Cu^{2+} in ZSM-5 zeolites produces an enhancement in the formaldehyde adsorption capacity. As observed in the first part of this study, a decrease in the specific surface area does not significantly affect the adsorption ability, providing a compelling evidence of the importance of surface chemistry on formaldehyde adsorption.

Despite their moderate adsorption capacity that prevents their use for pollutant removal, zeolites can be considered for gas analysis applications. On the one hand, they are expected to have lower affinity to water compared to HKUST-1. On the other hand, they exhibit acceptable breakthrough times for formaldehyde sampling. These times range from 4 to 21 min under the employed conditions (room temperature, flow rate = 15 mL/min and adsorbent mass = 1.6 – 6 mg) enabling to quantitatively samples from 9 to 51 ppm of formaldehyde without breakthrough observation. This range of

concentrations is relatively high compared to the ones found in indoor air, thus assuring a quantitative sampling even in highly polluted environments such as industrial working environment.

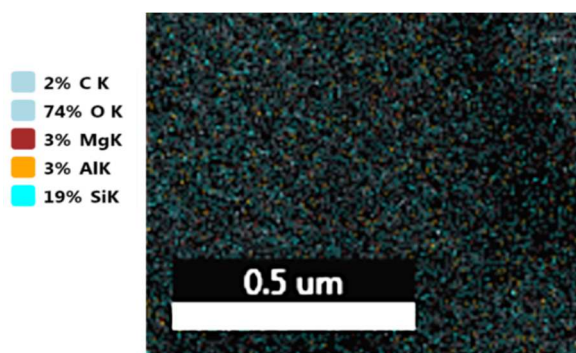


Figure 5-9. EDX mapping of Mg loaded CBV3020E zeolite

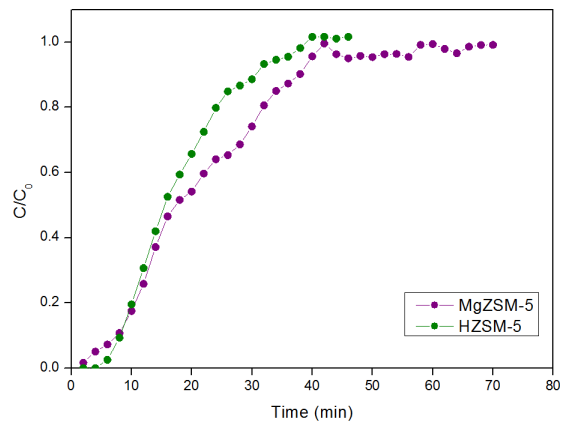


Figure 5-10. Breakthrough curves of gaseous formaldehyde over CBV3020E and CBV3020E-Mg zeolites ($C_0 = 164$ ppb, flow rate = 15 mL/min)

5.3.2.3 Performance evaluation of formaldehyde removal by conventional adsorbents

Due to the occurrence in indoor air and the harmful effects of formaldehyde, its adsorption has been studied on several conventional materials such as MOF, zeolites, AC and mesoporous silica. The adsorption capacities obtained in all those studies as a function of the concentration are plotted in Figure 5-11. As can be seen, the results are very different depending on the adsorbents and concentrations considered. Most of studies are conducted at a formaldehyde concentration from 3.65 to 150 ppm (corresponding to partial pressures from 0.015 to 13.7 Pa), thus being not representative of ambient conditions where formaldehyde is usually present at several tens or few hundreds of ppb. Moreover, the high variability in the partial pressures employed makes difficult a proper comparison between the adsorption capacities of different adsorbents.

As presented at the beginning of this section, comparing data obtained in the high-pressure region with those obtained in the low-pressure region can result in an inaccurate evaluation of the adsorption performance. Therefore, to reduce the possible errors in the adsorption performance assessment, instead of adsorption capacity, the Henry's constant (K_H) is commonly employed for comparison purposes [20], [43]–[45]. K_H is a relevant parameter to explain gas-solid adsorption behaviour [20] that can be used to evaluate the adsorption affinity of a material on a certain adsorbate.

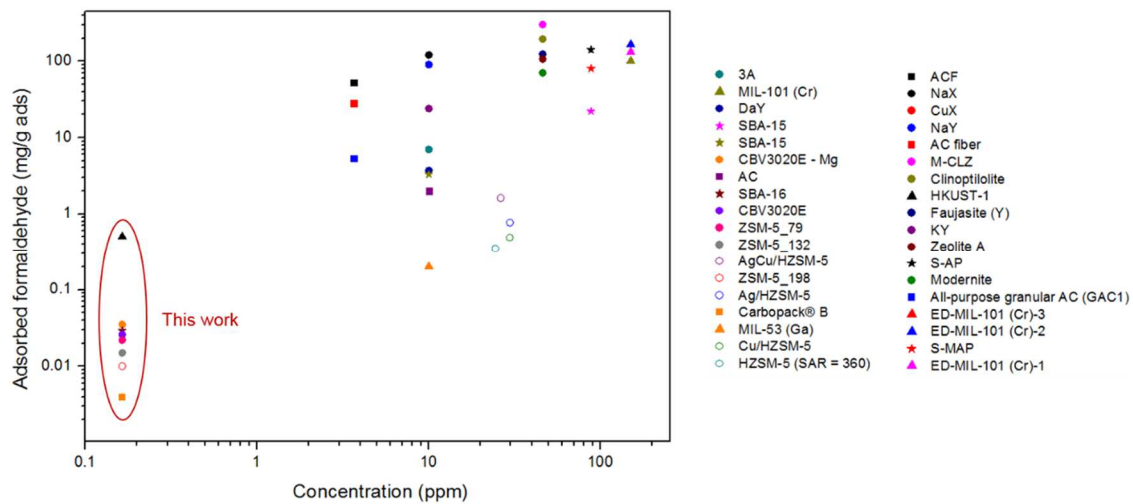


Figure 5-11. Formaldehyde adsorption capacities of diverse materials at different formaldehyde concentrations

This parameter is considered valid only at relatively low pressures (< 100 Pa corresponding to 1,094 ppm), where it is assumed that the adsorption capacity increases linearly with the adsorbate partial pressure. Thus, in this interval, Henry's law can be applied [44] and the Henry's constant K_H (mol/kg⁻¹Pa⁻¹) can be estimated as the slope of the adsorption capacity versus partial pressure plot as follows:

$$K_H = \frac{q}{P_f M_f} \quad \text{Eq. 5-1}$$

where q (kg/kg adsorbent) is the adsorption capacity, P_f is the formaldehyde partial pressure (Pa) and M_f is the molecular weight of formaldehyde (kg/mol).

In most studies, Henry's constant is not provided; hence, it has been calculated whenever possible from the data available in the experiments conducted at partial pressures lower than 100 Pa where Henry's law can be applied. In Table 5-5, adsorbents are listed in decreasing order of Henry constant. Apart from the comparison of the adsorptive properties of materials differing in nature, the determination of K_H values enables to draw some general conclusions about the most crucial factors in formaldehyde adsorption. Contrary to the general trend on the adsorption of non-polar compounds, specific surface area (SSA) seems not to be one of the most important factors on formaldehyde adsorption capacity as demonstrated by a relatively low K_H of MIL-101 (Cr) (SSA = 2,367 m²/g) and the high K_H obtained for S-AP (SSA = 422 m²/g). Several studies demonstrated indeed that functionalized materials with lower specific surface area exhibited an enhancement of the adsorption

capacity compared to the non-functionalized materials, owing to the formation of stronger interactions between the functional groups and formaldehyde molecules [24], [30]. This observation reveals that surface chemistry is a more decisive factor in formaldehyde adsorption than specific surface area.

Considering the pore size, it appears to be relevant when it is of the same order as the formaldehyde molecular diameter ($D_p = 2.5$ nm) due to the steric hindrance that can be caused, as observed in zeolite 3A ($D_p = 3$ nm) [28]. However, it seems not to be significant when it is much larger than formaldehyde kinetic diameter, as confirmed by the different K_H values obtained for DaY ($D_p = 0.74$ nm, $K_H = 0.135$ mol/kg Pa) and NaX ($D_p = 0.74$ nm, $K_H = 4.373$ mol/kg Pa), thus demonstrating that surface chemistry governs the adsorption of formaldehyde and, in general, polar molecules. Taking this into account, different strategies have been adopted to enhance adsorption capacity. Amine functionalization is the most common method employed to increase formaldehyde affinity in AC and mesoporous silica whereas high aluminium content and metal loading appear to be the most effective techniques in zeolites.

As mentioned previously, the calculation of K_H allows to evaluate the adsorbent affinity to formaldehyde and, thus, to assess their suitability for air pollution applications. As it is evident from K_H values, activated carbon fibers and some of metal loaded zeolites exhibited an outstanding affinity to formaldehyde attributed to the formation of strong adsorbate-adsorbent interactions. Therefore, it is expected that a high formaldehyde adsorption capacity be reached even at low concentrations, making these materials potential candidates for pollutant removal purposes. Concerning gas analysis applications, these adsorbents are probably not suitable since a complete desorption is required for the accurate formaldehyde quantification. Bellat *et al.* [28] observed that the adsorbed formaldehyde can polymerize into paraformaldehyde in the cages of zeolites NaX and NaY. The desorption of this latter compound becomes therefore much more difficult due to the size of the polymer, the complete desorption being only possible at 400 °C under dynamic vacuum, which is not compatible with gas analysis applications. Formaldehyde desorption from AC fibers was not investigated but the strong interactions of this compound with the acidic groups could potentially result in high desorption

Table 5-5. Formaldehyde adsorption capacities of various zeolites obtained in previous studies classified in descending order of the value of K_H .

Adsorbent	Adsorbent Type	S_{BET} (m ² /g)	V_{total} (mL/g)	Pore size (nm)	Concentration (ppm)	Partial pressure (Pa)	Temperature (°C)	Adsorption capacity (mg/g ads)	K_H (mol/kg ⁻¹ Pa ⁻¹)	Reference
ACF	AC	860	0.34	0.53	3.65	0.334	26	52.30	5.221	(Carter et al., 2011)
NaX	Zeolite	690	n. a.	0.74	10	0.914	25	120	4.373	(Bellat et al., 2015)
CuX	Zeolite	653	n. a.	0.74	10	0.914	25	90	3.279	(Bellat et al., 2015)
NaY	Zeolite	749	n. a.	0.74	10	0.914	25	90	3.279	(Bellat et al., 2015)
AC fiber	AC	1,084	0.41	0.53	3.65	0.334	26	28.20	2.815	(Carter et al., 2011)
M-CLZ	Zeolite	663.2	0.298	n. a.	46	4.204	25	300.5	2.380	(Kalantarifard et al., 2016)
Clinoptilolite	Zeolite	436.3	0.27	n. a.	46	4.204	25	194.5	1.541	(Kalantarifard et al., 2016)
HKUST-1	MOF	1,733	0.89	0.54 / 0.69	0.164	0.015	23	0.504	1.120	This work
Faujasite (Y)	Zeolite	415.2	0.136	n. a.	46	4.204	25	123.7	0.980	(Kalantarifard et al., 2016)
KY	Zeolite	703	n. a.	0.74	10	0.914	25	24	0.875	(Bellat et al., 2015)
Zeolite A	Zeolite	301.6	0.107	n. a.	46	4.204	25	106.7	0.845	(Kalantarifard et al., 2016)
S-AP	MS	422	0.72	7	88	8.042	r. t.	140.2	0.581	(Nomura and Jones, 2013)
Modernite	Zeolite	253.3	0.064	n. a.	46	4.204	25	70	0.555	(Kalantarifard et al., 2016)
All-purpose granular AC (GAC1)	AC	869	0.34	0.5	3.65	0.334	26	5.30	0.529	(Carter et al., 2011)
ED-MIL-101 (Cr)-3	MOF	382	0.34	< 2.3	150	13.708	r. t.	164.87	0.401	(Wang et al., 2016)
ED-MIL-101 (Cr)-2	MOF	n. a.	n. a.	< 2.3	150	13.708	r. t.	163.97	0.398	(Wang et al., 2016)
S-MAP	MS	401	0.69	6.6	88	8.042	r. t.	80.1	0.332	(Nomura and Jones, 2013)

ED-MIL-101 (Cr)-1	MOF	764	0.58	< 2.3	150	13.708	r. t.	131.54	0.320	(Wang et al., 2016)
3A	Zeolite	497	n. a.	0.3	10	0.914	25	7	0.255	(Bellat et al., 2015)
MIL-101 (Cr)	MOF	2,367	1.48	2.3	150	13.708	r. t.	100.30	0.244	(Wang et al., 2016)
DaY	Zeolite	717	n. a.	0.74	10	0.914	25	3.7	0.135	(Bellat et al., 2015)
SBA-15	MS	922	1.14	7	88	0.914	r. t.	22	0.120	(Nomura and Jones, 2013)
SBA-15	MS	595	0.4221	n. a.	10	8.042	25	3.3	0.091	(Bellat et al., 2015)
CBV3020E - Mg	Zeolite	296	0.11	0.55 ¹	0.164	0.015	23	0.035	0.078	This work
AC	AC	942	0.1011	n. a.	10	0.914	25	2	0.073	(Bellat et al., 2015)
SBA-16	MS	572	0.72	3.4 / 6.0	0.164	0.015	23	0.029	0.064	This work
CBV3020E	Zeolite	369	0.13	0.55 ¹	0.164	0.015	23	0.026	0.058	This work
ZSM-5_79	Zeolite	348	0.18	0.55 ¹	0.164	0.015	23	0.022	0.049	This work
ZSM-5_132	Zeolite	352	0.18	0.55 ¹	0.164	0.015	23	0.015	0.033	This work
AgCu/HZSM-5	Zeolite	299	n. a.	n. a.	26.2	2.394	RT	1.62*	0.023	(Zhao et al., 2011)
ZSM-5_198	Zeolite	367	0.17	0.55	0.164	0.015	23	0.01	0.022	This work
Ag/HZSM-5	Zeolite	310	n. a.	n. a.	29.7	2.714	RT	0.77*	0.009	(Zhao et al., 2011)
Carbopack® B	GCB	112	-	-	0.164	0.015	23	0.004	0.009	This work
MIL-53 (Ga)	MOF	560	-	n. a.	10	0.914	25	0.2	0.007	(Bellat et al., 2015)
Cu/HZSM-5	Zeolite	314	n. a.	n. a.	29.6	2.705	RT	0.49*	0.006	(Zhao et al., 2011)
HZSM-5 (SAR = 360)	Zeolite	n. a.	n. a.	n. a.	24.4	2.230	RT	0.35*	0.005	(Zhao et al., 2011)

¹Theoretical pore size; *Adsorption capacities calculated from mL of catalyst using a zeolite density of 0.72 g/mL [46]; *dynamic adsorption capacity; S-AP: primary aminosilica; S- MAP: secondary aminosilica. GCB: graphitised carbon black; MOF: metal organic frameworks; AC: activated carbon; MS: mesoporous Silica. K_H has been calculated from the formaldehyde partial pressure employed in each study and the obtained adsorption capacity following the Eq. 5- 1 assuming that Henry's law can be applied.

temperatures. Therefore, for preconcentration purposes, moderate adsorbate-adsorbent interactions are preferred. Hence, the adsorbents showing K_H values ranging from 0.1 to 1.5 mol/kg Pa seem to be more appropriate. These adsorbents exhibited a non-negligible formaldehyde adsorption capacity, thus enabling a quantitative sampling and, furthermore, the intermediate strength of the interactions may presumably lead to moderate desorption temperatures (150 - 250°C) similarly to the ones employed in conventional preconcentration systems. In this context, HKUST-1 could be a suitable candidate for this application. In this MOF, water molecules are adsorbed by interactions with copper sites and the carboxylic groups of the linkers and, since formaldehyde is a small polar molecule, similar interactions are expected in formaldehyde adsorption. Therefore, it may be reasonable to think that complete formaldehyde removal can be accomplished at a moderate temperature (~120 °C), as in the case of water.

Finally, K_H values lower than 0.1 mol/kg Pa are found for considerably hydrophobic materials such as ZSM-5 zeolites, some mesoporous silica and Carboxipack® B due to the weakness of the adsorbate-adsorbent interactions. It is obvious that these materials are not suitable for pollutant removal because of their limited adsorption capacity at low concentrations. However, some of them, such as Mg loaded and low SAR ZSM-5 zeolites or mesoporous silica (SBA-15 and SBA-16), can be used as a sampling material in moist environments since water is not expected to be adsorbed to a great extent.

5.3.2.4 Conclusions

A selection of conventional adsorbents including a graphitised carbon black, a mesoporous silica and a metal organic framework with different textural properties and surface chemistries has been investigated to evaluate their performance for gaseous formaldehyde adsorption at realistic concentrations (164 ppb). Among the investigated adsorbents, HKUST-1 appears to be the most efficient. This material exhibited the highest adsorption capacity and seems to be a good candidate for gaseous formaldehyde removal at low relevant concentrations. However, it is known from the literature that this material has high affinity to water, thus, more hydrophobic materials were investigated for formaldehyde adsorption. In this regard, a series of ZSM-5 zeolites with different Si/Al ratios and with Mg as compensating cation were also assessed in terms of formaldehyde adsorption capacity. Formaldehyde was only slightly adsorbed in ZSM-5 zeolites, but the results indicate that a considerable enhancement can be achieved by increasing the aluminium content. Moreover, it was demonstrated that the adsorptive performance can be further improved by

adding Mg^{2+} as a compensating cation due to the stronger adsorbate-adsorbent interactions formed.

To our knowledge, this is the first study to investigate formaldehyde adsorption at hundreds of ppb. This type of studies is needed because they provide accurate and reliable data of adsorption performance at ambient conditions. Thus, it allows to properly evaluate an adsorbent for real-world applications. More studies must be conducted at realistic conditions since adsorption capacity at high concentrations has been demonstrated to be not always linearly correlated to the capacity at low concentrations.

To enable a comparison between the experimental data obtained and the results from the literature, the Henry's constant was calculated for each adsorbent. The use of this parameter for comparison purposes allowed to shed light on the critical factors on formaldehyde adsorption, demonstrating that surface chemistry plays a major role in this process. Furthermore, it allows the comparison of adsorptive properties of different materials using adsorption data obtained under different experimental conditions. From the calculated Henry's constants, activated carbons and metal loaded X and Y zeolites seem to have potential applications in formaldehyde removal at low concentrations, whereas HKUST-1, more hydrophobic zeolites such as DaY, 3A or ZSM-5 and mesoporous silica could be more appropriate for gas analysis. Most of the experiments from the literature and the ones conducted in this work were performed in dry conditions (relative humidity < 5 %). Therefore, for real-world applications, it will be necessary to evaluate the competitive adsorption of water-formaldehyde binary mixtures to mimic the presence of humidity. HKUST-1 has indeed high affinity to water but there are no experimental data available in the literature on multicomponent adsorption. Another key aspect that requires further study is the desorption. Desorption temperature and decrease of adsorption capacity with regeneration cycles should be also investigated to properly evaluate the suitability of adsorbents for air pollution removal and analysis applications.

References

- [1] I. Lara-Ibeas et al., "BTEX near real-time monitoring in two primary schools in La Rochelle, France," *Air Qual Atmos Health*, vol. 11, no. 9, pp. 1091–1107, Nov. 2018.
- [2] C. Mandin et al., "Assessment of indoor air quality in office buildings across Europe – The OFFICAIR study," *Science of The Total Environment*, vol. 579, pp. 169–178, Feb. 2017.
- [3] R. Nasreddine, V. Person, C. A. Serra, C. Schoemaeker, and S. Le Calvé, "Portable novel micro-device for BTEX real-time monitoring: Assessment during a field campaign in a low consumption energy junior high school classroom," *Atmospheric Environment*, vol. 126, pp. 211–217, Feb. 2016.
- [4] R. Montero-Montoya, R. López-Vargas, and O. Arellano-Aguilar, "Volatile Organic Compounds in Air: Sources, Distribution, Exposure and Associated Illnesses in Children," *Annals of Global Health*, vol. 84, no. 2, Jul. 2018.
- [5] M. Verrièle et al., "The MERMAID study: indoor and outdoor average pollutant concentrations in 10 low-energy school buildings in France," *Indoor Air*, vol. 26, no. 5, pp. 702–713, Oct. 2016.
- [6] A. A. Arif and S. M. Shah, "Association between personal exposure to volatile organic compounds and asthma among US adult population," *Int Arch Occup Environ Health*, vol. 80, no. 8, pp. 711–719, Aug. 2007.
- [7] M. P. Tsakas, A. P. Siskos, and P. Siskos, "Indoor Air Pollutants and the Impact on Human Health," *Chemistry, Emission Control, Radioactive Pollution and Indoor Air Quality*, Jul. 2011.
- [8] M. A. Alghamdi et al., "Seasonal and diurnal variations of BTEX and their potential for ozone formation in the urban background atmosphere of the coastal city Jeddah, Saudi Arabia," *Air Qual Atmos Health*, vol. 7, no. 4, pp. 467–480, Dec. 2014.
- [9] N. L. Ng et al., "Effect of NO_x level on secondary organic aerosol (SOA) formation from the photooxidation of terpenes," *Atmospheric Chemistry and Physics*, vol. 7, no. 19, pp. 5159–5174, Oct. 2007.
- [10] G. B. Baur, "Development of Adsorbents for Selective Volatile Organic Compounds Removal from Diluted Gas Streams," *Infoscience*, 2015. [Online]. Available: <https://infoscience.epfl.ch/record/212805>. [Accessed: 30-Jun-2019].
- [11] D. Campagnolo et al., "VOCs and aldehydes source identification in European office buildings - The OFFICAIR study," *Building and Environment*, vol. 115, pp. 18–24, Apr. 2017.
- [12] O. Geiss, G. Giannopoulos, S. Tirendi, J. Barrero-Moreno, B. R. Larsen, and D. Kotzias, "The AIRMEX study - VOC measurements in public buildings and schools/kindergartens in eleven

European cities: Statistical analysis of the data," *Atmospheric Environment*, vol. 45, no. 22, pp. 3676–3684, Jul. 2011.

[13] R. Ortmann, C. Pasel, M. Luckas, S. Kraas, M. Fröba, and D. Bathen, "Sorption of Acetaldehyde and Hexanal in Trace Concentrations on Carbon-Based Adsorbents," *Chemical Engineering & Technology*, vol. 38, no. 1, pp. 125–130, 2015.

[14] D. Bourdin and V. Desauziers, "Development of SPME on-fiber derivatization for the sampling of formaldehyde and other carbonyl compounds in indoor air," *Anal Bioanal Chem*, vol. 406, no. 1, pp. 317–328, Jan. 2014.

[15] "Cooling baths," *Chemistry LibreTexts*, 02-Oct-2013. [Online]. Available: https://chem.libretexts.org/Ancillary_Materials/Demos%2C_Techniques%2C_and_Experiments/General_Lab_Techniques/Cooling_baths. [Accessed: 26-Jun-2019].

[16] J. G. Calvert, "Glossary of atmospheric chemistry terms (Recommendations 1990)," *Pure and Applied Chemistry*, vol. 62, no. 11, pp. 2167–2219, 2009.

[17] G. Busca, "Acidity and basicity of zeolites: A fundamental approach," *Microporous and Mesoporous Materials*, vol. 254, pp. 3–16, Dec. 2017.

[18] P. Losch, "Synthesis and characterisation of zeolites, their application in catalysis and subsequent rationalisation: methanol-to-olefins (MTO) process with designed ZSM-5 zeolites," p. 173, 2016.

[19] T. Terencio, F. Di Renzo, D. Berthomieu, and P. Trens, "Adsorption of Acetone Vapor by Cu-BTC: An Experimental and Computational Study," *J. Phys. Chem. C*, vol. 117, no. 49, pp. 26156–26165, Dec. 2013.

[20] E. Ahmed, A. Deep, E. E. Kwon, R. J. C. Brown, and K.-H. Kim, "Performance comparison of MOF and other sorbent materials in removing key odorants emitted from pigpen slurry," *Scientific Reports*, vol. 6, p. 31283, Aug. 2016.

[21] K.-Y. Andrew Lin and Y.-T. Hsieh, "Copper-based metal organic framework (MOF), HKUST-1, as an efficient adsorbent to remove p-nitrophenol from water," *Journal of the Taiwan Institute of Chemical Engineers*, vol. 50, pp. 223–228, May 2015.

[22] K. Vellingiri et al., "Metal organic frameworks as sorption media for volatile and semi-volatile organic compounds at ambient conditions," *Sci Rep*, vol. 6, p. 27813, 21 2016.

[23] S. Martens et al., "Periodic Mesoporous Organosilicas as Adsorbents of Toxic Trace Gases out of the Ambient Air," *Zeitschrift für anorganische und allgemeine Chemie*, vol. 640, no. 3–4, pp. 632–640, 2014.

[24] A. Nomura and C. W. Jones, "Amine-Functionalized Porous Silicas as Adsorbents for Aldehyde Abatement," *ACS Appl. Mater. Interfaces*, vol. 5, no. 12, pp. 5569–5577, Jun. 2013.

- [25] M. Woellner, S. Hausdorf, N. Klein, P. Mueller, M. W. Smith, and S. Kaskel, "Adsorption and Detection of Hazardous Trace Gases by Metal-Organic Frameworks," *Adv. Mater.*, vol. 30, no. 37, p. 1704679, Sep. 2018.
- [26] Z. Zhao, S. Wang, Y. Yang, X. Li, J. Li, and Z. Li, "Competitive adsorption and selectivity of benzene and water vapor on the microporous metal organic frameworks (HKUST-1)," *Chemical Engineering Journal*, vol. 259, pp. 79–89, Jan. 2015.
- [27] T. Salthammer, S. Mentese, and R. Marutzky, "Formaldehyde in the Indoor Environment," *Chemical Reviews*, vol. 110, no. 4, pp. 2536–2572, Apr. 2010.
- [28] J.-P. Bellat et al., "Capture of formaldehyde by adsorption on nanoporous materials," *Journal of Hazardous Materials*, vol. 300, pp. 711–717, Dec. 2015.
- [29] E. M. Carter, L. E. Katz, G. E. Speitel, and D. Ramirez, "Gas-Phase Formaldehyde Adsorption Isotherm Studies on Activated Carbon: Correlations of Adsorption Capacity to Surface Functional Group Density," *Environ. Sci. Technol.*, vol. 45, no. 15, pp. 6498–6503, Aug. 2011.
- [30] Z. Wang, W. Wang, D. Jiang, L. Zhang, and Y. Zheng, "Diamine-appended metal–organic frameworks: enhanced formaldehyde-vapor adsorption capacity, superior recyclability and water resistibility," *Dalton Trans.*, vol. 45, no. 28, pp. 11306–11311, Jul. 2016.
- [31] A. T. Hodgson and H. Levin, "Volatile organic compounds in indoor air: A review of concentrations measured in North America since 1990," Apr. 2003.
- [32] W. Liu et al., "Predicting personal exposure to airborne carbonyls using residential measurements and time/activity data," *Atmospheric Environment*, vol. 41, no. 25, pp. 5280–5288, Aug. 2007.
- [33] R. Cavalcante et al., "Exposure Assessment for Formaldehyde and Acetaldehyde in the Workplace," *Indoor and Built Environment*, vol. 14, pp. 165–172, Apr. 2005.
- [34] J. Rovira, N. Roig, M. Nadal, M. Schuhmacher, and J. L. Domingo, "Human health risks of formaldehyde indoor levels: An issue of concern," *Journal of Environmental Science and Health, Part A*, vol. 51, no. 4, pp. 357–363, Mar. 2016.
- [35] T. Dutta, K.-H. Kim, R. J. C. Brown, Y.-H. Kim, and D. Boukhvalov, "Metal-organic framework and Tenax-TA as optimal sorbent mixture for concurrent GC-MS analysis of C1 to C5 carbonyl compounds," *Scientific Reports*, vol. 8, no. 1, p. 5033, Mar. 2018.
- [36] H. Rong, Z. Ryu, J. Zheng, and Y. Zhang, "Effect of air oxidation of Rayon-based activated carbon fibers on the adsorption behavior for formaldehyde," *Carbon*, vol. 40, no. 13, pp. 2291–2300, Jan. 2002.

- [37] Y. Song, W. Qiao, S.-H. Yoon, I. Mochida, Q. Guo, and L. Liu, "Removal of formaldehyde at low concentration using various activated carbon fibers," *Journal of Applied Polymer Science*, vol. 106, no. 4, pp. 2151–2157, 2007.
- [38] P. Küsgens et al., "Characterization of metal-organic frameworks by water adsorption," *Microporous and Mesoporous Materials*, vol. 120, no. 3, pp. 325–330, Apr. 2009.
- [39] L. Deliere, "Adsorption et séparation des gaz rares sur des adsorbants dopés à l'argent," Nov. 2015.
- [40] S. M. Auerbach, K. A. Carrado, and P. K. Dutta, *Handbook of Zeolite Science and Technology*. CRC Press, 2003.
- [41] E. Kukulska-Zajac and J. Datka, "Transformations of Formaldehyde Molecules in Cu-ZSM-5 Zeolites," *J. Phys. Chem. C*, vol. 111, no. 8, pp. 3471–3475, Mar. 2007.
- [42] S. K. P. Veerapandian, N. De Geyter, J.-M. Giraudon, J.-F. Lamonier, and R. Morent, "The Use of Zeolites for VOCs Abatement by Combining Non-Thermal Plasma, Adsorption, and/or Catalysis: A Review," *Catalysts*, vol. 9, no. 1, p. 98, Jan. 2019.
- [43] C.-J. Na, M.-J. Yoo, D. C. W. Tsang, H. W. Kim, and K.-H. Kim, "High-performance materials for effective sorptive removal of formaldehyde in air," *Journal of Hazardous Materials*, vol. 366, pp. 452–465, Mar. 2019.
- [44] J. E. Szulejko, K.-H. Kim, and J. Parise, "Seeking the most powerful and practical real-world sorbents for gaseous benzene as a representative volatile organic compound based on performance metrics," *Separation and Purification Technology*, vol. 212, pp. 980–985, Apr. 2019.
- [45] K. Vellingiri, P. Kumar, A. Deep, and K.-H. Kim, "Metal-organic frameworks for the adsorption of gaseous toluene under ambient temperature and pressure," *Chemical Engineering Journal*, vol. 307, pp. 1116–1126, Jan. 2017.
- [46] "ZSM-5 Catalyst Supplier – Molecular Sieves - ACS Material." [Online]. Available: <https://www.acsmaterial.com/zsm-5-catalyst-1122.html>. [Accessed: 29-Jun-2019].

General conclusions and perspectives

During this thesis, different aspects related to the gaseous VOC quantification and removal have been addressed. At the beginning of this work, a field air quality campaign conducted in primary schools revealed the importance of near real time measurements in indoor air quality (IAQ) monitoring. These results, along with the new IAQ French legislation entered into force in 2018 disclosed an urgent need for portable analytical instruments sensitive enough to detect such low concentrations. This context was the motivation for the main objective to be met during this thesis, i.e. the development of a BTEX preconcentrator integrated in a portable GC prototype to achieve a LOD lower than $2 \mu\text{g m}^{-3}$ (0.6 ppb) for benzene. In parallel to this development, a complementary study of different adsorbents was also performed with a view to either better select and possibly enlarge the range of pollutants analysed or improve and characterize their adsorption/desorption cycles.

The literature review presented in **chapter 1** served to identify the main pollutants of indoor air and their range of concentrations. In this chapter, the most common methods for VOC quantification have been described and gas chromatography has proved to be the most suitable to meet with the objectives concerning portability and sensitivity defined at the beginning of this thesis. The state of the art performed on the gas preconcentrators allow to understand the importance of each parameter on the preconcentration performance and the current challenges in the miniaturization of gas preconcentration devices that were facing during this work. Finally, the review of the theoretical basis of the adsorption process helped me to understand and properly discuss the results obtained during the adsorption studies.

Chapter 2 was divided in two sections: VOC adsorption and preconcentrator development. In the first part, the main characteristics of the solid materials employed for VOC adsorption and the reasons for which they were selected for this study were presented. Then, all the techniques and the experimental conditions employed for their characterization were detailed. These techniques provide information about the different features of these solids in terms of textural properties and chemical composition which are essential for the interpretation of the adsorption behaviour (breakthrough time and adsorption capacity). Afterwards, the different homemade experimental setups used for the adsorption experiments have been described. These setups allowed to precisely monitor VOC adsorption and provide the data to generate the breakthrough curves. These curves were used for the

assessment of the breakthrough time and adsorption capacity. Both features playing a major role in gas analysis and pollutant removal applications.

In the second part of this chapter, the manufacturing process and the main elements of each preconcentrator developed in this thesis were described. This section illustrates the complexity and interdisciplinarity of the design process of an analytical instrument involving knowledge of different fields as analytical chemistry, thermodynamics, mechanics, fluid mechanics and electronics.

In **chapter 3** the results obtained during a field campaign of indoor air quality conducted in two French primary schools for 5 weeks were presented. The objective was to determine BTEX concentrations, identify their main emission sources and evaluate the efficiency of the different ventilation scenarios. To this purpose, preindustrial prototypes developed in our lab were employed to continuously monitor BTEX concentration under different occupation and ventilation conditions. These devices provided near-real time measurements that allowed to establish concentration-time profiles with high time resolution of 10 min. Such data, together with additional CO₂ measurements, demonstrated to be an effective method for source identification. Indeed, CO₂ levels can be used as confinement indicator, therefore, the correlation or anticorrelation of these with BTEX concentrations reveals the internal or external origin of the emission sources. Furthermore, repetitive patterns of pollution peaks measured at the same time in different weeks allowed to associate these emissions to children activities.

Our study revealed the importance of near-real time measurements compared to classical methods such as passive sampling since they provide average concentrations that are not useful for an accurate identification of the emission source. Therefore, our portable GC proved to be a valuable tool for BTEX source identification, and it has demonstrated its ability to monitor BTEX continuously at ppb levels over long periods of time. Nevertheless, a lower benzene threshold of 0.6 ppb was fixed by the new air quality legislation for public buildings in France. Therefore, an increasing sensitivity was required to comply with this new regulation. Due to the lack of portable analytical instruments sensitive enough to detect such low concentration, a preconcentrator was developed to improve the sensitivity of this instrument to ppt levels.

In **chapter 4** the performance of every preconcentrator prototype developed and tested in this work is described in terms of heating and preconcentration ability. The objectives fixed for this device, apart from a LOD lower than 0.6 ppb for benzene, were to maintain an energy consumption low enough to

be integrated in a portable instrument. This instrument must also have similar time resolution being able to perform an analysis cycle in ~10-15 min.

The first prototype developed, called MAP, was fully functional and exhibited LOD of 0.20 ppb for benzene. However, the high energy consumption due to its elevated thermal mass prevented its integration in portable commercial analysers. Therefore, to tackle this issue, several versions were developed by using diverse type of materials, adsorbents and heating systems. After many attempts, the last version developed, called μ AP2, met all the requirements set in the objectives of this thesis. GC system integrating μ AP2 exhibited a LOQ of 0.191 ppb for benzene with only 20 mL sample. To achieve this performance, the energy consumption was minimally incremented since only additional ~ 70 W were required for 70 s to perform this preconcentration step. Furthermore, the integration of this supplementary step had negligible influence in the total analysis time since in the case of consecutive analysis, the sampling of the next analysis can be performed simultaneously during the separation step of the ongoing analysis. As in any analytical device, reproducibility and repeatability were also evaluated. Our instrument demonstrated satisfactory performances for these critical features highlighting their suitability for reliable analysis over long periods of time. Furthermore, the manufacturing cost of the developed preconcentrator can be estimated in several tens of euros what leads to an outstanding price-performance ratio for this device.

The last part of this section consisted of a comparison with the existing portable GC in the literature. To our knowledge, our device showed the best sensitivity in terms of lowest detectable amount of pollutant being able to detect 3.6, 11.3, 32.0, 34.4 and 36.3 pg for benzene, toluene, ethylbenzene, m/p-xylenes and o-xylene, respectively. These amounts were 2 – 3 orders of magnitude lower than the best sensitivities reported to date for portable GC equipped with a preconcentration units and they were closer to the analytical performances typically found in bench-top instruments.

Chapter 5 summarizes the main results obtained in the sorption studies of BTEX, formaldehyde and hexanal on a wide variety of solid materials (adsorbents). The main objective of this study was to find an appropriate adsorbent for BTEX preconcentration and also for other common pollutants frequently encountered in indoor air, i.e. formaldehyde and hexanal. To this purpose, a series of dynamic adsorption experiments were carried out to evaluate the adsorption capacity and determine the key parameters affecting aromatics and aldehydes adsorption. This chapter was divided in three sections.

In the first section, toluene and BTEX adsorption at low concentration was evaluated on three commercial adsorbents differing in textural properties and surface chemistry. Among them, SBA-16 exhibited the highest adsorption capacity in both single and multicomponent adsorption studies. In this latter, SBA-16 showed minimum roll up preventing the desorption of the most volatile molecules when the adsorbent is close to the saturation. These features, together with a reasonable activation energy for the desorption, suggested that this material can be a good candidate for gas analysis applications.

In the second section, a similar adsorption study was presented but the adsorbents employed this time were zeolites synthesized in our research institute. Multicomponent BTEX adsorption experiments were carried out on five ZSM-5 zeolites with different Si/Al ratio (SAR) to elucidate the effect of chemical composition on BTEX adsorption. This parameter was proven to have a strong influence on BTEX adsorption, and the obtained results revealed that a compromise between SAR and hydrophobicity should be achieved to optimize BTEX adsorption. In this regard, the fluoride-mediated synthesis of ZSM-5 zeolite employed appears to be an advantageous strategy compared to the traditional alkaline route since it allowed to obtain highly hydrophobic materials even with low SAR.

Finally, the last section deals with the adsorption of formaldehyde and hexanal on the abovementioned materials (commercial adsorbents and zeolites) at realistic concentrations i.e. 164 ppb. This type of studies is required to properly evaluate adsorbent performances since adsorption capacity at high concentrations has been demonstrated to be not always linearly correlated to the adsorption capacity at low concentrations. To our knowledge, it has been the only study performed at such very low concentrations. Our results and their comparison with the experimental data from the literature highlighted that surface chemistry is a determining factor on aldehydes adsorption. HKUST-1 exhibited the highest adsorption capacity towards formaldehyde and hexanal presumably due to the strong interaction of carbonyl functions with copper ions of the HKUST-1 structure. SBA-16 and ZSM-5 zeolite showed a significant hexanal adsorption capacity whereas they were not very appropriate for formaldehyde capture. In fact, most of the materials investigated in this work were not very effective for formaldehyde capture because of its small size and high polarity.

The results obtained within the framework of this thesis open new prospects concerning the development of portable analytical instruments. Our compact GC exhibited satisfactory performances

under laboratory conditions, however, it should be tested in real environments, for example, by conducting a field campaign similar to the one performed during this thesis. This campaign can help to determine the real performances of the instrument as well as identifying the potential problems derived from the detection of interfering substances, the detector drift or fluctuating temperature and relative humidity conditions. Prior to this field campaign, an automatization of the preconcentration step resulting in a pre-industrialized prototype is needed. The automatization of the preconcentration step should lead to the improvement of repeatability and reproducibility of the measurements to reach levels of performance that meets the standards established for compliant air quality monitoring. In addition, the automatization of the overall system enables the programming of sequences of analysis and BTEX monitoring can be performed over long times without the constant supervision of a technician.

Undoubtedly, one of the main advantages of the preconcentrator developed in this work is its extremely low manufacturing cost (~tens of euros) which means that it can be easily placed on the market. Besides, this device can be filled with other adsorbents to capture different molecules and the separation column and the detector can be replaced or coupled to other sensors to enlarge the range of detected pollutants. In this regard, it is possible to think that the preconcentrator developed in this work can be rapidly adapted and used in many applications requiring very high sensitivity such as explosive and warfare agents detection, food industry or breath analysis.

Résumé (en français)

Ce résumé rédigé en français est une brève présentation du contexte dans lequel ce travail a été réalisé et des résultats les plus significatifs obtenus pendant ce travail de thèse. Si le lecteur souhaite avoir une vision plus approfondie de certains aspects, il est fortement recommandé de lire la version complète rédigée en anglais.

1. Introduction générale

Depuis ces dernières années, la pollution de l'air est devenue un des plus grands enjeux de notre temps en raison de son augmentation constante et de ses effets néfastes sur la santé. En 2016, l'Organisation Mondiale de la Santé a estimé que plus de 91 % des habitants de la planète respirent un air pollué, ce qui entraîne environ 7 millions de décès prématurés chaque année [1].

En effet, nombreuses preuves scientifiques ont démontré le lien entre l'exposition à la pollution atmosphérique et le développement d'un grand nombre de pathologies telles que les maladies cardiovasculaires, le cancer du poumon, les maladies pulmonaires obstructives chroniques et les infections respiratoires [2]–[4]. De plus, la pollution de l'air a également un impact économique notable en raison de la détérioration de la santé publique, de la baisse de la productivité des employés et de la dégradation de l'environnement. À cet égard, des politiques environnementales sont mises en œuvre pour protéger à la fois la santé humaine et l'environnement. Cependant, pour évaluer correctement la qualité de l'air et proposer ainsi des actions pour l'améliorer, des données expérimentales s'avèrent nécessaires.

a) La qualité de l'air intérieur

Un rapport publié par l'Organisation mondiale de la santé (OMS) en 2017 a révélé que la pollution de l'air (intérieur ou atmosphérique) est responsable de 11,6% des décès à travers le monde et constitue l'une des principales causes de mortalité, loin devant les grandes maladies transmissibles (voir Figure 1). Ce fort impact s'explique parce que l'Homme passe environ 85% de son temps dans des espaces clos [5] et que la concentration de polluants dans les environnements intérieurs est fréquemment de 2

à 10 fois plus élevée que celle des environnements extérieurs. Par conséquent, l'air intérieur constitue une voie majeure d'exposition à des nombreux polluants.

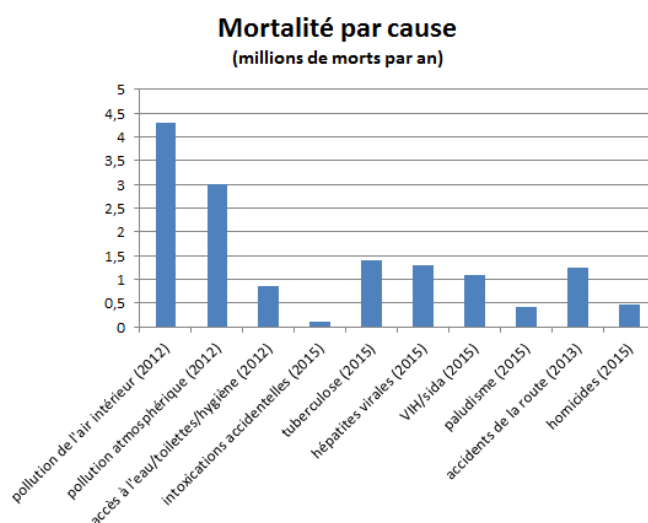


Figure 1. Principales causes de mortalité dans le monde enregistrées ces dernières années [6]

Dans les espaces clos, un large éventail de polluants peut être présent tels que composés organiques volatiles (COV), semi-volatiles (COSV), oxydes d'azote, etc. Parmi ces polluants, les COV sont fréquemment rencontrés à des concentrations élevées dans l'air intérieur [15] - [17]. Ce groupe de molécules est défini par le Conseil Européen comme des composés ayant une pression de vapeur de 0,01 kPa ou plus à 293 K. Les COV comprennent un large spectre de molécules caractérisées par des structures formées par des chaînes carbonées et, dans certains cas, d'autres atomes comme l'oxygène, le soufre ou l'azote. Le présent travail est focalisé sur l'analyse et l'élimination de certains COV, à savoir les BTEX (Benzène, Toluène, Ethylbenzène and Xylènes) et certains aldéhydes (formaldéhyde, hexanal) en raison de leurs abondances dans l'air intérieur [7], [8] et de leurs effets nocifs sur la santé. Les principales propriétés physico-chimiques des polluants étudiés sont présentées dans le Tableau 1.

Dans l'air intérieur, les sources d'émission sont très nombreuses et diverses. D'une part, les activités des occupants comme la cuisine, le tabagisme, le ménage ou le bricolage [9], [10] constituent des sources majeures d'émission des BTEX et des aldéhydes. D'autre part, les matériaux de construction et de décoration comme les revêtements de sol, revêtements muraux, adhésifs, vernis ou peintures ainsi que l'ameublement sont également considérés comme d'autres sources importantes de COV dans l'air intérieur [11]–[13].

Tableau 1. Propriétés physico-chimiques des composés étudiés dans ce travail.

	N° CAS	Masse molaire (g/mol)	Point d'ébullition (°C) at 1 atm	Pression de vapeur (kPa) à 20°C	Moment dipolaire (D)*	Diamètre cinétique (nm)
Benzene	71-43-2	78.11	80.1	10.00	0	0.585
Toluene	108-88-3	92.14	110.6	2.90	0.375	0.585
Ethylbenzene	100-41-4	106.17	136.0	1.00	0.59	0.60
o-Xylene	95-47-6	106.16	144.4	0.93	0.64	0.68
m-Xylene	108-38-3	106.16	139.0	1.20	0.35	0.68
p-Xylene	106-42-3	106.16	138.4	1.20	0	0.585
Formaldehyde	50-00-0	30.03	-19.4	101.32	2.33	0.25
Hexanal	66-25-1	100.16	131.0	1.33	2.64	0.52

La qualité de l'air dépend de la présence des sources d'émission mais aussi du taux de renouvellement de l'air. En effet, la ventilation joue un rôle clé sur les niveaux de polluants dans l'air intérieur. Une bonne ventilation peut permettre d'abaisser rapidement les concentrations de VOC présents en air intérieur [14], [15]. Par contre, si l'air extérieur est fortement pollué comme dans le cas d'une zone industrielle ou d'une zone de trafic intense, la ventilation peut contribuer à la dégradation de la qualité de l'air intérieur.

Comme conséquence de la multitude de sources d'émission existantes, les BTEX et les aldéhydes sont très souvent retrouvés à des concentrations élevées dans les environnements clos. Une étude dans 22 logements à Strasbourg a rapporté des concentrations maximales de formaldéhyde et d'hexanal variant entre 13,3-123,4 $\mu\text{g m}^{-3}$ et 0-47,2 $\mu\text{g m}^{-3}$, respectivement. Des niveaux plus élevés allant jusqu'à 92 $\mu\text{g m}^{-3}$ d'hexanal ont été signalés par Walgraeve *et al.* [16] dans une étude réalisée dans 6 foyers en Belgique. Dans cette étude, la concentration d'hydrocarbures aromatiques a atteint des concentrations de 88 $\mu\text{g m}^{-3}$ correspondant à 25% de la concentration totale de COV. Des niveaux significatifs des BTEX, de l'hexanal et du formaldéhyde ont également été détectés dans différents environnements à travers le monde, tels que les écoles [17]–[19], les universités [20], [21], les cafés ou les maisons d'agriculteurs [22]. Ces résultats ont montré que quels que soient le pays et le type d'environnement considérés, les COV sont toujours présents.

b) Effets sur la santé et législation

Au cours des dernières décennies, de nombreuses études ont été menées pour élucider les effets sur la santé causés par la pollution atmosphérique. De plus en plus de preuves scientifiques ont démontré la relation entre l'exposition aux polluants atmosphériques et les effets nocifs sur la santé humaine [33] comme les maux de tête, l'irritation des yeux et du nez ou le développement de pathologies telles que l'asthme [34], les allergies [35] ou même le cancer [36]. Ces effets dépendent du polluant, de sa concentration et du temps d'exposition. De plus, il est difficile d'évaluer les risques liés à la pollution de l'air car l'air extérieur et intérieur contiennent un mélange de polluants divers pouvant provoquer un effet synergique souvent appelé « effet cocktail ». Différents polluants peuvent en effet interagir les uns avec les autres, renforçant les effets néfastes que la somme des effets produits par chaque polluant unique. En outre, les effets sur la santé sont influencés par de nombreux facteurs tels que le sexe ou l'âge, les plus vulnérables étant les enfants, les femmes et les personnes âgées [37]. La présence de maladies cardiovasculaires ou respiratoires peut aggraver les effets néfastes de la pollution atmosphérique.

Parmi les composés étudiés dans ce travail, le benzène est considéré comme un de plus dangereux car il est classé cancérigène pour l'homme (Groupe 1) par le CIRC (Centre International de Recherche sur le Cancer). Pour ce type de composés, il n'y a pas de niveau d'exposition sûr, par conséquent, seule une estimation du risque associé à différentes concentrations peut être fournie.

Une fois le benzène absorbé dans le corps humain, il est transformé en substances qui sont extrêmement toxiques tels que le phénol, le catéchol et l'hydroquinone qui sont directement liées au développement de cancers [39].

Les autres composés aromatiques sur lesquels ce travail se focalise, sont classés comme probablement cancérigène (éthylbenzène) et non cancérigène (toluène et xylènes) pour l'homme. L'exposition courte à ces composés généralement entraîne l'irritation des yeux, du nez, de la gorge et des voies respiratoires [23]. Des effets plus graves tels que des lésions du système nerveux central et des reins, des vertiges, des étourdissements [24] ou des effets sur la mémoire à court terme [25] sont associés à des expositions de long durée à ces polluants.

Le formaldéhyde attire de plus en plus l'attention en raison de sa présence fréquente dans l'air intérieur. Cette substance est considérée comme cancérigène (Groupe 1) par le CIRC depuis 2006. En particulier, le formaldéhyde a été associé au développement d'un cancer du nasopharynx [26], [27].

Une exposition de courte durée au formaldéhyde peut provoquer une irritation de la gorge, du nez et des yeux ainsi que des maux de tête. Des effets plus graves tels qu'une diminution de la fonction pulmonaire, le larmoiement, la pneumonie et l'asthme ont été associés à une exposition à long terme au formaldéhyde [28].

Comme conséquence des effets néfastes de l'exposition à la pollution atmosphérique sur la santé humaine, une législation détaillée concernant la qualité de l'air a été élaborée dans plusieurs pays pour limiter l'exposition humaine et protéger la santé publique. Dans l'Union Européenne, la législation établie qu'un seuil de $100 \mu\text{g m}^{-3}$ pour le formaldéhyde ne doit être dépassé à aucun intervalle de 30 minutes au cours d'une journée [29]. Concernant le benzène, une valeur seuil de $5 \mu\text{g m}^{-3}$ a été établie pour une exposition à long terme (1 an) [30]. En France, la législation relative à la qualité de l'air intérieur des bâtiments publics est devenue plus stricte. Selon le décret no. 2011-1727 du 2 décembre 2011 [31], une valeur limite de $5 \mu\text{g m}^{-3}$ d'exposition à long terme a été fixée pour le benzène à partir du 1^{er} janvier 2013 et elle a été réduite à $2 \mu\text{g m}^{-3}$ à partir du 1^{er} janvier 2016. Dans le cas de formaldéhyde, une valeur limite de $30 \mu\text{g m}^{-3}$ a été fixée pour une exposition à long terme à partir du 1^{er} janvier 2015 et elle sera réduite à $10 \mu\text{g m}^{-3}$ à partir du 1^{er} janvier 2023.

c) Objectifs de ce travail

Le présent travail de recherche doctorale poursuit le travail effectué par Rouba Nasreddine [32] au cours de sa thèse focalisée sur le développement d'un GC portable pour la détection de BTEX dans l'air dont le schéma de fonctionnement est présenté sur la Figure 2a. Au cours de sa thèse, un premier prototype développé au laboratoire (Figure 2b) avait été déjà validé dans des conditions contrôlées [33] ainsi que dans des environnements réels [34]. En résumé, dans cet instrument, l'analyse des BTEX est effectuée en trois étapes : l'échantillonnage dans une boucle à l'aide d'une micropompe, la séparation des différents composés dans une colonne capillaire de chromatographie et la quantification au moyen d'un détecteur à photo-ionisation (PID) miniaturisé.

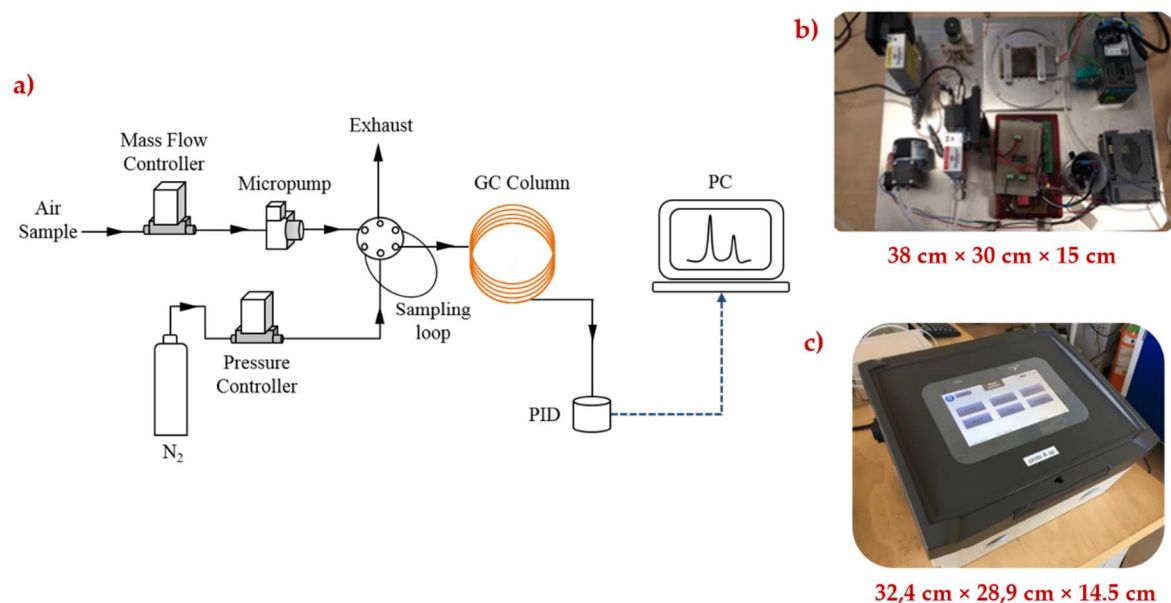


Figure 2. Schéma de fonctionnement du GC portable utilisé au cours de cette thèse (a), prototype de GC développé au laboratoire (b) et prototype de GC pré-industriel (c)

À la fin de sa thèse, un prototype pré-industriel du GC portable a été fabriqué (Figure 2c). Partant de ce point, les principaux objectifs du présent travail sont :

- L'évaluation des performances analytiques du prototype GC pré-industriel développé par Nasreddine *et al.* [33] en conditions réelles dans une campagne de terrain ainsi que la détermination des concentrations de BTEX et l'identification des principales sources dans l'air intérieur des écoles primaires.
- Le design, la conception et la fabrication d'un préconcentrateur BTEX afin d'être intégré dans le prototype GC développé et ainsi diminuer la limite de détection pour le benzène à une valeur inférieure à la valeur seuil fixée par le gouvernement français, soit $2 \mu\text{g m}^{-3}$ (0,6 ppb). Le prototype final devra conserver des caractéristiques similaires en termes de résolution temporelle ainsi que de consommation de gaz vecteur et d'énergie.
- Fournir des données expérimentales d'adsorption de COV sur différents matériaux à des concentrations réalistes (faible ppm - ppb). Évaluation de ces matériaux pour des applications d'analyse de gaz et d'élimination de polluants.

Ces trois objectifs principaux représentent les trois grandes parties de ce travail de thèse. La première partie présente les résultats obtenus dans une campagne de terrain sur la qualité de l'air intérieur menée dans deux écoles primaires françaises pendant 5 semaines. La deuxième partie porte sur le développement des différents prototypes de préconcentrateurs et sa caractérisation en termes de performances de chauffage et de préconcentration de BTEX. La troisième partie de ce travail est dédiée à l'étude de l'adsorption des BTEX, du formaldéhyde et de l'hexanal sur différents matériaux et l'influence des différentes propriétés texturales et chimiques sur l'adsorption de ces composés. A la fin de ce résumé, les conclusions générales et perspectives futures de ce travail sont présentées.

2. Campagne de mesure des BTEX dans deux écoles primaires à La Rochelle

Les polluants de l'air intérieur comme les BTEX ont des effets néfastes sur la santé humaine. Ces effets sont encore plus graves pour les enfants en raison de leur taux d'inhalation plus élevé, du développement continu de leurs tissus et organes et de leur système immunitaire immature [35]. De plus, les enfants passent beaucoup de temps à l'intérieur où les niveaux de polluants sont généralement de 2 à 10 fois plus élevés qu'à l'extérieur. Daisey *et al.* [36] ont ainsi rapporté que près de 30% du temps à l'intérieur est passé à l'école. Dans ce contexte, le projet Impact'Air visait à quantifier les profils concentrations-temps afin de mieux caractériser la pollution de l'air intérieur des écoles et de fournir des recommandations utiles pour améliorer leur qualité de l'air. Dans le cadre de ce projet, une campagne de terrain a été menée dans une école maternelle et deux écoles primaires de La Rochelle (France) pendant cinq semaines. Les principaux objectifs de ce projet étaient :

- Surveiller les polluants de l'air intérieur réglementés en France (formaldéhyde, benzène et CO₂) ;
- Identifier les principales sources d'émission de ces polluants ;
- Estimer l'efficacité de différents scénarios de ventilation sur la Qualité de l'Air Intérieur (QAI) ;
- Etablir de lignes directrices générales pour les bonnes pratiques en matière de QAI dans les écoles.

Bien que le formaldéhyde et le benzène soient les seuls COV réglementés, le toluène, l'éthylbenzène et les xylènes ont également été surveillés car l'exposition continue des enfants à ces polluants peut entraîner des problèmes de santé et une gêne physique [3]. De plus, la concentration de CO₂ a été

mesurée en continu car c'est un indicateur de confinement et donc de la ventilation à l'intérieur du bâtiment.

Afin d'identifier les principales sources de pollution et l'efficacité des différents scénarios de ventilation, des mesures de la qualité de l'air ont été réalisées dans différentes conditions chaque semaine. Au cours de la première semaine, les salles de classe étudiées étaient toujours fermées, non ventilées et occupées ni par les élèves ni par les enseignants (Figure 3a). Ainsi, la contribution des matériaux de construction à la pollution de l'air intérieur pourrait être estimée. Au début de la deuxième semaine, le mobilier a été ajouté et les salles de classe sont restées fermées pendant toute la semaine (Figure 3b). Ce scénario a permis de quantifier la pollution supplémentaire potentiellement émise par le mobilier. Enfin, au cours des trois dernières semaines, des activités scolaires normales ont été réalisées dans les salles de classe et différentes pratiques de ventilation ont été effectuées chaque semaine (Figure 3c).

Pendant une semaine, la ventilation habituelle a été suivie, où aucune instruction spécifique n'a été donnée aux enseignants, ils ont donc suivi ses critères subjectifs de ventilation. Ensuite, pendant une autre semaine, la ventilation était réalisée en fonction du niveau de CO₂ atteint dans la pièce. Ce niveau étant mesuré par un détecteur de CO₂ LUM'Air qui est équipé de trois LED différentes (verte, orange et rouge), qui s'allument en fonction de la concentration en CO₂. Pour des atmosphères qui ne sont pas confinées (concentration de CO₂ < 1000 ppm), la LED est verte. Lorsque les niveaux sont supérieurs à 1000 ppm (premier seuil d'alerte), la lumière est commutée à l'orange indiquant que les fenêtres et / ou les portes doivent être ouvertes. Si la concentration dépasse 1700 ppm (deuxième seuil d'alerte), la lumière passe au rouge et les fenêtres et / ou portes doivent être ouvrir rapidement afin de renouveler l'air intérieur.

Enfin, pendant une autre semaine, les enseignants ont suivi les consignes de ventilation données par l'Observatoire Français de la Qualité de l'Air Intérieur. Selon ces dernières instructions, les fenêtres ont été ouverts en moyenne 30 minutes dans les cas suivants : avant et après les cours, toutes les 2 h de cours, et après les opérations de nettoyage. Ainsi, toutes les portes de la classe sont restées ouvert la nuit.

Dans ce résumé, uniquement les résultats les plus significatives obtenus pendant cette campagne sont présentés. De plus amples détails sont donnés dans la publication « BTEX near real-time monitoring

in two primary schools in La Rochelle, France » [37] où tous les résultats obtenus pendant les cinq semaines de mesure en continu sont présentés.

Au cours de cette campagne de terrain, le benzène n'était présent que pendant les semaines d'occupation dans l'école Les Grandes Varennes indiquant que les matériaux de construction des bâtiments et le mobilier scolaire ne constituent pas une émission source de benzène. Par contre, cette école est proche de l'aéroport de La Rochelle et d'une route à voies avec un intense trafic, ce qui peut entraîner des concentrations élevées de COV dans la région, comme suggéré dans d'autres études [38]–[40]. Dans cette école, la plupart du temps, la concentration de benzène était inférieure à notre limite de détection de 1,1 ppb mais présentait parfois des pics à des périodes spécifiques. Par exemple, la Figure 3d illustre la concentration de benzène et de CO₂ mesurées à l'intérieur de la salle pendant la cinquième semaine. Le 15 mars, un pic de benzène atteignant presque 5 ppb peuvent être clairement identifiés pendant la nuit. Des valeurs jusqu'à 6 ppb ont également été enregistrées les 16 et 17 mars 2016 vers midi. La comparaison des concentrations de benzène et des niveaux de CO₂ montre qu'ils ne sont pas corrélés. En effet, le pic principal de la concentration de benzène a été enregistrée le 15 mars, lorsque le CO₂ le niveau a diminué, indiquant l'ouverture d'une ou plusieurs fenêtres. Le benzène a ensuite disparu, lorsque la concentration de CO₂ a commencé à augmenter, une fois les fenêtres fermées. Cette observation indique que la principale source d'émission du benzène n'était pas liée aux activités des élèves, mais était plus probablement attribuables aux travaux de rénovation de la chaussée avec du goudron à proximité de cette école à la même période.

D'autre part, les concentrations de toluène mesurées montrent un comportement complètement différent. Des concentrations faibles (0-3.2 ppb) ont été détectées pendant les 2 premières semaines dans l'école des Grandes Varennes indiquant que le mobilier constitue une source d'émission de toluène. Lorsque les occupants étaient présents (semaines 3 à 5), le toluène était présent dans les deux écoles et sa concentration variait respectivement de 0 à 29,5 ppb et de 0 à 3,5 ppb dans les écoles Les Grandes Varennes et Lavoisier. Les concentrations de toluène et de CO₂ mesurées dans Les Grandes Varennes au cours de la cinquième semaine sont présentés sur la Figure 3e. Contrairement aux résultats obtenus pour le benzène, cette figure montre que les niveaux de benzène et de CO₂ mesurés à l'intérieur de la salle étudiée étaient fortement corrélés. En effet, la concentration en toluène était faible (2 à 4 ppb) ou nulle lorsque les niveaux de CO₂ étaient d'environ 1000 ppm. Des concentrations plus élevées de toluène ont été enregistrés (8–17,6 ppb), lorsque les niveaux de CO₂ ont été supérieures à 1500 ppm. La diminution du niveau de CO₂ de 3500 ppm à moins de 1000 ppm indique que l'air à

l'intérieur de la salle a été renouvelé, soit par l'ouverture de fenêtres et / ou des portes. Afin de déterminer plus précisément l'origine de la source d'émission de toluène, les concentrations de toluène mesurées pendant les semaines 3 à 5 ont été comparées (Figure 3f). Cette figure met en évidence des pics de pollution répétitifs plus ou moins à la même heure (vers midi) du lundi au vendredi. Cette corrélation évidente tend à prouver que les émissions de toluène sont liées aux activités « artistiques » (dessins, peinture, bricolage) des enfants qui s'accompagnent de l'utilisation de colle et de peintures comme cela a été remarqué dans d'autres études antérieures [41], [42].

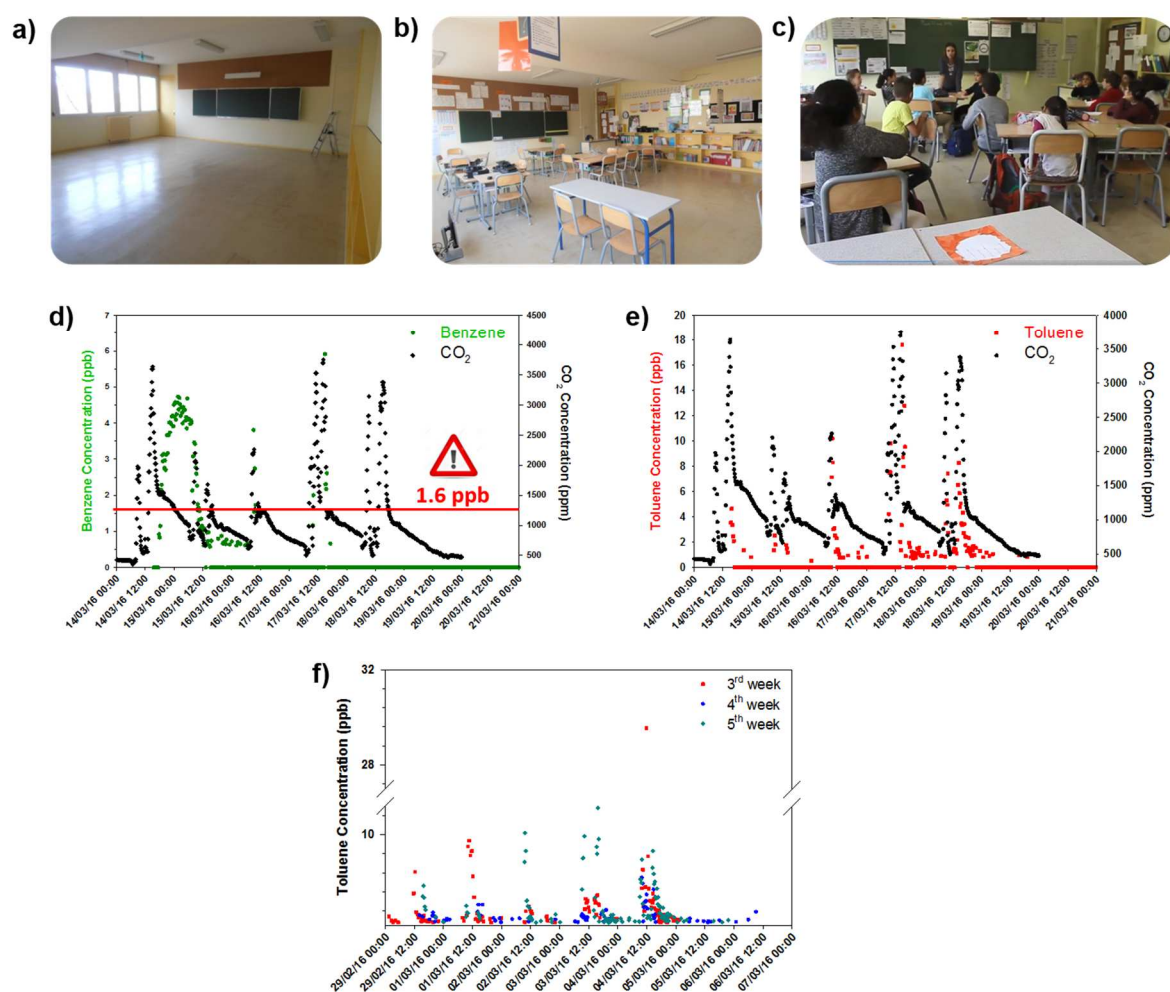


Figure 3. Les trois scénarios étudiés pendant la campagne de terrain : salle de cours vide (a), salle de cours avec le mobilier (b) et salle de cours pendant l'activité courante de l'école (c). Concentrations de benzène (d) et toluène (e) et CO₂ mesurées pendant la cinquième semaine à l'école des Grandes Varennes. Comparaison des concentrations de toluène mesurées à l'école des Grandes Varennes pendant la troisième, quatrième et cinquième semaines (f).

En conclusion, les mesures en temps quasi réel effectuées avec des prototypes de l'analyseur de BTEX ont permis de suivre finement les variations temporelles des concentrations de BTEX au cours des 5

semaines. Les niveaux de CO₂ ont été également mesurés en continu et ont été utilisés comme indicateur de confinement et ventilation. La comparaison entre les concentrations de CO₂ et de BTEX nous a permis d'identifier l'origine de leur principale source d'émission, qu'elle soit interne ou externe. Tous les BTEX étaient présents dans les classes étudiées à différents niveaux sauf dans l'école maternelle, où tous les niveaux de BTEX étaient inférieurs aux limites de détection de l'instrument analytique. Parmi les BTEX, le toluène était le composé le plus abondant dans les deux écoles. Sa concentration était fortement corrélée à la concentration de CO₂, ce qui suggère que la principale source d'émission était interne. De plus, des pics de pollution répétitifs ont été observés aux mêmes horaires au cours des trois dernières semaines, indiquant que ces niveaux élevés étaient certainement liés aux activités des enfants.

Cette étude met en évidence l'importance des mesures en temps quasi réel par rapport à l'échantillonnage passif traditionnel. En effet, ce type de mesures offre une haute résolution temporelle permettant de déterminer les périodes spécifiques où se produit une augmentation des concentrations de BTEX ainsi que d'identifier les sources potentielles de pollution. En outre, il a été démontré que la comparaison et les corrélations des concentrations de BTEX et de CO₂ constitue une méthode très utile pour déterminer l'origine de telles sources.

Pour conclure, nos prototypes de l'analyseur portable de BTEX a montré sa capacité à mesurer les concentrations de BTEX en continu sur de longues périodes et à enregistrer de petites variations de concentrations liées aux activités des enfants ou à la ventilation, ce qui n'est pas possible avec les méthodes classiques d'échantillonnage passif. Néanmoins, il est à noter que pendant une grande partie de la campagne, les concentrations de BTEX étaient inférieures à la limite de détection de l'instrument mais elles étaient probablement plus élevées que la limite fixée par la nouvelle réglementation française (0.6 ppb). C'est pourquoi une amélioration de la sensibilité du prototype de GC portable s'avère nécessaire. À cet égard, le développement et l'intégration d'une unité de préconcentration afin d'améliorer la sensibilité de l'instrument ont été réalisés au cours de ce travail de thèse et ils sont présentés dans la partie suivante.

3. Développement d'un préconcentrateur pour l'analyse des BTEX

L'un des principaux objectifs de ce travail de recherche était le développement d'un préconcentrateur pour améliorer la sensibilité de l'analyseur de BTEX présenté précédemment et atteindre une limite de détection inférieure à 0,6 ppb pour le benzène, afin de répondre à la nouvelle législation française

relative à la QAI des bâtiments publics. De plus, il s'agit de conserver des caractéristiques similaires à l'instrument actuel concernant le temps d'analyse (actuellement de 10 minutes) et la consommation énergétique afin de permettre le fonctionnement de l'appareil sur batterie.

Le principe de fonctionnement de cette nouvelle version de l'analyseur de BTEX intégrant une étape de préconcentration est illustré sur la Figure 4a. Dans cette version, la boucle d'échantillonnage est remplacée par un préconcentrateur. Ainsi, un volume d'air est prélevé à l'aide d'une micropompe couplé à un régulateur de débit massique et l'échantillon passe à travers le préconcentrateur qui est rempli avec un adsorbant spécifique pour piéger les BTEX. Une fois les BTEX piégés, la vanne 6 voies bascule et le préconcentrateur est chauffé rapidement jusqu'à une température de 200 - 330 °C en 1 minute ou moins. Cette brusque montée en température entraîne la désorption flash des molécules de BTEX et leur injection dans la colonne chromatographique. Ces molécules sont ainsi désorbées dans un volume beaucoup plus petit, augmentant ainsi la concentration des analytes dans l'échantillon avant l'analyse. Après la désorption, la vanne 6 voies retourne à sa position initiale. La séparation et la détection sont quant à elles similaires à celles du microanalyseur sans étape de préconcentration. L'efficacité de l'étape de préconcentration va dépendre, en grande partie, de la vitesse de la montée en température. Ainsi, plus rapide sera l'augmentation de température, plus petit sera le volume dans lequel les molécules seront désorbées et, par conséquent, plus élevée sera leur concentration au sein de l'échantillon. En outre, une montée en température lente entraîne une désorption échelonnée des molécules ce qui provoque l'élargissement de pics chromatographiques et, dans certains cas, leur coélution.

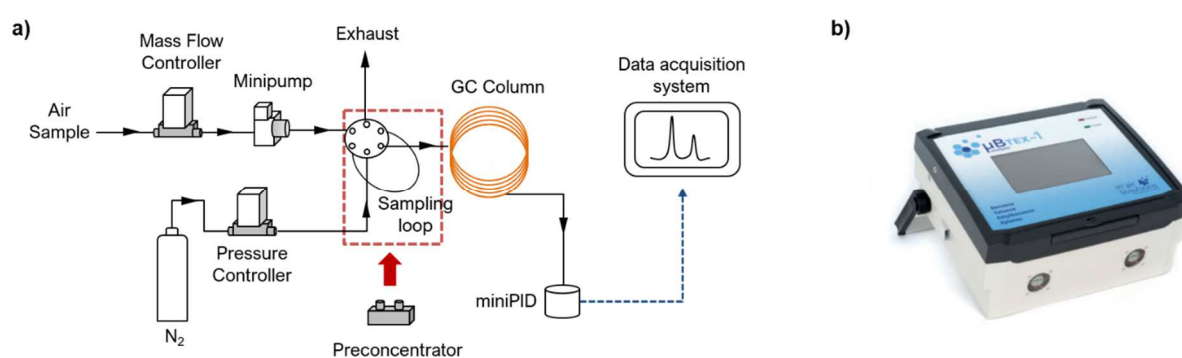


Figure 4. a) Schéma de fonctionnement de l'analyseur de BTEX avec l'étape de préconcentration et b) version commerciale (μ -BTEX-1, In'Air Solutions) utilisé pour l'intégration du préconcentrateur

Au cours de ce travail, plusieurs versions de préconcentrateur ont été développées (Figure 5) et testées en utilisant l'instrument présenté sur la Figure 4. Le premier prototype, nommé MAP [43], était fonctionnel mais sa masse thermique élevée impliquait une montée en température relativement lente (150 °C dans 1 min) associée de plus à une consommation énergétique très élevée (210 W) ce qui empêchait son utilisation dans un analyseur portable. Afin de réduire la masse thermique du dispositif, des nouvelles versions de préconcentrateur ont été fabriquées (voir Figure 5), la première d'entre-elles en utilisant des techniques de microfabrication.

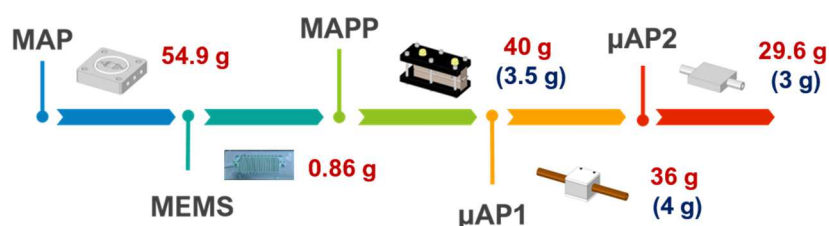


Figure 5. Différentes versions du préconcentrateur de BTEX développés au cours de ce travail de thèse. Masses thermiques avec connecteurs (rouge) et sans connecteurs (bleu).

L'utilisation de ces techniques a permis de fabriquer un dispositif miniaturisé, nommé MEMS, avec un système de chauffage intégré puissant et peu consommateur. Ce dispositif pesait 0,86 g, ce qui a entraîné non seulement une réduction de la consommation d'énergie (24 W), mais également une rampe de température beaucoup plus rapide qui permettait d'atteindre 220 °C en 10 s. Cette conception répond parfaitement aux objectifs fixés, néanmoins, ce dispositif n'était pas suffisamment robuste. C'est pourquoi, malheureusement, certaines des puces se sont fissurées pendant l'étape de fabrication et des autres après plusieurs cycles de chauffage-refroidissement. En effet, la différence de dilatation thermique de la résine SU-8 et du verre qui constituent la structure du dispositif a provoqué la fissuration du verre lorsque la température a changé rapidement et cette version n'a donc pas pu être opérationnelle.

En raison des inconvénients du processus de microfabrication concernant ses coûts, le délai de livraison, la complexité de la conception ainsi que les problèmes résultant de l'intégration de ces microdispositifs dans l'ensemble du système, il a été décidé de simplifier la conception ainsi que de réduire les coûts de fabrication en utilisant techniques disponibles dans notre laboratoire. Par conséquent, la plupart des pièces de ce nouveau prototype, nommé MAPP, ont été fabriquées à l'ICPEES en utilisant le micro-fraisage et l'impression 3D.

Ce dispositif a montré sa capacité pour la préconcentration de BTEX mais, malheureusement, la rampe de température atteinte était insuffisante en raison de sa masse thermique élevée ce qui a donné lieu à la coélution des pics de l'éthylbenzène et les xylènes. En outre, après certains cycles d'adsorption-désorption, les parties en plastique de la structure (y compris celles en PEEK) ont commencé à être endommagées ce qui a généré des fuites et, par conséquent, l'inopérance du dispositif. Afin de réduire considérablement la masse thermique du préconcentrateur en maintenant un coût abordable et avec une bonne robustesse, la version μ AP1 a été conçue.

Cette version était formée par un tube de cuivre de 1/8 "inséré dans un cube en aluminium percé en 1/8 " et avec un système chauffant composé des deux résistances en céramique. Cette configuration permettait d'atteindre 250°C en 62 s avec une consommation énergétique de seulement 80 W. Bien que le système chauffant était plus performant que celui de la version précédente, la coélution des pics de l'éthylbenzène et les xylènes était encore observée. En effet, la conception en deux parties indépendantes a entraîné un mauvais transfert de chaleur. C'est pourquoi, une version PC monobloc a été cette fois imaginée pour intégrer la partie cylindrique dans le cube (voir Figure 6a). De cette façon, toute la structure était en aluminium et le transfert de chaleur entre la résistance à la chaleur et le lit d'adsorbant était considérablement amélioré. Comme on peut le constater sur la Figure 6b, 330 °C ont été atteints en 68 s démontrant une amélioration considérable de la vitesse de la montée en température. A titre d'exemple, un chromatogramme d'un échantillon de 50 mL à une concentration de BTEX égale à 20 ppb est présenté sur la figure Figure 6c. Les pics BTEX y sont très bien définis et il n'y a pas de coélution entre l'éthylbenzène et les xylènes.

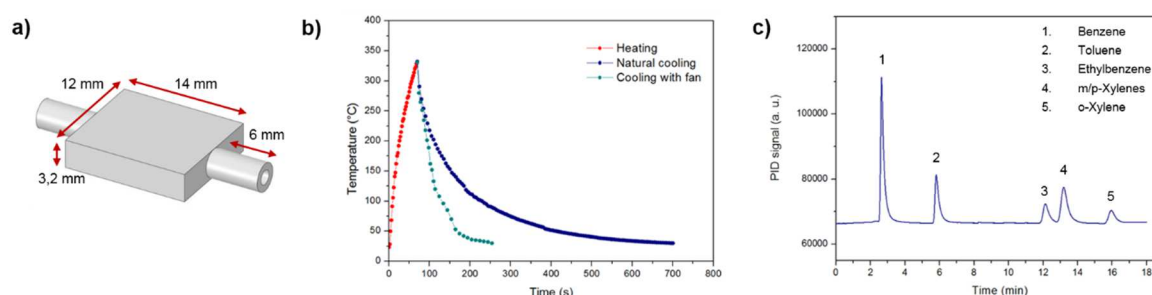


Figure 6. Design 3D du préconcentrateur μ AP2 (a). Performance du système de chauffage et refroidissement (b). Exemple d'un chromatogramme d'un échantillon de BTEX obtenu avec le prototype du GC intégrant le μ AP2 (V échantillon = 50 mL, $C_{\text{BTEX}} = 20$ ppb, température de désorption = 330 °C, temps d'injection = 75 s)

Afin de quantifier l'amélioration dans la sensibilité du GC dû à l'intégration de l'étape de préconcentration, une calibration du système a été réalisée en injectant une série de triplicat d'échantillons de 20 mL, prélevé pendant 4 min à 5 mL/min, de différentes concentrations allant de 2 à 50 ppb. Les aires moyennes des pics des échantillons analysés ont été tracées en fonction de la concentration injectée et les équations des courbes d'étalonnage résultantes sont présentées dans le Tableau 2.

Dans tous les cas sauf l'éthylbenzène, les coefficients de détermination obtenues sont supérieurs à 0,99 ce qui montre que les aires des pics augmentent parfaitement linéairement avec la concentration injectée, validant de fait le fonctionnement de ce préconcentrateur.

Les limites de détection (LDD) et de quantification (LDQ) de l'analyseur ont été calculées à partir d'un rapport signal / bruit de 3 et 10, respectivement, à partir de la plus faible concentration injectée, soit 2 ppb. Les limites de détection sont de l'ordre de centaines de ppt avec seulement 20 mL d'échantillon prélevé pour tous les composés, tandis que les limites de quantification dépassaient le ppb dans le cas de l'éthylbenzène et des xylènes (voir le Tableau 2). Il est important de noter que cette remarquable sensibilité répond désormais aux exigences de la législation française sur la qualité de l'air intérieur qui établit une valeur seuil de benzène de 0,6 ppb dans les bâtiments publics.

Tableau 2. Performances obtenues avec le prototype de l'analyseur de BTEX intégrant le μ AP2

Composé	Équation de calibration	R ²	LDD (ppb)	LDQ (ppb)
Benzene	$y = 9618.8 x$	0.9940	0.057	0.191
Toluene	$y = 3761.5 x$	0.9930	0.150	0.499
Ethylbenzene	$y = 1828.7 x$	0.9891	0.368	1.226
m/p Xylenes	$y = 1776.2 x$	0.9974	0.396	1.319
o-Xylene	$y = 1403.7 x$	0.9941	0.418	1.393

Comme tout appareil d'analyse, la répétabilité et la reproductibilité de l'analyseur doivent être évaluées pour garantir des résultats fiables à long terme. Pour évaluer la répétabilité, sept échantillons de 20 mL contenant 20 ppb de BTEX ont été analysés consécutivement le même jour en utilisant les mêmes conditions expérimentales (température de désorption = 330 ° C, temps d'injection = 75 s). Entre deux échantillons consécutifs, une étape de nettoyage a été réalisée. Les aires de pic et le temps

de rétention obtenus sont présentés dans la Figure 7a et b, respectivement. Une légère variabilité a été observée en termes d'intensité de pics : l'écart type relatif (% RSD) de l'aire de pic a été calculé à 4,9, 3,7, 4,3, 8,0 et 5,6% pour respectivement le benzène, le toluène, l'éthylbenzène, le m / p - xylènes et l'o-xylène. Ces valeurs inférieures à 10% pour tous les composés démontrent que les analyses effectuées avec le prototype de l'analyseur intégrant le préconcentrateur μ AP2 étaient hautement reproductibles même en mode d'injection manuelle. Le % RSD correspondant au temps de rétention a également été calculé, étant égal à 0,1% pour tous les analytes, ce qui montre l'excellente répétabilité en termes de temps de rétention. Dans cette version de l'analyseur de BTEX intégrant le μ AP2, l'injection d'échantillons et l'acquisition de données ont été automatisées ; par conséquent, bien que le temps d'échantillonnage ait été contrôlé manuellement, les résultats obtenus étaient très satisfaisants au niveau de la répétabilité des mesures.

Ensuite, la reproductibilité a été évaluée selon la méthode suivante : trois échantillons de 20 mL contenant 20 ppb de chacun des BTEX ont été analysés consécutivement sur trois jours différents. La Figure 7c et d montrent respectivement les résultats obtenus pour les aires de pic et le temps de rétention de chaque échantillon.

Les aires des pic obtenues sur trois jours différents étaient comparables et le % RSD était calculée étant égale à 3,2, 10,1, 21,8, 13,8, 13,9% pour respectivement le benzène, le toluène, l'éthylbenzène, le m / p - xylènes et l'o-xylène. La variation obtenue dans ce cas était évidemment supérieure à celle obtenue pour l'analyse effectuée en une seule journée ; cependant, toutes les % RSD, étaient inférieures à 15%, sauf celle de l'éthylbenzène, ce qui peut être considéré comme satisfaisant en termes de reproductibilité. Un % RSD plus élevée a également été observée pour le temps de rétention par rapport au test précédent, soit respectivement 1,0, 0,7, 0,5, 0,5 et 0,4% pour le benzène, le toluène, l'éthylbenzène, le m / p - xylènes et l'o-xylène. Malgré cette légère augmentation, la variation observée dans les temps de rétention était minime et les valeurs peuvent être considérées comme hautement reproductibles dans le temps. Les résultats obtenus dans les tests de répétabilité et de reproductibilité mettent en évidence la stabilité des mesures réalisées avec ce prototype dans le temps, même avec des concentrations de BTEX relativement faibles comme 20 ppb.

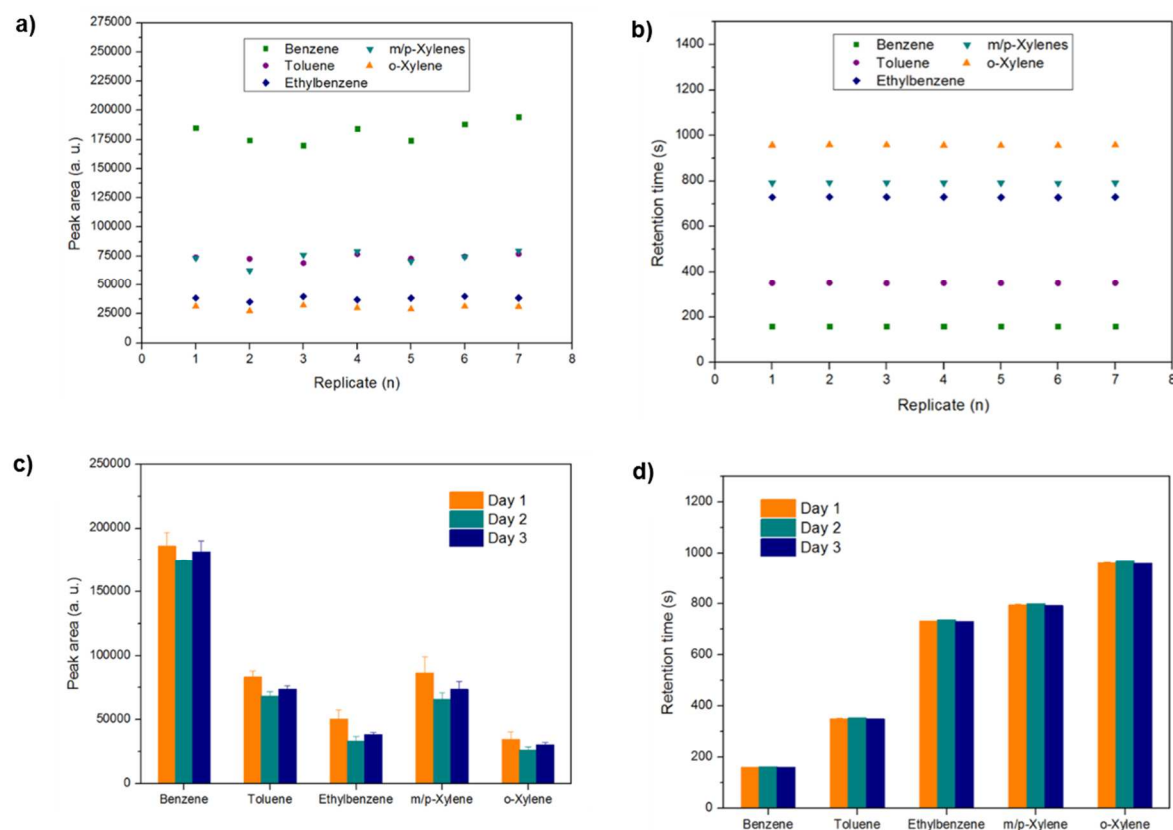


Figure 7. Résultats des tests de répétabilité obtenus pour 7 échantillons de BTEX analysés consécutivement le même jour : (a) aires de pic et (b) temps de rétention. Résultats des tests de reproductibilité obtenus pour 3 échantillons de BTEX analysés sur trois jours différents : (c) aires de pic et (d) temps de rétention. $V = 20$ mL, $C = 20$ ppb, température de désorption = 330 °C, temps d'injection = 75 s. Les barres d'erreur verticales représentent l'écart type des triplicats.

Ce dispositif a été comparé avec les GC miniaturisés intégrant un préconcentrateur pour la quantification des COVs les plus significatives de la littérature au cours de la dernière décennie. La plupart de ces appareils sont très portables (poids < 5 kg) et ont des dimensions relativement petites, ce qui les adaptent aux mesures sur site; cependant, leur sensibilité est en général de l'ordre de la ppb. Jusqu'à ce travail, seuls trois instruments avaient une LDD de l'ordre de la ppt. Zampolli *et al.* [44] ont proposé un GC-PID miniaturisé avec un PC rempli d'un adsorbant innovant à base de quinoxaline. Une LDD jusqu'à 0,1 ppb pour le benzène a été atteinte ; cependant, 55 min d'échantillonnage étaient nécessaires pour échantillonner les 2750 ml requis pour atteindre une telle sensibilité. Cette durée d'échantillonnage étant chronophage, elle ne permet pas d'établir des profils de concentration à haute résolution qui permettraient de déterminer l'exposition professionnelle ou d'identifier les sources de polluants [37]. Skog *et al.* [45] ont utilisé un temps d'échantillonnage plus court de 20 minutes pour collecter un échantillon de 4 L et atteindre une LDD de 2 à 11 ppt pour BTEX. Sun *et al.* [46] ont

rapporté une LDD inférieure à 1 ppb avec un temps d'échantillonnage de seulement 1 min mais le volume d'échantillon utilisé n'a pas été mentionné. Étant donné que la LDD dépend fortement du volume de l'échantillon, la sensibilité de chaque système a été calculée comme la masse d'analyte détectable la plus faible pour une meilleure comparaison.

Pour calculer la sensibilité, la LDD la plus basse atteinte pour chaque méthode a été multipliée par le volume d'échantillon. Par exemple, dans notre cas, le benzène LDD ($0,18 \mu\text{g m}^{-3}$ à $P = 1 \text{ atm}$ et $T = 25 \text{ }^\circ\text{C}$) a été multiplié par le volume d'échantillon ($2 \times 10^{-5} \text{ m}^3$), donnant une sensibilité égale à 3,6 pg. À notre connaissance, le système analytique développé dans ce travail a montré la sensibilité la plus élevée rapportée à ce jour pour l'analyse BTEX présentée par un GC portable. Cet instrument a atteint une LDD de 0,06 à 0,4 ppb ($0,18 - 1,82 \mu\text{g m}^{-3}$ à $P = 1 \text{ atm}$ et $T = 25 \text{ }^\circ\text{C}$) en utilisant un volume d'échantillon de seulement 20 ml ($2 \times 10^{-5} \text{ m}^3$). Cela signifie que la quantité détectable la plus faible avec ce GC compact était de 3,6, 11,3, 32,0, 34,4 et 36,3 pg pour le benzène, le toluène, l'éthylbenzène, les m / p-xylènes et l'o-xylène, respectivement.

A titre d'exemple, le GC portable développé par Zampolli *et al.* [44] avait une faible LDD pour le benzène de 0,1 ppb ($0,32 \mu\text{g m}^{-3}$ à $P = 1 \text{ atm}$ et $T = 25 \text{ }^\circ\text{C}$) mais il nécessitait un grand volume d'échantillon de 2750 mL ($2,75 \times 10^{-3} \text{ m}^3$) résultant une sensibilité de 878,5 pg pour ce composé. Une limite de détection inférieure a été trouvée avec le GC compact développé par Skog *et al.* [45] où une LDD du benzène de 0,01 ppb ($0,03 \mu\text{g m}^{-3}$ à $P = 1 \text{ atm}$ et $T = 25 \text{ }^\circ\text{C}$) a été atteint avec un échantillon de 4 L ($4 \times 10^{-3} \text{ m}^3$) donnant une sensibilité de 140,6 pg. Par conséquent, la sensibilité obtenue avec le GC portable développé dans ce travail différait de 2 à 3 ordres de grandeur par rapport à la plupart des valeurs rapportées dans la littérature, même celles rapportant des limites de détection très faibles. Pour l'analyse du BTEX, seule la première version de préconcentrateur (MAP) développée dans ce travail a donné des résultats similaires [43]. Malgré la sensibilité exceptionnelle pour le benzène de 6,4 pg obtenue avec le MAP, cette nouvelle version a permis d'améliorer cette performance dans un rapport de 1,8. Dans la littérature, uniquement Han *et al.* [47] ont rapporté une sensibilité comparable pour l'analyse de l'isoprène en utilisant un préconcentrateur développé au laboratoire couplé à un GC. Cependant, cette sensibilité ne correspond pas à un GC portable puisque le préconcentrateur développé dans ce cas était connecté à un GC-FID de paillasse. Ces résultats suggèrent que les performances obtenues par notre prototype en termes de sensibilité sont proches de celles généralement présentées par les instruments de paillasse.

En conclusion, plusieurs versions d'un préconcentrateur de BTEX ont été développées et testées au cours de ce travail de thèse. Le premier prototype, nommé MAP, était fonctionnel mais avec un inconvénient majeur liée à sa consommation d'énergie, qui empêche son utilisation dans un analyseur portable. À cet égard, plusieurs améliorations ont été proposées en changeant les matériaux utilisés dans la fabrication, l'adsorbant et le type de système de chauffage. Cependant, la plupart de ces dispositifs n'étaient pas entièrement fonctionnels et ne pouvaient pas être industrialisés, à l'exception du dernier, appelé μ AP2. Cet appareil a été testé dans des conditions contrôlées, démontrant qu'il répond aux exigences établies dans les objectifs de ce projet en termes de :

- Sensibilité : la limite de quantification du benzène atteinte (0,191 ppb) avec un échantillon d'air de seulement 20 mL est inférieure à la valeur seuil établie dans la récente législation française concernant la qualité de l'air intérieur (0,6 ppb) ;
- Consommation énergétique : la consommation d'énergie supplémentaire de ~ 70 W nécessaire sur une très courte durée estimée à 70 s (temps nécessaire pour atteindre la température de désorption) associée à l'étape de préconcentration est compatible avec un système d'analyse portable ;
- Temps d'analyse : l'ajout d'une étape de préconcentration n'a pas sensiblement augmenté le temps total d'analyse, permettant une surveillance BTEX en temps quasi réel.

De plus, contrairement à d'autres analyseurs de BTEX portables trouvés dans la littérature, le prototype développé dans ce travail a été évalué en termes de répétabilité et de reproductibilité. Le % RSD relativement faibles (<10% et <15%, respectivement) obtenues dans ces deux tests indiquent que les mesures effectuées sont stables dans le temps. Cette stabilité, la sensibilité remarquable et le temps d'analyse acceptable font de ce nouveau prototype de l'analyseur de BTEX un bon candidat pour les applications de surveillance de la qualité de l'air. Néanmoins, cet instrument doit être testé en conditions réelles pour évaluer l'influence possible des composés interférents et d'autres problèmes dérivés de l'utilisation dans des environnements réels. En outre, ce dispositif de préconcentration peut être autonome pour un couplage possible avec d'autres systèmes d'analyse comme des chromatographes en phase gazeuse et être utilisé pour d'autres applications nécessitant une sensibilité élevée, telles que la détection d'explosifs, le diagnostic précoce du cancer ou le contrôle de qualité des aliments.

4. Etude de l'adsorption des VOC sur des différents matériaux

Dans la dernière partie de ce travail de thèse, l'adsorption de certains COV à de faibles concentrations sur des adsorbants de nature différente a été étudiée pour évaluer leur application potentielle dans l'analyse via un système de préconcentration ou dans l'élimination de ces composés.

Dans la littérature, malgré le grand nombre d'études liées à l'adsorption de COV à ce jour, la plupart d'entre elles ont été menées à des concentrations très élevées, allant très souvent entre 5 300–800 000 ppm pour les BTEX [48] et entre 1 et 150 ppm pour le formaldéhyde [49]–[52]. De fait, il existe un manque d'études d'adsorption utilisant des concentrations plus réalistes (faible ppm – ppb). En outre, la plupart de ces études portent sur l'adsorption d'un seul composé ce qui est rarement le cas dans des environnements réels où un nombre considérable de composés (polluants) avec différentes polarités et tailles moléculaires coexistent. La présence des différents polluants peut conduire à des phénomènes d'adsorption préférentielle de certaines espèces par rapport à d'autres. Par conséquent, l'adsorption multi-composants est un point crucial à considérer lorsqu'un matériau est évalué pour son application dans l'élimination ou l'analyse de molécules gazeuses.

Afin de réaliser ces études de sorption, les dispositifs expérimentaux présentés sur la Figure 8a et b ont été utilisés, pour respectivement l'adsorption de BTEX et du formaldéhyde. Dans ces dispositifs, un débit d'air synthétique contenant les polluants ($C_{\text{BTEX}} = 10 \text{ ppm}$, $C_{\text{HCHO}} = 164 \text{ ppb}$) passe à travers le tube rempli avec l'adsorbant. Ensuite, le flux de gaz à la sortie du tube d'adsorption est analysé en ligne après avoir été dilué avec de l'azote ou de l'air synthétique pour éviter la possible saturation du détecteur. La représentation de l'évolution de la concentration de polluant dans l'effluent sortant du lit de l'adsorbant en fonction du temps constitue une courbe dite de perçage. Dans ces courbes, la concentration de polluant augmente avec le temps d'une façon généralement sigmoïdale jusqu'à atteindre un plateau qui indique la saturation totale de l'adsorbant. A partir de l'intégration de l'aire située au-dessus de la courbe entre le début de l'adsorption et le point de saturation, la capacité d'adsorption de l'adsorbant peut être calculée [53].

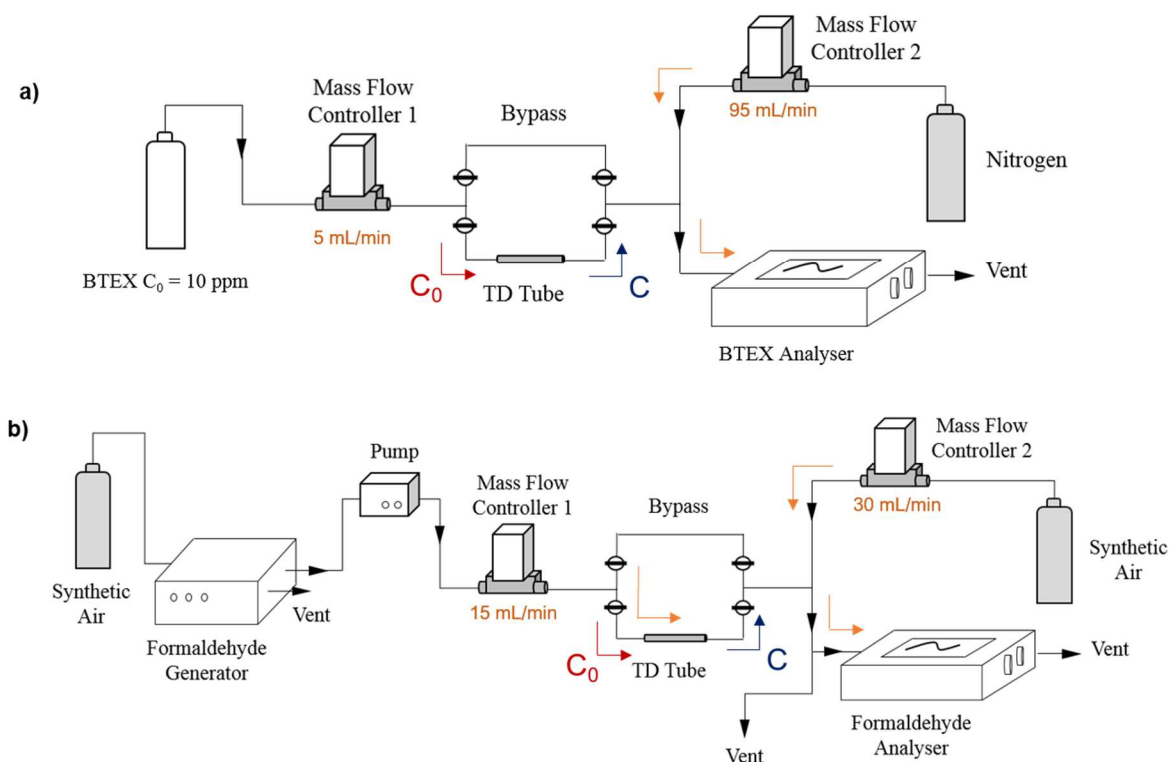


Figure 8. Dispositifs expérimentaux utilisés pour l'adsorption des BTEX (a) et du formaldéhyde (b)

Dans un premier temps, une étude de l'adsorption des BTEX sur trois adsorbants commerciaux a été réalisée, à savoir un noir de carbone graphitisé, le Carbpac® B, une silice mésoporeux, le SBA-16, et un squelette organométallique, le HKUST-1. La Figure 9 illustre les courbes de perçage obtenues pour les BTEX dans des conditions ambiantes ($T = 296 \text{ K} \pm 2 \text{ K}$). Pour chaque adsorbant, le tracé est composé de cinq courbes de perçage correspondant chacune à chaque composé du mélange de BTEX, à l'exception des m- et p-xylènes qui sont coélués et donc représentés par la même courbe. En général, les courbes obtenues pour les trois adsorbants sont comparables, étant adsorbés préférentiellement les composés avec un point d'ébullition plus élevé selon l'ordre benzène > toluène > éthylbenzène > m / p-xylènes > o-xylène. Un phénomène particulier est observé dans le cas du benzène et du toluène. En effet, leur concentration à la sortie du tube augmente jusqu'à atteindre des valeurs supérieures à la concentration d'entrée ($C/C_0 > 1$). Ce phénomène, appelé « roll-up », apparaît lorsque les effets thermodynamiques régissent le processus d'adsorption [54], c'est-à-dire que l'adsorbat avec des interactions plus faibles est remplacé par d'autres espèces avec des interactions adsorbat-adsorbant plus favorables. Le roll-up a été observé sur tous les matériaux dans différentes proportions,

entraînant la désorption des composés plus volatils, à savoir le benzène et le toluène, en faveur de l'adsorption des composés moins volatils. Ce phénomène est moindre sur le SBA-16 et le Carbopack® B tandis que sur HKUST-1, l'effet est plus prononcé. Selon la méthode décrite précédemment, les capacités d'adsorption ont été calculées pour chaque composé et chaque adsorbant (voir Figure 9d). Pour chaque adsorbant, le type des interactions adsorbat-adsorbant ainsi que la porosité varient, ce qui suggère que ces paramètres ont un fort impact sur la capacité d'adsorption. Parmi les adsorbants étudiés, le SBA-16 a montré la plus grande capacité d'adsorption (30,2 mg/ g adsorbant). En effet, dans les silices mésoporeuses, en plus des forces de London, les groupes hydroxyles situés à la surface peut se comporter comme des sites acides faibles interagissant avec le électrons π des anneaux aromatiques [55], [56] favorisant ainsi l'adsorption de composés aromatiques comme les BTEX.

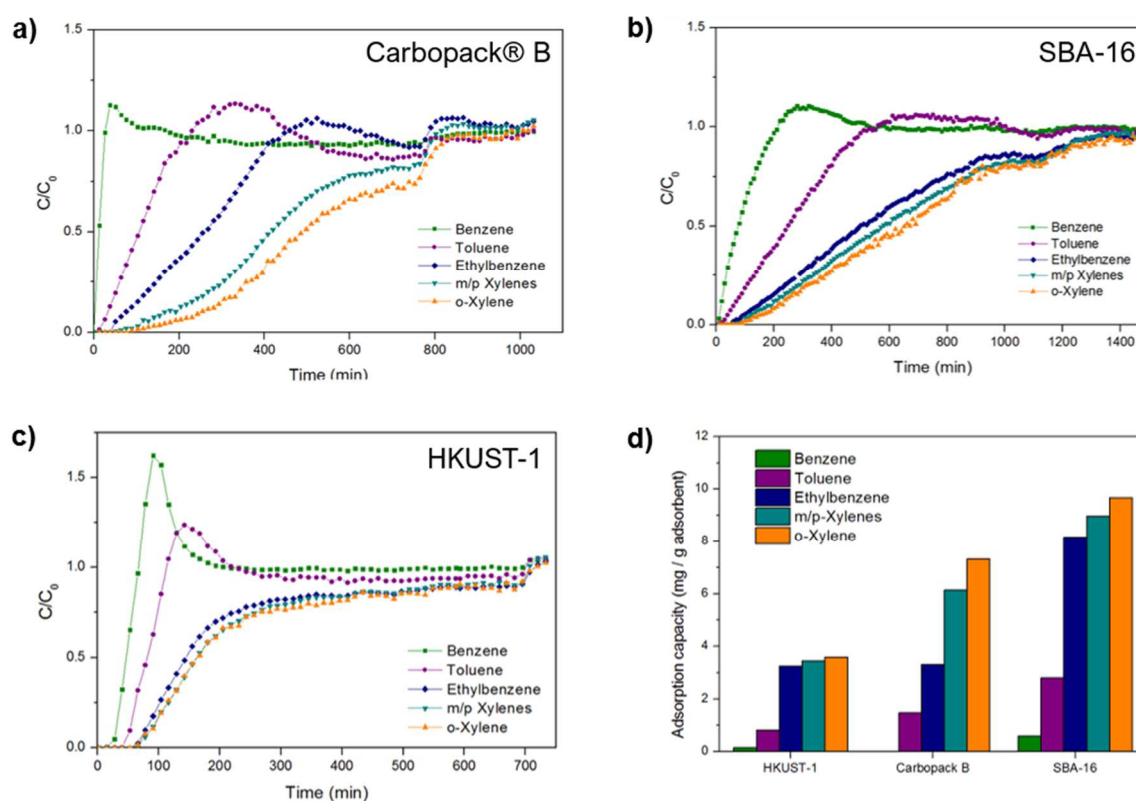


Figure 9. Courbes de perçage des BTEX sur Carbopack® B (a), SBA-16 (b) et HKUST-1 (c). Concentration BTEX = 10 ppm, débit = 5 mL / min. Capacités d'adsorption de BTEX des trois adsorbants étudiés (d)

L'adsorption des BTEX a été également testée sur cinq zéolithes ZSM-5 avec un rapport Si / Al différent (SAR) afin de déterminer l'influence de la composition chimique de l'adsorbant sur l'adsorption de BTEX. Les courbes de perçage obtenues pour les différentes zéolithes sont très similaires. La Figure

10a illustre un exemple de courbe de perçage typique de BTEX sur une zéolithe de type ZSM-5. Dans ce cas, un phénomène de « roll-up » est également observé pour le benzène. Néanmoins, cette fois un comportement différent est observé pour l'o-xylène et les m/p-xylènes. Pour ces composés, la concentration au début du test était égale à la concentration initiale (o-xylène) et égale à la moitié de la concentration initiale (m/p-xylène). Ce comportement peut être expliqué par un effet d'exclusion stérique qui se produit en raison de la plus grande taille de ces molécules comme il est illustré sur la Figure 10b. Les capacités d'adsorption de chaque zéolithe pour chaque composé ont été calculées (voir Figure 10c). Comme il peut être observé, il n'a pas une corrélation directe entre le rapport Si/Al et la capacité d'adsorption. Cette dernière semble dépendre de plusieurs paramètres, à savoir le nombre de sites acides, l'hydrophobicité et la diffusion des molécules dans le réseau cristallin.

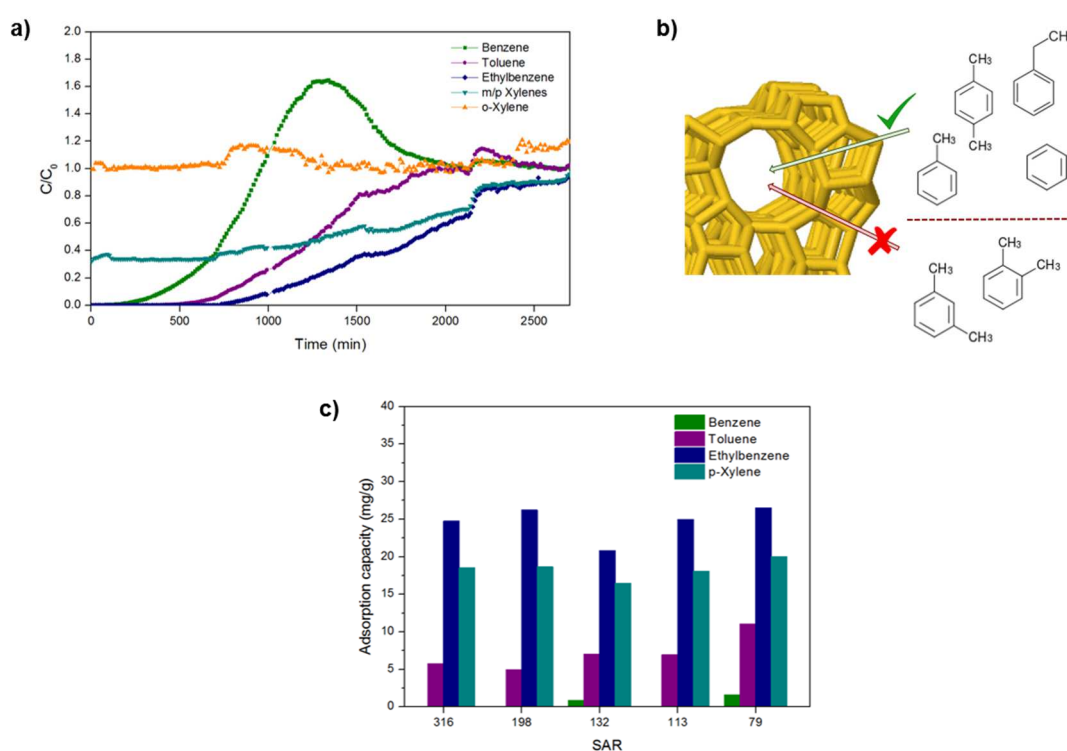


Figure 10. a) Courbe de perçage typique des BTEX sur une zéolithe ZSM-5, b) exclusion stérique des métha et ortho xylènes des pores de la zéolithe ZSM-5 et c) capacité d'adsorption des différents BTEX en fonction du rapport Si/Al.

La dernière étude est dédiée à l'adsorption de formaldéhyde à des concentrations très faibles (164 ppb) sur les matériaux précédemment utilisés pour l'adsorption de BTEX (adsorbants commerciaux et zéolithes). Ce type d'études est nécessaire pour évaluer correctement les performances des

adsorbants car il a été démontré que la capacité d'adsorption à des concentrations élevées n'est pas toujours corrélée linéairement avec la capacité d'adsorption à de faibles concentrations [49], [50].

Premièrement, l'adsorption était testée sur les adsorbants commerciaux. Les courbes de perçage obtenues sont présentées sur la Figure 11a.

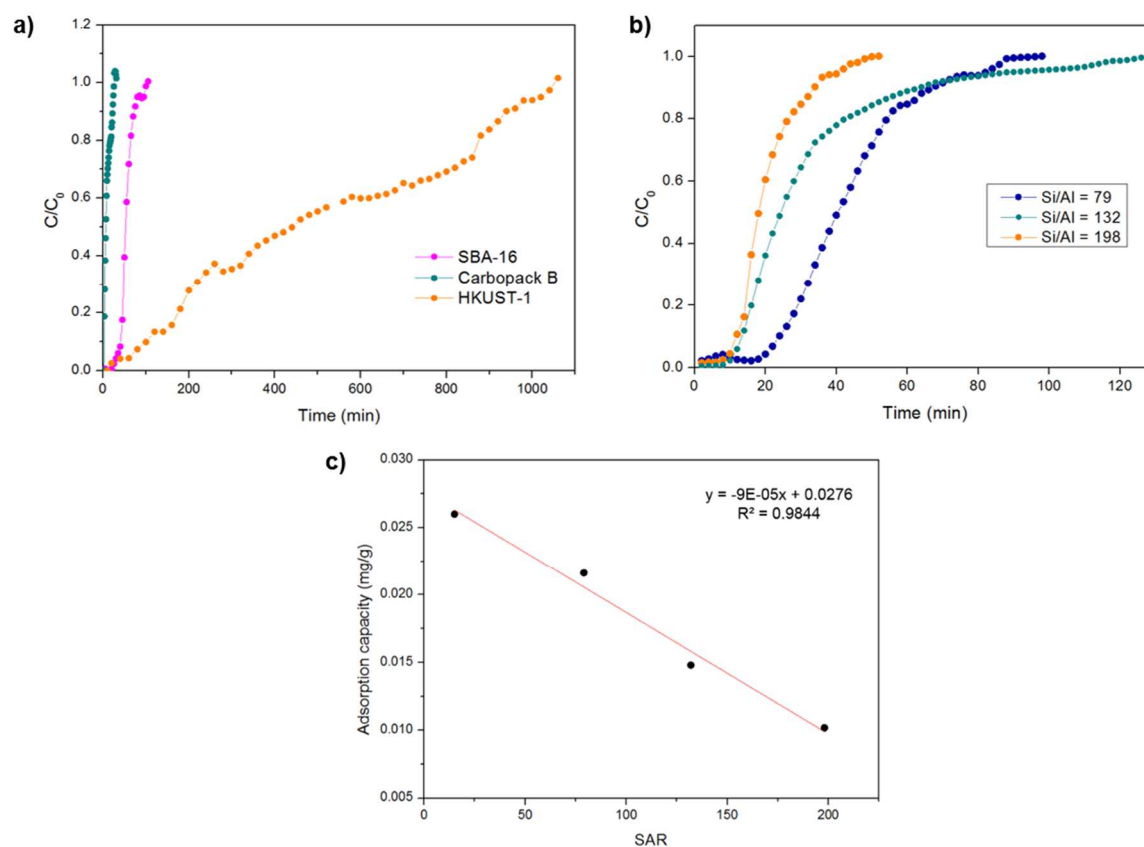


Figure 11. a) Courbes de perçage du formaldéhyde sur des adsorbants commerciaux, b) courbes de perçage du formaldéhyde sur des zéolithes ZSM-5 avec différents rapport Si/Al et c) corrélation linéaire de la capacité d'adsorption de formaldéhyde des zéolithes ZSM-5 avec le rapport Si/Al.

Il est évident que HKUST-1 présente une capacité d'adsorption très supérieure à celle du Carbo-pack® B et le SBA-16. Ce comportement peut être expliqué par la chimie de surface de chaque adsorbant. Dans le cas du Carbo-pack® B, les forces de London sont les seules interactions adsorbant-adsorbant, ce qui justifie un faible capacité d'adsorption. En revanche, le SBA-16 peut interagir avec la fonction aldéhyde des molécules de formaldéhyde *via* une liaison hydrogène [51] avec les groupes silanol (Si – OH) à la surface interne de ses mésopores favorisant ainsi l'adsorption des molécules de formaldéhyde. En conséquence, la capacité d'adsorption de SBA-16 est beaucoup plus élevée que celle obtenue pour Carbo-pack® B. Parmi les trois adsorbants, HKUST-1 a montré les meilleures

performances d'adsorption. Cette remarquable capacité obtenue s'explique par plusieurs facteurs. HKUST-1 a une surface spécifique très élevée qui fournit une grande quantité de sites d'adsorption. De plus, ce matériau présente des pores d'un diamètre de 5,4 et 6,9 Å. Ces pores conviennent à l'adsorption de formaldéhyde car ils sont suffisamment grands pour permettre l'entrée de la molécule de formaldéhyde (diamètre cinétique = 2,5 Å) et suffisamment étroits pour que les molécules établissent des interactions significatives avec les parois des pores. De plus, il est prévu que les atomes de cuivre présents dans la structure interagissent avec l'oxygène du groupe carbonyle de formaldéhyde, comme indiqué par Dutta *et al.* [57]. Par conséquent, il est évident que la surface spécifique influence l'adsorption du formaldéhyde, mais il semble que la capacité d'adsorption remarquable soit principalement attribuée à des interactions adsorbat-adsorbant très favorables et, donc, à la chimie de surface. Alors, le HKUST-1 pourrait être le candidat le plus approprié pour l'élimination du formaldéhyde gazeux en raison de son capacité d'adsorption élevée. Cependant, les molécules d'eau peuvent également interagir avec les cations cuivre présents dans la structure du HKUST-1 [58]. Si cette interaction est plus favorable que l'interaction avec le formaldéhyde, une diminution significative de la capacité d'adsorption du formaldéhyde en milieu humide pourrait être attendue, limitant son utilisation dans ces conditions. Dans l'analyse de gaz, cet inconvénient peut être partiellement surmonté en ajoutant un dispositif pour piéger les molécules d'eau avant l'échantillonnage de gaz sur le lit d'adsorbant, comme par exemple en utilisant un tube Nafion. Pour remédier à la problématique de l'humidité, l'adsorption de formaldéhyde sur des adsorbants plus hydrophobes tels que les zéolithes ZSM-5 a été également étudiée. Ce type de zéolithes est principalement hydrophobe, mais sa polarité est ajustable en modifiant la teneur en aluminium dans la structure. Ce contenu peut être facilement contrôlé en faisant varier les conditions utilisées lors de la synthèse. Lorsque la teneur en aluminium augmente, les atomes d'Al (+ III) remplacent les atomes de Si (+ IV), entraînant une plus grande quantité de charges négatives et, par conséquent, influençant la polarité du matériel. Par conséquent, l'hydrophobicité dans les zéolithes augmente lorsque moins de charges partielles sont présentes dans la structure, c'est-à-dire lorsque la teneur en Al diminue (SAR élevé) [59]. Dans ces structures, les charges négatives sont compensées par des protons coordonnés à l'un de ces atomes d'oxygène, formant ainsi des sites acides de Brønsted [60].

Des expériences d'adsorption de formaldéhyde ont été réalisées sur trois zéolithes avec un rapport Si/Al de 198, 132 et 79 afin d'évaluer l'influence de la teneur en aluminium sur la capacité d'adsorption. Les courbes de perçage obtenues sont présentées dans la Figure 11b. Pour toutes les zéolithes, les

courbes obtenues ont une forme assez similaire. Comme on peut l'observer sur la Figure 11b, les zéolithes avec une densité d'acide plus élevée, c'est-à-dire un rapport Si / Al inférieur, présentaient une plus grande capacité d'adsorption. Ces résultats suggèrent que l'adsorption des molécules de formaldéhyde est directement liée à la teneur en aluminium et, par conséquent, à la quantité de sites acides de Brønsted. Afin d'illustrer cette relation, les capacités d'adsorption des zéolithes ZSM-5 étudiées, y compris une autre zéolite commerciale ZSM-5 (Si / Al = 15) ont été tracées en fonction du SAR (voir Figure 11c). Une corrélation très linéaire est observée dans toute la gamme SAR étudiée suggérant que l'adsorption de formaldéhyde pourrait être attribuée aux interactions entre la fonction carbonyle et les groupes zéolithiques Si–(OH)–Al, comme indiqué précédemment par Kukulska-Zajac et Datka [61]. De plus, la réduction de la surface spécifique observée lorsque la SAR diminue semble avoir un effet négligeable sur l'adsorption du formaldéhyde. Cette observation renforce l'idée que l'adsorption du formaldéhyde est principalement dominée par la chimie de surface. Par conséquent, on peut conclure qu'à de faibles concentrations, une adsorption de formaldéhyde plus efficace peut être obtenue en utilisant des zéolithes à haute teneur en aluminium.

5. Conclusions générales

Au cours de cette thèse, différents aspects liés à la quantification et à l'élimination des COV gazeux ont été abordés. Au début de ces travaux, une campagne de terrain sur la qualité de l'air menée dans les écoles primaires a révélé l'importance des mesures en temps quasi réel dans la surveillance de la qualité de l'air intérieur. Ces résultats, ainsi que la nouvelle législation française sur la QAI entrée en vigueur en 2018, ont révélé un besoin urgent d'instruments portables d'analyse suffisamment sensibles pour détecter de si faibles concentrations. Ce contexte a été la motivation de l'objectif principal à atteindre au cours de cette thèse, à savoir le développement d'un préconcentrateur intégré dans un prototype de l'analyseur de BTEX portable pour atteindre une limite de détection inférieure à $2 \mu\text{g m}^{-3}$ (0,6 ppb) pour le benzène conformément à la valeur guide en France. Parallèlement à cette évolution, une étude complémentaire de différents adsorbants a également été réalisée afin de mieux sélectionner et éventuellement élargir la gamme des polluants analysés ou d'améliorer et caractériser leurs cycles d'adsorption / désorption. Ainsi ce travail est principalement composé de trois parties différentes.

Dans la première partie, les résultats obtenus lors d'une campagne de terrain sur la qualité de l'air intérieur menée dans deux écoles primaires françaises pendant 5 semaines ont été présentés. L'objectif

était de déterminer les concentrations de BTEX, d'identifier leurs principales sources d'émission et d'évaluer l'efficacité des différents scénarios de ventilation. À cette fin, des prototypes préindustriels développés dans notre laboratoire ont été utilisés pour surveiller en continu la concentration de BTEX dans différentes conditions d'occupation et de ventilation. Ces appareils ont fourni des mesures en temps quasi réel qui ont permis d'établir des profils concentration-temps avec une résolution temporelle élevée de 10 min. Ces données, ainsi que des mesures supplémentaires de CO₂, se sont avérées être une méthode efficace pour l'identification des sources. En effet, les niveaux de CO₂ peuvent être utilisés comme indicateur de confinement, par conséquent, la corrélation ou l'anti-corrélation de ceux-ci avec les concentrations de BTEX révèlent l'origine interne ou externe des sources d'émission. De plus, des schémas répétitifs de pics de pollution mesurés au même moment de la journée au cours de différentes semaines ont permis d'associer ces émissions aux activités des enfants. Notre étude a révélé l'importance des mesures en temps quasi réel par rapport aux méthodes classiques telles que l'échantillonnage passif, qui quant à elles fournissent des concentrations moyennes qui ne sont exploitables pour une identification de la source d'émission.

Notre analyseur de BTEX a montré également sa capacité à mesurer les concentrations de ces polluants en continu à des niveaux de ppb sur de longues périodes. Néanmoins, un seuil de benzène égale à 0,6 ppb a été fixé par la nouvelle législation sur la qualité de l'air des bâtiments publics en France. C'est pourquoi, la deuxième partie de ce travail a été dédiée au développement d'un préconcentrateur afin d'améliorer la sensibilité du prototype de l'analyseur de BTEX aux niveaux de la dizaine ou centaine de ppt.

A cet égard, plusieurs prototypes de préconcentrateur ont été développés et testés. Cependant, la plupart d'entre eux présentent des inconvénients majeurs concernant la robustesse et la consommation énergétique et seule la dernière version, nommé μ AP2, répondait à toutes les exigences fixées dans les objectifs de cette thèse. L'analyseur de BTEX intégrant le préconcentrateur μ AP2 présentait une LDQ de 0,191 ppb pour le benzène avec seulement 20 mL d'échantillon. Pour atteindre ces performances, la consommation d'énergie a été augmentée de façon minimale, car seulement 70 W supplémentaires ont été nécessaires pendant 70 s pour effectuer cette étape de préconcentration. De plus, l'intégration de cette étape supplémentaire a eu une influence négligeable sur le temps d'analyse total car dans le cas d'une analyse consécutive, l'échantillonnage de la prochaine analyse peut être réalisé simultanément à l'étape de séparation de l'analyse en cours. La reproductibilité et la répétabilité ont également été évaluées, l'instrument développé démontrant des performances

satisfaisantes pour ces caractéristiques critiques, soulignant sa fiabilité analytique sur de longues périodes. De plus, le coût de fabrication du préconcentrateur développé peut être estimé à plusieurs dizaines d'euros ce qui conduit à un rapport qualité-prix très raisonnable pour ce dispositif.

La troisième partie porte sur l'étude des différents adsorbants afin d'évaluer son potentielle application dans l'analyse de polluants gazeux. À cette fin, une série d'expériences d'adsorption dynamique ont été menées pour évaluer la capacité d'adsorption et déterminer les paramètres clés affectant l'adsorption des BTEX et du formaldéhyde. Tout d'abord, l'adsorption de BTEX à faible concentration a été évaluée sur trois adsorbants commerciaux dont les propriétés texturales et la chimie de surface étaient différentes. Parmi eux, le SBA-16 a montré la capacité d'adsorption la plus élevée et un effet de « roll-up » minimum empêchant la désorption des molécules les plus volatiles ce qui suggère que ce matériau peut être un bon candidat pour les applications d'analyse de gaz.

Ensuite, des études d'adsorption de BTEX ont été réalisées sur cinq zéolithes ZSM-5 avec un rapport Si / Al différent pour élucider l'effet de la composition chimique sur l'adsorption de BTEX. Il a été prouvé que ce paramètre a une forte influence sur l'adsorption de BTEX, et les résultats obtenus ont révélé qu'un compromis entre SAR et l'hydrophobicité devrait être atteint pour optimiser l'adsorption de BTEX. À cet égard, la synthèse par la voie du fluorure de la zéolite ZSM-5 utilisée semble être une stratégie avantageuse par rapport à la voie alcaline traditionnelle car elle a permis d'obtenir des matériaux hautement hydrophobes même avec un SAR faible.

La dernière étude est dédiée à l'adsorption du formaldéhyde à des concentrations très faibles (164 ppb) sur les matériaux susmentionnés (adsorbants commerciaux et zéolithes). Ce type d'études est nécessaire pour évaluer correctement les performances des adsorbants, car il a été démontré que la capacité d'adsorption à des concentrations élevées n'est pas toujours corrélée linéairement à la capacité d'adsorption à de faibles concentrations. À notre connaissance, il s'agit de la seule étude réalisée à des concentrations aussi faibles. Nos résultats et leur comparaison avec les données expérimentales de la littérature ont mis en évidence que la chimie de surface est un facteur déterminant de l'adsorption des aldéhydes. Parmi les adsorbants étudiés, HKUST-1 présentait la capacité d'adsorption la plus élevée vers le formaldéhyde probablement en raison de la forte interaction des fonctions carbonyle avec les ions cuivre de sa structure.

Les résultats obtenus dans le cadre de cette thèse ouvrent de nouvelles perspectives concernant le développement d'instruments d'analyse portables. Notre analyseur compact de BTEX a montré des

performances satisfaisantes dans des conditions de laboratoire, cependant, il doit être testé dans des environnements réels, par exemple, en menant une campagne sur le terrain similaire à celle réalisée au début de cette thèse.

Sans aucun doute, l'un des principaux avantages du préconcentrateur développé dans ce travail est son coût de fabrication extrêmement faible (~ quelques dizaines d'euros) ce qui signifie que le prix ne constituera pas un frein à sa mise sur le marché. En outre, ce dispositif peut être rempli avec d'autres adsorbants pour piéger différentes molécules ciblées. À cet égard, il est possible de penser que le préconcentrateur développé dans ce travail peut être rapidement adapté et utilisé dans de nombreuses applications nécessitant une sensibilité très élevée telles que la détection d'agents explosifs et de guerre, l'industrie alimentaire ou l'analyse de l'air exhalé pour le diagnostic précoce de maladies comme les cancers.

6. References

- [1] K. R. Smith, N. Bruce, K. Balakrishnan, H. Adair-Rohani, J. Balmes, Z. Chafe, M. Dherani, H.D. Hosgood, S. Mehta, D. Pope, E. Rehfuss, "Millions Dead: How Do We Know and What Does It Mean? Methods Used in the Comparative Risk Assessment of Household Air Pollution," *Annual Review of Public Health*, vol. 35, no. 1, pp. 185–206, Mar. 2014, doi: 10.1146/annurev-publhealth-032013-182356.
- [2] G. D'Amato, G. Liccardi, M. D'Amato, and M. Cazzola, "Outdoor air pollution, climatic changes and allergic bronchial asthma," *European Respiratory Journal*, vol. 20, no. 3, pp. 763–776, Sep. 2002, doi: 10.1183/09031936.02.00401402.
- [3] M. P. Tsakas, A. P. Siskos, and P. Siskos, "Indoor Air Pollutants and the Impact on Human Health," *Chemistry, Emission Control, Radioactive Pollution and Indoor Air Quality*, Jul. 2011, doi: 10.5772/18806.
- [4] R. A. Rinsky, B. Smith, R. Hornung, T.G. Filloon, R.J. Young, A.H. Okun, P.J. Landrigan, "Benzene and Leukemia," *New England Journal of Medicine*, vol. 316, no. 17, pp. 1044–1050, Apr. 1987, doi: 10.1056/NEJM198704233161702.
- [5] M. C. McCormack, P.N. Breyse, N.N. Hansel, E.C. Matsui, E.S. Tonorezos, J. Curtin-Brosnan, D.L. Williams, T.J. Buckley, P.A. Eggleston, G.B. Diette, "Common household activities are associated with elevated particulate matter concentrations in bedrooms of inner-city Baltimore

-
- pre-school children,” *Environmental Research*, vol. 106, no. 2, pp. 148–155, Feb. 2008, doi: 10.1016/j.envres.2007.08.012.
- [6] World Health Organization, *World health statistics 2017: monitoring health for the SDGs, sustainable development goals*. Geneva: World Health Organization, 2017.
- [7] S. Rovelli, A. Cattaneo, A. Fazio, A. Spinazzè, F. Borghi, D. Campagnolo, C. Dossi, D. Cavallo, “VOCs Measurements in Residential Buildings: Quantification via Thermal Desorption and Assessment of Indoor Concentrations in a Case-Study,” *Atmosphere*, vol. 10, no. 2, p. 57, Feb. 2019, doi: 10.3390/atmos10020057.
- [8] C. Mandin et al., “Assessment of indoor air quality in office buildings across Europe – The OFFICAIR study,” *Science of The Total Environment*, vol. 579, pp. 169–178, Feb. 2017, doi: 10.1016/j.scitotenv.2016.10.238.
- [9] Md. A. Bari, W. B. Kindzierski, A. J. Wheeler, M.-È. Héroux, and L. A. Wallace, “Source apportionment of indoor and outdoor volatile organic compounds at homes in Edmonton, Canada,” *Building and Environment*, vol. 90, pp. 114–124, Aug. 2015, doi: 10.1016/j.buildenv.2015.03.023.
- [10] P. Romagnoli, C. Balducci, M. Perilli, F. Vichi, A. Imperiali, and A. Cecinato, “Indoor air quality at life and work environments in Rome, Italy,” *Environ Sci Pollut Res Int*, vol. 23, no. 4, pp. 3503–3516, Feb. 2016, doi: 10.1007/s11356-015-5558-4.
- [11] D. Campagnolo, D.E. Saraga, A. Cattaneo, A. Spinazzè, C. Mandin, R. Mabilia, E. Perreca, I. Sakellaris, N. Canha, V.G. Mihucz, T. Szigeti, G. Ventura, J. Madureira, E. de Oliveira Fernandes, Y. de Kluizenaar, E. Cornelissen, O. Hänninen, P. Carrer, P. Wolkoff, D.M. Cavallo, J.G. Bartzis, “VOCs and aldehydes source identification in European office buildings - The OFFICAIR study,” *Building and Environment*, vol. 115, pp. 18–24, Apr. 2017, doi: 10.1016/j.buildenv.2017.01.009.
- [12] Y.-H. Cheng, C.-C. Lin, and S.-C. Hsu, “Comparison of conventional and green building materials in respect of VOC emissions and ozone impact on secondary carbonyl emissions,” *Building and Environment*, vol. 87, pp. 274–282, May 2015, doi: 10.1016/j.buildenv.2014.12.025.

-
- [13] E. M. Martins, P. F. de S. Borba, N. E. dos Santos, P. T. B. dos Reis, R. S. Silveira, and S. M. Corrêa, "The relationship between solvent use and BTEX concentrations in occupational environments," *Environ Monit Assess*, vol. 188, no. 11, p. 608, Oct. 2016, doi: 10.1007/s10661-016-5621-8.
- [14] R. Nasreddine, V. Person, C. A. Serra, C. Schoemaeker, and S. Le Calvé, "Portable novel micro-device for BTEX real-time monitoring: assessment during a field campaign in a low consumption energy junior high school classroom," *Atmospheric Environment*, doi: 10.1016/j.atmosenv.2015.11.005.
- [15] H. Willem, "Ventilation Control of Volatile Organic Compounds in New U.S. Homes: Results of a Controlled Field Study in Nine Residential Units," eScholarship, Apr. 2014.
- [16] C. Walgraeve, K. Demeestere, J. Dewulf, K. Van Huffel, and H. Van Langenhove, "Diffusive sampling of 25 volatile organic compounds in indoor air: Uptake rate determination and application in Flemish homes for the elderly," *Atmospheric environment*, vol. 45, no. 32, pp. 5828–5836, 2011.
- [17] L. Zhong, F.-C. Su, and S. Batterman, "Volatile Organic Compounds (VOCs) in Conventional and High Performance School Buildings in the U.S.," *International Journal of Environmental Research and Public Health*, vol. 14, no. 1, p. 100, Jan. 2017, doi: 10.3390/ijerph14010100.
- [18] J. Madureira, I. Paciência, J. Rufo, M. Severo, E. Ramos, H. Barros, E. de Oliveira Fernandes, "Source apportionment of CO₂, PM₁₀ and VOCs levels and health risk assessment in naturally ventilated primary schools in Porto, Portugal," *Building and Environment*, vol. 96, pp. 198–205, Feb. 2016, doi: 10.1016/j.buildenv.2015.11.031.
- [19] D. Norbäck, J. H. Hashim, Z. Hashim, and F. Ali, "Volatile organic compounds (VOC), formaldehyde and nitrogen dioxide (NO₂) in schools in Johor Bahru, Malaysia: Associations with rhinitis, ocular, throat and dermal symptoms, headache and fatigue," *Science of The Total Environment*, vol. 592, pp. 153–160, Aug. 2017, doi: 10.1016/j.scitotenv.2017.02.215.
- [20] E. Can, Ö. Özden Üzmez, T. Döğeroğlu, and E. O. Gaga, "Indoor air quality assessment in painting and printmaking department of a fine arts faculty building," *Atmospheric Pollution Research*, vol. 6, no. 6, pp. 1035–1045, Nov. 2015, doi: 10.1016/j.apr.2015.05.008.

-
- [21] S. Yurdakul, M. Civan, Ö. Özden, E. Gaga, T. Döğeroğlu, and G. Tuncel, "Spatial variation of VOCs and inorganic pollutants in a university building," *Atmospheric Pollution Research*, vol. 8, no. 1, pp. 1–12, Jan. 2017, doi: 10.1016/j.apr.2016.07.001.
- [22] K. Liu, C. Zhang, Y. Cheng, C. Liu, H. Zhang, G. Zhang, X. Sun, Y. Mu, "Serious BTEX pollution in rural area of the North China Plain during winter season," *Journal of Environmental Sciences*, vol. 30, pp. 186–190, Apr. 2015, doi: 10.1016/j.jes.2014.05.056.
- [23] "Toluène (FT 74). Généralités - Fiche toxicologique - INRS." [Online]. Available: http://www.inrs.fr/publications/bdd/fichetox/fiche.html?refINRS=FICHETOX_74. [Accessed: 10-May-2019].
- [24] "ATSDR - Public Health Statement: Ethylbenzene." [Online]. Available: <https://www.atsdr.cdc.gov/phs/phs.asp?id=381&tid=66>. [Accessed: 10-May-2019].
- [25] R. Kandyala, S. P. C. Raghavendra, and S. T. Rajasekharan, "Xylene: An overview of its health hazards and preventive measures," *J Oral Maxillofac Pathol*, vol. 14, no. 1, pp. 1–5, Jan. 2010, doi: 10.4103/0973-029X.64299.
- [26] M. Hauptmann, J. H. Lubin, P. A. Stewart, R. B. Hayes, and A. Blair, "Mortality from Solid Cancers among Workers in Formaldehyde Industries," *Am J Epidemiol*, vol. 159, no. 12, pp. 1117–1130, Jun. 2004, doi: 10.1093/aje/kwh174.
- [27] G. M. Marsh, A. O. Youk, J. M. Buchanich, S. Erdal, and N. A. Esmen, "Work in the metal industry and nasopharyngeal cancer mortality among formaldehyde-exposed workers," *Regulatory Toxicology and Pharmacology*, vol. 48, no. 3, pp. 308–319, Aug. 2007, doi: 10.1016/j.yrtph.2007.04.006.
- [28] S. Suresh and T. J. Bandosz, "Removal of formaldehyde on carbon -based materials: A review of the recent approaches and findings," *Carbon*, vol. 137, pp. 207–221, Oct. 2018, doi: 10.1016/j.carbon.2018.05.023.
- [29] World Health Organization, Ed., *Air quality guidelines for Europe*, 2nd ed. Copenhagen: World Health Organization, Regional Office for Europe, 2000.
- [30] Directive 2008/50/EC of the European Parliament and of the Council of 21 May 2008 on ambient air quality and cleaner air for Europe, vol. OJ L. 2008.

-
- [31] Décret n° 2011-1727 du 2 décembre 2011 relatif aux valeurs-guides pour l'air intérieur pour le formaldéhyde et le benzène. 2011.
- [32] R. Nasreddine, "Développement d'une méthode analytique et d'un microanalyseur miniaturisé pour la détection des BTEX dans l'air," thesis, Strasbourg, 2016.
- [33] R. Nasreddine, V. Person, C. A. Serra, and S. Le Calvé, "Development of a novel portable miniaturized GC for near real-time low level detection of BTEX," *Sensors and Actuators B: Chemical*, vol. 224, pp. 159–169, 2016, doi: 10.1016/j.snb.2015.09.077.
- [34] R. Nasreddine, V. Person, C. A. Serra, C. Schoemaeker, and S. Le Calvé, "Portable novel micro-device for BTEX real-time monitoring: Assessment during a field campaign in a low consumption energy junior high school classroom," *Atmospheric Environment*, vol. 126, pp. 211–217, Feb. 2016, doi: 10.1016/j.atmosenv.2015.11.005.
- [35] M. J. Mendell and G. A. Heath, "Do indoor pollutants and thermal conditions in schools influence student performance? A critical review of the literature," *Indoor Air*, vol. 15, no. 1, pp. 27–52, Jan. 2005, doi: 10.1111/j.1600-0668.2004.00320.x.
- [36] J. M. Daisey, W. J. Angell, and M. G. Apte, "Indoor air quality, ventilation and health symptoms in schools: an analysis of existing information," *Indoor Air*, vol. 13, no. 1, pp. 53–64, Mar. 2003, doi: 10.1034/j.1600-0668.2003.00153.x.
- [37] I. Lara-Ibeas, C. Trocquet, R. Nasreddine, C. Andrikopoulou, V. Person, B. Cormerais, S. Englaro, S. Le Calvé, "BTEX near real-time monitoring in two primary schools in La Rochelle, France," *Air Qual Atmos Health*, vol. 11, no. 9, pp. 1091–1107, Nov. 2018, doi: 10.1007/s11869-018-0611-3.
- [38] W. A. A. Madhoun, N. A. Ramli, A. S. Yahaya, N. F. F. M. Yusuf, N. A. Ghazali, and N. Sansuddin, "Levels of benzene concentrations emitted from motor vehicles in various sites in Nibong Tebal, Malaysia," *Air Qual Atmos Health*, vol. 4, no. 2, pp. 103–109, Jun. 2011, doi: 10.1007/s11869-010-0083-6.
- [39] H. D. Rad, A. A. Babaei, G. Goudarzi, K. A. Angali, Z. Ramezani, and M. M. Mohammadi, "Levels and sources of BTEX in ambient air of Ahvaz metropolitan city," *Air Qual Atmos Health*, vol. 7, no. 4, pp. 515–524, Dec. 2014, doi: 10.1007/s11869-014-0254-y.

-
- [40] Z. Liu, N. Li, and N. Wang, "Characterization and source identification of ambient VOCs in Jinan, China," *Air Qual Atmos Health*, vol. 9, no. 3, pp. 285–291, Apr. 2016, doi: 10.1007/s11869-015-0339-2.
- [41] P. N. Pegas, M.G. Evtyugina, C.A. Alves, T. Nunes, M. Cerqueira, M. Franchi, C. Pio, S.M. Almeida, M. do C. Freitas, "Outdoor/indoor air quality in primary schools in Lisbon: a preliminary study," *Química Nova*, vol. 33, no. 5, pp. 1145–1149, 2010, doi: 10.1590/S0100-40422010000500027.
- [42] J. Madureira, I. Paciência, J. Rufo, E. Ramos, H. Barros, J.P. Teixeira, E. de Oliveira Fernandes, "Indoor air quality in schools and its relationship with children's respiratory symptoms," *Atmospheric Environment*, vol. 118, pp. 145–156, Oct. 2015, doi: 10.1016/j.atmosenv.2015.07.028.
- [43] I. Lara-Ibeas, A. Rodríguez-Cuevas, C. Andrikopoulou, V. Person, L. Baldas, S. Colin, S. Le Calvé, "Sub-ppb Level Detection of BTEX Gaseous Mixtures with a Compact Prototype GC Equipped with a Preconcentration Unit," *Micromachines*, vol. 10, no. 3, p. 187, Mar. 2019, doi: 10.3390/mi10030187.
- [44] S. Zampolli, I. Elmi, F. Mancarella, P. Betti, E. Dalcanale, G.C. Cardinali, M. Severi, "Real-time monitoring of sub-ppb concentrations of aromatic volatiles with a MEMS-enabled miniaturized gas-chromatograph," *Sensors and Actuators B: Chemical*, vol. 141, no. 1, pp. 322–328, Aug. 2009, doi: 10.1016/j.snb.2009.06.021.
- [45] K. M. Skog, F. Xiong, H. Kawashima, E. Doyle, R. Soto, and D. R. Gentner, "Compact, Automated, Inexpensive, and Field-Deployable Vacuum-Outlet Gas Chromatograph for Trace-Concentration Gas-Phase Organic Compounds," *Anal. Chem.*, vol. 91, no. 2, pp. 1318–1327, Jan. 2019, doi: 10.1021/acs.analchem.8b03095.
- [46] J. Sun, N. Xue, W. Wang, H. Wang, C. Liu, T. Ma, T. Li, T. Tan, "Compact prototype GC-PID system integrated with micro PC and micro GC column," *Journal of Micromechanics and Microengineering*, vol. 29, no. 3, p. 29, 2018, doi: 10.1088/1361-6439/aaf42c.
- [47] B. Han, H. Wang, H. Huang, T. Liu, G. Wu, and J. Wang, "Micro-fabricated packed metal gas preconcentrator for enhanced monitoring of ultralow concentration of isoprene," *Journal of Chromatography A*, Aug. 2018, doi: 10.1016/j.chroma.2018.08.058.

-
- [48] J. E. Szulejko, K.-H. Kim, and J. Parise, "Seeking the most powerful and practical real-world sorbents for gaseous benzene as a representative volatile organic compound based on performance metrics," *Separation and Purification Technology*, vol. 212, pp. 980–985, Apr. 2019, doi: 10.1016/j.seppur.2018.11.001.
- [49] J.-P. Bellat, I. Bezverkhyy, G. Weber, S. Royer, R. Averlant, J.-M. Giraudon, J.-F. Lamonier, "Capture of formaldehyde by adsorption on nanoporous materials," *Journal of Hazardous Materials*, vol. 300, pp. 711–717, Dec. 2015, doi: 10.1016/j.jhazmat.2015.07.078.
- [50] E. M. Carter, L. E. Katz, G. E. Speitel, and D. Ramirez, "Gas-Phase Formaldehyde Adsorption Isotherm Studies on Activated Carbon: Correlations of Adsorption Capacity to Surface Functional Group Density," *Environ. Sci. Technol.*, vol. 45, no. 15, pp. 6498–6503, Aug. 2011, doi: 10.1021/es104286d.
- [51] A. Nomura and C. W. Jones, "Amine-Functionalized Porous Silicas as Adsorbents for Aldehyde Abatement," *ACS Appl. Mater. Interfaces*, vol. 5, no. 12, pp. 5569–5577, Jun. 2013, doi: 10.1021/am400810s.
- [52] Z. Wang, W. Wang, D. Jiang, L. Zhang, and Y. Zheng, "Diamine-appended metal–organic frameworks: enhanced formaldehyde-vapor adsorption capacity, superior recyclability and water resistibility," *Dalton Trans.*, vol. 45, no. 28, pp. 11306–11311, Jul. 2016, doi: 10.1039/C6DT01696K.
- [53] I. Lara-Ibeas, C. Megías-Sayago, A. Rodríguez-Cuevas, R. Ocampo-Torres, B. Louis, S. Colin, S. Le Calvé, "Adsorbent screening for airborne BTEX analysis and removal," *Journal of Environmental Chemical Engineering*, p. 103563, Nov. 2019, doi: 10.1016/j.jece.2019.103563.
- [54] D. Peralta, G. Chaplais, A. Simon-Masseron, K. Barthelet, C. Chizallet, A.-A. Quoineaud, G.D. Pirngruber, "Comparison of the Behavior of Metal–Organic Frameworks and Zeolites for Hydrocarbon Separations," *J. Am. Chem. Soc.*, vol. 134, no. 19, pp. 8115–8126, May 2012, doi: 10.1021/ja211864w.
- [55] R. Serna-Guerrero and A. Sayari, "Applications of Pore-Expanded Mesoporous Silica. 7. Adsorption of Volatile Organic Compounds," *Environ. Sci. Technol.*, vol. 41, no. 13, pp. 4761–4766, Jul. 2007, doi: 10.1021/es0627996.

- [56] X. S. Zhao, G. Q. Lu, and X. Hu, "Organophilicity of MCM-41 adsorbents studied by adsorption and temperature-programmed desorption," *Colloids and Surfaces A: Physicochemical and Engineering Aspects*, vol. 179, no. 2–3, pp. 261–269, Jan. 2001, doi: 10.1016/S0927-7757(00)00646-4.
- [57] T. Dutta, K.-H. Kim, R. J. C. Brown, Y.-H. Kim, and D. Boukhvalov, "Metal-organic framework and Tenax-TA as optimal sorbent mixture for concurrent GC-MS analysis of C1 to C5 carbonyl compounds," *Scientific Reports*, vol. 8, no. 1, p. 5033, Mar. 2018, doi: 10.1038/s41598-018-23391-6.
- [58] P. Küsgens, M. Rose, I. Senkovska, H. Fröde, A. Henschel, S. Siegle, S. Kaskel, "Characterization of metal-organic frameworks by water adsorption," *Microporous and Mesoporous Materials*, vol. 120, no. 3, pp. 325–330, Apr. 2009, doi: 10.1016/j.micromeso.2008.11.020.
- [59] L. Deliere, "Adsorption et séparation des gaz rares sur des adsorbants dopés à l'argent," Nov. 2015.
- [60] S. M. Auerbach, K. A. Carrado, and P. K. Dutta, *Handbook of Zeolite Science and Technology*. CRC Press, 2003.
- [61] E. Kukulska-Zajac and J. Datka, "Transformations of Formaldehyde Molecules in Cu-ZSM-5 Zeolites," *J. Phys. Chem. C*, vol. 111, no. 8, pp. 3471–3475, Mar. 2007, doi: 10.1021/jp066732g.

Communications

Peer reviewed publications

1. Lara-Ibeas, I.; Trocquet, C.; Nasreddine, R.; Andrikopoulou, C.; Person, V.; Cormerais, B.; Englaro, S. et Le Calvé, S., *BTEX near real-time monitoring in two primary schools in La Rochelle, France*. *Air Quality Atmosphere & Health* 2018, Volume 11, 1091 – 1107. D.O.I. 10.1007/s11869-018-0611-3
2. Lara-Ibeas, I.; Rodríguez-Cuevas, A.; Andrikopoulou, C.; Person, V.; Baldas, L.; Colin, S.; et Le Calvé, S., *Sub-ppb Level Detection of BTEX Gaseous Mixtures with a Compact Prototype GC Equipped with a Preconcentration Unit*. *Micromachines* **2019**, Volume 10, 187. D.O.I. 10.3390/mi10030187
3. Lara-Ibeas, I., Megías-Sayago, C., Rodríguez-Cuevas, A., Ocampo, R., Louis, B., Colin, S.; et Le Calvé, S., *Adsorbent Screening for Airborne BTEX Analysis and Removal*, *J. Environ. Chem. Engineering*, **2019**. D.O.I. 10.1016/j.jece.2019.103563.
4. Megías-Sayago, C., Lara-Ibeas I., Wang, Q., Le Calvé, S., et Louis, B., *Volatile organic compounds (VOCs) removal capacity of ZSM-5 zeolite adsorbents for near real-time BTEX detection*, *J. Environ. Chem. Engineering*, **2020**, D.O.I. 10.1016/j.jece.2020.103724.
5. Lara-Ibeas, I., Megías-Sayago, C., Louis, B., et Le Calvé, S., *Adsorptive removal of gaseous formaldehyde at realistic concentrations*, *Hazardous Materials*, **2020** (in preparation)
6. Lara-Ibeas, I., Rodríguez-Cuevas A., Le Calvé, S., *Recent developments and trends in miniaturized gas preconcentrators for portable VOC detection*, *Sensors and Actuators B: Chemical*, **2020** (in preparation).
7. Rodríguez-Cuevas A., Lara-Ibeas I., et al., *Low-cost micro-machined preconcentrator for ppt detection of BTEX*, *Sensors and Actuators B: Chemical*, **2020** (in preparation)
8. Trocquet C., Lara-Ibeas, I., et al., *Aldehydes monitoring over 5 weeks in indoor air in two primary schools and one kindergarten over 1 week in La Rochelle, France: part 1-Active sampling on DNPH tubes*, *Sensors and Actuators B: Chemical*, **2020** (in preparation)

9. Trocquet, C.; Lara-Ibeas, I., et al., *Aldehydes monitoring over 5 weeks in indoor air in two primary schools and one kindergarten in La Rochelle, France: part 2-Formaldehyde measurements in real time*, Sensors and Actuators B: Chemical, **2020** (in preparation)
10. Trocquet, C.; Lara-Ibeas, I., et al., *Data on comparison between formaldehyde analyser and reference method based on DNPH derivatization*, Data in Brief, **2020** (in preparation)

Patents

S. Le Calvé, A. Rodriguez, I. Lara-Ibeas, A. Leprince, M. Wolff, Micro-préconcentrateur pour la quantification de polluants gazeux., **déclaration d'invention n° 12395-02 soumise au CNRS.**

Conferences

1. I. Lara-Ibeas, R. Nasreddine, V. Person, S. Le Calvé, *Real-time monitoring of airborne VOCs using microdevices*, 1st Workshop MIGRATE "Research and training network on Miniaturized Gas flow for Applications with enhanced Thermal Effects", Strasbourg (France), **30 June - 1 July 2016**. Oral communication. Peer-reviewed conference proceedings.
2. I. Lara-Ibeas, C. Andrikopoulou, V. Person, A. Sharifi, D. Valougeorgis, S. Le Calvé, *Conception and development of microfabricated elements for microfluidic analytical devices*, 2nd Workshop MIGRATE "Research and training network on Miniaturized Gas flow for Applications with enhanced Thermal Effects", Sofia (Bulgaria), **29-30 June 2017**. Oral communication. Peer-reviewed conference proceedings.
3. I. Lara-Ibeas, C. Andrikopoulou, V. Person, A. Sharifi, D. Valougeorgis, S. Le Calvé, *Conception and development of microfabricated elements for microfluidic analytical devices*, 5th International Symposium on Sensor Science, Barcelona (Spain), **27-29 September 2017**. Oral communication & poster.
4. I. Lara-Ibeas, C. Andrikopoulou, S. Colin, L. Baldas, S. Le Calvé, *Fabrication and Integration of MEMS-based Devices for VOC monitoring*, MicroFluidics and Non-Equilibrium Gas Flows 2018, Strasbourg (France), **28 February - 2 March 2018**. Poster. **Best poster award**. Peer-reviewed conference proceedings.
5. I. Lara-Ibeas, A. Rodríguez-Cuevas, C. Andrikopoulou, A. A. Kassir, R. Kassem, L. Baldas, S. Colin, S. Le Calvé, *A Study of alternative granular adsorbents for benzene and toluene preconcentration*, 3rd Workshop MIGRATE "Research and training network on Miniaturized

- Gas flow for Applications with enhanced Thermal Effects”, Bastia (France), **27-29 June 2018**. Oral communication & poster. Peer-reviewed conference proceedings.
6. A. Rodríguez-Cuevas, I. Lara-Ibeas, C. Andrikopoulou, S. Le Calvé, *Increasing the sensitivity of a BTEX analyzer by integrating a preconcentrator: proof of concept*, 3rd International workshop MIGRATE, Bastia (France), **28-29 June 2018**. Oral communication & poster. Peer-reviewed conference proceedings.
 7. C. Andrikopoulou, S. Le Calvé, C. Sutter, A. Rodriguez-Cuevas, I. Lara-Ibeas, R. Kiefer, M. Verdines, Y. Ettrich, W. Schröder, S. Junk, *Development of an air-quality sensors Monitoring system for integration inside a drone*, 3rd International workshop MIGRATE, Bastia (France), **28-29 June, 2018**. Oral communication & poster. Peer-reviewed conference proceedings.
 8. I. Lara-Ibeas, A. Rodríguez-Cuevas, C. Andrikopoulou, A. A. Kassir, R. Kassem, L. Baldas, S. Colin, S. Le Calvé, *Study of alternative adsorbents for preconcentration of benzene and toluene: improving the sensitivity of a miniaturized GC to ppt levels*, 22nd International Conference on Miniaturized Systems for Chemistry and Life Sciences (MicroTAS), Kaohsiung (Taiwan), **11-14 November, 2018**. Poster.
 9. I. Lara-Ibeas, A. Rodríguez-Cuevas, C. Andrikopoulou, V. Person, L. Baldas, S. Colin, et S. Le Calvé, *Development of a microfluidic preconcentration device for sub-ppb level detection of BTEX*, Low-cost sensors and microsystems for Environment Monitoring, Toulouse (France), **20-21 May 2019**. Poster.
 10. I. Lara-Ibeas, A. Rodríguez-Cuevas, C. Andrikopoulou, P. Meyer, V. Person, C. Trocquet, R. Ocampo-Torres, M. Wolf, L. Baldas, S. Colin, S. Le Calvé, *Dispositifs de préconcentration microfluidiques pour l'analyse de COV par chromatographie en phase gazeuse*, Atmosfair, Lyon (France), **5-6 June 2019**. Oral communication.
 11. S. Le Calvé, C. Trocquet, I. Lara-Ibeas, P. Bernhardt, V. Person, *Analyseurs miniaturisés basés sur des dispositifs microfluidiques dédiés à quantification de la pollution de l'air intérieur*, Colloque interdisciplinaire Environnement(s), **June 2019**, Strasbourg, France. Oral communication.
 12. A. Rodríguez-Cuevas, I. Lara-Ibeas, A. Leprince, M. Wolf, S. Le Calvé, *Low-cost micro-machined preconcentrator for ppt detection of BTEX*, ISTE GIM 2019, Ettlingen, (Germany), **24-25 October 2019**. Oral communication & poster.

Appendix

Calculation of the error associated to generation of different BTEX concentrations using the experimental setup presented in page 177.

- Data of mass flow controllers (MFC) El-Flow that are part of the calibration bench:

Measurement accuracy = 0.5%

Accuracy of full scale = 0.1%

Full scale of BTEX MFC = 100 NmL/min

Full scale of N₂ MFC = 500 NmL/min

- Data of BTEX gas cylinder:

BTEX concentration = 100 ppb

Uncertainty about the concentration of the standard BTEX gas cylinder = 10 %

Uncertainty about the generated concentration ($\frac{\Delta C_{\text{final}}}{C_{\text{final}}}$) is expressed as a function of the flow rates set on the MFC and the uncertainty about the concentration of the BTEX gas cylinder according to the following equation:

$$\frac{\Delta C_{\text{final}}}{C_{\text{final}}} = \frac{\Delta F_{\text{BTEX}}}{F_{\text{BTEX}}} + \frac{\Delta [F_{\text{N}_2} + F_{\text{BTEX}}]}{[F_{\text{N}_2} + F_{\text{BTEX}}]} + \frac{\Delta C_{\text{BTEX}}}{C_{\text{BTEX}}}$$

where:

$\frac{\Delta C_{\text{BTEX}}}{C_{\text{BTEX}}}$ uncertainty about the concentration of the standard BTEX gas cylinder

$\Delta F_{\text{BTEX}} = (\text{measurement accuracy} \times F_{\text{BTEX}}) + (\text{accuracy of full scale} \times \text{full scale of BTEX MFC})$

$\Delta F_{\text{N}_2} = (\text{measurement accuracy} \times F_{\text{N}_2}) + (\text{accuracy of full scale} \times \text{full scale of N}_2 \text{ MFC})$

Where ΔC_{BTEX} is the uncertainty about the concentration of standard BTEX gas cylinder, C_{BTEX} is the concentration of the standard BTEX gas cylinder, F_{BTEX} is the flow rate set in the MFC of BTEX, F_{N_2} is the flow rate set in the MFC of N₂.

Composés Organiques Volatils dans l'air : étude de l'adsorption et la désorption sur différents matériaux, développement d'un préconcentrateur microfluidique et mesures sur le terrain

Résumé

Ce travail de thèse est consacré au développement d'outils plus performants pour la détection de polluants tels que les BTEX et les aldéhydes. Ces dispositifs très sensibles sont des outils de diagnostic en temps quasi-réel qui permettent de mesurer les variations temporelles et spatiales des polluants ciblés et donc faciliter l'identification des sources de ces polluants et ainsi développer des stratégies permettant de réduire leurs quantités ou même de les éliminer. Plus particulièrement, un dispositif portable basé sur la chromatographie gazeuse intégrant une étape de préconcentration a été développé pour atteindre des limites de détection de l'ordre de centaines de ppt, compatibles avec la surveillance de benzène conformément à la nouvelle législation française de la qualité de l'air intérieur. En outre, la sorption des BTEX et aldéhydes a été étudiée sur divers adsorbants pouvant être intégrés soit dans un préconcentrateur soit dans un épurateur dans un but analytique ou de remédiation.

Mots clés : qualité de l'air, Composés Organique Volatils, chromatographie en phase gazeuse, microfluidique, préconcentration, adsorption.

Résumé en anglais

This thesis is devoted to the development of highly efficient devices for the detection of pollutants such as BTEX and aldehydes. These sensitive devices are near real-time diagnostic tools that measure the temporal and spatial variations of the targeted pollutants facilitating the identification of their main emission sources and thus, the development of effective strategies to reduce their quantities or even eliminate them. More precisely, a portable device based on gas chromatography integrating a preconcentration step was developed to reach detection limits of the order of hundreds of ppt, compatible with benzene monitoring according to the new indoor air quality French legislation. In addition, the sorption of BTEX and aldehydes has been studied on various adsorbents for their potential integration either in a preconcentrator or in a purifier for analytical or remediation purposes.

Mots clés : air quality, Volatile Organic Compounds, gas chromatography, microfluidics, preconcentration, adsorption.